The Dissertation Committee for Michael Alan Kordosky
certifies that this is the approved version of the following dissertation:

Hadronic Interactions in the MINOS Detectors

Committee:

_____

Karol Lang, Supervisor

_____

Duane Dicus

_____

Sacha Kopp

_____

Roy Schwitters

_____

Don Winget

Hadronic Interactions in the MINOS Detectors

by

Michael Alan Kordosky, B.A.

Dissertation

Presented to the Faculty of the Graduate School of

The University of Texas at Austin

in Partial Fulfillment

of the Requirements

for the Degree of

Doctor of Philosophy

The University of Texas at Austin

August 2004

Acknowledgments

Particle physics experiments cannot succeed without the determined efforts of a multitude of people. The CalDet, though small, was no different and I would like to thank all those involved in the research and development, construction, operation and analysis. Jenny Thomas oversaw the effort from start to finish, offering me the hospitality of her home and the benefit of her advice. Without her it would have all fallen to pieces. I am especially grateful to Chris Smith, Ryan Nichol and Phil Adamson for their work on the detector calibration, upon which the quality of my results depend strongly, and of course for their football skills. Many people participated in the data collection, but nobody could surpass Gordon Crone's long hours in the counting house, resolute dedication to duty and generally amicable nature. Ruben Saakyan, Steve Boyd and David Petyt unselfishly and voluntarily donated a substantial portion of their time to CalDet, and their steady hands enabled me to focus on the analysis. My best wishes and thanks go to my colleagues Anatael Cabrera, Jeff Hartnell and Leo Jenner for their efforts.

In my time at the University of Texas I've had the opportunity to work with a wonderful group. Marek Proga has a tremendous work ethic and is a fantastic designer of scientific equipment with an unsurpassed attention to

detail and quality. It's impossible to truly understand Marek's value until you have seen him in action. Sacha Kopp accompanied me to my very first collaboration meeting, making me feel at home in a new world, and I've benefited much from his counsel during the years. Jing Liu joined the group in 2000 and immediately took on the lion's share of the M16 quality control analysis. Without Jing, I would not have been able to focus on CalDet.

I challenge anyone to find a better advisor than Karol Lang. Karol taught me an appreciation for the physics, an attention to details, a dedication to my work and every skill that I have as an experimentalist. I've become acquainted with many students over the last six years, both at the University of Texas and elsewhere, and I know of no advisor who is so firmly committed to the development and success of his students. The level of intellectual, moral and financial support that Karol has provided is astounding and I am deeply grateful to him.

I met Patricia Vahle during the initial week of classes in my first semester at the University of Texas and we've been co-conspirators ever since. I'm proud to have worked with her on the CalDet analysis and I'm grateful for her boundless support, good humor and close friendship. We've come a long way together!

<div align="right">

MICHAEL ALAN KORDOSKY

</div>

The University of Texas at Austin

August 2004

Hadronic Interactions in the MINOS Detectors

Michael Alan Kordosky, Ph.D.

The University of Texas at Austin, 2004

Supervisor: Karol Lang

MINOS, the Main Injector Neutrino Oscillation Search, will study neu-
trino flavor transformations using a Near detector at the Fermi National Ac-
celerator Laboratory and a Far detector located in the Soudan Underground
Laboratory in northern Minnesota. The MINOS collaboration also constructed
the CalDet (calibration detector), a smaller version of the Near and Far de-
tectors, to determine the topological and signal response to hadrons, electrons
and muons. The detector was exposed to test-beams in the CERN Proton
Synchrotron East Hall during 2001-2003, where it collected events at mo-
mentum settings between $200\,\mathrm{MeV/c}$ and $10\,\mathrm{GeV/c}$. In this dissertation we
present results of the CalDet experiment, focusing on the topological and sig-
nal response to hadrons. We briefly describe the MINOS experiment and its

iron-scintillator tracking-sampling calorimeters as a motivation for the CalDet experiment. We discuss the operation of the CalDet in the beamlines as well as the trigger and particle identification systems used to isolate the hadron sample. The method used to calibrate the MINOS detectors is described and validated with test-beam data. The test-beams were simulated to model the muon flux, energy loss upstream of the detector and the kaon background. We describe the procedure used to discriminate between pions and muons on the basis of the event topology. The hadron samples were used to benchmark the existing GEANT3 based hadronic shower codes and determine the detector response and resolution for pions and protons. We conclude with comments on the response to single hadrons and to neutrino induced hadronic showers.

Contents

Chapter 1

MINOS Physics Motivation

1.1   Introduction

Neutrinos have a long and interesting history. In 1930, Pauli proposed the neutrino to explain the energy spectrum of β decay but twenty-six years passed before neutrinos were directly observed by Reines and Cowan [1]. We now know that there are three neutrino flavors which couple to the $W^{\pm}$ and Z bosons and correspond to the three charged leptons[2]. It has long been clear that the neutrino is much lighter than any other known particle, aside from the photon. Indeed, experiments in the last half century have set ever lower limits on m_{ν} - now at $m < 3eV$ for $\bar{\nu}_e$[2]. These observations led to the assumption of massless neutrinos in the Standard Model.

During the last 30 years, neutrinos have been fruitfully employed as probes of the nucleon structure and the electroweak interaction. However, in the last decade the neutrino has returned as focal point for fundamental study. There is now compelling evidence that muon neutrinos produced in the

atmosphere change flavors as they propagate through the earth [3]. Thirty years of experiments to measure the solar neutrino flux have been augmented by recent and strong evidence [4] indicating that the deficit of ν_e from the sun [5, 6] is a result of a similar flavor change.

This section will review flavor changing processes in the neutrino sector as a motivation for the Main Injector Neutrino Oscillation (MINOS) experiment. The bulk of evidence supports the hypothesis that *neutrino oscillations* are the dominant flavor changing mechanism. Because of this, we will start with a description of neutrino oscillation theory and then discuss the experimental evidence. Such an approach is convenient because many of the important experimental results are interpreted in the framework of neutrino oscillations. Perhaps it is also worth noting that placing theory before experiment is in line with the historical development of neutrino oscillations. The theory was proposed by Pontecorvo in 1957 [7] with the first experimental hints coming more than a decade later and convicing evidence following more than 30 years after that.

1.2 Basic Oscillation Theory

The neutrino oscillation mechanism provides an elegant and simple explanation for neutrino flavor changing phenomena [2, 8, 9]. Neutrinos are most often referred to in terms of their weak (also called flavor) eigenstates Ψ_α. These are the states produced in association with the charged leptons e, μ, τ in the decay of the W boson. Experiments can then observe the flavor of an incoming neutrino by identifying the outgoing lepton in a charged current interaction. There also exist a set of states Ψ_i which are the mass eigenstates of the neutrino

system. Neutrino oscillations occur when the flavor eigenstates are mixtures of two or more mass eigenstates:

$$\Psi_\alpha = \sum_i U_{\alpha i}^* \Psi_i \tag{1.1}$$

Generally, Eq.1.1 implies that the number of mass eigenstates and flavor eigenstates is equal.

Neutrinos are produced in weak interactions as pure flavor eigenstates, which are superpositions of the mass eigenstates. Considering the system to be in a vacuum, the states then evolve according to the free particle Hamiltonian. For the mass eigenstate the evolution is simple:

$$
\begin{aligned}
\Psi(t) &= e^{-imt}\Psi \quad \text{(in the } \nu \text{ rest frame)} \\
&= e^{-i(Et-pL)}\Psi \quad \text{(in the lab frame)} \\
&\approx e^{-i(E-p)L}\Psi \quad \text{(as } \beta \to 1) \\
&\approx e^{-i\frac{m^2}{2p}L}\Psi \quad \text{(for } m_i/p \ll 1)
\end{aligned}
\tag{1.2}
$$

Here, and in the formulae that follow, the physical constants $\hbar$ and c are set to unity. The flavor eigenstates evolve as:

$$\Psi_\alpha(L) = \sum_i U_{\alpha i}^* \Psi_i e^{-iLm_i^2/2p} \tag{1.3}$$

Here, $\Psi_\alpha(L)$ is the wave function of a neutrino originally produced with flavor α having travelled some distance L away from the source. The Ψ_i denote the eigenstates of the free neutrino Hamiltonian. Equation 1.3 demonstrates the dynamic effect of mixing. As the system evolves the relative weight given to each Ψ_i component changes and the system is no longer in a pure flavor

3

eigenstate. Experiments directly measure the flavor composition of Ψ so it is more useful to express the right hand side of Eq. 1.3 in terms of the flavor eigenstates:

$$\Psi_\alpha(L) = \sum_\beta \sum_i U^*_{\alpha i} e^{-iL m_i^2/2p} U_{\beta i} \Psi_\beta \qquad (1.4)$$

The probability of finding the system, which started with flavor α to have flavor β is just $|\Psi_a(L)\Psi^*_\beta|^2$. Using Eq. 1.4 this probability can be expressed as:

$$
\begin{aligned}
P(\nu_\alpha \to \nu_\beta) &= \delta_{\alpha\beta} - 4 \sum_{i>j} \Re\left[U^*_{\alpha i} U_{\beta i} U^*_{\beta j} U_{\alpha j} \right] \sin^2\left(\Delta m_{ij}^2 L/4E \right) \\
&+ 2 \sum_{i>j} \Im\left[U^*_{\alpha i} U_{\beta i} U^*_{\beta j} U_{\alpha j} \right] \sin\left(\Delta m_{ij}^2 L/2E \right) \qquad (1.5)
\end{aligned}
$$

Here we have defined $\Delta m_{ij}^2 = m_i^2 - m_j^2$ and $\Re(z)$ and $\Im(z)$ indicate the real and imaginary components of the complex number z. The general expression presented above is rather complicated. In practice the transition probability simplifies greatly when specific experimental cases are considered. In the following sections we will attempt to decompose equation 1.5 into the forms typically quoted by experiments.

1.3   CP violation

We will consider CP violation first. The presentation given here is is simply intended to highlight the effect of CP violation as a way of simplifying equation 1.5. Past experiments have tended to assume that CP is convserved in the neutrino sector as the available data is insufficient to deterimine one way or the other. Also, many experiments have no sensitivity to CP violation, even in

principle. For example, as we will show, disappearance searches are inherently insensitive to CP violation.

Consider the effect that a CP transformation has on equation 1.5. The CP transformation is applied as:

$$P(\bar{\nu}_\alpha \to \bar{\nu}_\beta) \leftrightarrow P(\nu_\alpha \to \nu_\beta) \quad \text{when} \quad U_{\gamma k} \leftrightarrow U^*_{\gamma k} \qquad (1.6)$$

Applying 1.6 to 1.5, and using the fact that $\Re(z^*) = \Re(z)$ and $\Im(z^*) = -\Im(z)$, we find that:

$$P(\bar{\nu}_\alpha \to \bar{\nu}_\beta) - P(\nu_\alpha \to \nu_\beta) = 4 \sum_{i>j} \Im \left[U^*_{\alpha i} U_{\beta i} U^*_{\beta j} U_{\alpha j} \right] \sin \left(\Delta m^2_{ij} L/2E \right) \quad (1.7)$$

Therefore, if U is real there is no CP violation in the neutrino sector. Also, CP violation cannot be measured in an experiment which features only disappearance. To see this, consider the case where $\beta = \alpha$:

$$
\begin{aligned}
P(\bar{\nu}_\alpha \to \bar{\nu}_\alpha) - P(\nu_\alpha \to \nu_\alpha) &= 4 \sum_{i>j} \Im \left[U^*_{\alpha i} U_{\alpha i} U^*_{\alpha j} U_{\alpha j} \right] \sin \left(\Delta m^2_{ij} L/2E \right) \\
&= 4 \sum_{i>j} \underbrace{\Im \left[|U_{\alpha i}|^2 |U_{\alpha j}|^2 \right]}_{=0} \sin \left(\Delta m^2_{ij} L/2E \right) \\
&= 0
\end{aligned}
$$

So, CP violation does not modify the probability for a particular flavor to oscillate into *some* other flavor. Instead CP violation changes the probability for that flavor to oscillate into some *specific* flavor.

1.4   Two Neutrino Oscillations

Equation 1.5 simplifies enormously when only two mass eigenstates participate in the oscillations. This can happen when one of the Δm^2 splittings is small

5

compared to $4E/L$. In fact, this seems to be the case for ν_μ produced in the Earth's atmosphere. As an example, take $\alpha, \beta \to \mu$, $\Delta m_{12}^2 \ll 4E/L$ and $\Delta m_{32}^2 \approx \Delta m_{31}^2 \sim L/4E$. Equation 1.5 then simplifies to:

$$
\begin{aligned}
P(\nu_\mu \to \nu_\mu) &= 1 - 4|U_{\mu 3}|^2 \left(|U_{\mu 2}|^2 \sin^2\left(\Delta m_{32}^2 L/4E\right) + |U_{\mu 1}|^2 \sin^2\left(\Delta m_{31}^2 L/4E\right)\right) \\
&\approx 1 - 4|U_{\mu 3}|^2 \left(1 - |U_{\mu 3}|^2\right) \sin^2\left(\Delta m_{32}^2 L/4E\right) \qquad (1.8)
\end{aligned}
$$

Here, the unitarity relation $|U_{\mu 1}|^2 + |U_{\mu 2}|^2 + |U_{\mu 3}|^2 = 1$ has been used. Typically, atmospheric oscillation experiments define:

$$
\sin^2\left(2\theta_{atm}\right) = 4|U_{\mu 3}|^2 \left(1 - |U_{\mu 3}|^2\right)
$$

and then quote results in the $(|\Delta m_{32}^2|, \sin^2(2\theta_{atm}))$ plane. This practice corresponds to using a two component mixing matrix U of the form:

$$
U = \begin{pmatrix} \cos(\theta_{atm}) & \sin(\theta_{atm}) \\ -\sin(\theta_{atm}) & \cos(\theta_{atm}) \end{pmatrix}
$$

where the flavor indices run over the columns and the mass indices run over the rows. It is common to parametrize the 3 component mixing matrix in the form:

$$
U = \begin{pmatrix} c_{12}c_{13} & s_{12}c_{13} & s_{13}e^{-i\delta} \\ -s_{12}c_{23} - c_{12}s_{23}s_{13}e^{i\delta} & c_{12}c_{23} - s_{12}s_{23}s_{13}e^{i\delta} & s_{23}c_{13} \\ s_{12}s_{23} - c_{12}c_{23}s_{13}e^{i\delta} & -c_{12}s_{23} - s_{12}c_{23}s_{13}e^{i\delta} & c_{23}c_{13} \end{pmatrix} \qquad (1.9)
$$

where $c_{ij} = \cos\theta_{ij}$ and $s_{ij} = \sin\theta_{ij}$. The θ_{ij} are three parametric mixing angles and δ is a phase. In the case of a ν_μ disappearence measurement one has:

$$
\begin{aligned}
P(\nu_\mu \to \nu_\mu) &= 1 - 4|U_{\mu 3}|^2 \left(1 - |U_{\mu 3}|^2\right) \sin^2\left(\Delta m_{32}^2 L/4E\right) \\
&= 1 - 4s_{23}^2 c_{13}^2 \left(1 - s_{23}^2 c_{13}^2\right) \sin^2\left(\Delta m_{32}^2 L/4E\right) \\
&\approx 1 - \sin\left(2\theta_{23}\right) \sin^2\left(\Delta m_{32}^2 L/4E\right) \quad (\text{for } \theta_{13} \approx 0)
\end{aligned}
$$

So, in the limit of small θ_{13}, a ν_μ disappearance experiment directly measures $\sin^2 \theta_{23}$.

1.5   Evidence for ν_μ Disappearance
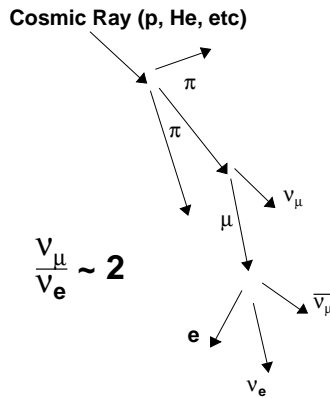
Figure 1.1: The production chain for atmospheric neutrinos. The ratio $\nu_\mu/\nu_e \sim$ 2 is expected without neutrino oscillations.

There is now a significant body of evidence supporting the hypothesis that atmospheric ν_μ undergo neutrino oscillations [3, 10, 11]. Atmospheric neutrinos are produced when cosmic rays interact in the upper atmosphere to produce π and K mesons. These mesons then decay in flight to produce ν_μ and ν_e in the approximate ratio of 2:1. Above energies of a few GeV the flux of the ν is spherically symmetric. In any period of time, the number of neutrinos entering the earth's surface is expected to be equal to the number leaving the earth's surface. Since the flux is spherically symmetric, each location on the

7

earth is equivalent. This means that at every point on the earth's surface, the flux of neutrinos within some slice of zenith angle $\theta + \Delta\theta$ is expected to be equal to the flux from the opposing angle $\pi - (\theta + \Delta\theta)$. So, the flux of upward going neutrinos must be equal to the flux of downward going neutrinos.

The best data come from the Super-Kamiokande experiment, which measured the flux of ν_μ, ν_e as a function of zenith angle and E_ν. The results of the measurement are shown in Fig. 1.2. For ν_e the flux is symmetric around
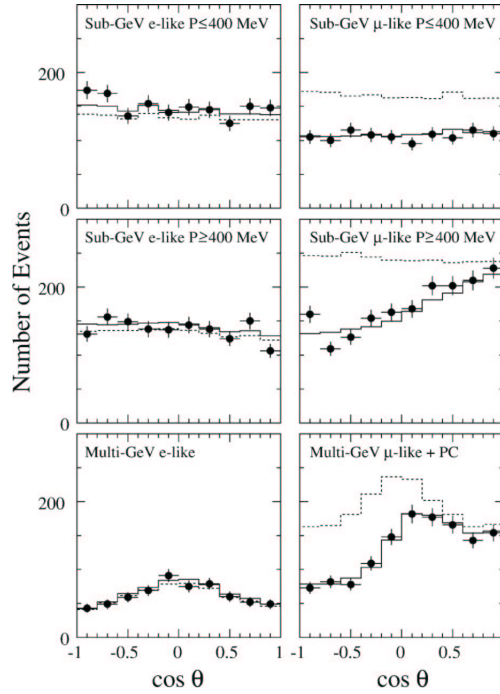
Figure 1.2: Zenith angle distributions for various event samples from the Super-Kamiokande atmospheric data set. The dashed histograms show the expected distributions without oscillations. The solid histograms show the best fit for $\nu_\mu \leftrightarrow \nu_\tau$ oscillations [12].

0. That is, the flux in opposing slices of zenith angle is equal. This is the

expectation in the case of no oscillations. On the other hand, the ν_μ flux is not symmetric for $E_\nu > 400MeV$. Figure 1.2 shows that the number of upward ($\cos\theta < 0$) going neutrinos is much less than the number of downward ($\cos\theta > 0$) going neutrinos. Additionally, the ratio ν_μ/ν_e was measured to be about 34% less than the expected value. The interpretation of these data is that the ν_μ are undergoing oscillations on their way through the earth, while the ν_e propagate largely unaffected.

Clearly, the majority of muon neutrinos cannot be oscillating into electron neutrinos. If that were the case, then the one would expect to see an increase in the number of upward going ν_e, corresponding to the decrease in the ν_μ. Therefore, if the oscillation hypothesis is correct, either $\nu_\mu \to \nu_\tau$ or $\nu_\mu \to \nu_s$, or some combination of the two, must form the dominant oscillation mode. Here, ν_s refers to a hypothetical *sterile* neutrino. Sterile neutrinos mix with the ν_e, ν_μ, ν_τ but do not participate in weak interactions.

The Super-Kamiokande data were found to favor $\nu_\mu \leftrightarrow \nu_\tau$ oscillations over $\nu_\mu \leftrightarrow \nu_s$ [13]. The experiment finds:

$$\sin^2 2\theta > 0.92 \quad \text{and} \quad 1.6 < \Delta m^2 < 3.9 \quad 10^{-3}eV^2$$

for the pure $\nu_\mu \leftrightarrow \nu_\tau$ mode [14]. The ν_μ disappearance results from Super-Kamiokande are supported by the measurments of several other experiments. Figure 1.3 compares the allowed regions from MACRO, Kamiokande and Soudan-II with the region from Super-Kamiokande.
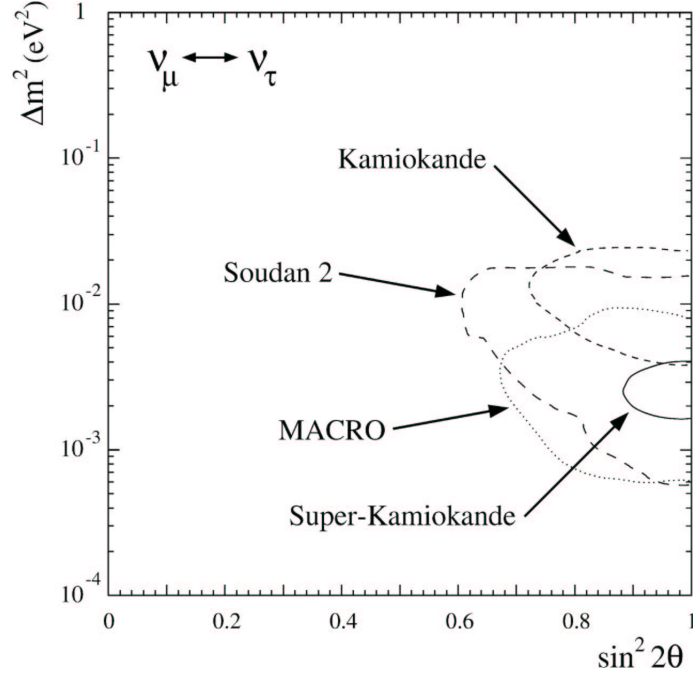
Figure 1.3: Results from several atmospheric neutrino experiments. The curves depict 90% CL allowed regions in a measurement of ν_μ disappearance. The parameters are extracted by assuming $\nu_\mu \to \nu_\tau$ oscillations [12].

1.6 Subdominant Mode: $\nu_\mu \to \nu_e$

The atmospheric neutrino data favor $\nu_\mu \leftrightarrow \nu_\tau$ oscillations as the dominant mode. The data are not sufficient however, to rule out some contribution from $\nu_\mu \to \nu_e$ and $\nu_\mu \to \nu_s$. In the case of $\nu_\mu \to \nu_e$, the oscillation probability from Eq. 1.5 is found to be:

$$
\begin{aligned}
P(\nu_\mu \to \nu_e) &\approx -4U_{\mu3}^* U_{e3} \underbrace{\left[U_{\mu1} U_{e1}^* + U_{\mu2} U_{e2}^* \right]}_{= -U_{\mu3} U_{e3}^*} \sin^2 \left(\Delta m_{32}^2 L/4E \right) \\
&= \sin^2 \left(2\theta_{13} \right) \sin^2 \left(\theta_{23} \right) \sin^2 \left(\Delta m_{32}^2 L/4E \right)
\end{aligned}
\tag{1.10}
$$

where the approximation corresponds to $|\Delta m_{12}^2 L/4E| \ll 1$ and matter effects are neglected. The data from Super-Kamiokande allow for $\sin^2 2\theta_{13} \lesssim 0.15$ at 90% CL when a fit to a $\nu_\mu \to \nu_\tau, \nu_e$ three neutrino oscillation scenario is done. The allowed region is then constrained by results from the $\bar{\nu}_e$ disappearance experiments CHOOZ and Palo Verde. The combined 90% CL contours allow $\sin^2 2\theta_{13} \lesssim 0.08$ [14].

1.7 Subdominant Mode: $\nu_\mu \to \nu_s$

The measured decay width of the Z boson strongly favors only three, light, active neutrinos [2]. The available data, however, do not rule out the existance of a fourth, sterile, neutrino which mixes with the three active neutrinos but does not participate in weak interactions. Oscillations between active and a sterile neutrino components would be observed as a distortion of the neutral current energy spectrum and a decrease in the neutral current event rate. Additionally, the ν_s and ν_τ have different effective potentials as they move through matter, since ν_τ experience neutral current interactions and ν_s do not. For oscillations between ν_μ and ν_τ the transition probability is (from Eq. 1.8):

$$P(\nu_\mu \to \nu_\tau) = sin^2\left(2\theta_{atm}\right)\sin^2\left(\Delta m_{32}^2 L/4E\right) \tag{1.11}$$

For ν_s this probability is modified by substituting,

$$sin^2\left(2\theta_{atm}\right) \quad \to \quad \frac{\sin^2\left(2\theta_{atm}\right)}{\left(\zeta - \cos\left(2\theta_{atm}\right)\right)^2 + \sin^2\left(2\theta_{atm}\right)} \tag{1.12}$$

$$\Delta m_{32}^2 \quad \to \quad \Delta m_{32}^2 \sqrt{\left(\zeta - \cos\left(2\theta_{atm}\right)\right)^2 + \sin^2\left(2\theta_{atm}\right)} \tag{1.13}$$

Where $\zeta = \sqrt{2}E_\nu G_F N_n/\Delta m_{32}^2$ and N_n is the number density of neutrons along the neutrino's trajectory [13, 15]. Therefore, including the matter effect differ-

ence introduces no new parameters. The ν_s and ν_τ components are typically weighted as:

$$\nu_\mu \to \nu_\tau \cos\xi + \nu_s \sin\xi \qquad (1.14)$$

Here ξ is a free parameter which must be extracted from the data (via fitting). When analyzed for ν_s and ν_τ combined oscillations, the Super-Kamiokande data allows for $\sin^2\xi < 0.19$ at 90% CL [14].

1.8 Alternatives to Oscillations

Two neutrino oscillations between ν_μ and ν_τ currently yield the best fit to the ν_μ disappearance data from Super-Kamiokande. However, there are a pair of *exotic* models that are also capable of describing the data [14]. These two models have been given the names *long neutrino decay* [16] and *neutrino decoherence* [17]. Table 1.8 shows the degree in which the exotic theories and standard oscillations are able to fit the data. The exotic models predict

Theory	$\chi^2/ndof$	$P(\chi^2)(\%)$
$\nu_\mu \to \nu_\tau$	173.8/190	79
long decay	194.0/190	41
decoherence	184.3/190	64

Table 1.1: A comparison of $\nu_\mu \to \nu_\tau$ oscillations with the exotic *long decay* and *decohenrence* scenarios. All three theories offer reasonable fits to the Super-Kamiokande data [14].

very diferent functional forms for the (L/E) dependence of the disappearance

probability. Briefly, these are:

$$P(\nu_\mu \to \nu_\mu) = \left(\sin^2(\theta_{atm}) + \cos^2(\theta_{atm}) e^{-\alpha L/2E}\right)^2 \quad \text{(long decay)} \quad (1.15)$$

$$P(\nu_\mu \to \nu_\mu) = \tfrac{1}{2}\sin^2(2\theta_{atm})\left(1 - e^{-\gamma L/E}\right) \quad \text{(decoherence)} \quad (1.16)$$

The MINOS experiment, throught it's superior (L/E) resolution, has the ability to definitively discriminate between standard oscillations and these exotic scenarios.

1.9   Summary

There is now compelling evidence for $\nu_\mu \to \nu_\tau$ flavor transformations in the atmospheric neutrino sector. The data are consistent with simple quasi-two neutrino oscillations as described by Eq. 1.8, but allow subdominant contributions from $\nu_\mu \to \nu_e$ and $\nu_\mu \to \nu_s$ oscillations. Additionally, though it has not been discussed here, there is also evidence that neutrinos produced in the Sun undergo oscillations described by a Δm^2 that is approximately 30 times smaller than Δm_{23}^2[18, 4, 19]. Finally, there is somewhat controversial evidence, from the LSND experiment, that $\nu_\mu \to \nu_e$ and $\bar{\nu}_\mu \to \bar{\nu}_e$ flavor transformations occur [20, 21]. When interpreted as oscillations, the resulting Δm^2 is at least 100 times larger than Δm_{23}^2. The LSND result is puzzling and, at the very least, would require a fourth, sterile neutrino. Clearly, neutrino physics is in a renaissance period, in which much has been learned but outstanding questions remain unanswered. The MINOS experiment will contribute to the field by verifying that $\nu_\mu \to \nu_\tau$ flavor transformations are indeed best explained as oscillations, by making a precision measurement of Δm_{23}^2 and $\sin^2(2\theta_{atm})$, and by conducting searches for the subdominant $\nu_\mu \to \nu_e$ and $\nu_\mu \to \nu_s$ modes.

13

Chapter 2

MINOS Overview

2.1 Introduction

The Main Injector Neutrino Oscillation Search (MINOS) experiment is designed to explore the region in $(\sin^2 2\theta_{atm}, \Delta m^2_{23})$ parameter space favored by Super-Kamiokande with an entirely different experimental technique. MINOS will utilize two detectors to measure the spectral composition of an accelerator produced muon neutrino beam at two locations, one close to the source, the other far away. The neutrino beam will be produced by the Neutrinos at the Main Injector (NuMI) facility at Fermilab. The two MINOS detectors are constructed to respond in the same way. Both detectors are iron-scintillator tracking-sampling calorimeters composed of $1\,\mathrm{cm}$ thick plastic scintillator planes each of which is backed by a $2.54\,\mathrm{cm}$ thick steel absorber plate. The scintillator planes are segmented into strips and read out by optical fibers coupled to multi-anode phototubes. The detectors are magnetized so that the μ charge-sign and momentum may be determined. The $1\,\mathrm{kt}$ Near

Figure 2.1: The geographical layout of the MINOS experiment.

detector is located on the Fermilab site, approximately 1 km from the NuMI target. The 5.4 kt Far detector is located 735 km away in the Soudan Underground Laboratory. Systematic uncertainties will be significantly reduced by comparing the beam composition, event rate and energy spectrum as measured at the two locations. Since neither the Near nor the Far detectors are able to be exposed to a test beam, MINOS constructed a third, calibration detector for that purpose. The calibration detector (CalDet) is a small version of the Near and Far detectors and has been used to measure the response of the MINOS detectors in test beams of known momentum and composition.

The NuMI (*Neutrinos at the Main Injector*) facility at Fermilab will
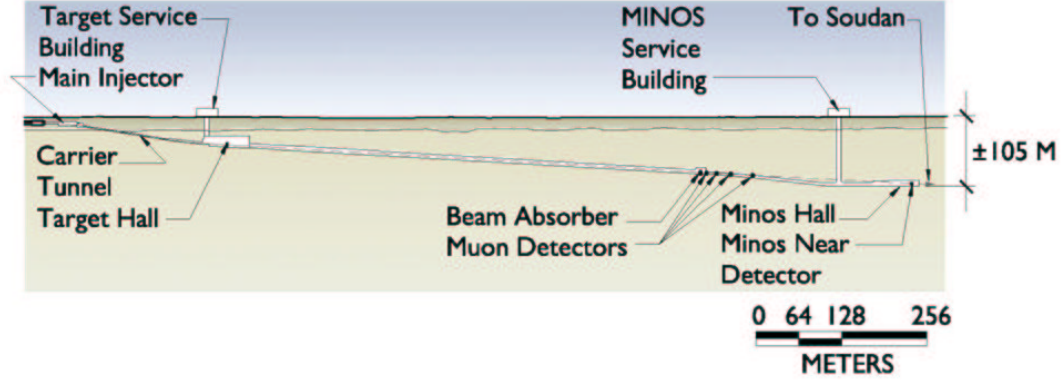
Figure 2.2: The layout of the NuMI facility on the Fermilab site [22].

provide the neutrino beam used by MINOS [22]. The NuMI beamline begins at the *Main Injector*, Fermilab's 120 GeV proton accelerator. Protons circulating in the Main Injector will be directed out of the ring and into the NuMI beamline by single turn extraction. The extraction process will bend the beam 8.9° downward into the initial section of the NuMI beamline, known as the NuMI stub. After traversing the stub, the beam is to be focused along the 131 m long *carrier tunnel* before being bent up by 5.6° and toward the *target hall*. A final 3.3° downward angle is required in order to point the beam at the Far detector. The beam will then undergo final focusing and be directed onto a segmented graphite target. Each beam spill will be approximately 8 μs long and consist of 2.5×10^{13} protons. The time between successive spills will be 1.9 s.

Mesons produced in the target will travel forward along the beamline toward a pair of magnetic focusing horns. The horns are designed such that mesons within a specific momentum range are focused parallel to the beamline.

16
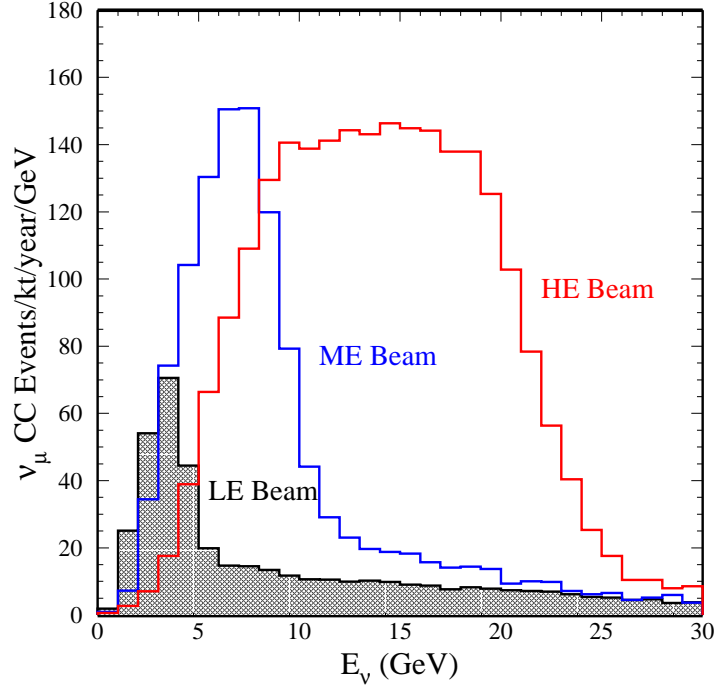
Figure 2.3: The energy spectrum of ν_μ CC events observed per kiloton-year at the Far Detector. Though the NuMI beamline is able to provide a flexible output spectrum, results from Super-Kamiokande suggest that NuMI will operate mostly in the LE configuration [23].

The momentum range to be focused may be altered by shifting the position of the horns, or the position of the target with respect to the horns [24]. The polarity of the horns may also be changed so as to focus mesons of the opposite sign, allowing NuMI to produce beams of both neutrinos and anti-neutrinos.

After being focused in the horns, the meson beam will propagate down a 2 m diameter, 677 m long evacuated pipe. Neutrinos are produced when mesons decay in flight. The kinematics of the decay $\pi \rightarrow \mu + \nu_\mu$ gives the

17

following formulae:

$$E_\nu = \frac{0.427 E_\pi}{1 + \gamma^2 \theta^2} \qquad (2.1)$$

$$Flux \propto \frac{4\gamma^2}{(1 + \gamma^2 \theta^2)} \frac{A}{4\pi r^2} \qquad (2.2)$$

Here γ is the pion boost, θ the angle between the π and ν momentum vectors, r the distance to the detector and A the area of the detector. A common rule of thumb results from Eq. 2.2: neutrinos produced by forward focused pions have an energy $\approx 0.43 E_\pi$. Both formulas assume $\theta << 1$ and are valid for a far away detector.

The muons resulting from the meson decays, undecayed mesons and beam protons will be stopped at the end of the decay tunnel by a section of steel and aluminum absobers followed by $240\,\mathrm{m}$ of rock. The absorber area is to be instrumented with ionization chambers which will measure the muon flux in order to monitor the beam focusing [25]. The neutrino beam will be about $80\,\mathrm{m}$ below the surface after passing through the absorber section and from there will travel on to the Near detector, located $30\,\mathrm{m}$ farther downstream.

Figure 2.3 shows the projected neutrino flux, expressed in terms of the number of ν_μ CC interactions at the Far detector, for three different focusing conditions. NuMI was wise to implement a flexible beam design. Prior to 1998 it was believed that most of the running would be done in the High Energy configuration based on the Kamiokande measurment of $\Delta m^2 \approx 1 \times 10^{-2} eV^2$. After Super-Kamiokande reported their first results ($\Delta m^2 \approx 3.5 \times 10^{-3} eV^2$) it became apparent that the Medium or Low Energy cofigurations would be more appropriate. The most recent results ($\Delta m^2 \approx 2.5 \times 10^{-3} eV^2$) suggest that NuMI will probably spend the majority of time in the Low Energy configuration. The Low Energy flux peaks in the range 1-6 GeV, the exact

range in which CalDet collected data.

2.2 Physics Goals

MINOS has four main physics goals. These are:

- To conclusively demonstrate the mechanism responsible for ν_μ disappearance.

- In the case of oscillations, to make a precision measurement of the oscillation parameters $(\sin^2 2\theta_{atm}, \Delta m^2_{33})$.

- To either observe $\nu_\mu \to \nu_e$ or set limits on $\sin^2 \theta_{13}$.

- To either observe $\nu_\mu \to \nu_s$ or set limits on $\sin^2 \xi$.

In order to meet it's physics goals, MINOS must posses a good understanding of:

The Absolute Energy Scale Signals in the detectors will be measured in units of charge. For physics analyses, MINOS will need a procedure for converting the observed charge into units representing the energy of the particles in the event. This conversion procedure is often known as "setting the energy scale". The conversion of signals to energy depends strongly upon the species of particle that deposited the signals as well as a myriad of details regarding the composition and construction of the detectors. Thus, the energy scale is not generally calculable from first principles and must instead be measured. MINOS's experimental goals require that the energy scale be known with a 5% absolute accuracy.

Event Topology The physics analyses depend on using event topology to classify each event as muon-neutrino charged current (ν_μ-CC), neutral current (NC) or electron-neutrino charged current ν_e-CC. The classification algorithms will be developed and characterized using simulated events in the Near and Far detectors. Correct results are crucially dependent on the accuracy of the simulation. To that end, MINOS requires a set of events, corresponding to particles of known identity and momentum, against which the detector simulation may be evaluated. A sample of hadronic events is particularly important since details of the underlying strong interaction physics are not well understood and therefore poorly modeled in simulations.

Near vs. Far differences The Near and Far detectors will be used to measure the neutrino flux close to and far away from the source. Each physics measurement will rely on using the neutrino flux measured in the Near detector to predict the unoscillated flux in the Far detector. The Near and Far detectors were designed to respond in the same way and to a large extent the composition of the two detectors will be identical. However, the disparity in rates between the two detectors forced MINOS to design separate electronics and readout schemes for the Near and Far detectors. The two readout schemes are expected to ultimately yield the same response. Nevertheless, calorimeters are complicated objects, leaving ample opportunity for subtle effects. Therefore, one would like to collected events, corresponding to particles of known identity and energy, using both the Near and Far detector readout schemes. Ideally, the the Near and Far detector electronics would be used to measure the

same events, removing sources of ambiguity unrelated to the readout.

The energy scale and event topology are usually measured by exposing the detector(s) in question to particle beams of known energy and composition. Direct exposure was not possible for MINOS, due to the locations and sizes of the detectors. The CalDet was constructed in order to remedy this problem. The CalDet's mission was to determine the energy scale, measure the topology of events in MINOS and characterize the response of the Near and Far detector readout schemes.

This remainder of this chapter describes the physics measurements that MINOS will make in greater detail. The intent is to provide concrete motivation for the CalDet program and the work presented in the follow-on chapters.

2.3 ν_μ disappearance

The evidence provided by Super-Kamiokande and other experiments strongly suggests that atmospheric neutrinos change flavor as they propagate. The data is consistent with $\nu_\mu \to \nu_\tau$ oscillations but is insufficient to rule out other, more exotic, models. The MINOS experiment will definitively demonstrate the oscillation mechanism by measuring the difference in the ν_μ energy spectrum between the Near and Far detectors.

The first step in the measurement is the classification of events by neutrino interaction type. Charged current (CC) events initiated by ν_μ are characterized by a track consistent with a muon extending out of the vertex shower region. Neutral current (NC) events are characterized by a single shower region without long tracks. Electron neutrino charge current events also have a single shower region with a somewhat different topology than NC events.

21
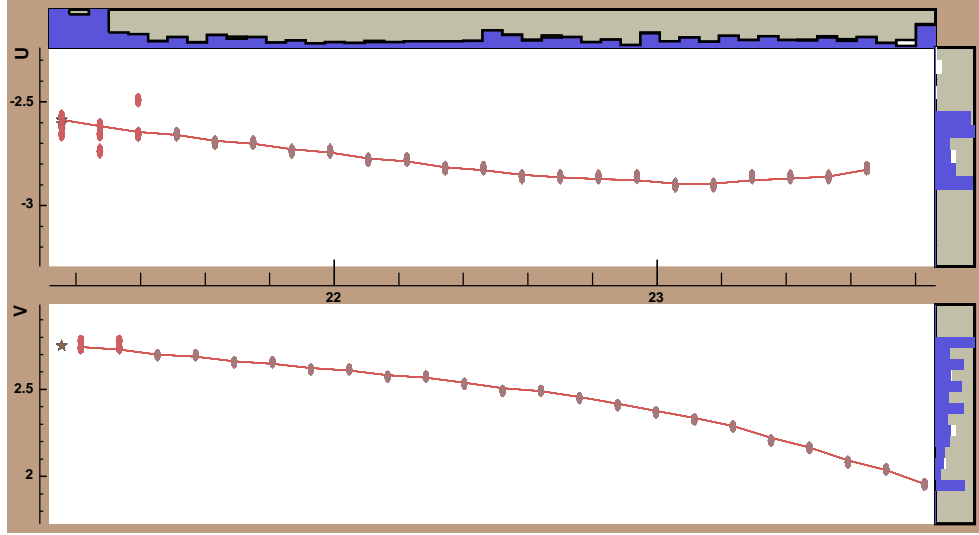
Figure 2.4: An example of a typical ν_μ CC event. The incoming neutrino had an energy of 2.6 GeV. The reconstructed muon track is displayed as a series of purple points connected by a line. The reconstructed vertex shower is shown as a set of red points. The reconstructed muon momentum was 1.8 GeV/c while the reconstructed shower energy was 1.1 GeV. Axis scales are in meters.

Event classification will be done by a pattern recognition procedure utilizing the detailed event shape information provided by the cellular structure of the MINOS detectors. The detector simulation and pattern recognition algorithms will be tuned to test beam data taken with the CalDet.

After identifying the interaction type the energy of the incoming neutrino (E_ν) is reconstructed. For CC events E_ν is computed from the muon momentum and the signals left in the detector by the vertex shower. The momentum of the muon is determined by the range in the detector, the curvature in the magnetic field, or a combination of both. The muon range to momentum conversion will be calibrated using measurements taken by the CalDet. The energy of the recoil system is computed from the vertex signals with a
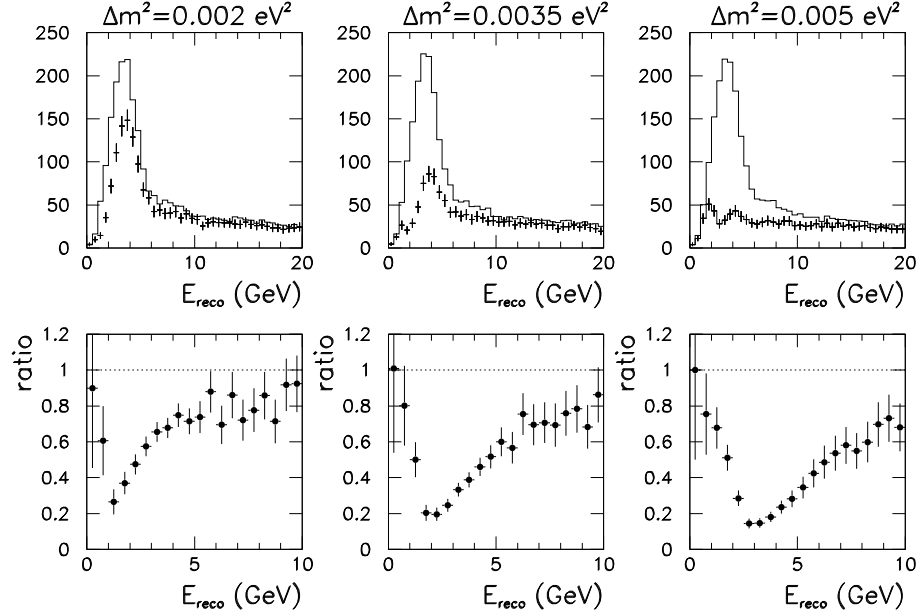
Figure 2.5: Reconstructed CC energy distributions from a Monte Carlo simulation of the MINOS experiment. The top row shows the reconstructed E_ν for three Δm^2 values. The full histogram corresponds to the no oscillation expectation. The crosses correspond to oscillations with $\sin^2 2\theta = 0.9$ and the stated Δm^2 values. The bottom row shows the ratio of the oscillated and unoscillated spectra [26].

calibration constant determined from the CalDet data.

By comparing the shape of the E_ν spectrum in the Far detector with that in the Near, MINOS will be able to measure $P(\nu_\mu \rightarrow \nu_\mu)$ as a function of E_ν, thereby discriminating between neutrino oscillations, decay and decoherence. MINOS will form a ratio between the E_ν spectrum measured at the Far detector and an expected spectrum based on Near detector measurements. In the case of neutrino oscillations in the Super-Kamiokande range, MINOS

expects to see a dip (the "oscillation maximum") in the spectral ratio. The position of the dip is directly related to the value of Δm_{23}^2 while the magnitude of the dip is related to $\sin^2 2\theta_{atm}$. Figure 2.5 shows reconstructed CC energy distributions from Monte Carlo simulations of the MINOS experiment (top row) and ratios of the expected (i.e. unoscillated) and measured (i.e. oscillated) spectra. In reality the no oscillation expectation of Fig. 2.5 will be derived from Near detector measurements. In all three cases MINOS is able to observe the oscillation structure through the shape of the dip and the low energy rise.
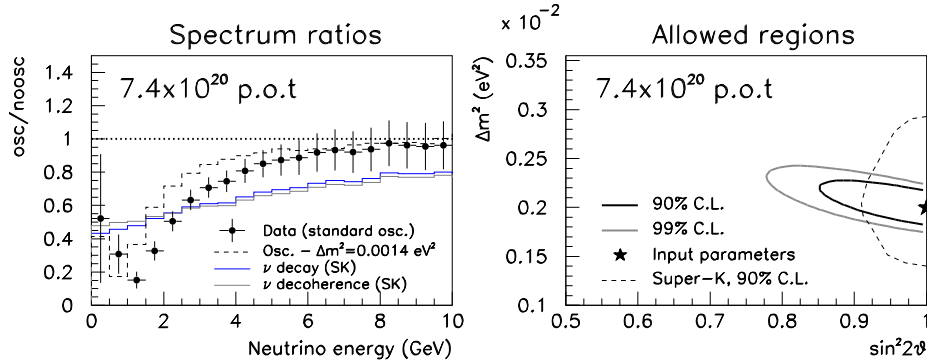
Figure 2.6: An example of oscillation parameter measurements. The figure on the left shows the ratio of the reconstructed oscillated spectrum and the unoscillated spectrum for $\Delta m^2 = 2.5 \times 10^{-3} eV^2$. The additional lines show the spectra for the ν-decay and decoherence scenarios with parameters corresponding to the best fit to Super-Kamiokande data. The figure on the right shows the result of a ML fit for $\Delta m^2, \sin^2 2\theta$ [23].

Figure 2.6 shows the precision with which MINOS can measure the oscillation parameters Δm^2 and $\sin^2 2\theta$ in a nominal three year run. The measurement quality for the Δm^2 parameter is directly affected by the uncertainty

in the overall energy calibration, providing motivation for the CalDet program. Generally a 10% measurement of Δm^2 is possible. The figure also shows that MINOS has an excellent ability to discriminate between standard oscillations and the exotic ν decay and decoherence scenarios.

Figure 2.6 assumes that there is a 20% systematic uncertainty in the determination of the NC background accepted in the CC sample. This uncertainty stems from those low energy NC events which contain a single energetic pion in the final state. Such NC events appear similar to low energy CC events leading to contamination of the CC sample. Though the 20% uncertainty is considered somewhat conservative, the true magnitude of this effect is not clear owing to the imperfect fashion in which hadronic showers are simulated[1]. The data obtained by the CalDet can shed some light on this problem. The CalDet collected relatively pure samples of single π and μ events at momenta in the range 400 MeV to 10 GeV. These data can be used to gauge the accuracy of the hadronic simulations as well as provide a direct measurement for single particle events.

2.4   Search for ν_e appearance

The results of the Super-Kamiokande and CHOOZ experiments permit a small contribution from the $\nu_\mu \leftrightarrow \nu_e$ mode in the dominant $\nu_\mu \leftrightarrow \nu_\tau$ oscillations. MINOS has some sensitivity to ν_e appearance and will be able to either discover oscillations into ν_e [27, 28] or else improve upon the existing limits.

The appearance analysis relies on the selection of a sample of events in which there is a single e-like shower. The main backgrounds in the sample are

---

[1]The GHEISHA code was used in the case at hand.

expected to consist of a small component of beam ν_e and of those NC events in which much of the energy of the final state is carried by a π^0. Previous analyses have found it helpful to place a cut on the visible energy corresponding to the area in which ν_μ disappearance is observed. This cut rejects a large fraction of the ν_e background present in the beam[2] as well as a significant fraction of NC events with $E_\nu > 10$ GeV . The remaining source of background is dominated by NC events. Additional cuts are placed on event shape variables and a neural network output. After all cuts one analysis finds the selection efficiency for ν_e is between 20-40% with a NC background misidentification probability of approximately 2% [27].

Figure 2.7 shows the limit MINOS can place on the sub-dominant mode $\nu_\mu \rightarrow \nu_e$ in the case of the three neutrino oscillation scenario $\nu_\mu \rightarrow \nu_\tau, \nu_e$. The limit is expressed in terms of the mixing angle $\sin^2 2\theta_{13}$ (see Eq. 1.10). In this figure, for each curve, the corresponding experiment can state "At 90% CL $\sin^2 2\theta_{13}$ must lie to the left of the presented contour".

The analysis that produced Fig. 2.7 classified events by using a series of cuts and a neural network output. However, the events used in the analysis did not pass through the full detector simulation and some truth information was used. Consequently, the derived signal and backround efficiencies are somewhat uncertain and perhaps not optimal. Clearly, the event simulation and the analysis procedure can be checked, perhaps improved, by using real e, π events collected by the CalDet.

---

[2]Beam ν_e are produced largely by kaon decays in flight.

90% CL Exclusion
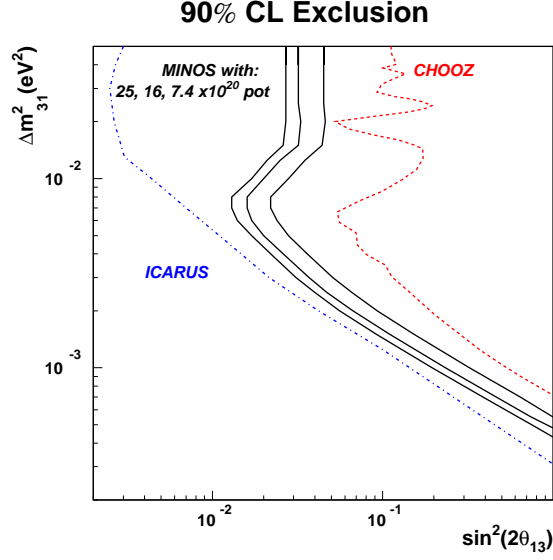
Figure 2.7: The region in parameter space for which MINOS can exclude the sub-dominant mode $\nu_\mu \rightarrow \nu_e$. The current CHOOZ limit, as well as the projected limit from ICARUS are shown for comparison. The three solid lines represent MINOS's capability for three different exposures [23].

2.5   Measurement of the ν_s component

The data from Super-Kamiokande allows $\nu_\mu \rightarrow \nu_\tau, \nu_s$ with the ν_s component accounting for no more than 20% of oscillated events. MINOS will have the ability to discriminate between ν_s and ν_τ oscillations based on the identification and energy reconstruction of neutral current events. The rate of neutral current events observed at the Far detector is expected to decrease if there are $\nu_\mu \rightarrow \nu_s$ oscillations . No decrease is expected for pure $\nu_\mu \rightarrow \nu_\tau$ oscillations. These expectations are often expressed in terms of a test statistic T:

$$T = \frac{1}{1 + (NC/CC)} \tag{2.3}$$

27

T is expected to remain relatively constant for ν_s oscillations and decrease for ν_τ oscillations.

The shape of the NC energy distribution can be utilized for parameter measurements and the setting of limits. For oscillations to ν_τ the ratio of observed to predicted NC events as a function of E_ν is expected to be unity. This assumes that a correction is applied for CC events misidentified as NC. Oscillations to ν_s will show a depletion in the observed/predicted ratio in the energy region that ν_μ disappearance occurs.

Figure 2.8 shows the result of one analysis [29]. In this analysis the ν_μ survival probability was parameterized by Eq. 1.8 and the oscillation to ν_s was parameterized by Eq. 1.14. The analysis began by generating CC, NC and ν_τ events according to the nominal beam flux. Individual events were then accepted or rejected as NC by applying the effect of cross sections, the detector's trigger efficiency and NC selection efficiencies for true NC, CC and ν_τ events. The trigger and selection efficiencies were derived from events simulated with the experiment's GEANT based detector simulation, GMINOS [31]. If an event was accepted as NC, it's energy was first smeared to simulate the detector's response and then used to fill a (unoscillated) E_ν reference spectrum.

Simulated experiments, corresponding to particular choices of Δm^2, ν_s mixing and detector exposure, were constructed by re-weighting and sampling the reference spectrum. A maximum likelihood fit of the simulated experiment was then done by re-weighting the reference spectrum using the transition probabilities corresponding to the fit parameters $(\Delta m^2, \sin^2 \xi)$. This procedure did not make use of the CC event sample, though doing so is expected to improve the measurement by acting as a constraint on Δm^2.

The key sources of uncertainty in the analysis were:
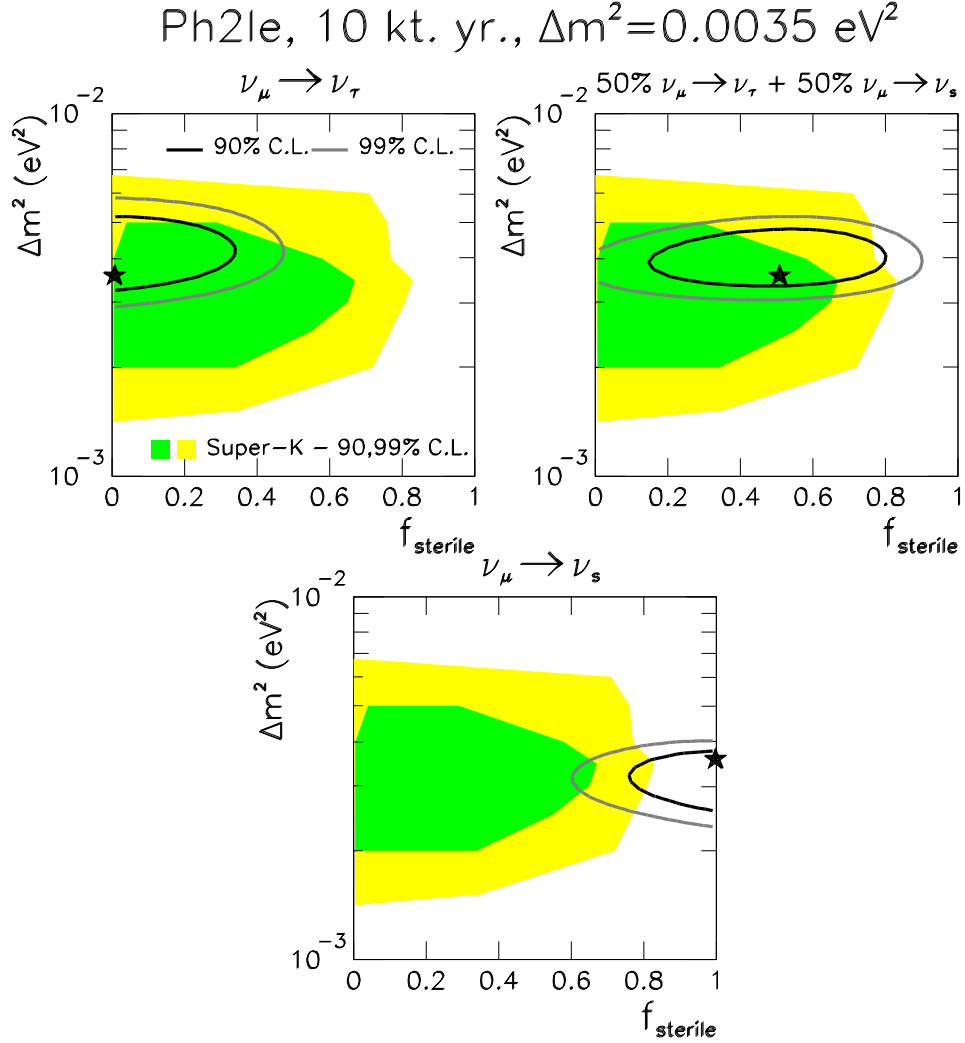
Figure 2.8: MINOS sensitivity to the mode $\nu_\mu \to \nu_s$. The figures were taken from [29] and show the MINOS capability for 3 different sterile mixing fractions. Here, $P(\nu_\mu \to \nu_\tau)$ is parameterized by Eq. 1.8 and the sterile fraction $f_{sterile}$ corresponds to $\sin^2 \xi$ in Eq. 1.14. The green and yellow areas correspond to 90 and 99% confidence limits derived from the Super-Kamiokande data [30]. The $\star$ corresponds to the true Δm^2 and $f_{sterile}$ values assumed in each figure. The black contours show the MINOS 90 and 99% confidence limits.

- The NC trigger efficiency

- The NC/CC selection efficiencies

- The NC cross section

The selection and trigger efficiencies are vulnerable to Monte Carlo inaccuracy. This is particularly true in regard to the simulation of hadronic showers. The hadronic data taken by CalDet will address this deficiency by providing single particle π, p events of known energy against which the simulation may be tuned.

2.6 Summary

MINOS physics analyses require a precise understanding of the detector's response to muons, electrons and hadrons in the energy range 0.5-10 GeV. The detector response includes event shape characteristics in addition to the overall energy scale. Because MINOS employs massive underground detectors direct test beam exposure is not possible. The CalDet program was intended to remedy this problem. The CalDet's mission was to measure the MINOS energy scale, characterize the topology of events in MINOS and search for any discrepancy in response caused by the differences between the Near and Far readout schemes.

Chapter 3

Detector Design

3.1 The MINOS Detectors

MINOS is a three detector experiment [32]. The first two detectors (Near and Far) will observe neutrinos produced by the NuMI facility. The two detector design allows MINOS to measure the unoscillated neutrino spectrum close to the source (the Near detector) and far from the source (the Far detector). The third detector, a scaled down version of the first two known as CalDet, was constructed to measure the response of MINOS to π, μ, e, p in the energy range 0.5-10 GeV. The three detectors are constructed to respond in an identical fashion to the greatest extent possible. The Near/Far/CalDet design coupled with the identical response dramatically decreases the systematic error in MINOS's measurements.

3.2   Calorimeter Composition

The MINOS detectors are tracking-sampling calorimeters with steel plates as the passive absorber and plastic scintillator planes as the active medium. The individual detectors are composed a series of these plates standing upright and front to back, like a sliced loaf of bread. The Near and Far detectors are magnetized so as to measure muon momentum and charge sign via curvature. The typical magnetic field inside the plates is approximately 1.3 T at the Far detector and 1.2 T in the Near detector target region. The CalDet has no magnetic field primarily due to it's smaller size and the need for portability. Light produced in the scintillator is conducted to photomultiplier tubes by wavelength shifting and clear optical fibers.

3.2.1   Steel

Steel, supplied by Olympic Steel Co., makes up approximately 95% of the mass of the MINOS Near and Far detectors. In order to maximize the magnetic permeability, the steel was required to have a relatively small carbon content (0.04-0.06%) and was produced by a hot rolling technique. The radioactivity of the steel was kept low in order to avoid a significant increase in the singles rate. In all three detectors the steel is formed into 2.54 cm[1] thick plates each of which provides the support for a 1 cm thick scintillator module.

The steel plates used in the Near detector are 6.2 m wide by 3.8 m high with a "squashed octagon" shape. The plates were produced as single 2.54 cm thick, 3.4 ton units. Each plane is required not to bow more than 1.5 cm in

---

[1] CalDet plates are slightly different, having been manufactured in Europe with a nominal width of 2.50 cm.
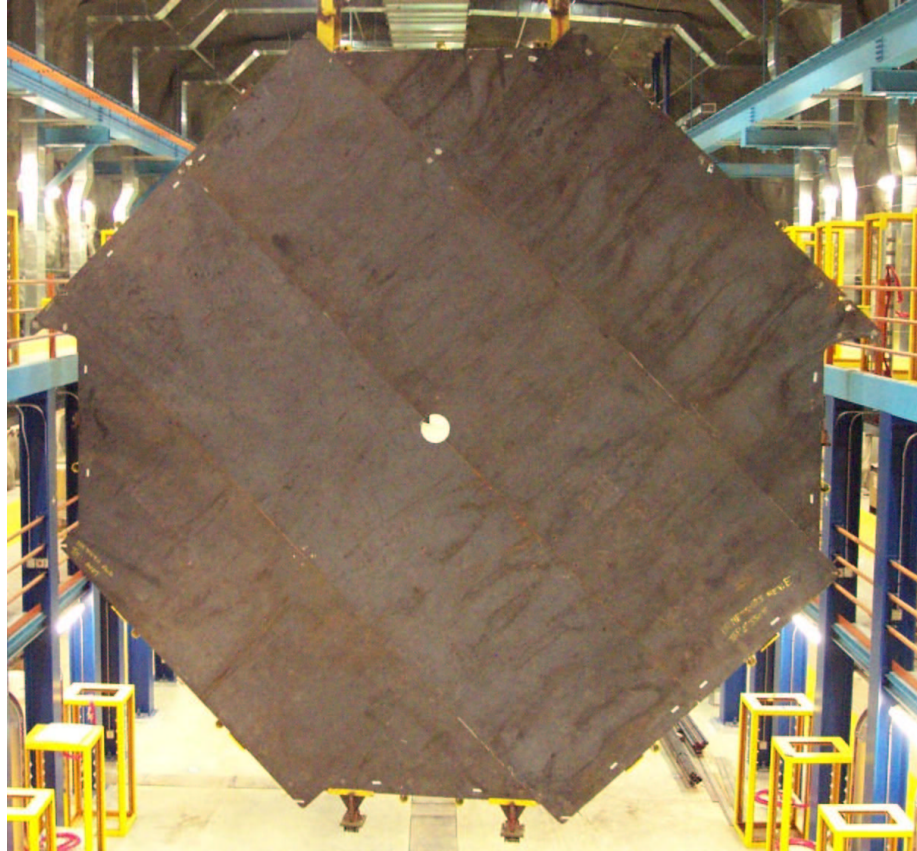
Figure 3.1: A Far detector steel plane being hoisted inside the Far detector cavern. The plane is 8 meters wide.

Figure 3.2: A Near detector steel plane. The plane is 6.2 m wide and 3.8 m across.

Figure 3.3: A CalDet steel plane. The plane is a $1\,\text{m} \times 1\,\text{m}$ square and rests atop a $\sim 80\,\text{cm}$ high base.

a 3.8 m length. Each plate has a 30×30 cm square hole, offset 56 cm from the horizontal center, to accommodate a current carrying coil which provides the magnetic field. The finished near detector will consist of 282 such plates hanging in a vertical array. The weight of each plate is borne by its two protruding ears which rest on the hall's steel support structure. Successive plates will be bolted together along the sides and around the coil hole in order to increase stability and prevent buckling.

The Far detector uses 8 m octagonal steel plates each with a central hole to accommodate the magnetic field coil. These plates were assembled from eight, 2 m wide and 1.27 cm thick, sub-plates welded together in a two-layer cross-lamination. Each 8 m plate weighs approximately 10.6 tons. All assembly was done in the Far detector hall. The 2 m plates are required to bow less than 0.8 cm in an 8 m length. The flatness specification was very important since any gaps, particularly those between layers, will cause local deviations in the magnetic field. During assembly, a 5000 lb compression rig is used to force the sub-plates together in order to minimize gaps and maximize flatness. Each finished plate is held together by a series of plug welds. The Far detector consists of 486 plates hanging in a vertical array and organized into two functionally identical super-modules of 249 (super-module 1) and 237 plates (super-module 2). As in the Near detector, successive plates are bolted together in order to increase stability with the weight of each plane being supported by its ears.

The CalDet consisted of sixty 1 m square, 2.50 cm thick steel plates organized in five modules of twelve vertically hanging planes each. Each module had it's own independent support structure which allowed it to stand alone. The center of each plane was at a height of 125 cm above the floor level. CalDet

CalDet Steel Composition

Plate thickness: 25.0 mm			Density: 7.85 g/cm^3			
Iron Isotopic		^{54}Fe	^{56}Fe	^{57}Fe	^{58}Fe	
Composition		5.85	91.75	2.12	0.28	
Impurities (% by weight)						
C	Si	Mn	P	S	Cr	Mo
0.18	0.29	1.01	0.015	0.008	0.018	0.002
Ni	Al	Cu	N	Sn	Ti	V
0.021	0.003	0.007	0.003	0.002	0.001	0.001

Table 3.1: The composition of the CalDet steel plates. The natural Fe composition is given in % for each isotope. Impurities are listed in % by weight [33].

was not magnetized. During data taking successive modules were bolted together in order to ensure proper alignment. Typically the five modules were arranged front to back and centered along the beamline. The modular design allowed CalDet to be portable and versatile. Modules were able to be easily lifted by the overhead cranes in the CERN East Hall. A module could even be moved on a heavy duty pallet jack if necessary. Less than the full complement of modules could be used and the modules could be arranged in a flexible manner. For example, during one running period, three of the modules were turned at an angle of 30° with respect to the beamline. The modules were also staggered with 36 cm horizontal offset in order to maximize the detector's thickness along the beam axis. The CalDet's flexibility facilitated a series of testbeam measurements with a particularly wide scope.
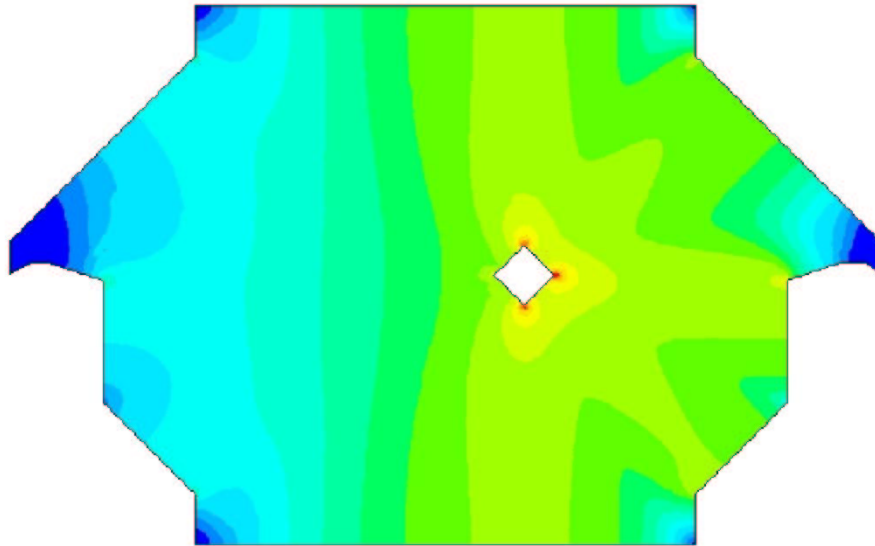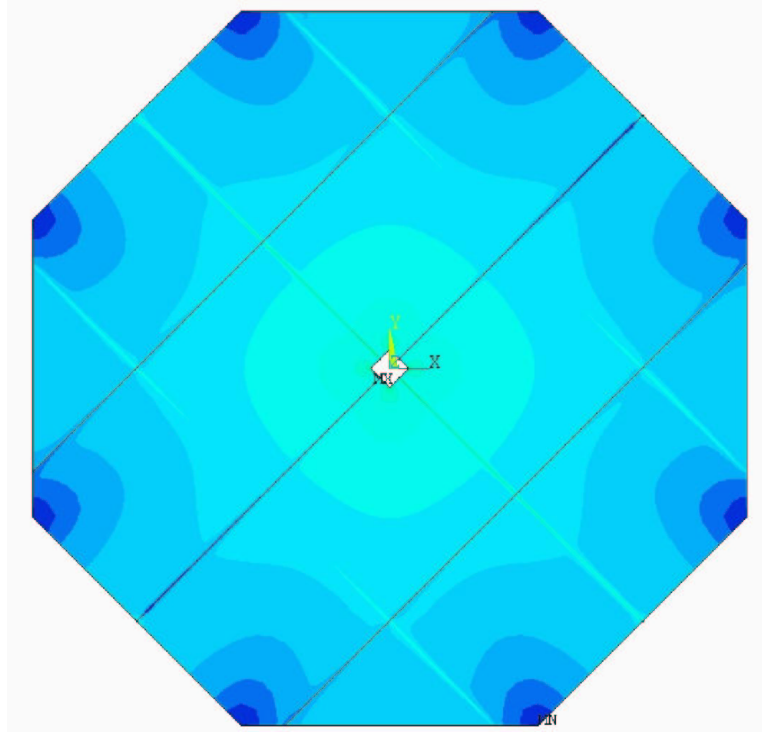
Figure 3.4: Magnetic field maps for Far (top) and Near (bottom) planes.

Near & Far Detector Steel Composition

Plate thickness: 25.4 mm			Density: 7.755 g/cm^3			
Iron Isotopic		^{54}Fe	^{56}Fe	^{57}Fe	^{58}Fe	
Composition		5.85	91.75	2.12	0.28	
Impurities (maximum % by weight)						
C	Si	Mn	P	S	Cr	Mo
0.06	0.40	0.40	0.07	0.01	0.05	0.01
Ni	Al	Cu	N	Sn	Nb	V
0.06	0.05	0.06	0.008	-	0.01	0.01

Table 3.2: The composition of Near and Far detector steel plates. The quoted density is the average from measurements on three heats. The spread in the measurements was 0.6%. The natural Fe composition is given in % for each isotope. The specified maximum amount of each impurity are listed as % by weight. All steel heats were within the specifications [34, 35].

3.2.2 Magnetic Field

The Near and Far detectors are magnetized in order to reconstruct the charge and momentum of muons produced in ν_μ CC interactions. In both detectors the field is created by running a current carrying coil along the detector through a hole in each of the steel planes. Thus, the field within each plane is toroidal. Both coils are water cooled and, for monitoring purposes, each plane has is equipped with a pickup coil wound around the toroid.

The two Far detector super-modules have separate coils and can be independently magnetized. The coils carry a 15 kA-turn current in order to produce a field strength that is approximately 1.3 T at a radius of 2 m from the coil hole. Each coil consists of 163 turns of 1/0 gauge stranded copper wire inside a 25 cm diameter copper jacket. The coils are cooled by water flowing in fifteen copper tubes routed along with the coil wires. Eight of the tubes

are arranged around the inside of each coil jacket with an additional seven tubes arrayed around the coil centers. The coils hang vertically down at the end of each super module with the coil returning inside a trench along the floor directly underneath the detector. The routing of the magnetic coil was designed to minimize the field strength in the areas occupied by the phototubes and electronics. After the coil of the first supermodule was energized the air fields close to the photomultiplier racks were measured to be in the range 3.2-14.1 G [36]. The photomultipliers themselves are encased in metal dark boxes which suppress the field experienced inside.

The Near detector coil must carry a 40 kA-turn current in order to produce a magnetic field of approximately 1.2 T in the region of the neutrino beam. Since the current in the Near detector coil will be much larger than the current in the Far coil, a design with a larger cooling capacity was required. The Near detector coil is made up of forty-eight turns of solid (not stranded) copper conductor arranged in a six by eight pattern. The individual coil turns consist of a copper tube with a 3.8 cm wide by 2.8 cm high rectangular cross section. Cooling is provided by deionized water which runs along a circular 1.65 cm passage inside of each tube. The near detector electronics and phototubes sit along the west side of the detector which allows the coil to return along the east side of the detector.

3.2.3 Scintillator

The active detector is composed of 4.1 cm wide by 1.0 cm thick plastic scintillator strips ranging in length between 1 and 8 m. Each strip is made of Dow STYRON 664 polystyrene doped with the fluors PPO (1% by weight) and

POPOP (0.03% by weight). The strips were produced by Itasca Plastics using an extrusion process developed by MINOS [37]. In that process the fluors are first mixed with dry polystyrene pellets. The mixture is then fed into a machine which melts the mixture, allowing the fluors to diffuse throughout. The same machine then extrudes the mixture through a die in order to produce strips of the desired shape. Mixing, melting and extrusion are all done under a nitrogen purge to remove oxygen. During the extraction process each strip is jacketed with a reflective layer of made of 85% polystyrene and 15% TiO_2 by weight. The strips are cooled by air and water before being cut to lengths of 8.0 and 11.3 m. This all-in-one extrusion process significantly reduced the cost of the scintillator.

Light produced in the scintillation process is collected by 1.2 mm diameter wavelength shifting (WLS) fibers glued inside a 2.0 mm deep groove along each strip. The glue used was Shell Epon 815C with TETA hardener mixed in a 100/13 ratio by weight. After gluing each groove was covered with a strip of aluminized mylar in order to maximize light collection. The WLS fibers have three layers. The innermost layer is made of polystyrene infused with the fluor Y-11. The middle layer is acrylic while the outer layer is a polyfluor. The three layer design maximizes the trapping fraction for green light. The Y-11 fluor in the fiber has an absorption spectrum which peaks around 420 nm and an emission spectrum with a maximum at ~ 520 nm. These two spectra overlap very little making re-absorption a relatively small effect. The attenuation process in the green fibers is well described by a double exponential distribution of the form:

$$f(x) = k \ e^{-x/\lambda_s} + (1 - k) \ e^{-x/\lambda_l} \qquad \text{with} \quad 0 \leq k \leq 1 \qquad (3.1)$$

41

CLEAR GROOVE

MN−3202

TiO₂ CAP

POLYSTYRENE
SCINTILLATOR

.020±.010
(0.5±0.25)
TYP.

FULL R.

.055±.006
(1.4±0.15)

R.020
(R0.5)
TYP.

.059±.010
(1.5±0.25)

.394±.020
(10.0±0.5)

MATERIAL:
POLYSTYRENE WITH
WHITE PIGMENTATION

.807±.010
(20.5±0.25)

.010
(0.25)
TYP.

1.614±.030
(41.0±0.8)

SCINTILLATOR BAR
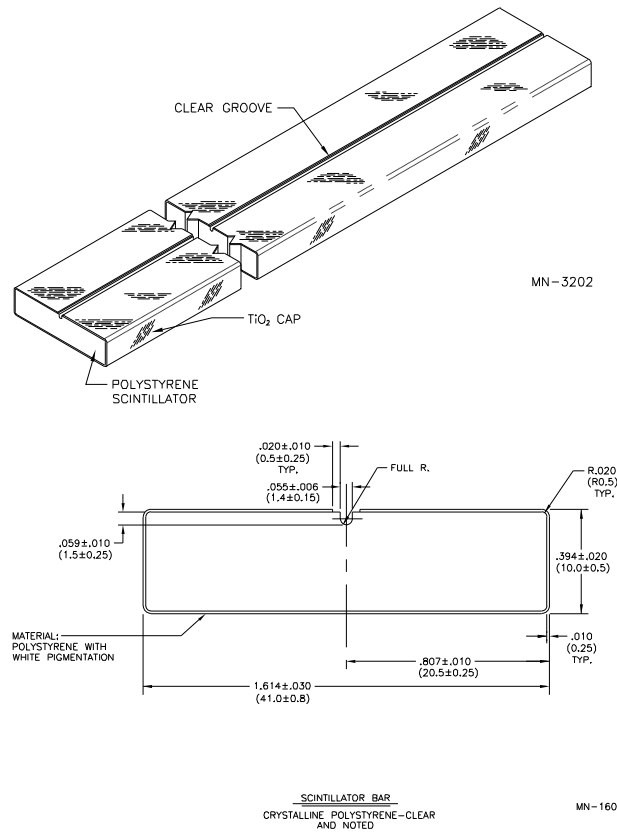CRYSTALLINE POLYSTYRENE−CLEAR
AND NOTED

MN−16011A

Figure 3.5: MINOS polystyrene scintillator strips.

42

Here, x is the distance along the fiber and λ_s, λ_l are the short and long attenuation lengths. Typical values for these parameters are:

$$\lambda_s \approx 80\,\mathrm{cm}, \quad \lambda_l \approx 650\,\mathrm{cm}, \quad k \sim 1/2$$

For the CalDet the parameters were determined using cosmic ray calibration data .

The scintillator strips are arrayed (with the 4.1 cm wide grooved side up) in modules of 16, 20, 24 or 28 strips. During construction the strips in each module were glued to a 0.5 mm aluminum skin in a tight formation in order to eliminate dead space. Plastic end-manifolds, terminating in a twenty-eight fiber bulk-connector, were attached to each end of the module (see Fig. 3.6). The WLS fibers were then routed through the manifolds and glued into place in the groove. A second sheet of 0.5 mm aluminum was glued down on the module's open face and then crimped with the lower aluminum sheet along the module's sides. Black RTV was used to seal each module along all seams and joins. Finally, the WLS fibers protruding from the bulk-connectors were fly cut and polished. The process resulted in modules that are light tight, rigid and easily stacked and packed.

All of the modules used by MINOS were constructed in the fashion described above. However, there are distinct module types due to the variance in size and shape between the different detectors. The Far detector scintillator planes are composed of two each of four different module types, for a total of eight modules per plane (see Fig. 3.7). The outermost module on each side has twenty-eight strips with the module end cut at a 45° angle with respect to the strip direction. The angle allows the module to match the octagonal shape of the detector. The next module in on each side is longer but also has
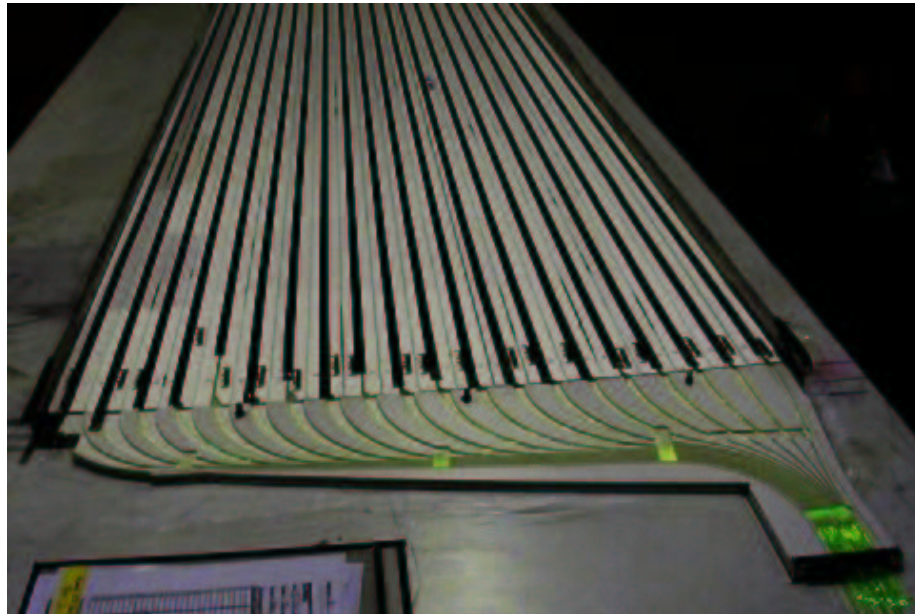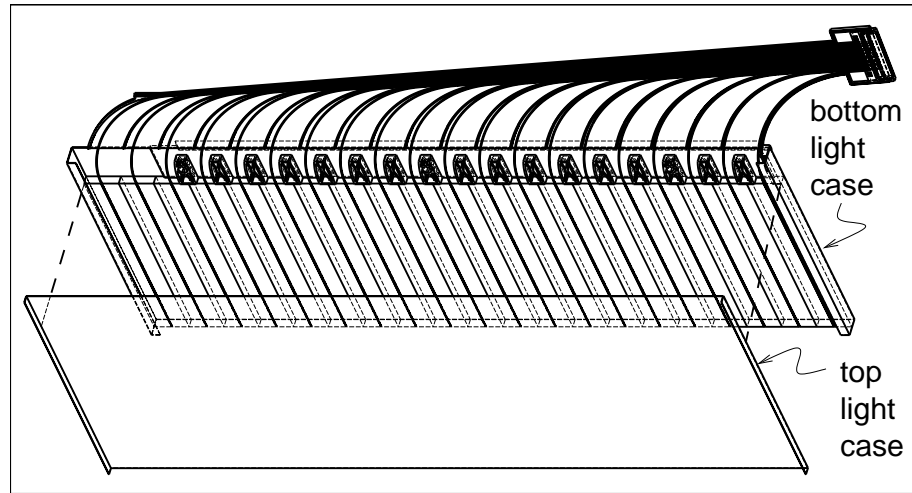
Figure 3.6: A scintillator module assembly schematic compared with an actual module. The photograph was taken just prior to crimping on the module's aluminum top. The photo was digitally enhanced to show the green WLS fibers. In the photo, the fiber ends have yet to be fly-cut and are visible protruding from the bulk connector at the bottom right. The black bars running along the module are strips of aluminized mylar used to cover the fiber grooves in each scintillator strip.
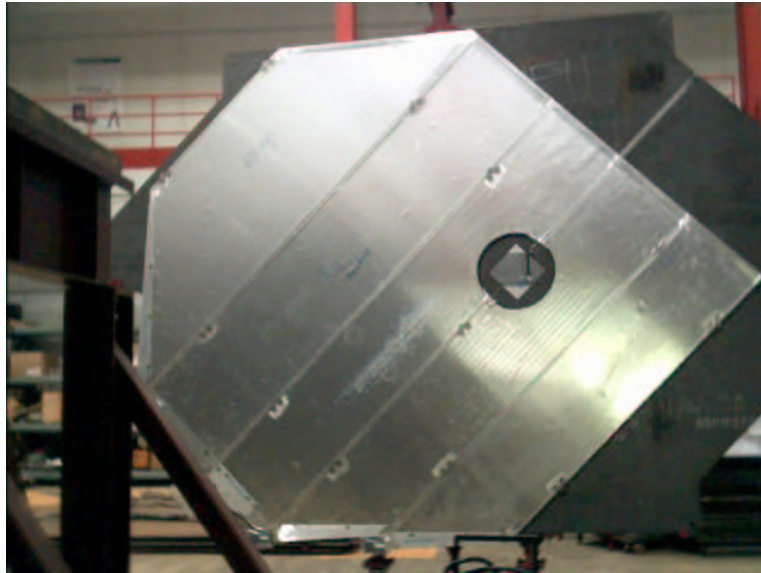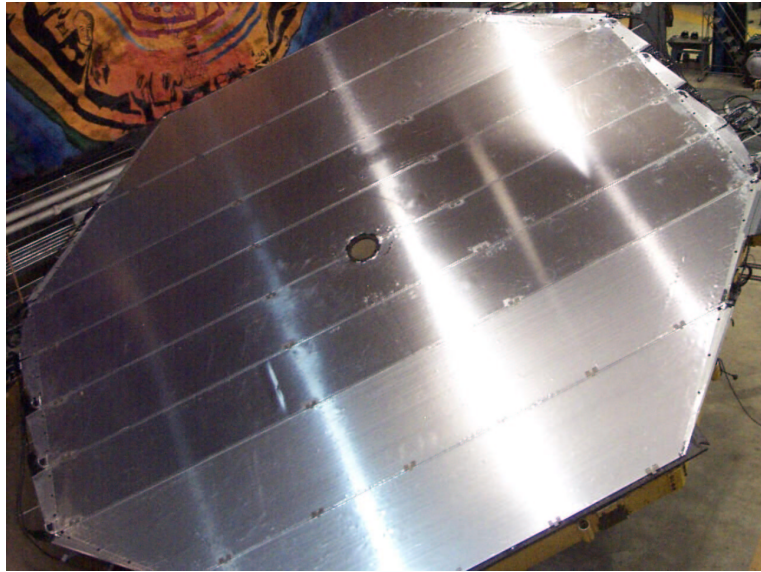
Figure 3.7: Far (top) and Near detector scintillator modules after being attached to their steel plane. Each Far detector plane is composed of eight modules. The Near detector photo shows a fully instrumented plane consisting of five modules. The Near detector also has partially instrumented planes made up of three modules.
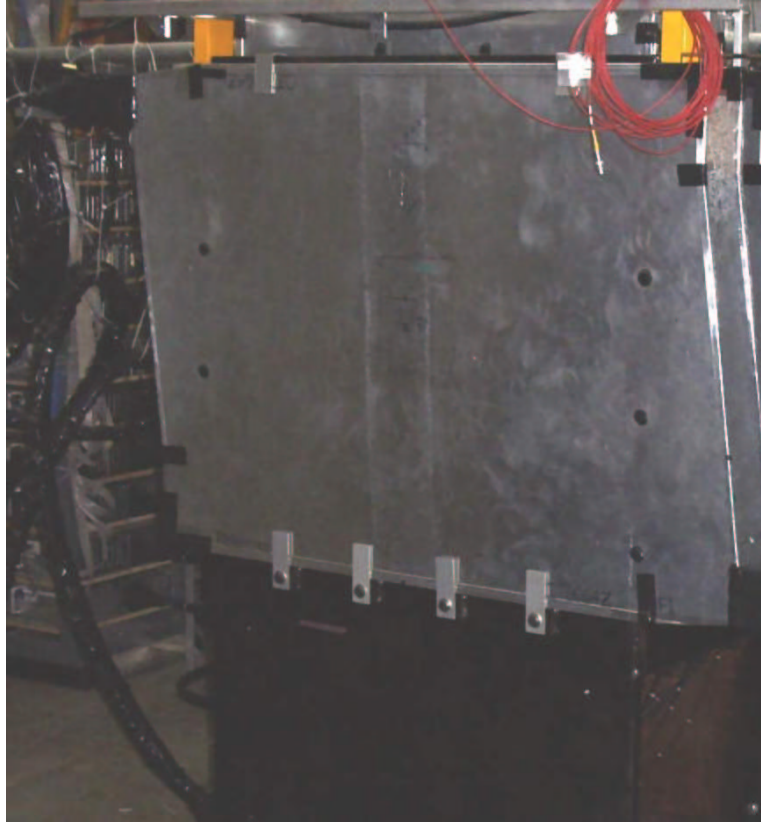
Figure 3.8: A CalDet scintillator module. Each CalDet module contains twenty-four strips which are read out at both ends. The strips run horizontally in the module shown in the photo. The active area is a 1 m square. The trapezoidal shape is due to the end-manifolds which route the WLS fibers from each strip end to the bulk-connector on the module's side.

twenty-eight strips and is cut at a 45° angle. The third module in toward the center has twenty strips with perpendicular ends. The central two modules are also twenty strips wide but have a bypass in the center to permit passage of the magnetic coil. A Far detector plane has one 192 strips each of which is read out on both sides. The strips in the Far detector run at an angle of 45° with respect to the vertical. Successive planes are rotated by 90°.

The Near detector has two different styles of scintillator planes: partially instrumented and fully instrumented. Fully instrumented Near detector planes are comprised of five different module types which together have ninety-six strips and cover a $\sim 13.2\,\mathrm{m}^2$ area. Because the neutrino beam is only about a meter wide in the Near detector hall, the scintillator planes in the upstream section of the detector are permitted to have a smaller area. These partially instrumented planes are comprised of three different module types, which cover a $\sim 6.0\,\mathrm{m}^2$ area with 64 strips. Near detector planes are only read out from one side. As in the Far detector, scintillator strips run at 45° angles with respect to the vertical and successive planes are rotated ±90°.

CalDet scintillator planes were built from the same components as the planes used in the Near and Far detectors. A single CalDet scintillator plane was composed of one twenty-four strip wide, 1 m long module. Each plane had an active area of approximately $1\,\mathrm{m}^2$ and could be readout on both sides. The strips in the CalDet run parallel (even numbered planes) or perpendicular (odd) to the floor rather than at a 45° angle as in the Far and Near detectors. Successive planes were rotated 90° with respect to one another.

The length of WLS fiber between the end of each scintillator strip and the optical connector on the module's side is known as the *pigtail*. Actual lengths vary from strip to strip with a median value of 67 cm. Table 3.3

47

CalDet Module Pigtail Lengths			
Fiber #	Length (cm)	Fiber #	Length (cm)
0	37.9	12	69.1
1	37.9	13	72.8
2	38.6	14	76.6
3	39.9	15	80.3
4	41.8	16	84.1
5	44.2	17	87.8
6	47.1	18	91.6
7	50.5	19	95.3
8	54.1	20	99.0
9	57.9	21	102.8
10	61.6	22	106.5
11	65.3	23	110.3

Table 3.3: The length of WLS fiber between the end of each 1 m long scintillator and the module's block connector. The values shown are for CalDet modules. Fiber numbers and strip numbers are the same for east side readout. On the west side, fiber 0 corresponds to strip 23, fiber 1 to strip 22, and so on [38].

lists the exact values for CalDet modules. The pigtail lengths are large and different enough that they must be accounted for when simulating the CalDet's response.

Scintillator modules were fabricated in factories at CalTech, Argonne and the University of Minnesota and then shipped to the detector sites. During the installation process the modules making up each scintillator plane are mounted on a horizontally oriented steel plane. There is a mounting bar at both ends of each module which is used to attach the module to brackets welded on the face of the steel plane. Additionally, modules are supported along their long edges by steel packing straps attached to switch plates welded to the face of each plane. The lowest module in each plane rests on a small shelf for additional support. The combined planes are eventually hung with the scintillator facing upstream.

3.3 Calorimeter Layout

The Far detector is located in the Soudan Underground Laboratory in Soudan, Minnesota. The 82 m long by 14 m wide by 12 m high detector hall was excavated at a depth of approximately 713 m. The hall was built specifically for MINOS and maintains nearly constant environmental conditions throughout the year. The detector is composed of 486 steel planes organized into two independent super-modules. Each steel plate in a super-module, with the exception of the most upstream one, is instrumented with scintillator. The completed detector weighs 5.4 kt and is held up by a steel support structure on each side. The photodetectors and electronics are installed in racks arranged along the three levels of the support structure.

Figure 3.9: The Far detector as it was after completion in July, 2003. Scintillator planes line the top and sides of the detector forming a veto-shield used to suppress downward going cosmic rays [39].

The Near detector will be located on the Fermilab site in a hall 1046 m downstream of the NuMI target. The near detector will consist of 282 steel plans organized into four sections. By order along the beamline these sections are:

Veto The Veto section will consist of a leading steel plane followed by 20 instrumented planes. This section is intended to act as a veto for particles produced by neutrino interactions in the upstream absorber.

Target The target section will be made up of 40 instrumented planes. Neutrino interactions used to make comparisons between the Near and Far detectors will be required to occur within the Target section.

Figure 3.10: The Near detector on July 9, 2004. At the time the photo was taken the detector was still being installed. The leading plane is partially instrumented and in the Hadron Calorimeter section of the detector [39].

Hadron Calorimeter The Hadron Calorimeter is designed to measure the energy of hadronic showers produced by interactions in the Target section. The calorimeter section will be comprised of 60 instrumented planes.

Muon spectrometer The last 161 planes will form the muon spectrometer. The spectrometer is designed to measure the momentum of muons produced by interactions in the Target section. Every fifth plane in the spectrometer will be fully instrumented. The rest are bare steel.

Four out of every five planes in the first three sections will be partially instrumented. The fifth plane will be fully instrumented in order to have a better

51

tracking capability for muons which leave the partially instrumented region. The detector will be held up by a two level support structure. Electronics and phototubes will be mounted in racks arrayed along the west side of the detector. The magnetic coil will return along the floor on the east side of the detector.

Figure 3.11: The CalDet in T7 beamline of the CERN East Hall during 2002. Phototubes reside inside the metallic mux-boxes located in the racks alongside the detector.

The CalDet was operated during 2001-03 in the T11 and T7 beamlines at the CERN PS East Hall. The detector is comprised of sixty steel plates each instrumented with a $1\,\mathrm{m}^2$ scintillator plane (see Fig. 3.11). The photodetectors and electronics were located inside the experimental area alongside the detector. The detector was controlled from inside a counting house located just outside the test beam area. Details of the operation and layout of the

Materials Budget

Material	Length (mm)	# of X_0	# of λ_I	$\Delta E|_{mip}$(MeV)
Al	1.0	11.2×10^{-3}	2.6×10^{-3}	0.44
Scint	10.0	23.0×10^{-3}	11.9×10^{-3}	2.00
Fe	25.4	1.423	0.149	28.58
Ti0$_2$ Layer	0.2	0.5×10^{-3}	0.2×10^{-3}	0.04
Air	23.0	-	-	-
Total	59.4	1.458	0.1655	31.06

Table 3.4: The materials budget for one plane assuming a normally incident particle. The third and fourth columns list number of radiation and interaction lengths per plane. Materials constants were taken from [2] and the nuclear interaction length is stated for protons. The iron density of Tab. 3.2 was used.

CalDet will be discussed in a following chapter.

3.4   Calorimeter Readout

3.4.1   Phototubes

MINOS employs Hamamatsu multi-anode photomultiplier tubes to convert light into charge. The Far detector utilizes sixteen-pixel phototubes (M16s); Near detector phototubes have sixty-four pixels (M64s). The individual pixels effectively act as miniature single anode phototubes. Each tube has a common dynode output that can be used to trigger readout by the front-end electronics. The PMTs were chosen because of their small size, low cost, relatively high efficiency and uniformity, fast timing and insensitivity to magnetic fields. Each tube is operated at an average (over pixels) gain of 1×10^6 and has a linear response for input pulses less than 100 photo-electrons.

The tubes were extensively tested at the University of Texas, Oxford

PMT Parameter	M16	M64
Typical HV (V)	765	813
Typical Gain	1×10^6	8×10^5
Single PE width	48%	50%
Average Gain Uniformity	13.3%	19.9%
Typical QE at 520 nm	$\geq$12%	12.8%
Average QE×CE Uniformity	8.5%	8.4%
Typical response non-linearity	<2%	<2%
Cross talk: Sum of 8 neighbor pixels	2.3%	4.7%
Cross talk: Sum of all non-neighbors	0.9%	2.1%
Average Dark Rate at 950 V	350 Hz	290 Hz

Table 3.5: Some PMT parameters extracted during the evaluation process. Single PE width refers to the fractional width of the single photoelectron charge spectrum. QE×CE is the effective collection efficiency. Uniformity is calculated as the RMS over all 128 fiber positions (M16s) or all pixels (M64s) for one tube. The response non-linearity is quoted for 100 PEs on a single pixel at the typical gain. Cross talk is defined as the amount of charge (in PEs) in a non-illuminated pixel divided by the amount of charge in an illuminated pixel [40, 41].

University and the University of Athens. Table 3.5 presents the results of the evaluation process. Generally the testing found that the PMTs performed as well as or better than expected and that M16s and M64s perform in a similar fashion.

3.4.2 Optical Cabling

The WLS fibers running through the strips in a module come together at a block connector on the module's end. The module block connector is coupled to a similar block connector carrying 1.2 mm diameter clear optical fibers. The clear fibers, which have a longer attenuation length (~ 12 m) than the green fibers, are used to carry the light to a dark-box in which a phototube resides. The dark-boxes (called *mux-boxes* at the Far detector and *Alner-boxes* at the Near) handle the connection between the clear optical fiber, the phototube face and the front-end electronics. The phototubes are secured, face down, to an optical connector (called a *cookie*) which holds the clear fibers.

One (Far detector) mux-box contains three M16 phototubes and serves one side of two adjacent planes of the same view (e.g. planes six and eight). The mux-boxes implement a 8:1 optical summing scheme in order to reduce the cost of electronics. The summing scheme (somewhat improperly known as *multiplexing*) was designed such that:

- The eight strips grouped on a single pixel are widely separated in the detector.

- The effect of cross talk is minimized

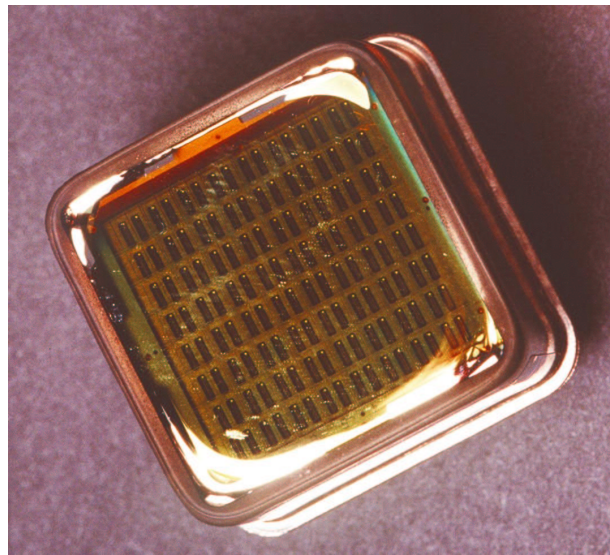- The scheme differs on each side so as to resolve ambiguity.

Figure 3.12: M16 (top) and M64 phototubes.

De-multiplexing is done during the event reconstruction phase. The standard algorithm reconstructs > 95% of the hits in more than 91% of muon tracks [42].

The Near detector does not have optical multiplexing and one M64 phototube resides in each dark-box. The sixty-four strips in a partially instrumented plane are read out by a single phototube. Fully instrumented planes in the Veto, Target and Calorimeter sections are read out by two M64s, each connected to forty-eight strips. In the muon spectrometer two successive planes in the same view are connected to a total of three phototubes. Additionally, in the muon spectrometer there is a 4:1 electronic multiplexing scheme that is implemented on the PMT base by directly connecting anodes together in groups of four.

The CalDet has no multiplexing. For M16 readout, three tubes (one mux-box) are connected to two successive planes (forty-eight strips) in the same view. After 2001, both ends of plane zero were read out by one mux-box so that signals in planes zero and two would not be correlated by PMT cross talk. Table 3.6 shows the mapping between (plane,strip,end) and (PMT,pixel) for M16 readout. Table 3.7 shows mapping for M64 readout.

CalDet scintillator planes were connected to PMT dark-boxes with both clear and green (WLS) fiber cables in order to model the Far and Near detectors. Table 3.8 lists the readout cable length and composition for different running periods. When CalDet was operated with M64s and Near electronics only, just the west side of the detector was read out by phototubes. In that case, the east side had WLS cables, either 1 or 3 m long, attached to a reflector connector rather than a phototube. The 1 m cables were intended to model the partially instrumented Near detector planes while the 3 m cables were intended to model the fully instrumented planes.

57

CalDet Strip to M16 PMT & Pixel Mapping				
Strip↓	Plane N	Plane N+2	Plane 0 (East)	Plane 0 (West)
0	(0,1)	(1,9)	(1,9)	(1,7)
1	(0,3)	(1,11)	(1,11)	(1,5)
2	(0,6)	(1,14)	(1,14)	(1,4)
3	(0,8)	(1,16)	(1,16)	(1,2)
4	(0,9)	(2,1)	(2,1)	(0,15)
5	(0,11)	(2,3)	(2,3)	(0,13)
6	(0,14)	(2,6)	(2,6)	(0,12)
7	(0,16)	(2,8)	(2,8)	(0,10)
8	(1,1)	(2,9)	(2,9)	(0,7)
9	(1,3)	(2,11)	(2,11)	(0,5)
10	(1,6)	(2,14)	(2,14)	(0,4)
11	(1,8)	(2,16)	(2,16)	(0,2)
12	(0,2)	(1,10)	(1,10)	(1,8)
13	(0,4)	(1,12)	(1,12)	(1,6)
14	(0,5)	(1,13)	(1,13)	(1,3)
15	(0,7)	(1,15)	(1,15)	(1,1)
16	(0,10)	(2,2)	(2,2)	(0,16)
17	(0,12)	(2,4)	(2,4)	(0,14)
18	(0,13)	(2,5)	(2,5)	(0,11)
19	(0,15)	(2,7)	(2,7)	(0,9)
20	(1,2)	(2,10)	(2,10	(0,8)
21	(1,4)	(2,12)	(2,12)	(0,6)
22	(1,5)	(2,13)	(2,13)	(0,3)
23	(1,7)	(2,15)	(2,15)	(0,1)

Table 3.6: The CalDet M16 readout scheme for two generic planes and plane 0. The notation (1,2) indicates pmt # 1, pixel # 2. The scheme for generic planes is shown for the top and east side readouts. The readout for the bottom and west sides have the strips in reverse order (e.g., take strip 0 to strip 23, strip 1 to strip 22, etc). Plane zero is readout by three phototubes in the same mux-box and has a slightly different scheme. The mapping for plane two follows the second column.

CalDet Strip to M64 Pixel Mapping				
Strip↓	Plane N	Plane N+2	Plane 0 (East)	Plane 0 (West)
0	51	43	0	43
1	46	38	5	38
2	41	33	10	33
3	36	28	15	28
4	31	23	20	23
5	26	18	25	18
6	21	13	30	13
7	16	8	35	8
8	11	3	40	3
9	6	62	45	62
10	1	57	50	57
11	60	52	55	52
12	55	47	60	47
13	50	42	1	42
14	45	37	6	37
15	40	32	11	32
16	35	27	16	27
17	30	22	21	22
18	25	17	26	17
19	20	12	31	12
20	15	7	36	7
21	10	2	41	2
22	5	61	46	61
23	0	56	51	56

Table 3.7: The CalDet M64 readout scheme for two generic planes and plane zero. The numbers in each column indicate the pixel number. One tube reads out one side of two planes (48 strips). M64s and Near electronics were used to read out only the west side of the detector, with the exception of plane zero where they were used on both sides in 2003. The mapping for plane two follows the second column.

CalDet Optical Readout Cable Lengths (m)							
where	when (dd/mm hh:mm)	U	D	W	E	p0W	p0E
2002	till ~1/8/03	C6	G4	C6	G4	C6	G4
T7NF03	1/8 - 26/9 15:00	C6	G3	C6	G3	C6	G3
T7N03A	26/9 15:00-1/10 18:30	C6	G3*	C6	G3*	C6	G4
T7N03B	1/10 18:30-6/10/03	C6	G1*	C6	G1*	C6	G4
T11N03	10/10 18:30-21/10/03	C6	G1*	C6	G1*	C6	G4

Table 3.8: Lengths and composition of the optical readout cables used in CalDet to connect scintillator planes to the dark-boxes. The notation C6 indicates 6 m of clear cable, while G3 indicates 3 m of green (WLS) cable. The presence of a * indicates that the cable was terminated with a reflector connector rather than connected to a phototube.

3.4.3 Readout Electronics

The design of the MINOS electronics required some compromises. The general philosophy of the experiment was to make the Near and Far detectors respond to neutrino interactions in the same way. Based on this, one might expect that the two detectors should use the same electronics to read and digitize photomultiplier signals. Indeed the experiment's initial design called for just that. Those plans, however, were based on running NuMI in *resonant extraction* mode rather than the *single turn extraction* mode that is now planned. From the electronics standpoint, the difference between the two is, in short, the neutrino interaction rate. The resonant extraction mode would have resulted in a 1 ms long beam-spill in contrast to the $8\,\mu$s spill provided by single turn extraction. The result is a large difference in rates between the two detectors. The high rate in the Near detector necessitates good time resolution (few tens of ns) and a small dead-time in order to resolve spatially overlapping events. Fast electronics are expensive and also unnecessary in the low-rate Far detec-
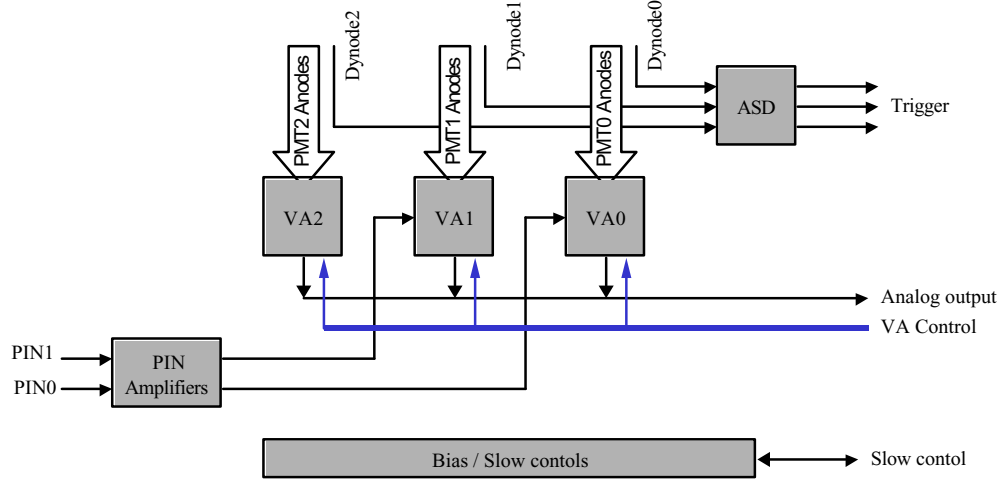
Figure 3.13: A block diagram for the VA Front-end Board [43].

tor. Additionally, the Far detector, given it's depth, has the ability to study atmospheric neutrinos provided that it is equipped with electronics having a time resolution in the few ns range. Thus, the two detectors use completely different electronics.

Far Detector Electronics

The Far detector readout electronics is based on the multi-channel VA chip produced by IDE Corp [43]. There is one chip for every PMT, with three chips residing on a *VA Front-end Board* (VFB) attached to each mux-box. Twenty-two channels on each VA chip can be read out, with sixteen connected to phototube anodes and one connected to a PIN diode input. The other five channels are used to correct common mode fluctuations. Each channel contains a pre-amplifier, a shaper, a track and hold stage and an output switch. Essentially, anode pulses are amplified and then shaped into a unipolar pulse.

61

The peaking time of the shaper circuit is about 500 ns. The shaper is connected through a transistor to a capacitor which tracks the shaper output.

The dynode signal from each PMT is connected to a discriminator (the *ASDLite*) on the VFB. The ASDLite has a variable threshold that is typically set to a level corresponding to approximately 0.3 photoelectrons. The discriminator output is sent over a ribbon cable to the *VA Readout Controller* (VARC) where a timestamp (with a 1.5625 ns LSB) is generated. The VARC waits for a period of time and then sends a signal back to the VFB which stops the tracking. The amount of delay in the VARC corresponds to the VA chip's shaper peaking time.

After sending the hold signal, the VARC instructs the VFB to begin the read out process. On the VFB, the voltage held on each capacitor is buffered to produce a differential current output which is then connected back to the VARC over a shielded analog signal cable. On the VARC the *VARC Mezzanine Module* (VMM) receives, amplifies and digitizes the VA output signal. The VMM has a 14-bit ADC with a dynamic range of 0.005-30 pC. Each VMM processes the signals from two VFBs, and each VARC can hold up to six VMMs. The readout and digitization process for a single chip takes 5-10 μs during which the chip does not respond to dynode triggers. The dead-time depends upon the hold time on the VA chip, the digitization time for the 21 channels on the chip and the settling time after digitization [43]. The time durations are configurable and different configurations yield the 5-10 μs dead-time range[2]. Since six chips are served serially by one VMM, the maximum dead-time is approximately 60 μs.

Digitizations from a single chip are matched with their timestamps (de-

---

[2]During standard running, CalDet was operated so as to achieve a 5 μs dead-time.

rived from the ASDLite trigger) and placed into a forty event (1 kb) FIFO. Each VMM has its own FIFO. A single *Sparsifier* unit on the VARC reads data from the six FIFOs in a round-robin fashion. The Sparsifier performs pedestal subtraction, common mode correction and zero suppression (sparsification). For each channel the VARC stores a pedestal value and a sparsification threshold which are determined from a dedicated run taken with random, rather than dynode, triggers (eg, a pedestal run). The Sparsifier then matches the remaining digitizations with their electronic address (channel, chip and VMM numbers) and writes them into two 32 k long-word buffers. Two buffers are used so that the Sparsifier can fill one while the other is being read out by the a VME processor.

A larger than expected singles rate was observed during the installation of the Far detector. Eventually, after much effort on the part of the collaboration, it was discovered that the rate was highest for recently installed planes, decreased exponentially with time with a decay constant of ~ 100 days, and was consistent with stress-induced phosphoresence in the WLS fibers [44]. The large rate caused an unacceptable dead-time in the Far detector. In order to reduce the rate a hardware trigger was implemented in the VARC. The trigger requires two out of the thirty-six chips in the VARC to recieve a dynode trigger before the VARC will output a hold signal. In principle the trigger requirement may be removed during beam spills.

Three VARCs occupy one VME crate, with sixteen crates servicing the entire detector. The digitized data is taken from each VARC's readout buffer by the crate's *Read Out Processor* (ROP). On the ROP the data from each of the VARCs is combined and time-sorted into (typically one second long) timeframes. The timeframes are transmitted to the trigger farm where event

63

building and filtering occurs.

Near Detector Electronics

The Near detector electronics system was designed to cope with the much higher rateof interactions expected in the Near detector[3]. The design allows the Near detector to digitize at the 53 MHz RF rate of the Main Injector (e.g. once every 19 ns) with zero dead-time during the $8\,\mu$s NuMI spills. The Near electronics has approximately the same dynamic range and charge resolution as the Far electronics.

The Near electronics is based on the Fermilab QIE (*Charge (Q) to Current (I) Encoder*) chip. The basic circuit in the chip is composed of a current splitter, a gated integrator and a range selector. The chip is able to achieve dead-time free operation by using four integrator/range selector pairs in parallel (see Fig. 3.14). The circuits operate in exactly the same way but are $90°$ out of phase with one another. A single 8-bit ADC digitizes the output voltage from the four range selectors. The details of the QIE read out process are described in the next few paragraphs. Much of the discussion closely follows the excellent and more exhaustive description of [45].

Readout begins when input current from a PMT anode is collected by the current splitter. The splitter divides the input current into eight binary-weighted ranges: I/2, I/4 ... I/256. The output of each current range is connected to the current integrator and used to charge a capacitor. The current integration phase ends when the switches connecting the eight ranges to their capacitors are closed. This leaves a voltage proportional to the input current

---

[3]Approximately forty neutrino intractions are expected to occur in the Near detector during each (low energy) beam spill.
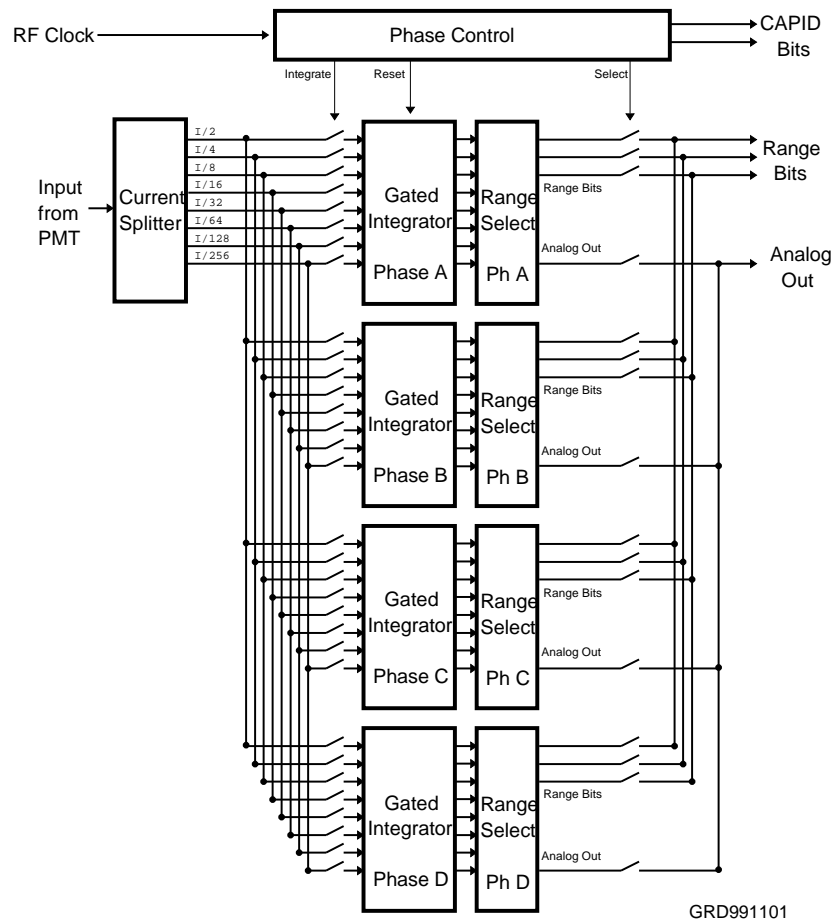
Fig. 1. Block Diagram of the QIE

Figure 3.14: A block diagram of the QIE chip [45]

held on each of the output capacitors. The integration phase takes one clock cycle (19 ns).

After current integration, the voltages held on the eight capacitors are output to one of the four the range selectors. The range selector uses a comparator to choose the range that is the most appropriate for digitization. The design of the current splitter assures that, in general, only one of the eight output voltages lies within the the input range of the ADC. The comparator outputs the selected voltage range in a three bit digital format and opens a channel from the corresponding capacitor (on the current integrator) to the ADC. Finally, the capacitors in the integrator are discharged to prepare for the next readout cycle.

The 8-bit ADC digitizes the comparator voltage and appends the 3-bit range to the result in order to give a floating-point-like representation of the signal from the photomultiplier. Two additional bits, known as the CAPID, are appended to identify which of the four circuits were used. The digitization process takes four clock cycles (76 ns) in total but is pipelined so that digitization can occur for each clock cycle. The range selection, voltage output and capacitor discharge phase takes three clock cycles (57 ns). The entire read out phase, beginning with the PMT input and ending with the start of digitization, takes four clock cycles. Thus, four parallel circuits are needed for dead-time free operation.

Figure 3.15 shows the ADC output from the QIE as a function of the input charge. The horizontal scale in the figure is somewhat arbitrary in that it depends on the individual components (in particular the integrators' capacitors) in the QIE circuit. Therefore, each channel must be independently calibrated. The calibration is done using a digital to analog converter driving a
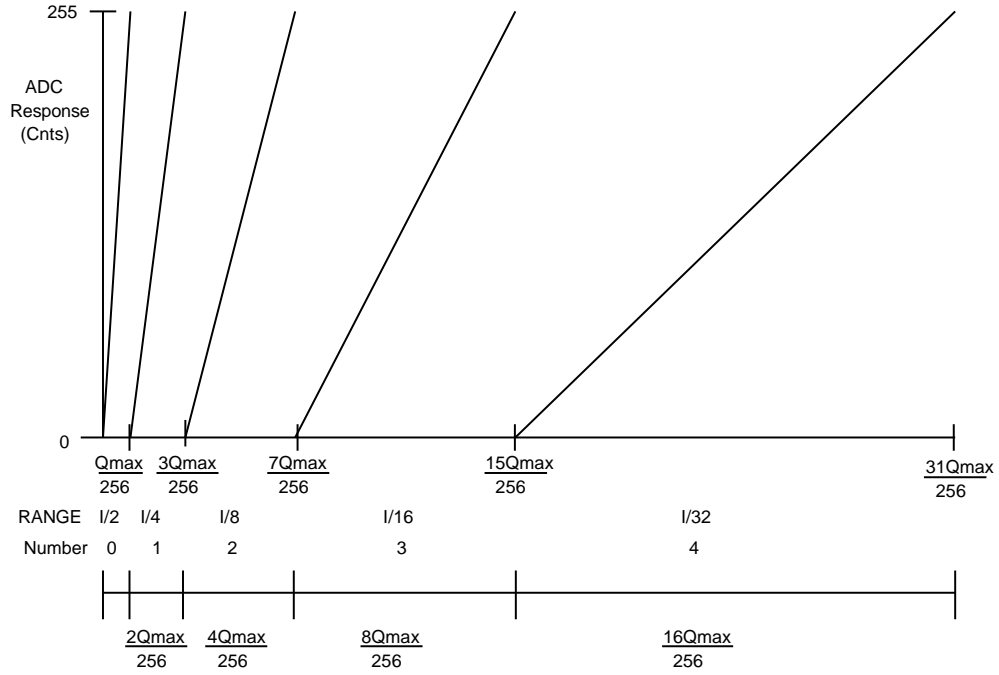
255

ADC
Response
(Cnts)

0

$\frac{Qmax}{256}$ $\frac{3Qmax}{256}$ $\frac{7Qmax}{256}$ $\frac{15Qmax}{256}$ $\frac{31Qmax}{256}$

RANGE   I/2 I/4   I/8   I/16   I/32

Number   0   1   2   3   4

$\frac{2Qmax}{256}$ $\frac{4Qmax}{256}$ $\frac{8Qmax}{256}$ $\frac{16Qmax}{256}$

Fig. 4. Ideal QIE Transfer Function
(Ranges 5-7 not shown.)

Figure 3.15: The QIE ADC output as a function of the input charge. The individual lines show the output for ranges 0-4. Ranges 5-7 are off scale to the right. In reality, the scale along the horizontal axis must be determined by calibration with a precision current source. For each 8-bit ADC count and 3-bit range the system then looks up the corresponding charge [45].

precision Howland Current Source which connects to the QIE input. The calibration procedure produces a slope and offset for each of the eight capacitors in the four circuits.

A MENU (*MINOS Electronics for Neutrinos*) board holds a single QIE chip, the associated ADC, the current source and a FIFO. The FIFO can hold digitizations from 1000 clock cycles (e.g. $19\,\mu$s of data) before readout is necessary. Sixteen MENUs reside on a MINDER (*MINOS Near Detector Readout*) board which controls and provides power and clock signals to the MENUs. Photomultiplier signals are routed from inputs on the MINDER to the MENU modules. The MINDER's (and hence the MENUs') clock signals are sequenced to a $53\,$MHz clock which is derived from the Main Injector clock. The MINDER uses the $53\,$MHz clock signal to timestamp each digitization. The timing resolution is then just one clock period (e.g. $1/53\,$MHz or $\sim 19\,$ns).

Data is saved in each of the MENU FIFOs for some period of time after the reception of a trigger signal by the MINDER. Triggers are derived either from the PMT dynodes (for cosmic ray calibration, as in the Far detector), from an external spill signal (for neutrino beam spills) or from another external process (including the light injection system and, in CalDet, from a coincidence of beam counters). The amount of time that the system is active and saving data after a trigger is configurable. For example, data are saved for $\sim 9\,\mu$s after the reception of a spill signal but only for a few (nominally twelve) clock cycles after the reception of a cosmic ray trigger. During CalDet operations twenty clock cycles were written after each external trigger.

Eight MINDERS are connected to a VME board called the MASTER (*MINOS Acquisition, Sparsifier, and Time-stamper for Event Records*). The MASTER controls the operation of each of its MINDERs through a special

68

module, known as a KEEPER (*Krate Electronics Port for Event Readout*), which resides, with the MINDERs, in a crate about a meter from the phototmultipliers. MASTERs receive and processes digitizations from their MINDERs. Each digitization contains the 8-bit ADC value, the 3-bit range and the 2-bit CAPID. The MASTER uses these values, as well as the channel ID, to construct an index into a lookup table. The values in the lookup table are derived from the slopes and offsets established through the current injection calibration described above. Thus, the raw ADC values from each MINDER are converted to calibrated values (known as DAC counts) with a least significant bit corresponding to 1.4 fC. Digitizations below a configurable threshold (nominally corresponding to 0.3 photoelectrons as at the Far Detector) are discarded by the MASTER. The channel ID, timestamp and DAC count of the remaining digitizations are written into one of a pair of buffers from which they can be read by the data acquisition system.

CalDet Electronics

The CalDet used both Near and Far detector electronics. Runs were taken with each type of electronics reading out the detector alone and with both types in parallel. Generally, the electronics operated as described above. However, because CalDet was operated in a particle beam and because runs were taken with both Near and Far electronics in parallel, there were some small deviations from the previous description. These differences are:

Beam Trigger Both types of electronics were able to be externally triggered. Trigger signals were derived from the coincidence of two time of flight counters or from a signal emitted by the light injection system. For the

Electronics used for each CalDet running period.			
where	when (dd/mm/yy)	Run Series	Comment
T11	9/01 - 11/01	1XXXX	Far, no beam trigger
T7	6/02	2XXXX	Far, no beam trigger
T11	4/9/02 - 14/9/02	3XXXX	Near+Far test
T11	15/9/02 - 3/10/02	4XXXX	Far only.
T7	4/10/02 - 16/10/02	5XXXX	Far only.
T7	1/8/03 - 26/9/03	7XXXX	Far on east side, Near on west side
T7	26/9/03 - 6/10/03	8XXXX,9XXXX	Near on west side, no Far
T11	10/10/03 - 21/10/03	1XXXXX	Near on west side, no Far

Table 3.9: The type of electronics used in each running period at CalDet. T11 and T7 are test beamlines in the CERN East Hall. The Near/Far running in 2002 had 6 planes on the west side of the detector read out with Near electronics and was useful only as an operational test of dual electronics data taking.

Far electronics each VARC took as input a TTL pulse which enabled the VARC to send hold signals to its VA chips. Each KEEPER in the Near electronics relayed a input TTL signal to its MINDERs. The reception of that signal caused twenty clock cycles to be saved by each MENU. Details of the trigger arrangement will be discussed in a subsequent chapter.

No 2/36 The Far detector electronics did not utilize the two out of thirty-six trigger.

Particle ID channels Six far detector chips, with one active channel on each, were used to read out signals from the CalDet particle identification system (Čerenkov counters and occasionally signals from the time of flight counters).

Fiducial timing Times in the Far and Near electronics differed by a phase shift of a few tens of nano-seconds. The shift changed each second. To permit (offline) event building, the Near electronics emitted a *fiducial timing* pulse when its clock began a new second. The fiducial signal was read out by a VA channel, allowing the Far and Near clocks to by synchronized offline.

Near clock The Near electronics clock signal was taken from a custom clock module rather than the accelerator complex.

Table 3.9 lists the electronics used by CalDet during each running period.

3.4.4   Data Acquisition

The data acquisition system, shown schematically in Fig. 3.16, is essentially the same for all three MINOS detectors. Front-end units (VARCs and MASTERs)
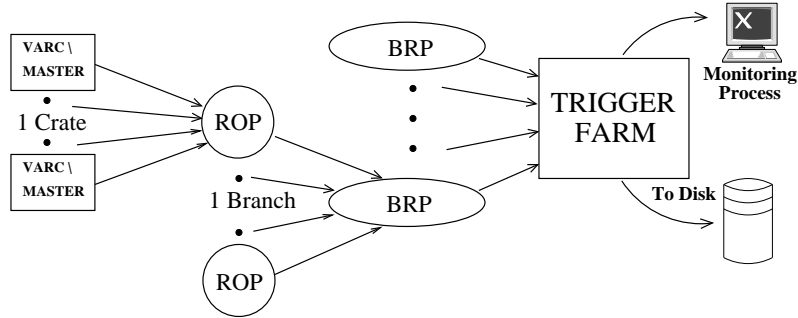
Figure 3.16: MINOS DAQ Layout. Multiple VARCs / MASTERs reside in a VME crate along with a Readout Processor (ROP). The ROP collects the data from its crate and exports it to a Branch Readout Processor (BRP). The BRP controls its ROPs and forwards their data on to the trigger farm. The trigger farm builds and filters events according to various trigger conditions. Events passing the trigger are saved to disk and made available for monitoring processes.

reside in VME crates along with a VME Readout Processor (ROP). The ROP provides a control interface to the front-end units and reads *timeblocks* of data from one of the two output buffers on each unit. Timeblocks are typically 10-50 ms long, with each read causing the front-end unit to switch to writing into the other buffer (known as a *buffer swap*). In CalDet, the time of flight data (see Ch. 4.4.1) are read out on each buffer swap. The ROPs assemble multiple timeblocks into a timeframe (typically one second long) and export the data to a Branch Readout Processor (BRP). The BRPs provide an interface between the front-end units and the interactive run control process as well as forwarding timeframes of data along to the trigger farm. The trigger farm is the first place where the entire detector's data is on-hand. For each time frame the farm does the following:

- Joins the timeframe from each BRP into a single one for the whole

detector.

- Monitors singles rates.

- Forms candidate events.

- Locates and processes light injection calibration data into summaries.

- Filters events according to various trigger algorithms.

- Writes triggered events to disk.

The trigger farm forms and filters events in a two step process. During the first stage, the algorithm constructs candidate events by searching for groups of hits clustered in time. The second stage filters the candidate events by requiring that there exist a spatial region in which M out of N planes (by default M=4 and N=5) are hit. Event candidates passing this requirement are saved to disk storage. The trigger farm also computes, for each channel, a running mean and RMS of the charge distribution for light injection calibration events. The individual digitizations from light injection events are then usually filtered out of the data-stream to reduce the data written to tape.

Event formation and filtering was generally not done in the trigger farm at CalDet. Instead, a conservative strategy was adopted in which the farm simply saved entire timeframes to disk. Event formation and filtering was subsequently done using an offline process. Details regarding the formation and selection of events at CalDet will be described in Ch. 4.

3.5 Slow Control

3.5.1 High Voltage Control

PMT high voltage is provided by LeCroy 1440 mainframes controlled via a homegrown program. The HV system at the Far detector includes an automated monitoring process which reads the PMT high voltages and adjusts any that are too far out of range. The system also has the ability to disable HV on a crate that shows serious errors. The system used at CalDet was more rudimentary. PMT high voltages were set once at the beginning of each running period. No automated corrections were done. Instead, calibration data was used to track and correct for gain drifts. During the data taking, the shift crews used a near-online monitoring process to search for serious errors (of which a very few were found).

3.5.2 Environmental Monitoring

The (inaccurately named) *Detector Control System* (DCS) is responsible for monitoring and logging a variety of environmental quantities. The system at the Far detector logs the temperature, humidity and radon content at various locations in the experimental hall. The system is also responsible for monitoring the current in the magnetic field coils. Voltages and currents in the front-end crates are monitored by the *Rack Protection System* (RPS) which can cut power in case of serious danger.

The DCS system was not available for the 2001-02 CalDet running periods. Instead, the hall temperature was monitored using a single, commercially purchased thermocouple read out by a dedicated PC. Synchronization of tem-

74

perature and detector data was done offline. No other quantities were logged during the 2001-02 running periods.

A DCS system was installed at CalDet prior to the 2003 running period. The system logged the temperature at various locations around the detector, recorded the pressure in the Čerenkov counters, and provided a number of generic scalers which recorded the rate in beam and Čerenkov counters. Finally, an interface to the CERN monitoring system was used to log the currents in beamline magnets. The monitoring data collected in 2003 was archived to the experiment's main database.

3.6   Detector Calibration

The MINOS detectors are calibrated using on board charge injection, an ultra-violet LED based light injection system, cosmic ray muons and finally the response to π, μ, e, p as measured by the CalDet. Each element of the calibration system was initially implemented and rigorously tested at the CalDet. A description of the calibration hardware and procedure is presented in Ch. 5.

3.7   Summary

The MINOS experiment uses three iron/scintillator tracking-sampling calorimeters, each constructed to perform in the same way. The Near detector will measure the composition of the neutrino beam about 1 km from the NuMI target while the Far detector will measure the composition in the Soudan iron mine - a distance of 735 km from the target. The two detector design will improve the quality of the oscillation measurement by suppressing systematic

errors associated with the event rate, beam composition, beam pointing and event reconstruction.

A smaller scale third detector, known as CalDet, was constructed to measure the response of MINOS to π, μ, e, p in the energy range 0.5-10 GeV. The major differences between the CalDet and the Near and Far detectors were

- The CalDet was not magnetized.

- The steel plate density, composition and thickness were slightly different (compare Tab. 3.1 and Tab. 3.2).

- The scintillator modules were shorter and had a unique routing scheme from the strip-ends to the module's optical connector.

- The lengths of the readout cables, though choosen to reproduce the Near and Far detector light levels, differed.

- The CalDet was not multiplexed.

- An external trigger was used; The M/N and 2/36 triggers were not used.

- Event formation was done offline.

The CalDet was responsible for validating the calibration procedure, establishing the absolute energy scale of the experiment, measuring the topological signature of π, μ, e, p events and providing a series of benchmarks against which detector response simulations may be validated. Details and results of the CalDet experiment will be presented in the following chapters.

Chapter 4

CalDet Operation

The MINOS calibration detector (CalDet) was exposed to test-beams in the CERN[1] PS East Hall in six running periods during the years 2001-03. The East Hall beamlines provided a mixed sample of hadrons and electrons with a tunable central momentum between 0.2-10 GeV/c and a momentum spread ($\delta p/p$) of approximately 1%. The identity of individual particles was established by a combination of Čerenkov and Time of Flight counters. An external, beam trigger was implemented prior to the fall 2002 running periods following an initial, and unsatisfactory, attempt to collect data using dynode triggers, as in the MINOS Far detector. The combination of beam trigger and particle identification allowed the CalDet to collect relatively pure samples of electrons, pions and muons, and protons, with well known momenta in the range between 0.2-10 GeV/c. These samples were used to precisely quantify the response of the MINOS detectors, prove the viability of the MINOS calibration procedure and provide a series of benchmarks against which Monte Carlo simulations were compared.

---

[1] *Conseil Européenne pour la Recherche Nucléaire*

4.1 Goals of the CalDet Program

The goals of the CalDet program were:

- Integrate the MINOS detector components into a small calibration module. Verify that the detector and production electronics operated properly away from the laboratory test bench.

- Exercise the MINOS light injection and cosmic ray calibration procedure, gauging the effectiveness with measurements of beam particles.

- Measure the response of the MINOS detectors to electrons, hadrons, and muons in the momentum range 0.5-10 GeV/c. The response includes the topological patterns induced by different particles as well as the signal response.

- Provide a series of benchmarks against which the detector simulation programs may be tuned.

- Compare the performance of the Near and Far detector readout schemes.

The CalDet, assembled in the spring and summer of 2001, was the first detector built by MINOS. The early goal of the CalDet program was to simply assure that the various components worked together as designed. Because CalDet came first many initial problems were discovered and corrected at CalDet, allowing for a smoother integration at the Far and Near detectors.

Samples of electrons, muons and hadrons were collected over a wide momentum range. These samples were used to gauge the effectiveness of the calibration procedure, by comparing the detector's response for samples of the

same particles taken at different times, in different beamlines and under different operating conditions. Measurements made with electrons and hadrons thereby served as benchmarks by which the calibration quality could be judged.

The CalDet was operated with both Near and Far detector electronics. One benefit was that both readout schemes would be fully exercised in a real world environment prior to installation at the detector sites. Additionally operating with both sets of electronics allowed CalDet to search for any discrepancy in response between the two detectors.

The ultimate goal of the program was to measure the response of the MINOS detectors to electrons, hadrons and muons in the energy range of interest to MINOS.

4.2 The Test Beamlines

The CERN PS (proton-synchrotron) East Hall (Fig. 4.1) provides mixed composition secondary beams in the momentum range 0.2-15 GeV/c [46]. The hall was used for some dedicated experiments (DIRAC, HARP) as well as test-beams. Beam was extracted from the PS machine according to a periodic super-cycle. The super-cycle varied in duration from 12 to 21.6 s and was subdivided into basic cycles, each of which corresponded to a specific extraction location.

Figure 4.2 shows an example of a super-cycle. Extractions to the East Hall are labeled EASTB and EASTC. EASTB cycles were sent to the T8 beamline for use by the DIRAC experiment. Beam from the EASTC cycles was split into two branches by an iron septum magnet and focused onto a pair of targets. Secondaries produced off the targets were distributed to the
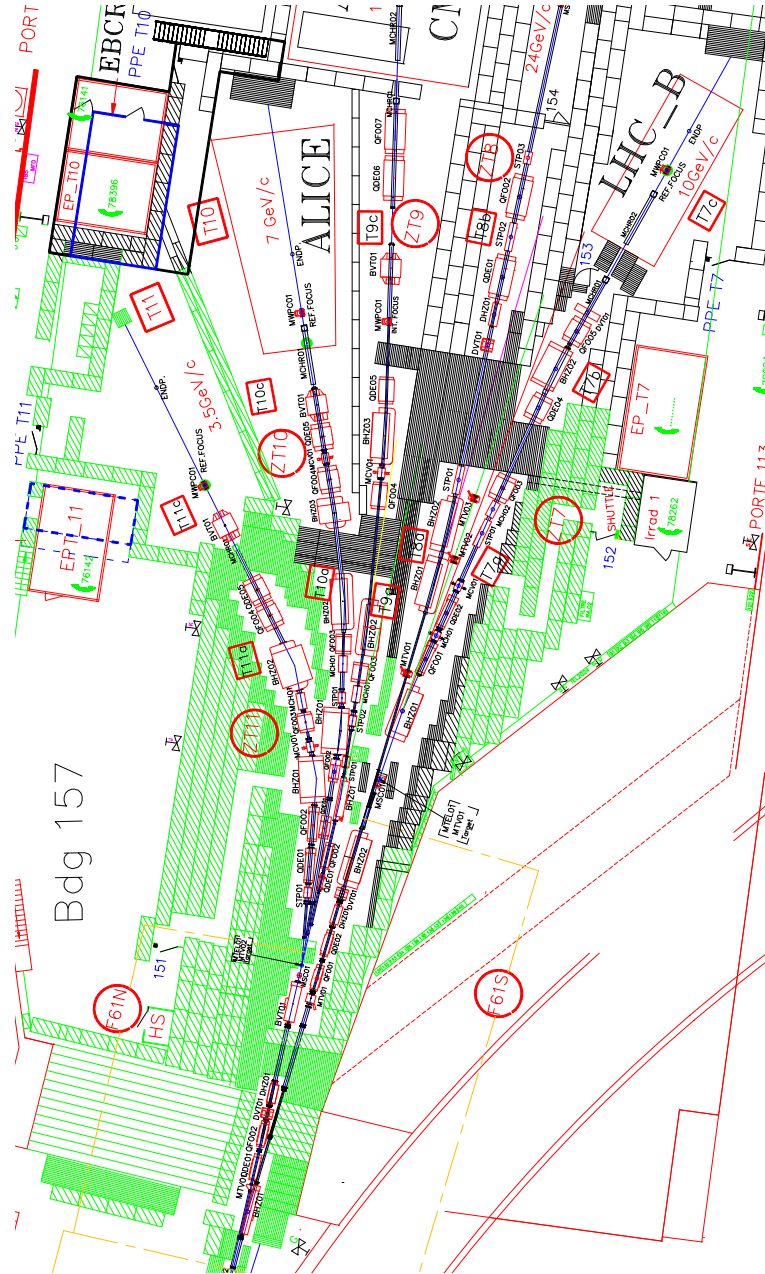
Figure 4.1: The CERN PS East Hall as viewed from above. The 24 GeV/c proton beam enters the hall on the lower edge of the figure. Particles are produced by proton interactions on two targets and distributed to the four secondary beamlines - T7,T9,T10 and T11.
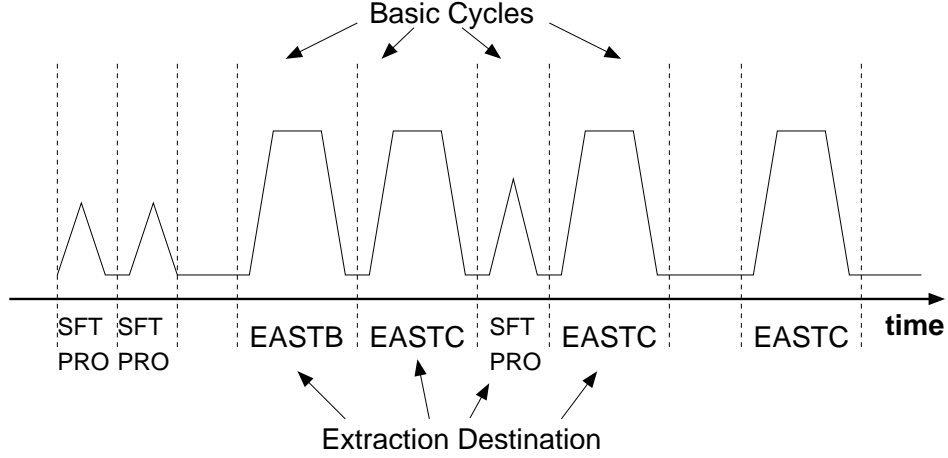
Figure 4.2: An example PS super-cycle. The nominal super-cycle is 16.8 s long and contains 14 basic cycles. Beam is extracted onto the East Hall production targets during the EASTC cycles. There were up to four EASTC cycles in each super-cycle.

T7,T9,T10 and T11 beamlines. The T11,T10 and T9 beamlines share one of the targets and the other is dedicated to the T7 beamline. The momentum range and composition of the secondary beamlines was largely determined by the angular acceptance of the lines with respect to the target.

There were up to four EASTC cycles per super-cycle with a minimum repetition time of 2.4 s. The duration of each spill was approximately 400 ms. The beamlines provided momentum selected, non-separated π, K, e and p particles. Each beam also contained μ produced in π, K decays. The beamlines could be operated in either polarity and at arbitrary momentum settings within their nominal range.

Each beamline has two focusing stages. In the first stage secondary particles produced off the target were focused in both transverse directions by a pair of quadrupole magnets, and the beam was bent horizontally by a dipole

81

magnet. The dipole added dispersion (e.g., correlation between momentum and transverse position) to the beam. The beam passed onto the second stage where it passed through a field lens quadrupole followed by a second dipole. The quadrupole-dipole pair recombined different momentum trajectories in order to make the beam dispersion free at its endpoint. The position and focusing at the endpoint could be altered by varying the currents in a final pair of quadrupoles located downstream of the second dipole. During standard data-taking the beam was focused onto a downstream beam counter located a few cm in front of CalDet.

The intensity of the secondary beams was controlled by using one or two collimators to limit the beam dimensions in the vertical and horizontal directions. The collimators were located in low dispersion sections of the beamline and had a negligible effect on the momentum spread. The momentum bite ($\delta p/p$) of the secondary beams was controlled by another collimator which limited the horizontal extent of the beam in the region between the two dipoles (i.e. in the high dispersion portion of the beamline). The collimators consisted of two brass jaws, 25-30 cm wide, set side by side to form a slit aperture [47]. Stepper motors were used to remotely control the aperture size. Individual collimators were 46, 75 or 90 cm long and reduced the beam intensity by approximately two orders of magnitude when fully closed.

In practice, collimators were never operated with less than a 2.3 mm half aperture in order to reduce scraping effects. The $\delta p/p$ for pions, protons and electrons was $\sim 1\%$. Very low intensities were achieved - based on advice from the PS staff - by defocussing the beam upstream of the intensity controlling collimators. The defocussing caused a larger proportion of the beam to be chopped by the collimators. It was intended that the jaw position always
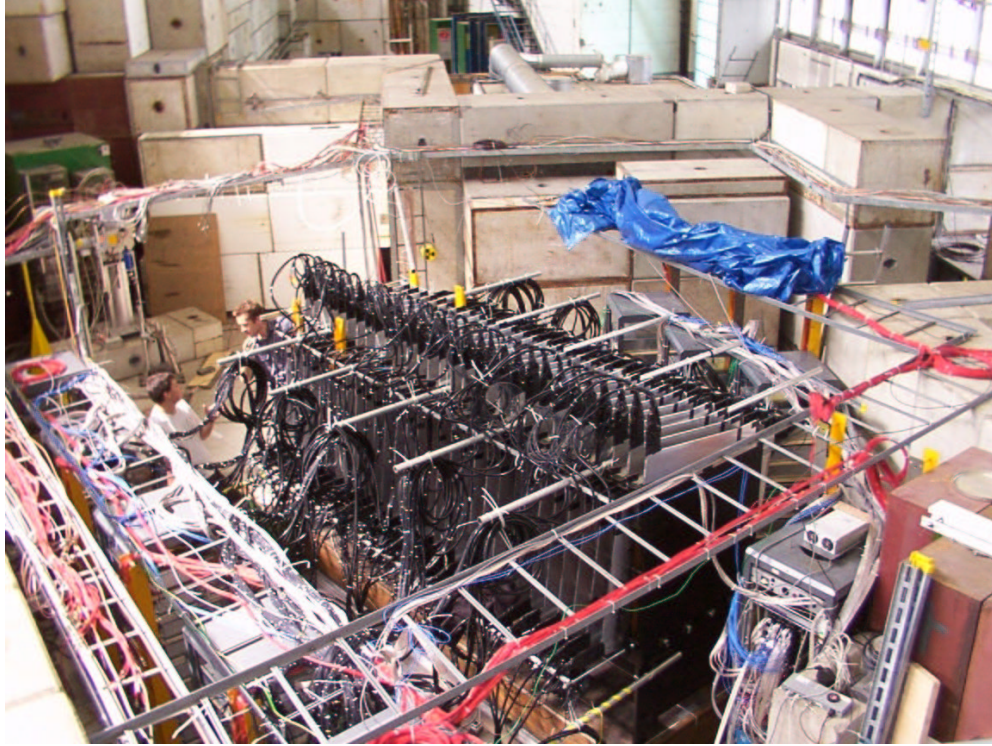
82

Figure 4.3: The CalDet in the T11 experimental area. The beam enters the area through the pitching magnet (in green) in the upper left-hand corner of the photo. Electronics and phototubes are stored in the racks alongside the detector.

be set symmetric to the beam axis. This was particularly important for the momentum selection collimator, since an asymmetric setting would cause a shift in the central momentum of the beam.

4.2.1 The T11 Beamline

CalDet collected data in two beamlines - T11 and T7. The T11 beamline (shown in Fig. 4.4) accepted secondary particles produced in the angular re-

Targets available for the T11 beamline.

Number	Composition	Dimensions (mm)	Comment
1	ZnS	thin screen	low intensity
2	Cu	$\emptyset\ \ 4 \times 25$	
3	Cu	$\emptyset\ \ 4 \times 50$	
4	Be + W	$\emptyset\ \ 4 \times 200 + \emptyset\ \ 20 \times 3$	electron enriched
5	Al	$\emptyset\ \ 5 \times 150$	
6	Be + W	$3 \times 5 \times 200 + \emptyset\ \ 10 \times 3$	electron enriched
7	ZnS	thin screen	low intensity
8	Cu	$\emptyset\ \ 4 \times 100$	
9	Al	thin screen	low intensity
10	Al	$\emptyset\ \ 5 \times 250$	maximum yield
11	Al	$\emptyset\ \ 5 \times 200$	
12	Al	$\emptyset\ \ 80 \times 1$	sheet - low intensity

Table 4.1: Targets available for use with T11. The targets were shared between the T9, T10 and T11 beamlines with the HARP experiment (T9) having de facto control. The notation $\emptyset\ \ A \times B$ indicates the target is cylindrical, A mm in diameter, B mm in length. The notation $A \times B \times C$ indicates the vertical and horizontal profile and thickness of a parallelepiped target. In order to enhance conversion of the photons produced in π^0 decays, a tungsten disk was attached to the downstream section of electron enriched targets.

Magnet current settings for the T11 beamline

P (GeV/c)	QDE01	QFO02	BHZ01	QFO03	BHZ02	QFO04	QDE05	BVT01
1.0	99.83	88.07	218	66.46	155.00	79.00	68.00	39.5
1.2	119.79	105.69	261.00	79.72	186.00	94.78	81.59	47.40
1.4	139.76	123.30	304.00	92.96	217.00	110.56	95.17	55.3
1.6	159.71	140.91	348.00	106.20	248.00	126.34	108.75	63.20
1.8	179.67	158.52	392.00	119.42	279.00	142.11	122.33	71.10
2.0	199.63	176.12	435.00	132.62	310.00	157.88	135.90	79.00
2.2	219.58	193.73	479.00	145.82	341.00	173.67	149.48	86.90
2.4	239.52	211.33	522.00	159.01	372.00	189.47	163.06	94.80
2.6	259.47	228.93	566.00	172.20	403.00	205.29	176.65	102.70
2.8	279.41	246.53	609.00	185.39	434.00	221.15	190.25	110.60
3.0	299.34	264.12	653.00	198.59	465.00	237.05	203.87	118.50
3.2	319.27	281.71	696.00	211.82	496.00	253.02	217.51	126.40
3.4	339.20	299.30	739.50	225.08	527.00	269.07	231.18	134.30
3.6	359.12	316.88	783.00	238.39	558.00	285.22	244.90	142.20

Table 4.2: The magnet current settings used in the T11 beamline. Currents are given in A. The notation QDExx (QFOxx) indicate vertical (horizontal) focusing quadrupoles. BHZxx (BVTxx) indicates horizontal (vertical) bending magnets. Momentum settings below 1 GeV/c were linearly extrapolated based on this table.

Figure 4.4: The layout of the T11 beamline in the CERN PS East Hall.
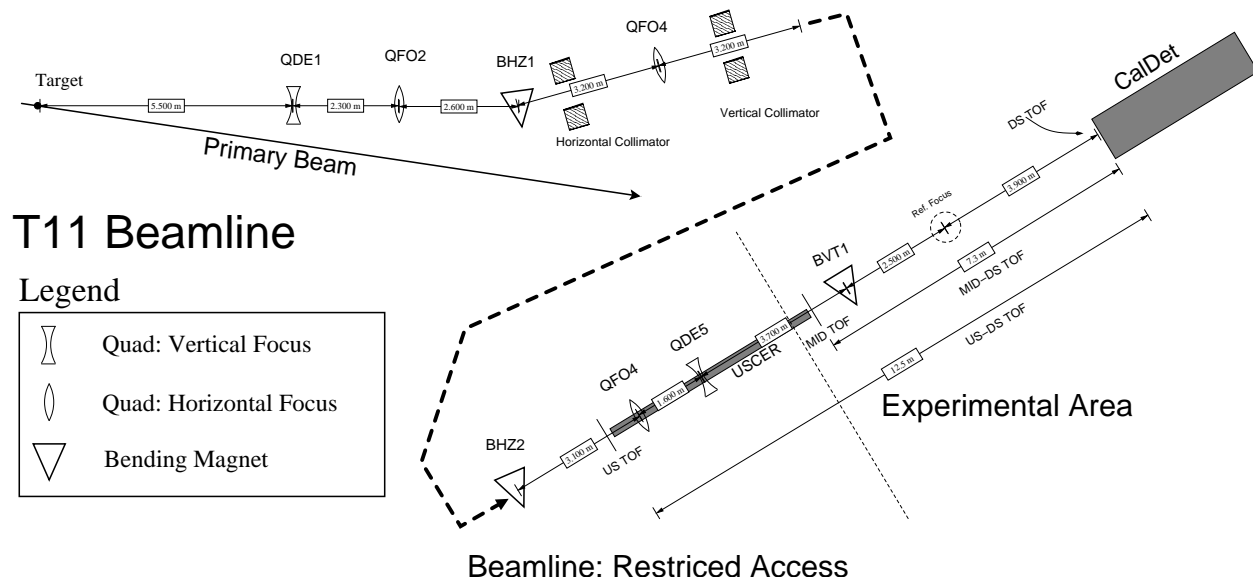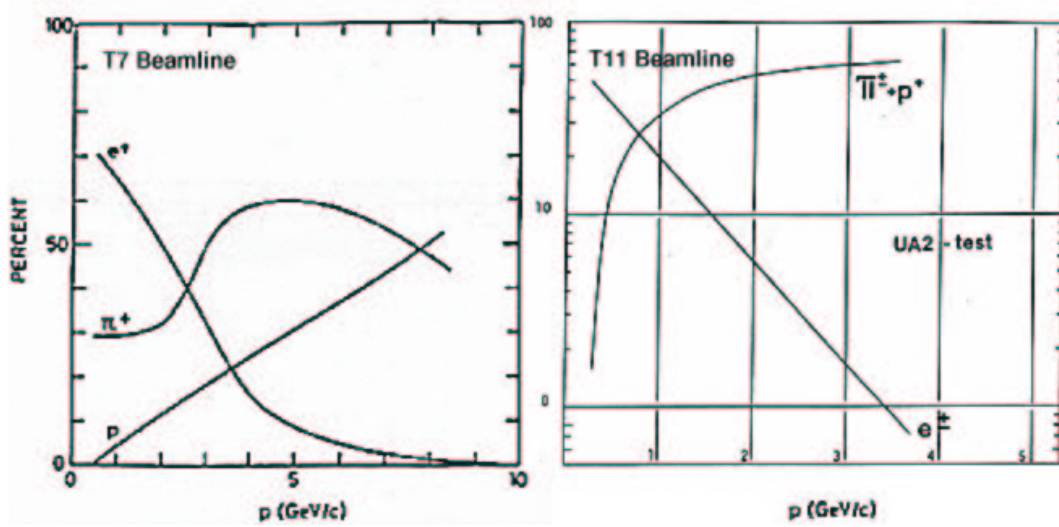
Figure 4.5: The composition of the T11 and T7 beamlines as published by the PS staff [46]. The PS 188 experiment made the measurements of T7 and T11 was characterized during a UA2 beam test. Both measurements are well over a decade old.

gion 148.4±6.2(H)×16.1±19.7(V) mrad with respect to the primary beam axis. The beamline had a nominal momentum range of 0.5-3.6 GeV/c. The (charged particle) beam composition was dominated by pions and protons for momentum settings above 500 MeV/c. Electrons were dominant below 500 MeV/c, but their contribution decreased exponentially with the beam momentum (see Fig. 4.5).

Magnet settings were derived from tables originally prepared by the PS staff [48]. In cooperation with machine experts, the MAD program [49] was used to recalculate some settings in order to account for small changes in the beamline layout. The program was also used to calculate magnet currents for the (originally untabulated) 0.4 and 0.6 GeV/c beam settings. Table 4.2 lists

the magnet currents that were used during data collection.

The T11 beamline shares its production target with the T9 and T10 beamlines. Table 4.1 shows the available targets. In 2002, the T9 user (HARP) had de facto control of the target selection; Targets six and eleven were used in the data-taking. The only difference between the two targets was that the electron content of the beam was somewhat larger with target six. Electrons were tagged, with high efficiency, by threshold Čerenkov counters (see Section 4.4.2), rendering the difference unimportant for the hadron analysis.

In T11, the horizontal (momentum selection) collimator half-aperture was set between 2.3-8.1 mm, depending on the beam intensity. The predicted $\delta p/p$ was less than 1% for all settings [48]. The vertical collimator half-aperture was set in the range 4.0-36.0 mm, according to the beam intensity and the desired rate of data collection . For momentum settings below $\sim 1.8\,\mathrm{GeV/c}$ the secondary flux at the detector decreased with the beam momentum. Consequently, collimators were opened in order to increase the rate of data collection. The $\delta p/p$ was not sensitive to the vertical collimator half-aperture.

4.2.2 The T7 Beamline

The angular acceptance of the T7 beamline was $\pm 12.8(\mathrm{H}), \pm 4.0(\mathrm{V})$ mrad with respect to the beam direction (e.g., a zero degree production angle). The beamline has a nominal momentum range of 0.5-10.0 GeV/c and is shown in Fig. 4.7. The beam composition was dominated by pions and protons for momentum settings above 2 GeV/c. Below 2 GeV/c electrons dominated, with their content decreasing exponentially with the beam momentum.

The T7 magnet settings, shown in Table 4.4, were derived from tables
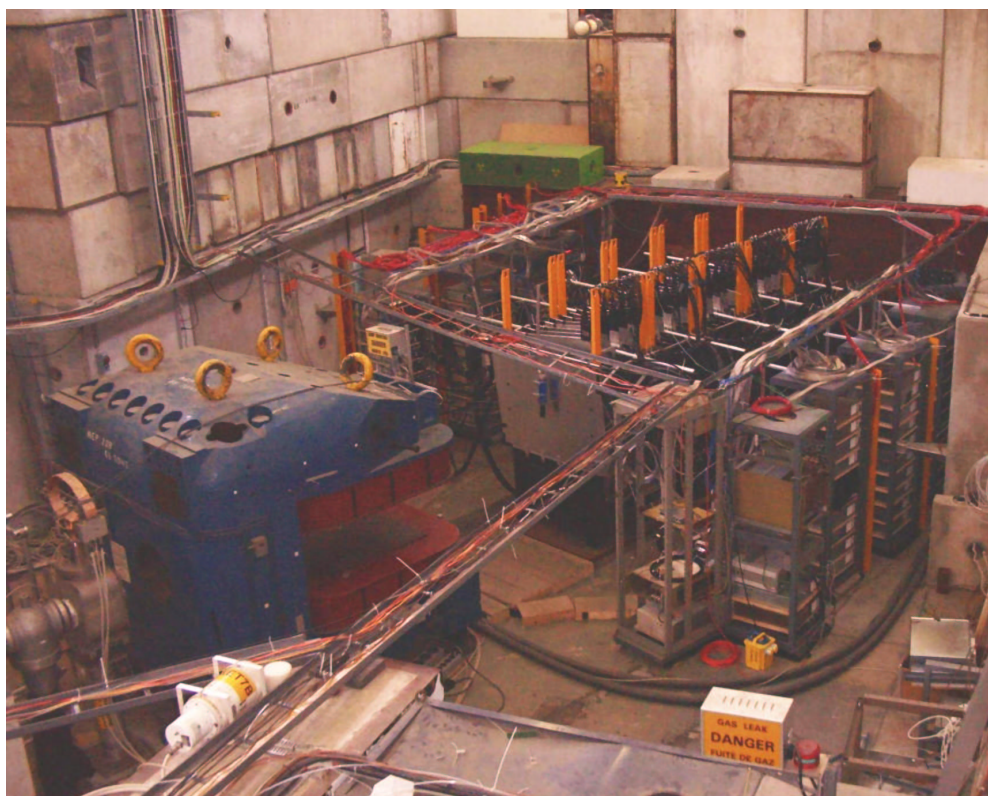
Figure 4.6: The CalDet in the T7 experimental area. The beam enters the area on the lower left-hand side of the photo and proceeds through a hole in the large spectrometer magnet (blue). The magnet was not energized during the data-taking.
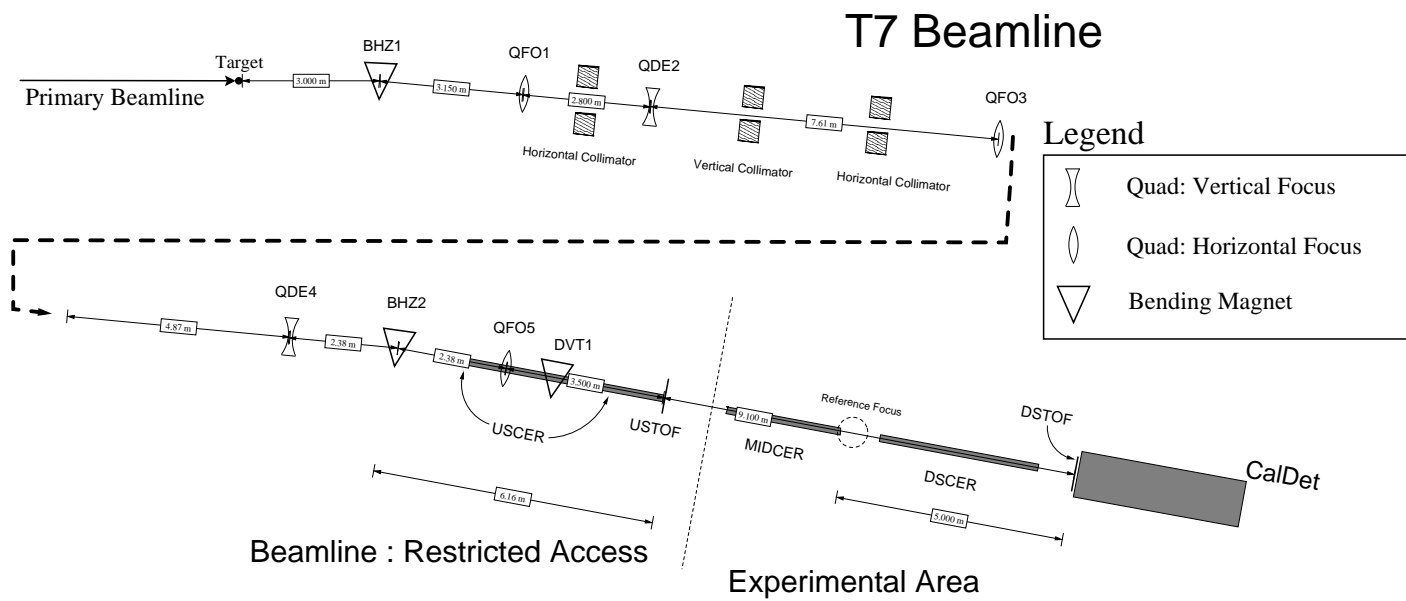
Figure 4.7: The layout of the T7 beamline in the CERN PS East Hall.

Targets available for the T7 beamline.

Number	Composition	Dimensions (mm)	Comment
1	ZnS	thin screen	low intensity
2	Al + W	$\emptyset \ 3 \times 50 + \emptyset \ 20 \times 3$	electron enriched
3	Al	$\emptyset \ 5 \times 250$	
4	-	-	passage (no target)
5	Al	$\emptyset \ 5 \times 190$	
6	$Al_2O_3 - Cr$	$\emptyset \ 5 \times 190$	
7	-	-	passage
8	Al + W	$\emptyset \ 3 \times 125 + \emptyset \ 20 \times 3$	electron enriched
9	Cu	$3 \times 2 \times 160$	
10	Al_2O_3	screen (?)	
11	Al	4×190	
12	-	-	passage

Table 4.3: Targets available for use with T7. The targets were dedicated to the T7 line and could be changed as desired. The notation $\emptyset \ A \times B$ indicates the target is cylindrical, A mm in diameter, B mm in length. The notation $A \times B \times C$ indicates the vertical and horizontal profile and thickness of a parallelepiped target. In order to enhance conversion of the photons produced in π^0 decays, a tungsten disk was attached to the downstream section of electron enriched targets.

Magnet current settings for the T7 beamline

P(GeV/c)	BHZ1	QFO1	QDE2	QFO3	QDE4	BHZ2	QFO5
0.5	19.00	39.81	39.84	20.02	23.23	35.00	14.98
1.0	38.00	79.63	79.67	40.03	46.46	70.00	29.96
1.2	45.60	95.55	95.61	48.03	55.75	84.00	35.95
1.4	53.20	111.47	111.54	56.03	65.03	98.00	41.94
1.6	60.80	127.40	127.47	64.03	74.32	112.00	47.93
1.8	68.40	143.33	143.41	72.05	83.63	126.00	53.93
2.0	76.00	159.24	159.33	80.02	92.87	140.00	59.91
2.2	83.60	175.15	175.26	88.02	102.16	154.00	65.89
2.4	91.20	191.11	191.21	96.07	111.50	168.00	71.90
2.6	98.80	206.98	207.11	104.01	120.71	182.00	77.87
2.8	106.40	222.96	223.08	112.08	130.09	196.00	83.89
3.0	114.00	238.81	238.95	119.99	139.24	211.00	89.84
3.2	121.60	254.71	254.86	127.97	148.53	224.00	95.82
3.4	129.20	270.62	270.78	135.96	157.80	238.00	101.80
3.6	136.80	286.52	286.69	143.95	167.08	252.00	107.78
3.8	144.40	302.42	302.60	151.94	176.36	266.00	113.76
4.0	152.00	318.32	318.51	159.93	185.63	282.00	119.75
5.0	189.00	397.75	397.99	199.94	232.22	352.00	149.65
6.0	227.00	477.09	477.38	240.16	279.33	419.00	179.57
7.0	266.00	556.32	556.65	280.80	327.46	494.00	209.56
8.0	305.00	635.42	635.79	322.22	377.46	564.00	239.68
9.0	347.00	714.36	714.78	364.93	430.74	640.00	270.04
10.0	395.00	793.14	793.61	409.75	490.08	708.00	300.78

Table 4.4: The magnet current settings used in the T7 beamline. Currents are given in A. The notation QDExx (QFOxx) indicate vertical (horizontal) focusing quadrupoles. BHZxx (BVTxx) indicates horizontal (vertical) bending magnets. Intermediate momentum settings, such as those between 0.5-0.8 GeV/c were interpolated based on values in this table.

prepared by the PS staff. As in the T11 beamline, the MAD program was used to update the settings in reaction to small changes in the magnet positions.

The T7 beamline has a dedicated target station, holding the set of user selectable targets listed in Table 4.3. The choice of target depended on the beam momentum, primary beam intensity and run plan. Generally, an electron enriched target (target 2 in Table 4.3) was used for momentum settings below $3\,\text{GeV/c}$. For beam momenta above $2.8\,\text{GeV/c}$, runs were taken in either hadron or electron mode. The electron mode included signals from the threshold Čerenkov counters in the trigger logic (see Section 4.3). Target 2 was used in the electron triggered runs. In order to reduce the beam intensity for hadron runs, a screen target (target 1 in Table 4.3) was typically used for momentum settings above $7\,\text{GeV/c}$. An aluminum target (target 3) was used during hadron runs at intermediate energies. The test-beam results are not expected to depend on the target composition.

The T7 beamline has one vertical and two horizontal collimators. The first horizontal collimator and the vertical collimator were used to control the beam intensity. The vertical half-aperture was varied in the range between 3-40 mm, while the horizontal half-aperture varied over 3-6 mm. Larger apertures were used at low momentum settings and when the screen target was employed. The second horizontal collimator was used to control the momentum spread and, to a lesser degree, the beam intensity. Half-aperture settings varied between 2.8-6 mm. The expected momentum spread was less than 1% for all runs.

4.3　Trigger System

Null Trigger Running (2001)

The calibration detector (with Far Detector electronics) was originally intended to operate in a free running mode identical to that of the Far Detector. In the free running mode each VA chip was independently read out when the signal from the associated dynode exceeded a threshold of approximately 1/3 photoelectron. The free running data was then time sorted and the Far Detector plane trigger algorithm was applied by the DAQ. The initial data from the fall 2001 beam test was taken in this mode.

Early analysis of the 2001 data showed that there was a significant effect due to readout dead-time. Each VA chip incurs at least a $\sim 5\,\mu s$ dead-time while being read out, the bulk which occurs during digitization. Since six VA chips are multiplexed onto one VMM ADC module, the dead-time becomes additive because the chips are digitized in succession. Thus, the readout dead time for one VA chip can be as large as $\sim 30\,\mu s$ and is dependent on the activity of the other chips served by the shared VMM.

The readout dead-time can be understood if a comprehensive record of the readout history of each chip is kept. Keeping such a record precludes the application of a plane trigger by the DAQ since some of the necessary information would be lost. Because of this, all data was written out to disk and analysis code was developed to track the dead time status of the detector. Good events were then selected by time sorting individual hits into events and requiring that the detector was alive at the time of those event. This mode of running is known as *null trigger*.

By tracking the dead-time status of the detector, a sample of good

events were isolated. Unfortunately the process was very inefficient for two reasons. First, high trigger rates made it necessary to inhibit readout of the entire detector for $\sim 80\%$ of each spill. Second, each VA chip was still dynode triggered and read out independently of all others. Large instantaneous rates and noise in the experimental hall (coming from residual radioactivity and neutrons from adjacent beamlines as well as PMT dark current) coupled with the independence of each chip and led to a high incidence of *asynchronous* dead time. The result was that many events had one or two dead chips. The combination of 80% read out inhibition and asynchronous deadtime made the overall efficiency for collecting fully live events on the order of a few percent.

External Trigger (2002-3)

Because of the the low efficiency of the 2001 operation, the ability to trigger CalDet with external signals was added for the fall 2002 beam test. Each VARC was reconfigured so that the free running mode could be enabled for a short time (500 ns) by the application of a TTL pulse. The TTL pulses were generated by the coincidence of two beam counters separated by several meters (see Tab. 4.6). The beam counters were also utilized by the time of flight system. The coincidence trigger logic is shown in Fig. 4.8. The trigger logic was used to ensure that:

1. A $50\,\mu s$ veto was asserted after each trigger. This was done to allow the detector to recover completely before the next trigger.

2. Triggering was inhibited whenever the time of flight TDC buffer was full. This ensured that every triggered event had a good time of flight measurement.

3. A veto was asserted during VARC buffer swaps.

4. Light injection flashing was inhibited during beam spills.

5. Between beam spills the detector was triggered in sync with flashes from the light injection system.

6. Optionally, threshold Čerenkov counters could be included in the trigger. The feature was typically used to collect electron (and suppress hadron) events for higher momentum beam settings (above $4\,\text{GeV/c}$ in T7 and $3\,\text{GeV/c}$ in T11).

The time of the trigger relative to the time of the event is rather important. The 2002 running period utilized VA electronics which shape and hold the PMT signal. Because of this, the trigger signal was allowed to arrive on the VARC inputs at any time up to $\sim 500\,\text{ns}$ after the event. This allowed cable lengths to be chosen in order to conveniently route signals from the beam counters to the trigger logic crate and from there to the VARCs. The 2003 running period featured a mixture of QIE and VA electronics. The QIE electronics required the trigger to arrive no later than $\sim 180\,\text{ns}$ after the event. This requirement made the use of very short, directly routed cables necessary.

Additionally, the trigger logic was able to use the beam spill signal from the accelerator complex to enable the detector to take null trigger data in between spills. This feature was used to take cosmic ray calibration data during some test beam runs. When running with Near Detector electronics the trigger logic was also used to insert a so called *fiducial timing* time stamp into the data stream. This was done each second and allowed the Near and
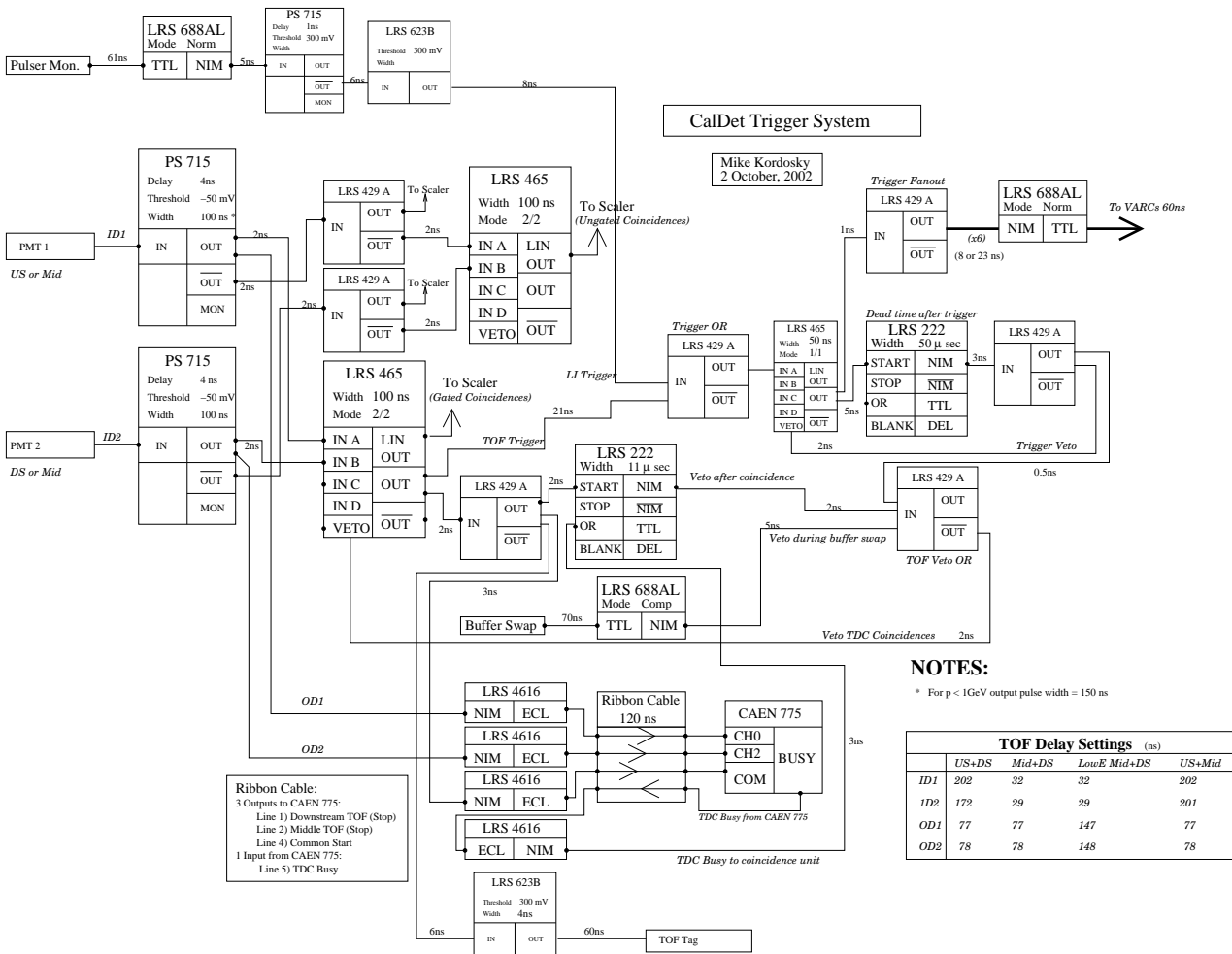
Figure 4.8: Beam trigger and time of flight electronics system: fall 2002 far+far running.

Far detector clocks to be precisely synchronized offline.

The external trigger increased the efficiency of data taking by a factor of almost 100. Comparisons with 2001 data showed that there was no apparent bias introduced by the trigger.

Some additional features were added to the trigger system for the 2003 fall beam test. This running period was used to directly compare the Near and Far detector electronics as well as run with Near Detector electronics only. The trigger system was modified slightly to better accommodate the Near Detector electronics. The modifications were:

1. The $50\,\mu s$ veto was increased to $70\,\mu s$.

2. The beam spill signal from the accelerator complex was used to (optionally) start SGATE readout in the Near Detector electronics. This running mode (known as *External SGATE*) prevented the electronics from being externally triggered. Instead, twenty contiguous Near Detector time slices were readout periodically during each spill.

3. When in External SGATE running mode, the TOF system was inhibited unless an SGATE readout was ongoing in the Near Detector electronics. This was done in order to assure that each event could be read out by both the Near and Far Detector electronics.

4. A coincidence between three beam counters was required. This feature was added to suppress events in which the particle traversed the light guide of the most downstream counter. The time of flight measured for these events differed systematically by about 2 ns from that measured when the particle traversed the scintillator.

PMT	Height (cm)	Width (cm)	Thickness (cm)	Comment
XP2030	12.5	5.5	1.5	2002 beam tests
XP2230	5.0	5.0	1.5	2003 beam tests

Table 4.5: The phototubes and scintillator dimensions for the beam counters used in 2002-03.

The flexible, but simple, external trigger enabled CalDet to collect high statistics, high quality data. The trigger was versatile and could be reconfigured as desired. On occasion, new triggering schemes were proposed at breakfast and implemented before lunch. As the 2001 running proved, CalDet would not have been able to meet its experimental goals without the external trigger.

4.4 Particle Identification Systems

4.4.1 The Time of Flight System

Hardware overview

The CalDet time of flight (TOF) system uses beam counters consisting of phototubes coupled via light guide to plastic scintillator paddles (see Tab. 4.4.1). One of the paddles (labeled USTOF in T11) is located between the magnets BHZ02 and QFO04 upstream of the T11 experimental area (see Fig. 4.10). This counter is not easily accessed due to the level of radiation in the area. The other two counters (called MIDTOF and DSTOF in T11) are movable. Figures 4.9 and 4.11 show the layout of the T11 and T7 beamlines with the location of the TOF counters marked. Table 4.6 lists the distances between paddles in different running configurations.
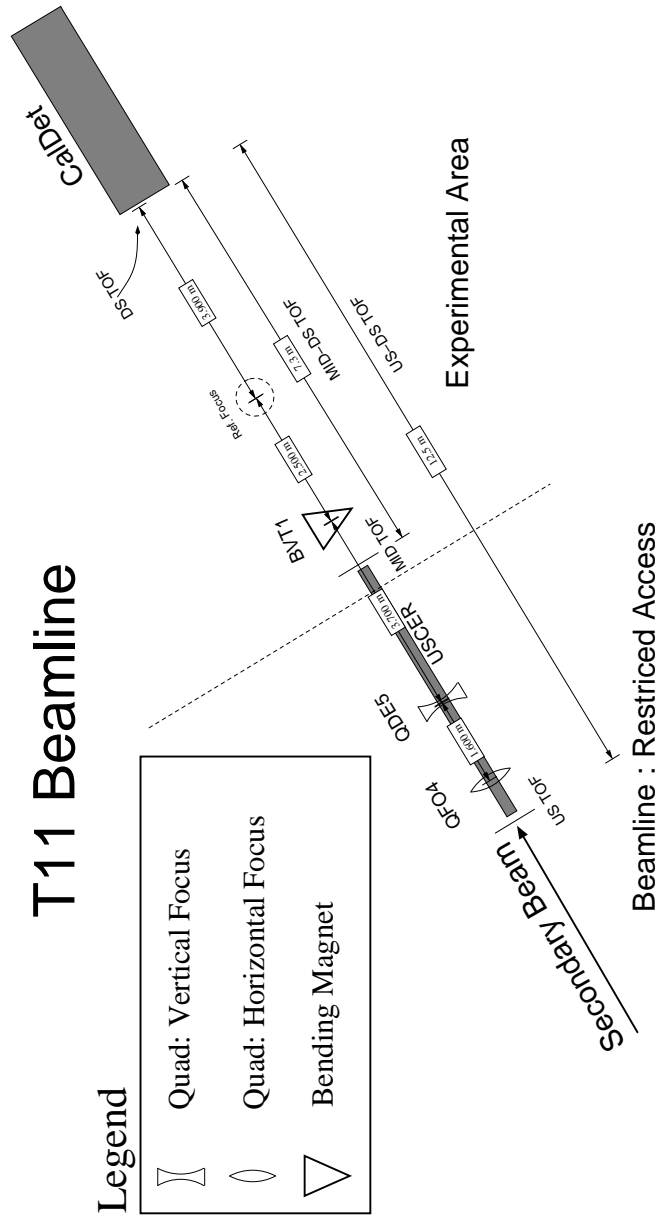
Figure 4.9: The downstream portion of the T11 beamline, showing the location of time of flight and Čerenkov counters.
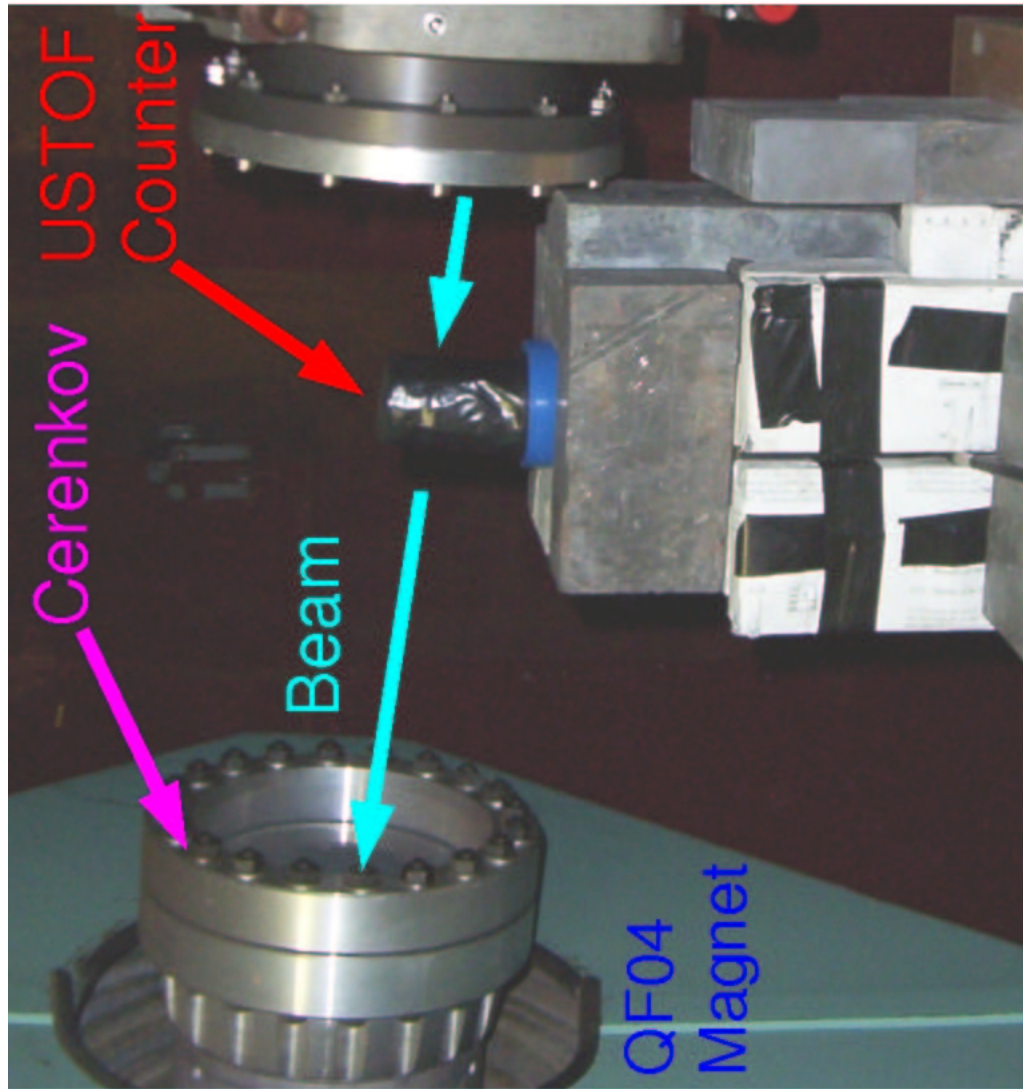
Figure 4.10: The upstream time of flight counter in T11.
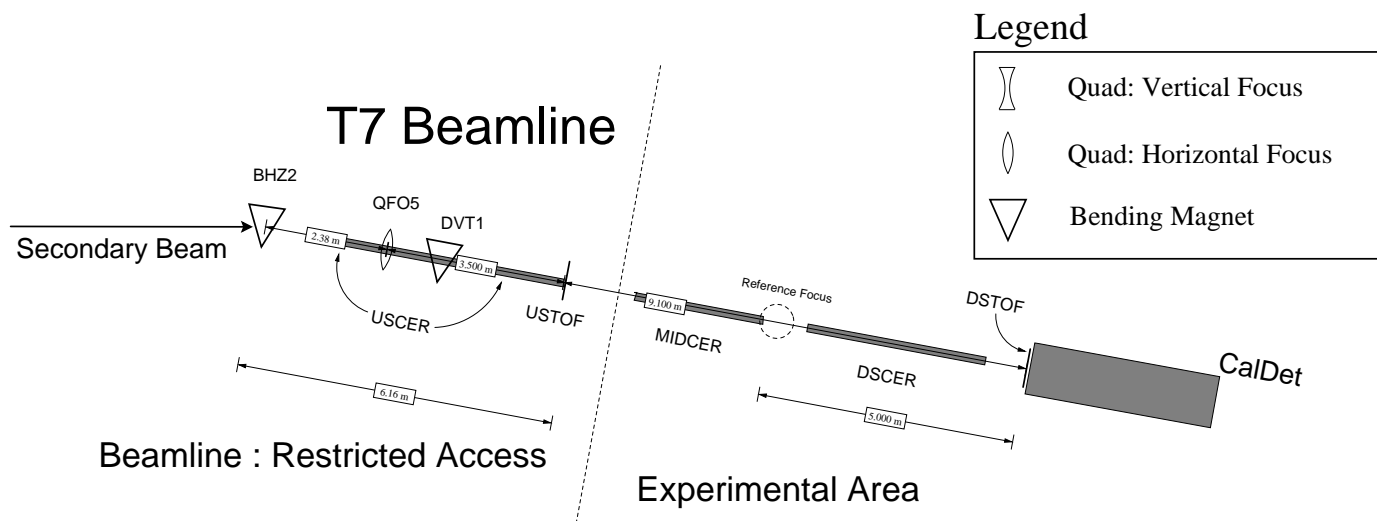
Figure 4.11: The downstream portion of the T7 beamline, showing the location of time of flight and Čerenkov counters.

Beam Line	Configuration	Distance (m)	Comment
T7	US to DS	9.1	normal running 2002
T11	US to DS	12.5	$0.8\,\mathrm{GeV/c} \leq p \leq 3.6\,\mathrm{GeV/c}$
T11	MID to DS	7.3	$p \leq 0.8\,\mathrm{GeV/c}$
T11	US to MID	4.5	angle running 2002
T7	US to DS	9.1	all running modes 2003
T11	US to DS	8.0	all running modes 2003

Table 4.6: The time of flight baselines used in the fall 2002-3 beam tests.

The signal from each counter was sent through coaxial cable to a NIM crate containing the trigger electronics. The length and type of cable depended on the position of the counters and the running mode. Low dispersion cables were used whenever practicable. The phototube high voltages were supplied by a LeCroy 4032 located in the counting house adjacent to the experimental area. Each phototube was encased in a cylindrical mu-metal shield in order to decrease the effect of magnetic fields from nearby beam elements.

Readout

Signals from each of the two counters were fed into a Phillips 715 constant fraction discriminator (CFD) channel. The CFD shaping time was set at 4 ns. One output from each channel of the 715 was routed to a LeCroy 465 logic unit (see Fig. 4.12). This unit constructed the coincidence trigger. The output of the 465 was sent to a LeCroy 4616 to be converted to ECL. The converted signal was then sent over a 120 ns ribbon cable to the common start input of a CAEN 775 VME TDC module.

The reception of common start by the TDC triggered the ramp-up of the time to amplitude conversion (TAC) section thereby beginning the time of flight measurement. The TOF measurement for each counter was terminated
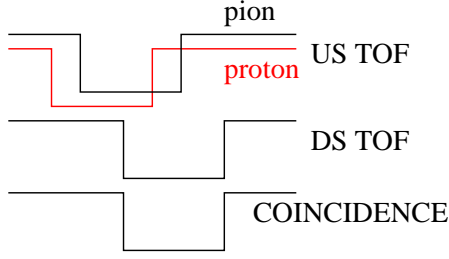
Figure 4.12: A "scope trace" schematic showing the inputs to the coincidence unit (US TOF and DS TOF) and the coincidence output. The DS TOF signal comes later than the US TOF signal and thereby sets the time of coincidence. The diagram is shown as it would be on an oscilloscope triggered on the coincidence.

upon the reception of a stop signal at the TDC. The stop signals were taken from the output of the Phillips 715 and cable delayed before being converted to ECL and passed over the 120 ns ribbon cable to the TDC. The amount of delay (77 ns in 2002, 147 ns in 2003) was chosen in order to assure that the stop signals arrive at the TDC more than 15 ns after the common start.

The TDC commenced with digitization following the reception of each stop signal. The module was operated in its most sensitive mode, yielding a 35 ps LSB with a 12-bit (143.36 ns) range. After digitization the results are placed into a thirty-two event buffer to await readout. Events in the buffer were time-ordered but not time-stamped. The digitization period lasted $\sim 11\,\mu s$. During that time the TDC could not respond to a new common start signal and notified the user by setting the BUSY output active. The BUSY signal was also asserted when the thirty-two event buffer on the TDC was full. The time of flight system used the BUSY signal to veto any further coincidences.
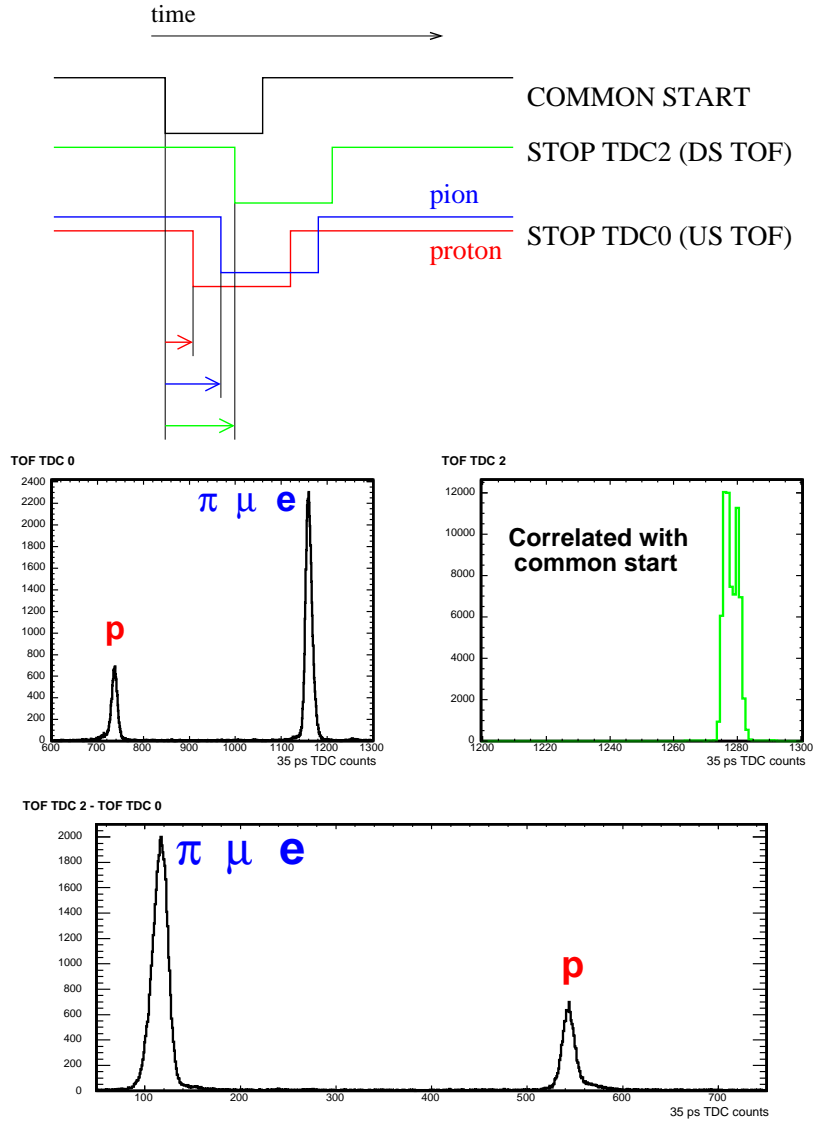
Figure 4.13: A scope trace schematic of signals input to the TDC module. The time of COMMON START is set by the counter corresponding to TDC2. This results in a narrow distribution of times on TDC2. Two traces are shown for TDC0, one for protons, the other for pions. The histograms show distributions for TDC0 and TDC2 (center right and left) and the difference TDC2-TDC0 (bottom). The data is from a 1 GeV run with a 12.5 m baseline.

The TDC module was read out by the DAQ once every 50 ms long time-block. Typically there were multiple events in the TDC buffer. Since the TDC did not time stamp each event, some additional information was needed in order to match up TDC digitizations with hits in the detector. The matching was accomplished by using the TDC coincidence output to generate a TOF-tag hit on an otherwise empty VA channel. The timing of the tag was adjusted (via cable delay) in order to synchronize it with hits in the detector. During the offline analysis each one second time frame was processed by time-sorting hits into events and matching the events with TDC readouts. The first event with a TOF-tag was then matched up with the first TDC readout, the second event with the second TDC readout and so on. This scheme relied on the fact that TDC events were stored in sequential order in the module's internal buffer. Occasionally the number of TOF-tag hits in a time block was not equal to the number of TDC events in the module's buffer. An unambiguous matching could not be done in this case and the TDC data from that time frame was ignored. The resulting events lacked time of flight information and were generally thrown out in subsequent analysis.

Analysis

The data from each TOF event consisted of one 12-bit word for each of the two counters. For each counter the word recorded the amount of time (in 35 ps counts) between the assertion of common start and the reception of the stop signal. The specific value of the data word was arbitrary since it depended on the amount of cable and electronics delay between the discriminator outputs and the inputs on the TDC. The measured TDC value from one of the counters (in this case the DS one) was highly correlated with the time of the coincidence

106

since the time of the coincidence (and hence common start) was determined by the overlap of the logic pulses from the two counters (see Fig. 4.13). The width of the correlated channel's TDC distribution was a measure of the jitter in the output of the coincidence module. A jitter of $\sim 2-3$ counts was observed.

The jitter in the coincidence was removed by considering the difference TDC2-TDC0. An arbitrary offset left due to cable lengths still remained. That offset was unimportant since the TOF system was primarily used for particle identification rather than an actual measure of the speed of relativistic particles. The distance in time of flight between particle species with masses m_1 and m_2 and momentum p is not arbitrary but is instead given by

$$\Delta t_{12} = \frac{L}{c} \left[\sqrt{1 + \frac{m_1^2}{p^2}} - \sqrt{1 + \frac{m_2^2}{p^2}} \right] \tag{4.1}$$

where L is the distance between counters and c is the speed of light.

Figures 4.14-4.15 show distributions measured in T11 during the fall 2002 running period. The distribution for hadrons (and muons) is shown in black. Electrons were independently selected by the Čerenkov system and are shown in blue. The position and width of the hadron peaks is estimated by a combined fit of 2 Gaussians with a flat background. Between 1.4-2.8 GeV/c a small contribution from kaons can be distinguished and an additional Gaussian is used in the fit. Below 1.2 GeV/c no kaons are observed and above 2.8 GeV/c kaons are too relativistic to be distinguished from pions. The parameters displayed on Fig. 4.14-4.15 correspond to the Gaussian mean (e.g., Xmean), RMS (e.g., Xrms) and scale (e.g., Xnorm)and a constant background (bkgrd). The X is a label taking on the values e,π,K and p which denote to electrons, combined pions and muons, kaons and protons respectively.

The resolution of the system was determined by the width of the Gaus-

107

run 40926 : + 3.6 GeV

		htof	
		Entries	44807
χ^2 / ndf	52.54 / 30	Mean	172.36
		RMS	20.40
		χ^2 / ndf	244.58 / 90
e norm	12.35± 1.16	π norm	1337.49 ± 11.52
		π mean	155.19± 0.04
		π rms	6.66± 0.04
		K norm	0.00± 0.00
e mean	154.80± 0.51	K mean	-9999.00± 0.00
		K rms	10.00± 0.00
		p norm	1204.90± 11.35
		p mean	193.94± 0.05
e rms	6.50± 0.44	p rms	5.82± 0.04
		bkgrd	7.40 ± 0.66

run 40912 : +2.4 GeV

		htof	
		Entries	17599
χ^2 / ndf	21.63 / 28	Mean	186.55
		RMS	39.10
		χ^2 / ndf	159.31 / 126
e norm	7.86± 1.09	π norm	624.87± 8.81
		π mean	157.34 ± 0.06
		π rms	5.53± 0.06
		K norm	15.76 ± 1.49
e mean	156.08± 0.58	K mean	79.59± 0.88
		K rms	6.09± 0.71
		p norm	355.19± 6.50
		p mean	238.63± 0.08
e rms	5.48± 0.63	p rms	5.38± 0.06
		bkgrd	2.67± 0.24

Figure 4.14: The time of flight distribution for runs 40926 (left, 3.6 GeV/c, positive polarity) and 40912 (right, 2.4 GeV/c, positive polarity). In each figure the two large peaks correspond to pions (left) and protons (right). The small peak on the far left corresponds to electrons. The baseline was 12.5 m. The shoulder on the pion peak in run 40912 is due the the presence of kaons. The abscissa is binned into single 35 ps TDC counts and the scale along the ordinate is arbitrary. The fit parameters are discussed in the text.
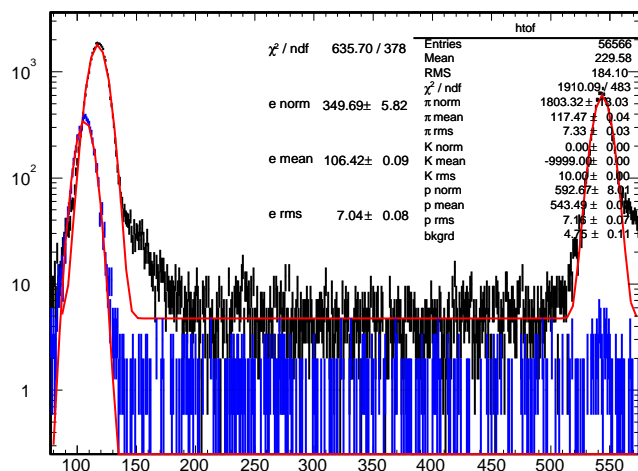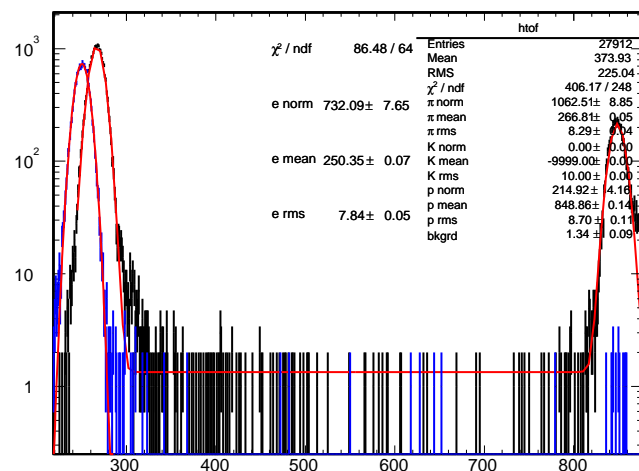
Figure 4.15: The time of flight distribution for run 40622 (left, 1 GeV/c, positive polarity) and 40781 (right, 600 MeV/c, positive polarity). In each figure, the leftmost peak corresponds to electrons, the middle peak to to pions and the rightmost peak corresponds to protons. The baseline was 12.5 m. The abscissa is binned into single 35 ps TDC counts and the scale along the ordinate is arbitrary. The fit parameters are discussed in the text.
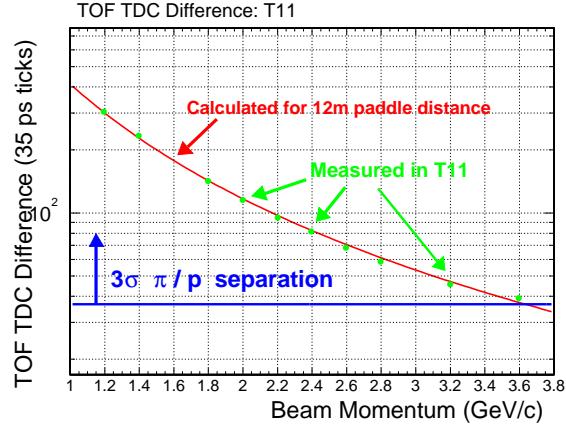
Figure 4.16: $TOF(p) - TOF(\pi)$ in TDC ticks vs. the primary beam momentum. The 210 ps resolution of the system and the 12 m baseline of T11 allowed for $> 6\sigma$ discrimination between pions and protons over the entire momentum range. The blue line in the figure corresponds to $3\sigma_p + 3\sigma_\pi$.

sian fits described above. For momenta higher than $2\,\mathrm{GeV/c}$ the measured resolution was $\sim 210\,\mathrm{ps}$. This allowed pions and protons to be easily distinguished over the entire range of momenta accessible in T11 (see Fig. 4.16).

The baseline in T7 was somewhat shorter, hence the separation power was not as great. Figure 4.17 shows the distribution for a $2.8\,\mathrm{GeV/c}$ run taken in T7. Events with a signal in one of the two Cerenkov counters are shown in blue. Most of those events are electrons though a small contribution from delta-rays, produced in the Cerenkov by protons, is also observed. The pion and proton peaks are separated by more than 6σ. In T7, the Čerenkov system was used to separate pions and protons at momenta above $2.8\,\mathrm{GeV/c}$. Figure 4.17 shows the TOF distribution from a $3\,\mathrm{GeV/c}$ run taken in T7. Events selected as pions by the Čerenkov are shown in blue and those selected as electrons are in green. The remaining events (corresponding to kaons and protons)
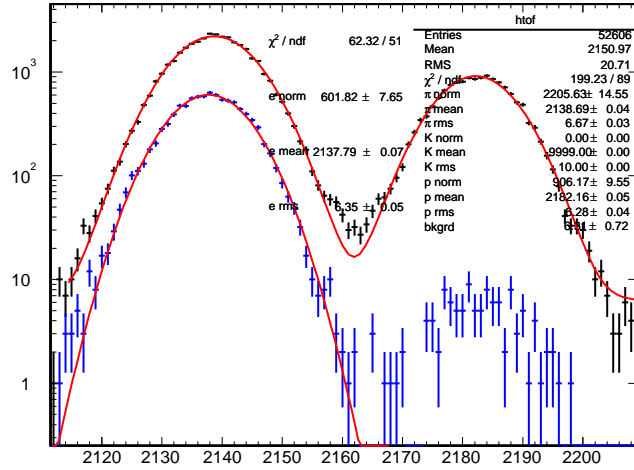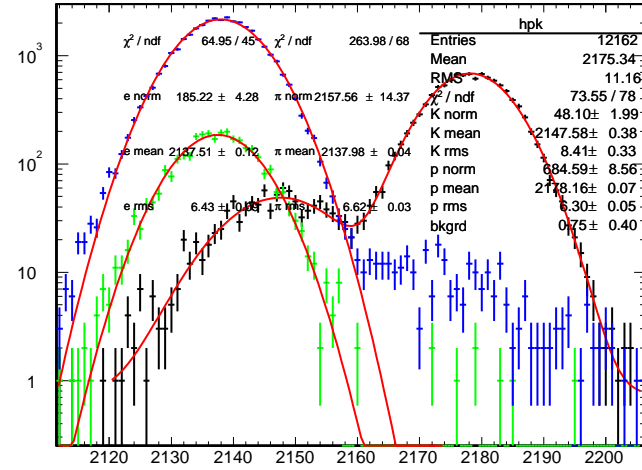
Figure 4.17: The time of flight distribution for runs 50487 (2.8 GeV/c, positive polarity) and 50266. In each figure, the the two large peaks correspond to pions (left) and protons (right). The smaller peak on the left corresponds to electrons. At 2.8 GeV/c pions, protons and kaons were below the Čerenkov threshold, but at 3 GeV/c pions were above threshold allowing the few % kaon content to be resolved as a shoulder on the proton distribution. The baseline was 9.1 m. The abscissa is binned into single 35 ps TDC counts and the scale along the ordinate is arbitrary. The fit parameters are discussed in the text.

Time of Flight : run 50549 : +4 GeV

π norm	1930.38	K norm	140.89
π mean	2138.83	K mean	2154.55
π rms	6.51	K rms	9.92
e norm	240.63	p norm	671.99
e mean	2138.73	p mean	2160.77
e rms	6.11	p rms	5.65
		bkgrd	0.12
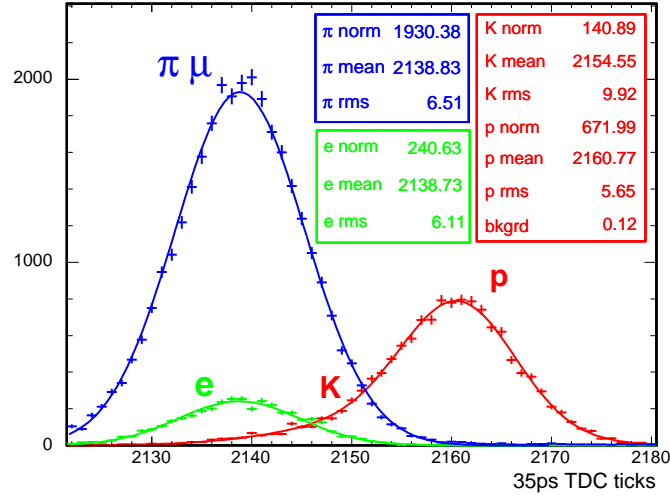
Time of Flight : run 70644 : +4 GeV

π norm	9913.86	K norm	352.35
π mean	417.08	K mean	423.69
π rms	3.51	K rms	5.16
e norm	1909.84	p norm	3860.36
e mean	416.08	p mean	437.90
e rms	3.37	p rms	3.21
		bkgrd	11.60
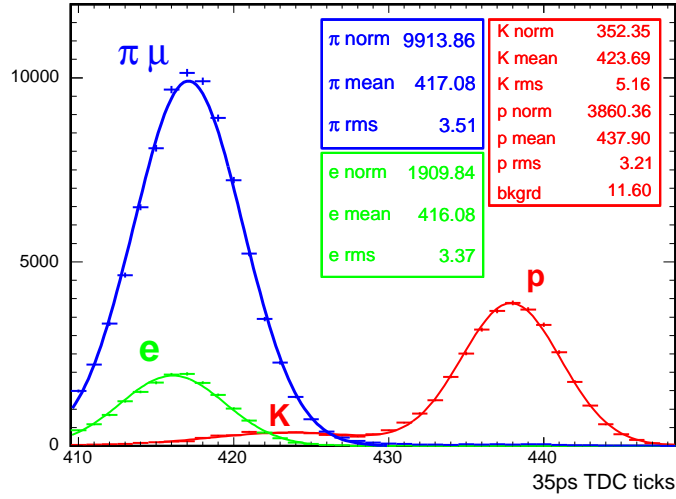
Figure 4.18: The time of flight distribution for two runs taken at $4.0\,\mathrm{GeV/c}$ in the T7 beamline. Pions and muons, as identified by a single Čerenkov counter, are shown in blue. Electrons, shown in green, were selected by requiring a signal in both Čerenkov counters. Protons (as well as a small number of kaons) were selected by requiring no signal in both Čerenkov counters. The data in the upper figure was collected in 2002, and the bottom is from 2003. The scale on the ordinate is the number of events per $35\,\mathrm{ps}$ TDC count (i.e., tick).

had no Čerenkov signal and are shown in black.

The time of flight resolution was improved in the T7 2003 running by installing new, higher quality counters. Figure 4.18 compares two distributions - one from 2002 and the other from 2003. The Čerenkov system was used to select electrons (green in the figure), pions/muons (blue) and protons/kaons (red). The resolution, as measured by the width of the Gaussian fits, improved by approximately 40%.

Unfortunately, the new counters were more sensitive to stray magnetic fields. In T7, both the upstream and downstream counters were located in field free regions (see Fig. 4.11). During the 2003 running in T11, the middle and downstream counters were used to form coincidences (the inaccesible upstream counter was too far away to provide the trigger signal for the Near Detector electronics). The middle counter was installed $\sim 30\,\mathrm{cm}$ from the BVT01 magnet (see Fig. 4.9), but stray fields reduced the resolution. In the end, the performance in T11 2003 was similar to the 2002 performance.

4.4.2 The Čerenkov System

Essential theory

Čerenkov radiation is emitted when charged particles travel through a medium at a speed larger than the speed of light in that medium. The radiation is emitted at an angle θ_c (the Čerenkov angle) with respect to the particle's trajectory according to the formula:

$$\theta_c = \cos^{-1}\left(\frac{1}{\beta n}\right) \qquad (4.2)$$

where n is the index of refraction.

When $\frac{1}{\beta n} < 1$, particles are above threshold and emit Čerenkov radiation with an intensity proportional to $\sin^2 \theta_c$. The Čerenkov angle may be expressed as a function of the particle momentum and gas pressure. The relationship between the pressure and the index of refraction is

$$n = 1 + kP \tag{4.3}$$

with the pressure P in atmospheres and $k = 4.1 \times 10^{-4} \, \text{atm}^{-1}$. The value of k depends on the gas and is listed here for CO_2. Using the identity

$$\sin^2 \left(\cos^{-1} x \right) = 1 - x^2 \tag{4.4}$$

one finds

$$\sin^2 \theta_c = 1 - \frac{1 + \frac{m^2}{p^2}}{(1 + kP)^2} \tag{4.5}$$

$$\approx 2kP - \frac{m^2}{p^2} \tag{4.6}$$

$$\rightarrow 2kP \quad \text{for electrons} \tag{4.7}$$

The relation for electrons was valid over the entire range of pressures and momentum settings used in the datataking. For moderate pressures ($< 5 \, \text{atm}$) and momenta ($< 10 \, \text{GeV/c}$) the Čerenkov angle is less than $4°$. Figure 4.19 shows the threshold pressure vs. the beam momentum for μ, π, K. Electrons are above threshold over the entire range of the figure.

Hardware overview

The PS complex supplied threshold Čerenkov counters for use in the East Hall test beams[46]. These counters consisted of aluminum tubes with a diameter of 15 cm. The tubes came in 1 m sections that could be joined to
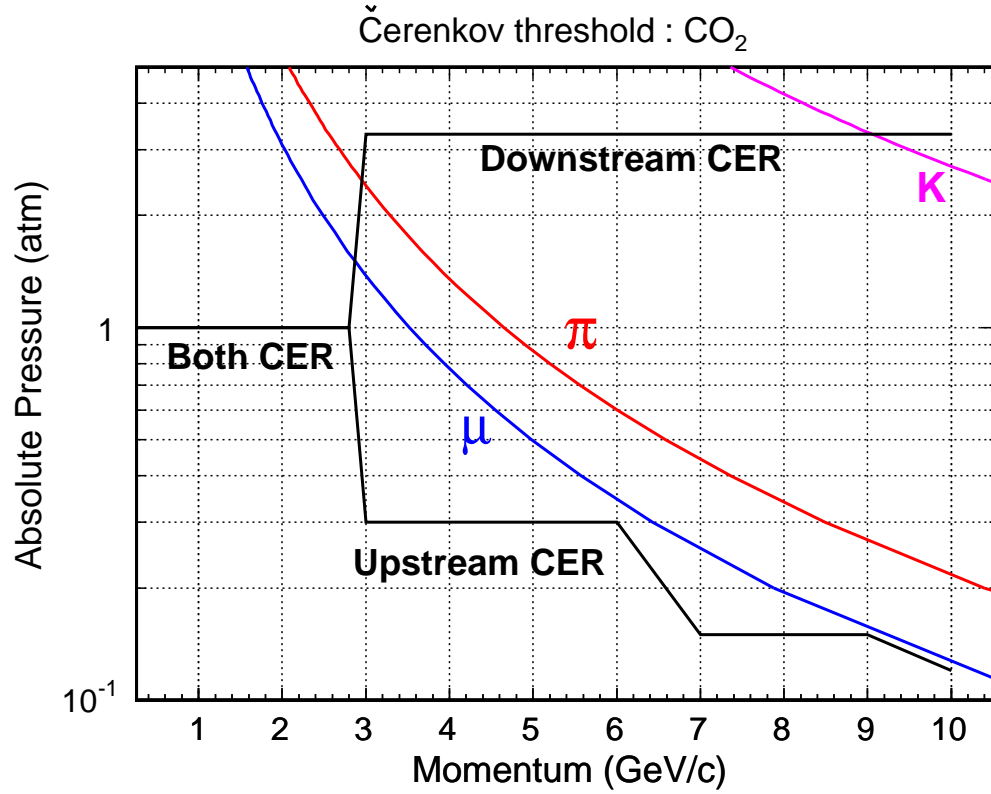
Figure 4.19: The Čerenkov threshold pressure vs. momentum for μ, π, K in CO_2. Black lines show the pressure settings for the T7 counters in 2002. The single T11 counter was pressurized at $1\,\text{atm}$ for all momenta.

make a counter of the desired length. Both ends of the counter were capped with $0.6\,\text{mm}$ thick aluminized Mylar foils. The counters were equipped with XP2020Q phototubes with quartz windows. The phototubes were operated between 2000 and $2300\,\text{V}$. The downstream end of each counter had a thin mirror which deflected Čerenkov light $\sim 90°$ downward to the phototube. The Čerenkov counters were filled with CO_2 at pressures between 0.1 and $4.3\,\text{atm}$ (absolute). One of the Čerenkov counters is shown in Fig. 4.20.

The T11 beamline has one $5\,\text{m}$ Čerenkov counter situated in an inaccessible portion of the beamline upstream of the experimental area. In 2003
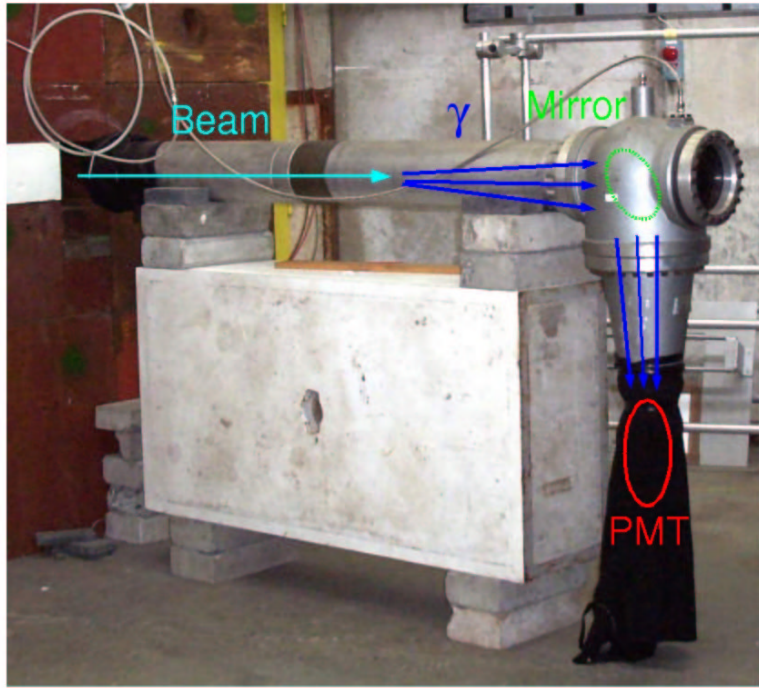
Figure 4.20: A threshold Čerenkov counter supplied for use in the East Hall. Beam enters the counter on the left. Čerenkov photons are radiated forward and then reflected downward off a mirror inside the counter. The photons are detected by a phototube located at the end of the counter's vertical arm.

a second 3.4 m counter was also used in T11. The counter was located in the experimental area with its downstream face 1.8 m from the front of the CalDet. The T7 beamline had one 4.4 m counter installed in the shielded area directly upstream of the experimental area. A second 3.4 m counter (the same counter was used in T11 during 2003) was situated in the experimental area with its downstream face $\sim$ 1 m from the detector. A third 2.5 m long counter was located between the upstream and downstream counters[2]. That counter was

---

[2]The counter was removed a week into the 2003 running period

quite inefficient, possibly broken, and not used in the analysis. All counters were read out using Far Detector electronics that had been modified to derive the trigger signal from the PMT anode pulse (rather than the dynode signal). The counter high voltages were supplied from an LeCroy 4032 located in the counting house adjacent to the experimental area.

Efficiency

Good knowledge of the Čerenkov efficiency was required for a number of analysis tasks. Each run was taken with at least one counter set to a pressure below the pion threshold. The signal from that counter was used identify to electrons. The counter efficiency was needed in order to estimate the electron contamination of the pion sample. As another example, some runs were taken with one of the Čerenkov counters pressurized so that muons with the nominal beam momentum were just above threshold and pions just below. These runs were taken in order to measure the muon content of the beam and isolate a clean stopping muon sample. Clearly the measurement depended critically on the efficiency for muon detection.

During the 2002 T7 beam test a number of runs were taken in which both counters were pressurized so that only electrons were over threshold. In these runs the two counters were set to the same pressure. Those pressures were adjusted when the beam momentum was changed in order to keep muons below threshold. The data were used to calculate the counter's efficiency. The computation proceeds with the following definitions:

$$\epsilon_1 = \frac{n_1}{N}, \quad \epsilon_2 = \frac{n_2}{N}, \quad \epsilon_1\epsilon_2 = \frac{n_{12}}{N}$$

Here, ϵ_x is the efficiency of counter x (an unknown), n_x is the number of events

117
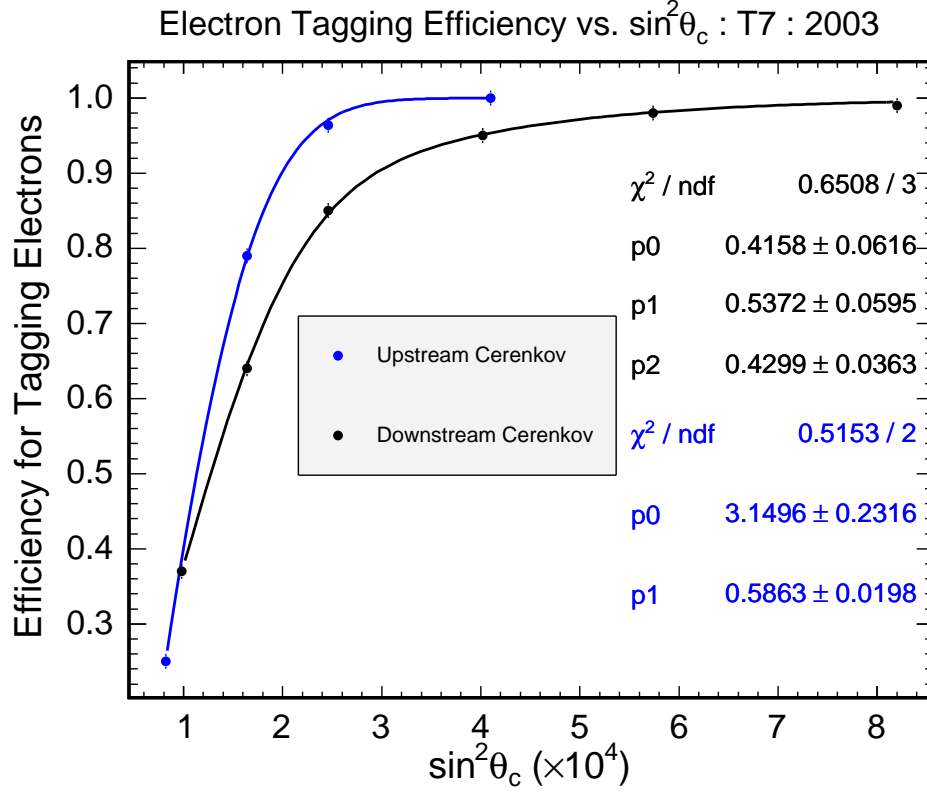
Figure 4.21: The electron tagging efficiency vs. $\sin^2\theta_c$. The parameterization vs. $\sin^2\theta_c$ allows the efficiency to be translated onto other particle species. The form of the parameterization is described in the text.

with a signal in counter x and n_{xy} is the number of events in which there was a signal in both counters. The total number of electron events is N (also an unknown). The efficiency and uncertainty of counter 1 were calculated as

$$\epsilon_1 \;=\; \frac{n_1}{N} = \frac{n_{12}}{n_2} \tag{4.8}$$

$$\delta\epsilon_1 \;=\; \sqrt{\frac{\epsilon_1\,(1-\epsilon_1)}{n_2}} \tag{4.9}$$

and likewise for ϵ_2.
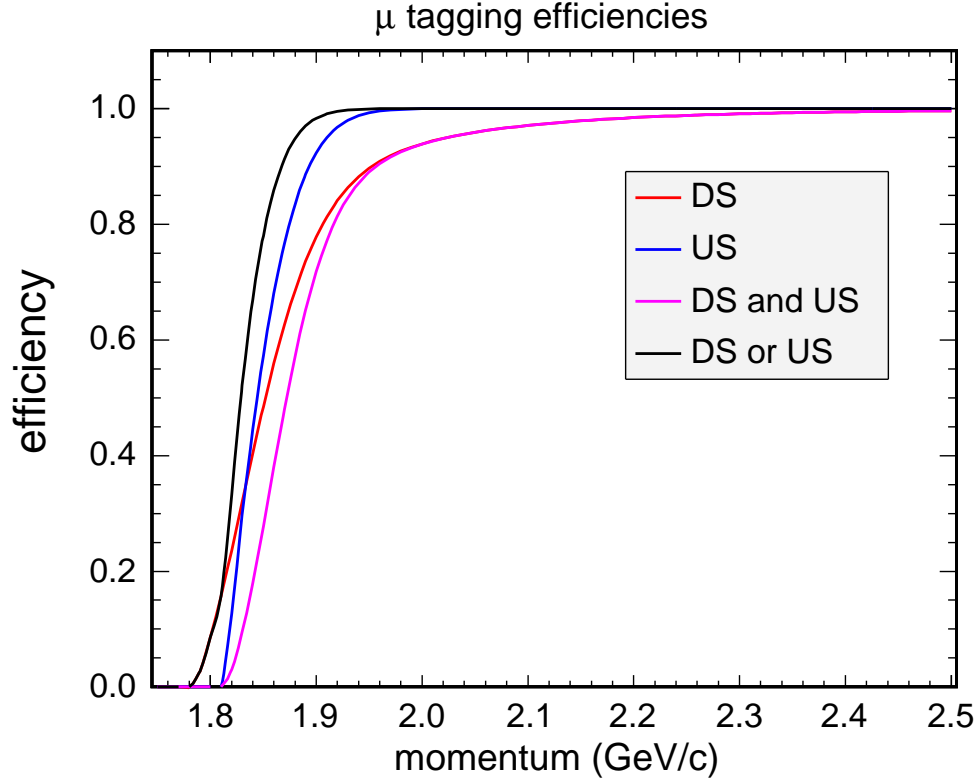
Figure 4.22: The muon tagging efficiency as a function of momentum. The upstream and downstream counters contain CO_2 at $4.3\,atm$. Curves were calculated using the parameterization shown in Fig. 4.21.

The T7 beamline had a small background of relatively energetic muons which could cause a signal in the Čerenkov counters. These muons (colloquially known as *PS-muons*) are believed to be caused by losses in the PS ring. The muons traversed the detector and hence had a momentum in excess of $2\,GeV/c$, independent of the nominal beam momentum. Events in the Čerenkov efficiency analysis were required to have a hit in no more than 20 planes, thereby assuring that the event did not contain a PS-muon. The
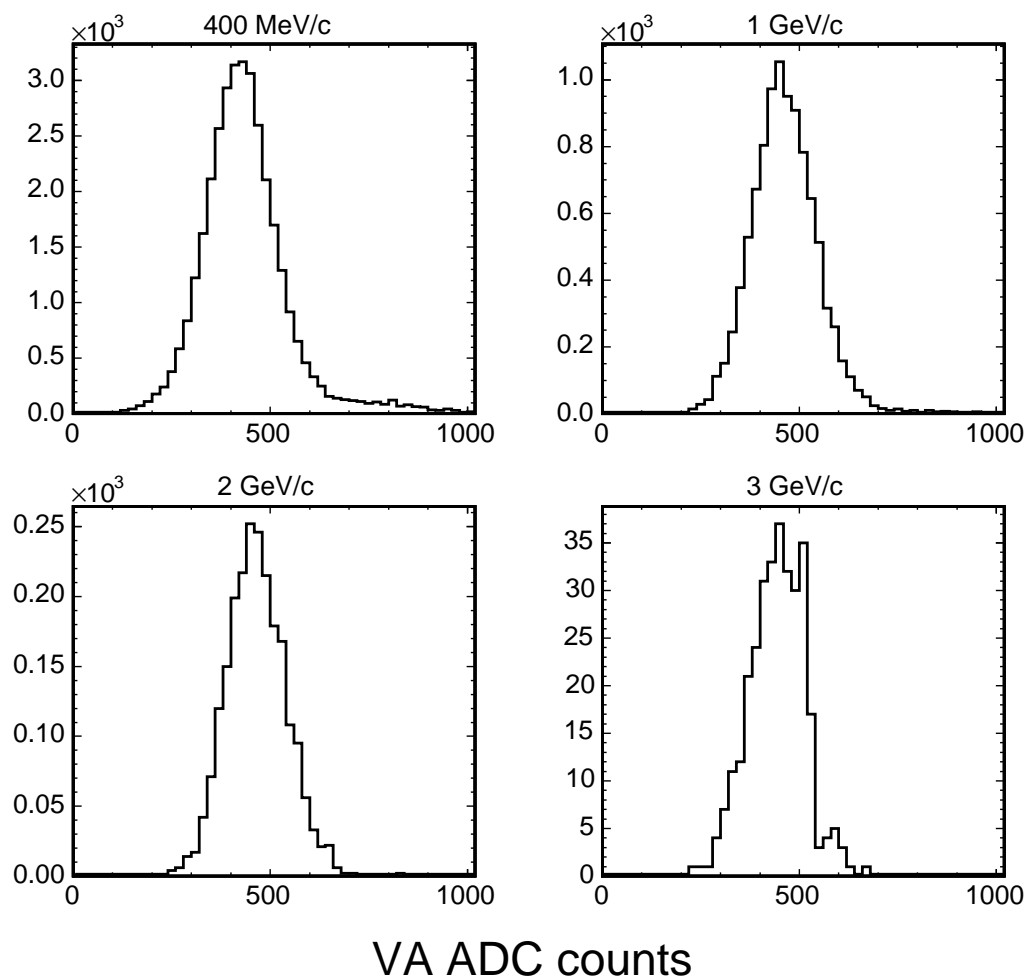
Figure 4.23: Čerenkov pulse-height distributions from the upstream counter in T11 during the 2002 running period. The scale on the ordinate is events per 20 VA ADC counts. The counter was pressurized to 1 atm - only electrons were above threshold. There are few entries in the 3 GeV/c histogram because the electron content of the beam was only 1-2%.

120

Pressure (atm)	$\sin^2\theta_c \times 10^4$	US Efficiency(%)	DS Efficiency(%)
0.08	0.66	40.3±1.3	-
0.14	1.15	80.6±0.4	53.7±0.4
0.28	2.30	99.40±0.04	60.4±0.2
1.0	8.20	99.95±0.03	99.26±0.02

Table 4.7: Electron tagging efficiency for the upstream (US) and downstream (DS) Čerenkov counters in T7, 2002.

results of the efficiency measurement are shown in Tab. 4.7.

At momentum settings below $3.0\,\mathrm{GeV/c}$ both counters were operated at $1\,\mathrm{atm}$ - well below the muon threshold. In the hadron analysis, events were rejected if either counter had a signal. The rejection factor was better than 1.5×10^5. Above $2.8\,\mathrm{GeV/c}$ the pressure in the upstream counter was adjusted downward to keep pions just below threshold. The downstream counter was operated well above the pion threshold, to discriminate between pions and protons. Though the upstream counter became inefficient as the pressure decreased, the electron composition of the beam fell as $\exp(-p)$, rendering electron tagging less important.

A different technique was used to measure the efficiency of the T7 counters in 2003. The measurement was made with the beam momentum set at $1\,\mathrm{GeV/c}$ (an arbitrary choice made only because the fraction of electrons was $\sim 90\%$ at $1\,\mathrm{GeV/c}$). While one counter was pressurized at 2 atmospheres runs were taken in which the pressure in the second counter was varied. Both counters are virtually 100% efficient at a pressure of 2 atmospheres. The efficiency

121

is then computed as:

$$\epsilon_1 \quad = \quad \frac{n_1}{n_2} \tag{4.10}$$

$$\delta\epsilon_1 \quad = \quad \sqrt{\frac{\epsilon_1(1-\epsilon_1)}{n_2}} \tag{4.11}$$

In the formulae above counter 2 is at two atmospheres and the pressure in counter 1 is varied. The results are shown in Tab. 4.8.

Upstream Counter (4.4m)

Pressure (atm)	$\sin^2\theta_c \times 10^4$	Efficiency(%)
0.10	0.82	25±1
0.20	1.64	79±1
0.30	2.46	96±1
0.50	4.10	100±1

Downstream Counter (3.4m)

Pressure (atm)	$\sin^2\theta_c \times 10^4$	Efficiency(%)
0.12	0.98	37±1
0.20	1.64	64±1
0.30	2.46	85±1
0.49	4.02	95±1
0.70	5.74	98±1
1.00	8.20	99±1

Table 4.8: Electron tagging efficiency for the upstream (US) and downstream (DS) Čerenkov counters in T7, 2003.

For a given counter, neglecting any drift effects (e.g., gain drift with time) and path length effects, the signal, and hence the efficiency, can only depend on $\sin^2\theta_c$. Therefore, to apply the measured efficiencies to other particle species one only needs to parameterize them with respect to $\sin^2\theta_c$. If the efficiency of the counters was dominated by Poisson statistics one would

expect a function of the form $\epsilon = 1 - \exp(-kx)$ to fit the data. Unfortunately this simple formula did not provide an adequate description of the data in Tab. 4.8.

The readout electronics used with the Čerenkov counters in 2003 had a threshold $\gtrsim 1$ photoelectron. For low light levels (i.e., small values of the Čerenkov angle) this made the efficiency of the counter decrease more rapidly with $\sin^2\theta_c$ than Poisson statistics allows. The upstream counter was operated at a gain approximately two times lower than that of the downstream counter, making the effect more severe there. A variety of functions were evaluated in order to parameterize the efficiency curve. The functions were required to monotonically increase with $\sin^2\theta_c$, asymptotically approaching unity for large values of the Čerenkov angle. Such a parameterization is presented in Fig. 4.21. The formulae used are:

$$
\begin{aligned}
\epsilon &= 1 - \big(\exp(-p_0 x) + \exp(-p_1 x^2)\big) \quad \text{Upstream} \qquad (4.12) \\
&= 1 - \big(p_0 \exp(-p_1 x) + (1 - p_0)\exp(-p_2 x^2)\big) \quad \text{Downstream} \quad (4.13)
\end{aligned}
$$

Here $x = \sin^2\theta_c$. The parameterizations can be used to calculate the counting efficiency for any particle species, given the pressure and momentum. As an example, Fig. 4.22 shows the calculated tagging efficiency for muons when both counters are pressurized at 4.3 atm - the maximum allowed value. Muons with momentum larger than $\sim 1.9\,\mathrm{GeV/c}$ can be tagged with high efficiency. For just that reason, during the 2003 running, data were collected at momentum settings of 1.8 and 2.0 GeV/c and 4.3 atm in both counters, in order to provide a high purity muon sample.

The T11 beamline only had a single Čerenkov counter in 2002 and therefore the efficiency could not be measured in the fashion outlined above.

The counter was 5 m long, but otherwise had the same design as the counters employed in T7. Figure 4.23 shows the counter pulse-height for different momentum settings and 1 atm pressure. The peak of the distribution did not depend strongly on the beam momentum (as expected) and was well above zero. The low pulse-height tail of the distributions did not extend below 100 ADC counts. The counter is thought to be at least as efficient as the upstream counter in T7 based on its somewhat greater length, the identical construction and the measured pulse-height.

4.5 The 2002 Run

Data were collected with CalDet running in external trigger mode during the fall 2002 running period in T7 and T11. The runs were taken at discrete beam momenta ranging from 200 MeV to 10 GeV, and in both polarities. Tables 4.9, 4.10 list the runs that were found useful for analysis of the hadronic response.

Care was taken to repeat a number low momentum settings in the T7 beamline in order to search for systematic differences between T11 and T7. Runs at momenta larger than 6 GeV/c were taken with the nominal high voltage and also with the high voltage reduced by 25 volts in order to understand (predominantly electronics) saturation effects. Certain special runs (e.g., with altered dynode thresholds) have been excluded from the figures.

Figures 4.24 and 4.25 show the number of $\pi^{\pm}, p$ collected at each beam momentum setting. The figures indicate the number of events before any cuts were applied. At least 1×10^4 and as many as 4×10^5 $\pi^{\pm}$ events were collected at each momentum setting. Multiple scattering and energy loss resulted in the

124

collection of relatively few proton events at the lowest momentum settings.

Data were collected with the detector turned at a $30°$ angle to the beam-line. Only the first twenty-four planes were read out due to space and time constraints. Low momentum settings were emphasized in order to maximize hadronic shower containment. The 2002 angle runs are listed in Tab. 4.11.

4.6   Particle Identification Selection Criteria

The hadron samples were selected using time of flight and Čerenkov information. The procedure differed somewhat between the two beamlines and changed with the beam momentum. The selection process can most logically be split up into low and high energy methods.

The low energy data included everything collected in T11 and the T7 data below $3\,\mathrm{GeV/c}$. For those data the time of flight system was used to distinguish between the $\pi\mu e$ and p samples. The separation was better than 6σ at all momenta (see Fig. 4.16). Gaussian fits, such as those in Fig. 4.14-4.15, were used to characterize the mean and σ of the pion and proton time of flight distributions. Events were selected from a region $\pm 2.5\sigma$ around the mean value of the π and p TOF peaks. For low energy running the Čerenkov counters were pressurized below the μ threshold and used to tag electrons. Events with a signal in any Čerenkov counter were not accepted for analysis as hadrons.

The high energy data were collected in T7 at momenta $\geq 3\,\mathrm{GeV/c}$. For momentum settings above $4\,\mathrm{GeV/c}$ the TOF system was unable to provide (on its own) a clean separation between the $\pi\mu e$ and p samples. To accomplish the discrimination, the upstream Čerenkov counter was pressurized below the μ threshold and the downstream counter was pressurized above the threshold

125

Runs used in the hadron analysis: T11 2002

Beam Line	Polarity	Momentum (GeV/c)	Runs
T11	+	0.4	40777
T11	-	0.4	40775
T11	+	0.6	40781
T11	-	0.6	40783
T11	+	0.8	40813
T11	-	0.8	40821
T11	+	1.0	40622
T11	-	1.0	40758
T11	+	1.2	40862
T11	-	1.2	40874
T11	+	1.4	40709
T11	-	1.4	40760
T11	+	1.6	40817
T11	-	1.6	40880
T11	+	1.8	40616
T11	-	1.8	40763
T11	+	2.0	40715
T11	-	2.0	40722
T11	+	2.2	40785
T11	-	2.2	40809
T11	+	2.4	40912
T11	-	2.4	40914
T11	+	2.6	40728
T11	-	2.6	40750
T11	+	2.8	40922
T11	+	3.0	40924
T11	+	3.2	40844
T11	-	3.2	40896
T11	+	3.6	40926
T11	-	3.6	40799

Table 4.9: T11 runs used in hadron analysis. The T11 beamline has an official range of 0.5-3.5 GeV.

Runs used in the hadron analysis: T7 2002

Beam Line	Polarity	Momentum (GeV/c)	Runs
T7	+	1.0	50505,50647($HV \downarrow$)
T7	-	1.0	50458, 50643($HV \downarrow$)
T7	+	2.0	50491
T7	-	2.0	50454
T7	+	2.4	50483
T7	-	2.4	50462
T7	+	2.8	50487
T7	-	2.8	50481
T7	+	3.0	50266
T7	-	3.0	50206
T7	+	4.0	50549
T7	-	4.0	50553
T7	+	5.0	50545
T7	-	5.0	50555
T7	+	6.0	50541
T7	-	6.0	50588
T7	+	7.0	50697($HV \downarrow$)
T7	-	7.0	50695($HV \downarrow$)
T7	+	8.0	50406
T7	-	8.0	50594
T7	+	9.0	50402,50687($HV \downarrow$)
T7	-	9.0	50412,50691($HV \downarrow$)
T7	+	10.0	50404,50683($HV \downarrow$)
T7	-	10.0	50408,50693($HV \downarrow$)

Table 4.10: T7 runs used in hadron analysis. The notation ($HV \downarrow$) indicates that the PMT high voltages were reduced. The T7 beam has an official range of 0.5-10.0 GeV.
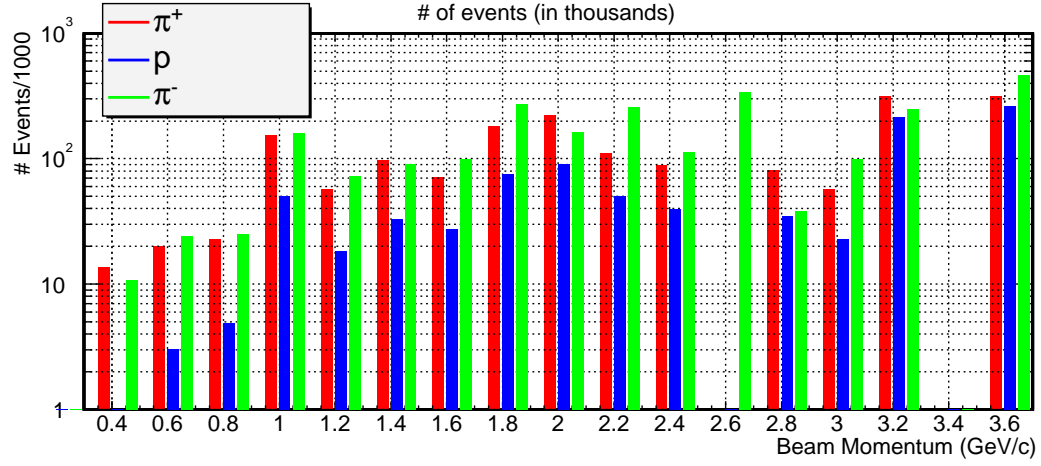
Figure 4.24: Number of low energy ($p \leq 3.6$ GeV) $\pi^{\pm}, p$ events collected during the fall 2002 running period.
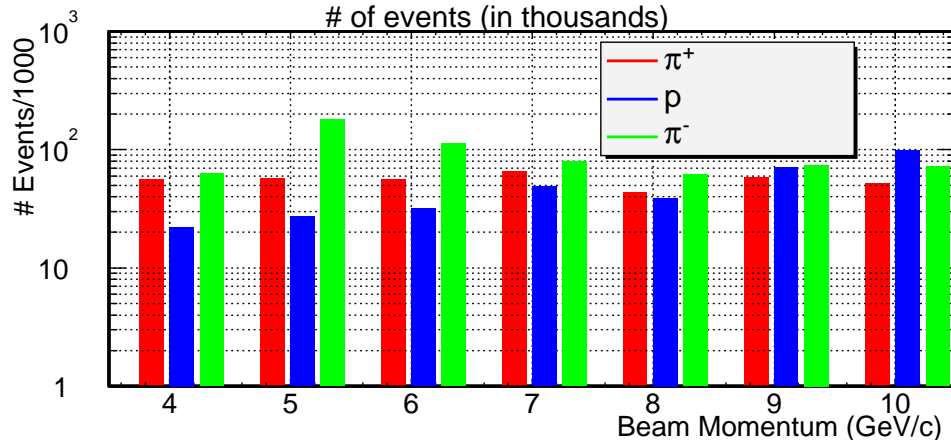
Figure 4.25: The number of high energy ($p > 3.6$ GeV) $\pi^{\pm}, p$ events collected during the fall 2002 running period.

Momentum (GeV/c)	Polarity	Runs
0.8	+	41008
0.8	-	41011
1.0	+	41013
1.0	-	41015
1.2	+	41017

Table 4.11: Runs taken with the detector oriented at a 30° angle to the beamline. Only the first 24 planes were read out.

(see Fig. 4.19). Pion events were selected by requiring a signal in the downstream Čerenkov counter but not the upstream. Events with signals in both counters were identified as electrons and those without a signal were identified as protons. Events were then required to be within $\pm2.5\sigma$ of the expected time of flight. This requirement rejected spurious triggers, particularly in the proton sample.

The selection procedure resulted in electron, combined pion and muon, and proton samples. At some momentum settings kaons were also identified. Figures 4.6-4.27 show the measured composition of the T11 and T7 beams. Statistical errors are too small to be seen. In the figures, data were collected with more than one target, which explains some of the scatter. The $+3\,\mathrm{GeV/c}$ point taken in T11 had an anomalously high pion content and was possibly collected with a screen, rather than thick, target. The general trend displayed in the two figures agrees with the results published by the PS staff (see Fig. 4.5).

The electron contamination in the pion sample was calculated for each beamline. Both the time of flight and Čerenkov information was used in the calculation. The electron and pion composition of the beam were taken from
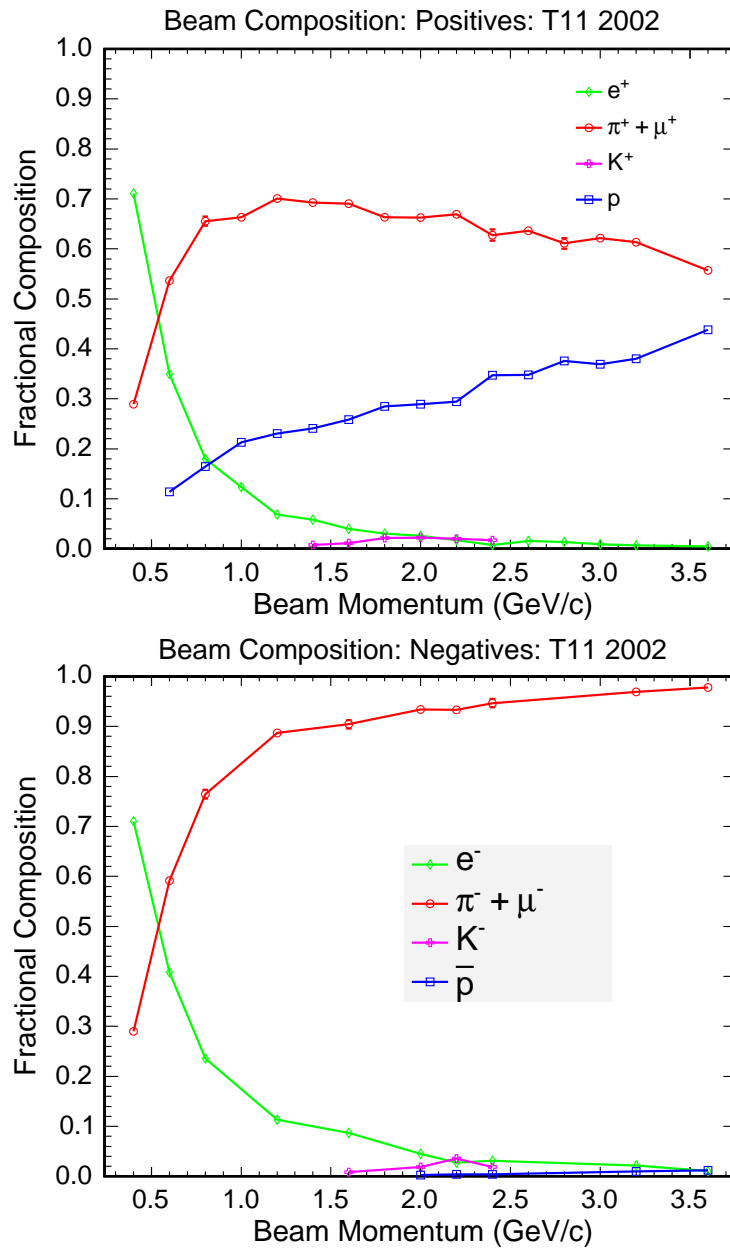
Figure 4.26: Measured composition of the T11 beamline, positive and negative polarities.
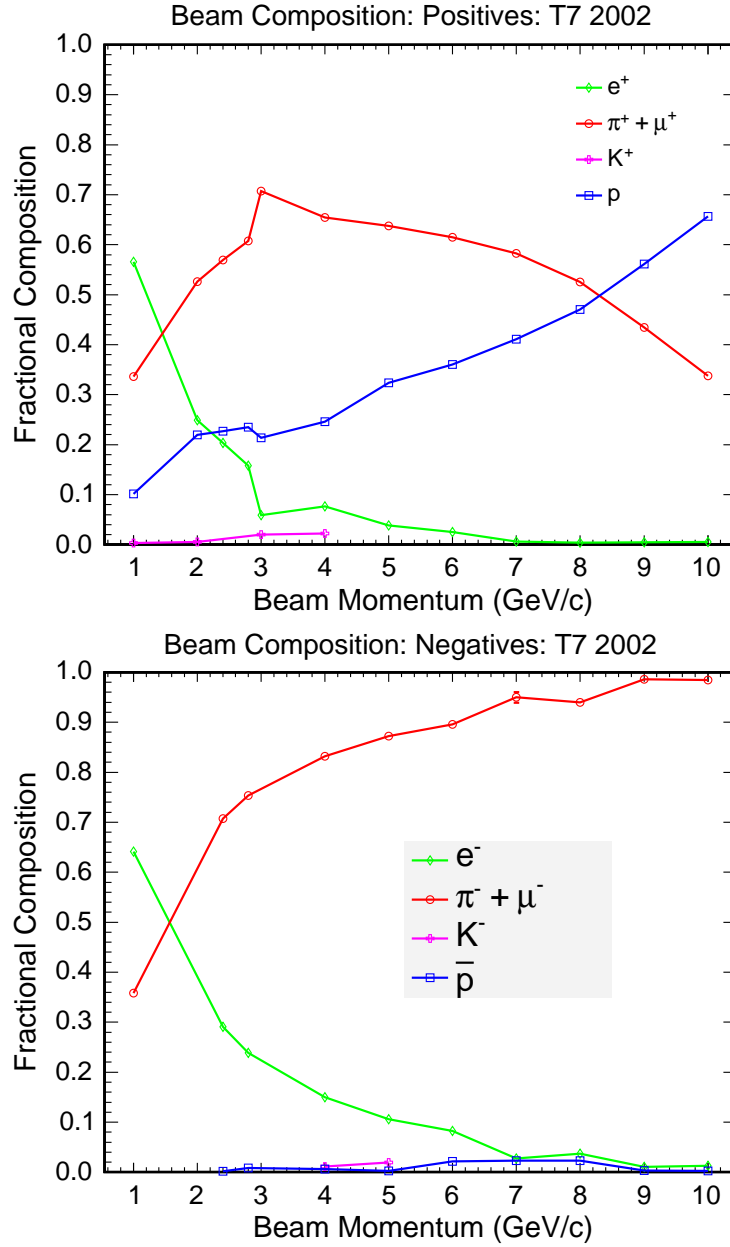
Figure 4.27: Measured composition of the T7 beamline, positive and negative polarities. The point at $+3\,\mathrm{GeV/c}$ is anomalous and was possibly taken with the screen target (rather than the electron enriched target of adjacent points).

131

Fig. 4.6. In T11, the single Čerenkov counter was conservatively estimated to be 98% efficient over the entire momentum range. This was somewhat less efficient than the T7 counters at the same pressure (1 atm). The calculated electron contamination was less than 0.3% over the entire momentum range, with a maximum at $1\,\mathrm{GeV/c}$[3].

Momentum (GeV/c)	Pressure (atm)	Efficiency(%)
$p < 3.0$	1.0	99.9±0.1
$3.0 \leq p \leq 6.0$	0.30	96±1
$6.0 < p \leq 9.0$	0.15	67±1
$p > 9.0$	0.12	40 ± 8

Table 4.12: Efficiencies used to calculate the electron contamination of the pion sample in T7. Below $3\,\mathrm{GeV/c}$ signals in either of the upstream or downstream Čerenkov counters were used to reject electrons. Above $3\,\mathrm{GeV/c}$ only the upstream counter was used.

In T7, the efficiency of the upstream Čerenkov counter was evaluated by using the pressure settings in Fig. 4.19 to calculate $\sin^2(\theta_c)$ and then looking up the efficiency using Fig. 4.21. The calculated efficiencies are shown in Tab. 4.12. The beam composition was taken from Figure 4.27. The resulting electron contamination was less than 0.5% for momentum settings below $10\,\mathrm{GeV/c}$. At $10\,\mathrm{GeV/c}$, the contamination was $2.3 \pm 0.9\%$, due to the low efficiency of the upstream Čerenkov counter.

Each event was required to have reasonable timing with respect to the time of the trigger as defined by a test statistic described below. This requirement suppressed pile-up events and occasional spurious triggers. For each

---

[3]The high electron composition below $1\,\mathrm{GeV/c}$ was suppressed by the time of flight seperation between electrons and pions.

event, the timing was calculated by histogramming the time of each hit and then comparing the resulting histogram to a template histogram constructed from data taken at low intensity. The height of each bin in the template histogram corresponded to the average fraction of hits per event in that bin. For each event a test statistic was calculated according to:

$$T = \frac{2}{N} \sum_i (\mu_i - x_i) + \ln\left(\frac{x_i}{\mu_i}\right) \qquad (4.14)$$

The sum is over the bins in the timing histogram. Here N is the number of hits, μ_i is the expected bin content and x_i is the measured bin content. The expected bin content was calculated as N multiplied by the height of the bin in the template histogram. The test statistic, colloquially known as *olchi2*, is similar to a reduced χ^2 in which the content of each bin is treated as a Poisson distributed random number. Events with anomalous timing had large values of olchi2. Figure 4.28 shows the test statistic at a few momentum settings. In the figure, the shaded histogram was computed by sampling the template histogram for events with N hits, where N itself was randomly generated from distributions of the number of hits at each momentum setting. The resulting histogram approximates the distribution for events with ideal timing.

Based on the shape of the ideal timing distribution and hand scanning, events were required to have olchi2 < 1.0. Two events removed by the cut are show in Fig. A.12. Events with large (> 5) values of olchi2 were easy to identify by eye as being caused by two particles (e.g., overlapping events). The olchi2 cut removed between one and five percent of events and was correlated with the beam intensity (see [50]). The fraction of events with olchi2 < 1.0 that had two particles was not characterized, but is estimated to be less than $\sim 2\%$ based on hand scanning.

133
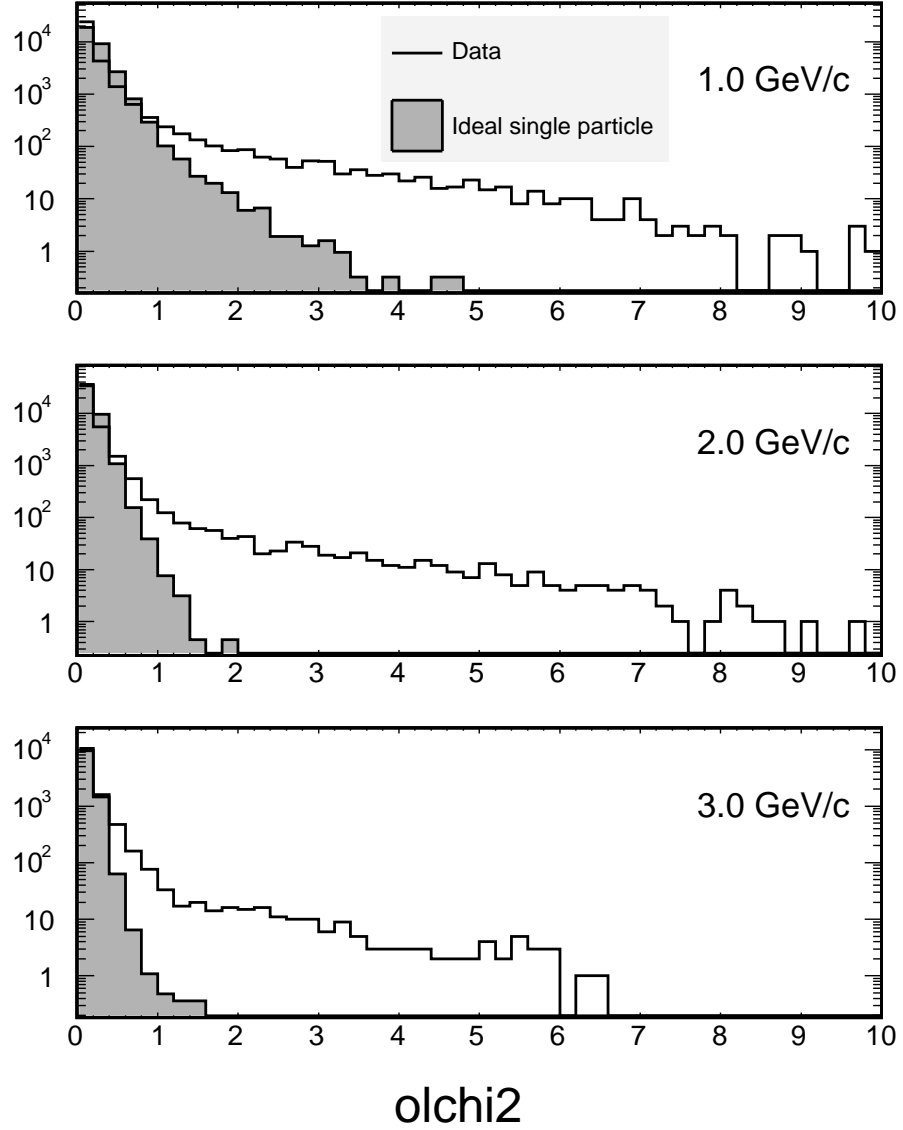
Figure 4.28: The olchi2 timing statistic for pions at a few momentum settings. The filled histogram corresponds to the ideal expectation calculated by sampling the timing template. The two histograms in each figure are normalized to have the same area.

Misidentified events were usually those in which the first particle was in time with the trigger and created hits on most of the chips in the first ~ 20 planes of the detector. The measured time of the hit from each channel on a given VA chip was determined according to the time of the dynode trigger which in turn was set by the first hit on the chip. Therefore, hits created by a second particle would be associated with the time of the first hit on the chip and could appear to happen at the same time as the initial particle. When the initial particle created hits on most of the chips in the first twenty planes there was little available information on the timing of the second particle. Such events were difficult to reject with the olchi2 statistic.

The identity of the overlapping particle is expected to be uncorrelated with the identity of the particle which caused the trigger. In that case, the particle type is distributed according to the beam composition shown in Fig. 4.6-4.27. For the majority of momentum settings the overlapping particle was most likely to be a hadron and thus the signal measured in overlapping events is expected, on average, to be no more than two times the signal measured in single hadron events. The bias introduced into the response would therefore be equal to the fraction of accepted events which had two particles. A more detailed study of pile-up events would require a full simulation of overlapping events which was difficult to implement in the MINOS detector simulation and is regarded as a topic for future investigation.

Chapter 5

CalDet Calibration

This section focuses on the calibration hardware and procedures employed at the CalDet. CalDet was the first detector built by MINOS and, as of this writing, is the only detector to fully exercise the calibration chain. The calibration procedure was pioneered at CalDet and is functionally identical to that planned for use in the Near and Far detectors. Indeed, it cannot be any other way if the hadronic and electromagnetic response measured at CalDet is to be transparently applied onto the other two detectors.

5.1 Overview of the Calibration Chain

The calibration procedure used by MINOS is designed to allow the energy deposited in the detector to be deduced from the signals observed from the detector. The system must:

- Correct for gain variations between phototube pixels.

- Track gain variations over time.

136

- Examine the response of the phototubes and electronics over a range of light levels.

- Correct for variations in the quantum and collection efficiency of the phototubes.

- Correct for strip-to-strip variations in light output as well as the effect of attenuation along readout cables and at optical connections.

The calibration procedure must finally translate the signals in the detector into a standard muon energy unit with which the response to hadrons and electrons can be transported to the Near and Far detectors.

5.2 Light Injection Calibration

The Light Injection (*LI*) system formed the core of the CalDet calibration scheme. The system was responsible for:

- Measuring the gain of the photomultipliers. That is, measuring the photomultiplier output charge (in ADC counts) for a known input light level.

- Characterizing the response of the photomultipliers at different light levels. The response of a PMT v. light level is known as a *gain curve*.

- Tracking short term gain changes.

- Making sure that the photomultipliers, electronics and optical cabling were functioning properly.

During LI data collection, individual photomultiplier pixels were illuminated with pulses of light at a well controlled level[1]. Prior to a beam running period, the photomultiplier gains were characterized using a dedicated, high statistics light injection run. The phototubes' gain curves were also measured at that time. The light injection system was then used to track the PMT gains throughout the beam running period. During beam running, each channel was illuminated with at least 2500 pulses every twenty minutes, with data taking occurring in between beam spills.

5.2.1 Light Injection Hardware

The light injections system utilizes blue light emitting diodes (LEDs) to illuminate each channel in the detector [51]. The LEDs resided in a pulser box located (at CalDet) alongside the photomultiplier racks. The CalDet pulser box contained 6 LEDs, each of which was optically fanned out to illuminate multiple channels. The optical connectors on the sides of each plane had a housing, known as a LIM (light injection module), which accepted the optical fibers from the pulser box, allowing them to illuminate the wavelength shifting fibers. The light from each LED was also directed onto two PIN photodiodes. The PIN diodes had an extremely linear response and were used to provide a stable measure of the LED intensity. This allowed the response of the photomultipliers and electronics to be determined at a wide range of light levels. In bench tests the PIN diodes were stable enough to track changes in the LED intensity to $\pm 0.5\%$ over a two month period [51].

---

[1]The LED intensity varied by $\pm 5\%$ over two months during bench tests [51]. As described in the text, PIN diodes were used to correct for these variations at CalDet.

5.2.2　Gain Calibration
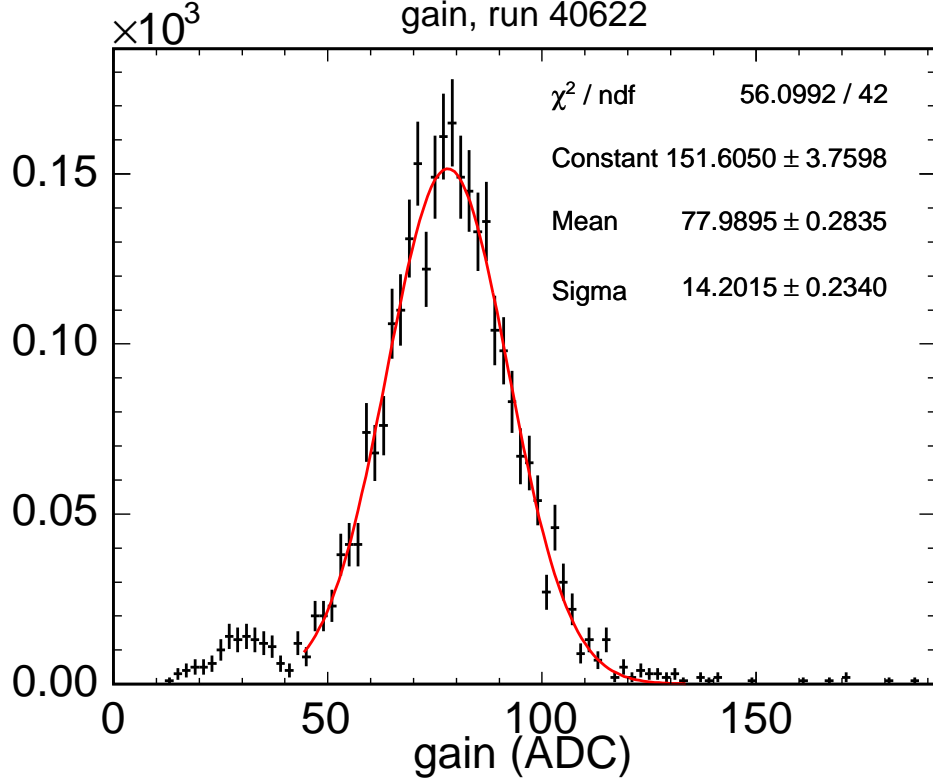
Figure 5.1: The gain for all channels in the calibration detector. Here the gain is expressed in units of ADC counts per photoelectron. The mean value 78 ADC is equivalent to a gain of 1×10^6. The peak at ~ 30 ADC were caused largely by faulty, low gain VA channels.

The charge distribution in each channel, measured during LI flashing, was used to calculate the channel gain (g) in units of VA ADC counts per photoelectron. The typical light level was a few tens of photoelectrons. The calculation, fully described in [52], begins with the pedestal subtracted mean (μ) and RMS (σ) of the charge distribution, both expressed in VA ADC counts.
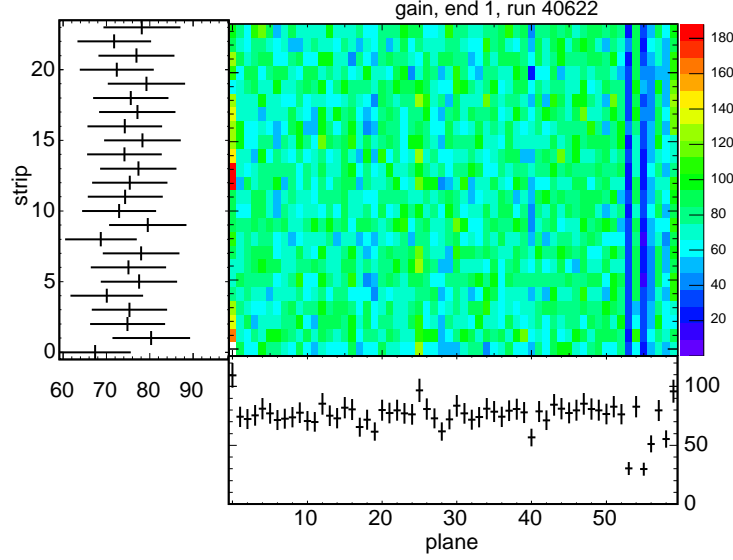
Figure 5.2: Gain for each plane and strip readout on side 1 of the calibration detector. The color scale is in VA ADC counts.

The mean is related to the gain and the number of photoelectrons n by:

$$\mu = ng \tag{5.1}$$

The RMS is given by the sum, in quadrature, of a contribution from the single-photoelectron width (σ_{1pe}) and a contribution from the pedestal width (σ_{ped}). The relation is:

$$\sigma^2 = n\sigma_{1pe}^2 + \sigma_{ped}^2 \tag{5.2}$$

In the limit $\sigma_{1pe} \ll g\sqrt{n}$ the shape of the charge distribution is established by the Poisson statistical process of photoelectron creation at the photocathode. In that case:

$$\sigma = g\sqrt{n} \tag{5.3}$$

$$n = \left(\frac{gn}{g\sqrt{n}}\right)^2 = \left(\frac{\mu}{\sigma}\right)^2 \tag{5.4}$$
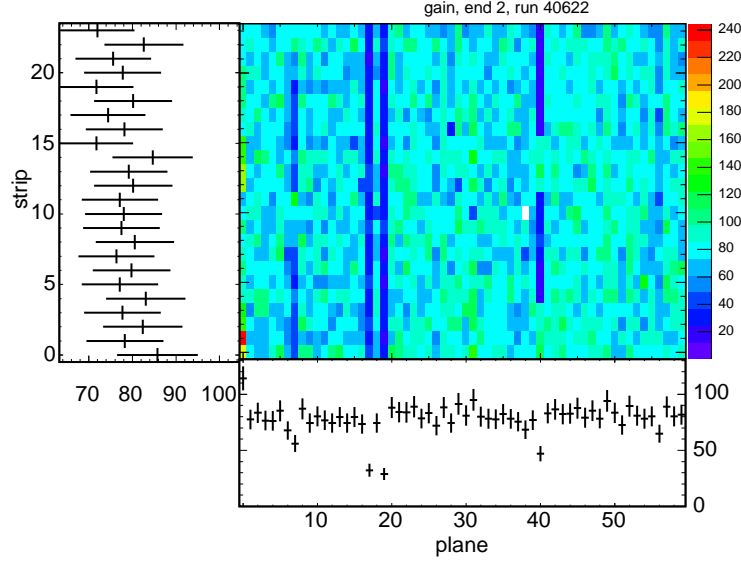
Figure 5.3: Gain for each plane and strip readout on side 2 of the calibration detector. The color scale is in VA ADC counts.

In a realistic case, the formula above must be corrected for a contribution from the single photoelectron width. The corrected formula is:

$$n = \left(\frac{\mu}{\sigma}\right)^2 \left(1 + \left(\frac{\sigma_{1pe}}{g}\right)^2\right) \tag{5.5}$$

The single photoelectron width was determined in-situ for all channels by directly fitting the single photoelectron charge distribution, visible when flashing at very low light levels. The typical fractional width (σ_{1pe}/g) was 0.5 ± 0.06, yielding corrections of $\approx 20 - 30\%$. Figure 5.1 shows the gain distribution for all channels in the calibration detector for a single time in 2002. The gain for each strip-end is shown in Fig. 5.2-5.3. Generally, the channel gains were uniformly distributed over the detector. Because the gain was expressed in units of ADC counts, the amplification of the VA electronics is directly included in

141

the measurement. The bands visible in the figures were caused by faulty low gain readout electronics. Gains were established once near the start of each running period and the light injection system was then used to track the gain drift in individual channels throughout the data-taking.

5.2.3 Drift Calibration

Phototube gains varied over the course of time, largely due to temperature fluctuations in the experimental hall. The light injection system was used to track and correct for the time dependent gain variations. Every 20 minutes during data-taking, a gain drift point was collected by flashing the full detector 2500 times at a fixed light level. Variations in the light output of the LEDs were monitored by a set of PIN diodes. Drift point calibration constants were determined from the mean of the charge distribution for each individual channel. For each channel the drift at time t, relative to the time $t = 0$ when the gains were initially determined, is calculated as [53]:

$$C(t) = \frac{\mu_{pmt}(t)/\mu_{pin}(t)}{\mu_{pmt}(0)/\mu_{pin}(0)} \tag{5.6}$$

The gain drift for individual channels is shown in Fig. 5.4-5.6. The run number, shown along the abscissa, increased with time. The oscillatory pattern visible in the plots was due to day-night temperature fluctuations. The drift point calibration typically corrected for drifts of $1 - 5\%$. The error on each point is $\approx 0.5\%$ and is dominated by statistics (i.e., the number of flashes).

5.2.4 Linearity Calibration

The light injection system was able to inject pulses over a large range of light levels. The injected light was independently monitored with PIN diodes,

142
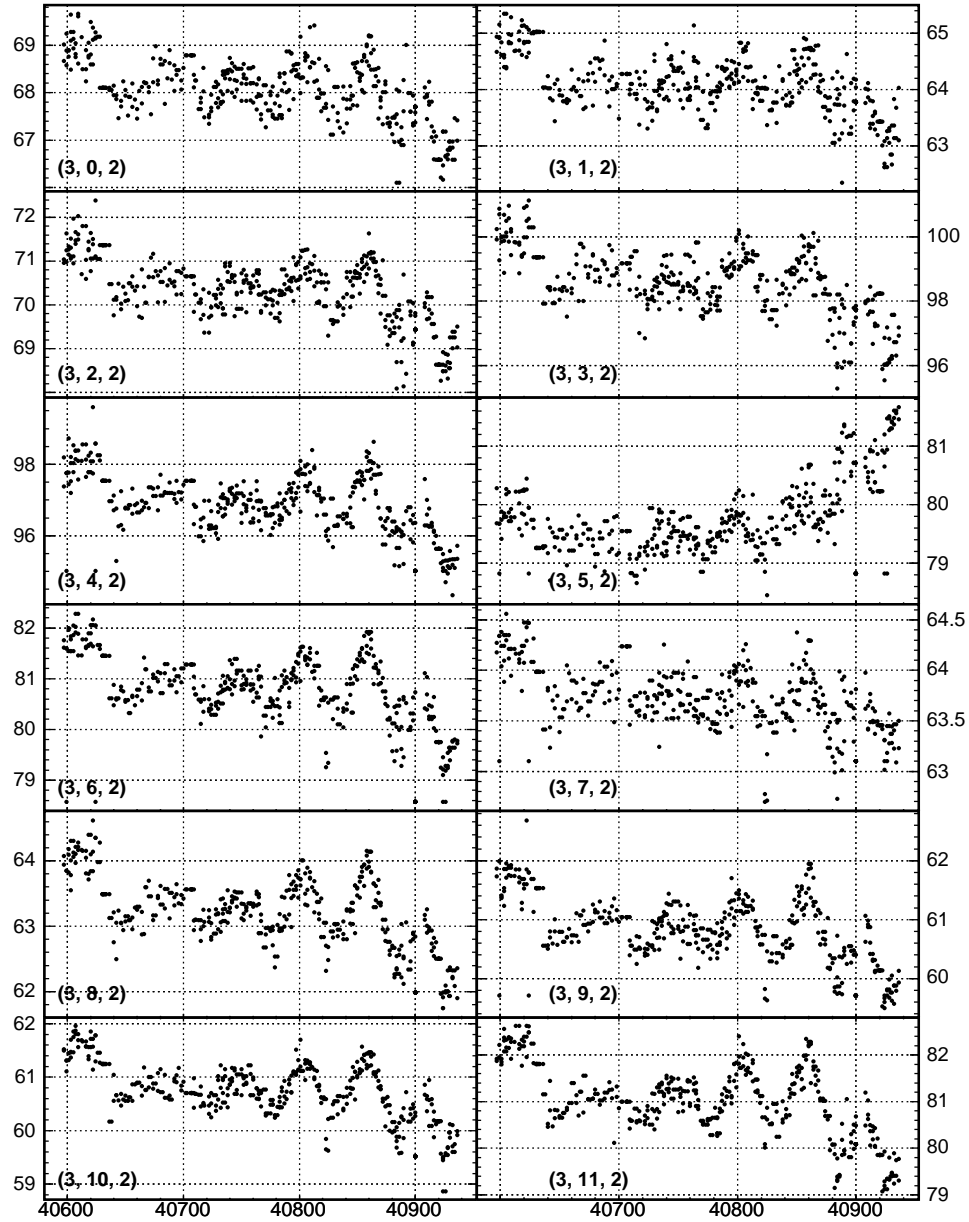
Figure 5.4: Gain variations over time. The abscissa gives the run number, while the ordinate gives the channel gain in VA ADC counts. The label on each figure refers to the plane, strip and end readout by each of the channels.

143
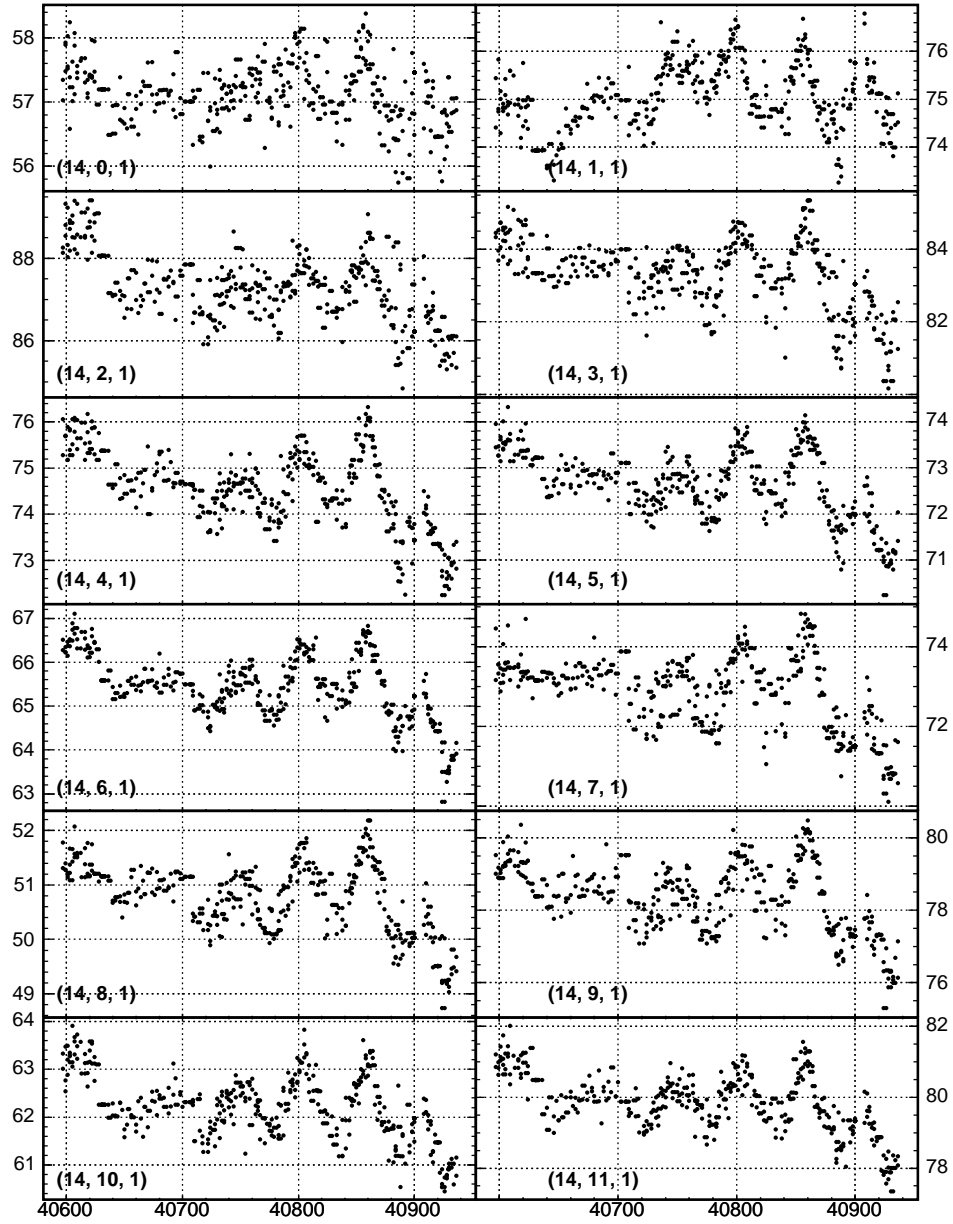
Figure 5.5: Gain variations over time. The abscissa gives the run number, while the ordinate gives the channel gain in VA ADC counts. The label on each figure refers to the plane, strip and end readout by each of the channels.

144
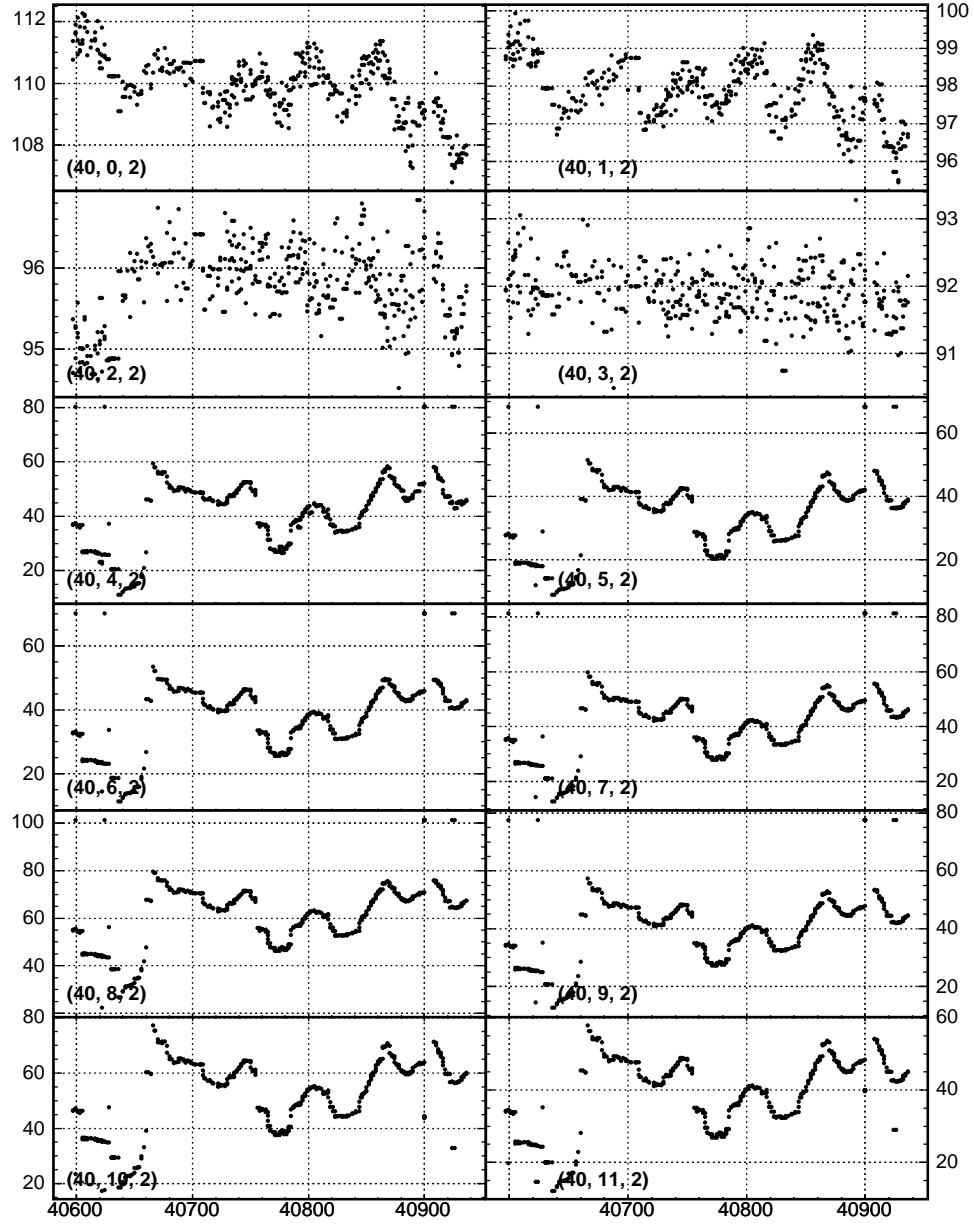
Figure 5.6: Gain variations over time. The abscissa gives the run number, while the ordinate gives the channel gain in VA ADC counts. The label on each figure refers to the plane, strip and end readout by each of the channels. The channels connected to strips 4-11 experienced wide variations, likely due to a malfunctioning VA amplifier.

145

which were shown to have a linear response in bench tests [51]. This capability allowed the response curve of the photomultipliers and electronics to be precisely determined. When response curves were measured at CalDet, a nonlinearity was observed at low light levels, a region in which previous tests had demonstrated that both the electronics and the photomultipliers were linear. After much effort the effect was traced to a dependence of the LED wavelength spectrum on the applied pulse-height [54]. The absorption quality of the wavelength shifting fibers depended strongly on the wavelength of the incoming light, causing the observed nonlinearity at low light levels. Before
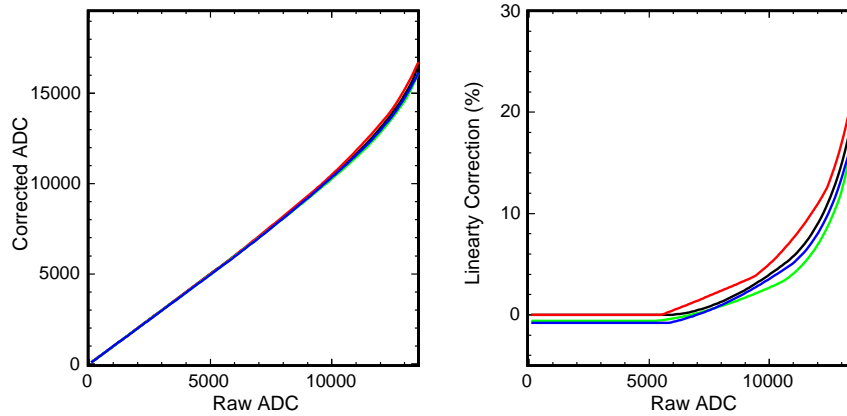
Figure 5.7: Correction for PMT and electronics nonlinearity. The figure on the left displays the corrected ADC value as a function of the raw (input) ADC. The figure on the right shows the correction (in %) as a function of the input ADC. For reference 7000 ADC counts corresponds to 90 photoelectrons.

the 2003 running period the original LEDs were replaced with a model in which the wavelength/voltage dependence is insignificant. For the 2002 data a special technique was applied in order to derive the linearity calibration. Strips on CalDet were readout on both ends and when LEDs were flashed

146

on one side of the detector, the other side saw a greatly attenuated signal. Generally, this light level was in the region where both PMTs and electronics have been demonstrated to be linear. When flashing on one side of the detector, phototubes on the opposite side were used in place of the PIN diodes to independently measure the light level.

Figure 5.7 shows the linearity calibration for a few channels. The nonlinearity was dominated by the VA electronics rather than the photomultiplier tubes. The vast majority of signals in beam induced events were well below $\sim 7000 \, \text{ADC}$ counts (90 PEs), in the region where no correction was needed[2].

5.3   Muon Calibration

The light injection system corrected for response differences caused by pixel to pixel gain differences, phototube and electronics nonlinearity, and time dependent gain drifts. A strip-to-strip calibration was needed in order to account for differences in the response of the individual strips in the detector. Such differences were caused by:

- Variations in the light output between individual strips.

- Differences in the lengths or attenuations lengths of the optical readout cables.

- Variations due to the quality of optical coupling between the the scintillator modules and the readout cables and between the readout cables and the phototube.

---

[2]As an example, in $10 \, \text{GeV/c} \, \pi$ induced hadronic showers 0.5% of hits were larger than 7000 VA ADC counts. Neutrino induced showers are not expected to differ significantly.

- Non-uniformity of light collection and quantum efficiency of the photo-multipliers.

Cosmic ray muons are a natural source for the strip-to-strip calibration since they are highly penetrating, illuminate the detector evenly, and deposit an amount of energy that is relatively independent of their momentum. Additionally, the Far and Near detector responses will be characterized in terms of cosmic ray muons, and the measurements made at CalDet must ultimately be translated to those detectors. A detailed discussion of the cosmic ray calibration is presented in [55]. Cosmic ray muon data were collected for each running period and whenever the detector was moved or re-cabled. Cosmic ray muons typically have an energy of a few GeV and appear as short, straight tracks in the detector. A relatively simple pattern recognition and tracking algorithm was used to reconstruct the angle and position of these tracks. The algorithm searched for track segments, fit a straight line to the hits in the segment, removed hits far from the fitted track, merged consistent track segments and required that the tracks found in the horizontal and vertical views were consistent. Figure 5.8 shows typical cosmic ray muon pulse-height distributions. For each hit along the muon track, the reconstructed angles were used to correct the observed pulse-height for the average path length through the scintillator strip. The path-length correction was especially important since the horizontal and vertical angular distributions were very different (cosmic rays come from above!). This resulted in a large difference in the path-length between the two views and neglecting any correction would have introduced an asymmetry in the calibration constants.

A correction was applied for *zeros*, that is cases in which a muon passed through a strip but no signal was observed. The correction was applied because
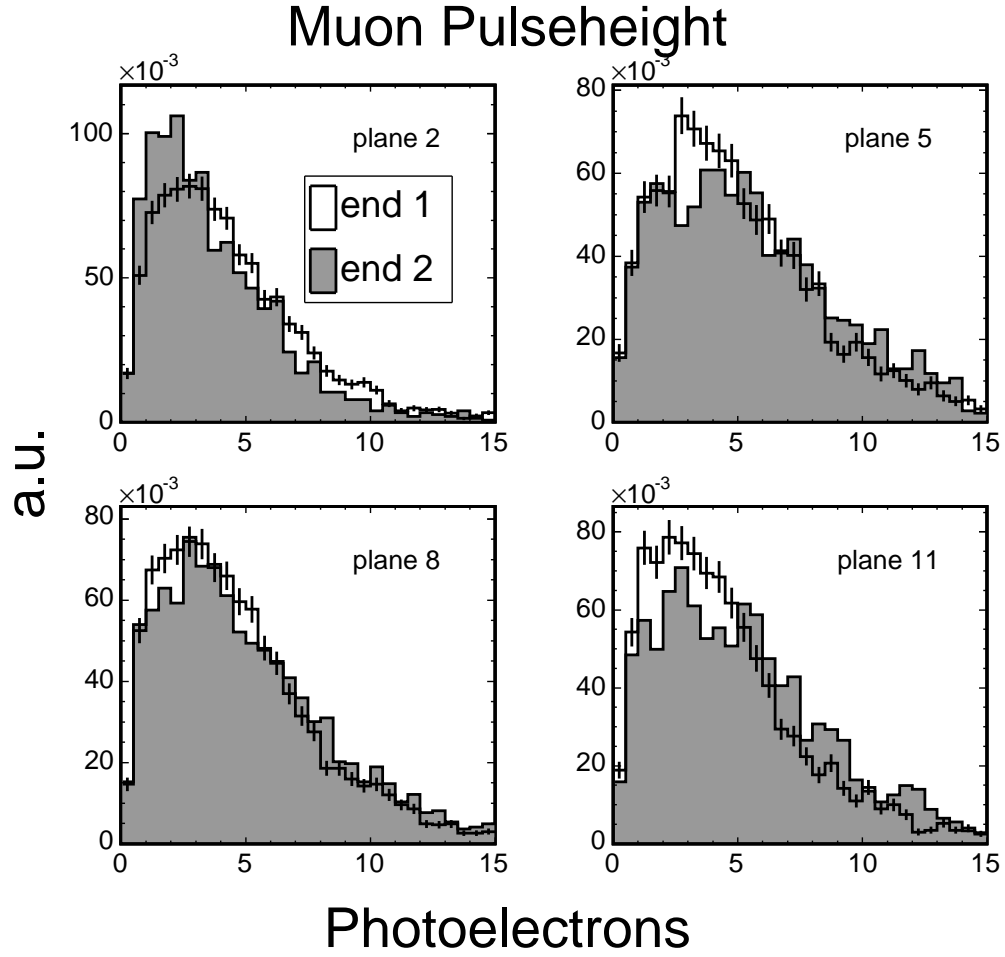
Figure 5.8: Example of raw muon pulse-height distributions used in the calibration. In this figure, the signals from all strips in a given plane were filled in each of the histograms but the actual calibration procedure considers each strip individually.

the true light output of each strip was proportional to the true mean of the muon pulse-height distribution rather than the mean of the zeroes truncated distribution. Neglecting such a correction would cause strips with a low light output to appear more luminous than they actually were, since the low light output strips were more likely to have zeroes. For each hit, the probability of obtaining a zero was calculated from the reconstructed angles and the light level for a normally incident muon. The method is iterative since the light level was not known at the start. For each hit, the associated strip-end pulse-height histogram was filled. The filling was done after weighting by the probability of not having a zero. The zeroes bin was also filled, weighted by the probability of having a zero. This approach correctly reproduced the true mean of the distribution.

The amount of light seen at the phototube depended on the position of the track along the length of the strip, due to light attenuation within the wavelength shifting and optical fibers. For tracks crossing near the strip ends, there was an additional suppression of light caused by photons leaking out the end. This effect was corrected for by mapping the response to muons along the length of the strip. Maps were constructed for each of the twenty-four strips readout from each end of both the horizontal and vertical planes. Individual strips were not separately mapped, as the statistical significance would have been too low. Instead, strips that had the same logical readout were combined. For example, the signals for all strip # 12s in vertical planes readout on the west side would be combined into one map. This gives 4×24 individual maps. Figure 5.9 shows an example of such maps. The maps were used to express the individual strip-end calibration constants in terms of the response to a muon crossing at the center of the strip. This convention is appropriate for the beam
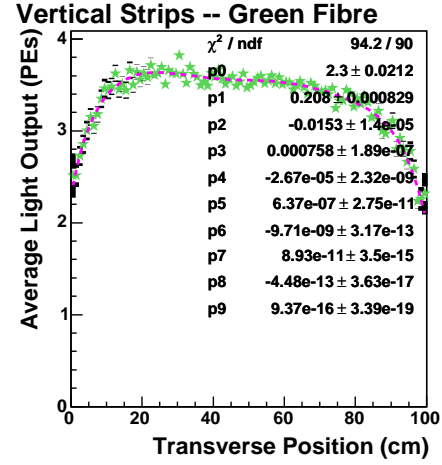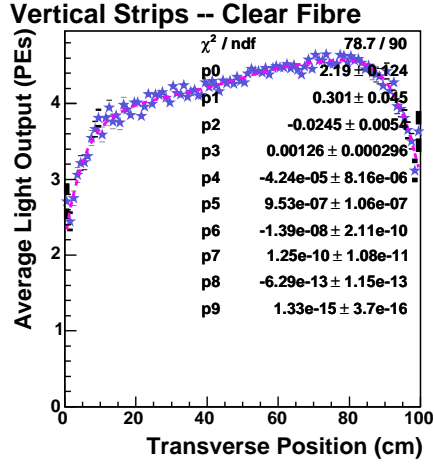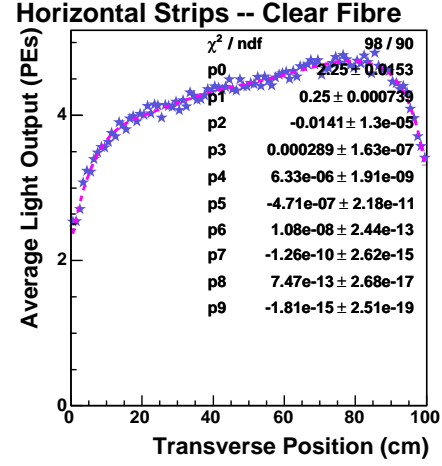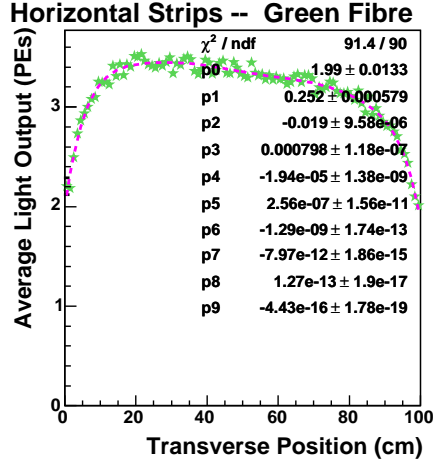
Figure 5.9: The scintillator response to muons, mapped along the length of the strip. Maps like these were used to correct the muon calibration constant back to the center of the detector. The parameters correspond to fits to a ninth degree polynomial. Taken with permission from [56].
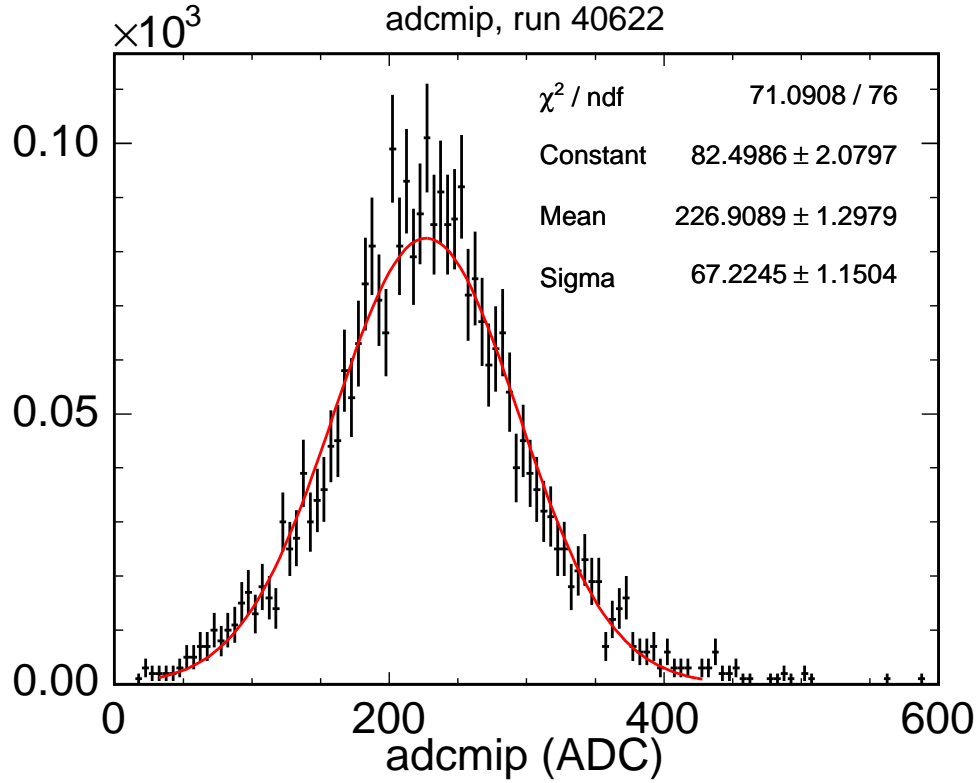
Figure 5.10: The muon calibration constants, in VA ADC counts, for all pixels in the calibration detector. The numerical value of each constant indicates the average pulseheight observed for a normally incident cosmic ray muon traversing the longitudinal center of the scintillator strip. Signals in ADC counts are converted to MIPs by dividing by these constants. The parameters correspond to a Gaussian fit. For reference 227 ADC counts ≈ 2.91 photoelectrons.
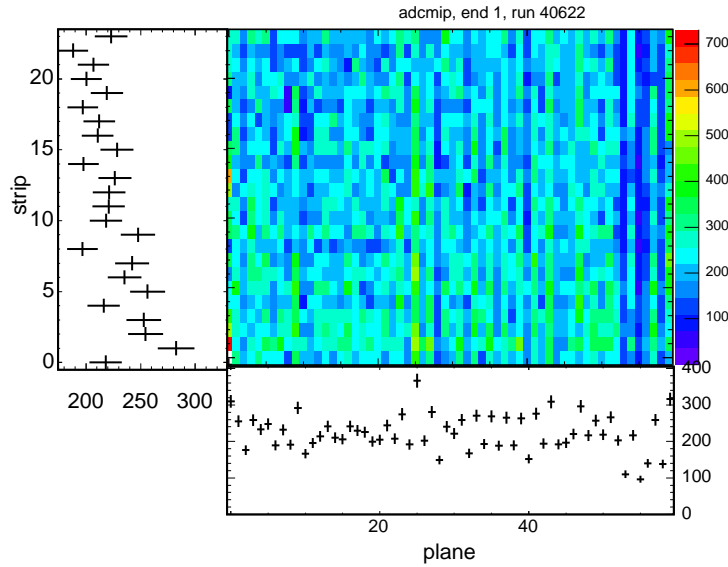
Figure 5.11: Muon calibration constants for each plane and strip readout on side 1 of the calibration detector. The color scale is in VA ADC counts.

analysis since the detector was only triggered on centrally located events.

Figure 5.10 shows the muon calibration constants, in units of VA ADC counts, for the entire calibration detector. The numerical value of each constant indicates the average pulseheight observed for a normally incident cosmic ray muon traversing the longitudinal center of the scintillator strip. The strip response varies by $\approx 30\%$ over the detector. Figures 5.11-5.12 show the response for each plane and strip in the detector. The color scale is in VA ADC counts. The bands in the figure are caused by channels which had a low gain, or instances in which the light reaching the phototube was rather low. The latter cases were caused by poor optical coupling between the readout cables and the phototubes. There was a clear and expected correlation between the muon calibration constants and the gain calibration constants, as demonstrated in

153
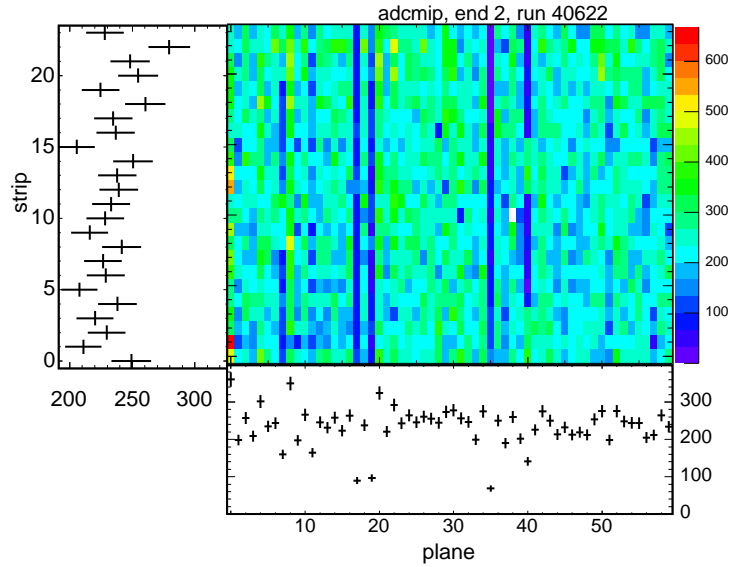
Figure 5.12: Muon calibration constants for each plane and strip readout on side 2 of the calibration detector. The color scale is in VA ADC counts.

Fig. 5.13.

After muon calibration, the pulse-height of each hit was expressed in units of *MIPs*. By construction, one MIP is the signal, measured at one end of the strip, deposited by a cosmic ray muon, incident normal to the 4.1 cm wide side of the strip and traversing it at its center. The MIP unit therefore has a semi-arbitrary scale that depends on the cosmic ray energy spectrum.

5.3.1 Results

A special cross check was devised to probe the effectiveness of the light injection calibration. In this test, the high voltage on the "-" (or East) side of the detector was reduced by 25 V and the high voltage on the "+" (or West) side of the detector was increased by 25 V. A run at 1 GeV/c beam momentum
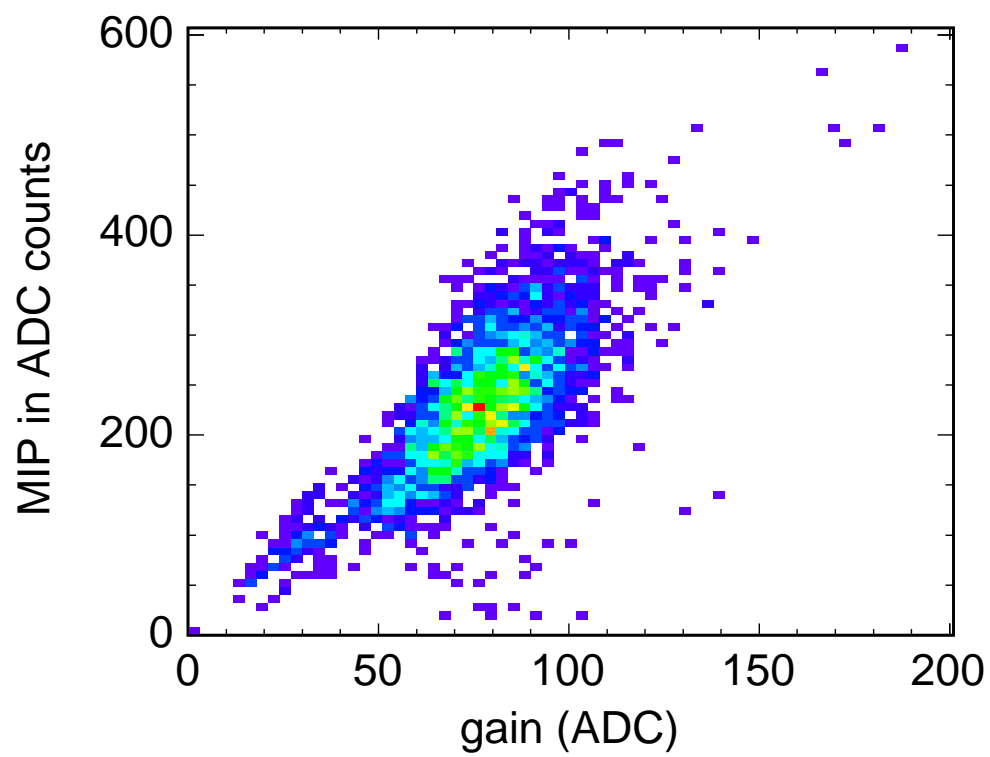
Figure 5.13: The muon calibration constants vs. the gain calibration constants. A clear and expected correlation is observed.
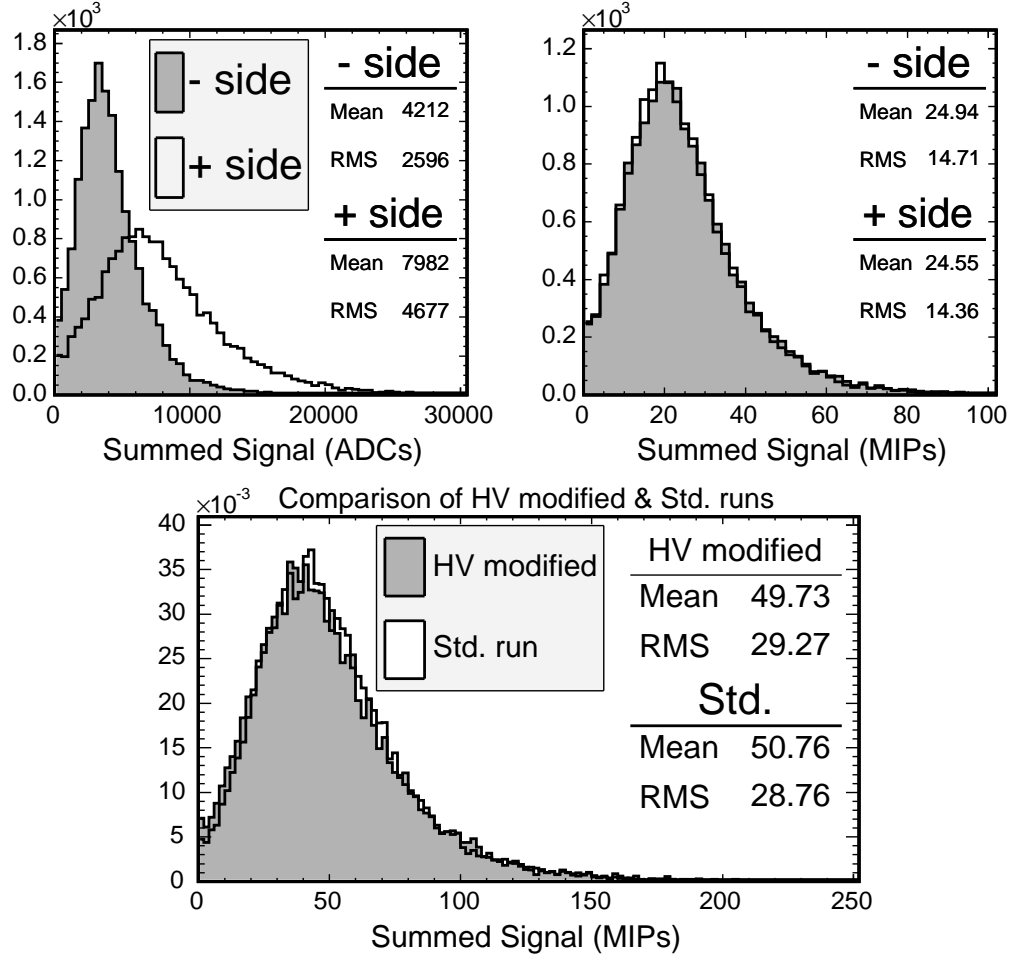
Figure 5.14: Results of a light injection calibration cross check. In this test, the high voltage on the "-" ("+") side of the detector was reduced (increased) by 25 V. A run at 1 GeV/c beam momentum was taken and pions were selected. The figure on the upper left shows the summed signal, in ADC counts, before calibration. The figure in the upper right shows that asymmetry was removed after the gain and muon calibrations were applied. The lower figure compares the total response, to pions, in the run with HV modified to a standard 1 GeV/c run. A 2% agreement was achieved.

was then taken and pions were selected. Results of the test are presented in Fig. 5.14. The plot in the upper left of Fig. 5.14 shows the summed signal, in ADC counts, on each side of the detector. A clear asymmetry was introduced by the high voltage changes. The plot in the upper right shows the response after the light injection and muon calibrations were applied. That asymmetry was removed by the calibration. The lower plot compares the total response, to pions, in the run with the modified high voltage to a standard $1\,\text{GeV}/c$ run. The high voltage modification in this test corresponds to an instantaneous gain change of $\approx 30\%$. Typical gain variations, caused largely by temperature fluctuations in the detector hall, were an order of magnitude smaller and varied slowly over each $24\,\text{hr}$ period. The cross check proves that the light injection calibration procedure is able to correct 30% gain deviations to within $\sim 2\%$. The remaining 2% disagreement was due to second order effects of the gain change, such as electronics trigger thresholds, as well as a run-to-run uncertainty caused by slight changes in magnet currents, collimator settings and Čerenkov pressure. The run-to-run uncertainty is discussed in Ch. 9.

The muon calibration was examined by studying the detector response to beam muons that transversed the entire detector lengthwise. Figures 5.15-5.16 show the average signal in each plane for punch-through muons at beam settings of $3.6\,\text{GeV}/c$ and $4\,\text{GeV}/c$ for data taken in the T11 and T7 beamlines respectively. The figures correspond to about two hours of data-taking. Only the signals from the central sixteen strips were considered in order to avoid including crosstalk hits created in the four strips along the edges of the detector. The average signal decreases with increasing plane number as the muon rolls off the relativistic rise portion of the dE/dx curve.

Residuals from a linear fit were used to quantify the quality of the cali-
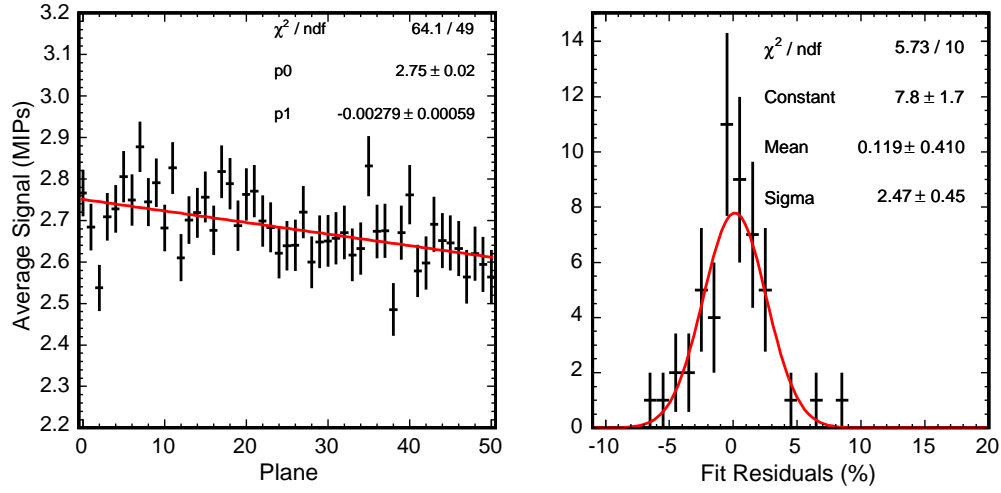
Figure 5.15: The average signal in each plane for beam muons. Note the suppressed zero of the ordinate. The beam momentum was set to $3.6\,\mathrm{GeV/c}$ and the detector was located in the T11 beamline. Muons that traversed the entire detector were selected. The decrease in signal with increasing plane number is caused by the falloff in dE/dx as the muon energy decreases toward minimum ionizing. The figure on the right shows the residuals to a linear fit. The width of the distribution indicates that the interplane calibration agrees to 2.5%.
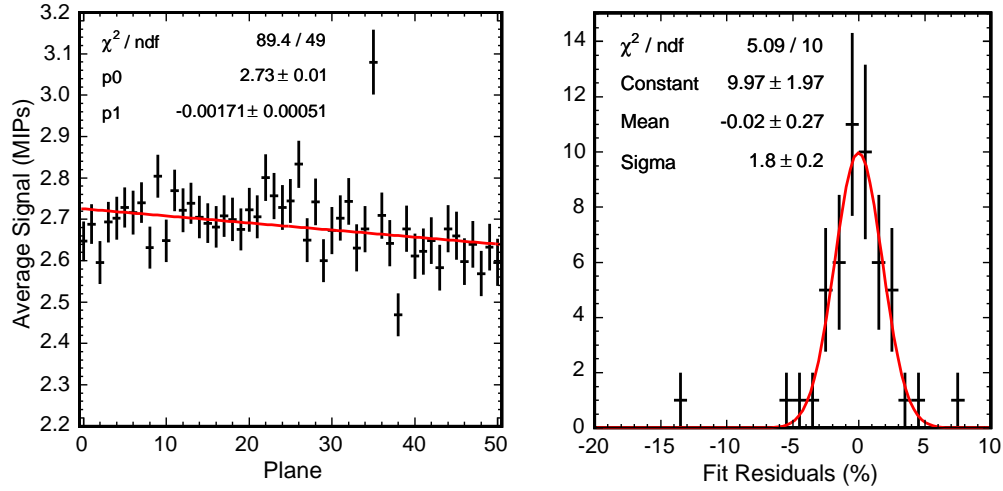
Figure 5.16: The average signal in each plane for beam muons. Note the suppressed zero of the ordinate. The beam momentum was set to $4\,\mathrm{GeV/c}$ and the detector was located in the T7 beamline. Muons that traversed the entire detector were selected. The decrease in signal with increasing plane number is caused by the falloff in dE/dx as the muon energy decreases toward minimum ionizing. The figure on the right shows the residuals to a linear fit. The width of the distribution indicates that the interplane calibration agrees to 1.8%.

bration[3]. The observed $\sim 2\%$ widths are considered quite acceptable, though the distribution for T7 shows that plane 35 was somewhat miscalibrated. The light output on this plane was low making the aforementioned zeroes correction difficult. The problem is not considered serious for calorimetry, since even high energy hadrons deposit most of their energy in the first thirty planes. The effect on certain pattern recognition tasks was somewhat larger.

5.4 Conclusions

For each event, signals observed in the detector are corrected for:

- Gain variations between pixels

- Gain drift with time

- Phototube and electronics response nonlinearity

- Differences, between channels, in the signals caused by muons traversing the detector.

The calibration procedure was able to correct for gain variations that were an order of magnitude larger than the typical gain drifts observed during data-taking. After calibration with cosmic ray muons, beam muons were used to demonstrate that the plane-to-plane response agrees to approximately 2%. This is considered acceptable for calorimetry.

After passing through the calibration chain, the detector's signals are expressed in units of MIPs. Many of the results of the following chapters will

---

[3]Second and third order polynomial fits were also performed but the conclusions drawn from those fits did not differ significantly from the linear fit.

160

use these units. The MIP has a somewhat arbitrary overall scale that depends on the cosmic ray energy spectrum. The final stage of the calibration will use the energy deposited by beam muons which range out in the detector[4] to set the overall scale, allowing results to be translated to the Near and Far detectors.

---

[4]The measured range of stopping tracks allows the initial momentum to be accurately determined, removing the arbitrary cosmic ray energy scale.

Chapter 6

Data Processing

The data processing was organized into four stages. Event data were held in gzip compressed binary format files (ROOT-files). The event IO and data compression were handled by the ROOT TTree class. Each processing stage read in a binary file and wrote out a processed file as well as various summary and log files. The four processing stages, summarized in Fig. 6.1, were:

Offline Trigger: Built events out of raw data blocks. Output triggered *tdaq* files. Each entry in the output file corresponded to one event. Light injection and cosmic ray muon events were filtered and written to a separate file.

CalDetDST Construction: Constructed *CalDetDSTs* from the tdaq files. Calibration was applied at this stage, particle identification was performed, tracks and showers were reconstructed and simple topological quantities were calculated. Events with DAQ errors were removed at this stage. The output file has one event per entry and was somewhat larger than the input file, owing to the additional reconstructed and

topological quantities.

Second Pass DST: Constructed a second pass DST from the input CalDetDST. Additional derived quantities were computed. Test statistics, used to discriminate between pions and muons were computed during this stage using weights read in from an external file. No events were removed from the data-stream at this stage.

Histogramming: Quantities in the CalDetDST and the second pass DST were histogrammed and written to disk. The resulting histogram files were significantly smaller and could be transferred over the network for follow-on analysis. Preselection cuts were applied at this stage in order to select specific samples for the final analysis.

Details of the data processing are described below.

6.1 Offline Event Assembly

The raw data collected by the CalDet is formed into blocks (called time-frames) by the data acquisition system. These blocks contain all the digitizations from one second of data taking. Individual events were collected after a positive signal from the trigger system but are merged together in these time-blocks. Thus, each time-frame must be formed into events before detailed analysis can take place. The formation of events is handled by the *OfflineTrigger* software package.

The offline trigger uses a gap trigger algorithm [57]. That algorithm has since been incorporated as the standard trigger algorithm at the Far detector. The gap trigger algorithm works in a two stage process. First, the algorithm

163

Raw Data

`C00012345_0000.mdaq.root`

Offline Trigger → Trigger Summaries

Calibration Constants
PID selection criteria
Run Information

`C00012345_0000.tdaq.root`

CalDetDST construction *(Track/Shower reco.)* *(Simple event quantities)*

`CalDetDST-12345_0000.root`

Discriminant Weights

Second Pass DST *(Derived quantities)* *(Discrimination variables)*

`CalDetDST-12345_0000.root`
`pmcv-12345_0000.root`

Cuts

Histogramming → Histograms

Figure 6.1: A schematic overview of the processing chain, beginning with the raw data and ending with histograms of derived quantities. Final analysis was conducted using the summary histograms.
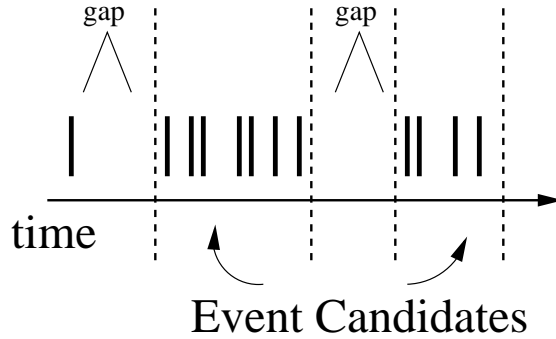
Figure 6.2: The gap trigger algorithm used by the OfflineTrigger. Candidate events are formed by searching for time-gaps of 156[ns].

iterates through the individual digitizations, searching for time gaps larger than 156 ns (that is 100 Far detector TDC counts). These time gaps mark candidiate event boundaries. Second, the candidate events are considered to see if they satisfy one of a number of trigger conditions. The conditions used are:

1. A hit on one of the VARC external input channels, marking an external trigger.

2. A hit in one of the Cerenkov channels.

3. A hit in the trigger PMT, signifying a light injection event.

4. N hits in a window N+1 planes long. This trigger is used to collect cosmic and atmospheric neutrino events at the Far detector but was not used at CalDet.

Figure 6.3 is an example of the distribution of trigger types for a 1 GeV run. A single event can satisfy more than one trigger condition. The bin

165

labeled *TOF* corresponds to the trigger formed from a coincidence of the beam counters. In the case of the $N/N+1$ conditions, the bin corresponding to the largest satisfied N value is filled. Events falling in the bin labeled *other* are primarily caused by accidental coincidences between the beam counters.
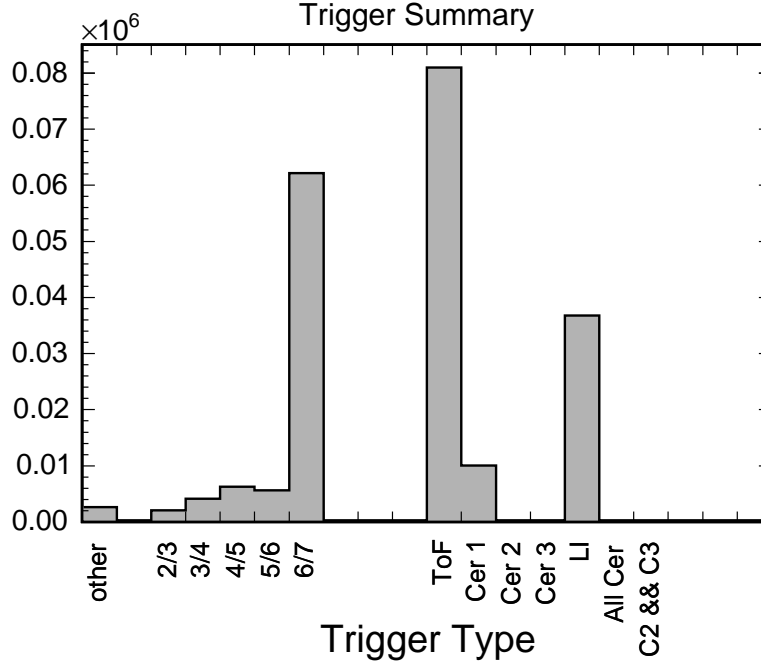
Figure 6.3: Distribution of trigger conditions found in run 40622, ($1\,\mathrm{GeV}$ positive polarity in the T11 beamline). Beam data were all required to fulfill the TOF trigger. In this run electrons were required to have Cer1 but in general the Cer trigger bit requirement depended on the particle type, beam momentum and pressure in the Čerenkov counters.

Offline trigger processing was run as an automated, near-online, process during the data collection. The algorithm was generally efficient enough to keep up with the data-taking without any prescaling. Raw data-files were reprocessed during the fall of 2003 on the Fermilab fixed target farm. In that

Table 6.1: The location and naming convention for triggered files stored in the Fermilab ENSTORE tape archive system.

Base directory	`/pnf/minos/caldet_reco/tdaq_data/`	
Beam events	`Crrrrrrrr_ssss.tdaq.root`	
Calibration events	`Crrrrrrrr_ssss.li.tdaq.root`	
The notation `rrrrrrrr_ssss` corresponds to the run and sub-run numbers		
Running Period	Run numbers	Sub-directories
T11 2002	`4XXXX`	`2002-09/`
T7 2002	`5XXXX`	`2002-10/`
T7 2003	`7XXXX, 8XXXX, 9XXXX`	`2003-09/, 2003-10/`
T11 2003	`11XXXX`	`2003-10/, 2003-11/`

processing, cosmic ray and light injection events, and beam events were written to a separate output files. The output files are stored in the Fermilab ENSTORE archive. Processing of the entire 2002 beam data set took approximately 17 days. Table 6.1 lists the locations and naming convention for the processed files. The entire CalDet 2002-03 beam dataset was processed and is available on ENSTORE. It's unlikely that further triggering will ever be needed.

6.2 CalDetDST construction

CalDetDSTs are constructed in the second phase of the data processing. During this stage, calibration is applied, particle identification (using the time-of-flight and Čerenkov information) takes place, tracks and showers are reconstructed and simple topological quantities are computed. Events not deriving from a coincidence of beam counters and events in which an error was reported by the online system were rejected at this stage. The level of rejection due

167

Table 6.2: Special database tables used to construct CalDetDSTs.

PLEXRAWCHANNEL-READOUTTYPE	Stored IDs for Čerenkov , TOF and LI channels
CALDETBEAM-MOMENTUM	A table used to lookup the beam momentum
CALDETTOFRANGE	Stored $2.5\,\sigma$ selection limits for TOF PID of π, μ, e, k, p
CALDETCERRANGE	Stored selection limits for Čerenkov PID of π, μ, e, k, p
CALDETOVERLAPWIN	Stored a time window around the nominal trigger. Used to reject pileup events and mis-triggers
CALDETCERTIMEWIN	Stored a time window, relative to the trigger, in which Čerenkov hits were required to fall

to errors was very low (most runs were completely error free). The data in CalDetDSTs are held by ROOT TTree objects which manage the storage and the IO of events.

A set of special, CalDet specific database tables were needed by the processing. These tables, listed in Tab. 6.2, held PID cut ranges, the beam momentum, IDs for the special CalDet TOF and Cerenkov channels, and timing windows. Briefly, CalDetDSTs contain:

Header information: The event number, the trigger word (from the offline trigger), the trigger time, the beam momentum, the temperature, a particle identification word and two words used in pileup rejection.

Response information: These included the total signal, the summed signal from even and odd planes and both ends, the signal of the largest hit, the time of the last hit in the event and the signal in planes 0 and 1.

Topological information: The strips in planes 0 and 1 with the largest signal (estimators of the event vertex), the longitudinal center of gravity of the event, the horizontal and vertical centers of gravity, the radius of the event and the plane of shower max. Also, the number of hits, the number of hit strips and the number of planes with a hit were computed and stored.

Particle ID information: The TDC value from each of the TOF counters, the Čerenkov ADC values and times of the Čerenkov hits.

Reconstructed information: NtpSRShower and NtpSRTrack objects. These objects held data from the MINOS standard track and shower reconstruction.

Individual Hits: An array of the individual hits in the event. The plane, strip, strip-end, pulse-height, and time of the hits were stored. Pulse-height was stored in ADCs, photoelectrons, drift and linearity corrected ADCs (known as SigLin), strip-to-strip uniformity corrected ADCs (known as SigCor) and MIPs. Storing the pulse-height in many formats was extraordinarily useful when studying the effect of calibration.

DST processing was done on the Fermilab user batch system using twenty-three 500 MHz dual processor nodes. To ease access, output DSTs were saved to disk rather than back into the ENSTORE tape archive. The average event size varied with the beam momentum, but 5 kb/Event at 2 GeV/c serves as a guide. The disk footprint is significantly smaller than the MINOS candidate output format, a major reason why DSTs were preferred. Processing time varied with the beam momentum. When the batch system was unoccupied

169

the majority of the 2002 beam dataset could be processed in 2-3 days.

6.3   Second Pass DST

A second round of processing was done on the CalDetDSTs and a summary
DST was created. The second pass processing focused on the computation
of a variety of topological quantities that were used to characterize hadronic
events and distinguish pions from muons. These variables fall into a seven
main categories:

Longitudinal profile: Variables which characterized the longitudinal profile
of events. The most useful of these were calculated by sliding a window N
planes long - with $N = 1, 3, 6, 9, 12$ - through the detector, and summing
the signal in that window. The position having the largest integrated
signal was saved to the DST along with the signal. These variables, called
EN (for the integrated signal) and EPN (for the window position) were
useful in distinguishing pions from muons. The variables were also used
to study and suggest improvements to the Far detector trigger algorithm.

Response regularity: Quantities designed to characterize the signal response
of the detector. These include the average signal per plane and the RMS
of the signal per plane. Hadronic showers were characterized by large
fluctuations in the longitudinal shower profile. The signal deposited by
muons was much more regular.

Event vertex: The event vertex was calculated as the strip with the largest
signal in planes zero (for the vertical position) and one (horizontal po-
sition). For events without a signal in plane zero or one, the next plane

in the same view was used. The vertex was also estimated by computing the center of gravity - weighting by the signal in each strip - in planes zero and one.

Shower angle: The shower angle in each view was estimated by first computing the center of gravity - weighting by the signal in each strip- in each plane and then fitting the result to a straight line.

Event end: The longitudinal end of the event was computed by looking for the last plane with a signal larger than 0.5 MIP, subject to the condition that one of the preceding four planes also has a signal larger than 0.5 MIP. Making a tighter requirement on the number of preceding planes with a signal larger than 0.5 MIP did not yield significantly different results for muon events. The transverse position of the event end was estimated as the strip with the largest signal in the end plane (for one of the two views) and the preceding plane (for the other view). The sum of the signals in the ending plane and the previous three planes was also tabulated and used to discriminate between pions and muons.

Shower vertex Generally hadrons penetrate a few planes before the first strong interaction, at which point a hadronic shower may occur. The longitudinal shower vertex was estimated by looking for the first plane with an integrated signal above a variable threshold. Thresholds of 2,3,4,5,6,7,8 and 10 MIPs were used. After determining the shower vertex, the shower width and summed signal was also computed.

Shower-like activity The number of planes having a summed signal larger than thresholds of 2,3,4,5,6,7,8 and 10 MIPs were computed. The number

171

of hits in the highest occupancy plane, and the three highest occupancy planes were counted. During the counting, hits with a signal less than 1.5 PEs were disregarded, in order to reject phototube cross-talk.

A set of test statistics (for example, the output of a linear discriminant) was also calculated during the second pass processing. The test statistics were used to discriminate between pions and muons. The formation of the test statistics will be described in a following chapter.

The second pass processing was done on the Fermilab user batch system. The processing was rather quick; When the batch system was unoccupied, the entire 2002 dataset could be processed in less than a day.

6.4 Histogramming

Histograms were created during the final stage of the processing. The histogramming stage read in a CalDetDST and the associated second pass DST in parallel, allowing joint distributions, with one variable from each DST, to be constructed. The procedure only processed events passing a freely configurable cut. The cut was typically used to separate the sample into pions, muons and protons, constructing identical histograms for each. Histogramming a single run usually took less than half an hour and produced over 300 histograms. The output files were relatively small ($\sim 1\,\mathrm{Mb}$) and could easily be copied off the Fermilab site for the final analysis.

6.5   Conclusion

Data processing was done in four stages, each of which produced an output file to be used by follow-on stages. The multi-stage processing - a traditional model in high energy physics - was useful because the downstream stages could be run multiple times in order to add variables and construct new histograms. The OfflineTrigger stage was only run once, CalDetDSTs were constructed 4-5 times, while the second pass and histogramming stages were run many tens of times. CalDetDSTs contained fully calibrated, reconstructed and identified events. Some topological information was included in the CalDetDSTs. The second pass DST contained an enhanced set of topological quantities, used to discriminate pions from muons and characterize hadronic events. The final analysis was done using histograms created in the last, histogramming, phase of the processing.

Chapter 7

Beamline Simulations

CalDet collected data in the T7 and T11 beamlines in the CERN East Hall. The beamlines have been partially characterized by the PS staff [46] and were operated using currents and collimator settings derived from [48]. The two beamlines are functionally similar but differ in their specific layout, energy range and acceptance. Additionally, the characterization done by the PS staff did not address a few issues of specific interest to the CalDet program. These include:

- The muon content of the beams.

- The kaon content of the beams.

- Energy loss in material upstream of the detector.

- Acceptance of the trigger.

Monte Carlo studies were conducted in order to address these issues. The studies broke down into three categories:

- Beam optics studies with the Decay TURTLE program.

- Energy loss and acceptance studies with a GEANT3 based program.

- Target modeling with the FLUKA03 code.

Results of the studies are presented below.

7.1   Beam Optics Studies

The optics of the T11 and T7 beamlines were simulated with a version of the widely used Decay-TURTLE program. Decay-TURTLE is designed to simulate charged particle transport through magnetic and electrostatic beamlines, accounting for second and higher order chromatic and geometric aberrations. The program optionally includes particle decay into a two body final state. The decay option was used to simulate the $\pi \rightarrow \mu\ \nu$ process.

The specific program employed, known as PSI-TURTLE [58], was based on and shared code with the original TURTLE program [59] but included a number of additional features. The PSI version of the code was used because the original code did not work properly on a modern LINUX system. The PSI did not implement some of the features found in the original program, the source code was not distributed and the program had a feature which prevented it from running in a batch environment making high statistics simulations very difficult.

The beamlines were modeled using the magnetic fields and magnet apertures listed in Tab. 7.1-7.2. Field values for a $1\,\mathrm{GeV/c}$ momentum setting are shown; fields for other momentum settings were determined by scaling the

175

Magnet Apertures and Fields for T11

Magnet	Half-aperture (cm)	B (kG) @ 1 GeV/c
QDE01	10	1.051
QFO02	10	0.927
BHZ01	70	4.017
QFO03	5	1.341
BHZ02	70	3.772
QFO04	10	1.515
QDE05	10	1.306
BVT01	70	1.129

Table 7.1: Magnet apertures and pole-tip fields used to simulate the T11 beamline. The nominal fields and apertures were recommended by the PS staff, but corrected to conform to the currents used in the data-taking (see page 87). For dipoles, the half-aperture refers to half the distance between the two poles. For quadrupoles, the half-aperture is the distance between the pole tip and the beam axis.

Magnet Apertures and Fields for T7

Magnet	Half-aperture (cm)	B (kG) @ 1 GeV/c
BHZ01	70	1.206
QFO01	10	0.839
QDE02	10	0.840
QFO03	10	0.794
QDE04	10	0.978
BHZ02	70	1.390
QFO05	10	0.745

Table 7.2: Magnet apertures and pole-tip fields used to simulate the T7 beamline. The nominal fields and apertures were recommended by the PS staff, but corrected to conform to the currents used in the data-taking (see page 87). For dipoles, the half-aperture refers to half the distance between the two poles. For quadrupoles, the half-aperture is the distance between the pole tip and the beam axis.

tabulated values by the ratio of the momenta. The beamlines layout, shown in Fig. 4.4-4.7, was based on References [48, 46] and confirmed by the PS staff.

Figure 7.1 shows the simulated T11 beam profile, for the nominal magnet currents (top) and the recalculated currents used during the data-taking (bottom). The beam profile corresponds to primary particles (e.g., pions rather than muons). The magnet currents were recalculated in order to improve the beam focusing, moving the focus onto the downstream time of flight counter. The simulated beamline begins at the target ($z = 0\,\mathrm{m}$) and ends at the front face of the detector ($z \approx 32\,\mathrm{m}$). Aperture and beam trigger constraints were not imposed.

The input phase space, visible as the initial size and angular spread of the beam in Fig. 7.1, was estimated from similar figures found in Ref. [48]. The initial momentum spread ($\delta p/p$) was set to 5%. The momentum spread of particles produced on the target is quite wide, but particles with momenta that differ by more than a few percent from the nominal beam momentum were lost on collimator and magnet apertures or were not accepted by the beam coincidence trigger. Figure 7.1 was in good agreement with a TRANSPORT based model of the beamline prepared by the PS staff.

Optionally, TURTLE can impose constraints on the beam dimensions in order to account for collimator slits, quadrupole apertures and trigger counters. Tracks passing outside the apertures are automatically stopped. Electromagnetic energy loss and hadronic showers are not modeled by the program. Figure 7.2 shows the result of applying aperture constraints. In the upper figure, tracks passing outside magnet apertures are stopped. The lower figure includes the constraints from collimator slits and the upstream time of flight counter. The imposition of constraints, particularly the requirement

177
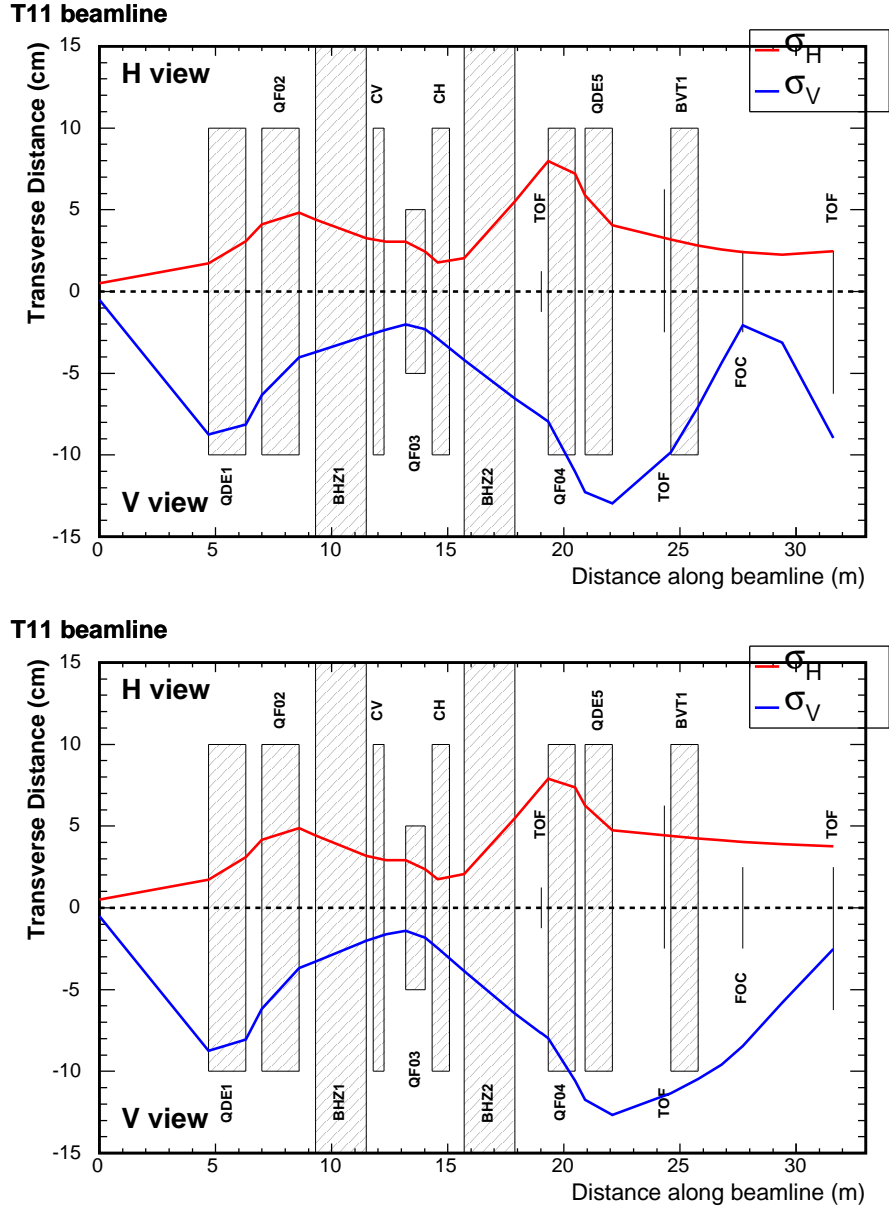
Figure 7.1: The RMS size of the T11 beam, in the horizontal and vertical planes, vs the position along the beamline. In the upper figure, the field values recommended in Ref. [48] were used. The field values in Tab. 7.1 were used in the lower figure.

178
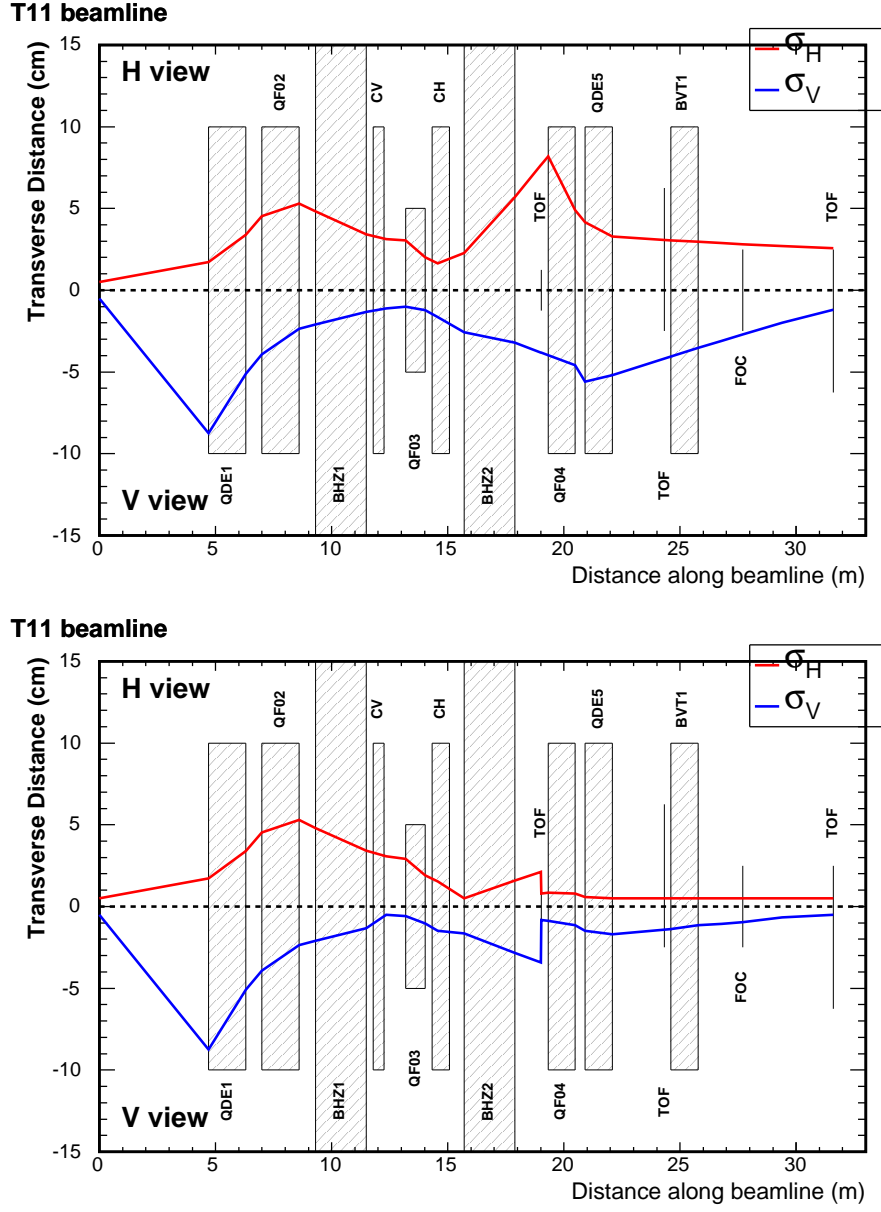
Figure 7.2: The RMS size of the T11 beam, in the horizontal and vertical planes, vs the position along the beamline. The field values in Tab. 7.1 were used in the simulation. In the upper figure, magnet aperture constraints were imposed. In the lower figure, collimator apertures and the acceptance of the USTOF counter were also included. Collimators, labeled CV and CH, were simulated with a 0.5 cm half apertures.

179

that tracks pass through the upstream TOF counter, dramatically decreased the size of the beam-spot and the momentum spread at the face of the detector. The upstream counter only accepts tracks passing within a $2.54 \, \text{cm}^2$ area centered on the beam axis. The accepted tracks are essentially parallel to the beam axis. Since the simulation does not include scattering, the result is that - neglecting decays - all of the tracks which pass through the upstream counter also pass through the downstream counter and are accepted by the trigger.

Figure 7.3 shows the T7 beam profile, without any constraints (top) and including all constraints (bottom). Similar to T11, the imposition of constraints dramatically decreased the spot size at the detector face.

Decay-TURTLE includes a simulation of particle decay, a feature that was used to model the muon content of the beam. The simulated beam at the target consisted solely of pions which were then allowed to decay as they traversed the beamline. Muons produced by decays were tracked through the beamline starting at the decay vertex and obeyed the same aperture constraints as pions.

Muons produced in pion decay have a broad momentum spectrum. In the pion rest frame the muon energy and momentum are:

$$E_\mu = \frac{m_\pi^2 + m_\mu^2}{2m_\pi} \tag{7.1}$$

$$p_\mu = \frac{m_\pi^2 - m_\mu^2}{2m_\pi} \tag{7.2}$$

The decay is isotropic. Boosting to the lab frame, the muon energy (E_μ') and momentum along the beam axis ($p_{\mu\|}'$) are:
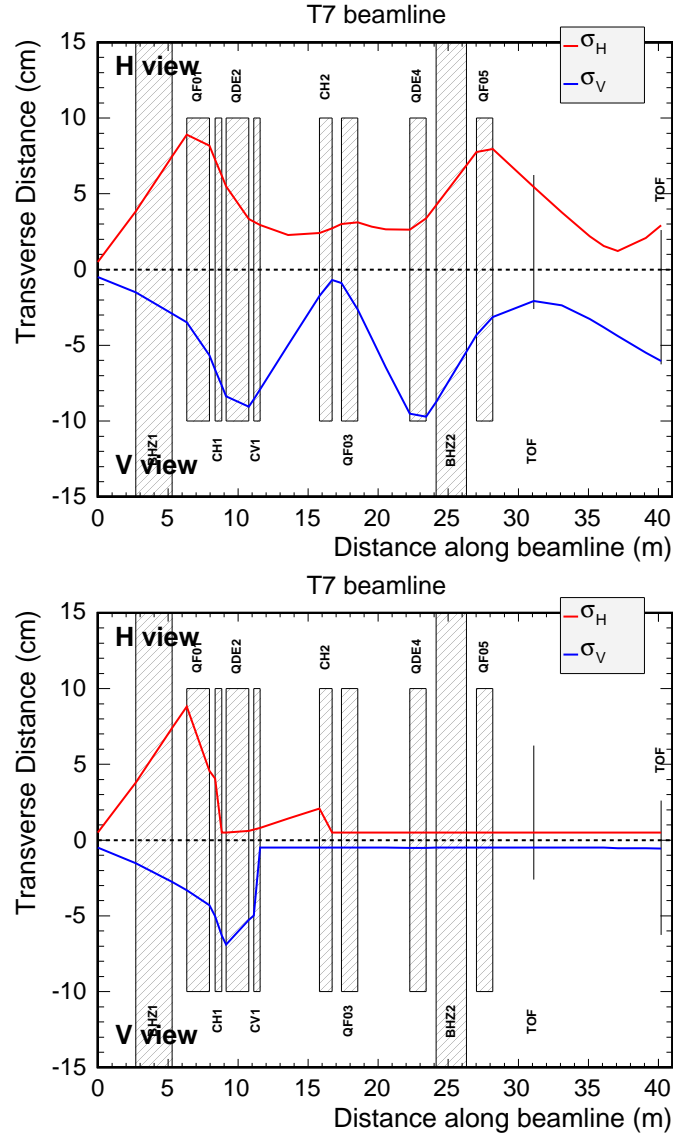
Figure 7.3: The RMS size of the T7 beam, in the horizontal and vertical planes, vs the position along the beamline. The field values in Tab. 7.2 were used in the simulation. In the upper figure, no aperture constraints were imposed. In the lower figure, magnet aperture and collimator constraints as well as the acceptance of the USTOF counter were included. Collimators, labeled CV1 and CH1,2 , were simulated with a 0.5 cm half aperture.

181

$$E'_\mu = \gamma E_\mu + \gamma \beta p_\mu \cos(\theta) \tag{7.3}$$

$$p'_{\mu \parallel} = \gamma p_\mu \cos(\theta) + \gamma \beta E_\mu \tag{7.4}$$

$$p'_{\mu T} = p_{\mu T} = p_\mu \sin(\theta) \tag{7.5}$$

Here, θ is the angle, in the pion rest frame, between the outgoing muon and the pion (i.e., beam) direction. The muon momentum along the pion's original direction is $p_{\mu \parallel} = p_\mu \cos(\theta)$. The muon momentum is maximized when $\theta = 0$ and minimized when $\theta = \pi$. In the limit $\beta \to 1$ and $\theta = 0, \pi$:

$$p_\mu = p'_{\mu \parallel} \approx \gamma (E_\mu \pm p_\mu) \quad (\cos(\theta) = \pm 1, \quad \beta \to 1) \tag{7.6}$$

$$= \gamma m_\pi = E'_\pi \quad (\cos(\theta) = +1) \tag{7.7}$$

$$= \left(\frac{m_\mu}{m_\pi}\right)^2 \gamma m_\pi = 0.573\ E'_\pi \quad (\cos(\theta) = -1) \tag{7.8}$$

Thus, the muon momentum falls in the range $0.573 E_\pi < p_\mu < E_\pi$. Figure 7.4 shows the predicted muon momentum spectrum at the CalDet face. The spectra peak near the nominal beam momentum and have an *off-momentum* tail extending down to $0.573 E_\pi$. The beam trigger has a large effect on the muon spectrum, suppressing the off-momentum tail. This is intuitive, since the *on-momentum* muons are in the momentum channel of the beamline and decay forward along the parent pion's direction.

Figure 7.5 shows the predicted muon composition of the T11 and T7 beamlines, after considering the trigger acceptance. The composition, expressed as a fraction of the total number of pions and muons, is nearly independent of the beam momentum, varying between 2-4%. Perhaps the result is not too suprising. The probablility for a pion to decay in a small distance
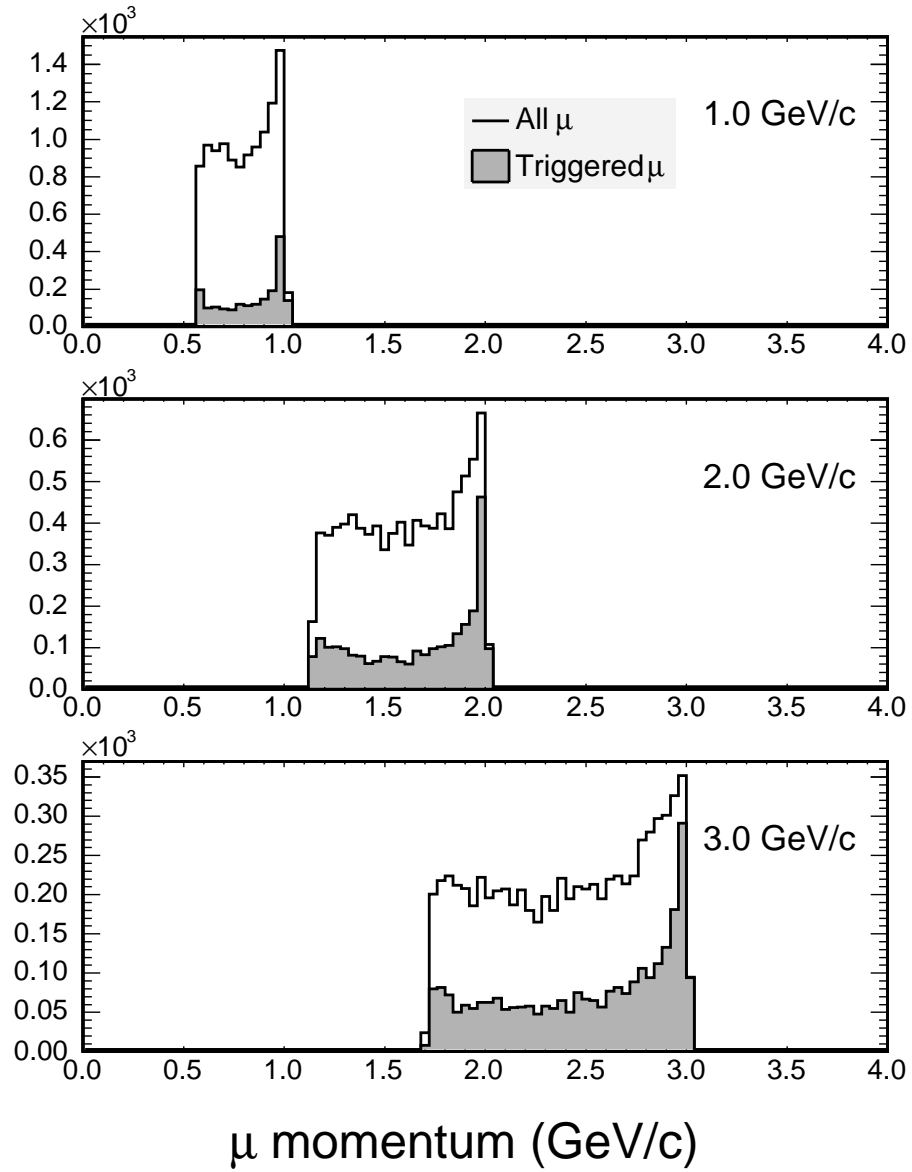
Figure 7.4: Muon momentum spectra, as predicted by TURTLE, for tracks accepted by the CalDet trigger. The muons are created in pion decay. The spectra peak near the on-momentum value, but have a tail extending down to $\sim 0.57\,E_\pi$. Results are from a simulation of the T11 beamline. T7 is similar.

δx is

$$\frac{m_\pi}{\tau p_\pi} \delta x$$

In the relativistic limit, the angle (with respect to the pion direction) of the daughter muon is

$$\phi \approx \frac{p_\parallel}{p_T} \propto \frac{1}{p_\pi}$$

where $p_T, p_\parallel$ are the longitudinal and transverse muon momenta in the lab frame. If the detector is a distance L away, the muon will enter the detector at a distance $L\phi$ from the projected pion impact point (i.e., the beam-spot). The muon acceptance is expected to roughly scale in inverse proportion to $L\phi$, that is as p_π. Therefore, the product of the decay probability and the acceptance, and hence the muon content, does not depend on the beam momentum. This simplistic argument implicitly assumes a sufficiently narrow pion beam, such that there are no pions outside the acceptance of the downstream counter that could decay into a muon that is accepted. Scattering is also neglected. The effect (on muons) of focusing has not been considered. TURTLE does predict a narrow pion beam (see Fig. 7.2) and completely neglects scattering, lending some justification to the argument.

7.2 GEANT Simulation

The GEANT3 code was used to construct a model of the downstream portion of the T11 and T7 beamlines (see Fig. 7.6, 4.9 and 4.11). The code was originally intended to predict the energy lost in trigger paddles, Čerenkov windows and gas, a multi-wire chamber, and the air in the detector hall. The code was later extended to model trigger acceptance and study the muon con-

184
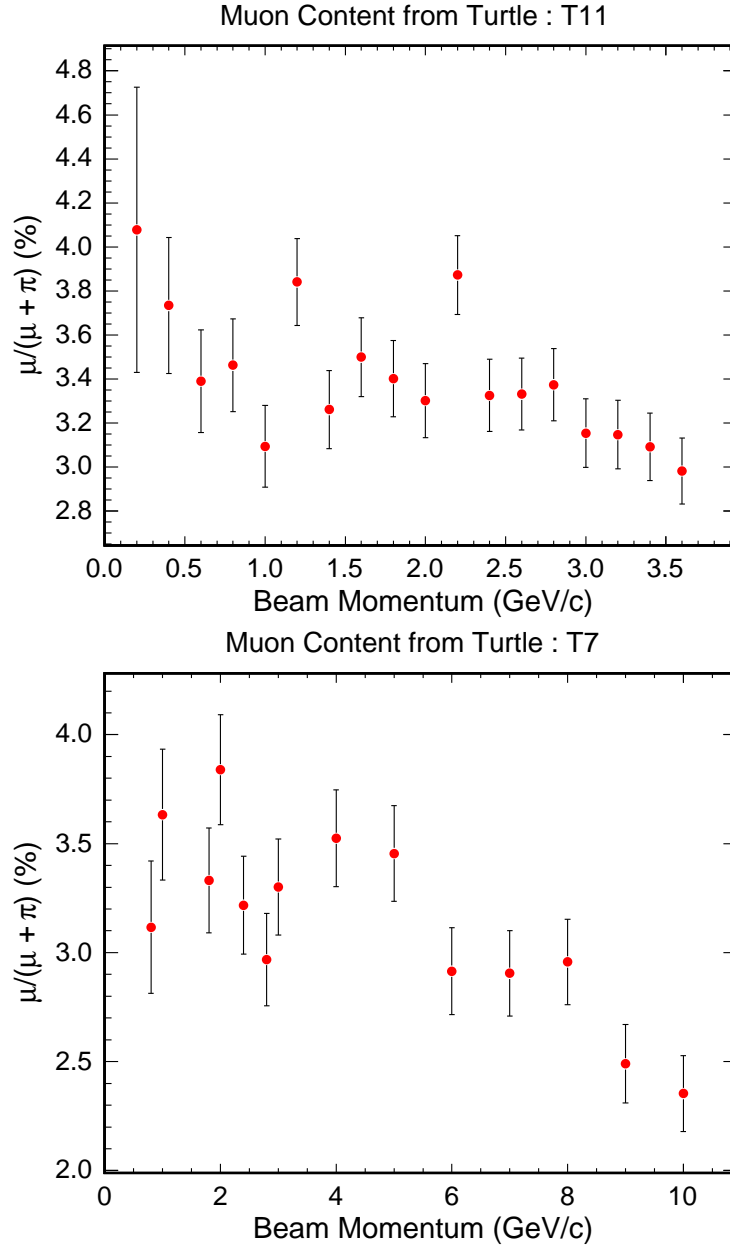
Figure 7.5: The muon content, expressed as a fraction of the total number of muons and pions accepted by the trigger, as a function of the beam momentum. The results are a prediction of the TURTLE simulation of T11 and T7.

185
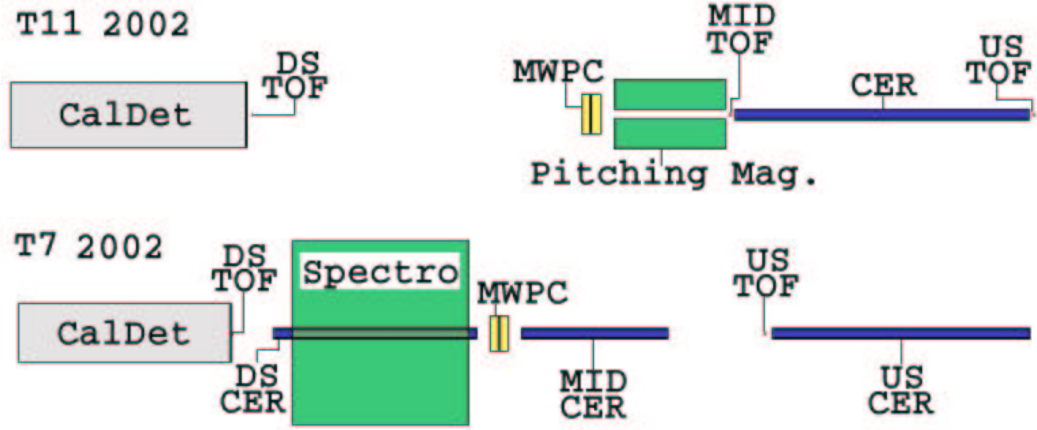
Figure 7.6: Cartoon layouts of the T11 and T7 beamlines, showing elements included in the GEANT beamline simulation.

tent. Events produced by the beamline simulation were also inserted into the GEANT simulation of the detector.

Only the downstream section of the beamlines was modeled. The T11 model began at the upstream time of flight counter. The simulation of T7 started just before the front face of the upstream Čerenkov counter. Tracks were extracted from the Decay-TURTLE simulation at those points and inserted into the beam-line simulation.

The upstream Čerenkov counters in both beam-lines run through the aperture of one (T7) or two (T11) quadrupole magnets. The fields of these magnets were simulated using a scalar potential:

$$\Phi = \frac{Bxy}{a} \tag{7.9}$$

where B is the magnitude of the field at the pole tip radius a and x, y are the coordinates perpendicular to the beam direction. At any point, the magnetic field is given by $\boldsymbol{B} = \boldsymbol{\nabla}\Phi$. The parameters in Tab.7.1-7.2 were used in the

186

simulation with the pole tip fields scaled according to the beam momentum. The actual magnet yokes were not included in the simulation. Instead, fields were restricted to the Čerenkov counter volume. The field values dropped sharply to zero outside the Čerenkov radius and at both ends of the quadrupole. Though the discontinuity is clearly not a good model of the quadrupole's fringing field, the exact form of that field is not expected to be very important (see Ref. [60, page 41]).

TURTLE predicted a very small pion beam-spot size, but did not include the effect of multiple scattering. The GEANT beamline simulation included a detailed treatment of multiple scattering in all volumes, including Čerenkov gas and the air in the experimental hall. As shown in Fig. 7.7-7.8, the inclusion of scattering dramatically increased the size of the pion beam-spot. Therefore the pion acceptance in the GEANT beam simulation is less than the TURTLE prediction. The muon spot size is also quite wide, but most of the spread is due to the decay kinematics rather than multiple scattering.

The predicted spot-size as function of momentum is shown in Fig. 7.9-7.10. Generally, focusing improved with momentum since the effect of scattering decreased. For pions in T11, the x,y asymmetry at low momentum settings was caused by particles scattering away from the beam axis upstream and inside of the last quadrupole (QDE05), which focused in the vertical plane and defocussed horizontally (see Fig. 7.1). The effect of multiple scattering decreased with the particle momentum, shrinking the asymmetry at high momentum settings. The asymmetry for muons at low energy - which is opposite to that of the pions - was caused by the BVT01 dipole, which limited the horizontal extent of the beam just downstream of the Čerenkov counter (see Fig. 7.6,4.9). At higher energy, the asymmetry turned over and was caused
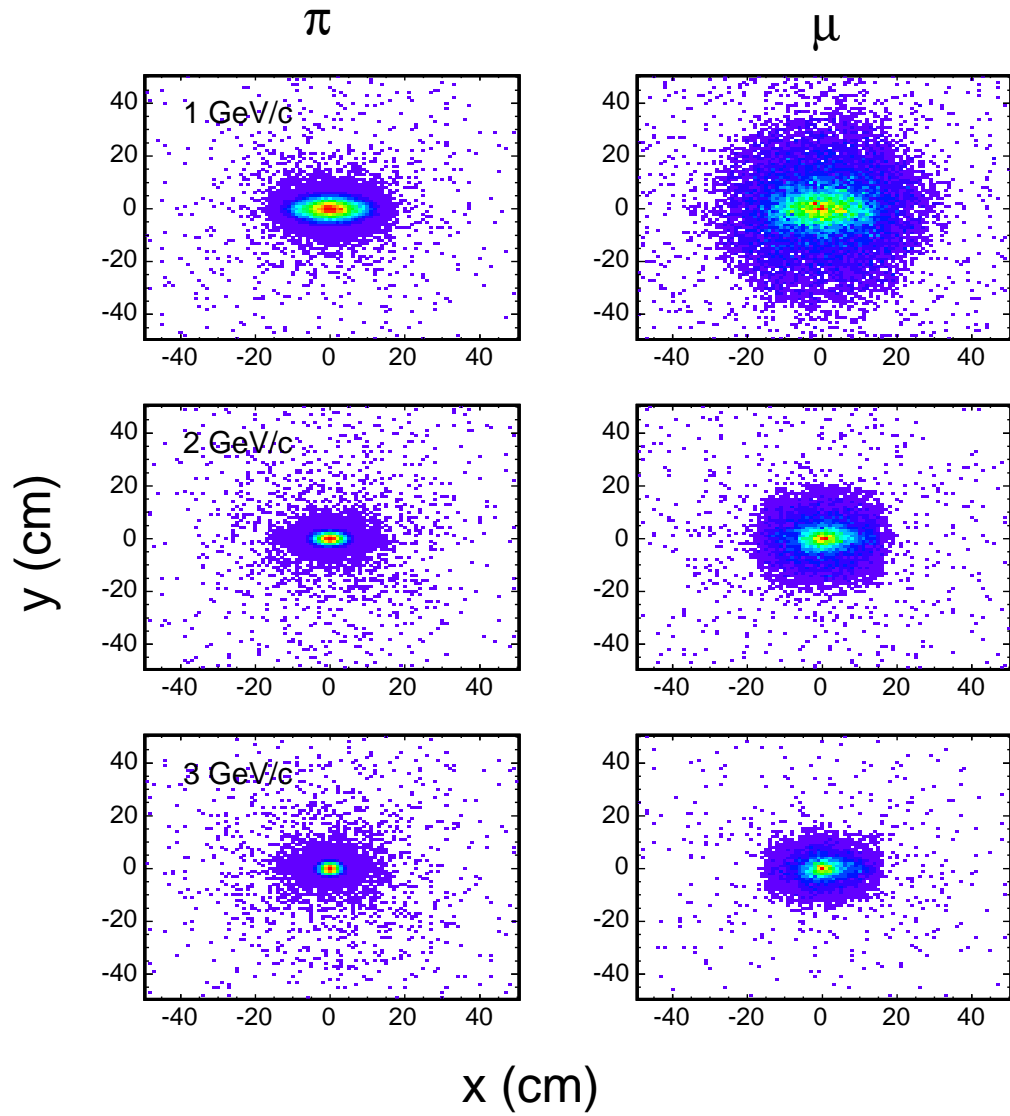
187

Figure 7.7: π^+ and μ^+ beam spots, at CalDet's front face, as predicted by the GEANT simulation of the T11 beamline. Momentum settings of 1, 2 and 3 GeV/c are shown. The downstream trigger paddle is centered on (0,0).
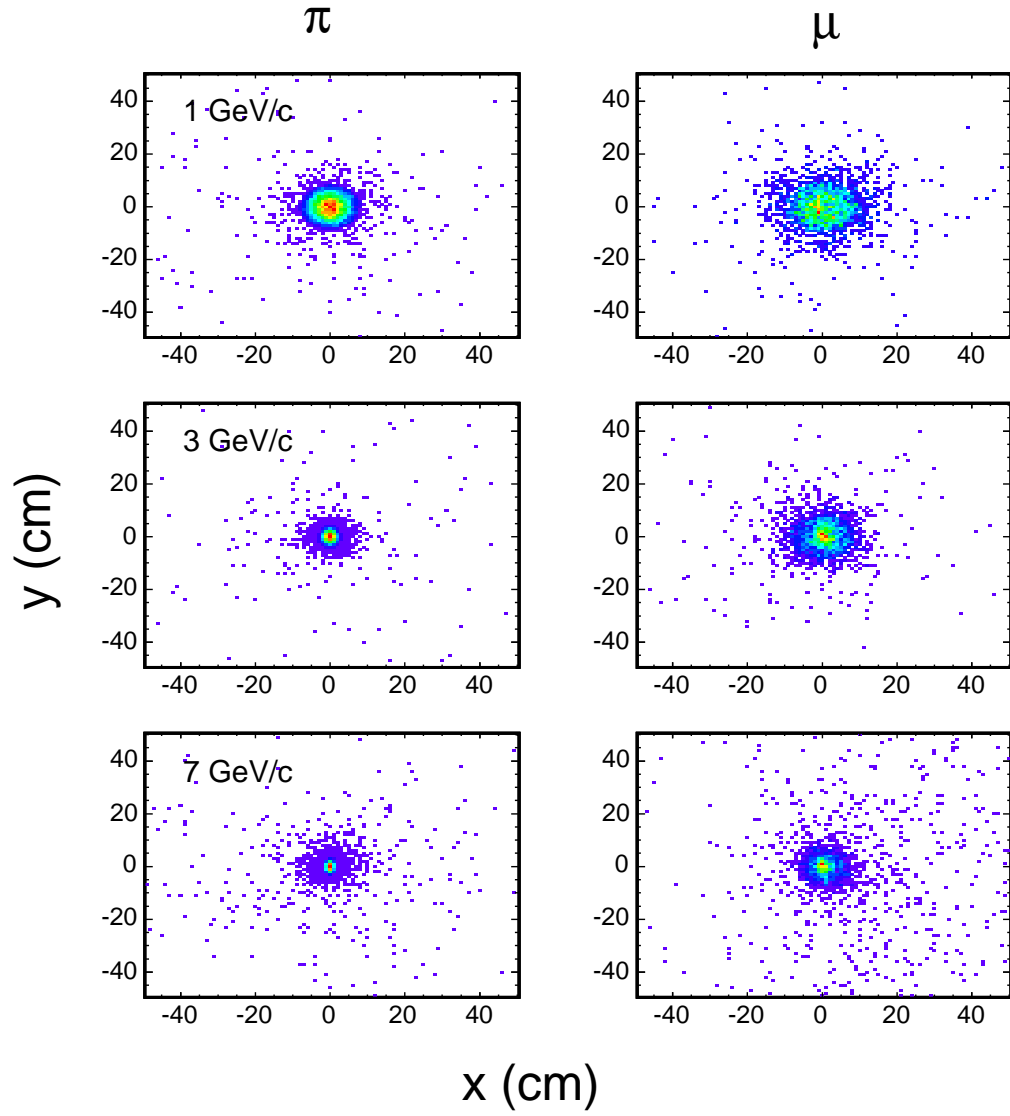
Figure 7.8: π^+ and μ^+ beam spots, at CalDet's front face, as predicted by the GEANT simulation of the T7 beamline. Momentum settings of 1, 3 and 7 GeV/c are shown. The downstream trigger paddle is centered on (0,0).
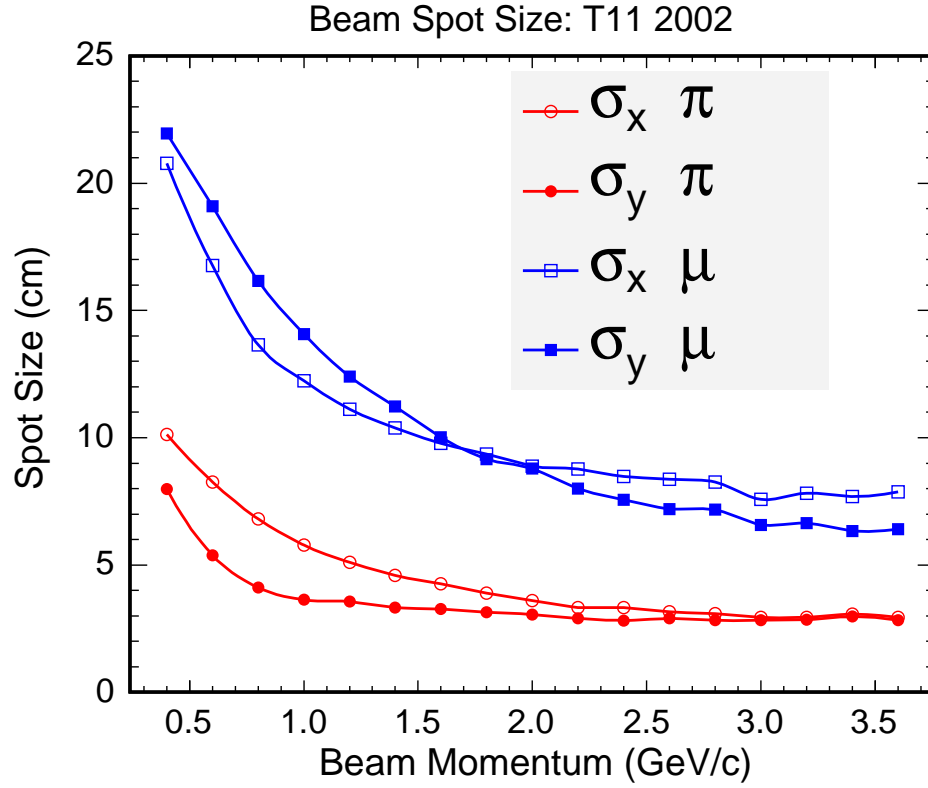
Figure 7.9: The RMS spot size, in the horizontal and vertical dimensions, as a function of the beam momentum. Results are from the GEANT simulation of the T11 beamline. In this figure, particles were required to pass through the upstream beam counter.
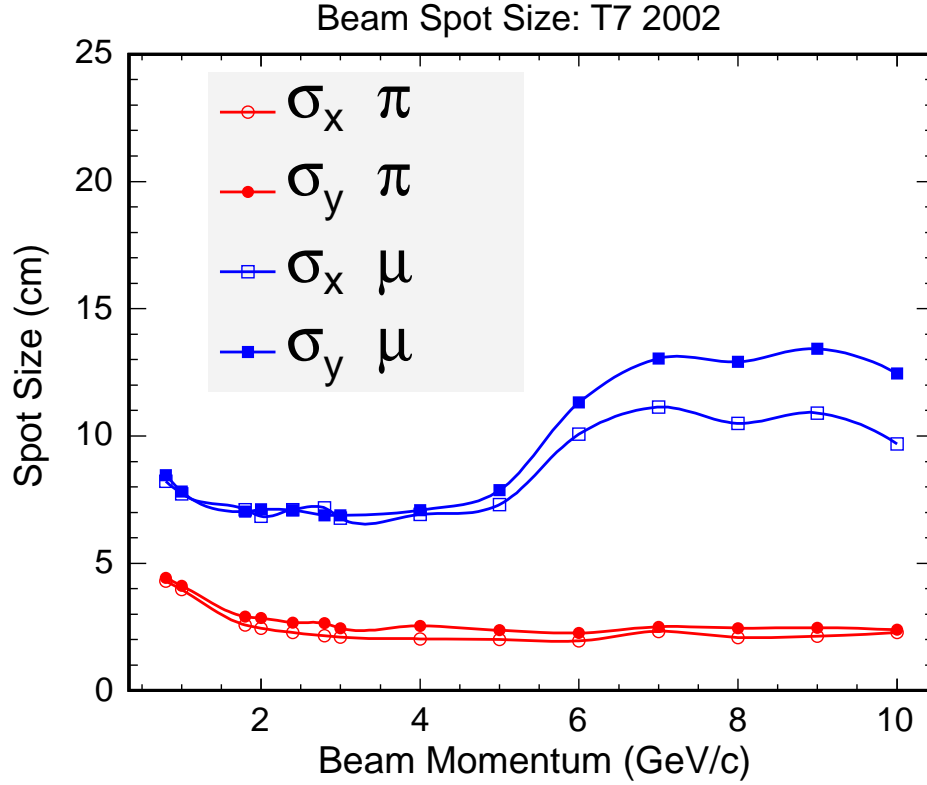
Figure 7.10: The RMS spot size, in the horizontal and vertical dimensions, as a function of the beam momentum. Results are from the GEANT simulation of the T7 beamline. Above $4\,\mathrm{GeV}/c$ muons which scatter out of the beam-pipe are able to punch through the (unused) spectrometer magnet upstream of the detector. The spectrometer magnet is shown in Fig. 4.6. The vast majority of punch-through muons are not accepted by the trigger.

by the same focusing effect that was present in the low energy pions. For T7, Fig. 7.10 displays a noticeable increase in the muon spot size for momentum settings above 5 GeV/c. The increase was caused by muons which were able to punch through the large iron spectrometer[1] magnet upstream of the detector. The vast majority of those muons were not accepted by the trigger.

Particles lose energy as they traverse the beamline. For μ, π, p, the majority of losses occur by ionization, rather than radiation. Pions and protons may also interact hadronically. Approximately half the losses occur in the scintillator paddles used for triggering, while the other half occur in the Čerenkov gas, mirrors and windows, and in the air present in the detector hall. Figure 7.11 shows the effect, on the particle momentum, of energy loss in beamline material. At high energy, protons and pions lose approximately the same amount of energy. As the beam momentum decreases, proton dE/dx climbs away from minimum ionizing and losses increase. For example, in T11 at 1 GeV/c, pions lost approximately 2.5% of their momentum, while protons lost about 3%. At 600 MeV/c pions lost about 3% but protons lost nearly 12% of their momentum.

Some pions and protons interacted hadronically upstream of the detector, experiencing a large energy loss that left them significantly *off-momentum*. Figure 7.12 shows the fraction of particles that had less than 95% of the average momentum - a relatively large loss. Events were required to satisfy the beam coincidence trigger. At high energy, approximately 2% of particles were off-momentum. At low energy in T7, the number of large proton (and pion) losses increased dramatically. These losses were caused by hadronic in-

---

[1]The spectrometer magnet was not energized during the data-taking and residual magnetic fields in its vicinity were measured and found to be negligible.
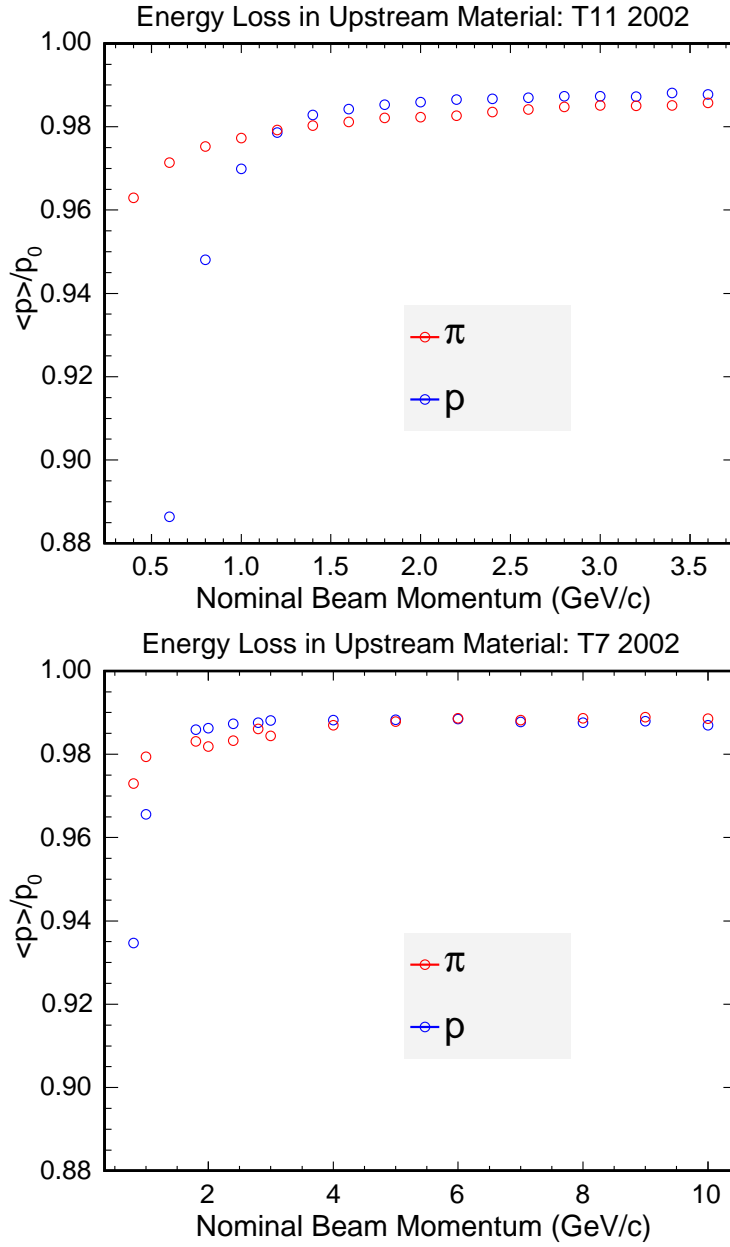
Figure 7.11: The effect, on the momentum, of energy loss in material in the T11 and T7 beamlines. The average momentum, as a fraction of the beam momentum, of particles accepted by the trigger is shown as a function of the beam momentum. In T7, the scatter between 2-3 GeV/c is not statistically significant.
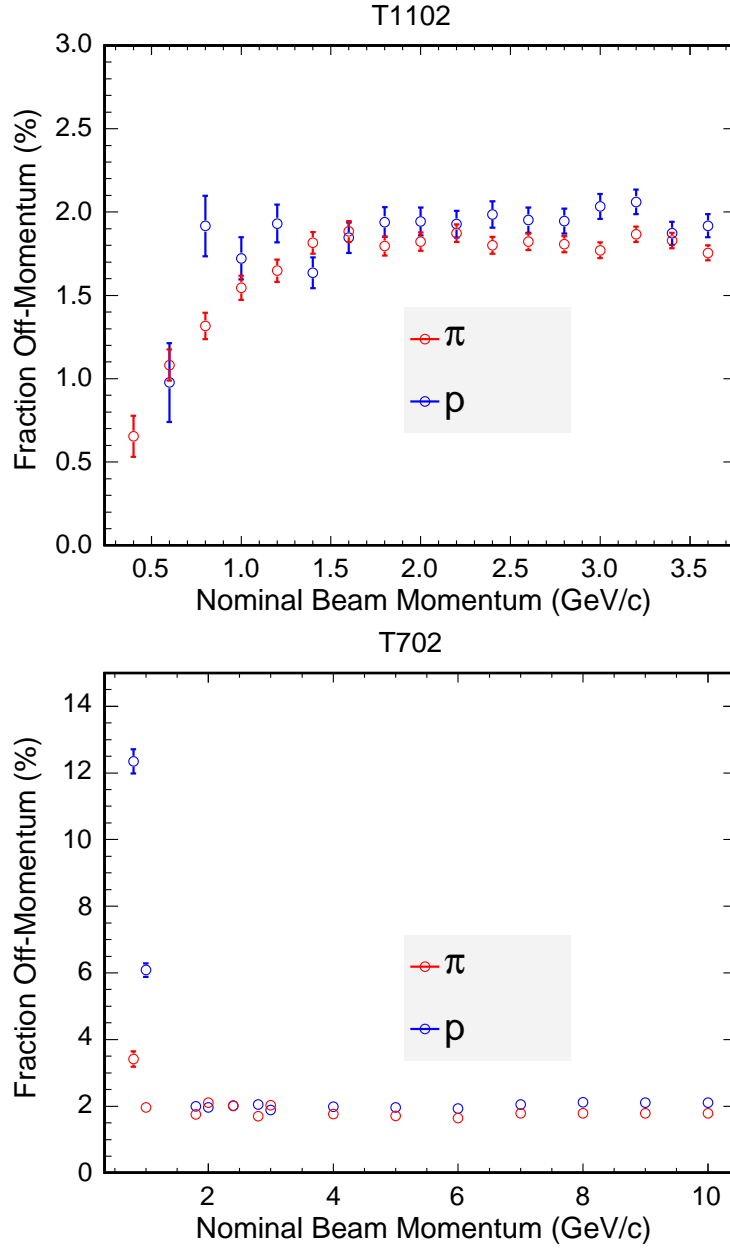
Figure 7.12: The fraction of significantly off momentum particles accepted by the trigger. The particles are defined as those having less than 95% of the average momentum. Most of these particles have either experienced a hadronic interaction or scattered through/off the walls of the Čerenkov counter.
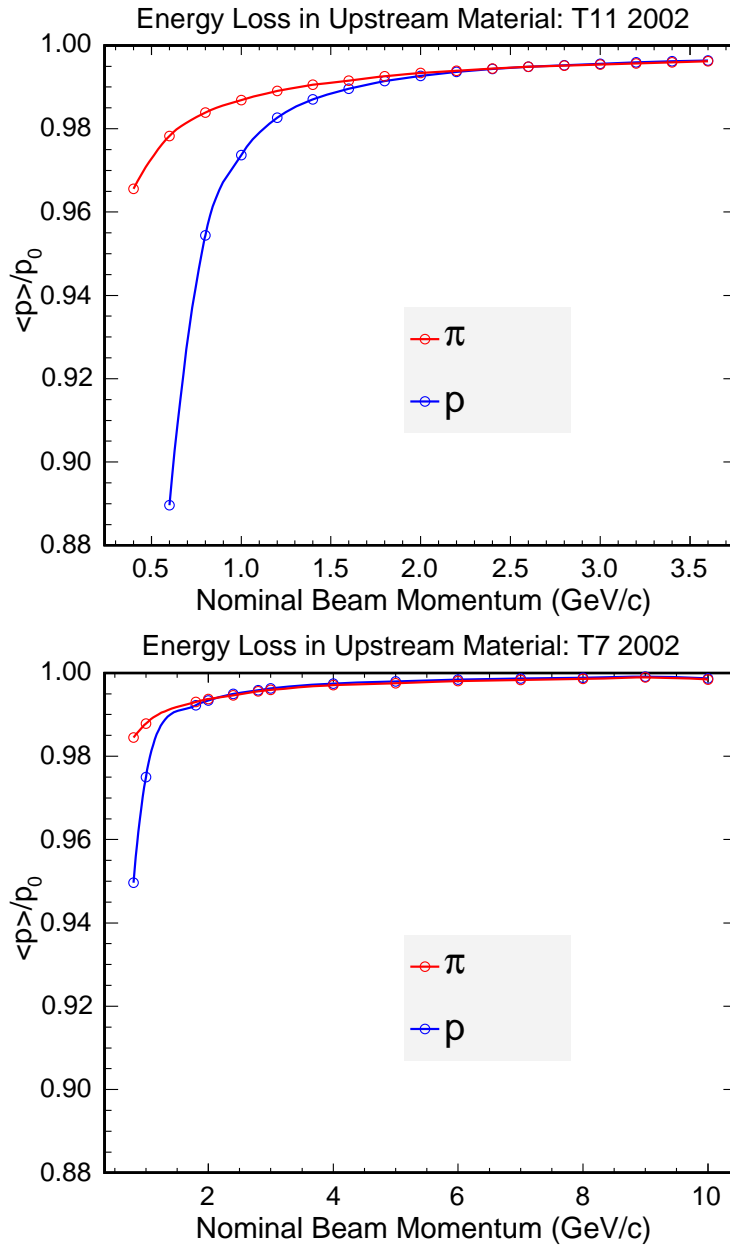
Figure 7.13: The effect, on the momentum, of energy loss in material in the T11 and T7 beamlines. All events were required to satisfy the beam trigger and off-momentum events (see Fig. 7.12) were removed. The average momentum, as a fraction of the beam momentum, is shown as a function of the beam momentum.

195

teractions in the downstream Čerenkov counter gas, window and walls, and to a lesser degree in the spectrometer magnet. Because the end of the downstream Čerenkov was only 80 cm from the detector face, the acceptance for off-momentum events was significantly enhanced. By comparison, in T11 the 4 m in front of the detector was occupied only by air. Figure 7.13 shows the effect of energy loss after the significantly off-momentum events were removed.

The GEANT beamline simulation allowed the muon content to be further characterized. The PSI version of the Decay-TURTLE code did not report the pion decay vertex - an unfortunate omission[2]. The vertex was recorded by the beamline simulation and yielded additional insight into the muon content. Figures 7.14-7.15 show the decay vertex versus the muon momentum for all muons striking the CalDet face and for those that were triggered. At low energy, the majority of accepted muons were produced within a few meters of the detector face. The exceptions are those muons that are either on-momentum $(\cos{(\theta)} = +1$ in Eq. 7.8), or maximally off-momentum $(\cos{(\theta)} = -1)$. These are the muons which follow the original pion's trajectory. As the energy increases, muons are accepted from greater distances. Figures 7.16-7.17 display the decay vertex for all muons and those accepted by the trigger. Muons input from Decay-TURTLE caused the high occupancy in the first bin. Figures 7.18-7.19 show the muon momentum spectrum before and after the trigger condition was applied. The spectra are similar to those produced by Decay-TURTLE (Fig.7.4), with the addition of some events in which p_μ is below the nominal kinematic limit $(\sim 0.57 E_\pi)$. These low energy muons were produced by pions which scattered or were created in Čerenkov walls and the BVT01

---

[2]The Decay-TURTLE manual lists an option to record the vertex, but apparently it was never implemented in the PSI version.
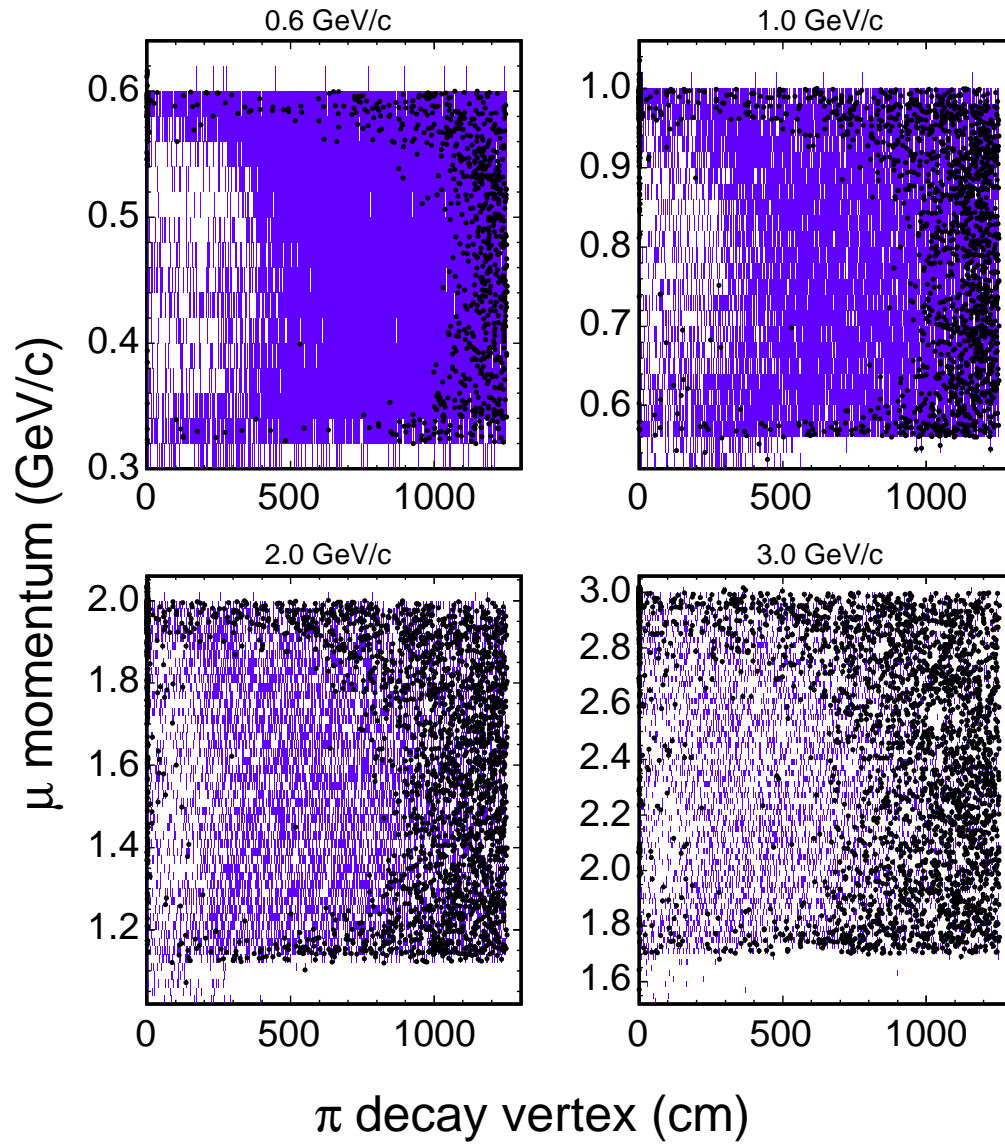
Figure 7.14: The muon momentum as a function of the pion decay vertex along the beamline. All tracks striking the 1×1 m CalDet face are shown in color. Muons accepted by the trigger are shown in black. Results are from the GEANT simulation of the T11 beamline. The upstream face of the CalDet was located at 1253 cm.

197
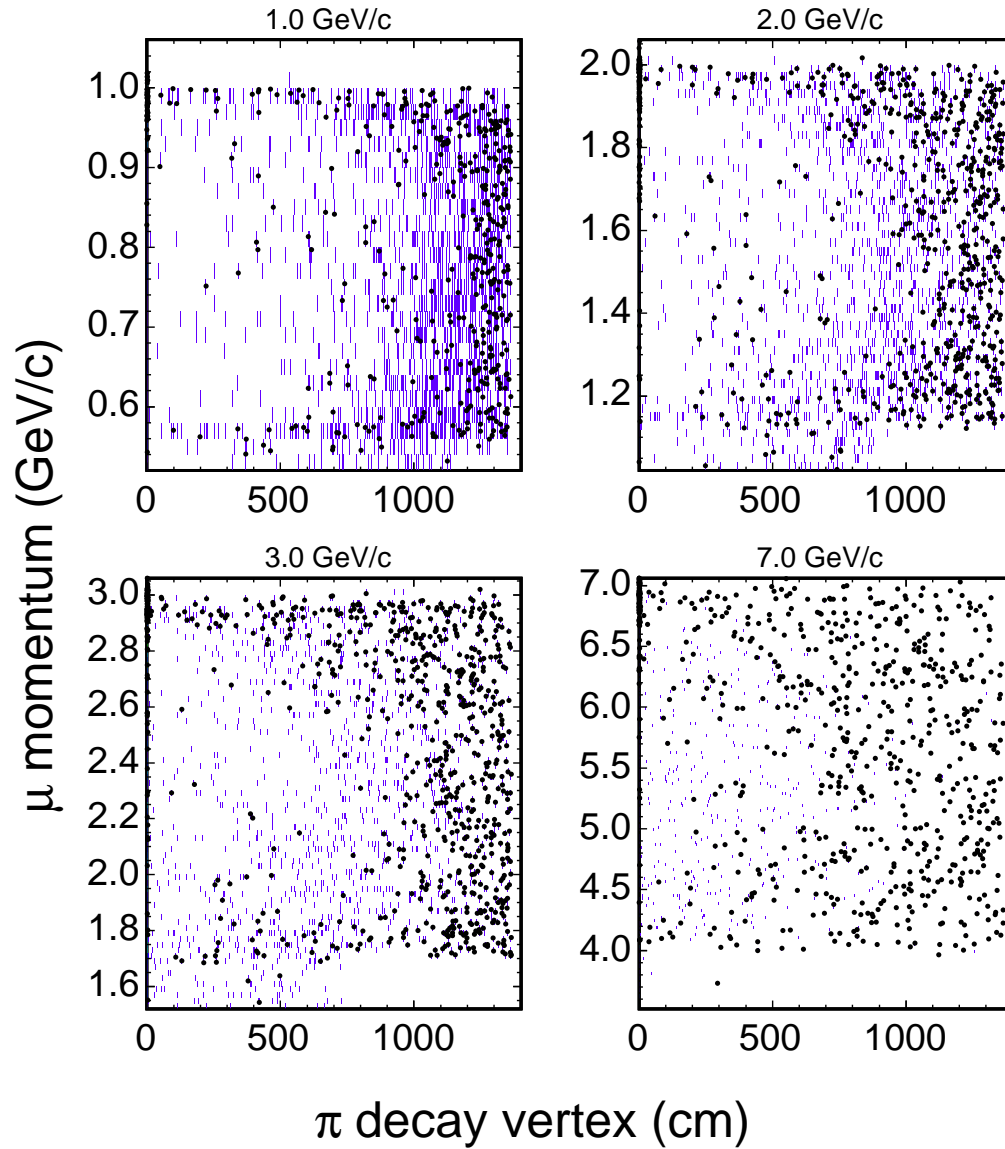
Figure 7.15: The muon momentum as a function of the pion decay vertex along the beamline. All tracks striking the 1×1 m CalDet face are shown in color. Muons accepted by the trigger are shown in black. Results are from the GEANT simulation of the T7 beamline. The upstream face of the CalDet was located at 1364 cm.
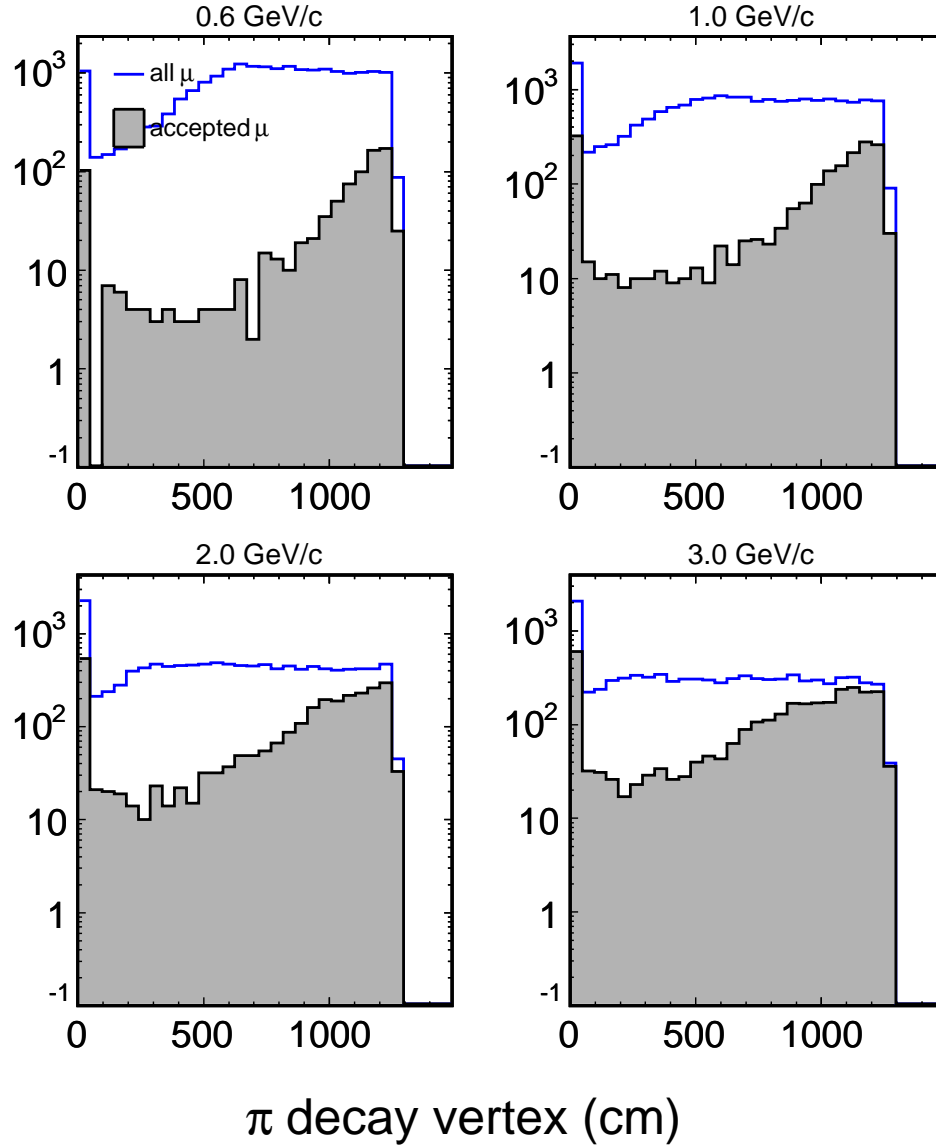
Figure 7.16: The pion decay vertex along the beamline for muons which strike the front face of the detector (open histogram), and for muons which are accepted by the trigger (shaded). The upstream face of the CalDet was located at 1253 cm. Results are from the GEANT simulation of the T11 beamline. The vertical scale is arbitrary.
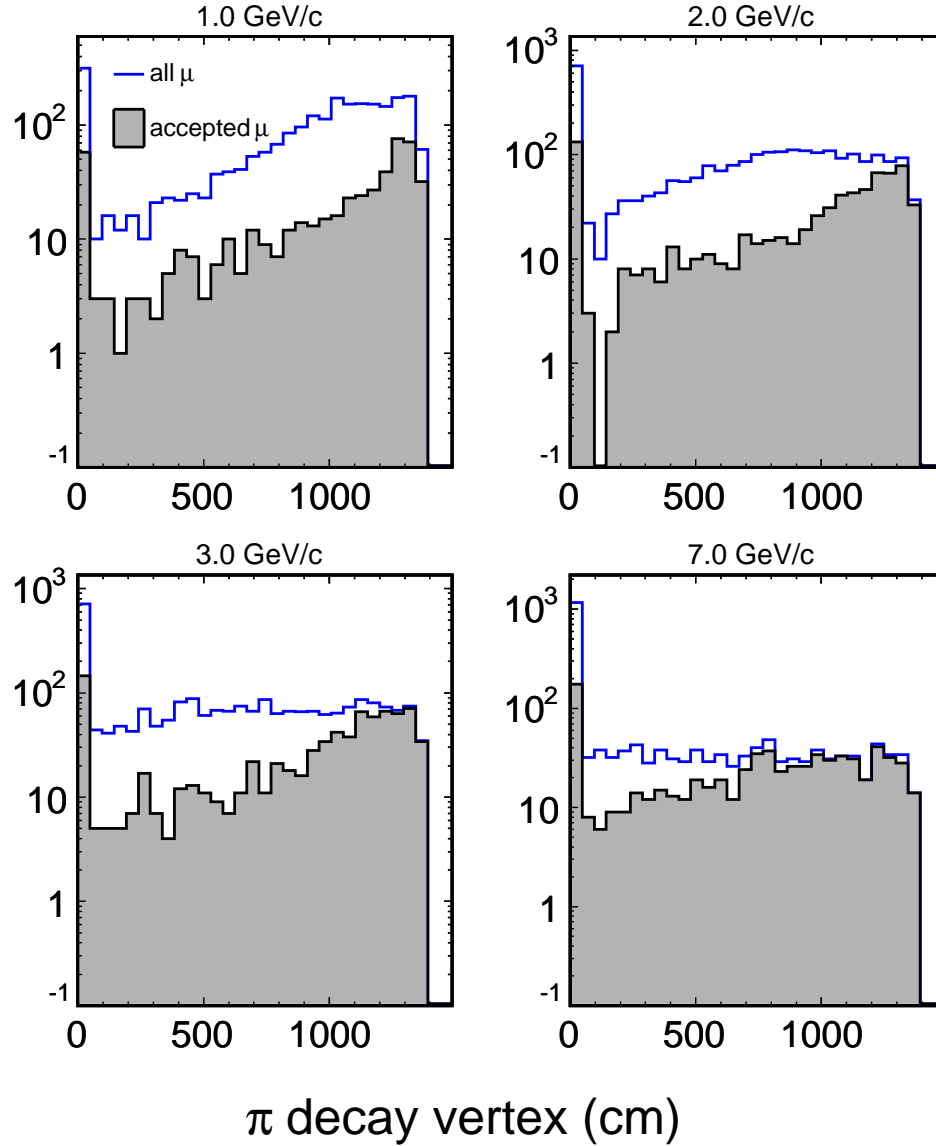
Figure 7.17: The pion decay vertex along the beamline for muons which strike the front face of the detector (open histogram), and for muons which are accepted by the trigger (shaded). The upstream face of the CalDet was located at 1364 cm. Results are from the GEANT simulation of the T7 beamline. The vertical scale is arbitrary.
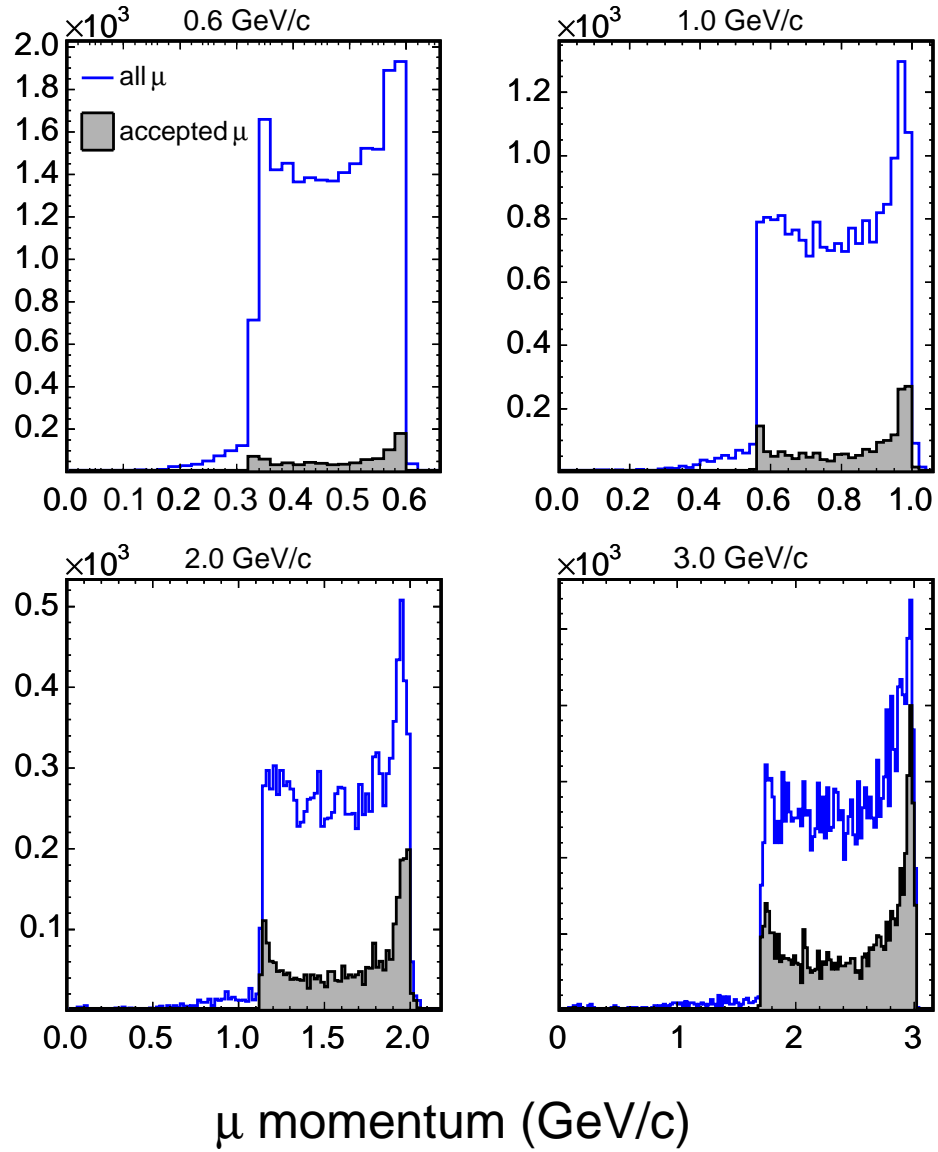
Figure 7.18: The momentum of muons which strike the front face of the detector (open histogram), and for muons which are accepted by the trigger (shaded). Results are from the GEANT simulation of the T11 beamline. The vertical scale is arbitrary.
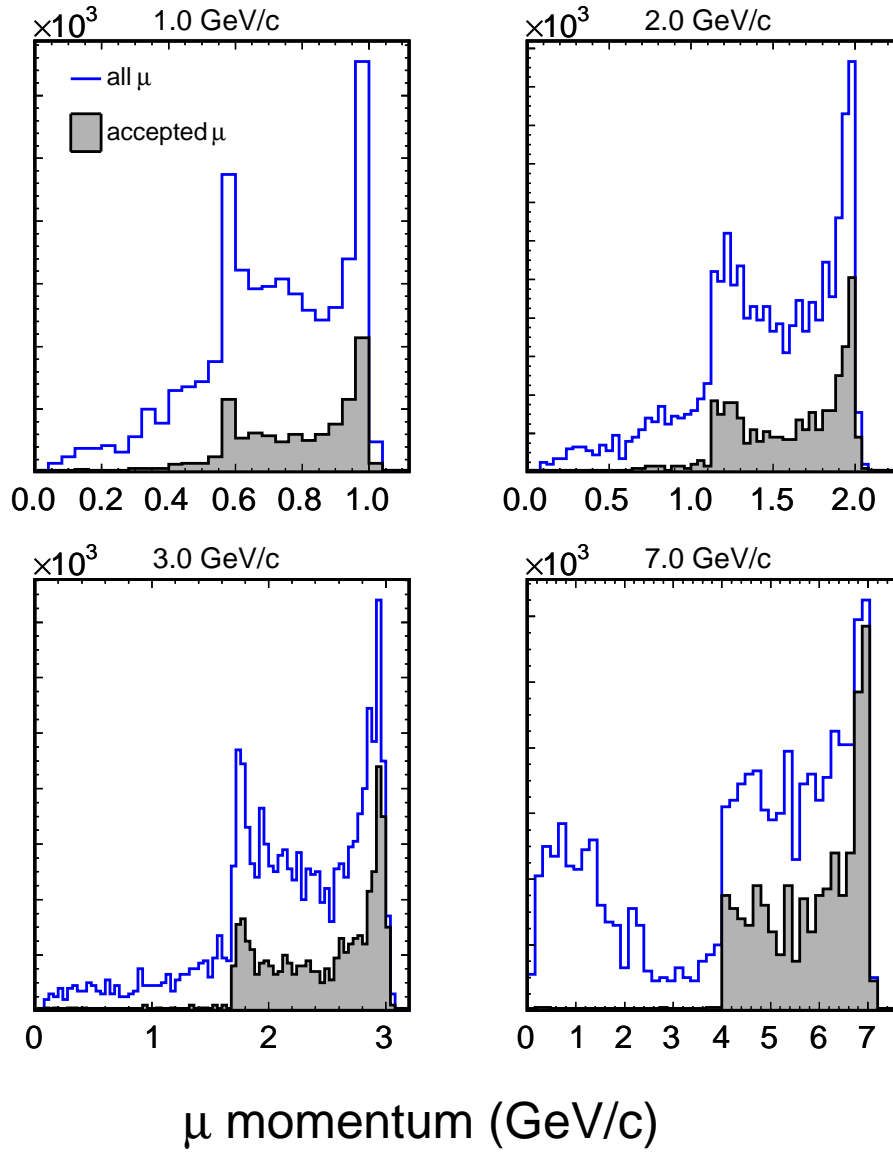
Figure 7.19: The momentum of muons which strike the front face of the detector (open histogram), and for muons which are accepted by the trigger (shaded). Results are from the GEANT simulation of the T7 beamline. The vertical scale is arbitrary.

202

and spectrometer magnets. Some muons also scattered after production. The low energy muons have a broad angular distribution and are suppressed by the trigger.

The muon content predicted by the GEANT simulation is larger than the Decay-TURTLE prediction. As Figure 7.20 shows, the fraction of muons is no longer constant, and instead falls with energy. The larger ratio was caused by the increase in the pion spot size due to scattering, and a consequential decrease in the pion acceptance. Muons were not strongly affected since the pion decay kinematics caused a naturally wide muon beam-spot even in the absence of scattering.

The beamline simulation was used to evaluate the trigger acceptance for π, μ, p and e. Starting at the target, particles were tracked through TURTLE and removed upstream of the first time of flight (T11) or Čerenkov counter (T7) at which point they were injected into the GEANT beamline simulation. The acceptance was defined as the ratio of triggered to total events of each type striking CalDet. The muon acceptance, when calculated in this way, is somewhat over-estimated at low energy since some muons do not hit the detector.[3] The result is shown in Fig. 7.21. The acceptance curves were parameterized as functions of the beam momentum with second, third, fourth or fifth degree polynomial fits. The acceptance for pions, electrons and protons each converge to unity at high energy. The acceptance of protons decreases somewhat more rapidly with decreasing momentum than it does for pion and electrons - a consequence of the $1/\beta$ dependence of the multiple scattering angle [2, page 166]

---

[3]The muon acceptance is not used in any of the calculations that follow but was presented here for completeness.
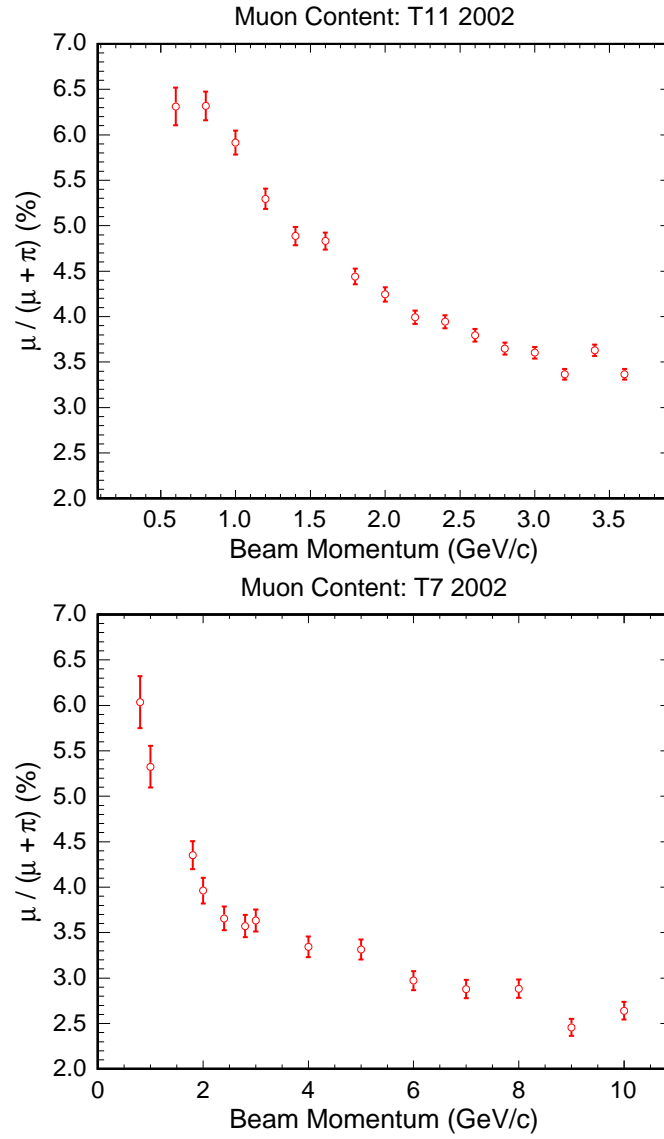
Figure 7.20: The muon content, expressed as a fraction of the total number of muons and pions accepted by the trigger, as a function of the beam momentum. The results are a prediction by the GEANT simulation of the T11 and T7 beamlines.
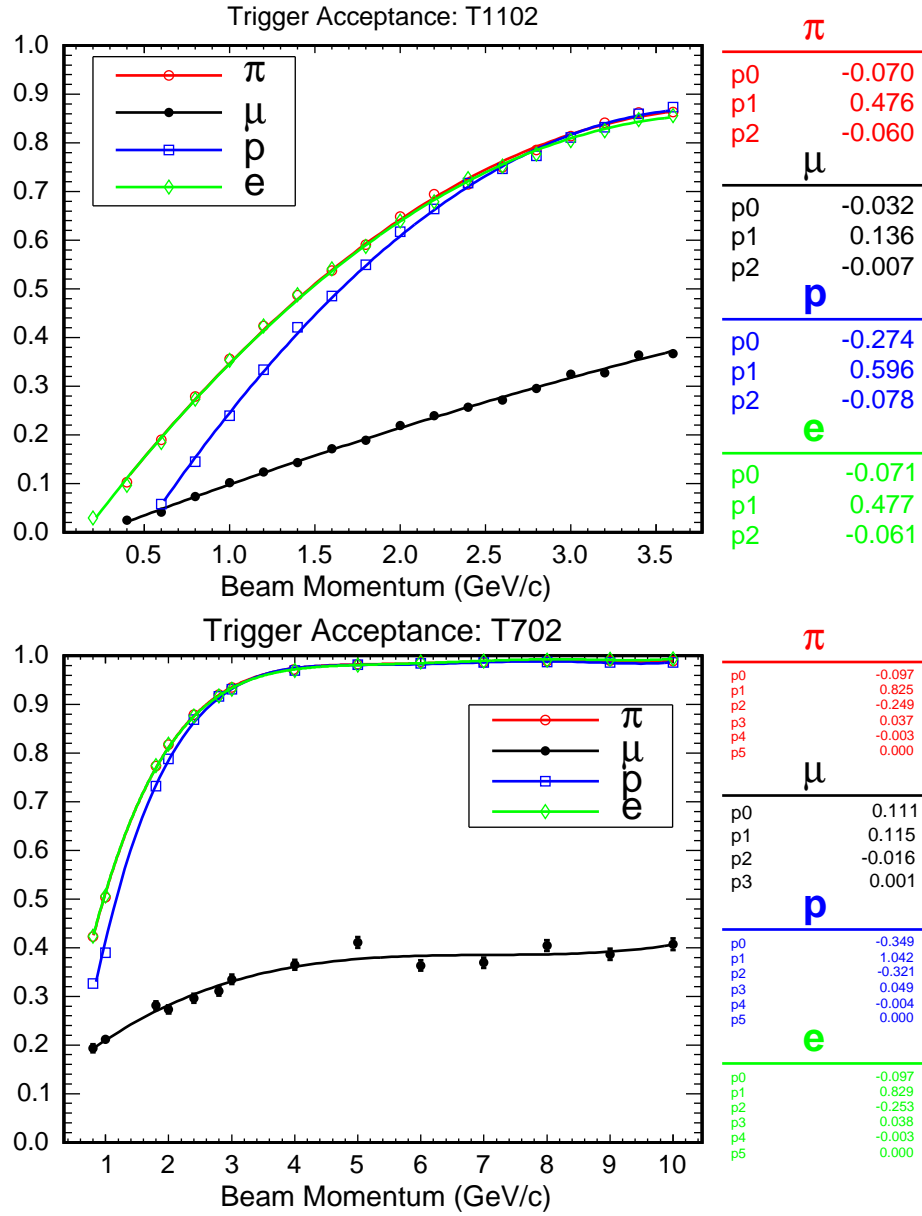
Figure 7.21: The trigger acceptance (on the ordinate) as a function of the beam momentum for the T11 and T7 beamlines. The acceptance was evaluated using the GEANT beamline simulation. The pion and electron acceptances were nearly equal over the entire momentum range and in the figures the pion curve is hidden beneath the electron curve. The parameters are the results of polynomial fits.

7.3 Target simulation

Particle production off the T11 and T7 targets was simulated with the FLUKA03 program [61]. A geometric model of each target was constructed according to the information in Tab. 4.1-4.3. The FLUKA geometry consisted of the target centered in an evacuated sphere 5 m in diameter. Only the targets used during the data-taking were modeled. A pencil beam of 24 GeV/c protons was directed onto the simulated target at 0° and the produced particles were recorded as they passed through an solid-angular region defined on the sphere surrounding the target. The angular region was defined to mimic the acceptance of the T11 and T7 lines.

The momentum spectra of particles accepted into the T11 and T7 beamlines are displayed in Figure 7.22. Targets 11 (hadron) and 6 (electron) from Tab. 4.1 were modeled. The largest difference is just one of scale: more particles are produced in the longer hadron target. The electron enriched target increased the electron content by approximately 20-30%. The kaon content is approximately 5% and anti-proton production is negligible. The number of negative pions is less than the number of positives - a feature that was apparent during the data-taking.

The results from simulating the T7 electron and ZnS screen targets are shown in Figure 7.23. The screen target was quite thin and it was necessary to enable a biasing feature in FLUKA in order to achieve significant results. The biasing featured decreased the hadronic interaction length for the *first* hadronic interaction of the 24 GeV/c primary protons in the target. Electrons were produced when photons from π^0 decay converted in the target - explaining why few electrons were produced in the thin screen target. However, the
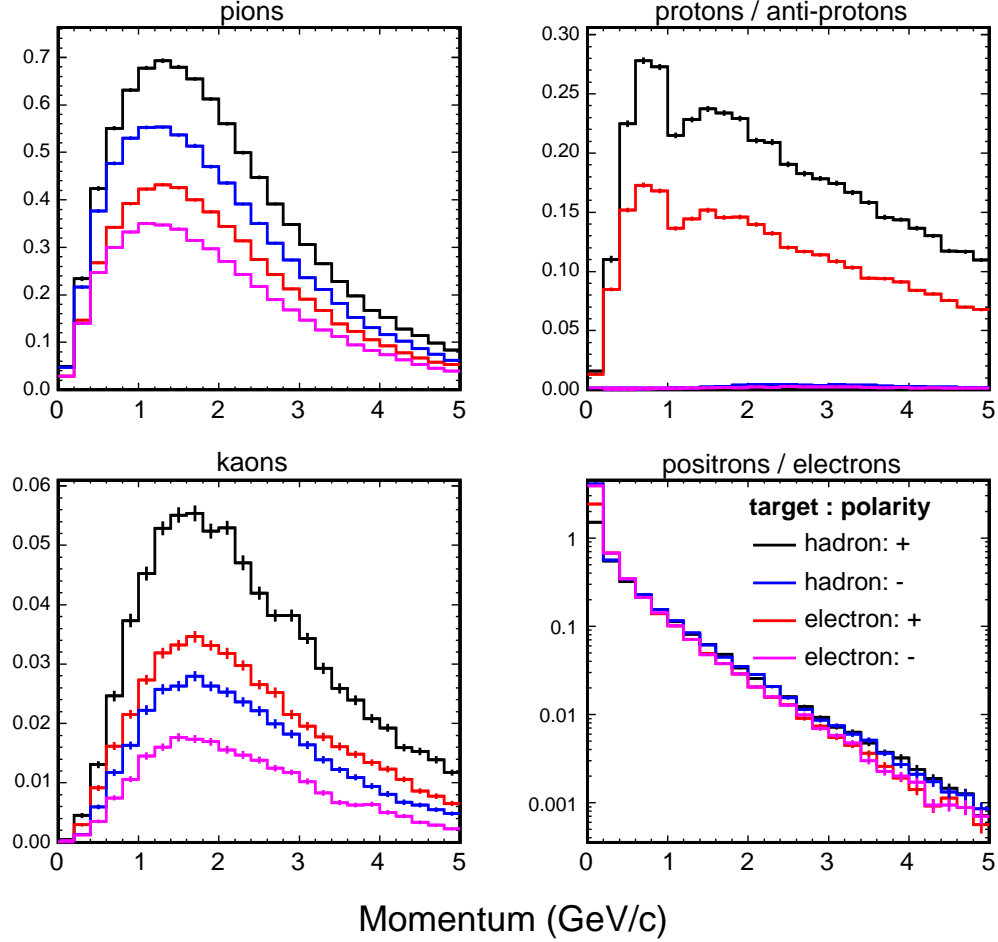
Figure 7.22: Momentum spectra of particles accepted into the T11 beamline. The program FLUKA03 was used to simulate targets six (electron) and eleven (hadron) of Tab. 4.1. The majority of data were collected with the hadron target. The electron/positron spectrum, shown in log scale, falls with increasing momentum as $\exp(-p)$. The ordinate scale is arbitrary but is consistent between each target and between the four figures.
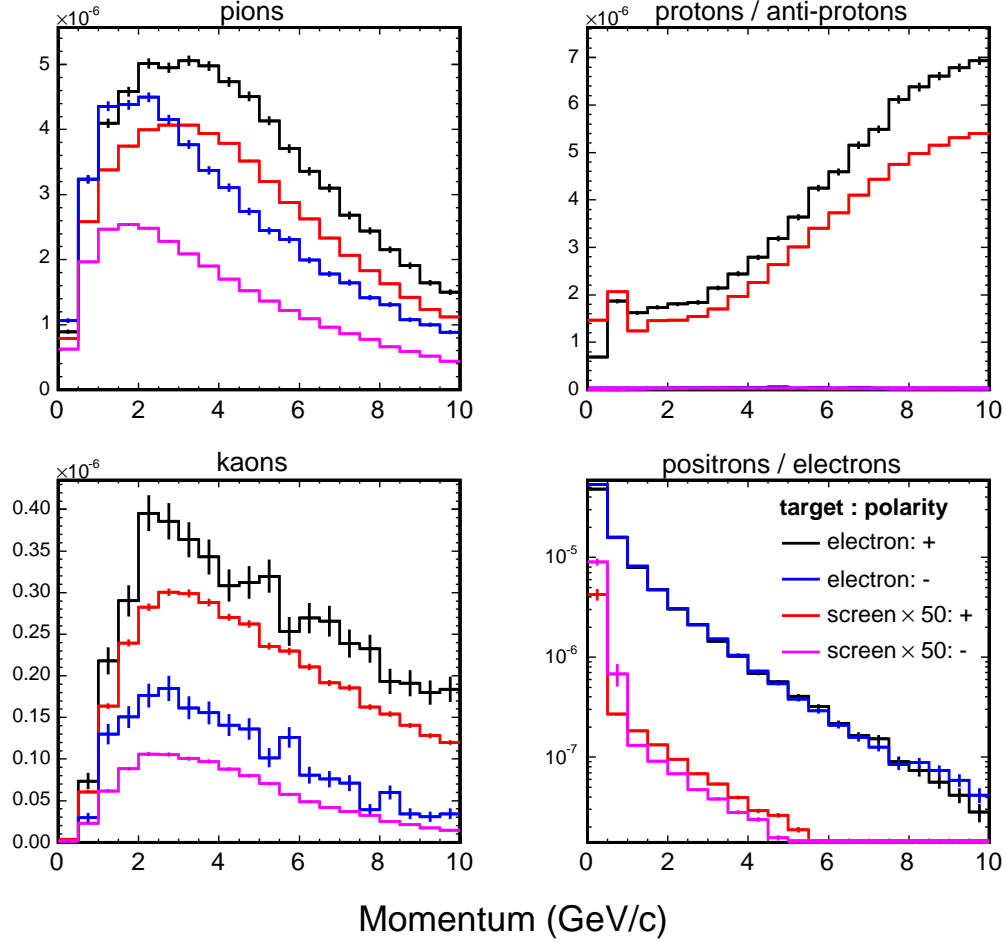
Figure 7.23: Momentum spectra of particles accepted into the T7 beamline. The program FLUKA03 was used to simulate targets one (screen) and two (electron) of Tab. 4.3. Spectra from the screen target were scaled up by an (arbitrary) factor of 50 in order to make them visible. The electron/positron spectrum, shown in log scale, falls with increasing momentum as $\exp(-p)$. The ordinate scale is arbitrary but consistent between the four figures.

fraction of electrons may be somewhat underestimated in this case since the air surrounding the target was not modeled.

The FLUKA prediction of the beam composition was compared to the measured values in T11 and T7. Figure 7.24 displays the results for T11. The figures on the left show the fractional composition of the beam at the target as a function of the particle momentum. The pion and kaon curves were then corrected for decay between the target and CalDet and the momentum dependent trigger acceptance, shown in Fig. 7.21, was applied.[4]. Finally, in order to compare to the data in which pions and muons were counted together, the pion curve was corrected by adding in the measured muon content. The figure on the right compares the FLUKA predictions - after these corrections - to the measured particle fractions.

The corrections made to the FLUKA curves are approximations since the actual acceptance is difficult to estimate without a complete simulation of the entire beamline - a substantial project. Even so, the agreement for T11 is reasonable. The main discrepancy appears to be an under-estimation of the π/e ratio, possibly caused by a deficiency in modeling $\pi^\pm/\pi^0$ at the target. The kaon content, only 1-2% at the detector, agrees with the data to approximately a factor of two.

Below $6\,\mathrm{GeV/c}$ in T7 the FLUKA predictions agreed with the data to within $\sim 10\%$ (absolute), though the π/e ratio was systematically under-estimated by FLUKA (see Fig. 7.25). Above $5\,\mathrm{GeV/c}$ the predicted proton content rises more rapidly than the data allow. The effect was seen when modeling both targets 2 (electron) and 1 (screen) (see Fig. 7.25). In the 6-10 $\mathrm{GeV/c}$ region, pions and muons were tagged with the downstream Čerenkov counter

---

[4]The correction for pions was used on the kaons
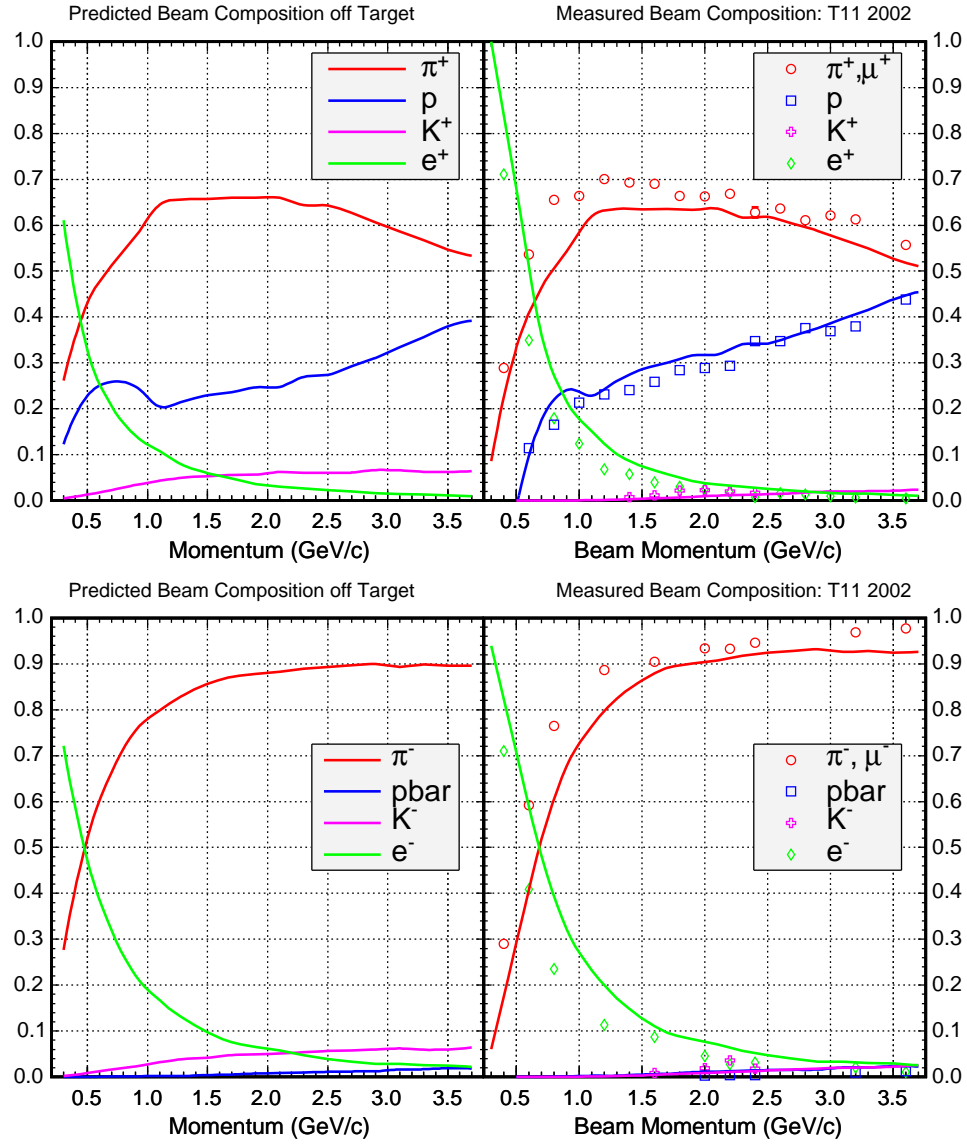
Figure 7.24: The T11 beam composition as a function of momentum. The ordinates show the fractional composition for each particle species. The prediction of FLUKA03 (shown as lines) is compared to the measured data (points). Positive particles are shown on the top row. Negatives are shown on the bottom row. The figures on the left show the beam composition at the target, while those on the right show the composition at the detector. The results from a simulation of Target 11 from Table 4.1 are shown.
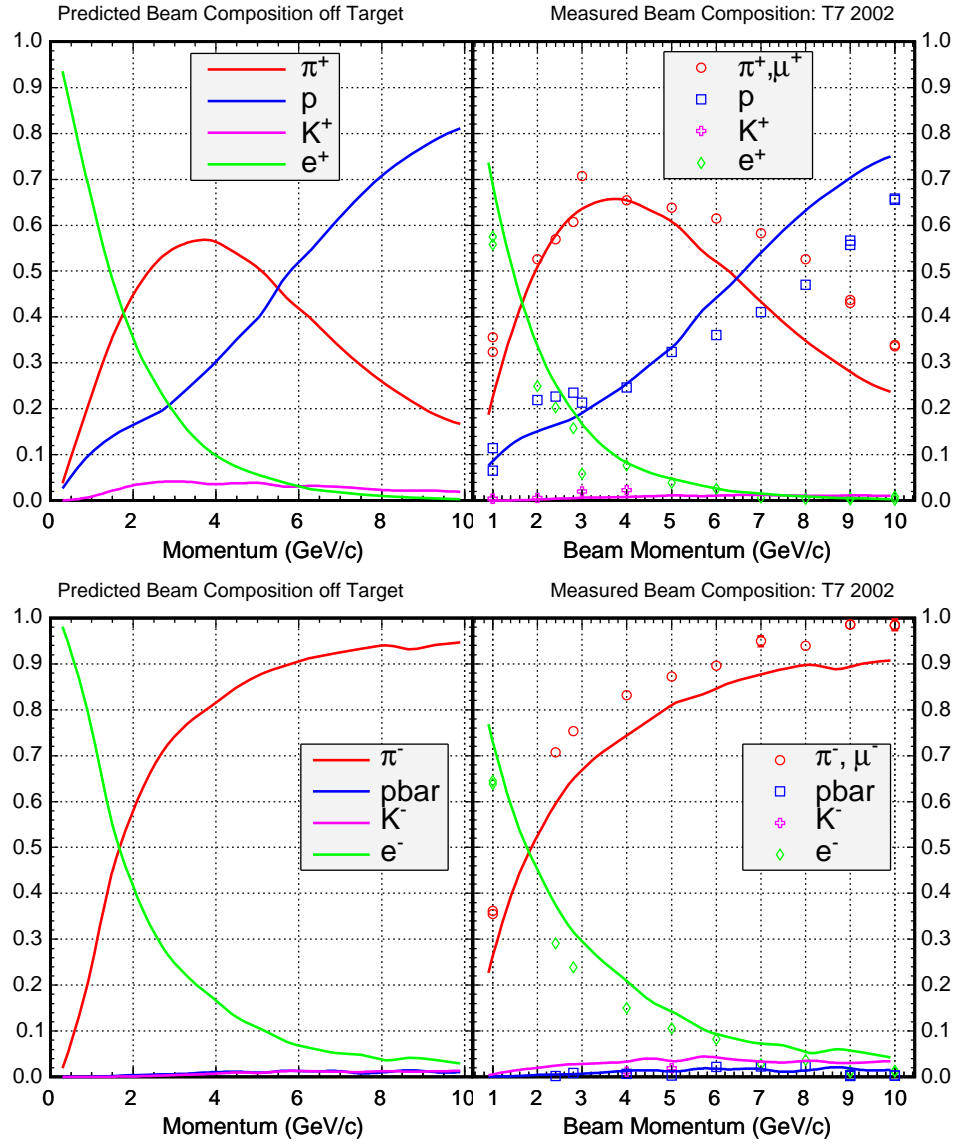
Figure 7.25: The T7 beam composition as a function of momentum. The ordinates show the fractional composition for each particle species. The prediction of FLUKA03 (shown as lines) is compared to the measured data (points). Positive particles are shown on the top row. Negatives are shown on the bottom row. The figures on the left show the beam composition at the target, while those on the right show the composition at the detector. Target 2 from Table 4.3 was simulated. It was generally used below 7 GeV/c.
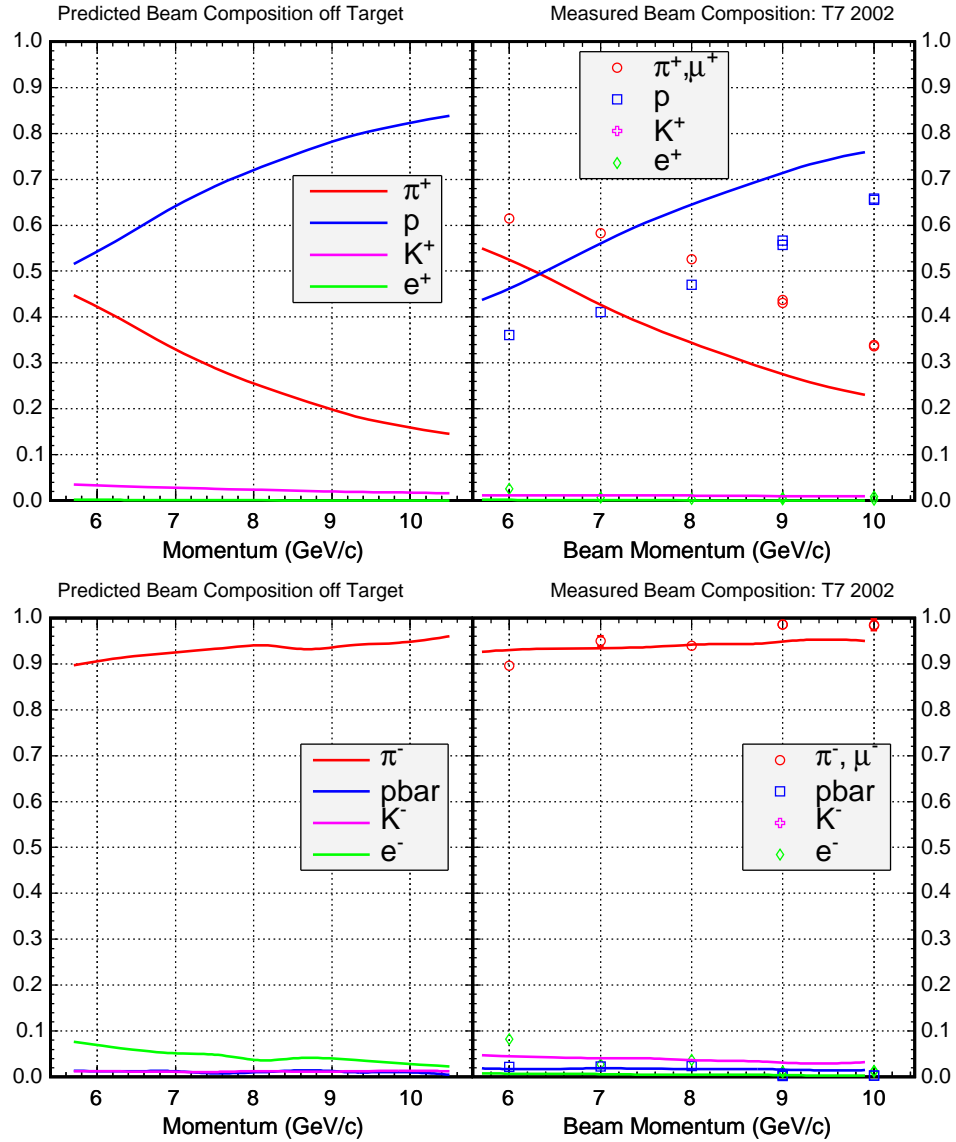
Figure 7.26: The T7 beam composition as a function of momentum. The ordinates show the fractional composition for each particle species. The prediction of FLUKA03 (shown as lines) is compared to the measured data (points). Positive particles are shown on the top row. Negatives are shown on the bottom row. The figures on the left show the beam composition at the target, while those on the right show the composition at the detector. Target 1 from Table 4.3 was simulated. It was generally used above 7 GeV/c.

212

pressurized at 3.3 atm - well below the proton threshold. The efficiency, which was ~ 100% over the range, does not matter since an inefficient counter would count fewer pions rather than more. The time of flight difference between the resulting pion and proton samples was in excellent agreement with expectations. The discrepancy is not believed to indicate a problem with the data. The trigger acceptance was estimated to be nearly 100% for both pions and protons in the 5-10 GeV/c range. Possibly the acceptance through the upstream portion of the beamline (not evaluated by the beamline simulation) could cause such a difference. That said, no mechanism causing a large acceptance difference between high energy pions and protons has been identified.

For most momentum settings the small number of kaons and relatively poor time of flight separation from pions and protons made a significant kaon sample difficult to select. Kaons therefore formed a background to the pion and proton analysis. The results of the target modeling were used to predict the kaon contamination of the pion and proton samples. Disregarding any information from the Čerenkov counters, the background from kaons depends on the relative fraction of kaons, the momentum and the time of flight baseline and resolution.

The kaon fraction was derived from Fig. 7.24 (T11) and Fig. 7.25 (T7). The pion and proton content was taken directly from the data, rather than the FLUKA prediction. The FLUKA prediction of the kaon content was used, but only after being propagated to the detector (the right hand plots in Fig. 7.24, 7.25). The times of flight for pions, kaons and protons, were modeled using normal distributions with a mean computed based on the baseline,mass and momentum, The RMS was chosen between three and nine 35 ps

213
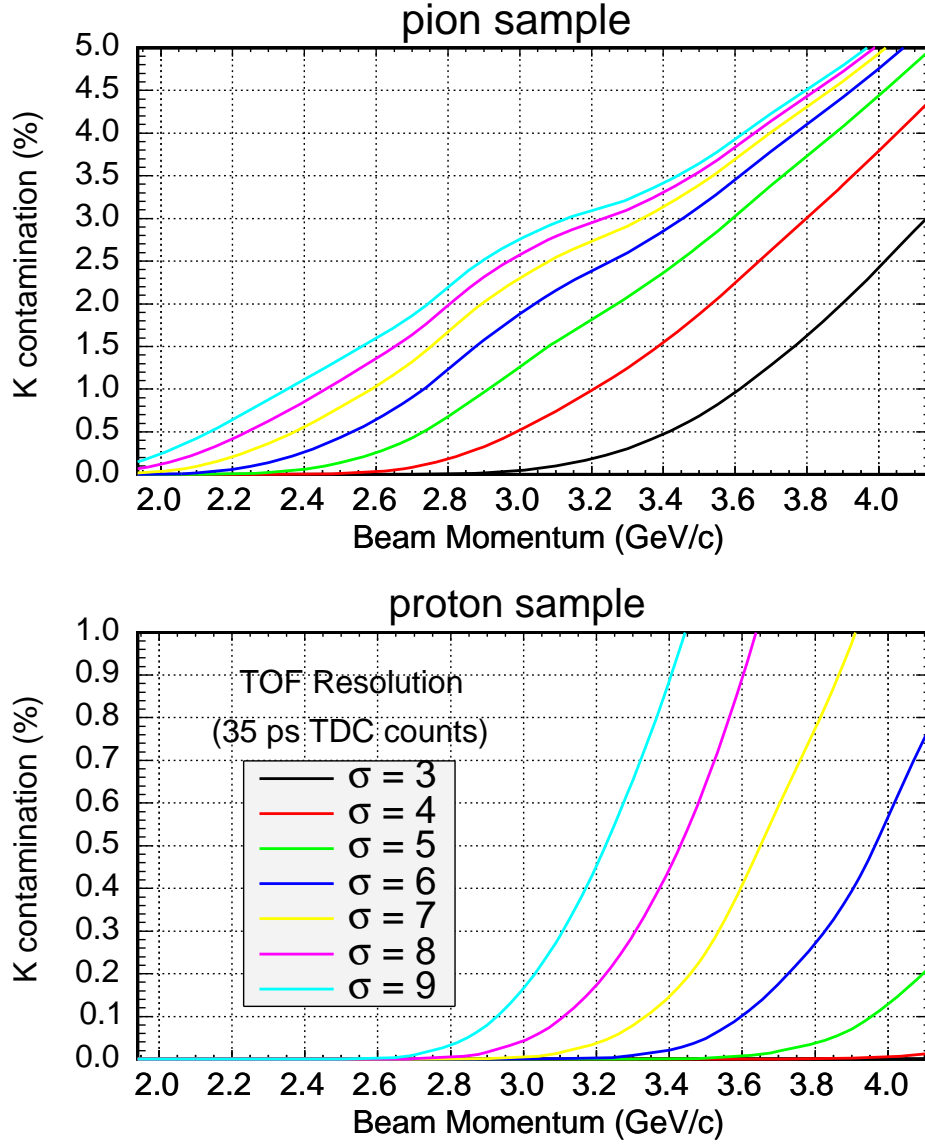
Figure 7.27: The calculated kaon contamination of the positive pion and proton samples in T11. The contamination is shown as a function of the beam momentum and for a range of TOF resolutions.
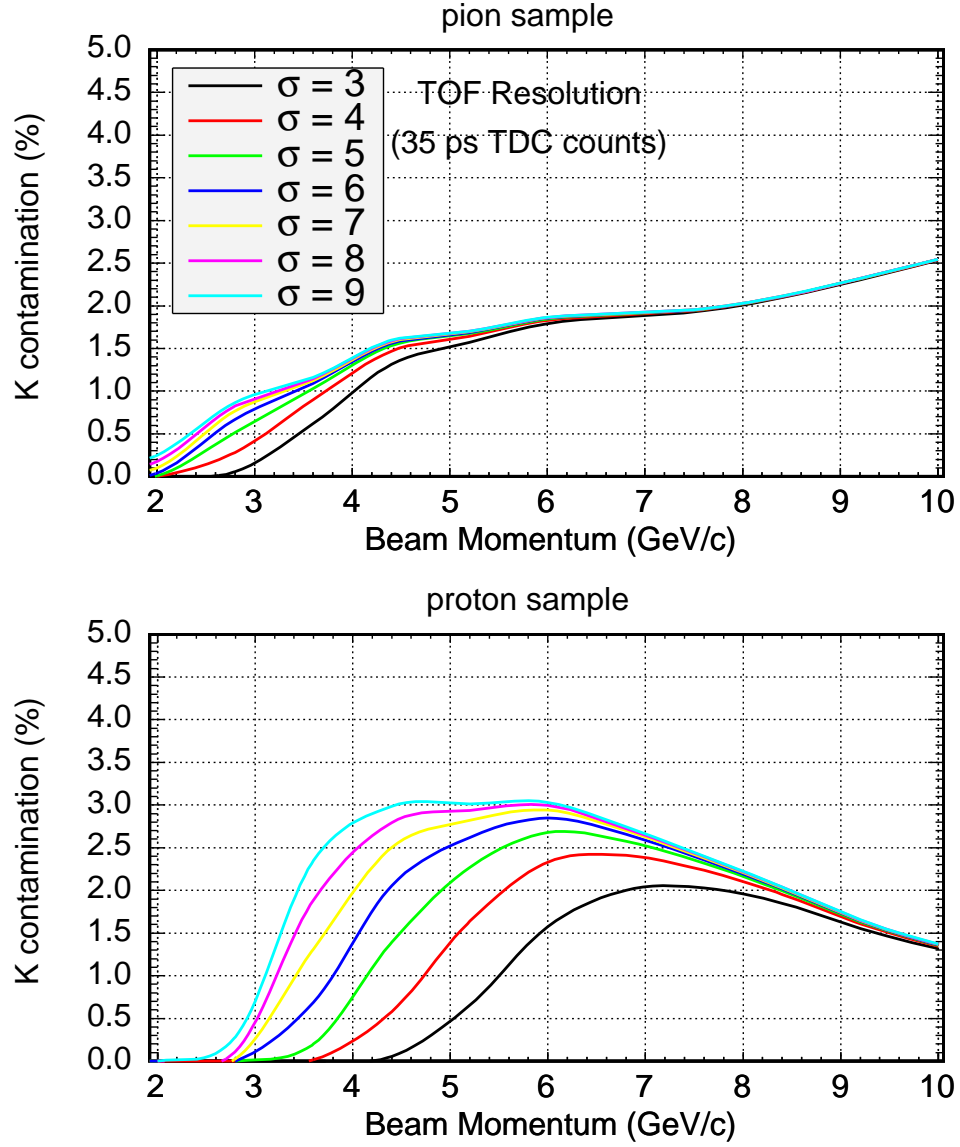
Figure 7.28: The calculated kaon contamination of the positive pion and proton samples in T7. The contamination is shown as a function of the beam momentum and for a range of TOF resolutions.

TDC counts[5]. The same RMS was used for each species. The acceptance for pions and protons was computed by integrating the region $\pm 2.5\,\sigma$ around the mean pion and proton times of flight. The kaon time of flight distribution was integrated over the pion and proton acceptance regions in order to compute the kaon misidentification probability.

The results of the computation are shown in Fig. 7.27-7.28. Using the measured $210\,\mathrm{ps}$ time of flight resolution, the kaon background was less than 4% everywhere. Additionally, in T7, the downstream Čerenkov counter was used to identify pions and muons (but not kaons) between $3\text{-}9\,\mathrm{GeV/c}$. Therefore, the contamination of the pion sample was zero over that range. The counter did identify kaons in the $10\,\mathrm{GeV/c}$ sample.

Hadronic activity and the hadronic response of the detector depend, to first order, on the *available energy* [6] carried by the incoming particle. The few % contamination from kaons is negligible in most studies. As a somewhat extreme example, at $3\,\mathrm{GeV/c}$, the kaon avaliable energy is $3.041\,\mathrm{GeV}$, for pions it is $3.003\,\mathrm{GeV}$ and for protons it is $2.205\,\mathrm{GeV}$. Assuming a 3% contamination of the proton sample, the apparent shift in the average proton energy is

$$1 - \frac{E_p * (1 - f_K) + E_K * f_K}{E_p} = 1 - \frac{2.205 \times 0.97 + 3.041 \times 0.03}{2.205} = 1.1\%$$

The effect on pions is much smaller.

---

[5]The typical resolution was 6 TDC counts.

[6]Total energy for mesons, kinetic energy for protons. The distinction is that the meson mass is eventually converted into (possibly) visible energy.

Chapter 8

Event Topology

MINOS will classify events as ν_μ-CC, ν_e-CC or NC based on the topological patterns induced in the detector. For example, ν_μ-CC events will be selected by requiring that the events contain a track, consistent with a muon, eminating from the vertex. Electron neutrino charged current events and neutral current events will have shower topologies, similar to those observed by CalDet for electron and pion induced events. The primary differences between ν_e-CC and NC events will be a more dense, shorter shower-core and a relative reduction in the hadronic activity in ν_e-CC events due to the energy carried by the electron. The classification efficiencies will be evaluated, at least partially, by using comprehensive GEANT based Monte Carlo simulations of neutrino interactions in both the Near and Far detectors. Neutral current events are of particular interest because they are on one hand the dominant background for the ν_μ and ν_e CC measurements and on the other are themselves sensitive to oscillations involving ν_s. Therefore, accurate simulation of neutral current event topology is of considerable importance to MINOS. The CalDet data provides a powerful tool that may be used to confront simulations in the

217

relatively simple case of single particles with a well known momentum and identity. The Monte Carlo must correctly reproduce the test-beam data in order to be used with confidence in the neutrino analysis. The simulation of neutrino events is, of course, more complicated since there is an additional dependence on the generator and ν flux. The test-beam data at least allows the problem to be factorized into two parts: the generation of the final state and the simulation of the detector's response to the final state.

The hadron analysis in CalDet faced a problem that was analogous to the NC/CC separation task. As discussed in Ch. 7, simulations indicated that the pion sample contained a muon background of 3-7%[1]. These muons had to be identified in order to accurately characterize the signal and topological response to pions. The identification procedure utilized the topological differences between pion and muon events, and though not 100% efficient, yielded a pion sample which could be compared to simulated pions subjected to the same selection criteria.

8.1 Summary of the Hadron Samples

Figures 8.1-8.5 summarize the hadron sample present after the selection criteria of Ch. 4.6 were applied. The figures shown were constructed during the histogramming phase of the data processing, using inputs from the CalDetDST and second pass DST(see Ch. 6). The variables shown are:

Number of strips (planes) hit: The number of strips (planes) with a signal. Both variables measure the "activity" of the event. The # planes hit is also a relatively robust measure of the penetration of the event into

---

[1]As will be shown, the measured muon background appears significantly higher

the calorimeter. At energies above $\sim 3\,\mathrm{GeV}$ the two variables provide a reasonable separation between pions and muons, since, neglecting noise, muon tracks are expected to have ~ 1 hit strip / hit plane and penetrate the entire calorimeter. Pion showers are expected to be shorter with a larger strip/plane ratio.

Shower maximum plane and signal: The plane with the largest signal and the signal in that plane. For muons, the signal in shower max is expected to be $\lesssim 15\,\mathrm{MIPs}$ and the plane of shower max is expected to be relatively flat with some peaking at the stopping planes for on-momentum and off-momentum muons[2]. For pions, the shower max plane distribution is expected to peak below ~ 10 planes with a high-side tail. Above $2\,\mathrm{GeV/c}$ the signal in shower max is expected to be significantly larger than $\sim 10\,\mathrm{MIPs}$, allowing pions to be separated from muons.

Summed signal: The amount of signal, summing every hit in the event. The average, over many events, of the summed signal is the conventional measure of the detector's response.

Figure 8.1 summarizes the low energy combined pion and muon sample. On-momentum muons cause the small peaks visible on the high side tail of the number of planes hit distribution. The calorimeter signal and the number of hits both scale approximately linearly with the beam momentum. The plane of shower maximum distribution changes more slowly with energy, with the mean scaling approximately as $\log{(E_\pi)}$. Figure 8.2 summarizes the high

---

[2]By convention, due to the double ended readout, two MIPs (rather than one) are expected for a normally incident cosmic ray muon crossing a strip. Landau fluctuations then cause the maximum signal to be somewhat higher for events in which the muon crosses a few tens of planes.
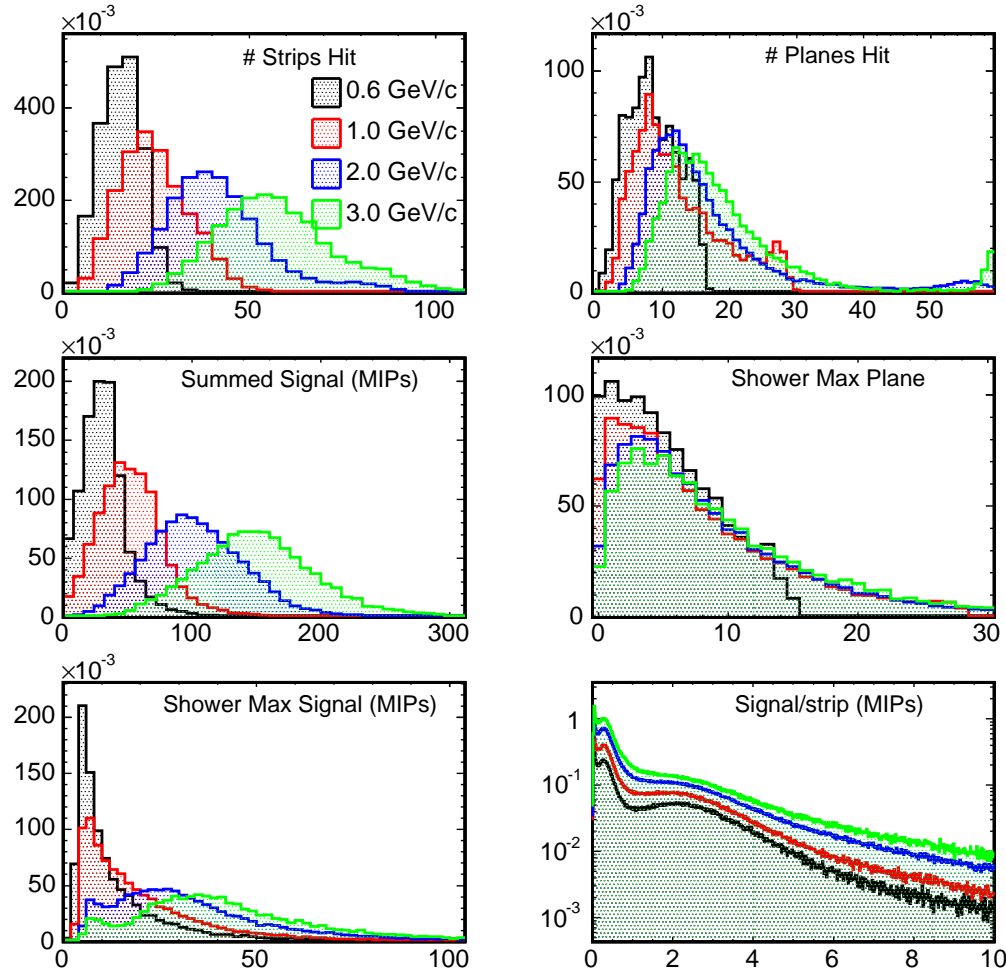
Figure 8.1: Some basic quantities summarizing the low energy combined pion and muon sample. The data were collected in the T11 beamline at positive polarity. The histograms were normalized to the number of events.
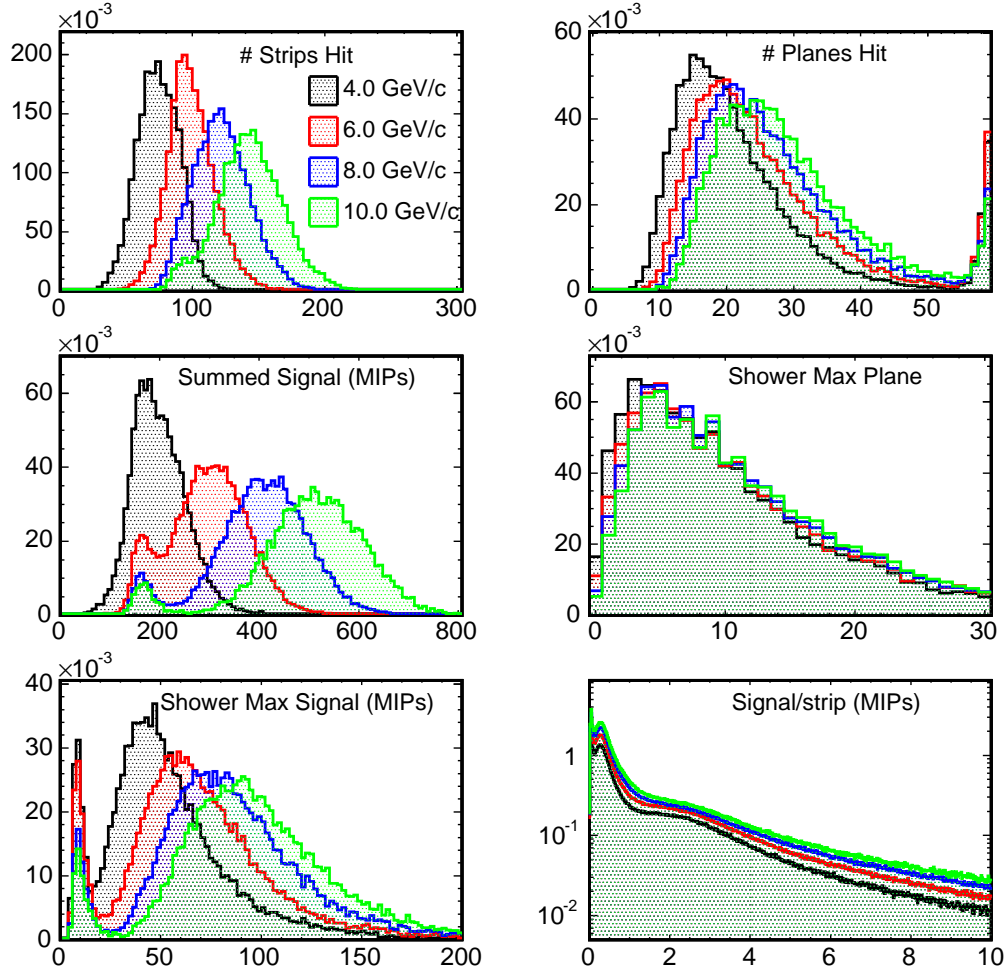
Figure 8.2: Some basic quantities summarizing the high energy combined pion and muon sample. The data were collected in the T7 beamline at positive polarity. The histograms were normalized to the number of events.

energy combined pion and muon sample. Muons punch through the detector and are visible in the peak above 55 planes hit as well as in the peak around 160 MIPs in the summed signal distribution, and in the peak at ~ 10 MIPs in the shower max signal distribution.

Characteristics of the low energy proton sample are shown in Fig. 8.3-8.4. Below 1 GeV/c, protons lose the majority of their energy by ionization and range out in the detector without participating in a hadronic interaction. The effect is particularly noticeable in the shower max plane distributions, in which the peaks at 1, 3 and 6 planes correspond to the stopping plane for 0.6, 0.8 and 1 GeV/c protons. As the energy increases an ever larger proportion of protons shower prior to ranging out and the distributions in Fig. 8.4 begin to look more similar to the pion distributions in Fig. 8.1. This behavior should allow MINOS to identify non-interacting proton tracks. The data could be useful in determining the ν four-momentum in quasi-elastic events, assuming events with a proton track traversing more than six planes are selected. A few percent of protons range out at momenta as high as 1.6 GeV/c (18 planes traversed). The angular reconstruction of those tracks should be quite good and it may be possible to amass a significant sample in the high rate Near detector.

8.2   The Detector Monte Carlo

The physics component of CalDet events was simulated using a GEANT3 based model of the detector known as GMINOS [62, 63, 64]. The active detector response, that is the response of the scintillator, optical cables, phototubes and electronics, was simulated in the MINOS offline framework using the Det-

222
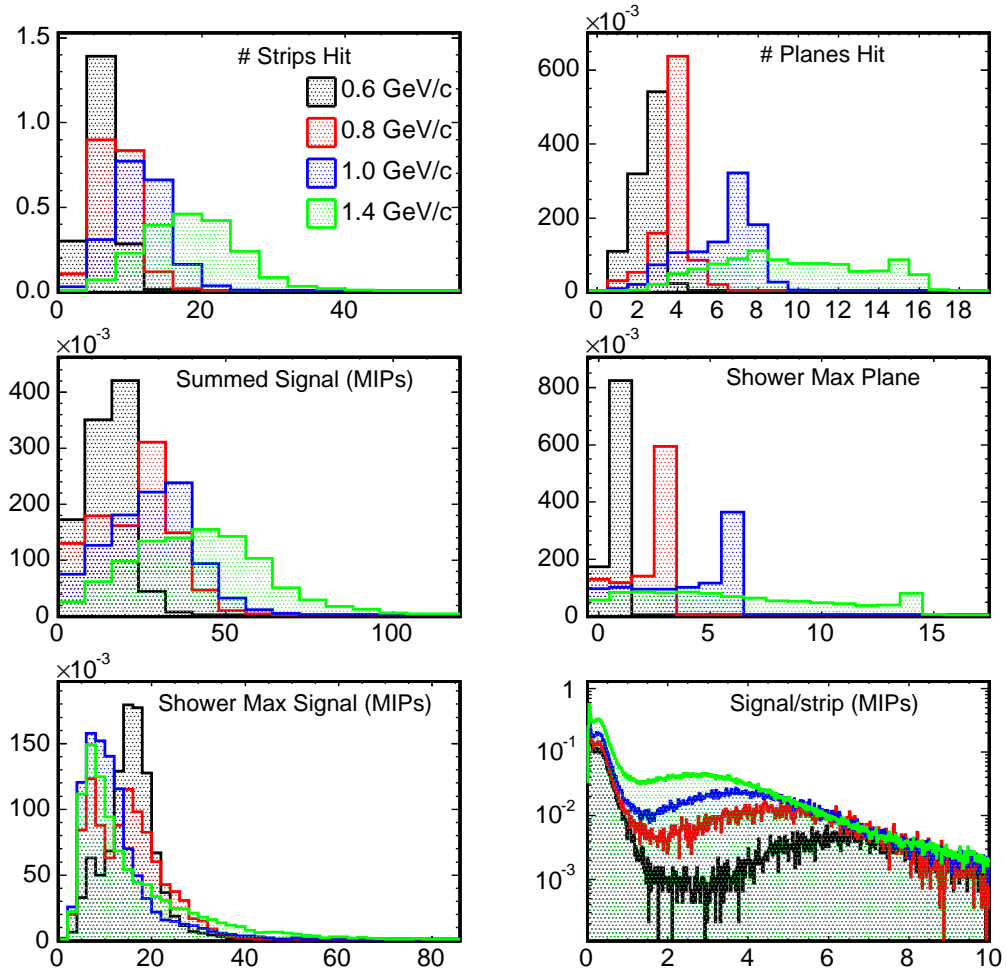
Figure 8.3: Some basic quantities summarizing the low energy proton sample. The data were collected in the T11 beamline. The histograms were normalized to the number of events.
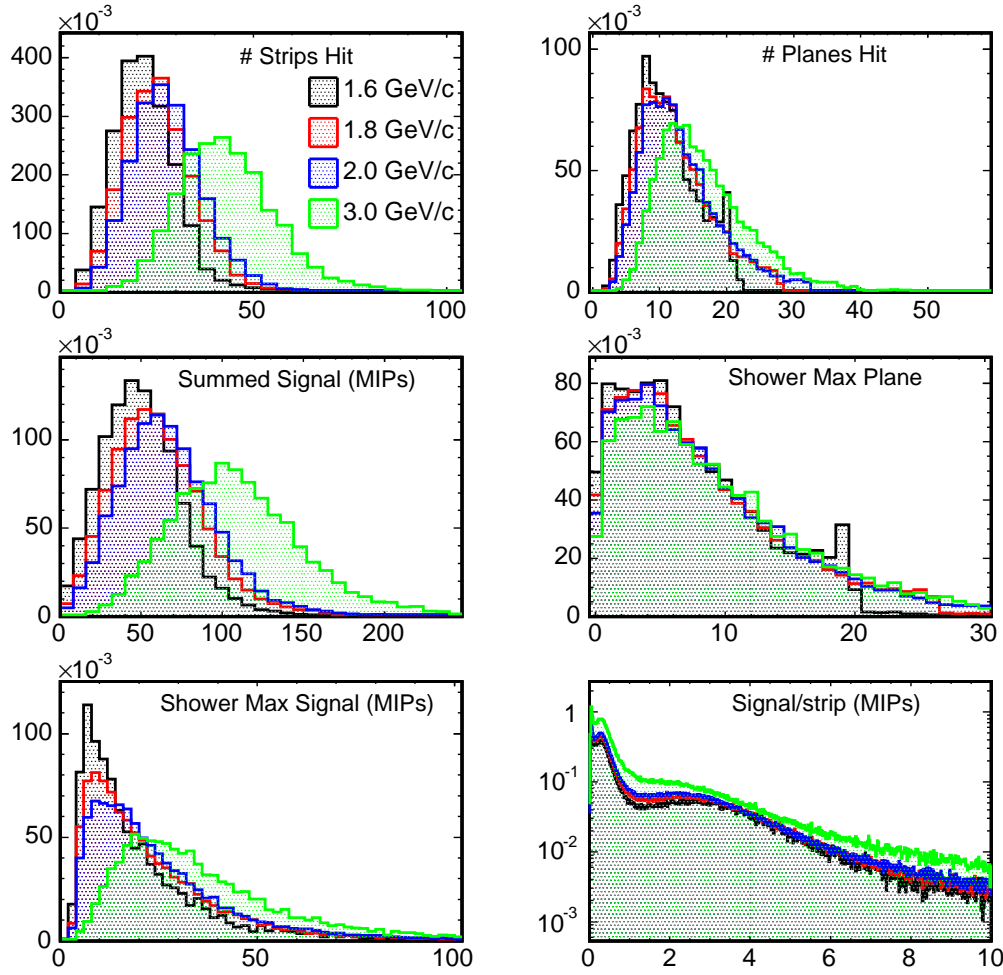
Figure 8.4: Some basic quantities summarizing the low energy proton sample. The data were collected in the T11 beamline. The histograms were normalized to the number of events.
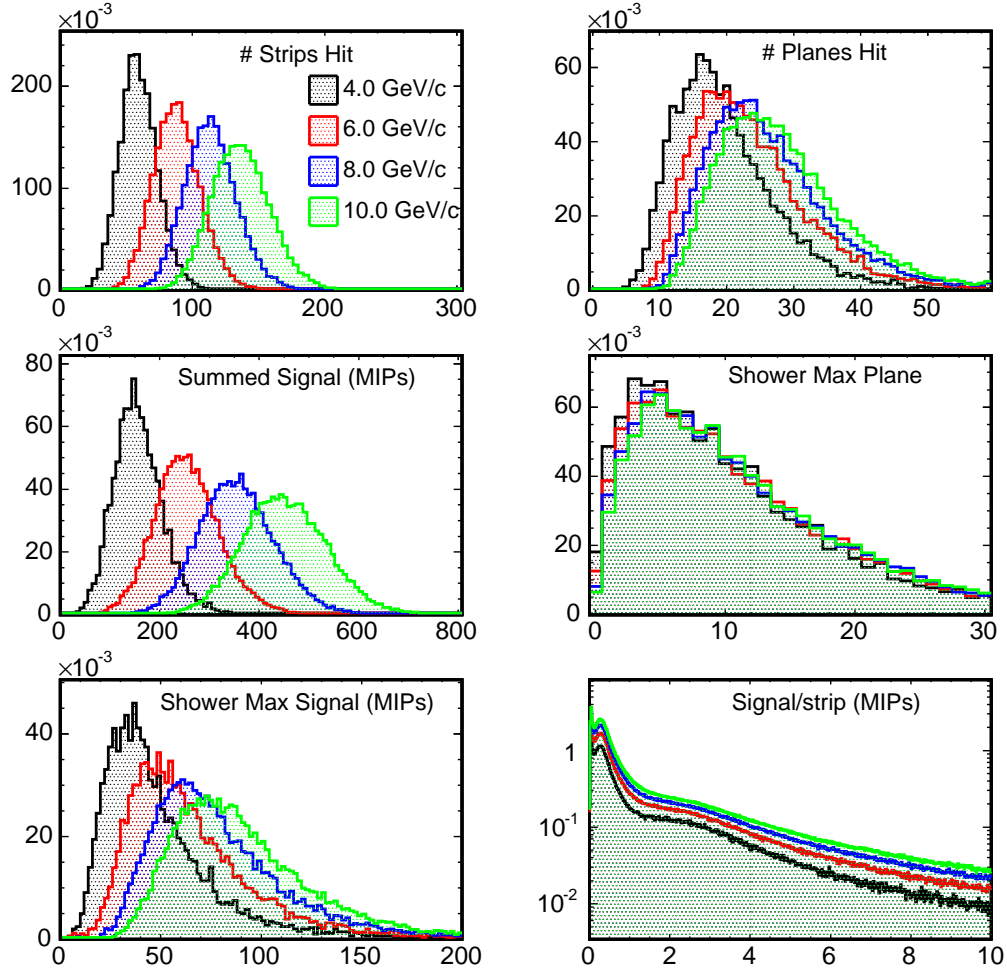
Figure 8.5: Some basic quantities summarizing the high energy proton sample. The data were collected in the T7 beamline.

Sim and PhotonTransport packages. The event simulation had two goals. First, muon, hadron and electron events must be well simulated since MINOS will select NC, CC and ν_e-CC event samples based on event topology. The event topology and resulting selection efficiencies will be derived largely from GMINOS simulations. CalDet provided an ideal data set to which the simulations could be compared and possibly tuned. Second, the CalDet pion sample included a muon background which had to be quantified and possibly removed in order to characterize the detector's response to pions. The simulation was therefore used to develop a strategy to discriminate between pions and muons and was also compared to the selected pion sample. Though this work presents results of the selection and comparison, it is clear that Monte Carlo characterization and tuning will continue, possibly throughout the lifetime of the experiment.

8.2.1 GMINOS Simulations

GMINOS was developed during the design phase of the experiment so that the collaboration could study the performance of a variety of detector designs and technologies. The program was upgraded over the years to implement the geometry and composition of all three actual MINOS detectors in GEANT3. The CalDet geometry originally had 1 in thick, pure iron planes, but was modified to account for the actual 2.50 cm thickness and the measured density, isotopic composition, and impurity abundance (see Tab. 3.1). GMINOS also provided an interface for user specified neutrino (or cosmic ray) fluxes. This interface was modified in order to receive CalDet events. Events could be input from the command line (monochromatic particles), from an ASCII flux file or

226

from the CalDet beamline simulation. The beamline simulation provided the most realistic input events and, unless noted, was used in the work presented in this section. Only events which would have passed the CalDet beam trigger were simulated.

GMINOS employed GEANT3 to track particles, simulate interactions and record energy deposition in the scintillator strips. Table 8.1 lists the physics settings used in the simulation. The settings were chosen to give the most realistic simulation at the expense of disk space and CPU time. In particular, the low tracking cutoffs were necessary in order to correctly model the hit multiplicity of electron (and to a smaller extent, hadron) events. The TOFMAX card was used to terminate tracking after 500 ns - the approximate time window of each CalDet trigger. The cut removed hits at large times caused by neutrons and, as shown in Fig. 8.6, slightly reduced the range, hit multiplicity and signal for hadronic events. Multiple hadronic interaction models were evaluated and will be discussed in Ch. 8.2.4. The code output truth information, including a detailed history of all interactions[3], and a record of the energy deposition in a form that could be read by MINOS' C++ based offline code.

8.2.2 Active Detector Simulation

The active detector response was simulated in the MINOS offline framework using the DetSim and PhotonTransport packages [65]. The PhotonTransport code began the simulation by reading the record of energy depositions (hits) created by GMINOS. For each hit, the code generated a number of photons

---

[3]The detailed history, while useful, had a very large disk footprint and was only used in special cases.

Physics settings used with GMINOS

FFREAD card	setting	Comment
DRAY	1	δ-ray production with e^- generation
LOSS	1	Continuous energy loss, with Landau fluctuations and δ production
ANNI	1	e^+ annihilation
BREM	1	Bremsstrahlung with γ generation
COMP	1	Compton scattering with e^- generation
DCAY	1	Particle decay with generation of daughters
MULS	1	Molière multiple scattering
PAIR	1	Explicit $\gamma \to e^+e^-$ simulation
DCUTE/M	10 keV	δ-ray production threshold
CUTS	10 keV	Hadron, electron and muon tracking cutoffs
TOFMAX	500 ns	Tracking time cutoff.
HADR	*	Hadronic interaction model Discussed in Ch. 8.2.4

Table 8.1: GEANT3 physics settings used to simulate events in CalDet. In general the settings were chosen to give the most detailed simulation possible at the expense of CPU time and disk space. Multiple hadronic interaction models were studied.
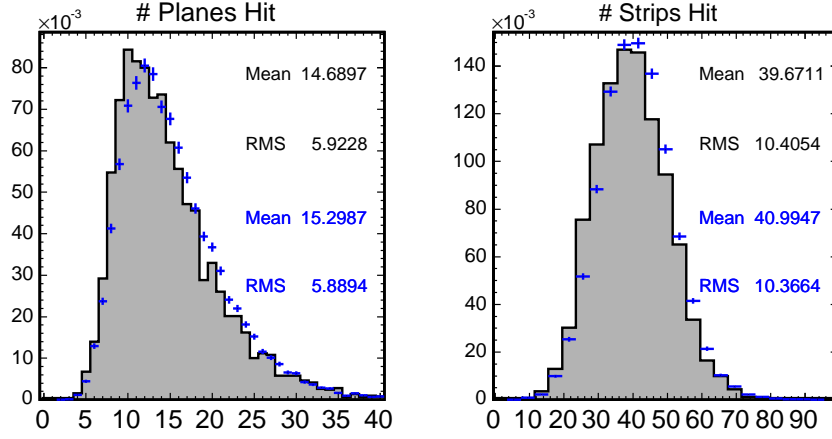
Figure 8.6: Simulated $2\,\mathrm{GeV/c}\ \pi^+$ with the TOFMAX tracking cutoff set to $500\,\mathrm{ns}$ (filled) compared to simulation without a time cutoff (crosses).

along the particle track according to the formula:

$$N = C \times S_i \times \frac{dE}{1 + k_b \frac{dE}{dx}} \tag{8.1}$$

Here, C is an overall normalization constant corresponding to the number of photons produced per unit of deposited energy and S_i corresponds to the relative light output of the strip in question. The constant C also accounts implicitly for the PMT quantum efficiency in order to make the simulation more efficient. Since approximately 13% of photons striking the photocathode will create photoelectrons, the quantum efficiency is accounted for up-front, so that 87% of the generated photons are not processed and then lost on the PMT face. For simplicity, and because the simulation code was in active development, CalDet events were simulated with S_i set to unity for all strips. The denominator in Eq. 8.1 accounts for scintillator saturation by large localized energy depositions (Birks' Law), with the constant k_b set to $0.1\,\mathrm{m/GeV}$ [66].

229

The photons generated along the particle track were then distributed along the wavelength shifting (WLS) fiber according to a probability density function relating the initial position and time of the photon to the position and time when captured on the fiber. The probability density function was constructed from a detailed model that created individual photons in the scintillator strip according to a realistic emission spectrum and then tracked the photons through the strip, accounting for wavelength dependent absorption, reflection off the TiO_2 co-extrusion, and reflection, refractions and eventual absorption in the WLS fiber. Photons captured in the WLS fiber were propagated to the phototube face accounting for attenuation in the WLS and clear fibers:

$$f(x) = k \ e^{-x_g/\lambda_s} + (1-k) \ e^{-x_g/\lambda_l} e^{-x_c/\lambda_c} \qquad (8.2)$$

Where $\lambda_s = 1.052 \, \text{m}$, $\lambda_l = 7.078 \, \text{m}$, $k = 1/3$ and $\lambda_c = 11.4 \, \text{m}$, and x_g, x_c are the lengths of travel through the WLS and clear optical fibers [63]. The detector was simulated with the clear and WLS fiber lengths (including pigtails) that were used in the data-taking (see Tab. 3.3, 3.8).

Each photon that made it to the phototubes was converted into a photoelectron, since the PMT quantum efficiency was accounted for when the photons were originally generated. The DetSim package handled the simulation of the phototube response, dynode triggering, electronics response and triggering by the data acquisition[4]. The M16 response simulation included a complete model of electron multiplication in the phototube dynode chain, high light-level non-linearity, dark noise, transit time, and optical and electri-

---

[4]The trigger conditions were appropriate for the Near and Far detectors and were not used when simulating the CalDet. The CalDet had an external beam trigger rather than a DAQ trigger.

cal cross talk (discussed in Ch. 8.2.6). All phototube pixels were simulated with a gain of 0.8×10^6. The phototube simulation output the charge on each pixel of all the phototubes involved in the event. The charges were accepted by the electronics simulation, converted into ADC counts, and joined with the time and channel identification words to make a hit (known as a RawDigit) which had a format that was identical to the hits output by the actual data acquisition system. The hits were then processed as if they were real data.

8.2.3 Monte Carlo Calibration

It was necessary to calibrate the simulated hits. As a first step, the individual ADC values were converted to photoelectrons assuming perfect knowledge of the electronics and PMT gains. The parameter C in Eq. 8.1 controls the overall light output and was tuned in order to correctly reproduce the mean number of photoelectrons observed in 1 GeV electron events. The simulated hits included the effect of attenuation in the optical readout cables. In the real data, the strip-to-strip calibration procedure corrected for attenuation and defined the MIP calibration constants in terms of normally incident cosmic ray muons passing through strips at the center of the detector(see Ch. 5). For simulated events, the MIP calibration constants were constructed by assuming perfect knowledge of the attenuation lengths and then inverting Eq. 8.2 at the center of each strip. The resulting constants were then multiplied by a single overall scale factor having units of MIPs/PE. The scale factor was chosen in order to reproduce the total signal, in MIPs, observed in 1 GeV electron events.

The calibration procedure for simulated events was, admittedly, somewhat of an idealization, in that it assumes perfect knowledge of phototube

gains, strip light output and cable attenuation. Clearly, if one was studying some aspect of the calibration, such as the strip-to-strip correction, the approach would not be valid. For the studies presented here, the Monte Carlo calibration procedure effectively factored out calibration related effects, allowing a more direct comparison between the data and Monte Carlo.

8.2.4 Hadronic Shower Simulations

GEANT3 is able to interface with several external hadronic shower simulation codes. The codes were essentially developed during the late-1970's and 1980's to simulate hadronic interactions in bulk matter, such as calorimeters and shielding blocks, and have generally been benchmarked for primary particle energies in excess of $10\,\text{GeV}$. Additionally, the majority of calorimeters used in the benchmarking did not have the degree of segmented readout present in MINOS. It was not clear, therefore, if any of the existing codes would correctly simulate few-GeV hadronic showers in the MINOS calorimeter. As a primary motivation, the CalDet program was undertaken to provide a sample of pions and protons, in the 0.5-10 GeV range, with which hadronic shower codes could be evaluated.

Each of the hadronic interaction codes available for use in GEANT was evaluated during the test-beam program. Briefly the codes are:

GFLUKA: A *circa* 1993 version of the FLUKA code [67]. The GEANT implementation is incomplete and disavowed by the current FLUKA authors. The code was found to overestimate the activity induced in the detector with a signal response that was too high (by $\sim 30\%$) and a resolution that was too good ($\sim 36\%/\sqrt{E}$). The code was not found useful for
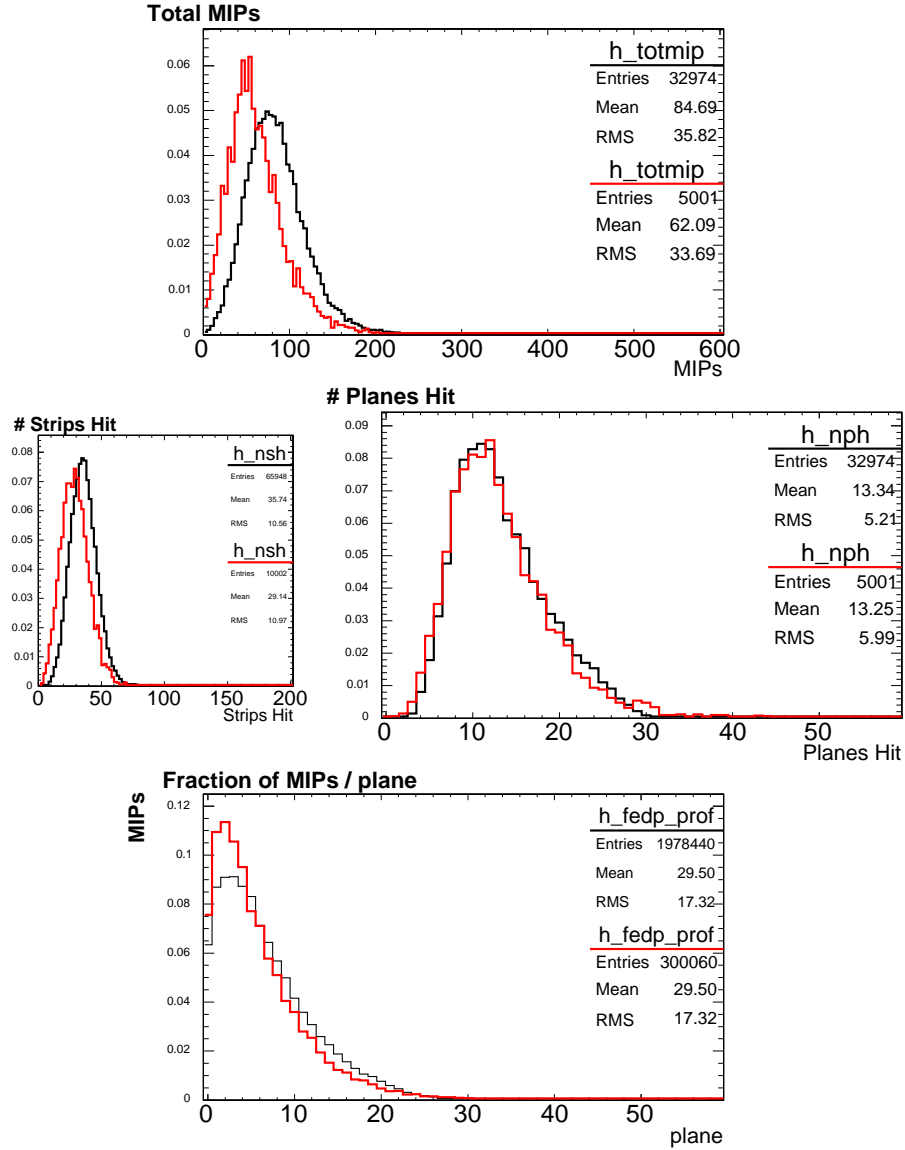
Figure 8.7: A comparison between $1.8\,\mathrm{GeV/c}$ π^+ data (black) and pions simulated with the original GHEISHA code (red). GHEISHA was found to underestimate the activity in hadronic events, as evidenced by the signal distribution (top) and the hit strip multiplicity (left). The number of planes hit was well modeled(right), but the simulation appeared to shower too early (bottom).

simulating MINOS events and was little used.

GHEISHA: The GEANT3 implementation of the GHEISHA code [68]. The code is based on parameterizations extrapolated downward into the few-GeV energy region. Figure 8.7 presents a basic comparison between $1.8\,\mathrm{GeV/c}$ π^+ data and the GHEISHA simulation. The simulation was in better agreement with the data than GFLUKA but underestimated the activity in hadronic events.

SLAC-GHEISHA: An enhanced, bug-fixed version of the GHEISHA code [69]. The simulation was found to agree somewhat better with the data than the original GHEISHA.

GCALOR: A version of the CALOR code system adopted for use with GEANT3 [70]. The GCALOR version is most similar to CALOR89 [71] which is widely used for shielding calculations. The original CALOR code was written in the 1970's and as such was tuned to lower energy interactions than GFLUKA or GHEISHA were. Charged pions below $2.5\,\mathrm{GeV}$ and protons below $3.5\,\mathrm{GeV}$ are transported with code (NMTC) based on Bertini's intra-nuclear cascade model [72]. As the primary particle energy increases above 2.5 and $3.5\,\mathrm{GeV}$ a linear probability function is used to determine whether NMTC or GFLUKA is called to model the interaction, with the probability of calling GFLUKA reaching unity at $10\,\mathrm{GeV}$. GCALOR includes a detailed simulation of low energy ($< 20\,\mathrm{MeV}$) neutron interactions based on the MICAP code coupled to an ENDF/B neutron cross section data file. The GCALOR code was in good agreement with π^+ data, and somewhat poorer agreement with protons and π^-.

234

In CalDet, the GCALOR code was in the best agreement with the data at low energies and as such was adopted for use in the pion muon discrimination procedure. SLAC-GHEISHA was also a good model and could be used in neutrino event simulations as a way of probing MINOS' sensitivity to the details of the hadronic interaction simulation. Detailed comparisons between GCALOR, SLAC-GHEISHA and the CalDet data are presented in Ch. 8.4.

8.2.5 Muon Energy Loss

Muons in the energy range 10 MeV-10 GeV lose energy almost entirely by ionization. The energy loss per unit length is described by the famous Bethe-Bloch equation [2, 73]:

$$-\frac{dE}{dx} = K\frac{Z}{A}\frac{1}{\beta^2}\left[\frac{1}{2}\ln\frac{2m_ec^2\beta^2\gamma^2 T_{max}}{I^2} - \beta^2 - \frac{\delta}{2}\right] \quad \frac{\text{MeV}}{\text{g/cm}^2} \qquad (8.3)$$

Here $K = 0.307\,\text{MeVcm}^2/\text{g}$ is a numerical constant, I is the mean excitation energy (in eV), M is the particle mass, and $\beta\gamma = p/M$ is the muon velocity multiplied by the relativistic boost. The variable T_{max} represents the maximum kinetic energy which can be transfered to an electron in a single collision:

$$T_{max} = \frac{2m_ec^2\beta^2\gamma^2}{1 + 2\gamma m_e/M + (m_e/M)^2} \qquad (8.4)$$

Above $\sim 200\,\text{MeV/c}$ the medium begins to become polarized by the muon's electric field, which in turn suppresses distant collisions and decreases dE/dx. In the Bethe-Bloch equation the variable δ, known as the density effect parameter, accounts for the decreased energy loss. The density effect correction

235

Density Effect Parameters

Material	I (eV)	$\bar{C}$	x_1	x_0	k	a	δ_0
Fe	286.0	4.291	3.153	-0.0012	2.963	0.1468	0.12
	(280)	(4.252)	(3.000)	(0.2000)	(3.000)	(0.1517)	(0.00)
scint	68.7	3.300	2.503	0.1647	3.222	0.1645	0.00
Al	166.0	4.240	3.013	0.1708	3.635	0.0802	0.12
	(162)	(4.190)	(3.000)	(0.2000)	(3.000)	(0.1489)	(0.00)

Table 8.2: Density effect parameters as tabulated in [75] and used to correct GEANT. The standard GEANT3 parameters for Fe and Al are shown in parenthesis but are not listed for scintillator since standard GEANT considered scintillator a composite material when calculating dE/dx.

is usually expressed as an eight parameter function of p/M [74]:

$$
\delta(x) = \begin{cases}
Qx - \bar{C} & \text{for} \quad x \geq x_1 \\
Qx - \bar{C} + a\left(x_1 - x\right)^k & \text{for} \quad x_0 \leq x < x_1 \\
0 & \text{for} \quad x < x_0 \quad \text{(nonconductors)} \\
\delta_0 10^{2(x-x_0)} & \text{for} \quad x < x_0 \quad \text{(conductors)}
\end{cases}
\tag{8.5}
$$

Here, $Q = 2\ln 10$ is a numerical constant and $x = \log_{10}\left(p/m\right)$ [73]. Over the course of time a variety of different methods have been used to calculate the (material dependent) parameters $\bar{C}, x_1, x_0, k, a, \delta_0$. Because the parameters are correlated, significantly different tabulations can often give the same final result. The mostly widely used and highly regarded values have been tabulated for a large number of materials by Sternheimer [75].

CalDet collected a modest sample of stopping muons in the momentum range 0.4-2.0 GeV/c, allowing muon energy loss and range to be characterized. Motivated by the data, the GEANT prediction for dE/dx was compared to the results of the detailed calculation in [73]. The comparison highlighted a shortcoming in the simulation: the dE/dx predicted by GEANT was system-

atically higher than the calculated values by about 2%. As it turned out, GEANT determined the density effect parameters according to the algorithm used by the EGS4 electromagnetic shower code for *untabulated* materials [62]. This in turn caused the energy loss to be overestimated.

The shortcoming was corrected by modifying the GEANT routines GDRELA, GDRELE and GDRELX[5]. The modified routines read in tabulated values for $\bar{C}, x_1, x_0, k, a, \delta_0$, and used Eq.8.5 to calculate δ. The tabulated values for Fe, Al and scintillator are shown in Table 8.2. The result of the correction, a $\sim$ 2% decrease in dE/dx, is shown in Figure 8.8. The modified version of GEANT was in excellent agreement with the calculations of Groom et al. As shown in Fig. 8.9 the correction increased the range of $1.8\,\mathrm{GeV/c}$ muons by about one plane. A comparison between the range of measured and simulated muons is presented in Ch. 8.4.4.

8.2.6 The Effect of PMT Cross Talk

Multi-anode phototubes, such as the Hamamatsu M16 and M64 tubes used in MINOS, suffer from cross talk amongst the individual pixels. During the MINOS R&D and construction phases a significant effort was made to investigate the cross talk phenomenon, using data from dedicated bench tests as well as the results from the PMT teststands built at the University of Texas and Oxford University. Details of the analysis [76] and a description of the simulation of M16 response and cross talk [77] are outside the scope of this document but are summarized here with an emphasis on the topological consequences.

Cross talk comes in two phenomenological modes: optical and electrical.

---

[5]The density correction was applied not only to muons but to pions, protons and electrons as well.
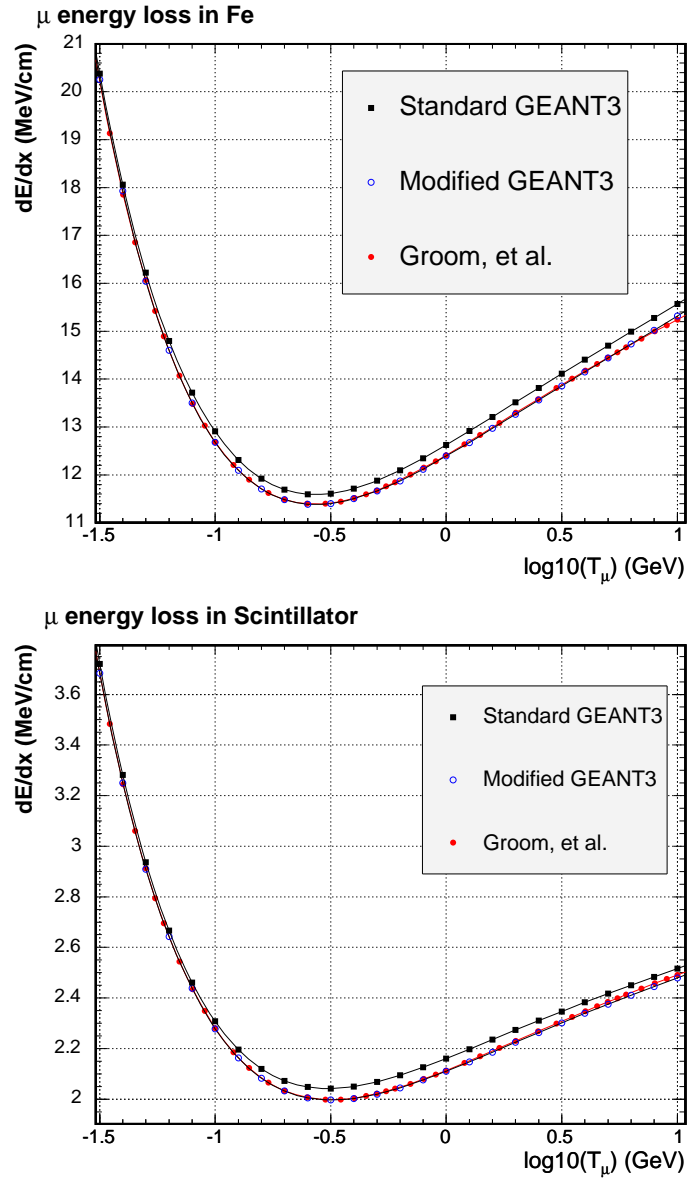
Figure 8.8: Muon dE/dx in iron and scintillator. The default GEANT prediction is compared to the modified GEANT version and the calculation of Groom, et al. [73].
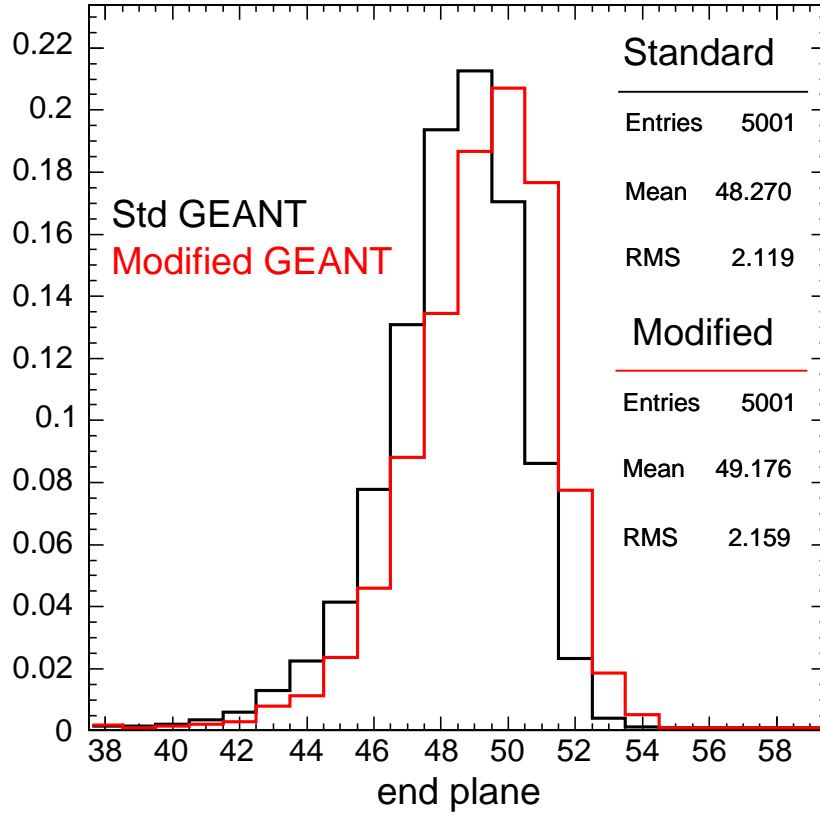
Figure 8.9: The effect of the dE/dx correction on the range of 1.8 GeV/c muons. Normally incident, mono-energetic muons were simulated in CalDet with the standard (black) and modified (red) GEANT codes. The $\sim 2\%$ decrease in dE/dx is easily visible as a 1 plane increase in the muon range.

Optical cross talk is a stochastic process in which photons or photoelectrons originally incident on one pixel scatter into another pixel. Electrical cross talk is a quasi-continuous process in which charge leakage in the dynode chain or inductive/capacitive coupling between pixels causes charge to appear on a non-illuminated pixel. For moderate pulseheights ($\sim 30\,\mathrm{PEs}$ or less) the signals created by electrical cross talk were generally below the $\sim 1/3\,\mathrm{PE}$ sparsification threshold. On the other hand, optical cross talk signals were usually single photoelectrons, above the readout threshold $\sim 90\%$ of the time, and were therefore the dominant effect.

The cross talk strength (i.e. magnitude) was characterized by the average charge measured on the cross talk pixel as a fraction of the charge on the illuminated pixel. The strength was found to depend on the geometric relationship between the two pixels, with pixels sharing a border having the largest coupling (0.1-1.6%). Figure 8.10 displays the couplings for CalDet M16s[6]. The up/down and left/right asymmetries visible in the figure were largely caused by the position of the optical fiber on the illuminated pixel (not shown) and the pixel architecture.

Cross talk caused low pulseheight "ghost" hits to be associated with strips in which no energy was deposited. At CalDet, three phototubes read out one end of two planes, with one of the PMTs being shared by the two planes. The coupling between any two strips was then a function of the optical mapping back on the phototube face (see Tab. 3.6). Figures 8.11-8.14 display the optical cross talk strength when each of the four strips at the center of the detector were illuminated. For phototubes that read out only one plane,

---

[6]The CalDet did not utilize the 8:1 optical summing used at the MINOS Far Detector. Instead, each fiber was located on one of the eight Far Detector fiber spots. The same readout scheme was used on all pixels.
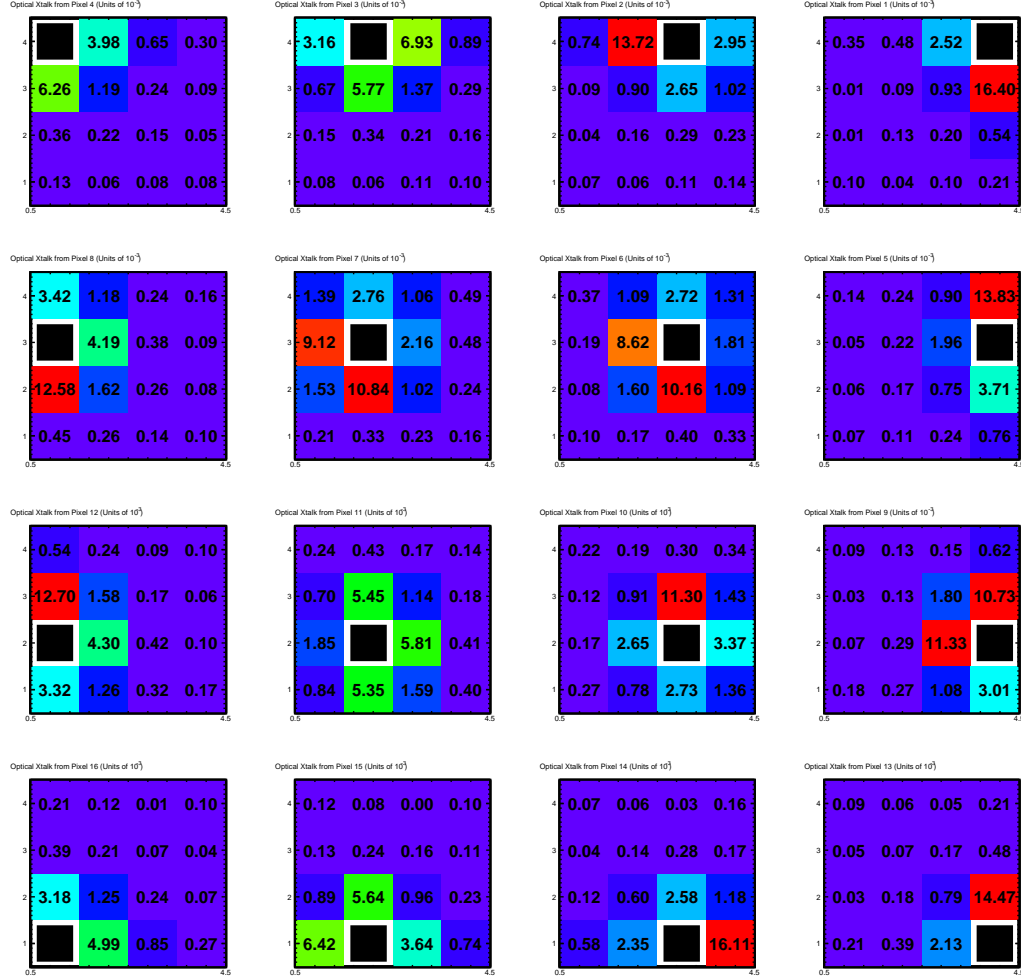
Figure 8.10: Optical cross talk strength as a function of the illuminated M16 pixel. Each individual figure represent a face on view of a Hamamatsu M16 phototube, with the individual squares corresponding to the sixteen pixels. The illuminated pixel is denoted by a black square. The cross talk strength between the illuminated pixel and and each of the others is shown in the color map with the numerical values superposed. The strength is in units of 10^{-4}.

the largest couplings were to one or more of the four strips at the edge of the plane. The shared phototube also coupled to the edge strips but had an additional, rather strong, coupling forward or backward into the other plane. This forward cross talk occurred in the showering region and was therefore quite difficult to identify on an event by event basis.

On average, 20% of the hits in each π event were caused by optical cross talk. In the analysis, a pulseheight cut of 1.5 PEs was applied when calculating cross talk sensitive quantities (e.g. the radius of an event). Charge weighting was also used in some quantities. In principle, a sophisticated cross talk removal algorithm could be devised by using the couplings of Fig. 8.10. Such an algorigthm was not considered necessary, ran the risk of biasing some topological quantities, and was not pursued. A complete *simulation* of M16 cross talk and response was devised on the basis of teststand measurements, tuned with CalDet data, and is now part of the standard simulation code [76, 77].

8.3   Topological Discrimination of Pions and Muons

The topological differences between hadronic showers and muon tracks can be used to classify events as pion-like or muon-like. For energies above a few GeV, the relatively fine longitudinal and transverse segmentation of the MINOS calorimeters facilitated the task by providing frequent sampling of hadronic showers and muon tracks. More specifically, hadronic showers above a few GeV may be identified by looking for signals inconsistent with a min-
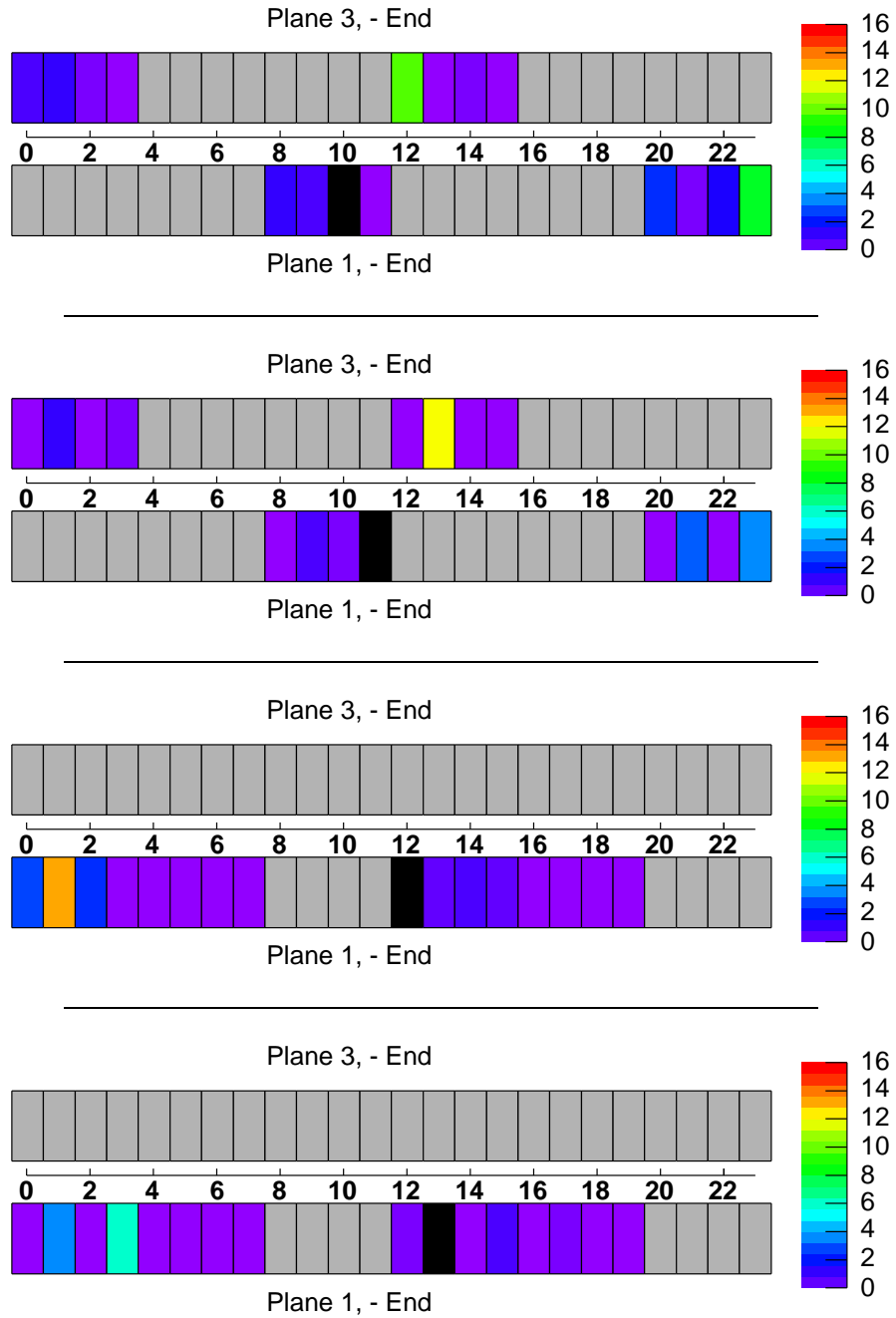
Figure 8.11: Average cross talk magnitude, as a fraction of the light level on the illuminated pixel, shown for different illuminated strips (in black). The color scale is in units of 10^{-4}. Strips marked with grey were not served by the illuminated PMT.
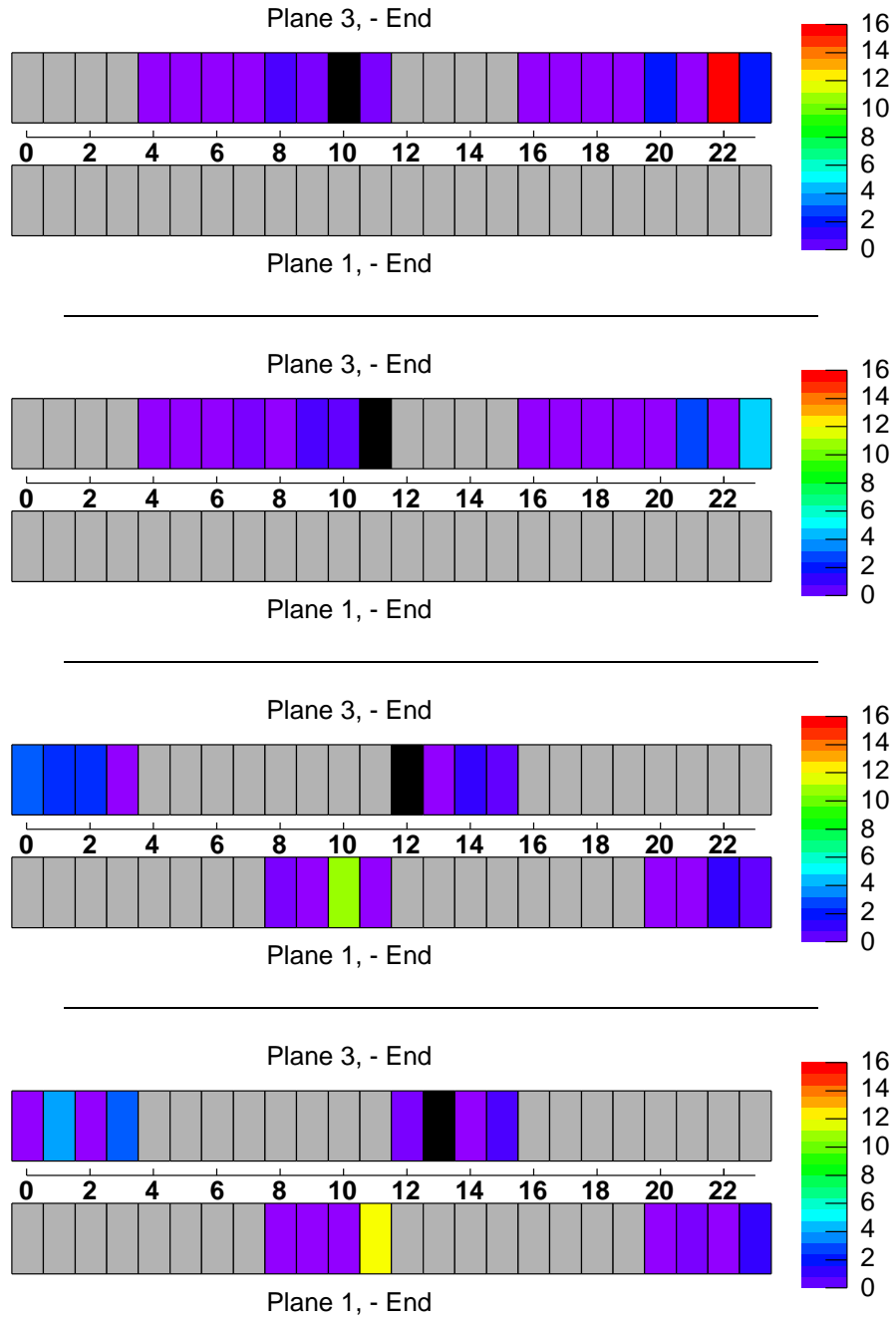
Figure 8.12: Average cross talk magnitude, as a fraction of the light level on the illuminated pixel, shown for different illuminated strips (in black). The color scale is in units of 10^{-4}. Strips marked with grey were not served by the illuminated PMT.
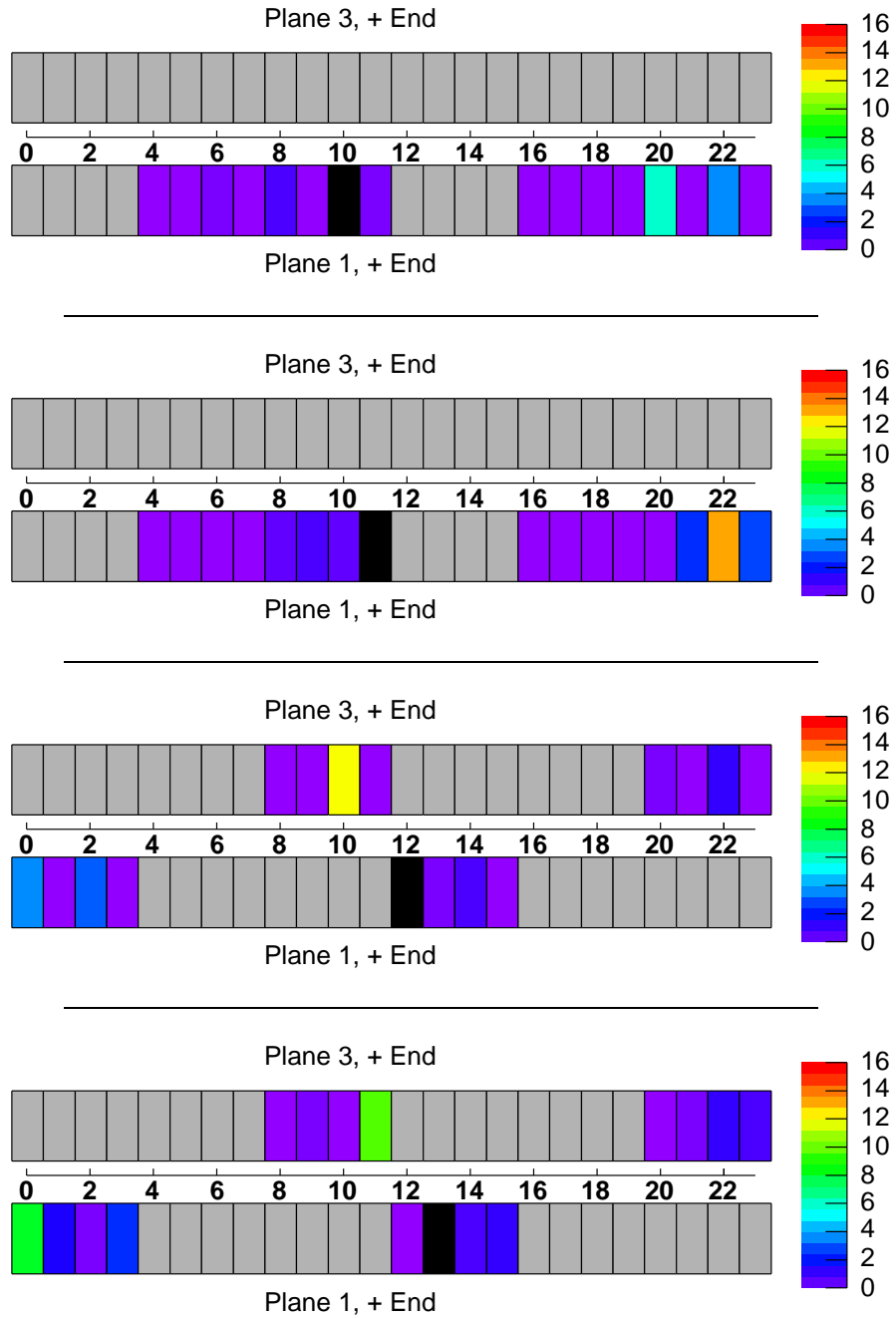
Figure 8.13: Average cross talk magnitude, as a fraction of the light level on the illuminated pixel, shown for different illuminated strips (in black). The color scale is in units of 10^{-4}. Strips marked with grey were not served by the illuminated PMT.
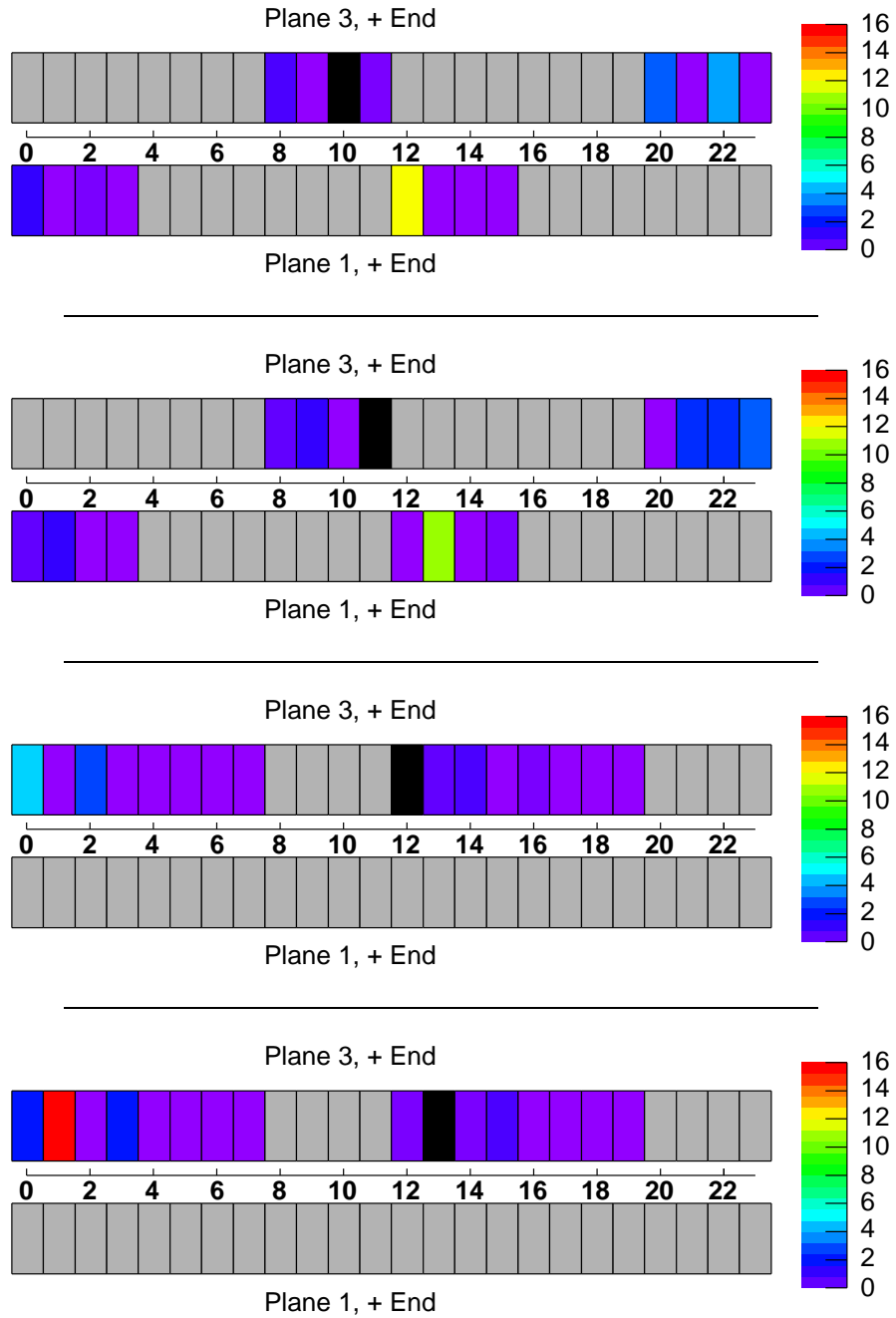
Figure 8.14: Average cross talk magnitude, as a fraction of the light level on the illuminated pixel, shown for different illuminated strips (in black). The color scale is in units of 10^{-4}. Strips marked with grey were not served by the illuminated PMT.

imum ionizing particle, multiple strips hit in a plane, isolated signals larger than 2-3 PEs, and large fluctuations in the magnitude of signals, even between successive planes. Additionally, above the 4 GeV/c momentum setting, all muons traversed the detector whereas most pions did not. Figures A.2 shows typical 5.0 GeV/c pion events. The showering behavior allowed those events to be clearly distinguished from muons, an example of which is shown in Fig. A.3.

Pion-muon separation in MINOS is relatively easy above $\sim 3\,\text{GeV/c}$. As an example, consider Fig. 8.15, which displays the average signal per plane verus the signal in the plane with the largest (integrated) signal for the combined pion and muon dataset. The quantities essentially estimate the typical signal from a plane and the magnitude of the largest fluctuation. Muons occupy the region centered on $\sim 2.5\,\text{MIPs/plane}$ on the abscissa and $\sim 10\,\text{MIPs}$ on the ordinate. Pions, characterized by a higher average signal and larger local fluctuations in the energy deposition, occupy the region on the upper right-hand side of the figure. The number of hit planes per event, a simple estimate of the range, is shown in Fig. 8.16 for four beam momentum settings. Muons were expected to traverse the entire detector, depositing on average $\sim 2.5\,\text{MIPs} \approx 7.8\,\text{PEs}$ per plane. Therefore, muons should be counted with high efficiency and occupy the last few bins of the histograms in Fig. 8.16[7].

Muons were selected by requiring that the average signal per plane was less than 4 MIPs, the maximum signal in a plane was less than 22 MIPs and the number of planes with a hit greater than 55. Figure 8.17 shows the summed calorimeter signal in MIPs for the all events and for those identified as muons

---

[7]Based on the light level, muons should have left a signal in virtually every plane. Each plane, however, has approximately 2% dead space caused by the crack between adjacent scintillator strips
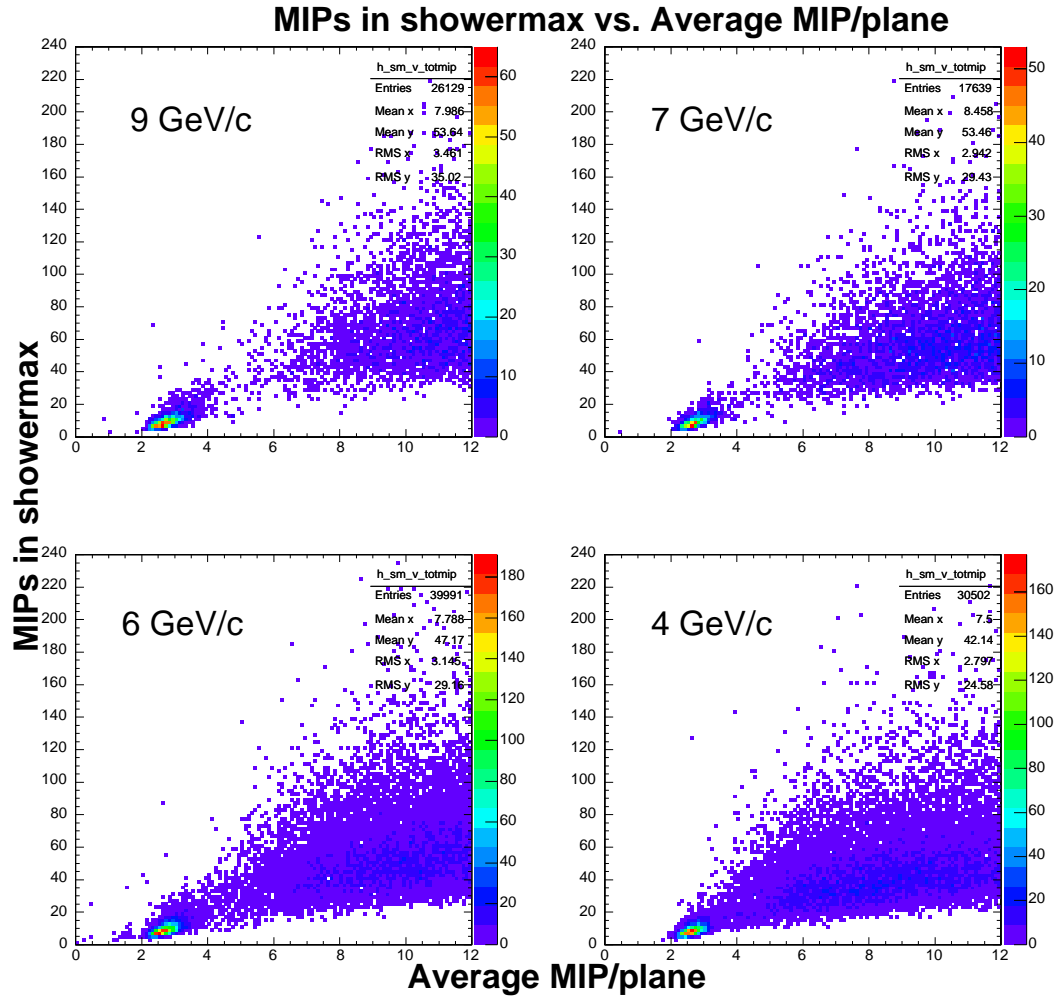
Figure 8.15: Simple topological quantities distinguishing high energy pions and muons. Data were collected in the T7 beamline in 2002. The average signal per plane is shown along the abscissa, while the signal in the plane with the most signal (e.g. shower max) is shown along the ordinate. Muons occupy the island in the lower left hand region of each figure.
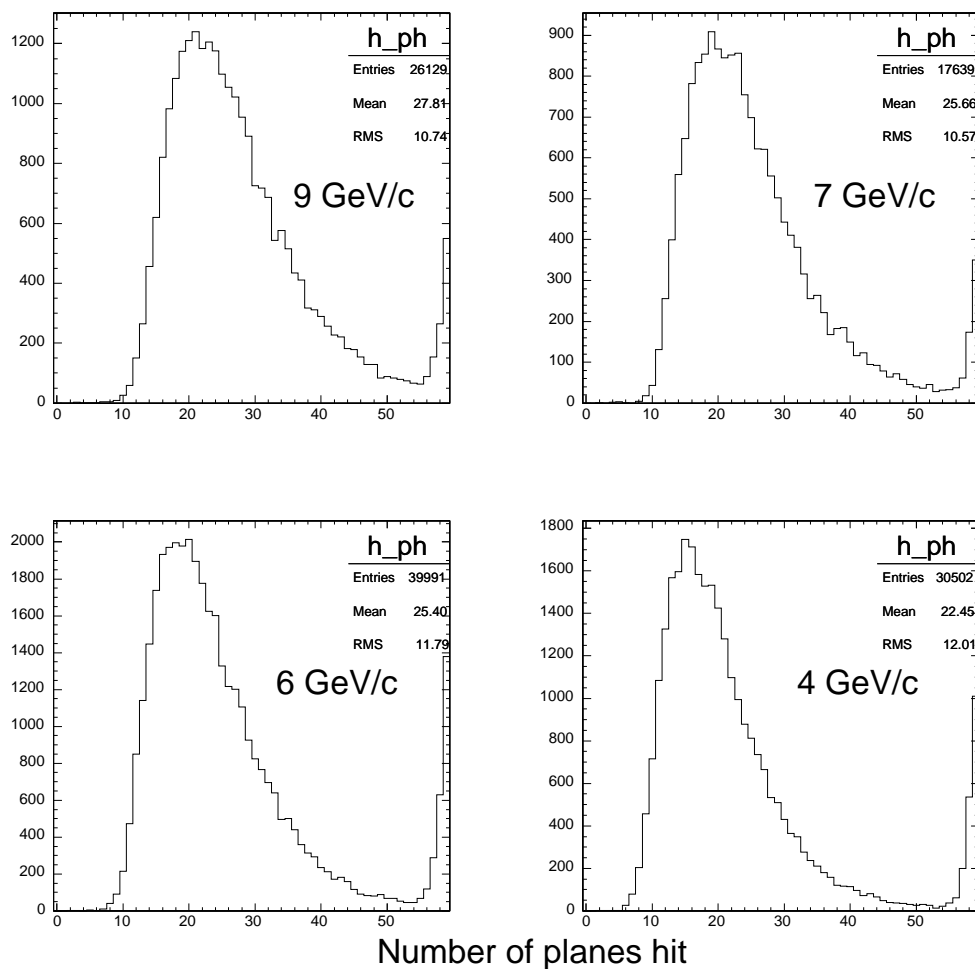
Figure 8.16: The number of planes-with-a-signal per event. Data were collected in the T7 beamline in 2002. At the energies shown here muons punch through the calorimeter, and occupy the five rightmost bins. The vertical scale is the number of events in each one plane bin.

249
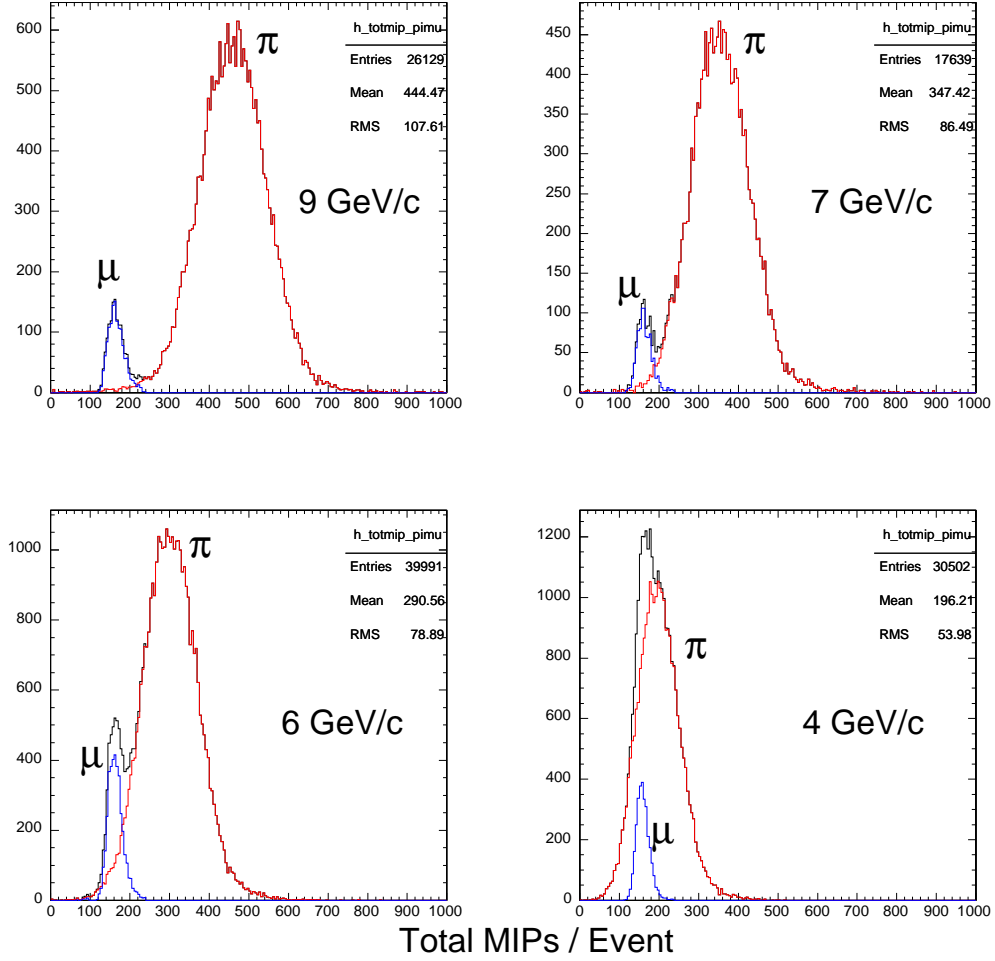
Figure 8.17: The summed signal per event after selecting pions and muons using the average signal per plane, the signal in the shower max plane, and the number of planes hit in the event. Data was taken in the T7 beamline in 2002. Because muons punch through the calorimeter, the signal per event, for muons, does not change with energy. The vertical scale is events per 2 MIP bin.

The fraction # μ / # (π + μ) vs. Beam Momentum : T7 2002
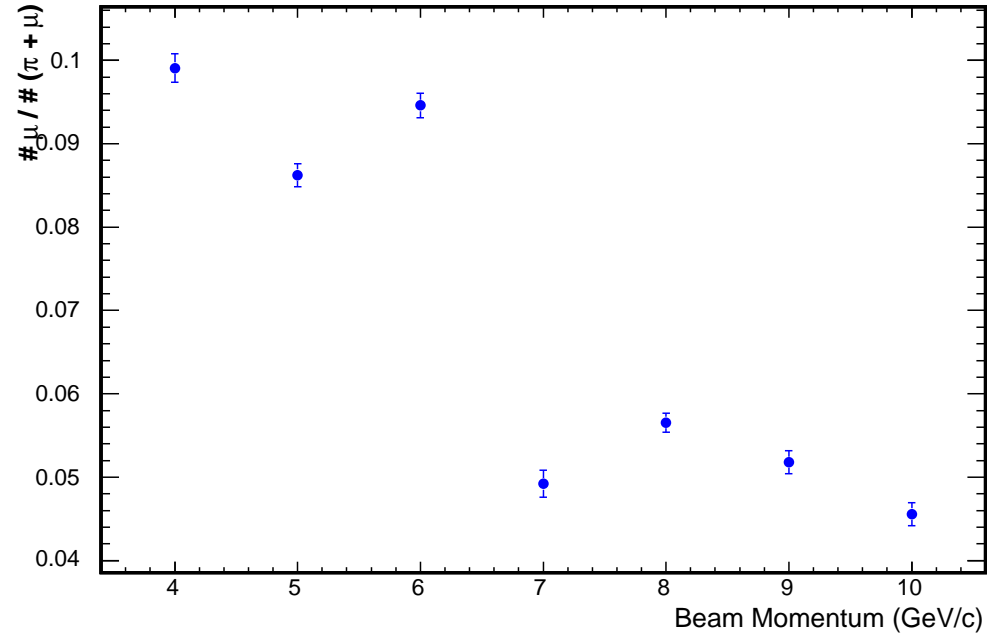
Figure 8.18: The fraction of events selected as muons in the muon+pion sample as a function of the beam momentum. Muons and pions were selected using the topological quantities in Fig. 8.15-8.16. The selection efficiency was not evaluated, but is assumed to be 100% in this figure, given the way in which the muon shoulder behaves and is removed in Fig. 8.17.

and pions. As expected, the muon signal distribution did not change between the different momentum settings.

Figure 8.18 shows the fraction of muons measured at beam momentum settings between 4-10 GeV/c, assuming 100% selection efficiency. The muon fraction rises with decreasing energy, though not entirely smoothly considering the 6 GeV/c and 7 GeV/c points. The behavior of those points is not well understood. One hypothesis is that the muon content was influenced by collimator apertures which changed between the two runs. Additionally, the measured muon content was a factor of 1.8-3.0 times higher than the prediction in Fig. 7.20. The discrepancy cannot be caused by non-interacting pions traversing the detector or by pion decay in flight. For example, the pion inelastic interaction length λ_I is estimated to be 16.8 cm or 6.7 MINOS planes [2]. The calorimeter is therefore 9 interaction lengths deep, and the probability that a pion will not interact on its way through the detector is 0.01%. The contribution from pion decay in flight is somewhat larger but still negligible. As an example, at 5.0 GeV/c the probability for a pion to decay in flight is roughly:

$$
\begin{aligned}
P(x = d) &= 1 - \exp\left(\frac{m_\pi d}{p_\pi \tau_\pi}\right) \\
&\approx \frac{m_\pi d}{p_\pi \tau_\pi} = 0.14\%
\end{aligned}
$$

where $d = 6.7$ planes ≈ 0.4 m is the distance traveled through the detector in one iron interaction length, and $\tau_\pi = 26$ ns is the pion lifetime. Recall, CalDet planes were separated by 5.94 cm of which only 2.5 cm was iron, the remainder being scintillator (1 cm) and air. The fraction of pions which decay in flight increases with decreasing momentum. Using the formula above, at 400 MeV/c the fraction is calculated to be 1.8% which is an overestimate since
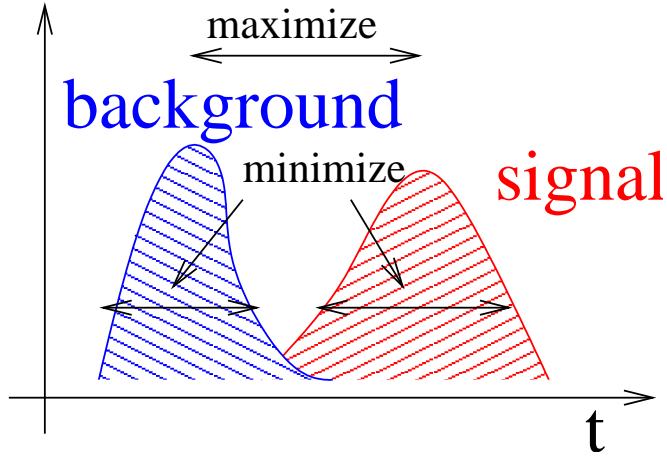
Figure 8.19: The goal of a linear discriminant. The discriminant calculates a test statistic which is distributed such that distance between the two classes is maximized while the variance within each class is minimized.

the hadronic cross section (proportional to d^{-1}) increases with decreasing beam momentum. The higher than expected muon content cannot be caused soley by pion decay in flight or punch through.

8.3.1 Linear Discriminant

Pion-muon discrimination is relatively simple at higher beam momentum settings but becomes increasingly difficult as the momentum decreases. A multivariable linear discriminant technique was adopted in order to assist in the classification. The procedure was useful because it constructed a scalar quantity that was optimized such that the pion and muon distributions were maximally separated. The quantity could then be cut on to yield pion-like and muon-like samples, and the efficiency for correctly classifying pions (or muons) could be varied by changing the cut parameter. Other than the input vari-

ables, the procedure had no tunable parameters, in contrast to neural networks which require choosing an architecture, minimization procedure and transfer functions[8].

For each event, the discriminant technique constructed a single test statistic t from a set of N event variables $\boldsymbol{x} = \{x_1 \ldots x_N\}$. The discriminant was just a mapping $\boldsymbol{x} \to t$ from the N dimensional event variable space to the one dimensional test statistic space. The simplest mapping was linear

$$t\left(\boldsymbol{x}\right) = b + \boldsymbol{w}^\top \cdot \boldsymbol{x} \tag{8.6}$$

where $b, \boldsymbol{w}$ are the bias and a vector of weights. The weights were free parameters which were optimized by minimizing the variance (in test statistic space) within each class (pions and muons in the present case) while maximizing the separation between the classes (see Fig. 8.19). The optimization procedure consisted of varying the weights in order to minimize a quantity Q given by [78]:

$$Q = \frac{\sum_{i,j=1}^{N} w_i w_j \left(\boldsymbol{m}_\mu - \boldsymbol{m}_\pi\right)_i \left(\boldsymbol{m}_\mu - \boldsymbol{m}_\pi\right)_j}{\sum_{i,j=1}^{N} w_i w_j \left(C_\mu + C_\pi\right)_{ij}} \tag{8.7}$$

where π, μ label the two classes, $C_{\mu,\pi}$ are the covariance matrices of the event variables for muons and pions and $\boldsymbol{m}_{\mu,\pi}$ are vectors of the means of the event variables. Q was maximized when the numerator was large (the classes are well separated) and the denominator was small (the variance with each class is minimized). Up to an arbitrary scale factor, the weights were found by inverting the sum of the covariance matrices and multiplying by $\left(\boldsymbol{m}_\mu - \boldsymbol{m}_\pi\right)$ [78]:

$$\boldsymbol{w} \propto \left(C_\mu + C_\pi\right)^{-1} \cdot \left(\boldsymbol{m}_\mu - \boldsymbol{m}_\pi\right) \tag{8.8}$$

---

[8]Linear discriminants, also known as single layer perceptrons, have an architecture that is identical to a single layer neural network with linear transfer functions and a linear output.

The overall scale a of $\boldsymbol{w}$ and the bias b were still arbitrary. For convenience, a, b were fixed by maximizing

$$L = \sum_\pi \log\left[\frac{1}{1 + \exp\left(-b - a\boldsymbol{w} \cdot \boldsymbol{x}\right)}\right] + \sum_\mu \log\left[1 - \frac{1}{1 + \exp\left(-b - a\boldsymbol{w} \cdot \boldsymbol{x}\right)}\right]$$
$$(8.9)$$

with respect to a, b, where the sums were over all pion and muon events. L is a log likelihood in which the probability that a particular value of the test statistic $t' = b + a\boldsymbol{w} \cdot \boldsymbol{x}'$ corresponds to a pion event was modeled as a logistic sigmoid:

$$P\left(\pi|t'\right) = \frac{1}{1 + \exp\left(-t'\right)} \qquad (8.10)$$

The procedure essentially mapped the test statistic for pion events to positive values and the statistic for muon events to negative values. The logistic sigmoid model was adopted as a convention in order to fix the scale of t. In the analysis $1/1 + \exp(-t')$ was never assumed to reflect the actual probability that t' corresponded to a pion induced event.

The discriminant bias and weights were constructed from samples of pions and muons simulated in CalDet using GMINOS and the DetSim and PhotonTransport packages. GCALOR was used to simulate hadronic showers and the input events were taken directly from the output of the beamline simulation. Weights were separately constructed for positive and negative pions at each beam momentum setting. For momentum settings less than $4\,\mathrm{GeV/c}$ the weights were constructed using events simulated in the T11 beamline, above $4\,\mathrm{GeV/c}$ the events were simulated in the T7 beamline. This is in contrast to building the weights for T7 and T11 separately, a procedure that was not adopted because it was desirable to make identical selections on runs taken at the same momentum setting in T11 and T7.
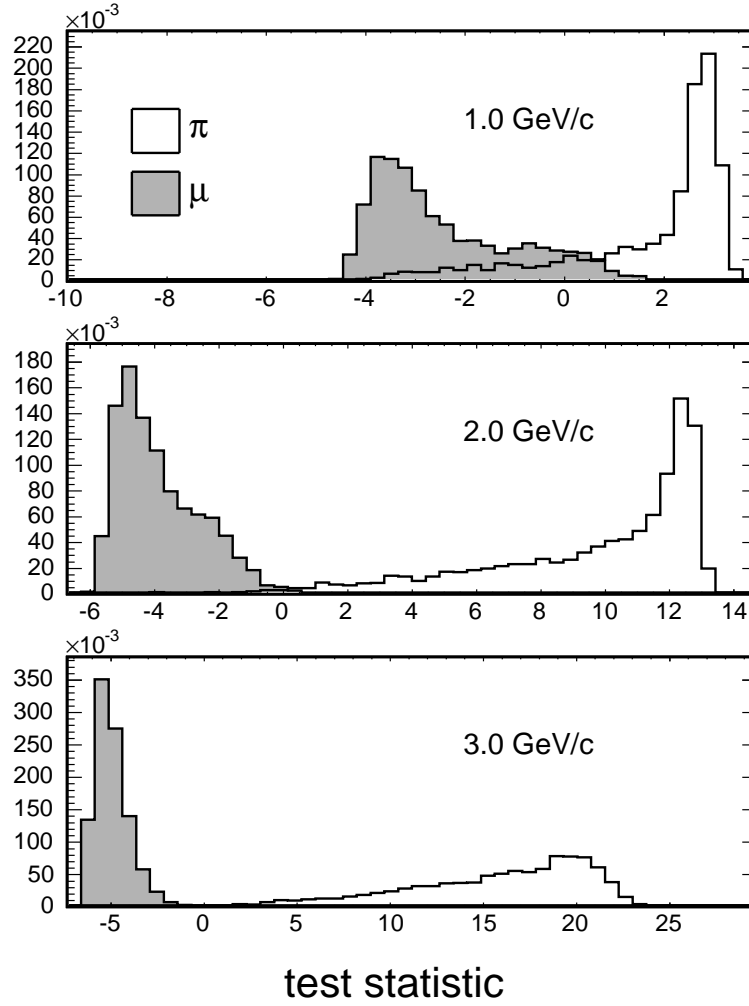
Figure 8.20: The distribution of the test statistic for muons and low energy π^- simulated with GCALOR. The right-hand shoulder on the muon distribution corresponds to maximally off-momentum muons. Pions and muons are more easily separated as the beam momentum increases. The histograms are normalized to unit area.

Six event variables were used in the discrimination procedure. The variables were selected according to their ability to individually discriminate between pions and muons, their applicability over a wide range of momentum settings (but with a focus on the region below $2\,\mathrm{GeV/c}$) and their relative simplicity. The variables were:

E3: The signal in the three-plane window having the largest integrated signal. The variable is expressed as a fraction of the total signal.

E9: Just as E3 but for a nine-plane window.

SIGDEV: The absolute deviation of the pulseheight per plane. The quantity was calculated as
$$\mathrm{SIGDEV} = \frac{1}{59} \sum_{i=1}^{59} \left| S_i - \bar{S} \right|$$
where S_i is the pulseheight observed in plane i, and $\bar{S}$ is the average pulseheight per plane. Before being used in the discriminant process the quantity was multiplied by $1/40$ in order make the scale similar to the other quantities.

NBP: The number of planes with an integrated signal greater than $7\,\mathrm{MIPs}$.

MAX: The number of strips hit in the plane with the largest number of strips hit. In order to suppress the effect of PMT cross talk, the strips were required to have a signal larger than $1.5\,\mathrm{PEs}$ before being counted.

MAX3: Just as MAX, but the three planes with the largest number of strips hit were used.

257

The quantities probed different aspects of the detector's response to pions and muons. The E3 and E9 variables characterize the pattern of longitudinal energy deposition. The SIGDEV variable characterizes the magnitude of fluctuations in the signals deposited in each plane. NBP roughly represents the number of planes with a pulseheight that was inconsistent with a minimum-ionizing particle. The MAX and MAX3 variables characterize the width of the shower. Originally, an estimator for the range of events was used in the procedure, but the resulting discriminant was found to depend too strongly on the muon range and hence on the muon momentum spectrum. The E3 and E9 variables provided the strongest discrimination followed by the SIGDEV and NBP and then MAX and MAX3 variables.

Figures 8.21-8.23 display the event variables for three momentum settings. In the figure, the distributions from simulated pions and muons are shown, along with the combined muon and pion distribution from the data. The distribution shown in magenta with error bars is a sum of the simulated pion and muon distributions in which the muon content was scaled according to the measured composition of muons (discussed below). In general the simulation was in reasonable agreement with the data for the E3,E9, SIGDEV and NBP distributions. The MAX and MAX3 variables are shifted toward somewhat larger values for simulated pions.

The discriminant weights and bias were constructed from Monte Carlo samples of 5000 pion and muon events each. The efficiency of the selection was determined by using the weights and bias to calculate the discriminant for a second sample of 5000 pions and muons. The fraction of pions with $t > t_{test}$ (the pion efficiency) and the fraction of muons with $t > t_{test}$ (the muon misidentification probability) were determined using the second sample
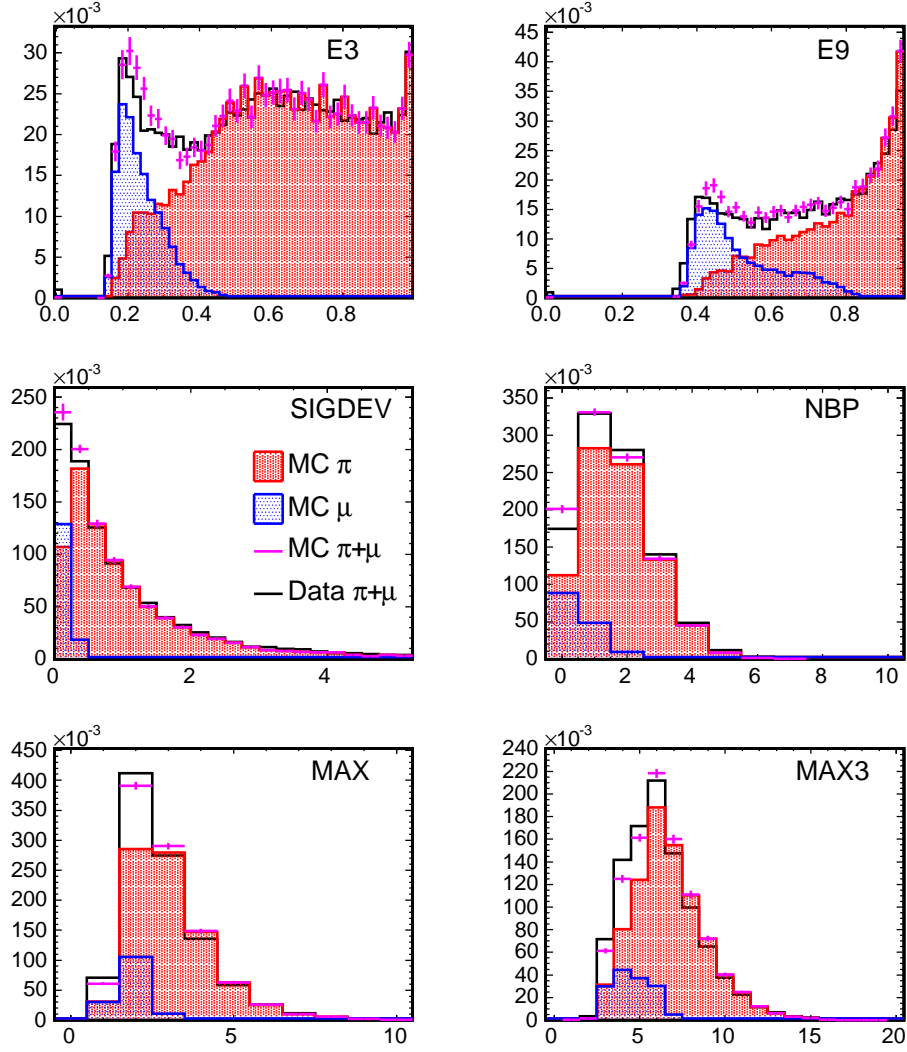
Figure 8.21: Variables used to form the discriminant. Distributions are shown for $1\,\mathrm{GeV}/c$ π^+, μ^+ simulated using the flux from the beamline simulation and combined pion and muon data collected in T11. The relative proportion of simulated muons and pions was established based on the calculated discriminant efficiency and the measured fraction of muons. The combined π and μ histograms are normalized to unit area.
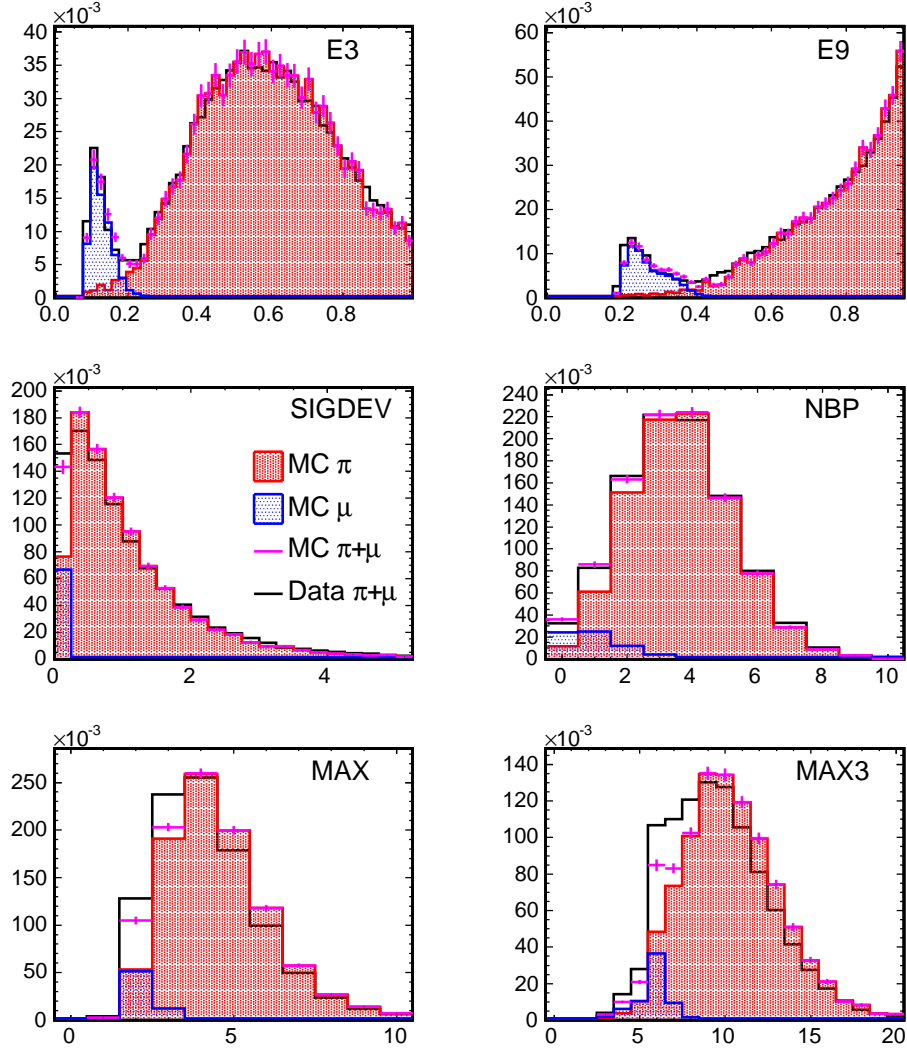
Figure 8.22: Variables used to form the discriminant. Distributions are shown for $2\,\mathrm{GeV/c}$ π^+, μ^+ simulated using the flux from the beamline simulation and combined pion and muon data collected in T11. The relative proportion of simulated muons and pions was established based on the calculated discriminant efficiency and the measured fraction of muons. The combined π and μ histograms are normalized to unit area.
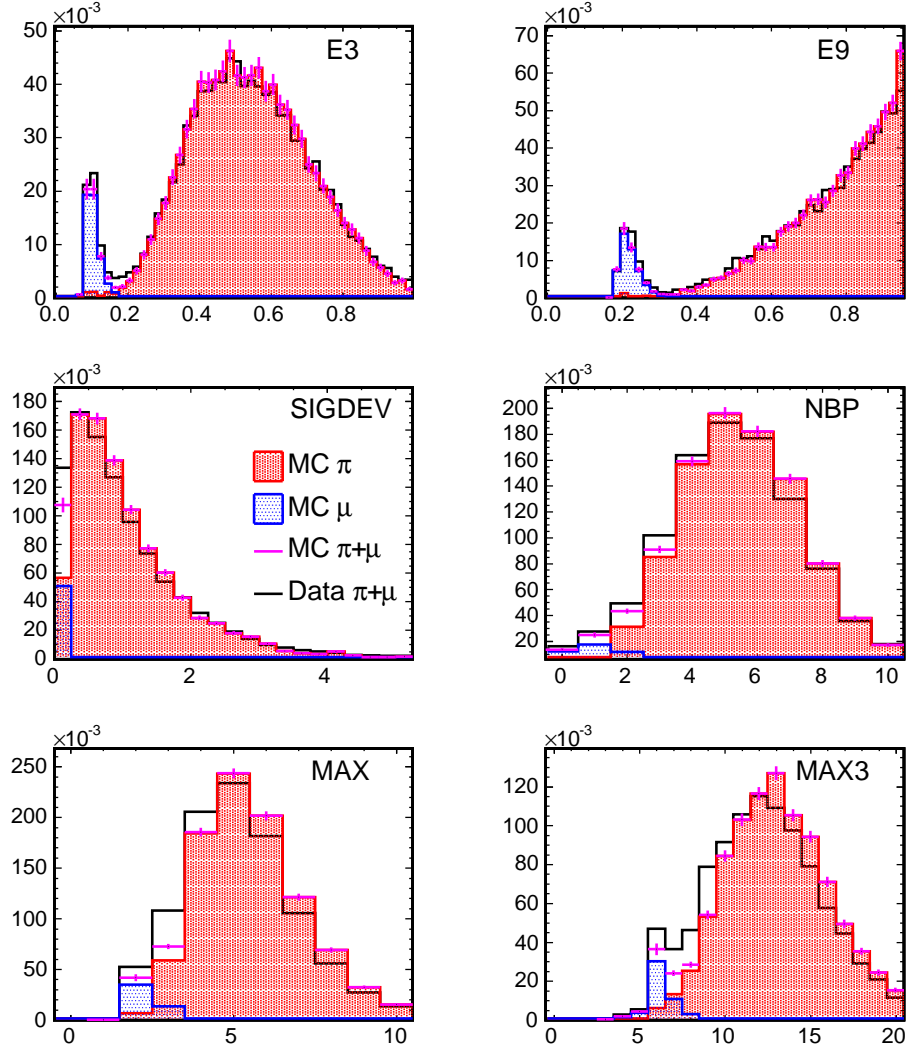
Figure 8.23: Variables used to form the discriminant. Distributions are shown for $3\,\mathrm{GeV}/c$ π^+, μ^+ simulated using the flux from the beamline simulation and combined pion and muon data collected in T11. The relative proportion of simulated muons and pions was established based on the calculated discriminant efficiency and the measured fraction of muons. The combined π and μ histograms are normalized to unit area.
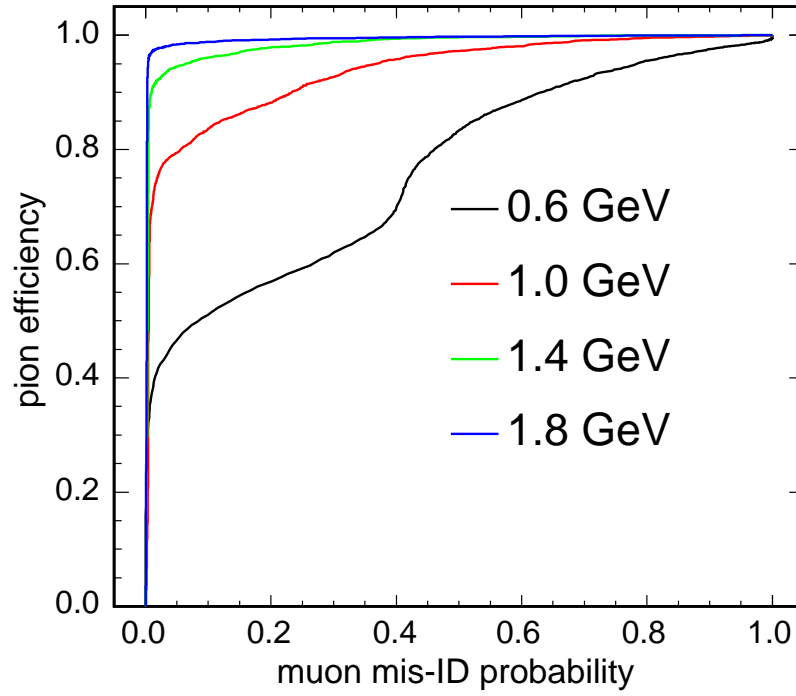
Figure 8.24: The efficiency for selecting pions vs. the muon misidentification probability for π^- simulated with GCALOR. The linear discriminant technique was used in the selection. The figure for π^+ is nearly identical.

for a range of values t_{test}.

Figure 8.24 shows the calculated pion efficiency versus the muon misidentification probability. Different locations along the curves correspond to different values of t_{test}. For momentum settings above $1.0\,\mathrm{GeV/c}$ pions could be selected with $> 90\%$ efficiency while rejecting $> 90\%$ of muons. The ability to seperate pions and muons decreased with the beam momentum. Part of the decrease is likely due to both the event variables used and the nature of the discriminant procedure. A neural network technique or multi-dimensional cuts could possibly give a superior result. These results illustrate that the MINOS detector was not optimized for hadronic events in the $1\,\mathrm{GeV/c}$ range and below. The 2.5 cm thickness of the MINOS iron planes coupled with the relatively small amount of energy available in the hadronic showers caused many of the shower particles to be absorbed before traversing scintillator. This resulted in pion events with few large hits and little information which distinguished them from muons. Figures A.7-A.8 display a selection of events taken at a $1\,\mathrm{GeV/c}$ momentum setting.

If all muons were on-momentum then a relatively simple selection could have been made on the event length. The presence of the off-momentum tail in the muon sample complicated matters. At and below $1\,\mathrm{GeV/c}$ the off-momentum muon event length merged significantly with the pion event length rendering a simple selection using the event length unfeasible. Though the event length was not used in the discrimination procedure there was some correlation between the length and the discriminant variables. The effect of the correlation was largest at very low energies and had consequences for the discriminant behavior. As an example, the kink in the $600\,\mathrm{MeV/c}$ curve in Fig. 8.24 was caused by the off-momentum muons.
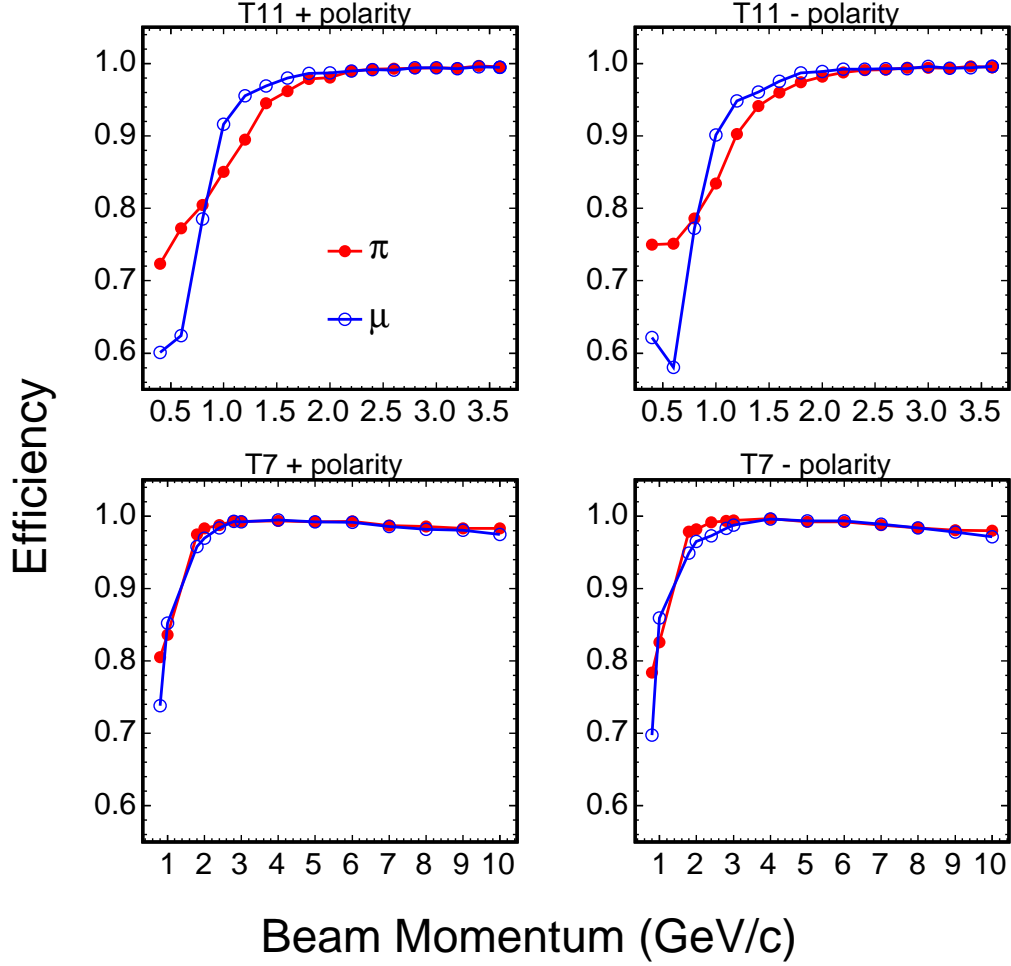
Figure 8.25: The efficiency for selecting pions and muons with the linear discriminant technique. Below $4\,\text{GeV/c}$ in T7, weights were calculated using events from the T11 simulation but the efficiency was re-evaluated using events from the T7 beamline simulation. The efficiency drop at low momenta is a consequence of the composition and granularity of the MINOS calorimeter as well as the relatively small amount of activity induced by low energy pions. The discriminant variable were optimized for momentum settings below $4\,\text{GeV/c}$ which caused the slight decrease in the efficiency at high energy.

Pion and muon (or more properly pion-like and muon-like) events were selected by placing a cut t_0 on the test statistic distribution. Events with $t > t_0$ were classified as pions and those with $t < t_0$ were classified as muons. The position of the cut is somewhat arbitrary and depends on the goals of the study at hand. This work aimed at a general characterization of pion and muon events. As such, considering an example based on the 600 MeV curve in Fig. 8.24, a cut which rejected 90% of muons from the pion sample while only accepting 50% of pions did not seem advisable. A perfect selection would accept 100% of the pion sample while rejecting all muons and, except at the lowest energies, the position of the cut t_0 was chosen to most closely approximate that ideal case. That is, the cuts were choosen to correspond to the point of closest approach to $(0, 1)$ in Fig. 8.24.

For the 400 and 600 MeV momentum settings, the closest approach was located on the left-hand side of an inflection like that shown in Fig. 8.24. In that region, the pion efficiency increased rapidly as a function of the muon misidentification probability and the position of the cuts were adjusted in order to move to the right of the inflection, accepting more pions at the expense of an increase in the muon background. Figure 8.25 shows the selection efficiencies as a function of the momentum setting for positive and negative polarities in T7 and T11. The pion selection efficiency increased with the beam momentum up to $\sim 5\,\mathrm{GeV/c}$ and was greater than 98% above $2\,\mathrm{GeV/c}$. The discriminant variables were optimized for momentum settings less than $4\,\mathrm{GeV/c}$ which caused the slight decrease in efficiency at high energies.

The determination of the discriminant weights and efficiency for one run took about half an hour on a 500 MHz processor. The weights and a record of the selection efficiency were saved to disk and later applied to the data

during the second pass DST construction phase of the processing as described in Ch. 6. Each DST entry contained a word holding the value of the test statistic allowing different cuts to be applied with ease.

8.3.2   Muon Content

The discriminant was used to count the number of muons and thereby measure the muon content of the beam. In each run, the number of events n'_π with $t > t_0$ and the number of events n'_μ with $t < t_0$ were tabulated. The numbers n'_μ, n'_π do not precisely correspond to the actual number of muons and pions in the beam, since n'_μ contains a contribution from pions that were misidentified as muons and n'_π contains a contribution from muons that were misidentified as pions. The actual number of muons and pions, n_μ and n_π, are related to n'_μ and n'_π by

$$n'_\mu \;\; = \;\; n_\mu \epsilon_\mu + n_\pi \left(1 - \epsilon_\pi\right) \tag{8.11}$$

$$n'_\pi \;\; = \;\; n_\pi \epsilon_\pi + n_\mu \left(1 - \epsilon_\mu\right) \tag{8.12}$$

where $\epsilon_{\pi,\mu}$ are the muon and pion selection efficiencies. Solving for ϵ_μ gives:

$$n_\mu = \frac{n'_\mu + N\left(\epsilon_\pi - 1\right)}{\epsilon_\mu + \epsilon_\pi - 1} \tag{8.13}$$

Here $N = n'_\mu + n'_\pi = n_\mu + n_\pi$ is the total number of pions and muons.

Figure 8.26 shows the measured muon content, as a fraction of the total number of pions and muons. The errors in the figure account for the statistical uncertainty in the selection efficiencies due to the size of both the Monte Carlo and data samples. The muon content was consistent between the positive and negative polarities, but not between T11 and T7. As predicted by Fig. 7.20 the muon content increased when the beam momentum decreased, but the actual

266
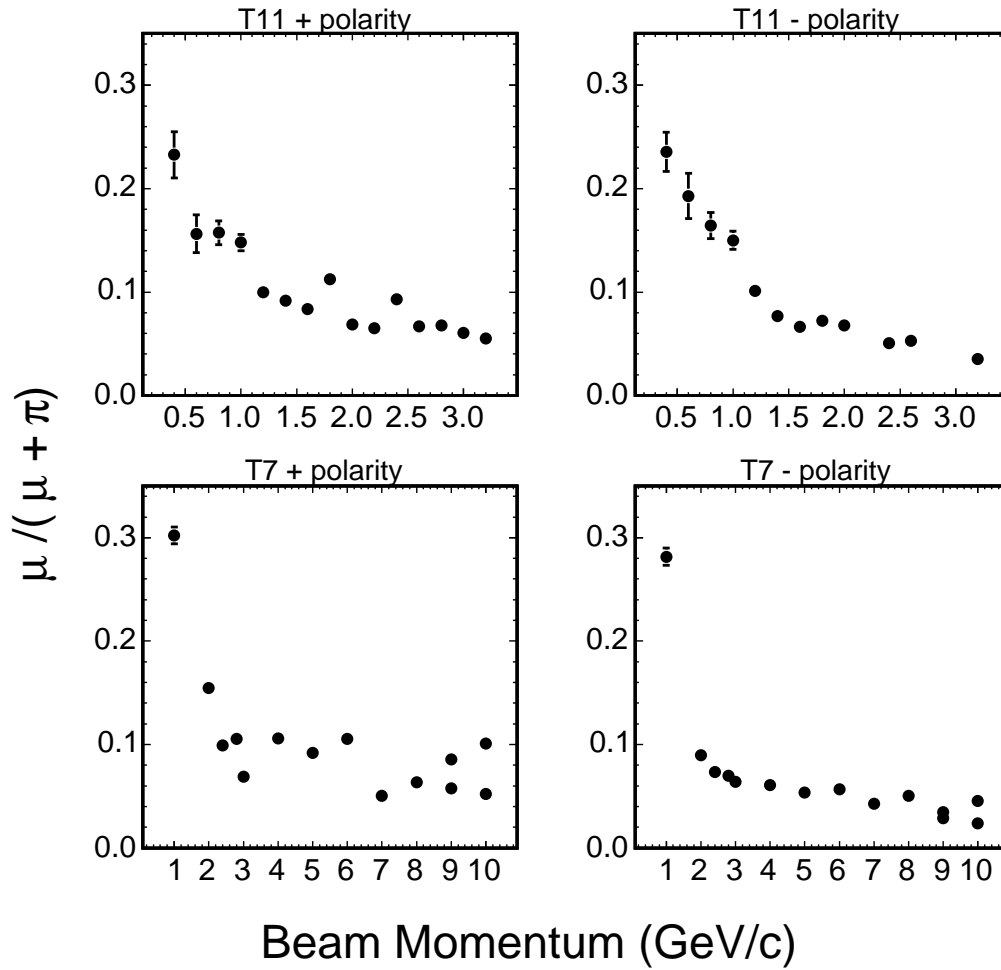
Figure 8.26: The measured muon content as a fraction of the total number of pions and muons. Efficiencies were taken from Fig. 8.25. The scatter, particularly noticeable for the positive polarity beams, is statistically significant and believed to be caused by differing beam conditions and collimator settings.

fraction of muons was much higher than the predicted fraction. In the region below $4\,\mathrm{GeV/c}$ the muon content in T7 was significantly larger than in T11 even though the same discriminant weights and selection criteria were used.

The muon content exhibited more scatter as a function of the beam momentum for the positive beam polarities than the negative, and T7 was more scattered than T11. The scatter is not believed to be due to any deficiency in the selection procedure. For example, the muon content determined with simple selection criteria and shown Fig. 8.18 is in good agreement with the same points in Figure 8.26. Even at $10\,\mathrm{GeV/c}$, where the pion/muon selection is essentially unambiguous, the muon content was observed to differ by a factor of two between two separate runs. The cause of the scatter is not understood but is hypothesized to be due to differing beam conditions. For example, the two runs at $10\,\mathrm{GeV/c}$ positive polarity differed in the target used and also the collimator settings[9]. In fact, considering the eight points at ± 9 and $\pm 10\,\mathrm{GeV/c}$, the point at each momentum setting with the lowest muon content was measured during one continuous, $4\,\mathrm{hr}$ timespan and the point with the highest content was measured during a second, $2\,\mathrm{hr}$ timespan later in the running period. The detector was operated with PMT high voltages lowered by $25\,\mathrm{V}$ during the second period but the change was not expected to cause any difference in the muon counting. A complete understanding of the muon content would probably require a detailed simulation, in GEANT or FLUKA, of the entire beamline, including all the magnets and interactions in collimators, magnet apertures and beam-pipe walls.

Figure 8.27 shows the muon contamination of the pion sample after pions were selected with the discriminant procedure. The contamination was

---

[9]The log of the collimator settings is not unambiguously clear.
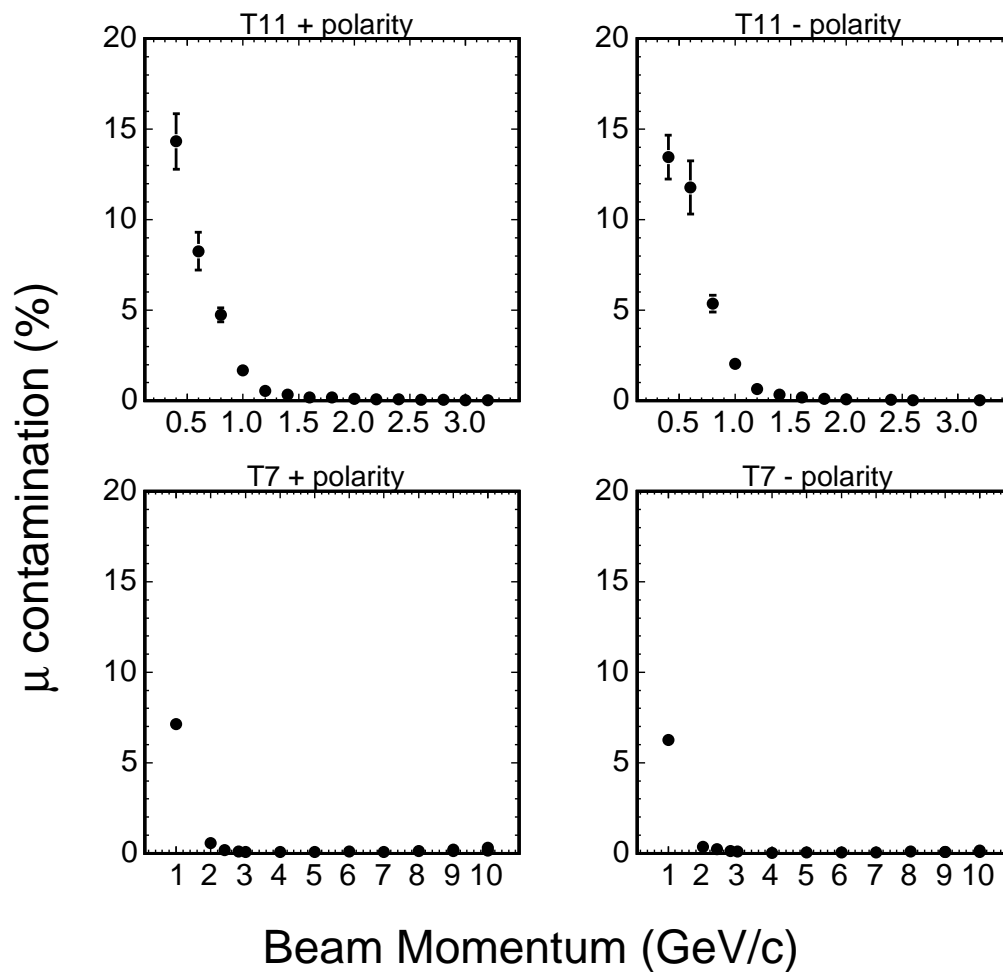
Figure 8.27: The muon contamination of the pion sample as a function of the beam momentum. For momentum settings above 1 GeV/c the contamination was negligible. The muon content increased with decreasing beam energy (Fig. 8.26) and at the same time the ability to distinguish pions from muons decreased (Fig. 8.25). The two effects caused the contamination to increase as the beam energy dropped.
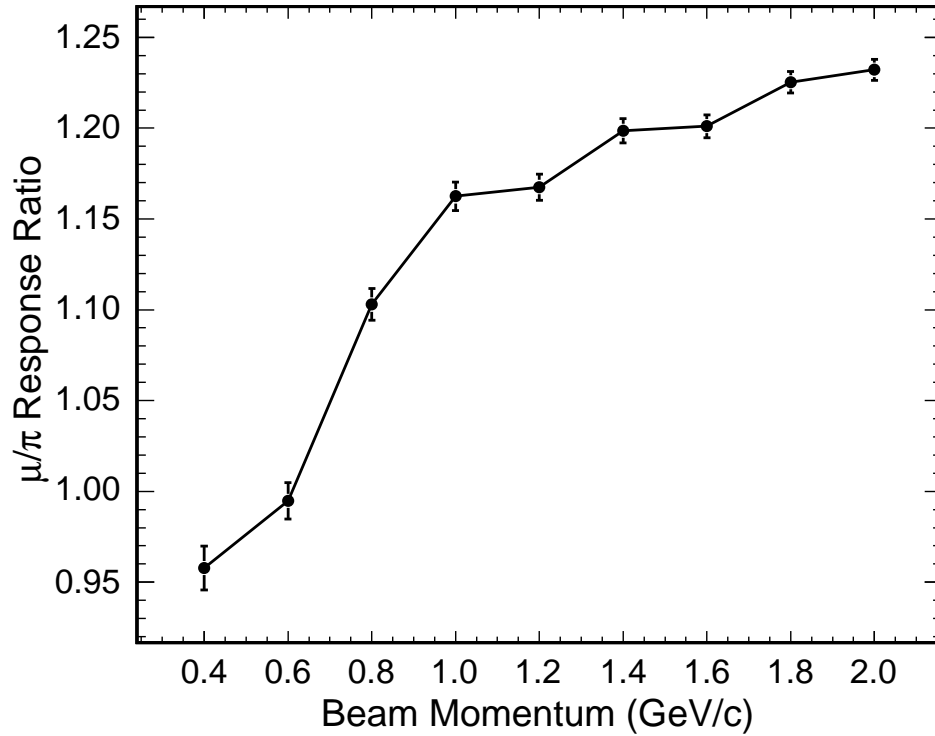
Figure 8.28: The ratio of the detector's response to muons and pions. The figure is the result of Monte Carlo calculations using the GCALOR hadronic shower code. The discriminant procedure was not used to select pions and muons. Events were input from the beamline simulation, thereby including off-momentum muons. The μ/π ratio gradually decreased from ~ 1.23 at $2\,\mathrm{GeV/c}$ to ~ 1 at $600\,\mathrm{MeV/c}$.

less than 1% for momentum settings above $1\,\mathrm{GeV/c}$ but rose steadily as the beam momentum decreased below $1\,\mathrm{GeV/c}$, reaching a maximum of $\sim 14\%$ at the $400\,\mathrm{MeV/c}$ setting. The relatively high contamination at low energy was a result of the large muon content of the beamlines as well as the relatively poor ability of the MINOS calorimeter to discriminate between muons and pions in the sub-GeV region (see the discussion on p. 263). Figure 8.28 shows the ratio of the (signal) response of pions and muons according to a Monte Carlo simulation. The effect of the contamination on the signal response is less severe than the $\sim 10\%$ contamination might indicate because the (albeit simulated) μ/π response ratio decreases to unity at low energy.

8.4 Comparison of Data and Monte Carlo

MINOS will classify neutrino events as ν_μ-CC, NC and ν_e-CC based on the topological patterns induced in the detector. The development of selection algorithms and the resulting efficiencies will depend in a large part on Monte Carlo simulations conducted with GMINOS. As such, the CalDet program was undertaken, at least in part, in order to provide a sample of π, μ, e, p events with which the quality of the Monte Carlo could be judged. There was a particularly acute need to validate the hadronic shower simulation since multiple codes were available and those codes had most often been benchmarked for energies above $10\,\mathrm{GeV}$ or so. Prior to the advent of the CalDet program there was no significant reason for preferring one code over another.

All of the hadronic shower codes commonly employed with GEANT3 have been compared to the CalDet data. The first comparisons focused on the two most often used hadronic shower codes, GHEISHA and GFLUKA,

271

and proved that neither code was able to correctly model π and p events in CalDet (see, for example, Fig. 8.7). Two additional packages, GCALOR and SLAC-GHEISHA, were adopted and preliminary results indicated that each was in better agreement with the data than either GHEISHA or GFLUKA. Results of a more comprehensive comparison between the π, p data and the SLAC-GHEISHA and GCALOR codes are presented below.

8.4.1 Comparison of Pions

Pion events were selected from the data according to the discriminant procedure and the same selection was applied to the simulated events. The Monte Carlo events were read in from the beamline simulation, which accounted for energy loss upstream of the detector and made comparisons at the few % level possible. Pure π events were used in the study and there was no attempt to correct the Monte Carlo distributions for the estimated muon contamination.

Figures 8.29-8.32 display the hit-strip multiplicity observed in $\pi^{\pm}$ events. The hit-strip multiplicity is a general but robust indicator of the activity induced in the detector. In the figures, the column on the left shows the distribution when all hit strips were counted while the column on the right shows the distribution when hits with a pulseheight less than 1.5 PEs were ignored. The pulseheight cut is interesting because it provides a simple way of rejecting the majority of the hits created by PMT cross talk. At all energies, GCALOR was observed to create more activity in the detector than SLAC-GHEISHA. Below 6 GeV/c the means of the GCALOR distributions agreed rather well with the data but SLAC-GHEISHA under-predicted the activity. Both Monte Carlo distributions were somewhat narrower than the data, though the pulseheight

272

Figure 8.29: π^+ hit-strip multiplicity, with and without a 1.5 PE cut. Data collected in T11 are shown shaded, pions simulated with GCALOR are shown in blue and those simulated with SLAC-GHEISHA are shown in red. The histograms are normalized to unit area.

Figure 8.30: π^- hit-strip multiplicity, with and without a 1.5 PE cut. Data collected in T11 are shown shaded, pions simulated with GCALOR are shown in blue and those simulated with SLAC-GHEISHA are shown in red. The histograms are normalized to unit area.

274
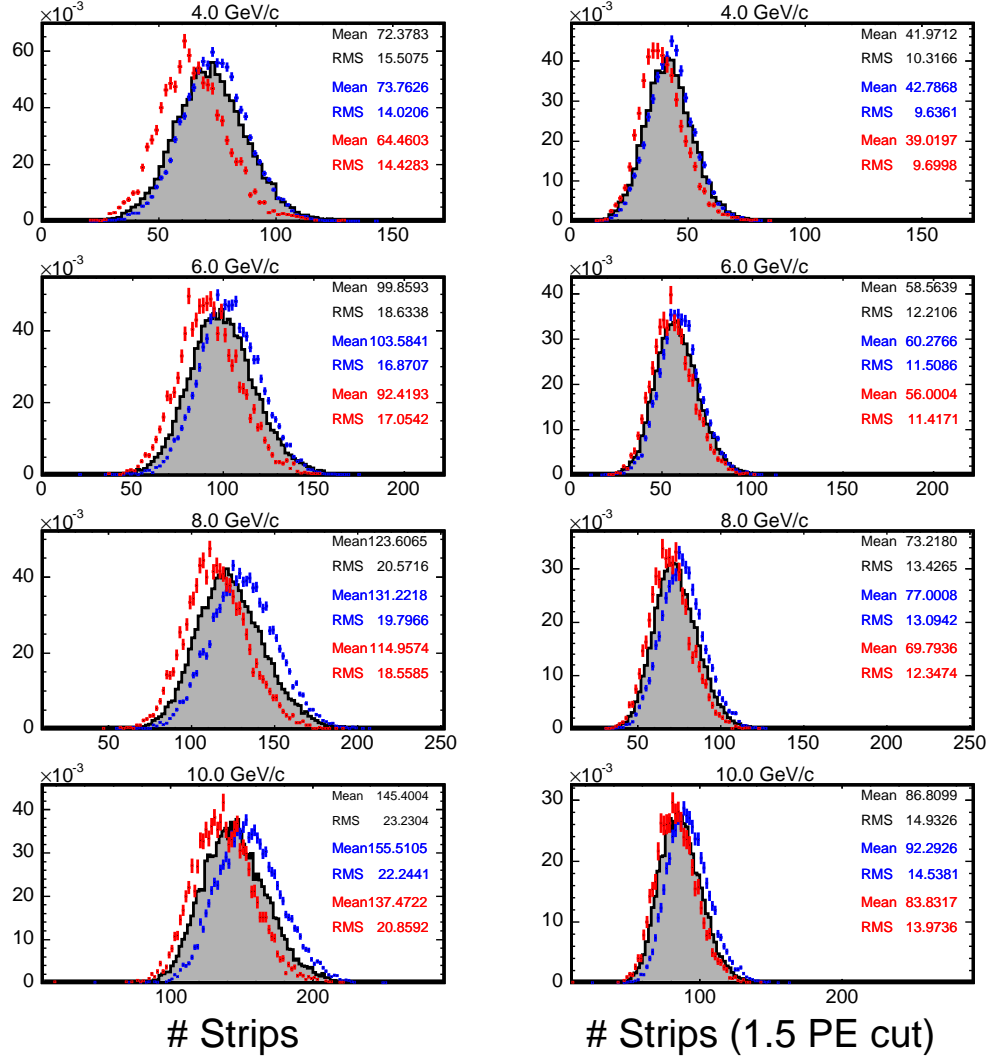
Figure 8.31: π^+ hit-strip multiplicity, with and without a 1.5 PE cut. Data collected in T7 are shown shaded, pions simulated with GCALOR are shown in blue and those simulated with SLAC-GHEISHA are shown in red. The histograms are normalized to unit area.

Figure 8.32: π^- hit-strip multiplicity, with and without a 1.5 PE cut. Data collected in T7 are shown shaded, pions simulated with GCALOR are shown in blue and those simulated with SLAC-GHEISHA are shown in red. The histograms are normalized to unit area.

cut reduced the discrepancy. GCALOR gradually began to overestimate the activity at about $6\,\mathrm{GeV/c}$ and the agreement between SLAC-GHEISHA and the data became somewhat better.

Figures 8.33-8.36 display the hit-plane multiplicity and the shower profile of $\pi^{\pm}$ events. The distributions are interesting in part because the relatively fine longitudinal segmentation of the MINOS calorimeter has been used in many analyses to discriminate between NC and ν_{μ}-CC events through a cut on the event length. The shower profiles may also be used to derive the depth necessary to contain a given fraction of the energy in hadronic showers with the result being utilized to establish constraints on the fiducial volume and estimate the inter-event contamination in the Near detector.

The hit-plane multiplicity was modeled rather well by GCALOR over the entire energy range, though the Monte Carlo distributions were somewhat more narrow than the data. The SLAC-GHEISHA code tended to underestimate the hit-plane multiplicity and π^- were modeled slightly worse than π^+. Both codes appeared to shower early, depositing energy less deeply into the detector than was observed in the data. SLAC-GHEISHA modeled the shower profile much more poorly than GCALOR except at the highest momentum settings.

A simple procedure was devised to estimate the longitudinal shower vertex (i.e. interaction plane) and thereby allow a quantity that was similar to the hadronic interaction length to be compared between the data and the simulation. Showers were defined to begin on the first plane with an integrated signal above some threshold value. Multiple threshold values between 2-10 MIPs were utilized, though it was clear that reasonable values had to be significantly larger than the typical minimum ionizing signal ($\sim 2\,\mathrm{MIPs}$). Fig-

277

Figure 8.33: π^+ hit-plane multiplicity and shower profile. Data collected in T11 are shown shaded, pions simulated with GCALOR are shown in blue and those simulated with SLAC-GHEISHA are shown in red. In the shower profile figures, the abscissa corresponds to the plane number and the ordinate corresponds to the average fraction of shower energy deposited per plane. The hit-plane multiplicity histograms are normalized to unit area.
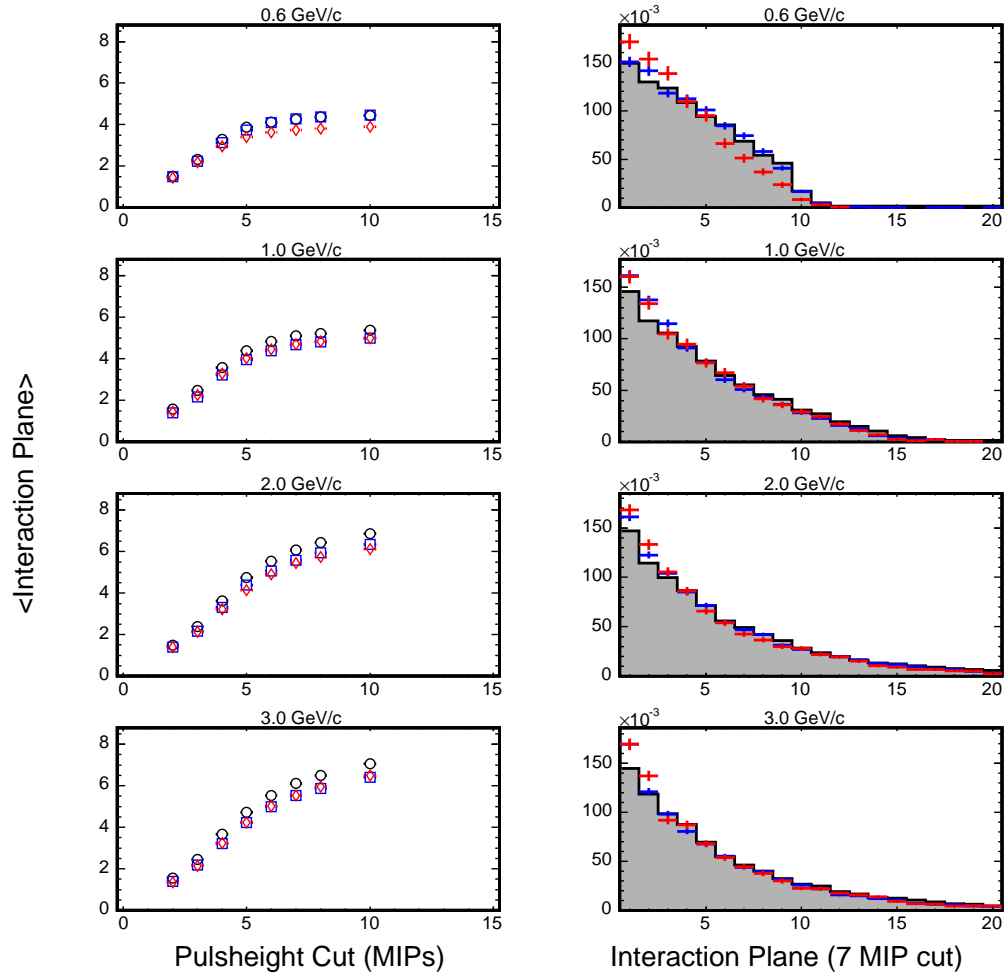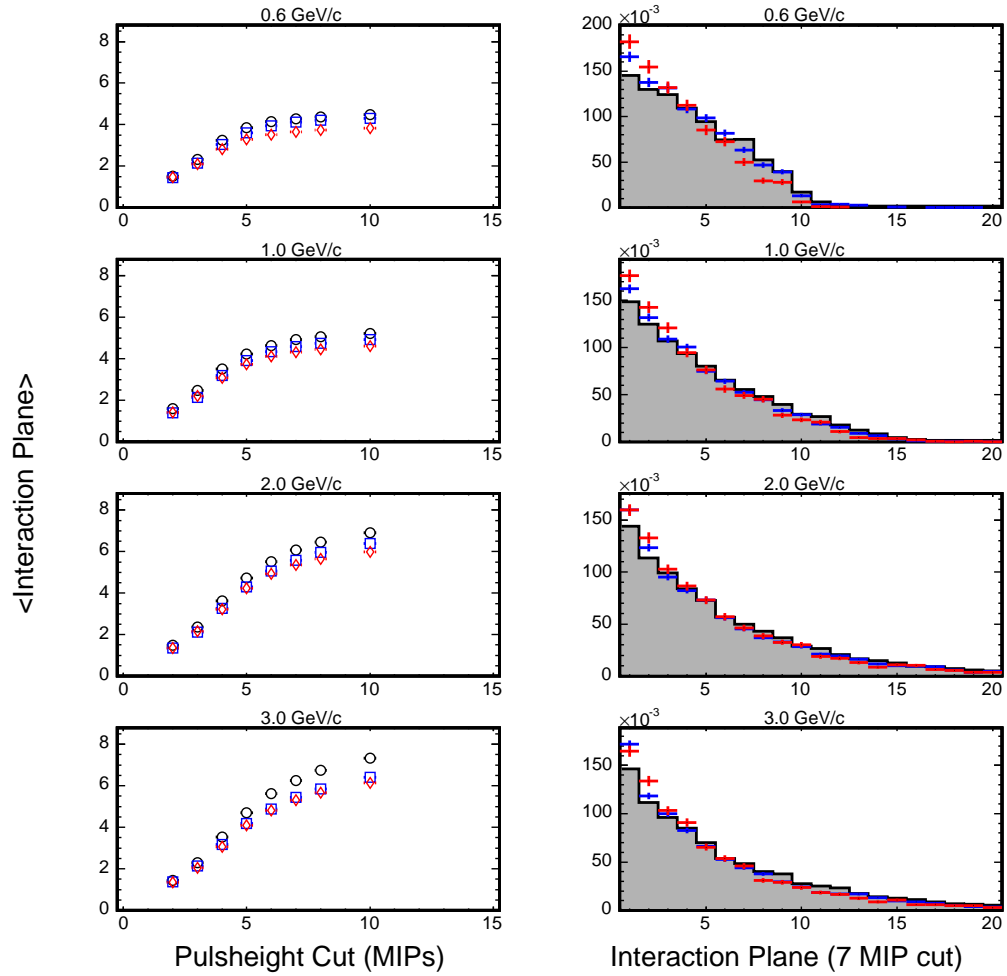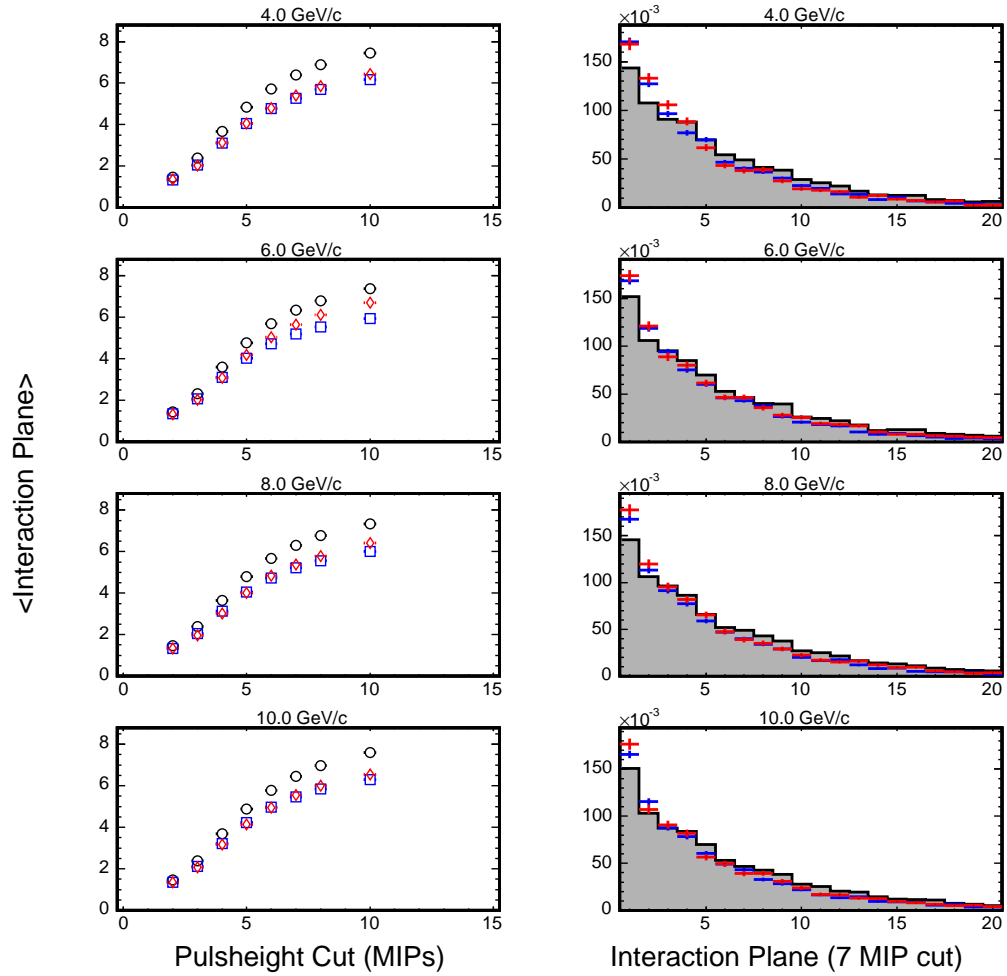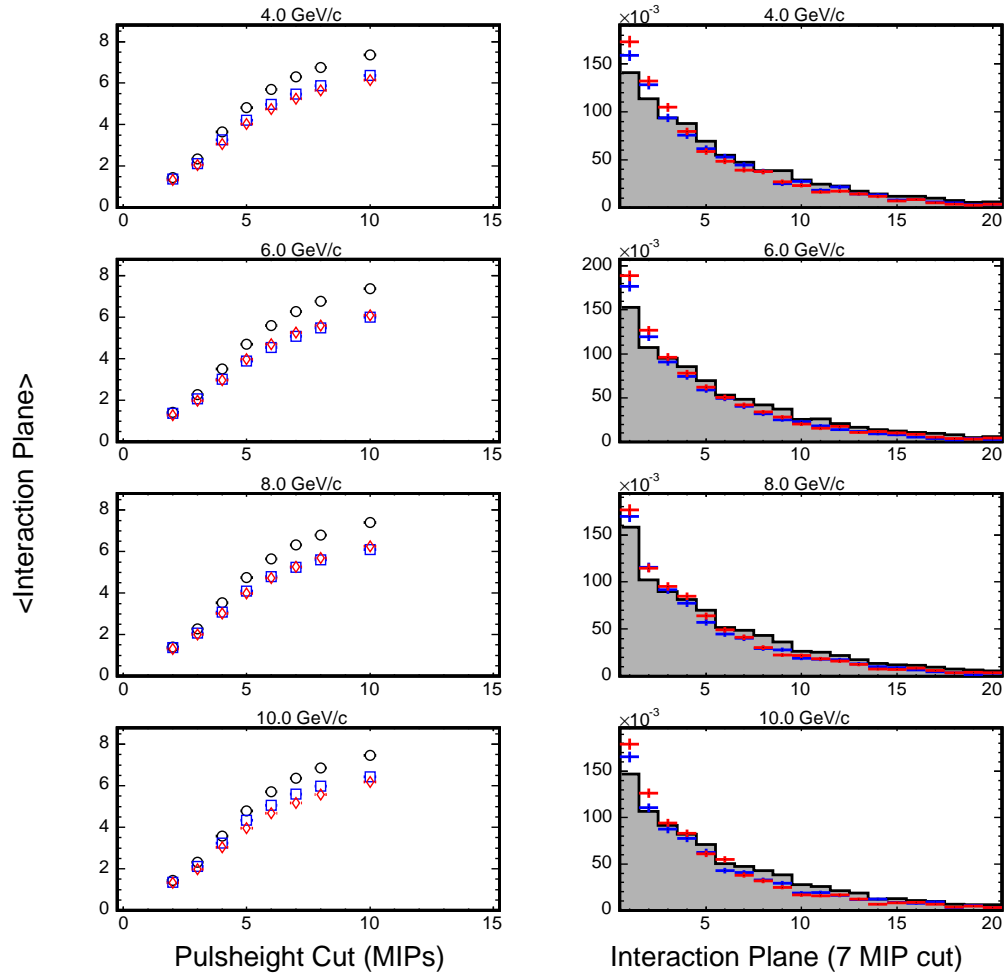
Figure 8.34: π^- hit-plane multiplicity and shower profile. Data collected in T11 are shown shaded, pions simulated with GCALOR are shown in blue and those simulated with SLAC-GHEISHA are shown in red. In the shower profile figures, the abscissa corresponds to the plane number and the ordinate corresponds to the average fraction of shower energy deposited per plane. The hit-plane multiplicity histograms are normalized to unit area.

Figure 8.35: π^+ hit-plane multiplicity and shower profile. Data collected in T7 are shown shaded, pions simulated with GCALOR are shown in blue and those simulated with SLAC-GHEISHA are shown in red. In the shower profile figures, the abscissa corresponds to the plane number and the ordinate corresponds to the average fraction of shower energy deposited per plane. The hit-plane multiplicity histograms are normalized to unit area.

Figure 8.36: π^- hit-plane multiplicity and shower profile. Data collected in T7 are shown shaded, pions simulated with GCALOR are shown in blue and those simulated with SLAC-GHEISHA are shown in red. In the shower profile figures, the abscissa corresponds to the plane number and the ordinate corresponds to the average fraction of shower energy deposited per plane. The hit-plane multiplicity histograms are normalized to unit area.

Figure 8.37: π^+ mean interaction plane versus the pulseheight cut to define the shower vertex (left) and the interaction plane distribution for a 7 MIP cut (right). The interaction plane distributions are normalized to unit area. Data collected in T11 are shown shaded, pions simulated with GCALOR are shown in blue and those simulated with SLAC-GHEISHA are shown in red.

Figure 8.38: π^- mean interaction plane versus the pulseheight cut to define the shower vertex (left) and the interaction plane distribution for a 7 MIP cut (right). The interaction plane distributions are normalized to unit area. Data collected in T11 are shown shaded, pions simulated with GCALOR are shown in blue and those simulated with SLAC-GHEISHA are shown in red.

283

Figure 8.39: π^+ mean interaction plane versus the pulseheight cut to define the shower vertex (left) and the interaction plane distribution for a 7 MIP cut (right). The interaction plane distributions are normalized to unit area. Data collected in T7 are shown shaded, pions simulated with GCALOR are shown in blue and those simulated with SLAC-GHEISHA are shown in red.

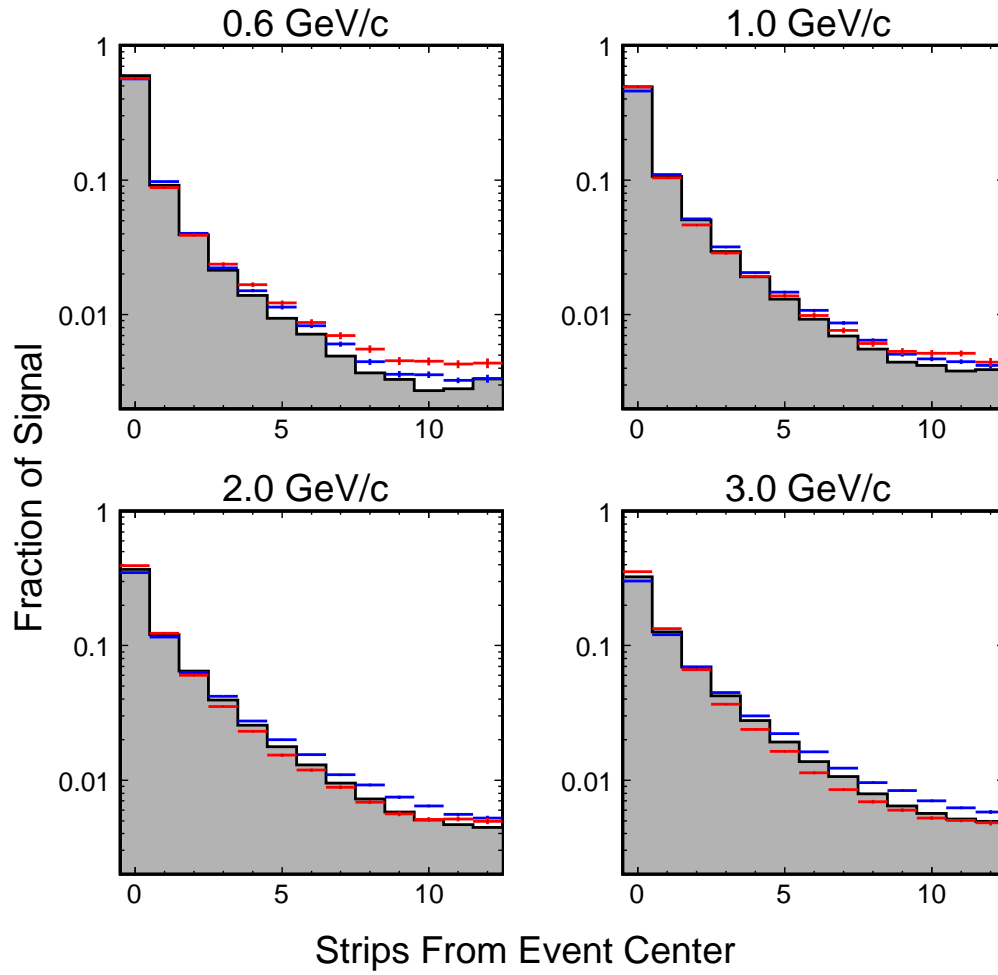Figure 8.40: π^- mean interaction plane versus the pulseheight cut to define the shower vertex (left) and the interaction plane distribution for a 7 MIP cut (right). The interaction plane distributions are normalized to unit area. Data collected in T7 are shown shaded, pions simulated with GCALOR are shown in blue and those simulated with SLAC-GHEISHA are shown in red.

285

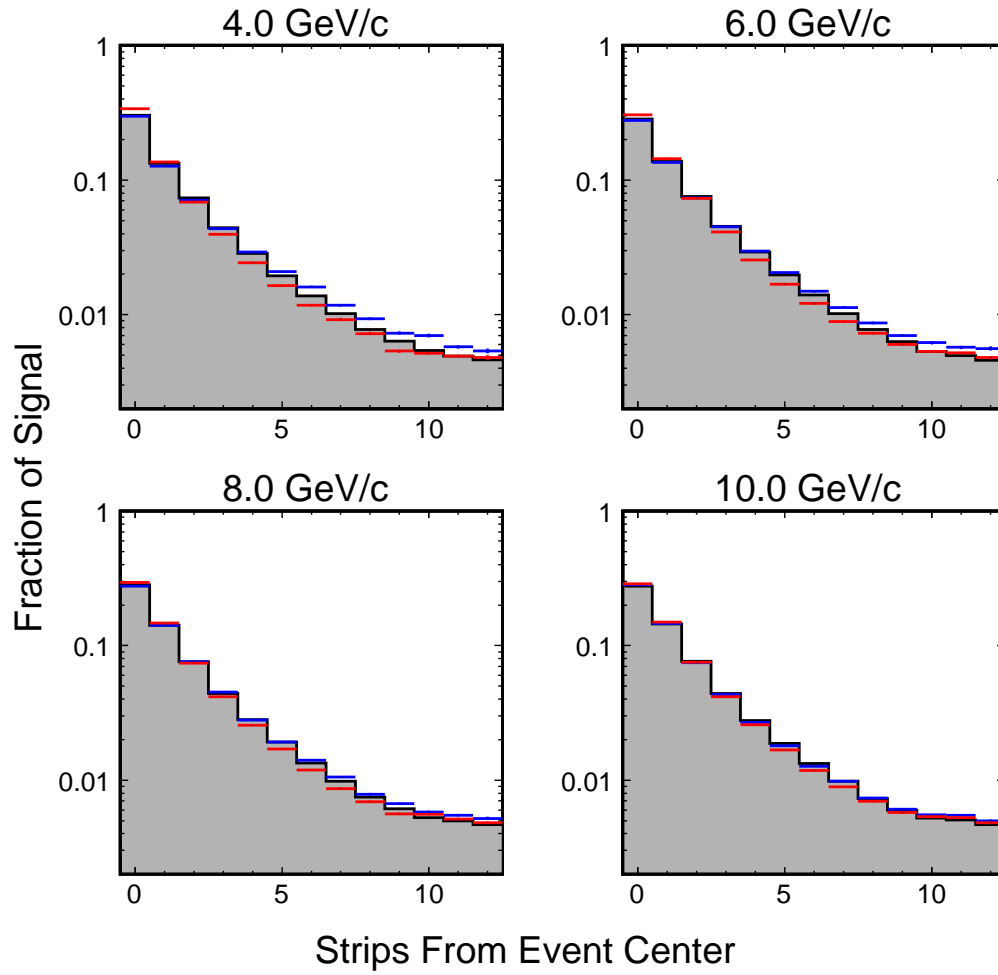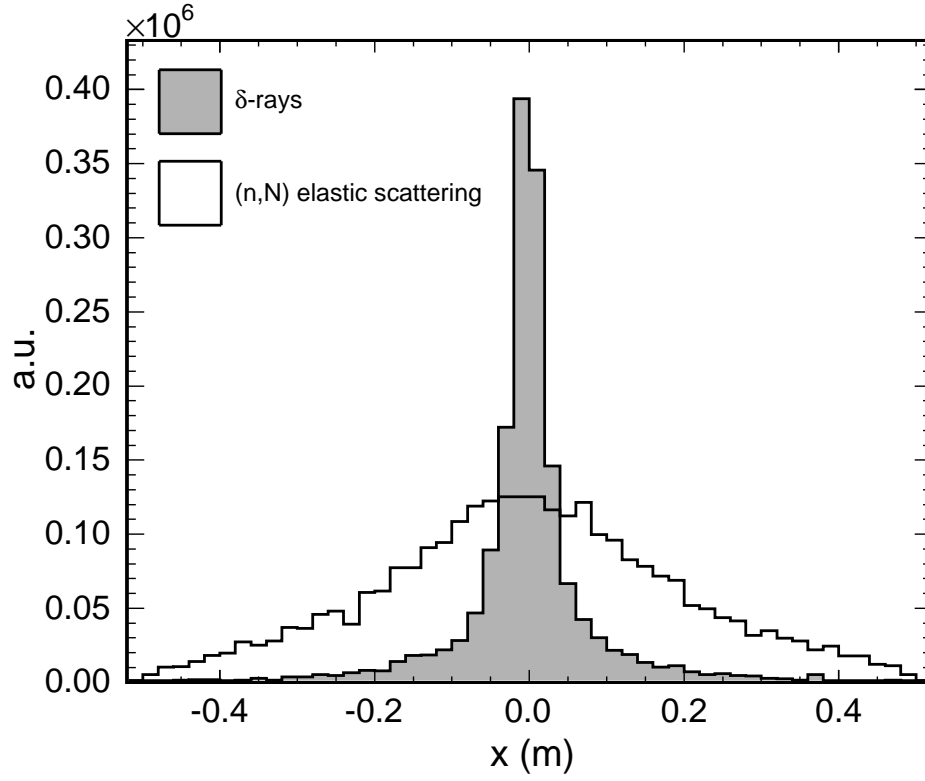ures 8.37-8.40 display the result of the study. The column on the left shows the average interaction plane as a function of the magnitude of the cut used to define the vertex. The column on the right shows an example of the interaction plane distribution for a 7 MIP cut. Both shower codes appear to underestimate the average interaction plane, an observation that is possibly connected to the early showering behavior noticed in Fig. 8.33-8.36. For the data, at momentum settings above 2 GeV/c, a 7-8 MIP cut yields an average interaction plane between 6.2-7.0, in agreement with the simple estimate of 6.7 planes taken from [2].

Figures 8.41-8.44 display the fractional energy deposition as a function of the distance, in MINOS strips, from the shower axis. The energy deposition was integrated over the entire depth of the calorimeter and the horizontal and vertical views were added in order to construct the figures. Signals less than 1.5 PEs were not included in order to limit the effect of cross talk from the shower core to the edges of the detector(see Fig. 8.11-8.14). Hadronic showers had a narrow core in which the majority of energy was deposited and broad non-Gaussian tails. Different mechanisms contribute to the shower core and shower tails [79]. Figure 8.45 shows the lateral distribution of δ-ray production and (n, N) elastic scattering interactions according to a GCALOR simulation. Relative to the δ-ray production, the tails of the distribution receive a larger contribution from (n, N) scattering than the shower core. In CalDet, more than 90% of the signal was contained within ± 5 strips of the shower axis (see Fig. 8.46). At momentum settings below ~ 2.0 GeV/c both shower codes overestimated the width of the energy deposition profile. As the beam momentum increased into the 2-3 GeV/c region SLAC-GHEISHA appeared to model the tails somewhat better than GCALOR, and above the

286

Figure 8.41: π^+ fractional energy deposition per strip versus the transverse distance, in strips, from the shower axis. Data collected in T11 are shown shaded, pions simulated with GCALOR are shown in blue and those simulated with SLAC-GHEISHA are shown in red.

Figure 8.42: π^- fractional energy deposition per strip versus the transverse distance, in strips, from the shower axis. Data collected in T11 are shown shaded, pions simulated with GCALOR are shown in blue and those simulated with SLAC-GHEISHA are shown in red.
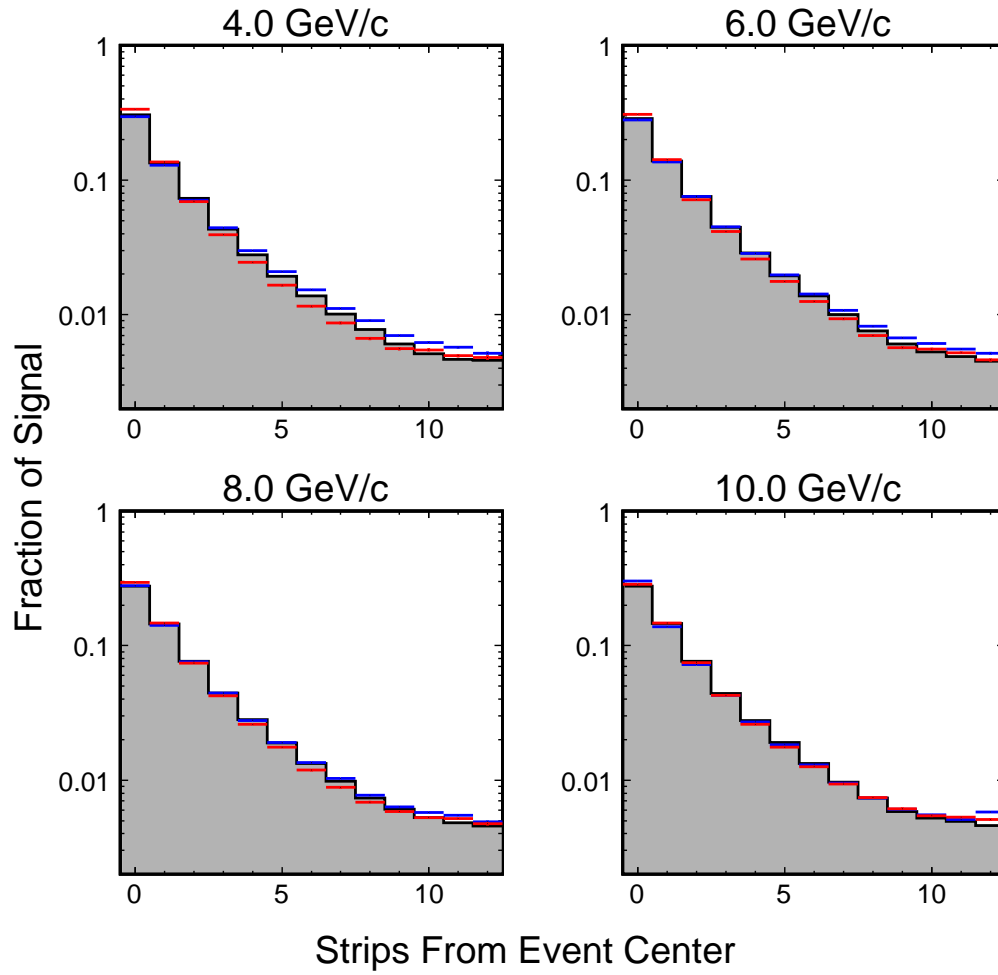
Figure 8.43: π^+ fractional energy deposition per strip versus the transverse distance, in strips, from the shower axis. Data collected in T7 are shown shaded, pions simulated with GCALOR are shown in blue and those simulated with SLAC-GHEISHA are shown in red.

Figure 8.44: π^- fractional energy deposition per strip versus the transverse distance, in strips, from the shower axis. Data collected in T7 are shown shaded, pions simulated with GCALOR are shown in blue and those simulated with SLAC-GHEISHA are shown in red.

Figure 8.45: The lateral distribution of δ-ray production and (n, N) elastic scattering processes integrated over the entire depth of CalDet. The figure was constructed from a simulation of $1\,\mathrm{GeV/c}$ π^+ using the GCALOR code and only interactions producing a particle with a kinetic energy larger than $10\,\mathrm{keV}$ were recorded. Most δ-rays are produced within $\sim 10\,\mathrm{cm}$ of the shower core, but (n, N) interactions are distributed much more broadly. The scale along the ordinate is arbitrary.

few-GeV region both simulations converged and were in good agreement with the data.

Figures 8.48-8.51 compare measured $\pi^{\pm}$ signal distributions with the result of GCALOR and SLAC-GHEISHA simulations. A major goal of the CalDet program was to determine the relationship between the measured signal and the original hadron energy so that the energy of hadronic showers observed in the Near and Far detectors may be determined. Consequently, there was a significant interest in quantifying the ability of the Monte Carlo to reproduce the observed signal distributions. While it may be possible to scale the Monte Carlo signal from hadrons in the case of a discrepancy, the best case is obviously the one in which the simulation agrees with the data without particle specific scale factors.

The signals from all channels in the calorimeter - with the exception of those reading out plane zero - were summed in and are shown in units of photoelectrons (left column) and MIPS (right column) in Fig. 8.48-8.51. The scintillator plane zero was the first CalDet element encountered by beam particles, and was therefore vulnerable to relatively soft particles created in upstream interactions, such as δ-rays and $e^{\pm}$ pairs from photon conversion. Because neutrino interactions will, on average, begin at the center of a steel plane the inclusion of plane zero in the sum was not considered advisable or necessary as it would have simply added a more-or-less constant offset of $\sim$ 2 MIPs to the summed signal. Additionally, the plane was difficult to calibrate properly.

The signal distributions have a characteristic asymmetric shape with a long high-side tail that is especially prominent at low energies. Such shapes
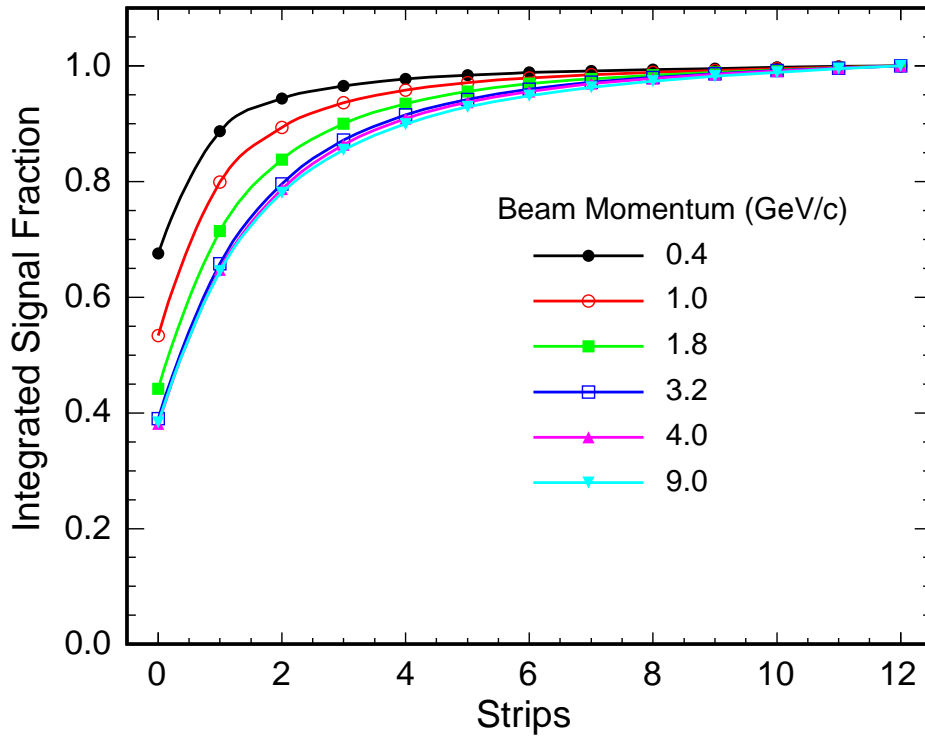
Figure 8.46: The integrated signal fraction versus the transverse distance from the shower axis for π^- observed in CalDet. The shower width gradually increased with the beam momentum, but even at $9\,\mathrm{GeV/c}$ more than 90% of the signal was contained within ± 5 strips. The result for π^+ is nearly identical.
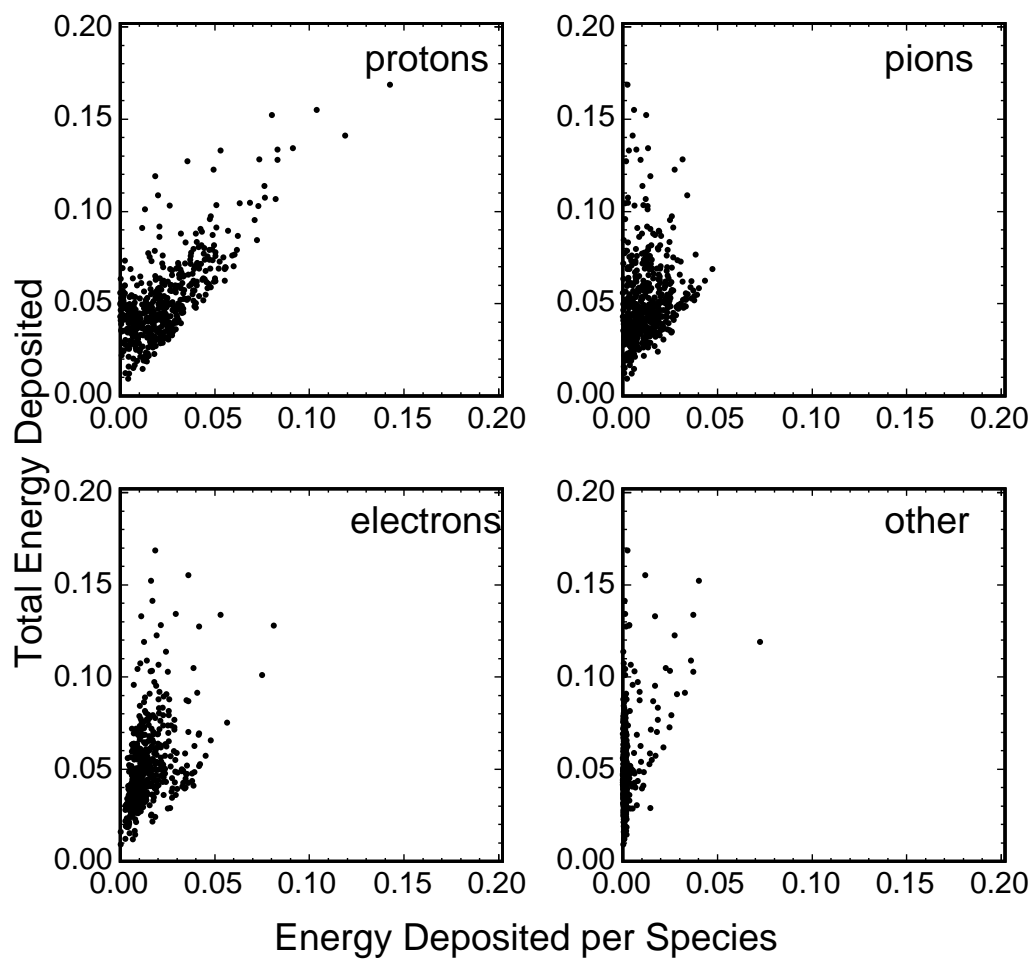
Figure 8.47: The correlation between the total energy deposited in the scintillator strips and the energy deposited by pions, protons, electrons and other particles (μ, α, etc). The figure is the result of a GCALOR simulation of $1\,\mathrm{GeV/c}$ π^+ showers in CalDet.

are traditionally observed in non-compensating[10] calorimeters and are generally attributed to fluctuations in the electromagnetic component of the showers [79]. While this is certainly true for the MINOS calorimeters, particularly above the few-GeV/c region, the tail at low energies appears to be caused predominantly by protons. Figure 8.47 shows the GCALOR prediction of the correlation between the total energy deposited in the scintillator strips and the energy deposited by pions, protons and electrons in $1\,\mathrm{GeV/c}$ π^+ showers. Events in the tail of the signal distribution clearly occur when much of the energy is deposited by protons.

Both shower codes reproduced the shape of the signal distributions including the high-side tail. The GCALOR simulation was superior to SLAC-GHEISHA, which systematically underpredicted the the mean of the signal distributions and more substantially overpredicted the widths. The behavior of SLAC-GHEISHA in this regard was similar to what was observed in the hit-strip multiplicity comparison. Below $6\,\mathrm{GeV/c}$ GCALOR was found to correctly predict the mean of the π^+ distributions (in MIPs) at the level of $\sim 2-3\%$, but with a slightly greater width. The π^- distributions, which have a mean that was $\sim 5\%$ smaller than the positives, were not modeled quite as well. The π^+/π^- response discrepancy was momentum dependent and will be discussed in greater detail in Ch. 9.

Above $6\,\mathrm{GeV/c}$ both simulations diverged from the data, with GCALOR overpredicting the response and SLAC-GHEISHA underpredicting it. The performance of GCALOR was reminiscent of GFLUKA, which also predicted too much signal, and could have a common cause since GCALOR's high energy

---

[10]That is, calorimeters in which the response to the hadronic component of showers (h) differs from the response to the electromagnetic component (e). The MINOS calorimeters are non-compensating.

Figure 8.48: π^+ summed signal in photoelectrons (left) and MIPs (right). Data collected in T11 are shown shaded, pions simulated with GCALOR are shown in blue and those simulated with SLAC-GHEISHA are shown in red. The histograms are normalized to unit area.
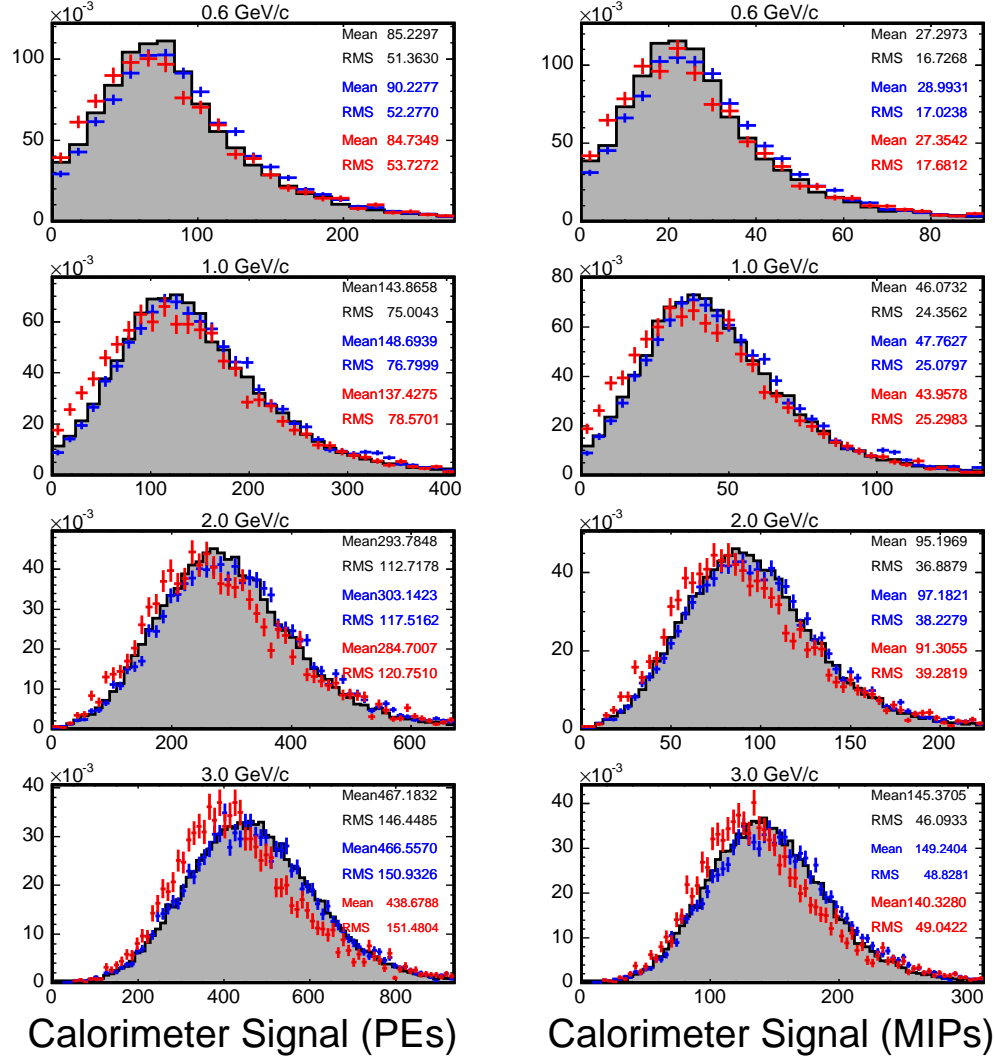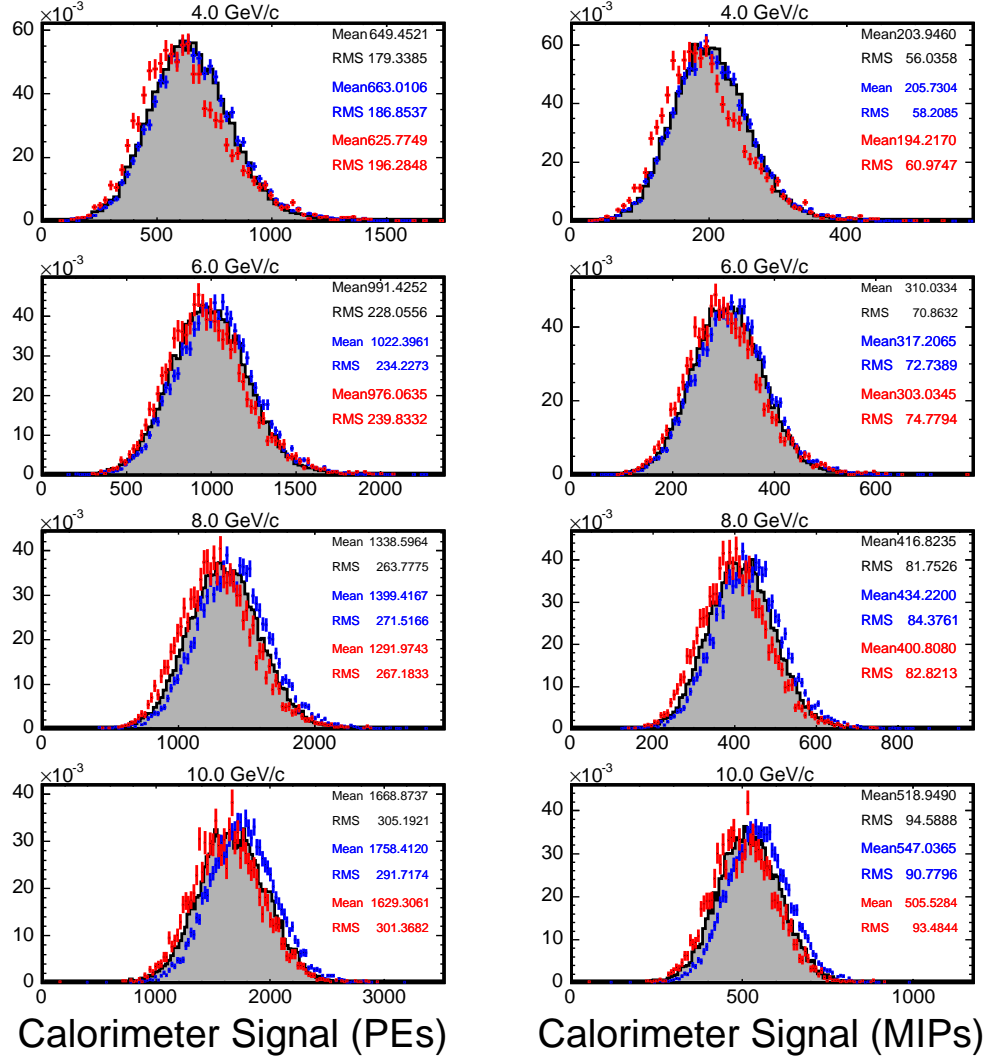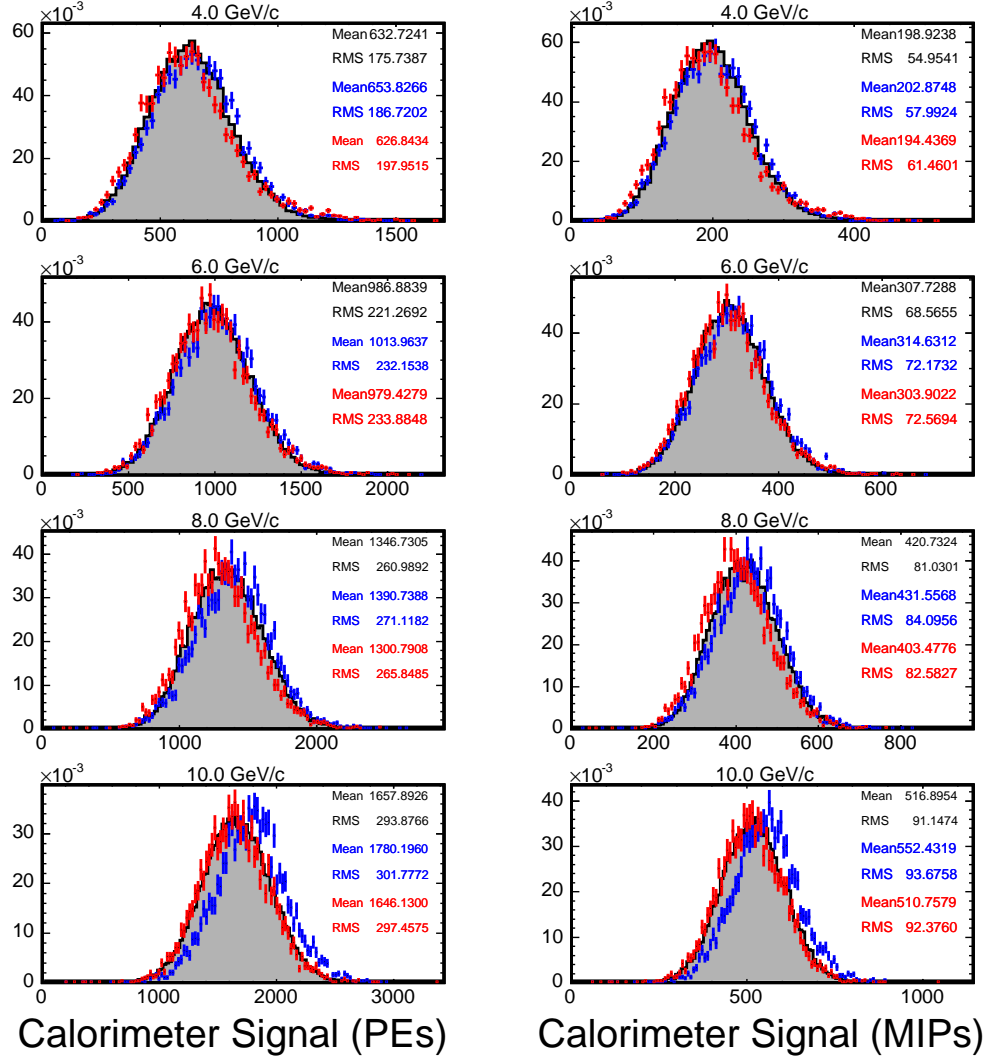
296

Figure 8.49: π^- summed signal in photoelectrons (left) and MIPs (right). Data collected in T11 are shown shaded, pions simulated with GCALOR are shown in blue and those simulated with SLAC-GHEISHA are shown in red. The histograms are normalized to unit area.

297

Figure 8.50: π^+ summed signal in photoelectrons (left) and MIPs (right). Data collected in T7 are shown shaded, pions simulated with GCALOR are shown in blue and those simulated with SLAC-GHEISHA are shown in red. The histograms are normalized to unit area.

Figure 8.51: π^- summed signal in photoelectrons (left) and MIPs (right). Data collected in T7 are shown shaded, pions simulated with GCALOR are shown in blue and those simulated with SLAC-GHEISHA are shown in red. The histograms are normalized to unit area.

interaction model called GFLUKA to simulate interactions for pion energies above 2.5 GeV. The frequency of calls to GFLUKA gradually increased with the primary particle energy, perhaps explaining the divergence at the higher momentum settings. It should be possible, in the future, to modify GCALOR to remove calls to GFLUKA or to call GHEISHA instead. Such a strategy may improve the agreement at high energy.

8.4.2   Comparison of Protons

The results of a comparison between the proton data and the simulations are shown Fig. 8.52-8.61. For momentum settings above 1 GeV the general features and level of agreement between the data and the simulations was similar to the pion comparisons. That is, SLAC-GHEISHA was observed to underestimate the activity in the detector, both codes appeared to shower early, the hit-plane multiplicity agreed reasonably well, and the calorimeter signal was modeled more correctly by GCALOR though there was some divergence at the highest momentum settings.

The results at and below 1 GeV/c require some comments. As discussed on p. 222, when the beam momentum dropped to 1 GeV/c and below it became ever more likely that protons would lose all of their energy via ionization and range out prior to interacting hadronically. The topological quantities and the signal measured in each event were then directly dependent on the proton's range, and through that on the proton's initial momentum and it's energy loss per unit length. The detector's response became quantized since protons which, for example, range out 1/4 of the way through a steel plane do not look significantly different than those which range out 3/4 of the way through

the plane. On the other hand, protons which barely make it through a steel plane emerge with a very low momentum, are heavily ionizing and leave a large signal in the following scintillator plane. This is the scenario that occurred at the 600 MeV/c and possibly 1 GeV/c momentum settings in Fig. 8.52-8.61.

At the 600 MeV/c setting nearly all of the simulated protons ranged out in the first steel plane (plane zero) and very little signal was measured. Those simulated protons originally had 175 MeV of kinetic energy but, according to the beamline simulation (see Fig. 7.13), typically lost 34 MeV in upstream material, leaving them with an average kinetic energy of 141 MeV. Such protons have a range of 2.6 cm in CalDet steel [80] and would emerge from the steel with only a few MeV of kinetic energy. It is not clear that the detector was sensitive to such low energy protons. The calculation for the 1 GeV/c setting is less transparent since not all protons range out, but it seems likely that a similar thresholding effect occurred. The discrepancy in the low energy response is possibly caused by excessive energy loss in upstream material or an overestimation of the material in the beamline. Low energy protons would be much more sensitive to such an effect than pions or muons since the latter are nearly minimum ionizing while the former occupy the steeply rising portion of the dE/dx curve below minimum ionization. The proton range and response are discussed in greater detail in Chapter 9.

MINOS will not be able to make useful measurements on protons with a momentum around 600 MeV/c, other than to perhaps surmise that a proton was present by observing a single, possibly very large, hit close to the vertex. Protons in the 1-2 GeV/c range are certainly measurable but additional effort will be necessary to improve the simulation of such protons.

301
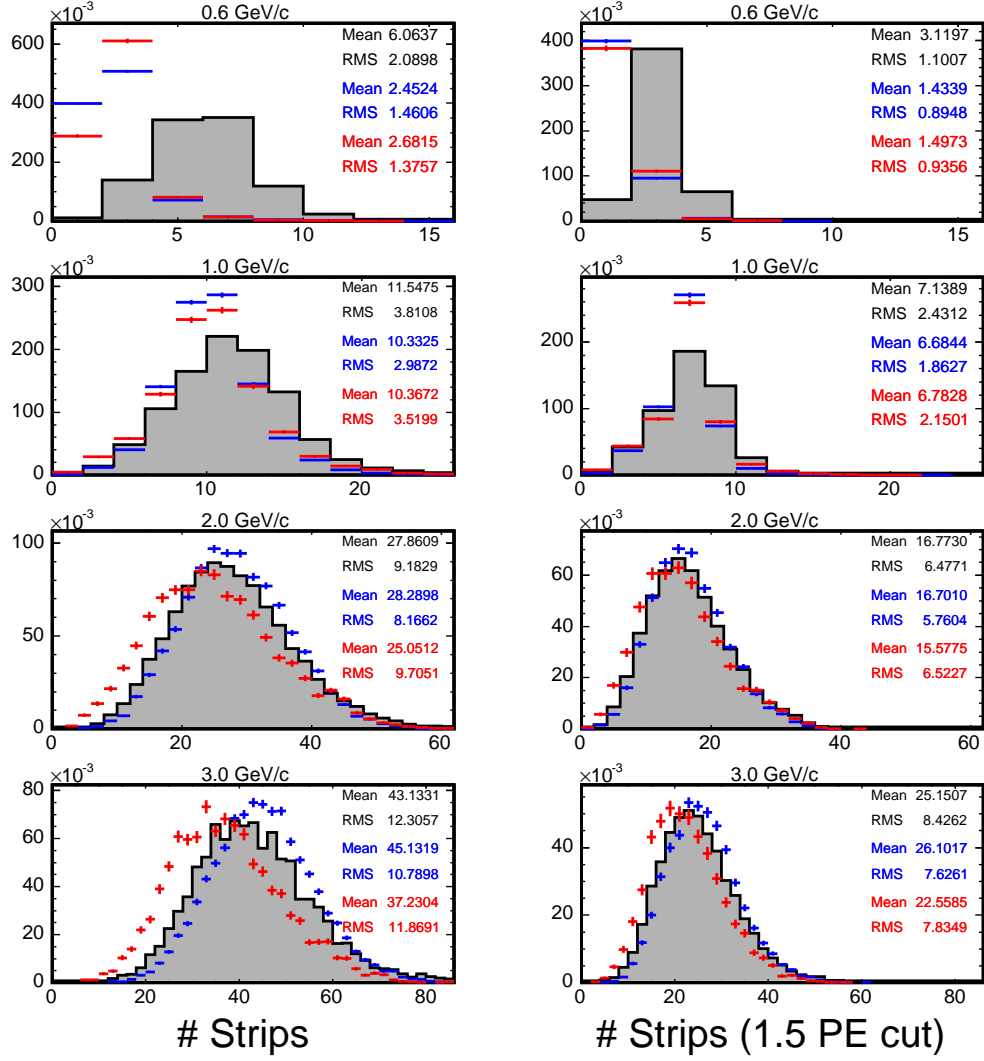
Figure 8.52: Proton hit-strip multiplicity, with and without a 1.5 PE cut. Data collected in T7 are shown shaded, protons simulated with GCALOR are shown in blue and those simulated with SLAC-GHEISHA are shown in red. The histograms are normalized to unit area.
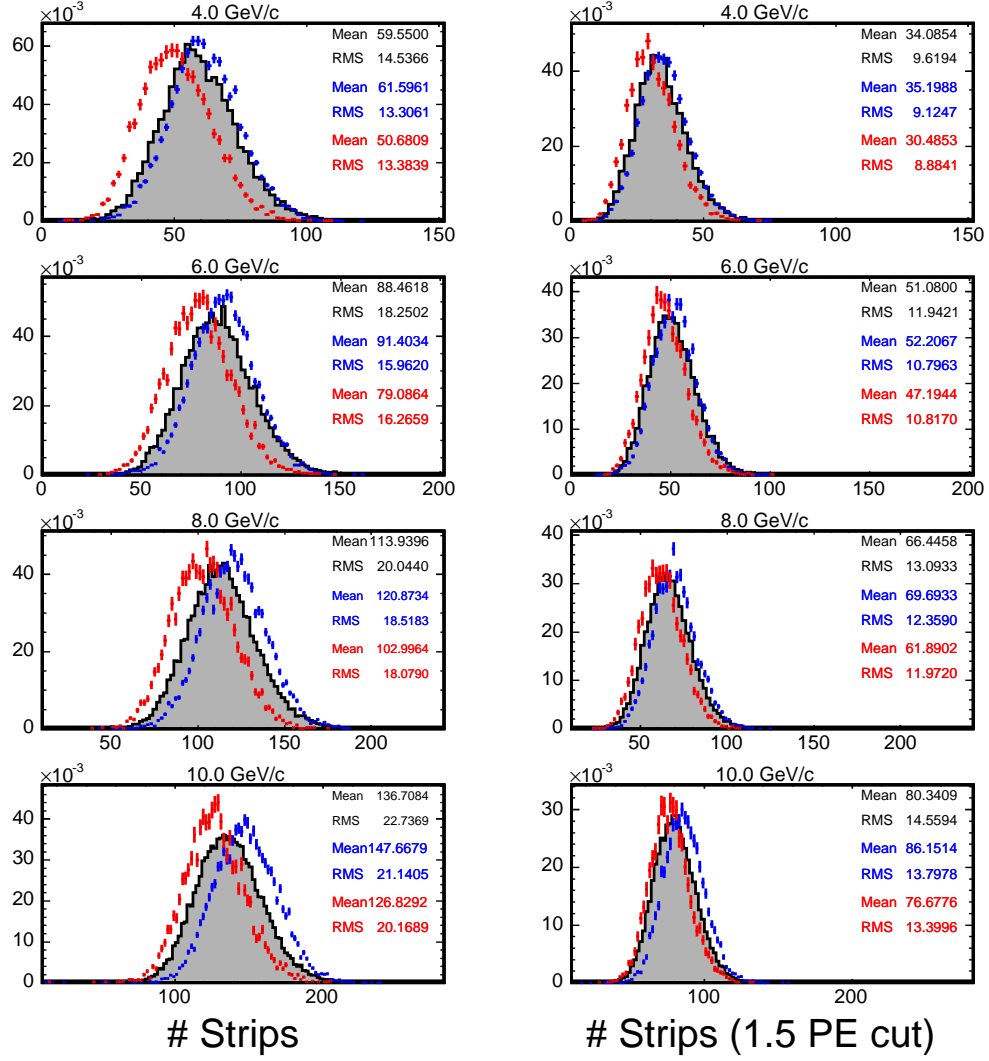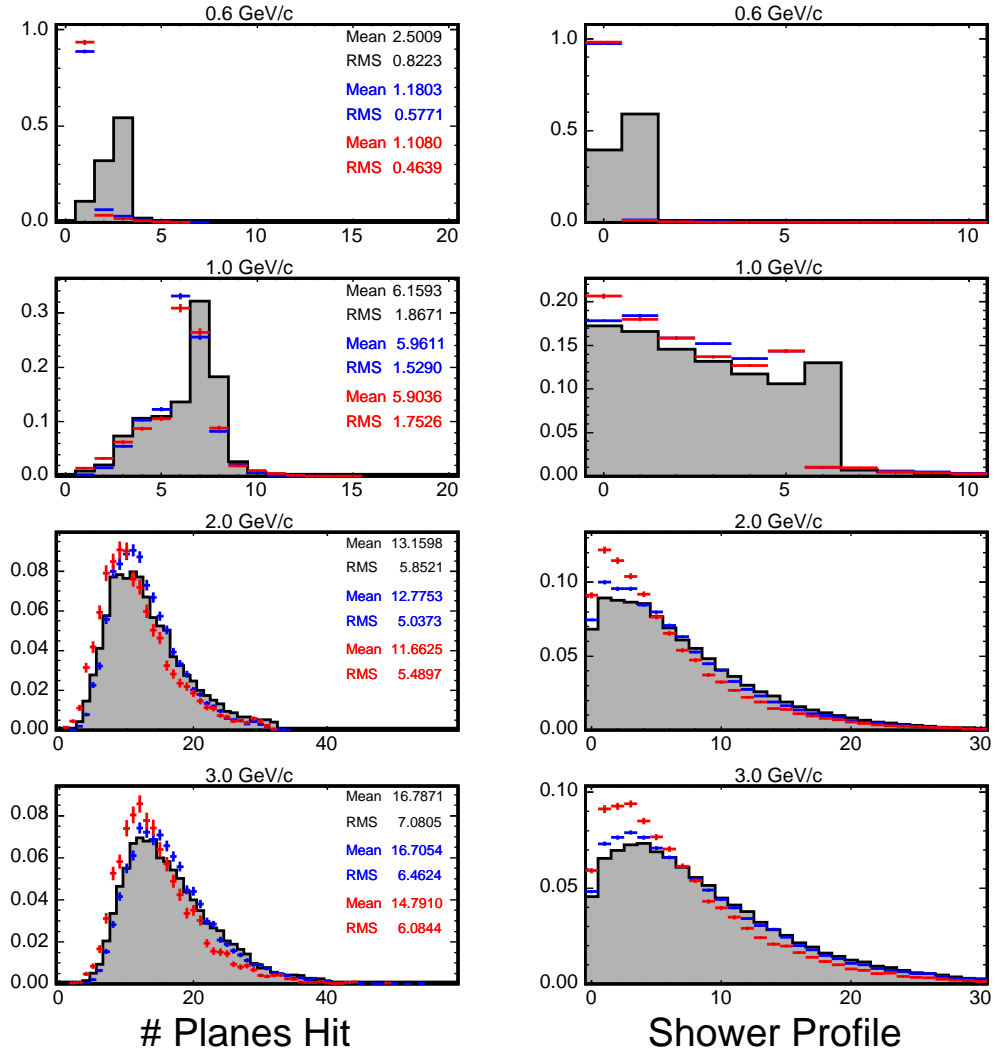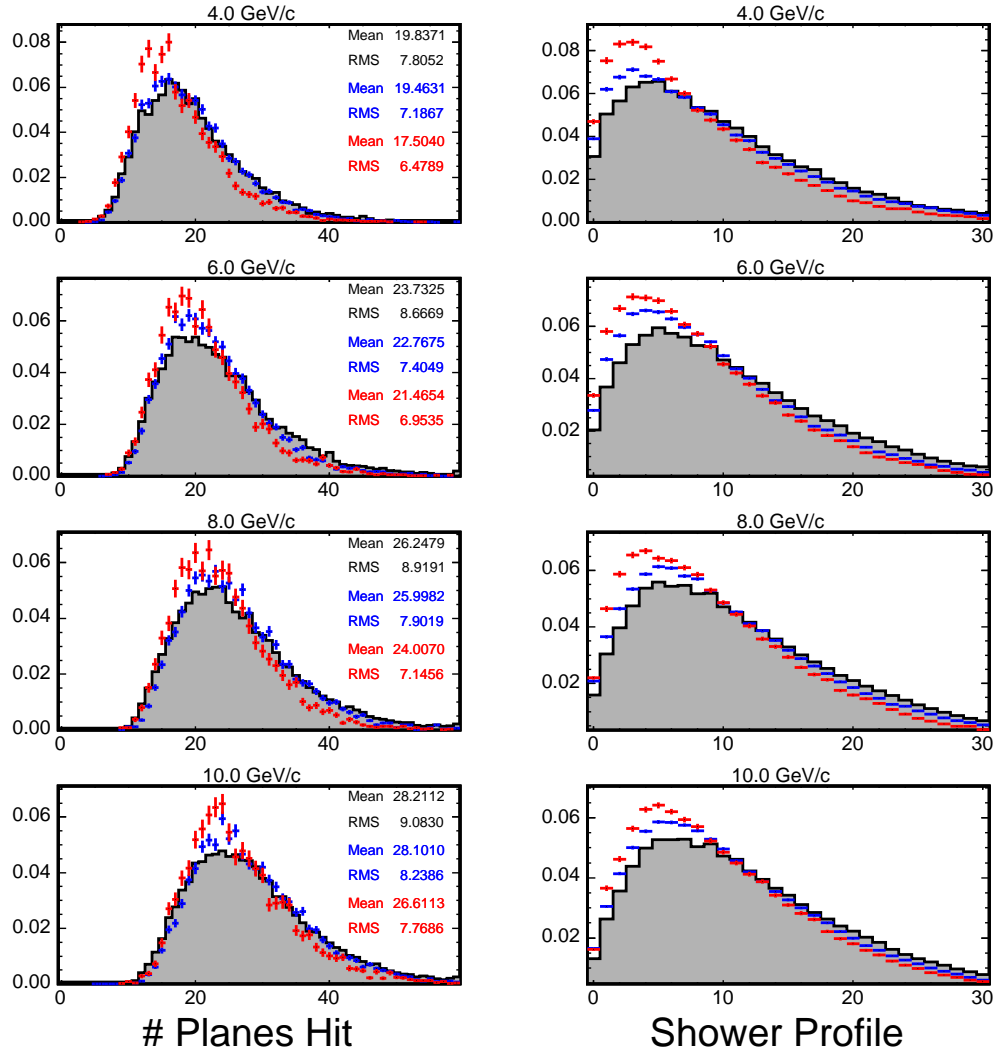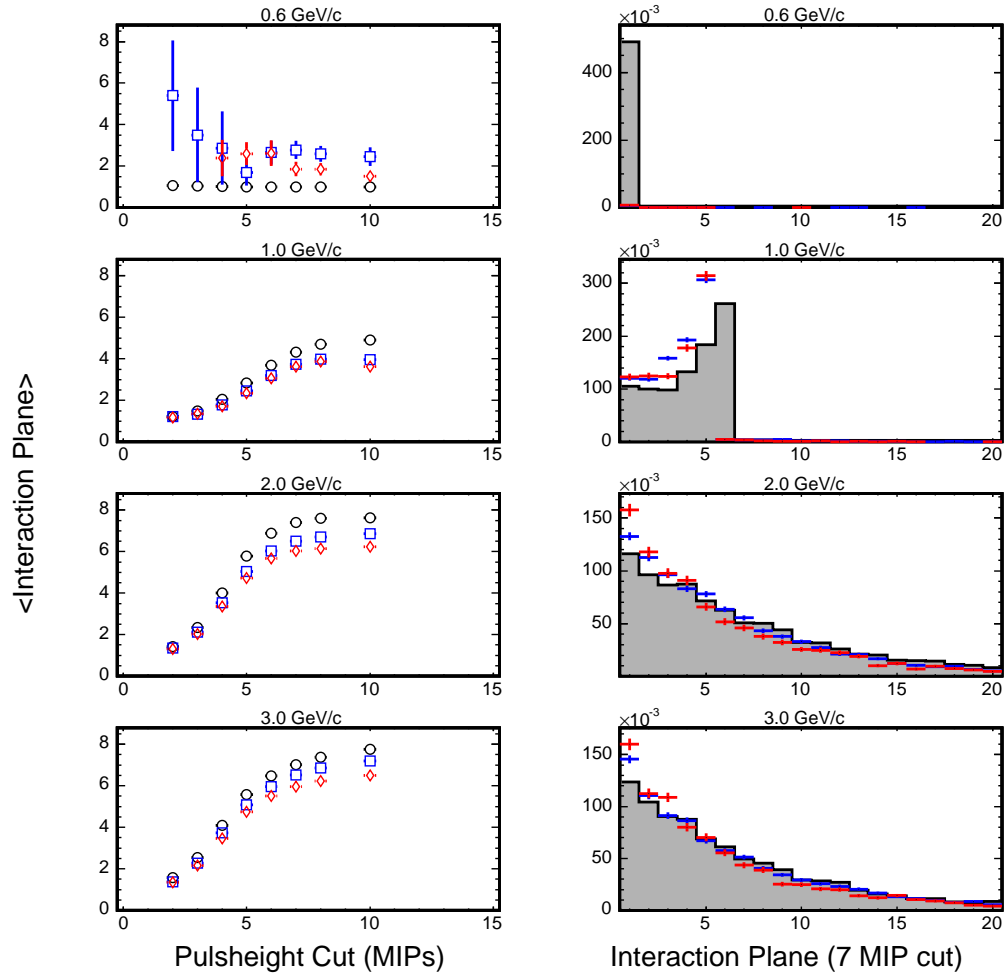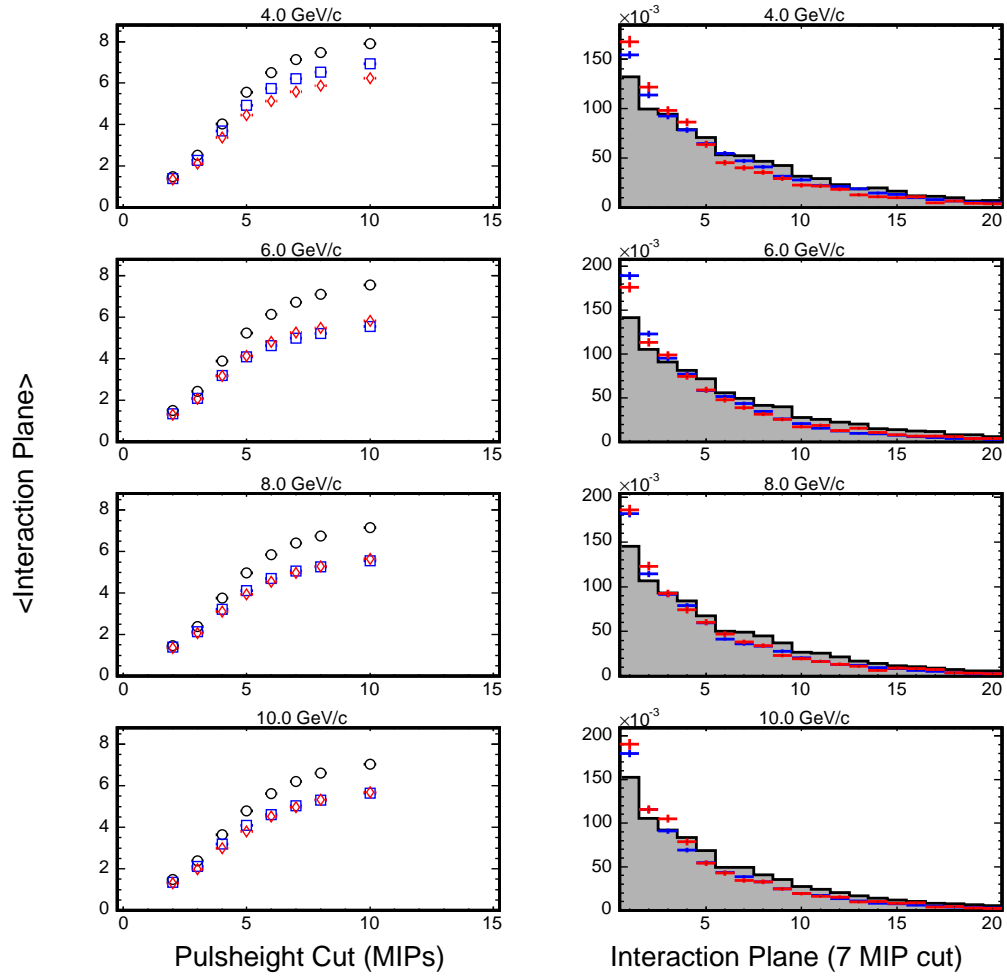
Figure 8.53: Proton hit-strip multiplicity, with and without a 1.5 PE cut. Data collected in T7 are shown shaded, protons simulated with GCALOR are shown in blue and those simulated with SLAC-GHEISHA are shown in red. The histograms are normalized to unit area.

Figure 8.54: Proton hit-plane multiplicity and shower profile. Data collected in T7 are shown shaded, protons simulated with GCALOR are shown in blue and those simulated with SLAC-GHEISHA are shown in red. The histograms are normalized to unit area.
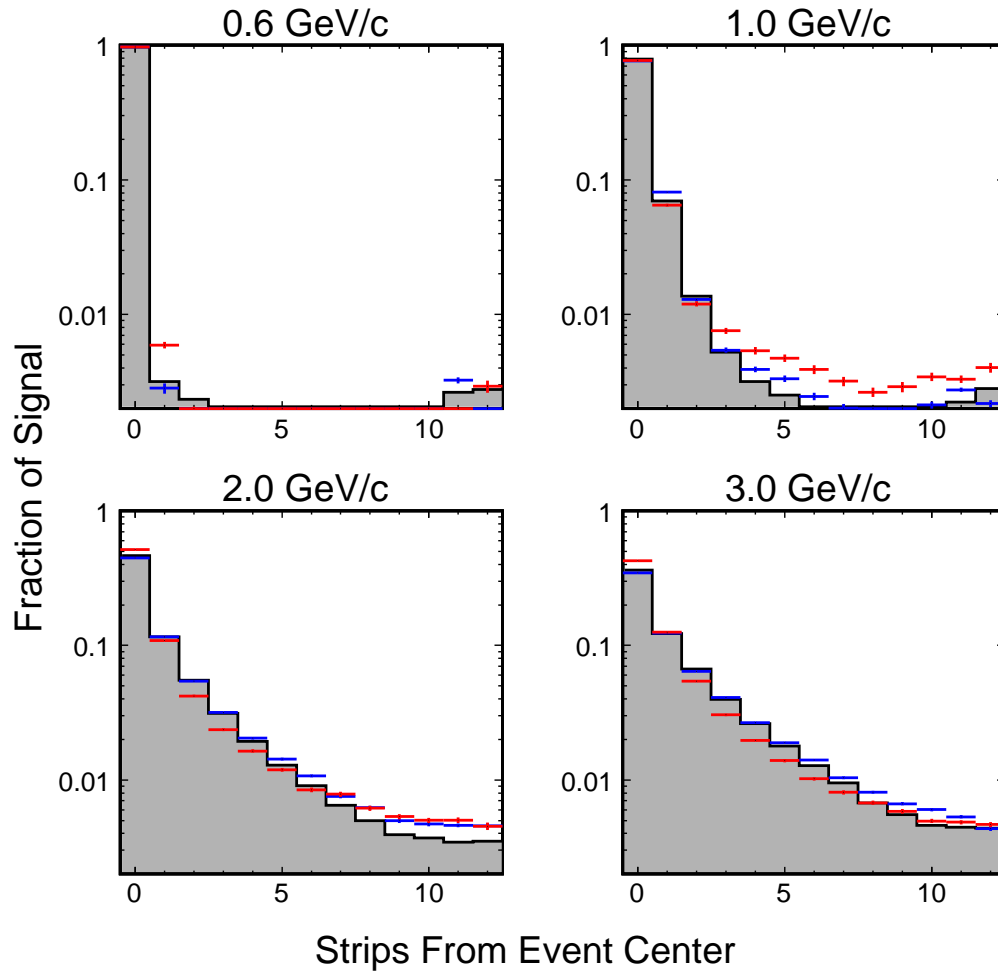
Figure 8.55: Proton hit-plane multiplicity and shower profile. Data collected in T7 are shown shaded, protons simulated with GCALOR are shown in blue and those simulated with SLAC-GHEISHA are shown in red. The histograms are normalized to unit area.

Figure 8.56: Proton mean interaction plane versus the pulseheight cut to define the shower vertex (left) and the interaction plane distribution for a 7 MIP cut (right). The interaction plane distributions are normalized to unit area. Data collected in T11 are shown shaded, protons simulated with GCALOR are shown in blue and those simulated with SLAC-GHEISHA are shown in red.

Figure 8.57: Proton mean interaction plane versus the pulseheight cut to define the shower vertex (left) and the interaction plane distribution for a 7 MIP cut (right). The interaction plane distributions are normalized to unit area. Data collected in T7 are shown shaded, protons simulated with GCALOR are shown in blue and those simulated with SLAC-GHEISHA are shown in red.

Figure 8.58: Proton fractional energy deposition per strip versus the transverse distance, in strips, from the shower axis. Data collected in T11 are shown shaded, pions simulated with GCALOR are shown in blue and those simulated with SLAC-GHEISHA are shown in red. The histograms are normalized to unit area.
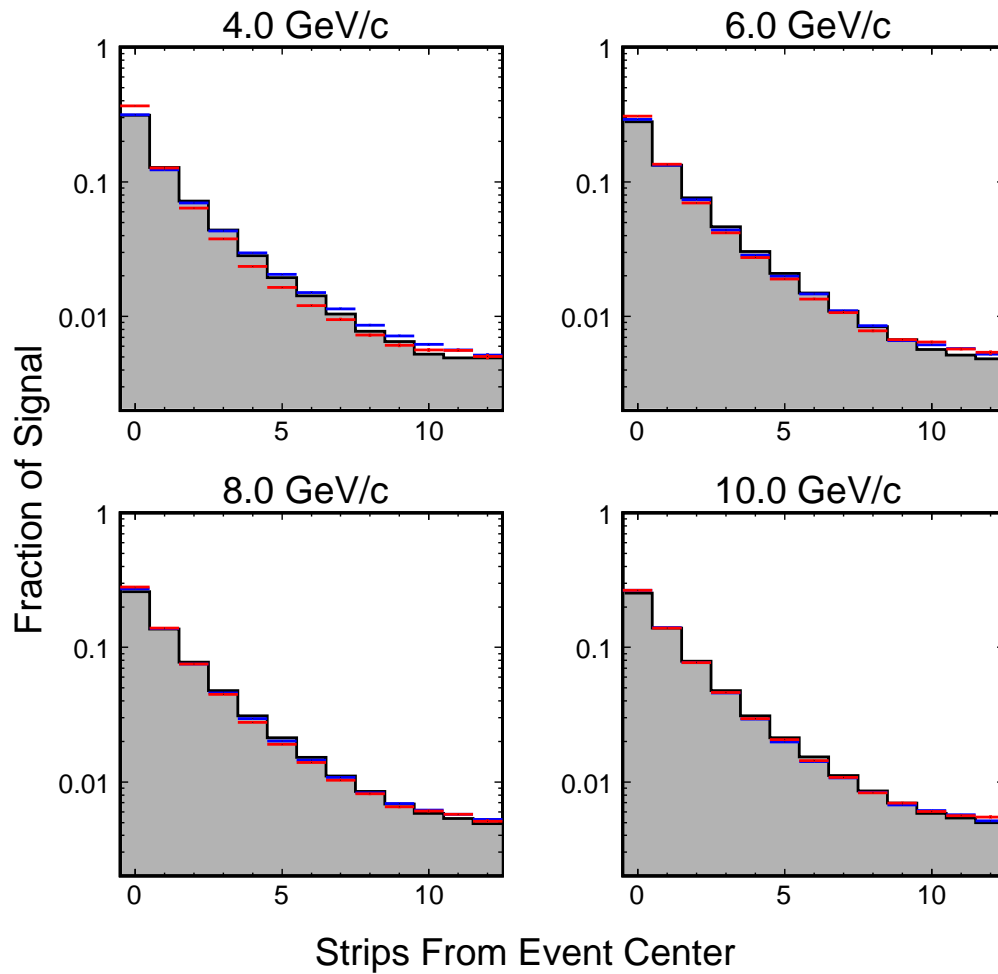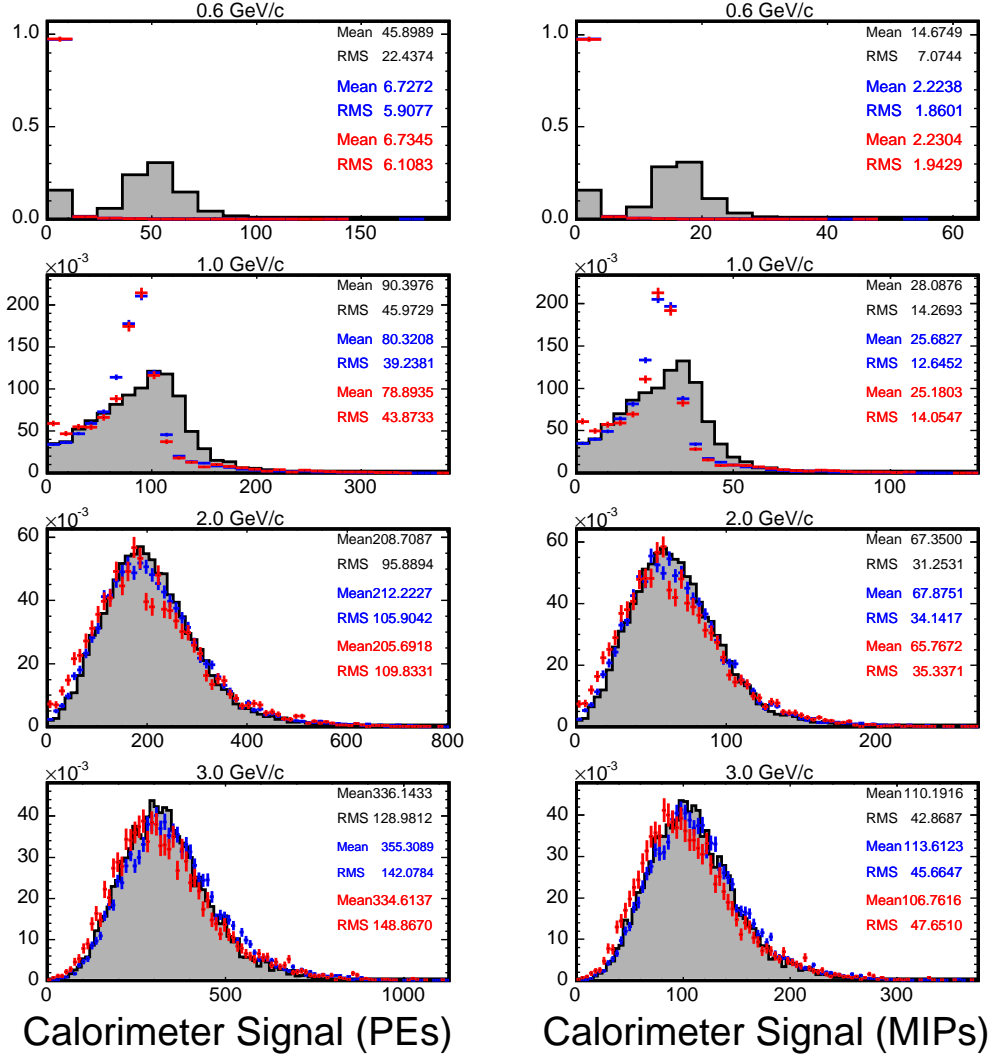
Figure 8.59: Proton fractional energy deposition per strip versus the transverse distance, in strips, from the shower axis. Data collected in T7 are shown shaded, pions simulated with GCALOR are shown in blue and those simulated with SLAC-GHEISHA are shown in red. The histograms are normalized to unit area.

Figure 8.60: Proton summed signal in photoelectrons (left) and MIPs (right). Data collected in T7 are shown shaded, pions simulated with GCALOR are shown in blue and those simulated with SLAC-GHEISHA are shown in red. The histograms are normalized to unit area.
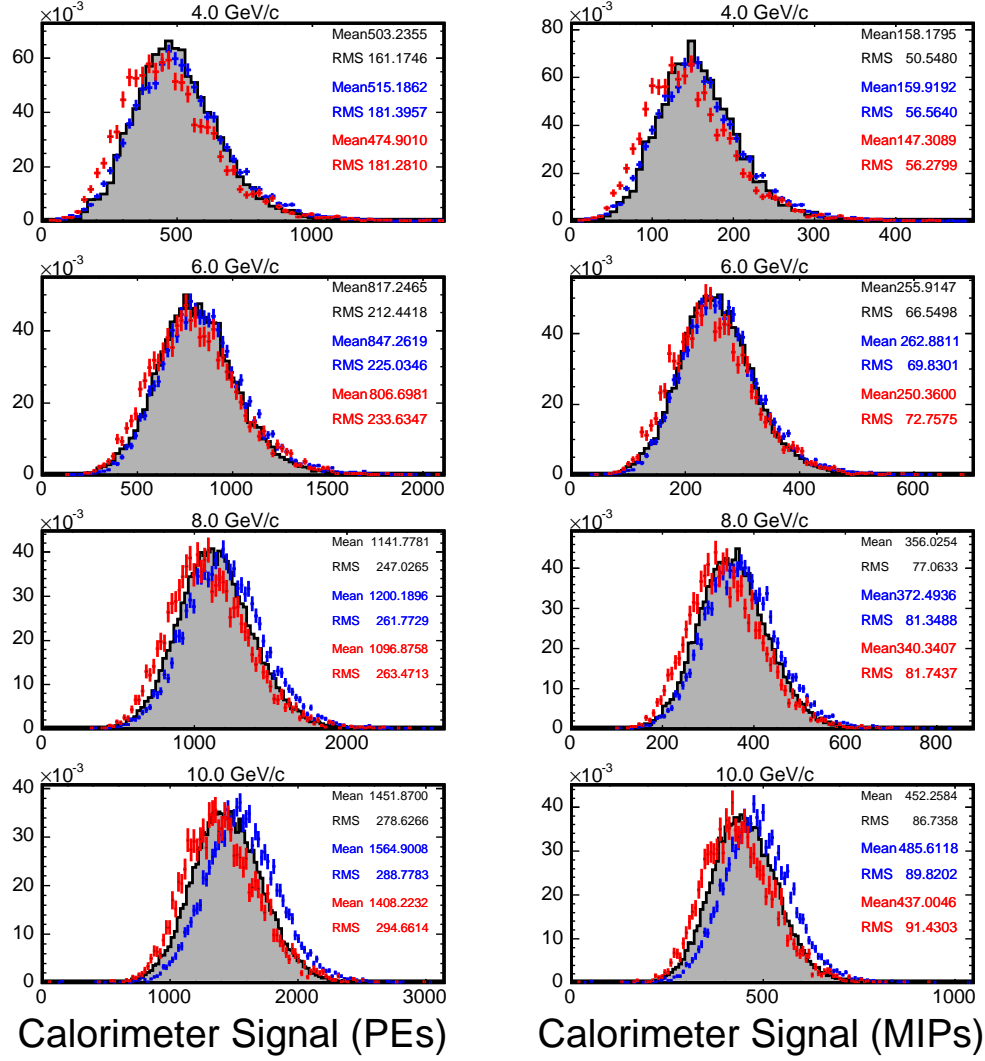
Figure 8.61: Proton summed signal in photoelectrons (left) and MIPs (right). Data collected in T7 are shown shaded, pions simulated with GCALOR are shown in blue and those simulated with SLAC-GHEISHA are shown in red. The histograms are normalized to unit area.

8.4.3 Shower Profile Fits

Some effort was made to parameterize the average longitudinal hadronic shower shape. The results of the parameterization were used to compare the data with simulations and could also be used in fast simulations and as a way to "guide the eye" when scanning neutrino events. In an often used parameterization [81] the average shower shape is modeled as a combination of an electromagnetic component, developing on the scale of the radiation length X_0, and a hadronic component, developing on the scale of the interaction length λ_I:

$$f(x) = N \left[\omega s^{\alpha-1} e^{-\beta s} + (1 - w) t^{\alpha-1} e^{-\delta t} \right] \tag{8.14}$$

Here, $f(x)$ is the fraction of (visible) energy deposited per plane as function of depth in the calorimeter. The depth x in MINOS planes was used to calculate s, t in units of radiation length and interaction length (1.76 cm and 16.8 cm respectively for Fe) [2]. The first term in Eq. 8.14 describes the electromagnetic portion of the shower, and the second the hadronic. The free parameters $\omega, \alpha, \beta, \delta$ characterize the shower shape; Their values are expected to change with beam momentum. The parameter N is a normalization constant, which in this work is unitless. Equation. 8.14 was originally developed in the context of 10-500 GeV/c hadronic showers [81, 82], so it wasn't clear *a priori* if it would properly describe the relatively low energy test-beam data.

For both pion and proton data, fits were done to profiles of the average fractional signal per plane versus plane. The first bin, corresponding to scintillator plane 0, was ignored in the fitting procedure since it is not preceded by iron and is rarely part of a shower. The upper end of the fit range was set to the 98% truncation point. When fitting the data, in each bin a 2% uncertainty was added (in quadrature) to the statistical error in order to account

for uncertainties in the muon calibration constants (see Fig. 5.15-5.16). The overall normalization N was fixed by constraining $\int f(x)\mathrm{d}x = 1$ during the final stage of the minimization.

Some results of the fitting are shown in Fig. 8.62-8.65. Equation 8.14 provided an excellent description of the pion data from $10\,\mathrm{GeV/c}$ to $\sim 1\,\mathrm{GeV/c}$. The fits to negative pion shower profiles agreed, within parameter errors, with the fits to the positive profiles. Below $1\,\mathrm{GeV/c}$ the fits were relatively poor, though the shape of the curve did seem to crudely represent the data. The poor fits at low energy reflect the sparse activity of low energy hadronic showers. For example, in the sub-GeV range, π induced showers consist of approximately 0-2 secondary pions and 5-10 each of protons and neutrons [79]. The charged particles lose most of their energy via ionization within a few planes of the initial hadronic interaction and few tertiary pions are produced - a significant difference compared to shower development for few-GeV and above pions. Proton induced showers were also fit, with the results shown in Fig. 8.66-8.67. Above $\sim 2\,\mathrm{GeV/c}$ the data is well described by Eq. 8.14.

8.4.4 Muon Range

During the development of the π/μ discriminant analysis, simulated muons were discovered to have a range that was s5-6% shorter than the muons measured by CalDet. The discrepancy was particularly noticeable for the 1.8-2.0 GeV/c momentum settings, where muons (particularly on-momentum muons) were identified with high efficiency but still stopped in the detector. In reaction to the new information an evaluation of muon dE/dx in GEANT was conducted and, as discussed in Ch. 8.2.5, the treatment of the density
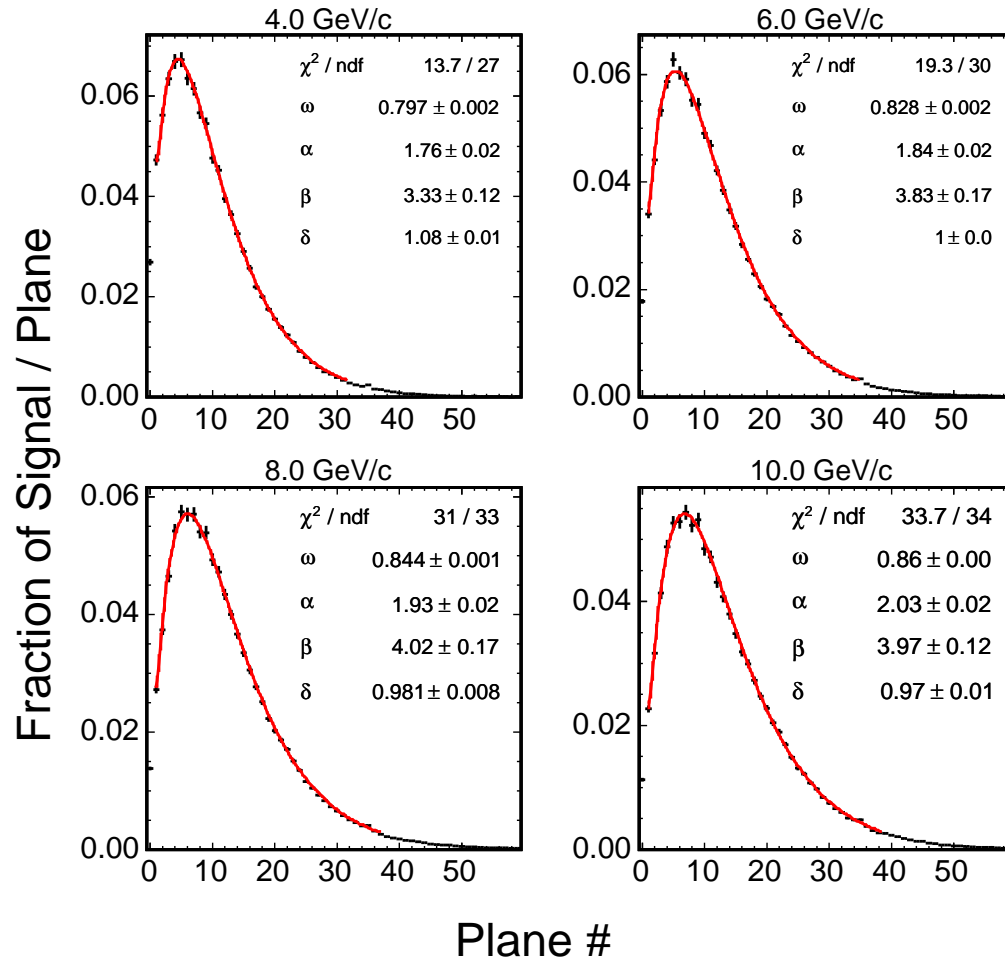
Figure 8.62: High energy (4.0-10.0 GeV/c) π^+ shower profiles fit to Eq. 8.14. The data were collected in the T7 beamline in 2002.
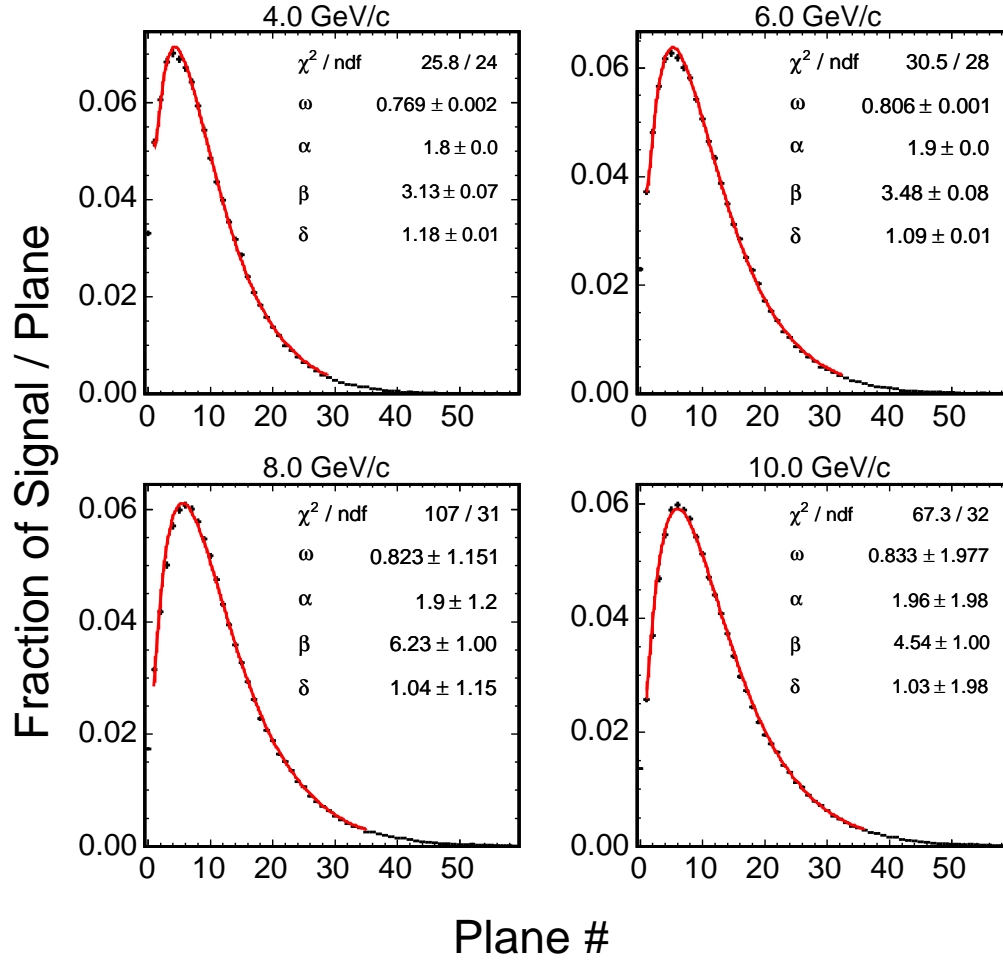
Figure 8.63: Simulated high energy (4.0-10.0 GeV/c) π^+ shower profiles fit to Eq. 8.14. The GCALOR code was used in the simulations.
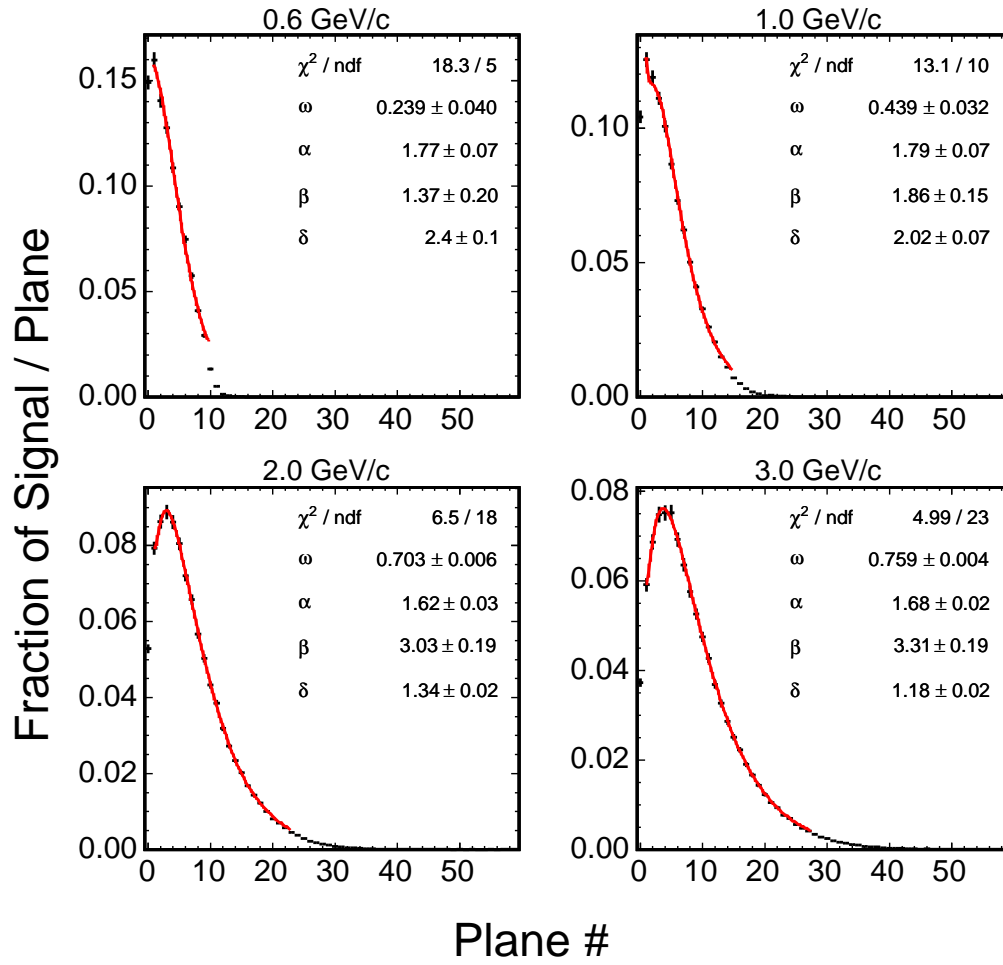
Figure 8.64: Low energy (0.6-3.0 GeV/c) π^+ shower profiles fit to Eq. 8.14. The data were collected in the T11 beamline in 2002.
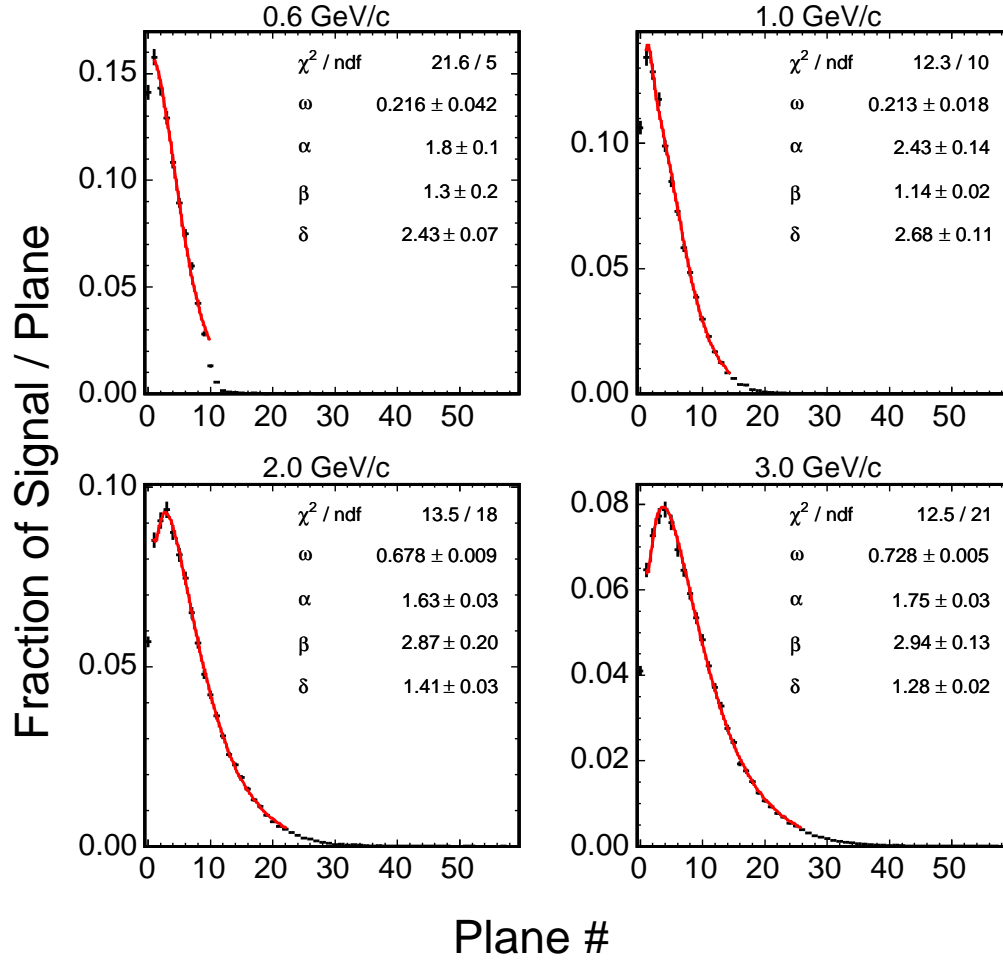
Figure 8.65: Simulated low energy (0.6-3.0 GeV/c) π^+ shower profiles fit to Eq. 8.14. The GCALOR code was used in the simulations.
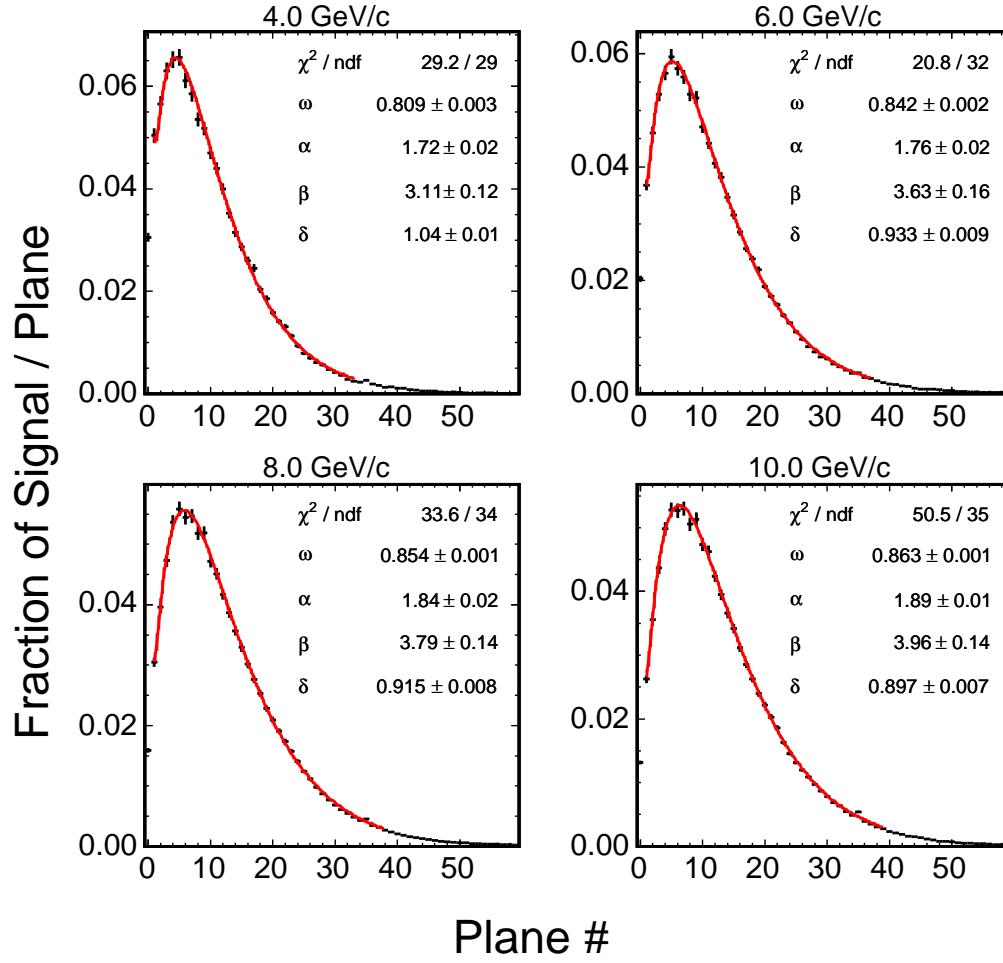
Figure 8.66: High energy (4.0-10.0 GeV/c) proton shower profiles fit to Eq. 8.14. The data were collected in T7 during 2002.
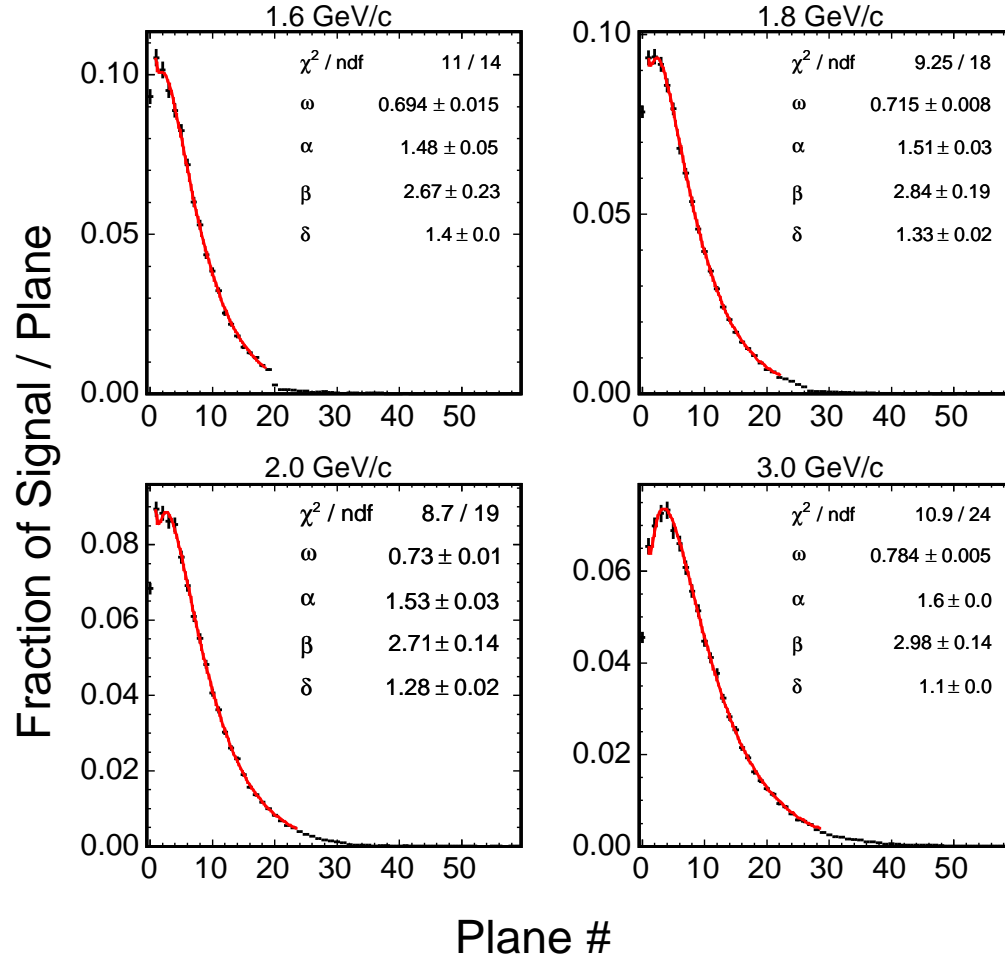
Figure 8.67: Low energy (1.6-3.0 GeV/c) proton shower profiles fit to Eq. 8.14. The data were collected in T11 during 2002.
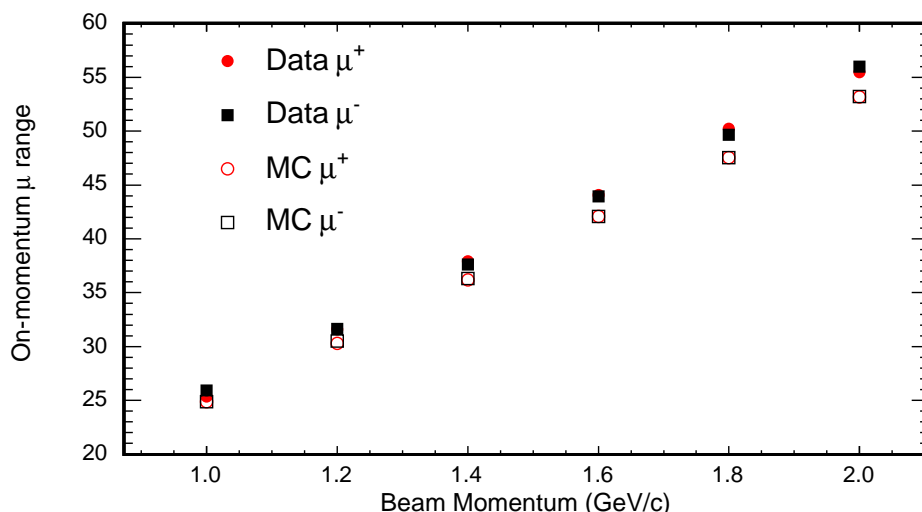
Figure 8.68: The range, in units of MINOS planes, of on-momentum muons identified by the discriminant procedure. The range was computed by looking for the most downstream plane with a signal larger than 0.5 MIPs allowing for a gap of at most 3 planes. The range estimate was consistent with the result from MINOS' standard track finder but was less sensitive to forward cross talk hits near the end of the track. Though the range of μ^+ and μ^- was consistent, the range of simulated muons was approximately 3-4% lower than in the data. The data are from T11 and are consistent with measurements in T7.

effect was found to be at the root of the discrepancy. The original simulation overestimated the energy loss in iron and scintillator by approximately 2% in the minimum ionizing region which led to a corresponding decrease in the range (see Fig. 8.9).

The density effect treatment was corrected not only for muons, but also for pions, protons and electrons. Figure 8.68 shows a comparison of the muon range after the correction was applied. In the figure, muons were identified by the discriminant procedure and their range was calculated by looking for the

most downstream plane with a signal larger than 0.5 MIPs allowing for a gap of up to three planes. At each momentum setting the on-momentum peak, examples of which are shown in Fig. 8.69, was identified and a truncated fit to a normal distribution was performed in order to estimate the range. The figures make it apparent that a significant ($\sim 3-4\%$) discrepancy existed for all momentum settings between 1 and 2 GeV/c. It is also clear that the data and Monte Carlo samples were internally consistent in the sense that positive and negative muons had equivalent ranges.

A comparison of Fig. 8.9 and the upper plot in Fig. 8.69 indicates that the range of simulated monochromatic muons is in much better agreement with the on-momentum peak observed in the data. That observation correctly indicates that the muon spectrum derived from the beamline simulation, and also the spectrum derived from the simpler TURTLE program, did not peak precisely at the nominal beam momentum value. At 1.8 GeV/c muons lost approximately 15 MeV/c to material in the T11 beamline, accounting for some of the discrepancy. However, because of the decay kinematics and the finite (rather than infinitesimal) size of the beam trigger paddles, the fraction of muons which were exactly on-momentum was negligible. The kinematics and acceptance account for an additional 15 MeV/c at the 1.8 GeV/c momentum setting. Both the energy loss and kinematics/acceptance effects should occur in the data and there is nothing to indicate that the modeling is incorrect.

The discrepancy, in which simulated muons had a range 3-4% shorter than those observed by CalDet, remains somewhat of a mystery. The dE/dx simulation in GEANT was evaluated and, after correcting the density effect, the tabulated dE/dx agreed with recently published range tables [73]. The DCUTM, DRAY, CUTS, LOSS and MULS settings of Tab. 8.1 were varied
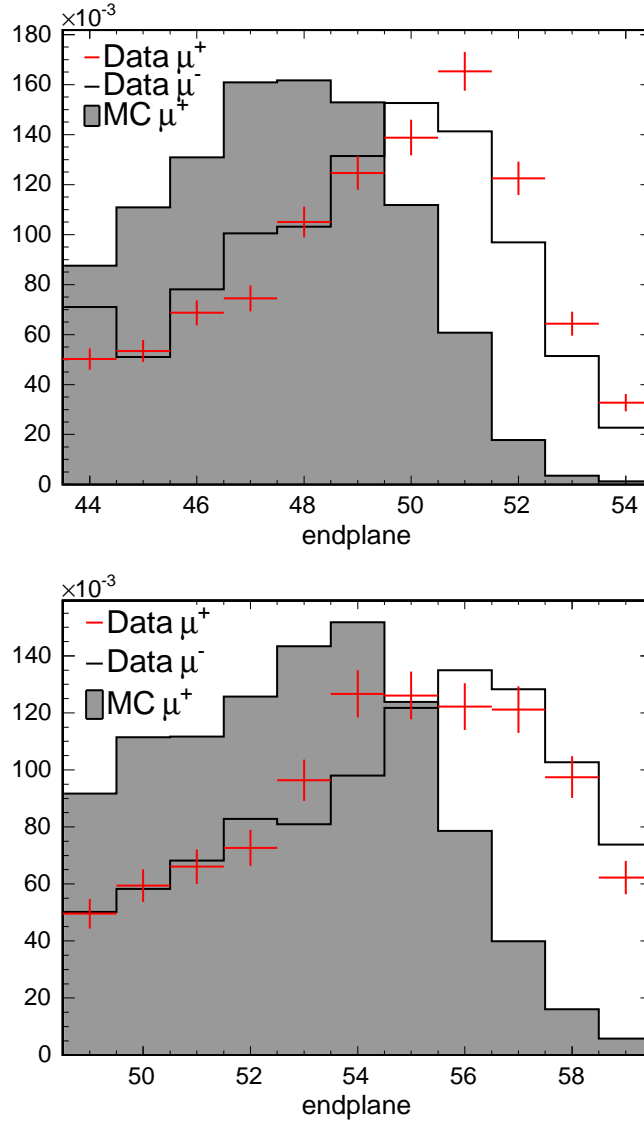
Figure 8.69: A comparison of the range, in units of MINOS planes, of μ events. The upper figure corresponds to a $1.8\,\text{GeV/c}$ beam setting, while the lower figure corresponds to a $2.0\,\text{GeV/c}$ setting. Both figures have been zoomed in to show the region around the nominal stopping plane for on-momentum muons. For the momentum settings shown, an approximately two plane discrepancy was observed between the data and Monte Carlo, with the simulated events being shorter.

without significantly increasing the range while still preserving a reasonable simulation[11]. A cursory study of energy loss fluctuations found that the tabulated mean dE/dx was preserved to within 1%. Multiple Coulomb scattering was not investigated in great detail and it is possible that some of the discrepancey may lie there.

As discussed in Ch. 7.2, the majority of muons which were accepted by the beam trigger were produced within a few meters of the detector. The exception were the on-momentum and maximally off-momentum muons which decayed along the pion's line of flight. It is possible that the range discrepancy was caused by an additional contribution from muons which were created far up the beamline and accepted into its magnetic channel. The TURTLE simulation predicted a negligible contribution from those muons, but features of the program prevented a full study of the issue.

A systematic shift in the beam momentum may also be responsible for the range discrepancy. The shift would have to occur with approximately the same magnitude for both polarities and in both beamlines. There are no published measurements of the absolute momentum in the beamlines, many users of the PS test-beams are not sensitive to a few percent shift and the PS staff do not firmly quote the systematic error on the beam momentum. The muon range provides the best measure[12] of the beam momentum through a comparison to the simulated muon range but additional work will be necessary in order to assure that the simulation is correct.

---

[11]Completely removing multiple scattering and energy loss fluctuations did increase the range but the resulting events were not realistic.

[12]That is, the best measure that can be derived from the CalDet data.

8.5 Conclusions

Detailed simulations of CalDet π, μ and p events were conducted using GEANT3 to model the physics of the events and energy deposition in the active elements of the detector. Details of the CalDet detector, such as the exact width and density of the steel planes, the isotopic composition of the iron and impurities in the steel were corrected in the Monte Carlo. A mistreatment of the Bethe-Bloch density effect, and hence dE/dx, was discovered and corrected in GEANT3. The active detector response was simulated using the DetSim and PhotonTransport packages of the MINOS offline framework. Non-uniformity due to varying optical cable lengths and compositions was correctly accounted for and a detailed model of the M16 response, including cross talk, was implemented. The light level and PE to MIP conversion constants were tuned using $1\,\mathrm{GeV/c}$ electrons.

The simulations were used to develop a procedure that discriminated between pions and muons on the basis of event topology. The discriminant procedure was used to characterize the muon content of the beamlines and provide a sample of pions which were compared to pions simulated with the GCALOR and SLAC-GHEISHA hadronic shower codes. The comparison indicated that GCALOR most correctly modeled the data for momentum settings below $6\,\mathrm{GeV/c}$ and that SLAC-GHEISHA systematically underpredicted the activity in the detector. The results of the study motivated the experiment to change the default hadronic interaction model used in simulating neutrino events from (old) GHEISHA to GCALOR. Though not discussed here, the change had a significant effect on the reconstruction and analysis of neutrino events.

324

Chapter 9

Response and Resolution

MINOS' primary goal is to conclusively demonstrate the mechanism responsible for ν_μ disappearance and, in the case of oscillations, to measure the parameters $(\sin^2 2\theta_{atm}, \Delta m_{23}^2)$ to an accuracy of approximately 10%. Additionally, MINOS will conduct a search for the subdominant transition $\nu_\mu \to \nu_e$ and attempt to set tighter limits on $\nu_\mu \to \nu_s$. To achieve these goals MINOS must accurately reconstruct the orignal neutrino energy, a task that requires the absolute response to hadrons, electrons, and muons be known to within 5% [32]. The CalDet program was specifically conducted to measure the detector response and resolution in a well controlled setting.

9.1   Response to Pions and Protons

We understand the detector response to refer to the amount of signal output by the detector per unit of incident energy. In the case of CalDet, the signal was expressed in terms of the MIP unit established by the cosmic-ray calibration procedure discussed in Ch. 5.3. Generally, calorimeters respond differently

to hadrons, muons and electrons, and therefore each species must be independently characterized. This section presents the response of the MINOS calorimeters to pions and protons.

Figure 9.1 shows the detector response to positive and negative pions as measured in the T11 and T7 beamlines and compared with the results from GCALOR and SLAC-GHEISHA. The pions were selected according to the procedure described in Ch. 8.3.1. In the figure, the values along the abscissas denote the available energy, defined as

$$E = \sqrt{p^2 + m^2} \qquad \text{(pions)}$$
$$E = \sqrt{p^2 + m^2} - m \qquad \text{(protons)}$$

That is, the available energy corresponds to the total energy for pions but the kinetic energy for protons. The distinction is that pions eventually release their mass energy by being absorbed on a nucleus or by decaying whereas protons ultimately stop and become part of the matter through which they were traveling. The energy that could be used to create signals in the detector, the relevant quantity for calorimetry, does not include the proton mass.

In Fig. 9.1 the values along the ordinates represent the mean of the signal distribution measured at each momentum setting (see Fig 8.48-8.51) divided by the available energy. In each event, the measured signal was computed by summing the signal recorded from each strip-end in planes 1–59. Plane zero was ignored because it fronted the detector and would have contributed a constant $\sim 2\,\text{MIP}$ for each event, roughly independent of the momentum setting and particle type. In addition, neutrinos will interact (largely) in the steel planes of the detector and the particles produced in the interaction will initially encounter steel rather than scintillator.
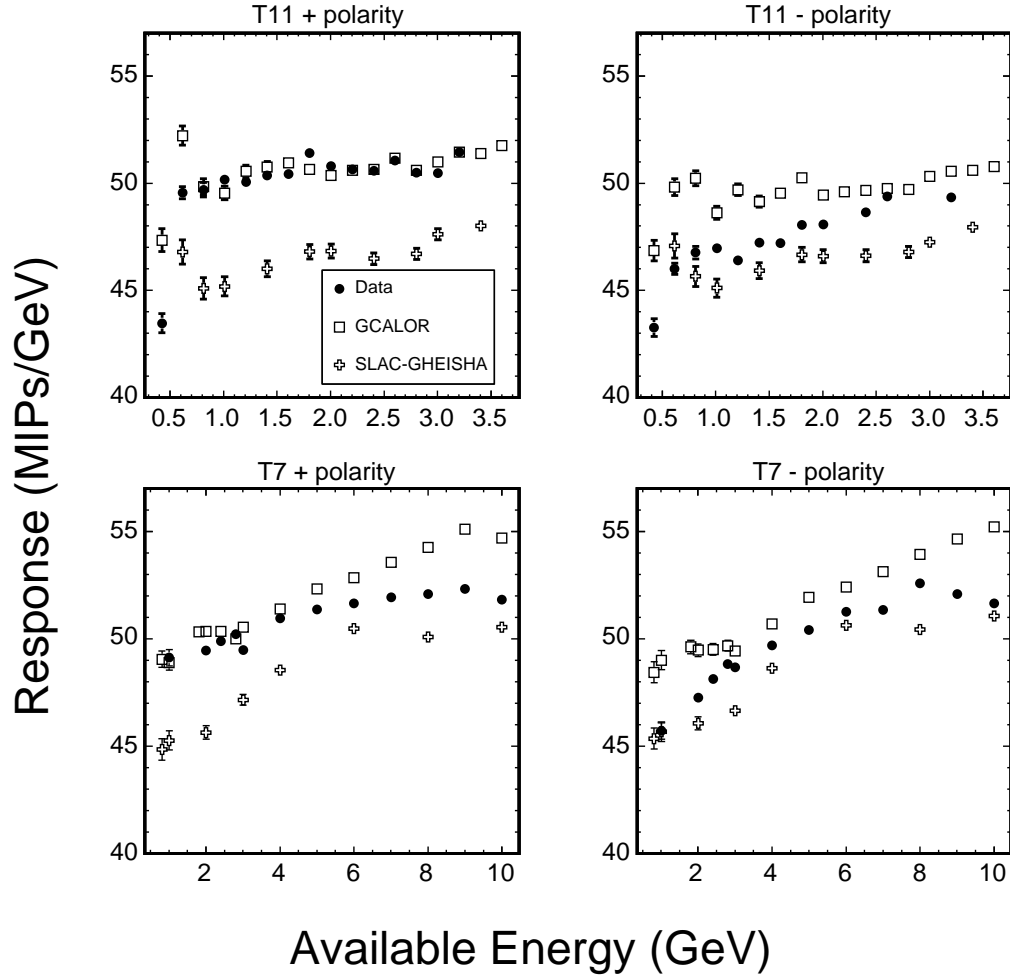
Figure 9.1: The signal response to $\pi^{\pm}$ as a function of the available energy. Here the pion response was taken as the mean of the signal distribution divided by the available energy. The errors in this figure are statistical and, for lack of better knowledge given the long tails present in the low energy signal distributions (see Fig. 8.48), were computed as $\sigma/\sqrt{N}$.

Very roughly, one expects that the measured signal will scale in propor-
tion to the available energy and also that the signal will vanish in the limit
in which the energy decreases to zero. This scenario would be borne out with
the individual points in Fig. 9.1 falling along a horizontal line. The vertical
position of the line would correspond to the constant of proportionality relat-
ing the measured signal to the initial particle energy. In such a case MINOS
would characterize the response with a single number - the position of the line.

Figure 9.1 indicates that the simple scenario elucidated in the previous
paragraph is only a crude approximation of reality. At low energy, the positive
pion response was flat to within 3%, neglecting the point at 400 MeV/c. On
the other hand, the response to negative pions decreased with the beam energy,
from approximately 49 MIP/GeV at 3 GeV/c to 46 MIP/GeV at 800MeV/c.
There was a clear charge asymmetry in the pion response at low energies
which gradually became smaller as the beam momentum increased, ultimately
vanishing at ~ 6 GeV/c. Further discussion of the asymmetry is presented
below. Above 4 GeV/c, and for both polarities, the response slowly increased
with the beam momentum. The trend was modeled by both hadronic shower
codes and is postulated to be due to an increase, with energy, in the fraction of
shower energy carried by electromagnetic particles (generally π^0s) [79, p. 56–
60]. Because the response of the MINOS calorimeter is larger for electrons
than it is for pions, an increase in the electromagnetic content of the showers
would cause the response to increase in the fashion observed.

At 400 MeV/c and 600 MeV/c a significant fraction of pion events re-
sulted in no observed signals in planes 1–59. The events generally did deposit
energy in plane zero, had a good time of flight measurement and are not
thought to be the result of accidental triggers. The effect, as seen in Fig. 9.2,
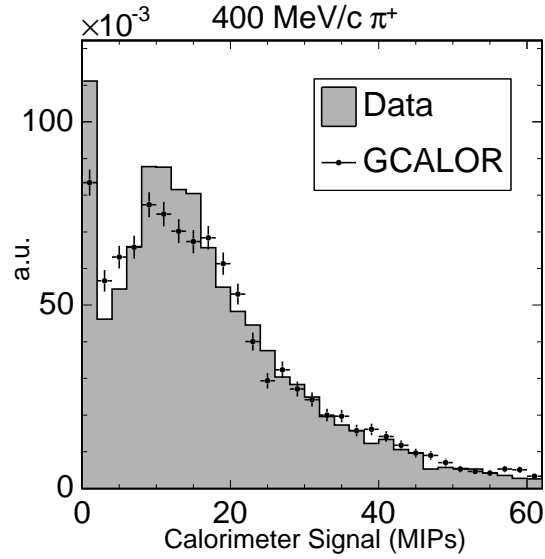
328

Figure 9.2: The calorimeter signal for $400\,\mathrm{MeV/c}\ \pi^+$. The pileup in the lowest bin was largely due to events in which no signal was observed.

was observed in both the data and the Monte Carlo and was largely due to pion interactions in the first steel plane which produced shower particles that stopped within the plane[1]. When reconstructing the hadronic energy in neutrino events, MINOS will obviously only be able to measure those events in which a signal is present. It is therefore improper to include events with no signal when determining the pion response. Figure 9.3 shows the response to $\pi^\pm$ determined by ignoring the first bin of the signal distributions. The correction, which increased the response, had a significant effect only for the $400\,\mathrm{MeV/c}$ and $600\,\mathrm{MeV/c}$ momentum settings.

Figure 9.4 shows the detector response to protons collected in T11 and

---

[1]As an example, protons with a momentum of $400\,\mathrm{MeV/c}$ range out in approximately $1\,\mathrm{cm}$ of steel.
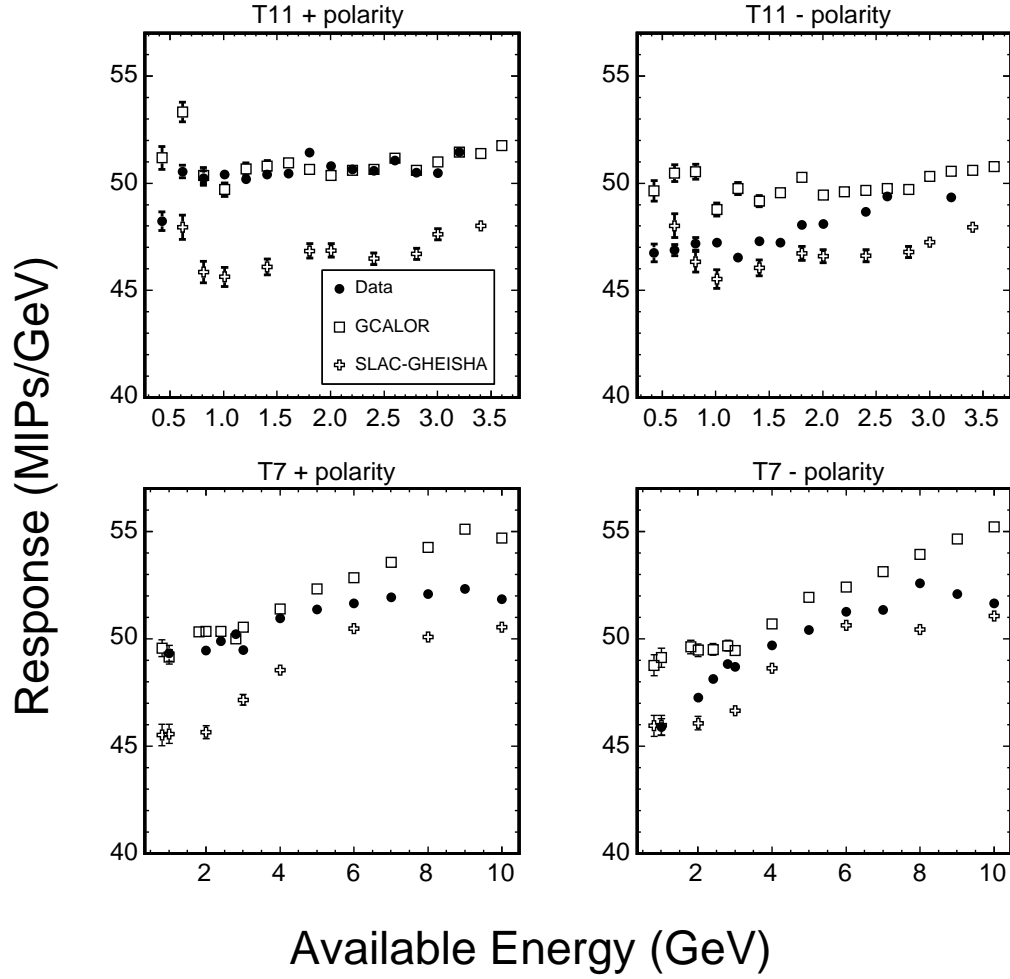
Figure 9.3: The signal response to $\pi^{\pm}$ as a function of the available energy. Here the pion response was taken as the mean of the signal distribution divided by the available energy. The first bin of the signal distribution (see Fig. 9.2) was neglected when calculating the mean for each run. The errors in this figure are statistical and were computed as $\sigma/\sqrt{N}$.
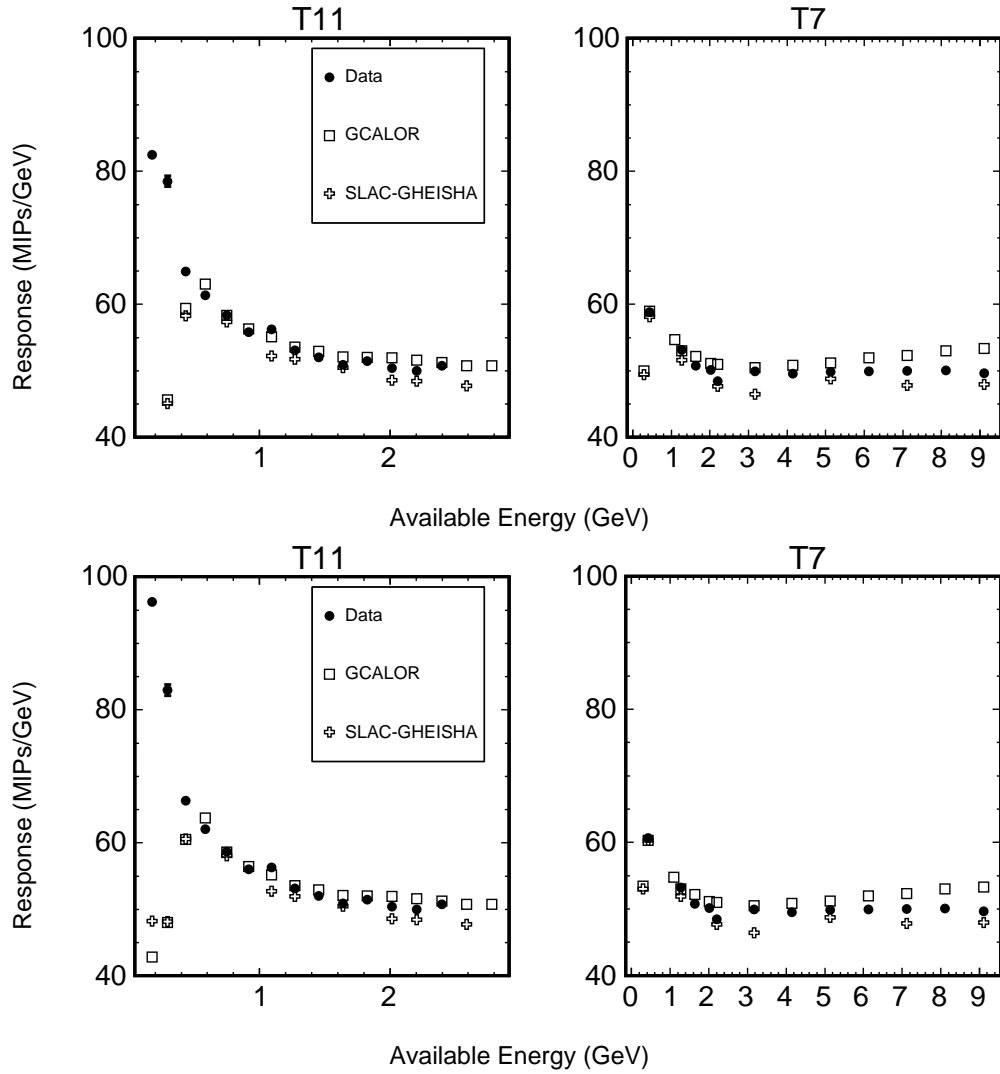
Figure 9.4: The signal response to protons as a function of the available energy. In the upper figure the response was taken as the mean of the signal distribution divided by the available energy. The first bin of the signal distribution was neglected when calculating the means in the lower figure.

331

T7, including and neglecting the first bin in the signal distribution. The proton response differs significantly from the pion response at low energies because low energy protons lose most of their energy by ionization rather than hadronic interactions. Additionally, $1\,\mathrm{GeV/c}$ protons lose $\sim 50\%$ more energy per unit of length than minimum ionizing particles and the difference increases as the proton momentum drops. The shape of the curves indicate a difficulty with calorimetric measurements of low energy protons, namely that the response, in MIPs/GeV, increases very rapidly as the energy decreases.

Figure 9.5 highlights the manner in which the measured signal depends on the proton range. In the figure, the calorimeter signal is shown as a function of the range for protons collected at the $800\,\mathrm{MeV/c}$ and $1\,\mathrm{GeV/c}$ beam settings. The measured signal was clearly quantized according to the stopping plane. For example, $1\,\mathrm{GeV/c}$ protons which penetrated the first five planes emerged with a momentum of 300-400 MeV/c, deposited approximately five times more energy in plane six than a minimum ionizing particle, and thereby created about 50% more signal than those that range out in plane five or below. The range effect was even larger for $800\,\mathrm{MeV/c}$ protons, for which the signal from tracks which traversed three planes was more than two times larger than for those that only penetrated two. In addition, the signal observed for $800\,\mathrm{MeV/c}$ protons which ranged out in plane three was consistent (to within 15% or so) with the signal observed for $1\,\mathrm{GeV/c}$ protons which stopped in plane five. This behavior suggests that, in the momentum interval in which protons range out in the detector, the best measurement of the proton energy may be achieved by considering both the stopping plane and the calorimeter's signal.

An additional curiosity of the proton response measurements is shown in Fig. 9.6. Two runs taken at $1\,\mathrm{GeV/c}$, the first in T11 and the second in
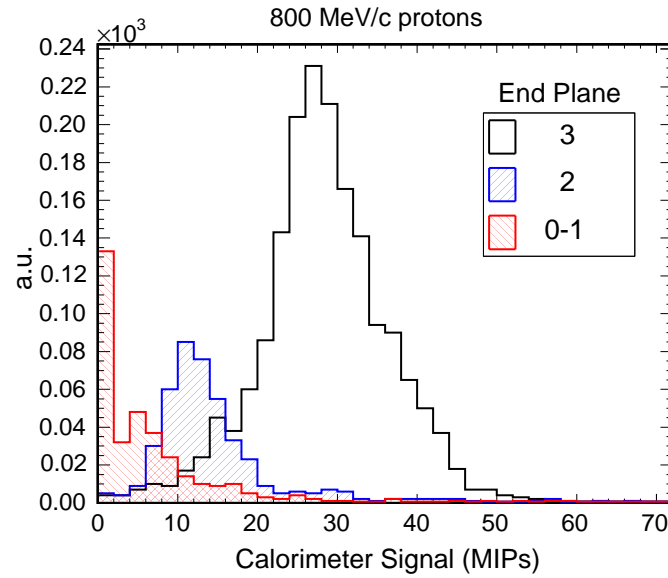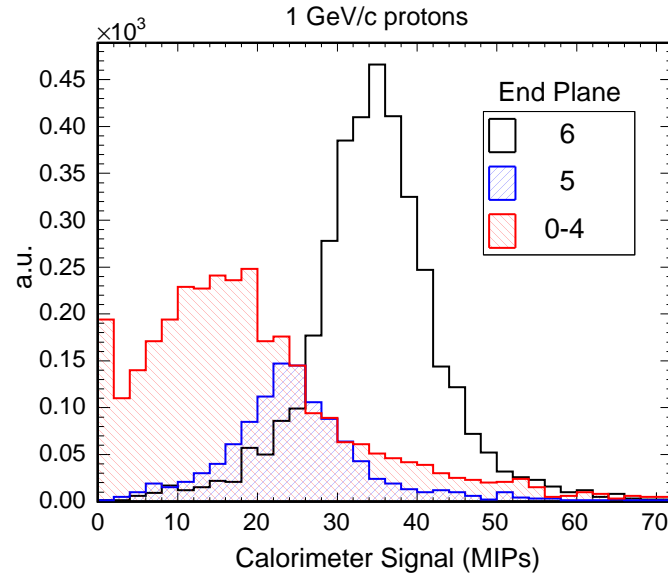
332

Figure 9.5: The signal response to protons as a function of the end-plane in the event. The end-plane is an estimate of the proton range. Protons were likely to range out in the detector for momentum settings at and below 1 GeV/c, causing a strong correlation between the signal and the proton range.
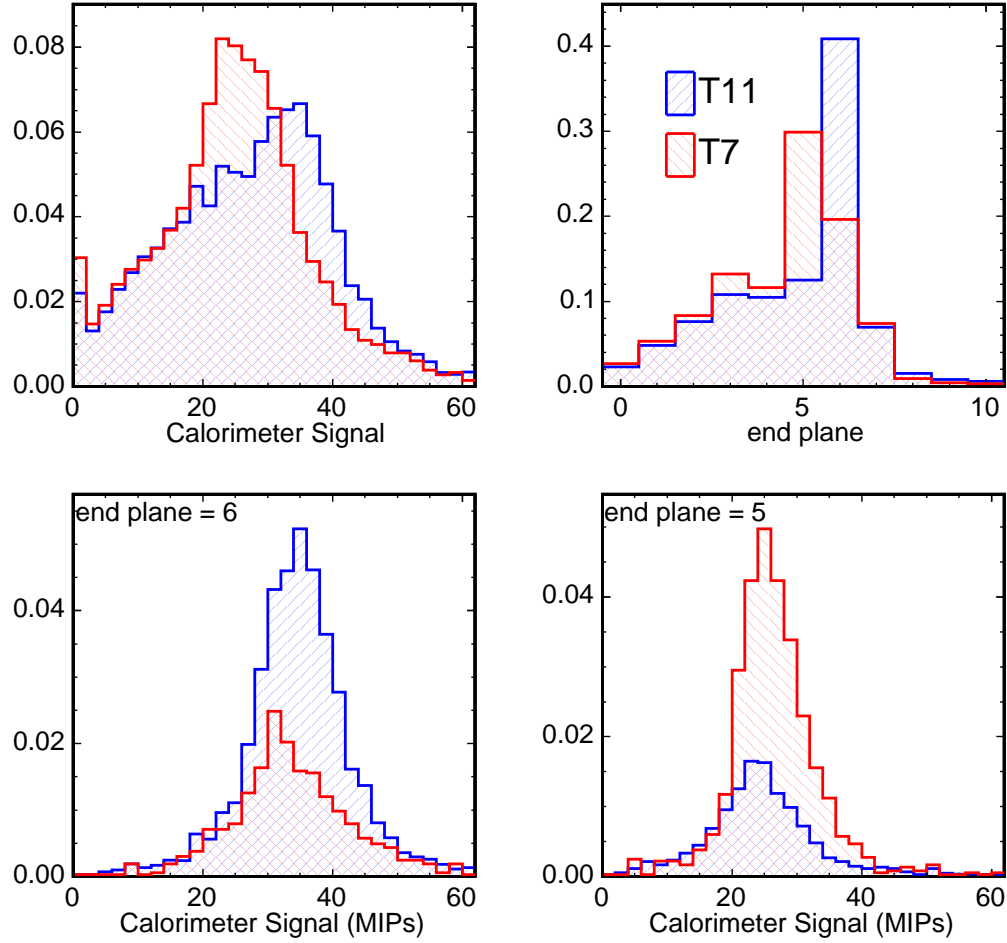
Figure 9.6: A comparison of the end-plane and its effect on the calorimeter signal for two $1\,\mathrm{GeV}/c$ runs, one taken in T7 the other in T11. The response measured in the T11 run was $\sim 10\%$ higher than the response measured in T7. Protons in T11 were more likely to penetrate planes 0-5 and deposit energy in scintillator plane six, and that additional sampling caused the discrepancy in the response. The lower two figures show that the response was in better agreement when the signal distributions corresponding to specific stopping planes were compared.
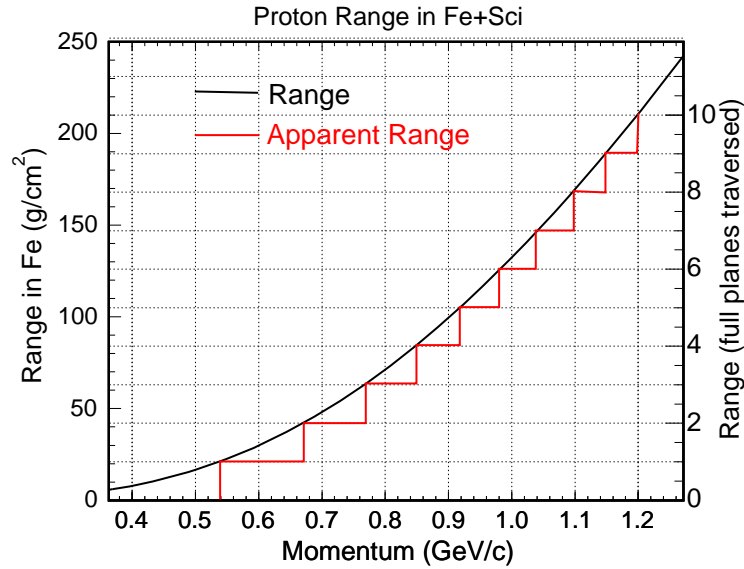
Figure 9.7: Estimated proton range in iron and scintillator as a function of the momentum. The range data, in iron, were taken from reference [80] and a correction was made to incorporate the effect of the scintillator when the axis on the right was constructed. See text for details.

T7, are compared in the figure. A 10% difference in the detector response to protons was observed between the two runs. In contrast, the pion response measured in the two runs was consistent to within 2%. The proton discrepancy was correlated with the range, which was somewhat larger in T11 than in T7. Protons in T11 were more likely to traverse five full planes and subsequently deposit energy in plane six, and that additional sampling was responsible for the discrepancy. The figure surely indicates that there was a difference in the proton momentum between T11 and T7, owing either to the beam setting or to energy loss upstream of the detector.

Figure 9.7 shows the estimated proton range in the MINOS calorimeter

as a function of momentum. The figure was constructed from published range tables for iron [80] but, when determining the range in MINOS planes shown on the right, a correction for the scintillator was made. An effective density for the MINOS iron-scintillator planes was derived by multiplying the density of iron by a correction factor

$$C_r = \frac{\left(\frac{dE}{dx}\right)_{Sci} + \left(\frac{dE}{dx}\right)_{Fe}}{\left(\frac{dE}{dx}\right)_{Fe}}$$

When evaluated at minimum ionizing for $1\,\mathrm{cm}$ of scintillator and $2.5\,\mathrm{cm}$ of iron: $C_r = 1.07$. According to Fig. 7.13, $1\,\mathrm{GeV/c}$ protons lost approximately $25\,\mathrm{MeV/c}$ in the material upstream of the detector. In Fig. 9.7 the protons, having a momentum of $0.975\,\mathrm{GeV/c}$ at the front face of the detector, reside right at the transition between tracks which range out in plane five and those which make it to plane six. Variations in the momentum of 1–2% are enough to push the range firmly above or below the transition. Despite the 10% difference in response, the proton measurments are consistent with one another when the range threshold effect descibed here is accounted for.

9.2   Run-to-Run Uncertainty

The statistical uncertainty of the data points in Fig. 9.1, 9.3 and 9.4 was difficult to evaluate given the non-Gaussian shape of the low energy pion signal distributions, but as an estimate the simple Gaussian approximation $\sigma/\sqrt{N}$ was used. An additional source of run-to-run uncertainty, encompassing small variations in the magnet currents and Čerenkov pressures, residual calibration errors and temperature fluctuations, must also be accounted for. These uncertainties were estimated on the basis of electron data collected during 2003
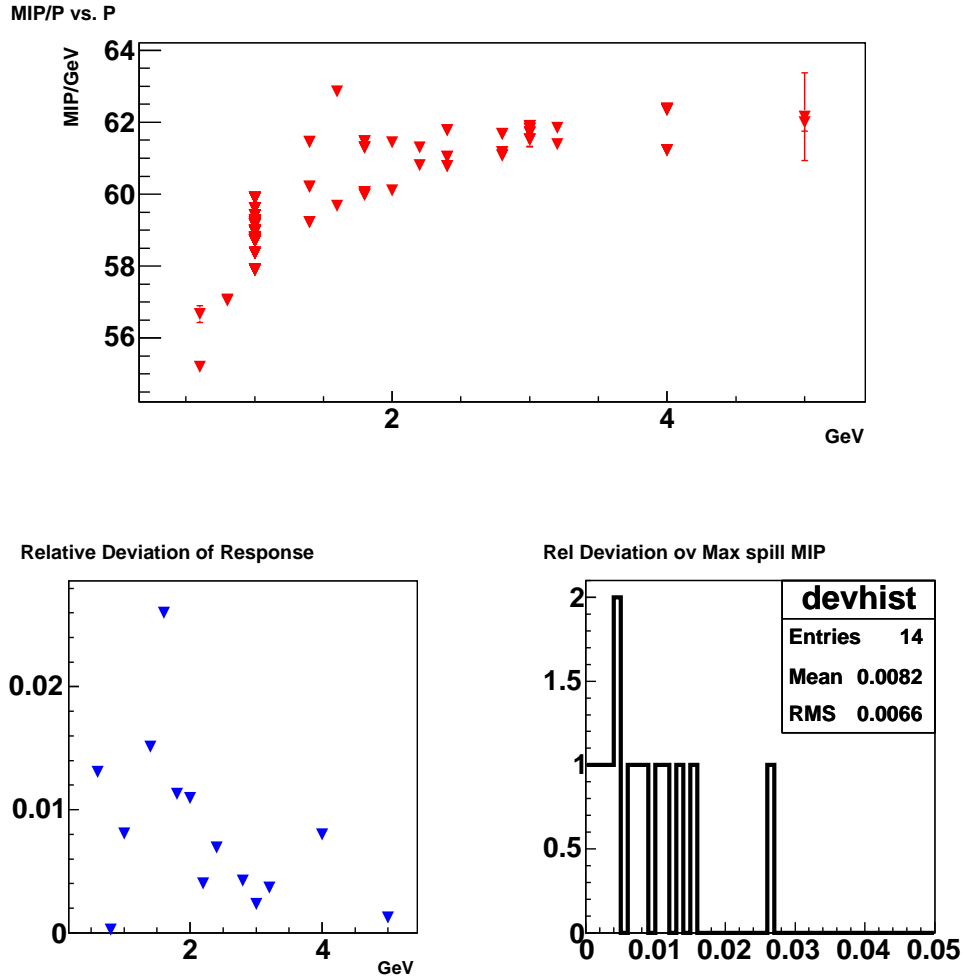
Figure 9.8: The run-to-run uncertainty in the detector response as estimated from repeated measurements over a range of momentum settings in the T7 beamline. The upper figure displays the electron response as a function of the beam momentum. At each momentum setting, a mean (μ) and RMS (σ) were calculated from the response measured in the individual runs. The fractional width (σ/μ) at each momentum setting is displayed in the lower-left hand figure. The histogram shown on the lower-right is a projection of the figure to its left and was used to estimate the run-to-run uncertainty in T7 as 0.8%. Taken with permission from [50].

in both T11 and T7 [50]. Runs were repeatedly taken at momentum settings between $600\,\mathrm{MeV/c}$ and $5\,\mathrm{GeV/c}$ with a concentration on the region between 1–$3\,\mathrm{GeV/c}$. Figure 9.8 shows the result for T7. The uncertainty was estimated from the repeatability of the response measurements at each momentum setting by computing the RMS over the individual runs and dividing by the mean. This procedure resulted in a fractional uncertainty at each momentum setting. A single, global error was computed for each beamline by averaging over the uncertainties at each momentum setting. For each data point, the global errors, calculated to be 0.8% in T7 and in 0.5% in T11, were added in quadrature to the statistical error on the response.

9.3   Correction for Energy Loss

Pions and protons lost energy as they traversed the beamline. The majority of losses were due to ionization in trigger counters, Čerenkov counter windows and gas and in the air present in the detector hall. As an example, according to the GEANT beamline simulation (as described in detail in Ch. 7.2), $1\,\mathrm{GeV/c}$ pions lost approximately $15\mathrm{MeV/c}$ prior to arriving at the detector face and protons lost $25\,\mathrm{MeV/c}$. For each run, the results of the beamline simulation were used to correct the available energy E_a for the energy lost due to ionization. The correction was applied as

$$E = \sqrt{\left(p_0 \left\langle \frac{p}{p_0} \right\rangle\right)^2 + m^2} \qquad \text{(pions)}$$

$$E = \sqrt{\left(p_0 \left\langle \frac{p}{p_0} \right\rangle\right)^2 + m^2} - m \qquad \text{(protons)}$$

where p_0 denotes the nominal beam momentum and $\langle p/p_0 \rangle$ was taken from the ordinate in Fig. 7.13. The corrections were largest at the lowest momentum settings. The available energy for pions at the $400\,\mathrm{MeV/c}$ momentum setting was corrected by 3.1%, while protons at the $600\,\mathrm{MeV/c}$ setting received a 19.4% correction.

9.4　Parameterization of the Response

The hadronic shower energy in each neutrino interaction will be carried from the vertex by one or more mesons (mostly pions) and nucleons. Thus, the response to neutrino induced hadronic showers will necessarily involve a convolution of the response to single pions and protons. A parameterization of the detector response to single pions and protons is presented here as the first step toward the eventual hadronic calibration of MINOS.

The hadronic response curves were corrected for energy loss and, a measurement error, derived from the repeatability measurements made in 2003 and discussed above, was added in quadrature to the statistical error on the mean signal $\bar{S}$. The mean signal was computed by excluding the lowest (zeros) bin of the signal distributions. The data points $\left(\bar{S}, E\right)$ were fit to second and third order polynomials

$$S\left(E\right) \;=\; p_0 + p_1 E + p_2 E^2 + \ldots$$

to parameterize the response. The fits were not intended as a test of any model and as such the quality of the fits was judged on the basis of MINOS's physics needs by gauging the ability of regions $\pm 1\%$ and $\pm 2\%$ about the best fit curve to encompass the data.
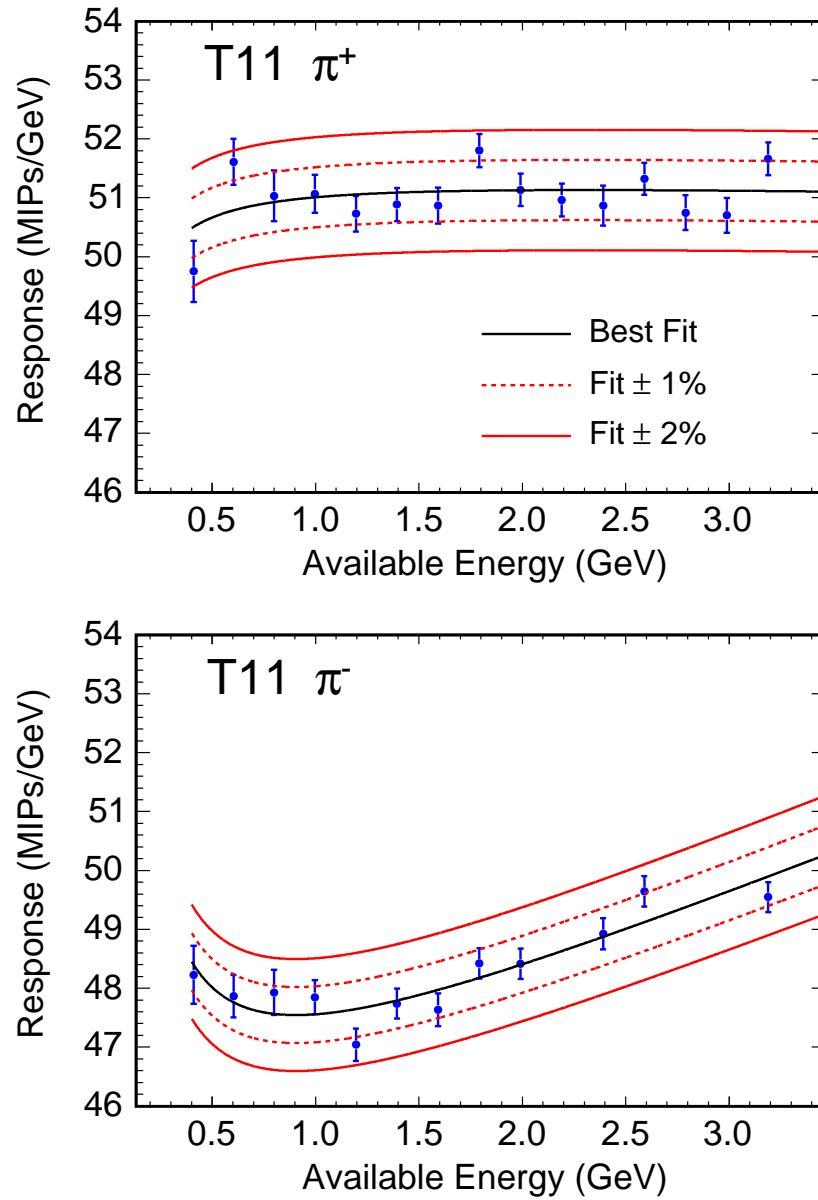
Figure 9.9: Second order polynomial fits to the pion response curves. The data were collected in the T11 beamline.

Figure 9.9 displays the result of second order fits to the data collected in the T11 beamline. The low energy data were the most important since, although MINOS will measure many hadronic showers with energy larger than 3 GeV, even high energy hadronic showers will, in general, consist of multiple lower energy particles. The fits represented the data rather well. Most points were contained within $\pm 1\%$ of the fitted curve and all were contained within $\pm 2\%$. Figure 9.10 shows the result of a combined fit to the data collected in T11 and T7. When a point was measured in both T11 and T7 the weighted mean of the two points was used in the fit. The positive pions were fit to a second order polynomial but a third order equation was necessary to properly represent the negative pion data. With the exception of the 400 MeV/c π^+ point, the data were all contained within $\pm 2\%$ of the best fit curves. The numerical values of the fit parameters are presented in Tab. 9.1.

The proton response curve was also parameterized, and the result is shown in Fig. 9.11. As discussed above, the response to protons rose rapidly at low momentum settings, became highly correlated with the proton range, and should probably be used in conjunction with a range measurement when reconstructing the proton energy. For momentum settings above 1.4 GeV/c the majority of protons showered and the response converged to an asymptotic value of 50 MIPs/GeV. The high energy (> 6 GeV) pion and proton response differ by approximately 4%, an effect possibly attributable to the bias toward having a leading baryon in proton induced events and a leading meson (possibly a π^0) in pion induced events [79, p. 61].

Figure 9.9 shows an approximately 7% discrepancy in the detector response to π^+ and π^- in the low energy region. The response asymmetry was somewhat surprising and warranted additional investigation, particularly be-
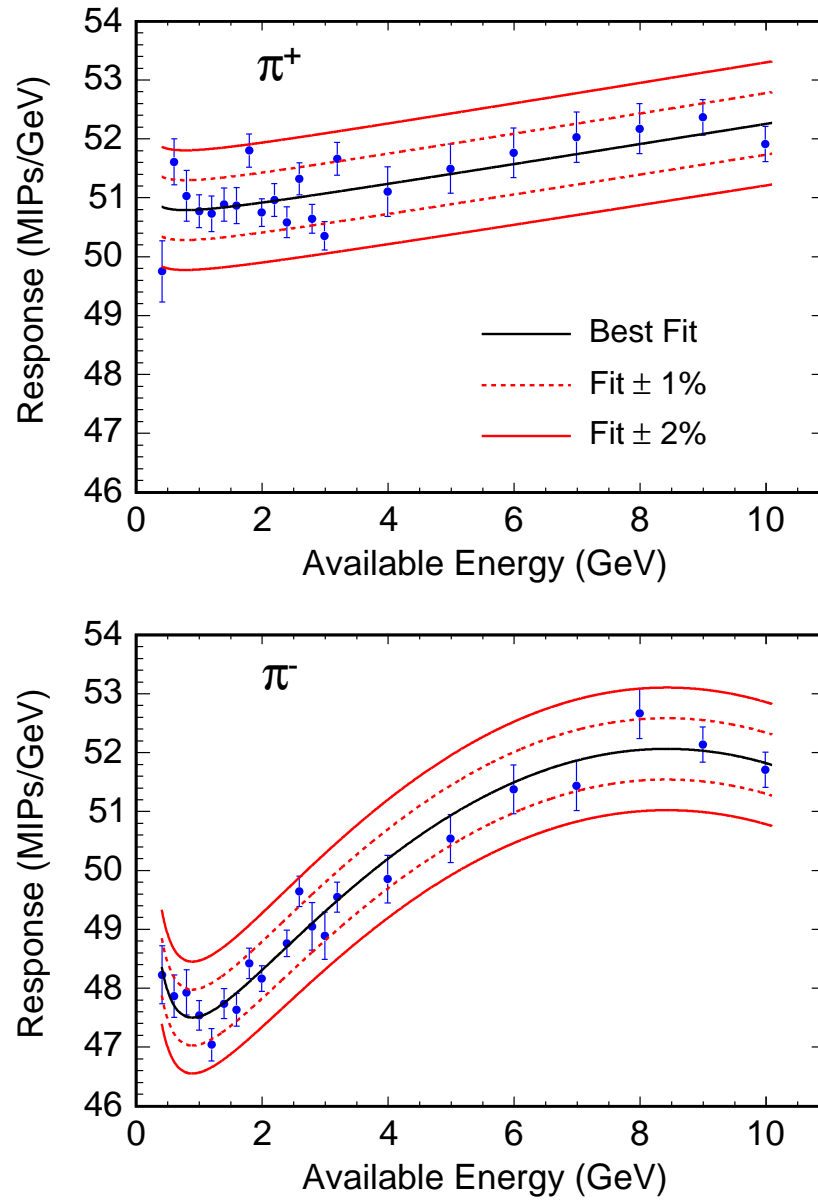
341

Figure 9.10: Fits to the pion response curves. The data from T11 and T7 are combined in the fits.
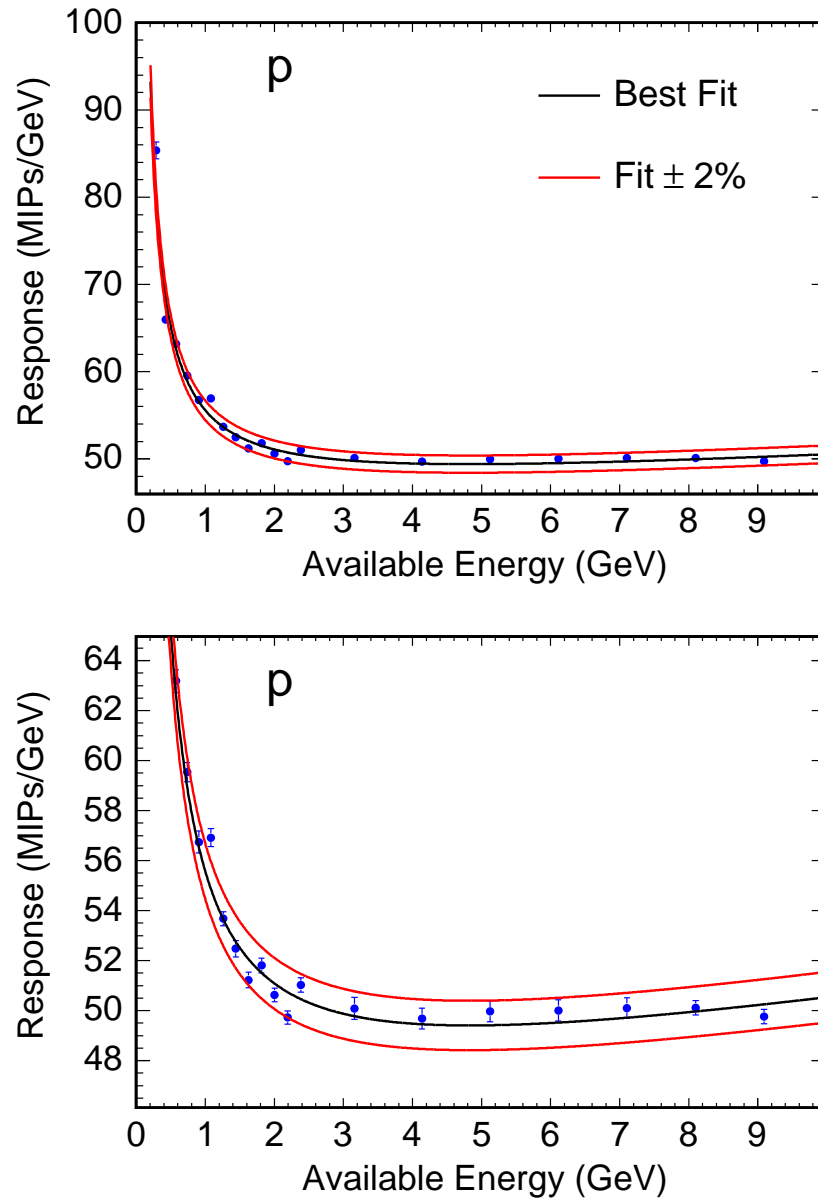
Figure 9.11: Fits to the proton response curves. The upper figure shows the entire momentum range, while the lower figure is zoomed to the momentum range, above $1.4\,\mathrm{GeV/c}$, in which most protons shower. The data from T11 and T7 are combined in the fits.

Response Fit Results: $\pi^\pm$, p

	χ^2 NDF	p_0 δp_0	p_1 δp_1	p_2 δp_2	p_3 δp_3	$\# \pm 1\%$	$\# \pm 2\%$ tot.
T11 π^+	23.8 12	-0.38 0.35	51.46 0.58	-0.07 0.19	- -	11	4 15
T11 π^-	15.4 9	1.18 0.34	44.94 0.58	1.44 0.19	- -	10	2 12
T7 π^+	12.2 11	-0.80 0.96	50.03 0.61	0.249 0.065	- -	11	1 12
T7 π^-	18.0 11	-4.01 0.95	49.54 0.59	0.325 0.064	- -	7	5 12
T7 and T11 Combined							
π^+	43.0 19	0.10 0.21	50.52 0.21	0.172 0.033	- -	17	5 23
π^-	23.0 17	1.20 0.30	44.72 0.48	1.69 0.19	-0.100 0.016	18	3 21
p	153.7 17	9.80 0.18	45.34 0.23	0.421 0.038	- -	-	15 17

Table 9.1: Best fit parameters from second and third order polynomial fits to the pion response curves. The $\# \pm 1, 2\%$ fields count the number of data points within $\pm 1, 2\%$ of the parameterized response.

cause neither Monte Carlo Code predicted the effect[2]. The difference appears to be a real effect as indicated by the following points:

- The discrepancy was not due to a gross error, such as a momentum offset between the positive and negative polarities. Two facts support the assertion. First, as shown in Fig. 8.68-8.69, the range of on-momentum muons was consistent to within $\sim 1\%$ between the two beam polarities. Second, no significant difference was observed between e^+ and e^-, despite

---

[2]GCALOR does show a $1 - 2\%$ response asymmetry, with π^- being lower, over most of the 1–$3\,\mathrm{GeV}$ range

the fact that the data were, for the most part, collected during the same runs as the low energy pion data presented here [50]. In addition, a consistent asymmetry was observed in both the T11 and T7 beamlines which indicated that any systematic error would have had to be present in both beamlines.

- The response asymmetry was not caused by a systematic error in the calibration procedure. Quite simply, during the calibration, no distinction was made between positive and negative beam polarities. Additionally, any serious discrepancies would have been observed in the muon and electron responses.

- The effect was not caused by protons leaking into the pion sample for the positive polarity runs. Proton leakage would make the average signal appear smaller rather than larger. For example, at $1\,\mathrm{GeV/c}$ the proton signal distribution had a mean of 28.1 MIPs but the mean of the pion distribution was 50.7 MIPs. Additionally, the pion and proton peaks in the TOF distribution were separated by at least $6\sigma = 1.26\,\mathrm{ns}$ for all momentum settings in T11 (see Fig. 4.16).

- Electrons were not responsible for the asymmetry. The electron content, as a fraction of the pion content, agreed to approximately 10% between the two beam polarities and electrons were identified and rejected with high efficiency in the 1–$3\,\mathrm{GeV/c}$ range (see Ch. 4.6).

- Pile-up (overlapping events) did not cause the discrepancy. Positive and negative polarity runs were intentionally taken with the same trigger rate, the hit timing was used to reject pile-up events, and a 7% difference

in the response suggests at least a 7% overlap rate. Such a high rate is inconsistent with event scanning.

- The difference was not caused by operating the detector at different temperatures or during different time periods for positive and negative polarity runs. For example, it was not the case that all negative polarity runs were taken at night while positives were collected during the day. Runs were taken semi-randomly and positives and negatives were often collected in back-to-back runs over the span of a few hours.

- The discrepancy was not caused by stray magnetic fields from beamline magnets influencing the operation of the detector. The detector was located more than 5 m from any beamline magnet and the stray fields were measured and found to be negligible in the area around the detector.

- The procedure used to discriminate between pions and muons was not the cause of the response asymmetry. This was verified by using a simple cut on the range to select pions. Figures 9.12-9.13 show the result. The cut used to define pions, shown in the figures as a dashed line at fifteen (Fig. 9.12) or twenty-eight planes (Fig. 9.13), was chosen to sit just below the nominal range for maximally off-momentum muons. Events with a range less than the cut value were accepted as pions. Additional cuts were placed at twenty-three or fifty-two planes, and events with a range greater than the cut values were accepted as on-momentum muons. The signal distributions for the pion and muon samples were studied and an asymmetry, consistent with the one observed when employing the discriminant to select pions, was seen in the pion sample but not in the muons. At 1 GeV/c the pion cut was varied between planes four

346

(accepting 15% of the events) and thirty (accepting all events) and the asymmetry was observed for all cut values.

No reason has been found to suspect that the π^+, π^- response asymmetry was not a real effect. Though there is a relatively small amount of published calorimetric data in the few-GeV region, two experiments have been found in which a response asymmetry appears to occur in the few-GeV region[83, 84]. In addition, some calorimeters may not be sensitive to the effect given the complex fashion in which the response of a calorimeter depends upon its composition and construction.

9.5   Energy Resolution for Pions and Protons

The energy of individual hadronic showers may be measured with an accuracy determined by the energy resolution, defined here as the root-mean-square of the hadron signal distribution divided by the mean, (σ/μ). The resolution is energy dependent and may be parameterized as [79]

$$\left(\frac{\sigma}{\mu}\right) = A \oplus \frac{B}{\sqrt{E}} \quad \text{(quadratic)} \tag{9.1}$$

$$\left(\frac{\sigma}{\mu}\right) = A + \frac{B}{\sqrt{E}} \quad \text{(linear)} \tag{9.2}$$

where the $\oplus$ symbol indicates that the two terms are to be added in quadrature and E is the available energy. Figures 9.14-9.15 show fits of the energy resolution using Eq. 9.2.

For pions, the fits were made to the entire range of the data, but for protons a good fit could only be made to the data above $1.5\,\text{GeV}$. At low energy, the proton resolution was better than a $1/\sqrt{E}$ scaling would indicate because much of the proton energy was lost by ionization (characterized
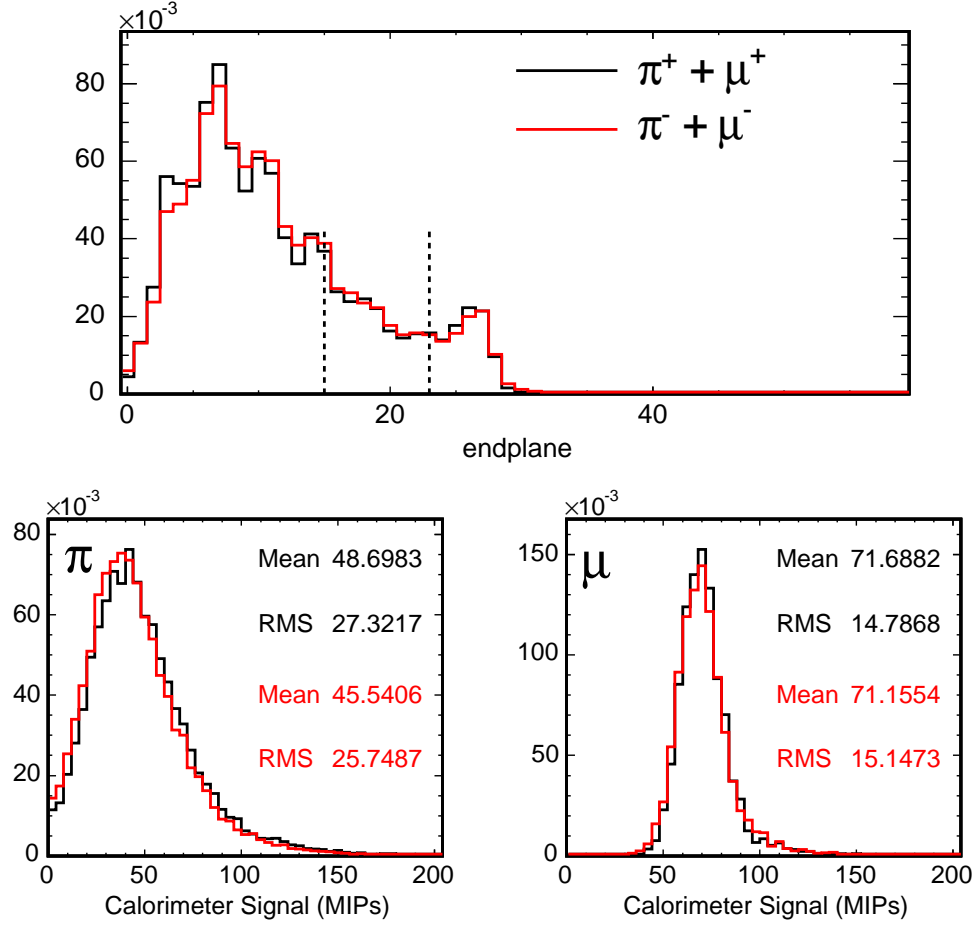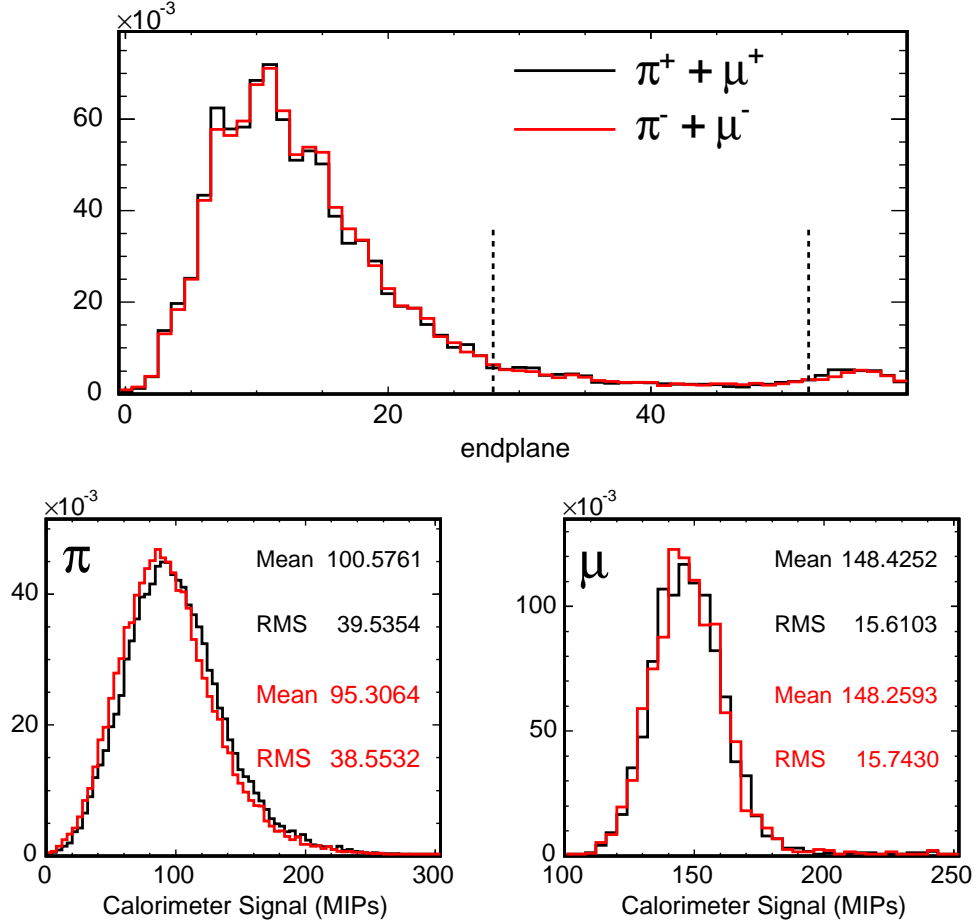
347

Figure 9.12: The observed π^+, π^- signal response asymmetry when a simple cut on the range is made. The upper figure shows the end-plane, an estimate of the range, for the combined pion and muon samples collected at $1\,\mathrm{GeV/c}$ for both beam polarities. Cuts, shown as dashed lines, were made on the range to define a sample of pions and on-momentum muons. The lower two figures show the pion response (left) and the on-momentum muon response (right). The asymmetry is observed in the pion sample but not in the muons.

Figure 9.13: The observed π^+, π^- signal response asymmetry when a simple cut on the range is made. The upper figure shows the end-plane, an estimate of the range, for the combined pion and muon samples collected at $2\,\mathrm{GeV/c}$ for both beam polarities. Cuts, shown as dashed lines, were made on the range to define a sample of pions and on-momentum muons. The lower two figures show the pion response (left) and the on-momentum muon response (right). The asymmetry is observed in the pion sample but not in the muons.
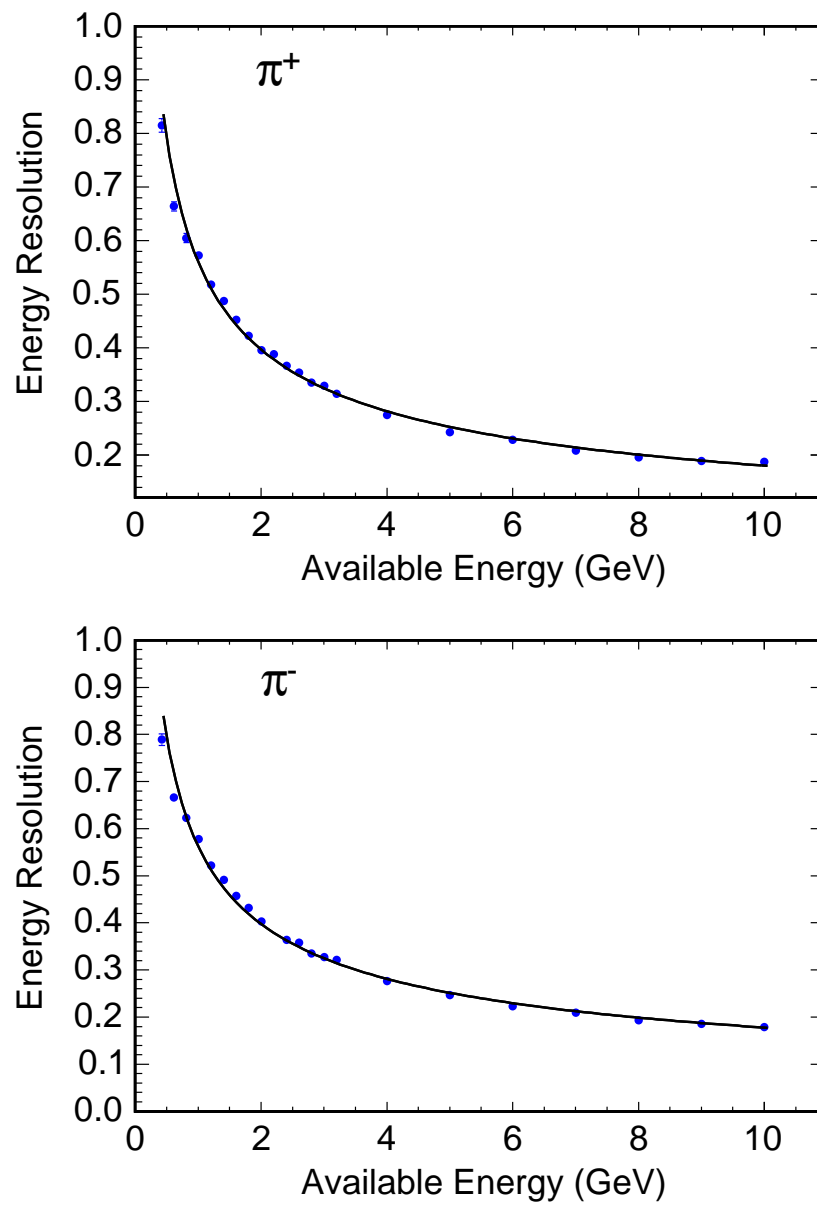
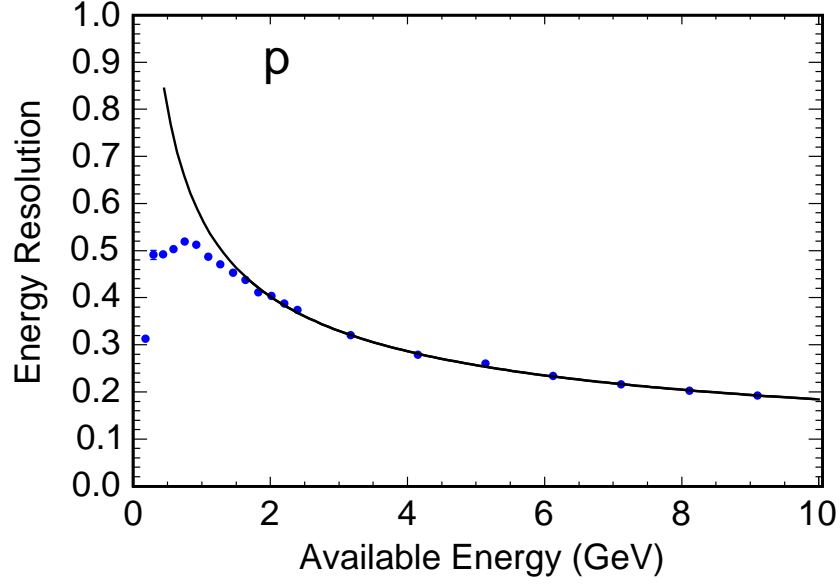Figure 9.14: The pion energy resolution fit to Eq. 9.2.

Figure 9.15: The proton energy resolution fit to Eq. 9.2. Points below 1.5 GeV were neglected in the fit.

Fits to the energy resolution for $\pi^\pm$ and p

	A (%)	B (%)	
π^+	4.2 ± 1.5	55.7 ± 0.5	quadratic
π^+	0.7 ± 0.4	55.1 ± 0.9	linear
π^-	0.0 ± 3.3	56.2 ± 0.3	quadratic
π^-	-0.1 ± 0.4	56.3 ± 0.9	linear
$\pi^+ + \pi^-$	2.1 ± 1.5	56.1 ± 0.3	quadratic
$\pi^+ + \pi^-$	0.3 ± 0.2	55.8 ± 0.4	linear
p	4.3 ± 1.4	56.6 ± 0.6	quadratic
p	0.7 ± 0.5	55.9 ± 1.0	linear

Table 9.2: Best fit parameters from linear and quadratic fits to the energy resolution.
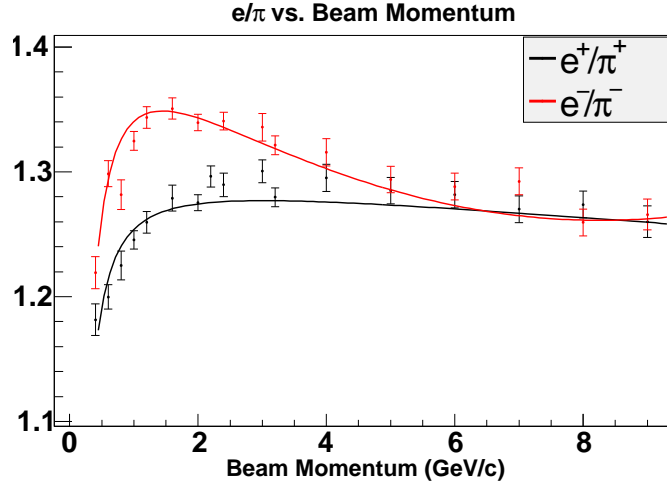
Figure 9.16: The electron/pion response ratio as a function of the beam momentum for for positive and negative pions [50].

by small fluctuations) rather than in hadronic interactions (characterized by large fluctuations). Between $300\,\mathrm{MeV}$ and $1.2\,\mathrm{GeV}$ the proton resolution was approximately 50% and did not depend on the energy.

9.6   Electron to Pion Response Ratio

The electron to pion response ratio (e/π) is shown as a function of the beam momentum in Fig. 9.16. The difference in the ratio between the positive and negative beam polarities was due to the signal asymmetry observed between π^+ and π^-; The response to e^+ and e^- was consistent to within 2% [50]. For both polarities, the ratio gradually converged to a value of 1.27 ± 0.01 at high energy.

9.7 MEU Calibration

Results thus far have been presented in terms of the MIP (minimum ionizing particle[3]) unit defined during the cosmic-ray calibration described in Ch. 5.3. The unit depends, implicitly, on the cosmic-ray spectrum which is different at the three detector locations. A more portable calibration constant, called the MEU (Muon Energy Unit or Muon Equivalent Unit), may be defined in terms of muon tracks which stop in the detector. Stopping muons are useful as a standard "candle" since, at each point along the track, the muon energy may be computed by reverse integrating the Bethe-Bloch equation from the track endpoint, thereby removing any dependence on the cosmic-ray spectrum.

The MEU is itself an arbitrary (but portable!) unit, since it depends on the way in which the calibration is performed. Two calibrations will be offered here as examples, both of them employing beam muons collected in the CalDet at momentum settings between 1–$3\,\mathrm{GeV/c}$. In both calibrations, the muons were selected according to the discriminant procedure of Ch. 8.3.1 and were required to stop between planes twenty-five and and fifty-eight[4]. Positive and negative muons were combined in the analysis and a total of thirty-five runs were used, yielding a sample of 65500 muons.

For each muon track, the signals in each plane were summed and then used to fill a two dimensional histogram of the signal per plane versus the distance from the stopping plane. That histogram, displayed in the upper left of Fig. 9.17, was used to compute the average signal per plane as function of the distance from the end point, as is shown on the upper right. Two intervals

---

[3]A misnomer, given the way in which the MIP constant was defined.

[4]The stopping plane (end plane) was defined as the most downstream plane with a signal larger than $0.5\,\mathrm{MIPs}$ allowing for a gap of at most three planes.
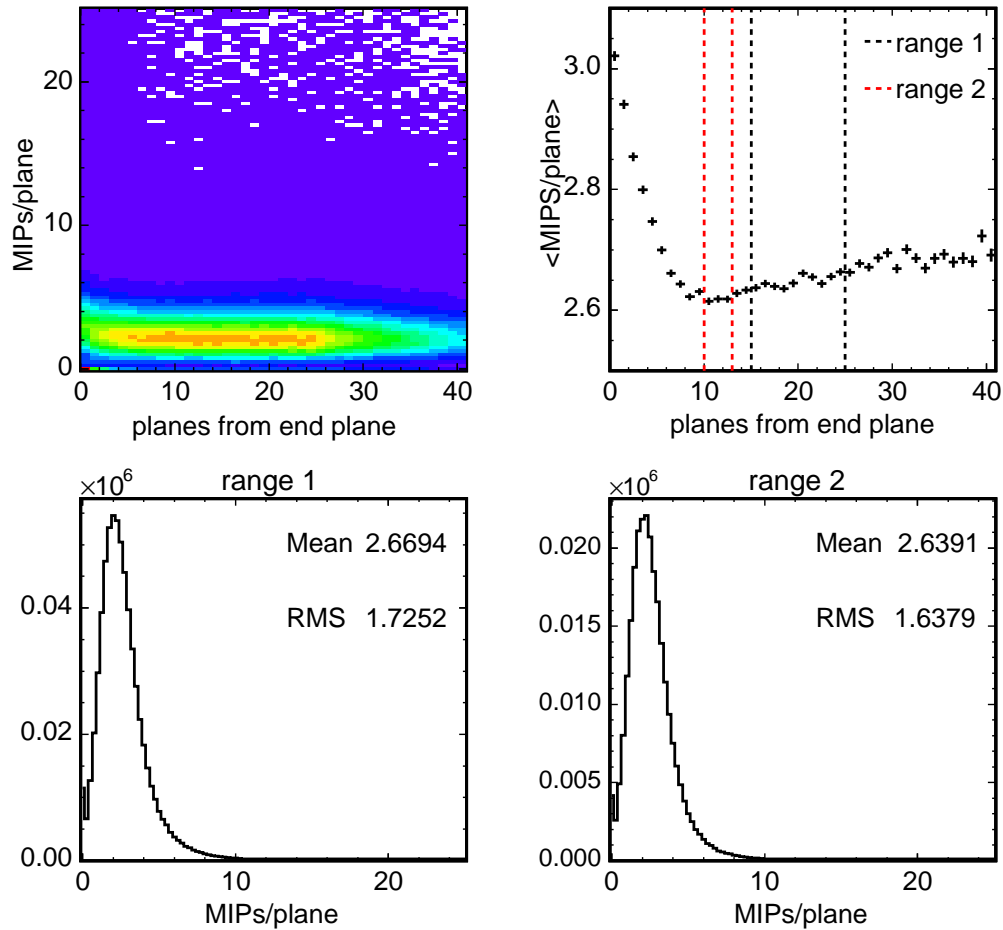
Figure 9.17: Two definitions of a MEU calibration constant in terms of the MIP calibration described in Ch. 5.3. The figure on the upper left shows the signal observed per plane as a function of the distance from the end of on-momentum muon tracks selected by the discriminant procedure. The figure on the upper right, derived from the one beside it, shows the mean signal per plane as a function of the distance from the end of the track. Dashed lines indicate the regions over which the signal per plane was used to construct the lower two histograms. Further details are discussed in the text.

along the muon track are plotted as dashed lines in Fig. 9.17. The first interval spanned the relativistic rise portion of the curve between fifteen and twenty-five planes from the track's end while the second included the three bins between ten and twelve planes. The second region, chosen to encompass the three bins with the lowest signal per plane, is assumed to approximately correspond to a ~ 60 MeV/c range containing the minimum ionizing point. Histograms of the signals per plane within each interval are shown in the lower left and right of Fig. 9.17. The mean value of each histogram defines the conversion between MIPs and MEUs as

MIP to MEU conversion constants

	MIPs/MEU	σ	entries
range 1	2.669	1.725	655306
range 2	2.639	1.638	262144

The two numbers are expected to disagree since they are derived from different portions of the dE/dx curve. The constant determined using range 2 may be used to derive a conversion between MIPs and visible energy. According to references [73, 85], muon dE/dx in scintillator is within 0.5% of the minimum ionizing value in the ± 60 MeV/c range about the minimum ionizing momentum. This allows the energy loss at minimum ionizing (1.936 MeV cm^2/g) to be used to derive a conversion factor of

$$0.734 \, \frac{\text{MeV cm}^2}{\text{g MIP}}.$$

The conversion to visible energy has a certain advantage in that any other method which provides such a conversion should, in principle, yield the same result.

The MIP/MEU conversions offered here are intended to anchor the results presented above to a more tangible unit system than the rather amorphous (and misnamed) MIP. Some effects, notably the effect of multiple scattering on the local track angle, have been neglected and tracking was not performed. All signals in each plane were summed in contrast to a possible scheme which neglects those hits not along the track. The difference is not expected to be large since normally incident muons traverse essentially one strip per plane, the noise rate is negligible, and any cross talk hits are a consequence and partial measurement of the original light pulse.

9.8   Fitting Hadronic Line Shapes

Figures 9.21-9.22 show the result of fitting proton signal distributions. The fits were acceptable for proton momenta $> 1.5\,\mathrm{GeV/c}$. As the momentum dropped below $\sim 1.5\,\mathrm{GeV/c}$, an ever increasing fraction of protons ranged out in the detector prior to experiencing a hadronic interaction. The calorimeter signal for those protons was highly correlated with the range - leading to the peaked signal distributions shown in Fig. 9.22. The different peaks correspond to specific planes in which the protons ranged out.

Pion signal distributions (sometimes called *line-shapes*) are asymmetric, having a Gaussian shape around the most probable value and a high-side tail. At low energy ($< 600\,\mathrm{MeV/c}$) the tail extends out to values as much as 10 times larger than the most probable value. Motivated by similar distributions observed in CsI crystal calorimeters [86], the pion line-shapes were described
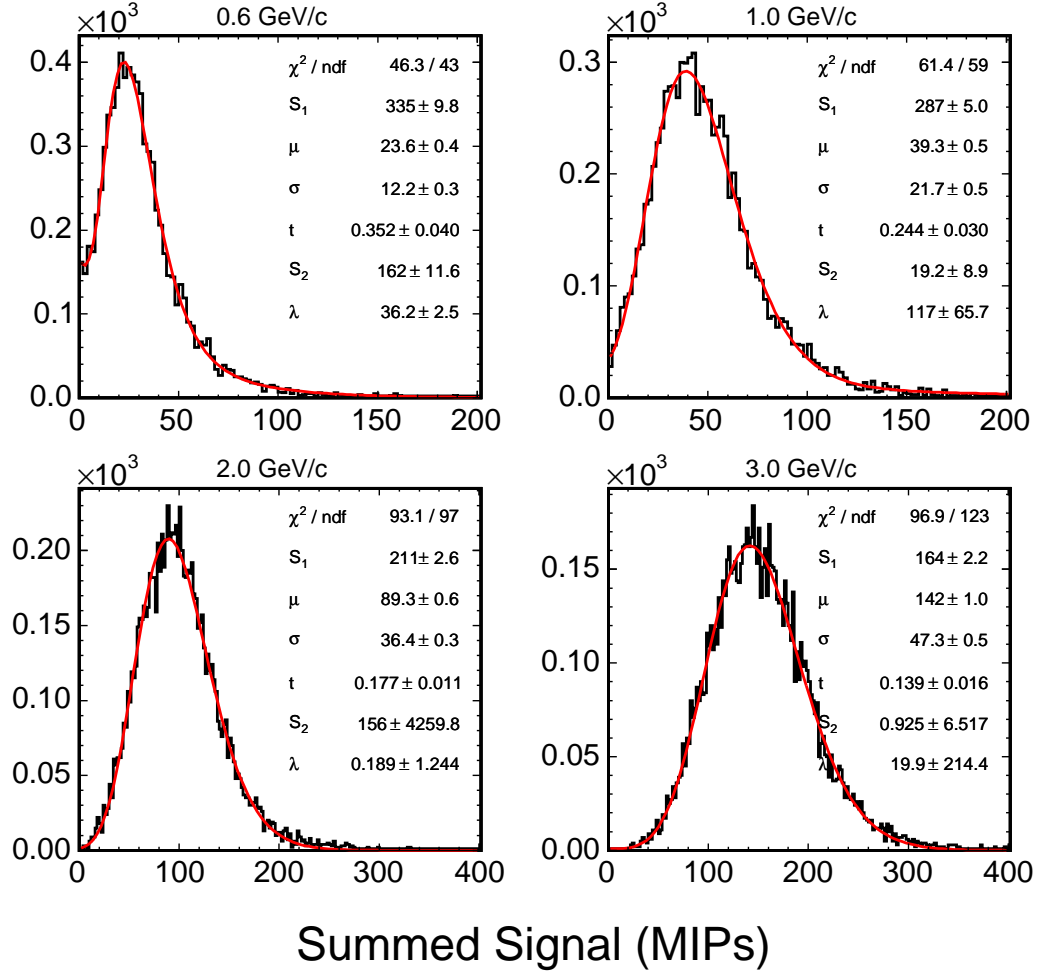
Figure 9.18: Simulated π^+ signal distributions fit with the lognormal function of Eq. 9.3. The GCALOR hadronic shower code was used in the simulation.
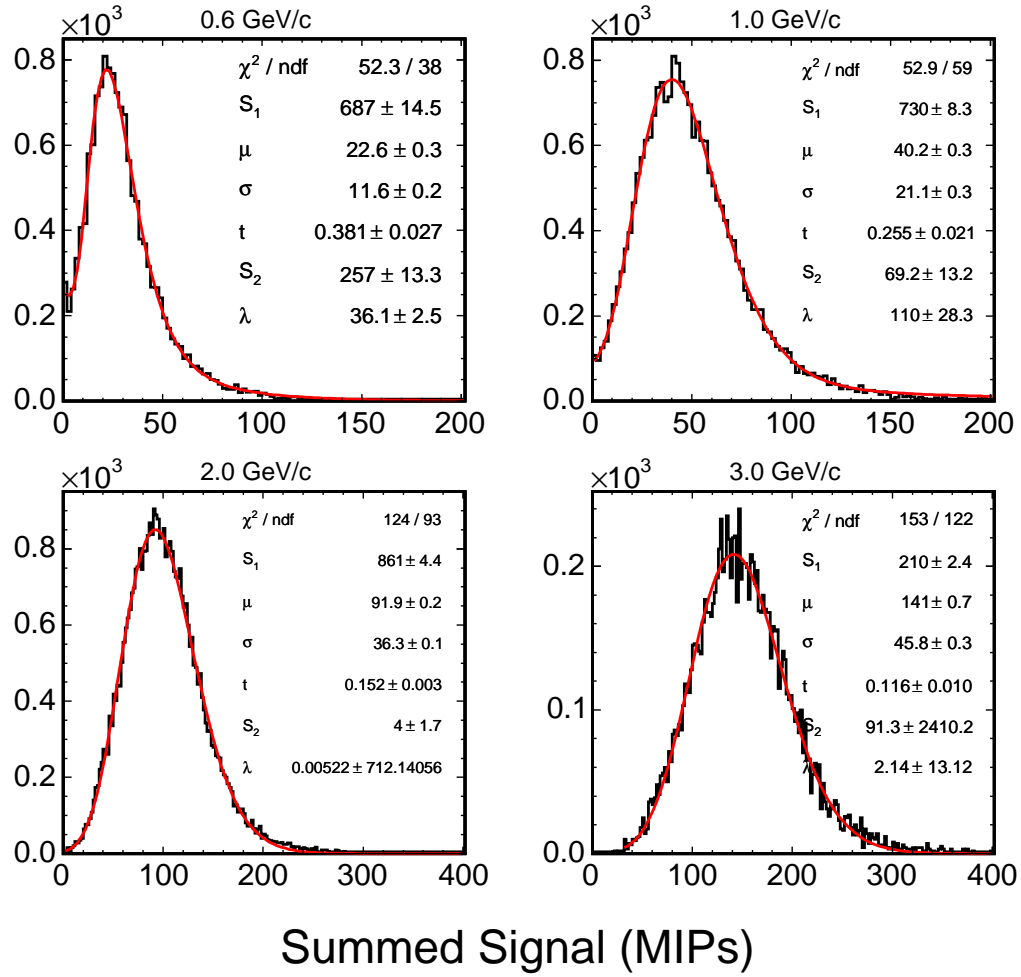
Figure 9.19: π^+ signal distributions fit with the lognormal function of Eq. 9.3. The data are from the T11 run in 2002.
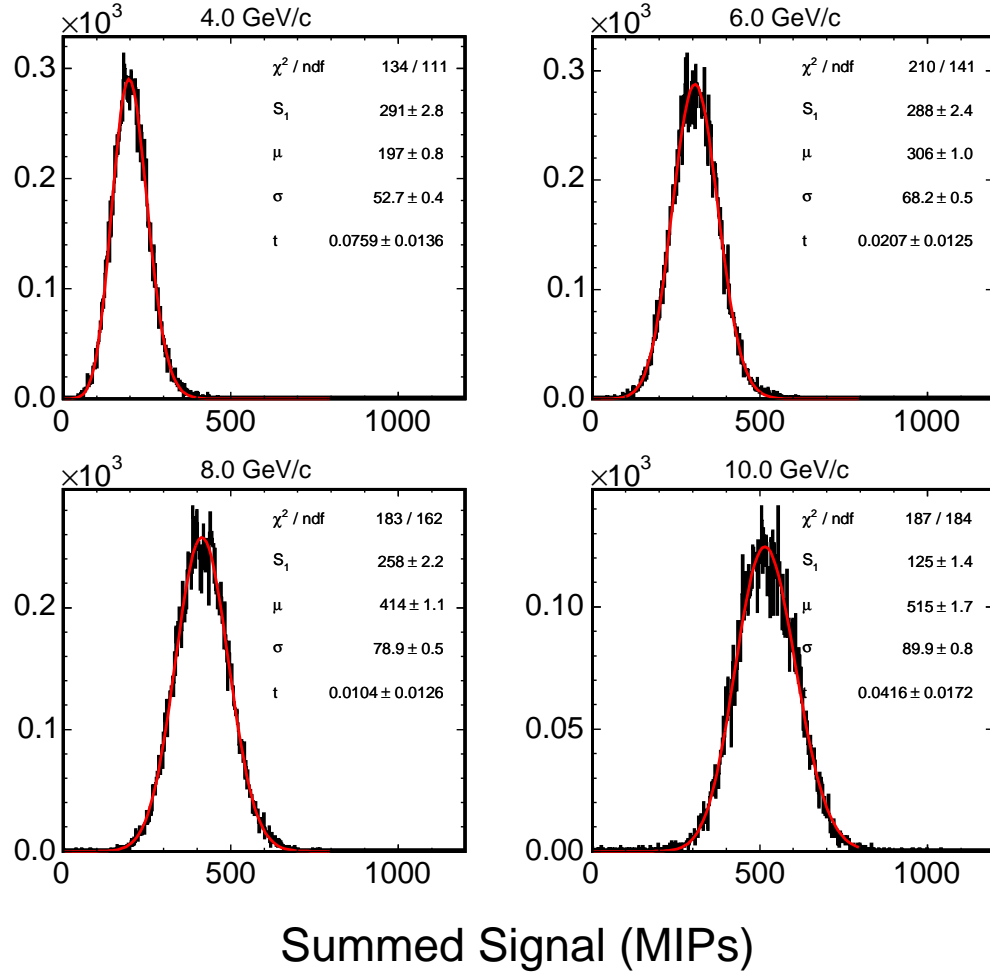
Figure 9.20: π^+ signal distributions fit with the lognormal function of Eq. 9.3. The $S_2 \exp(-x/\lambda)$ term was explicitly set to zero in the fit. The data are from the T7 run in 2002.
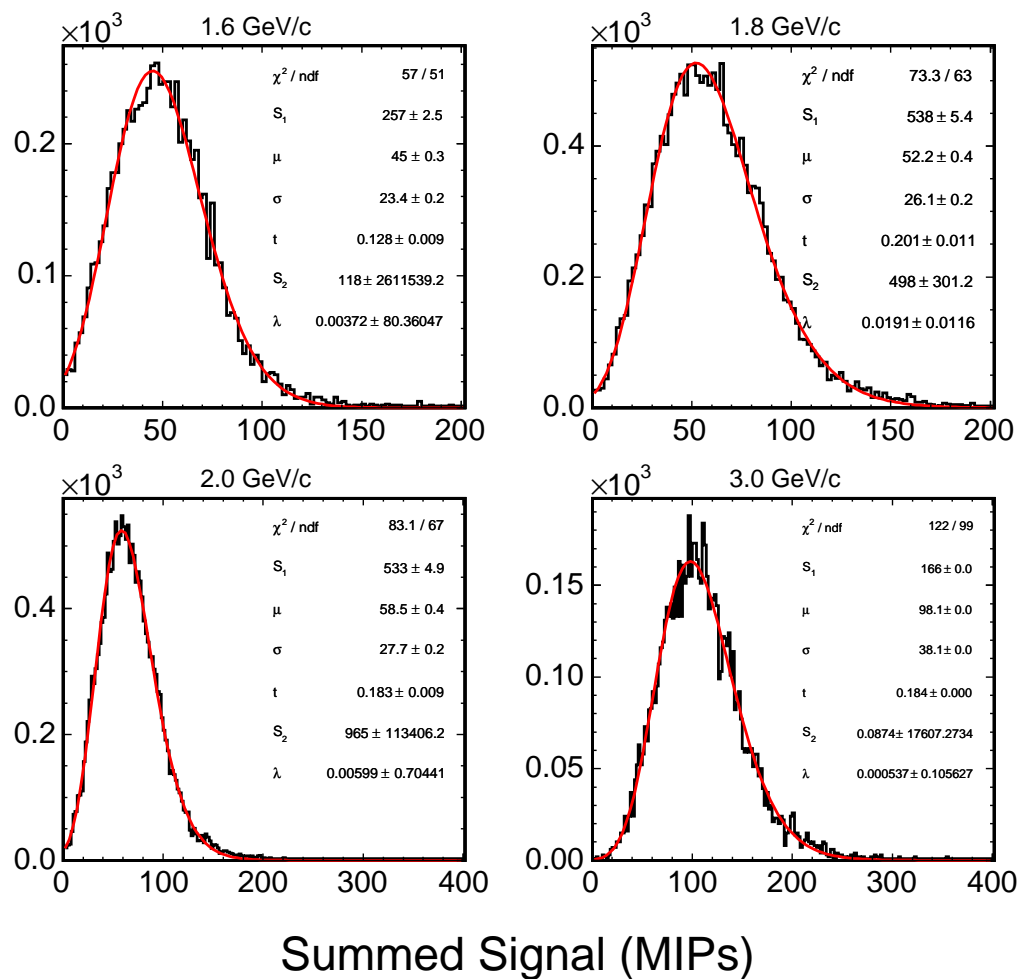
Figure 9.21: Proton signal distributions fit with the lognormal function of Eq. 9.3. The data are from the T11 run in 2002.
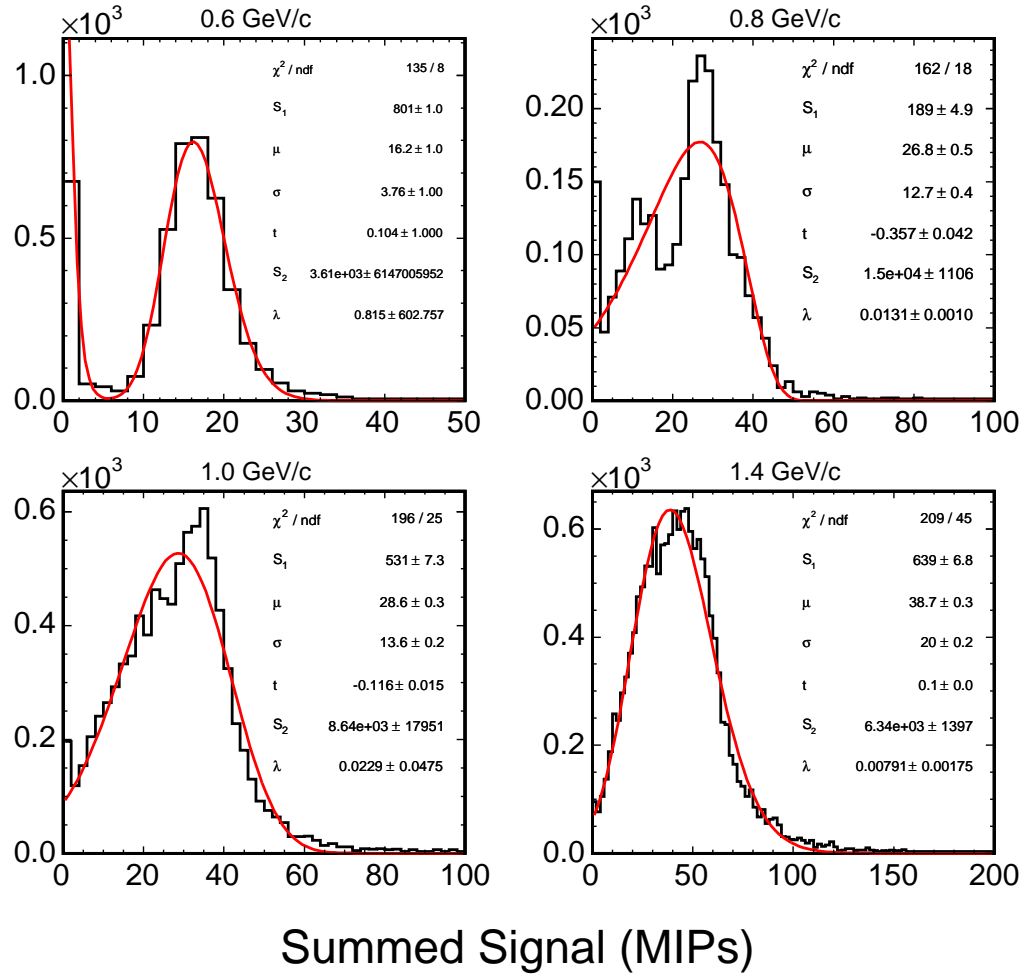
Figure 9.22: Low energy proton signal distributions "fit" with the lognormal function of Eq. 9.3. The data are from the T11 run in 2002. At the energies shown, a significant fraction of protons did not experience a hadronic interaction and instead lost all their energy via ionization. The calorimeter signal was then highly correlated with the proton range - giving rise to the multiple peak structures visible in the upper two figures.

by a modified lognormal function [87]:

$$f(x) = S_1 \exp\left[-\frac{1}{2}\log\left(\frac{1}{t} + \left(\frac{x-\mu}{\sigma}\right)\frac{\sinh Kt}{Kt}\right)^2 - \frac{t^2}{2}\right] + S_2 \exp\left(-x/\lambda\right)$$

$$(9.3)$$

Here, $S_{1,2}$ are normalization factors and $K = \sqrt{\log 4}$. Neglecting the second term in Eq. 9.3, the parameter μ corresponds to the most probable value and $\sigma = \mathrm{FWHM}/\sqrt{4\log 4}$. The parameter t describes the tail of the distribution. The $S_2 \exp\left(-x/\lambda\right)$ term was added to account for an excess of events on the left-hand side of very low energy distributions and is unimportant above $800\,\mathrm{MeV/c}$.

Using Eq. 9.3, log-likelihood fits were done to pion signal distributions. The upper limit of the fit range was chosen in order to contain 98% of the data[5]. Figures 9.18-9.19 display the results for a few low energy beam settings. Generally, Eq. 9.3 described the data well, even at the lowest energies where the distributions were most asymmetric. The function also described the high energy line-shapes, as shown in Fig. 9.20.

Equation 9.3 provided a good fit to more than 90% of the pion data and Monte Carlo signal distribions. Fits were poorest at the lowest two momentum settings, and there were occasional instances in which the fit could not converge. Additionally, the second term in Eq. 9.3 was needed in order to fit the low energy data but its presence meant that the μ fit parameter no longer corresponded to the most probable value. Finally, the fits did not always represent the $\sim 1\%$ of events in the long high-side tail of the hadronic signal distributions, and when integrated to find the mean was found to bias the result in a way that depended on the fit range. Equation 9.3 could be

---

[5]For some distributions, the fitting program did not report correct errors when fitting to the full range.

considered as a starting point for efforts determined to parameterize the line shape[6].

9.9   Conclusions

MINOS will characterize ν_μ disappearance, measure the parameters $(\sin^2 2\theta_{atm}, \Delta m_{23}^2)$ if oscillations exist and search for the sub-dominant $\nu_\mu \to \nu_e$ and $\nu_\mu \to \nu_s$ modes. These experimental goals require that the absolute response to muons, electrons and hadronic showers be known to approximately 5%. The CalDet program was conduced in order to provide an anchor for the neutrino energy reconstruction by measuring the response to single pions, protons, electrons and muons with well known momenta.

Pions and protons were identified with the Čerenkov and time of flight systems and, in addition, pions were distinguished from muons using the procedure outlined in Ch. 8.3.1. The detector response was defined as the measured signal, presented here in MIPs, per unit of available energy. In this work, the measured signal was characterized as the mean of the hadronic signal distributions, examples of which are shown in Fig. 9.18-9.22. The mean was calculated by ignoring the small number of low energy events with zero response, and a correction was applied for energy lost upstream of the detector. The measurement uncertainty on each response point was estimated from the repeatability of the electron response measured in multiple runs collected in 2003. The response curves were parameterized with second and third order polynomials

---

[6]As an example of such an effort, a more crude parameterization of the line shapes was used in the past for fast Monte Carlo calculations.

$$\begin{aligned} S(E) &= 0.10 + 50.52E + 0.172E^2 & (\pi^+) \\ S(E) &= 1.20 + 44.72E + 1.69E^2 - 0.100E^3 & (\pi^-) \\ S(E) &= 9.80 + 45.34E + 0.421E^2 & (p) \end{aligned}$$

where E is the available energy in GeV and S is the mean signal in MIPs. The quality of the parameterization was judged by the ability of regions $\pm 1\%$ and $\pm 2\%$ about the best fit curve to contain the data. Details of the fitting procedure were shown in Tab. 9.1 and Fig. 9.10-9.11.

In the 1-3 GeV/c region, the detector response to negative pions was $\sim$ 7% smaller than the response to positive pions. The asymmetry decreased with the beam momentum and was not observed above 6 GeV/c. The asymmetry was also observed in the e/π ratio (Fig. 9.16). Although other experiments may have observed a similar effect [83, 84], the result was considered somewhat of a suprise. There is, however, no evidence to suggest that the asymmetry was due to a gross error in the data collection, calibration or event selection.

The pion and proton energy resolutions were fit to Eq. 9.2, with the results

$$\begin{aligned} \left(\frac{\sigma}{\mu}\right) &= (4.2 \pm 1.5) \oplus \frac{55.7 \pm 0.5}{\sqrt{E}}\% & (\pi^+) \\ \left(\frac{\sigma}{\mu}\right) &= (0.0 \pm 3.3) \oplus \frac{56.2 \pm 0.3}{\sqrt{E}}\% & (\pi^-) \\ \left(\frac{\sigma}{\mu}\right) &= (2.1 \pm 1.5) \oplus \frac{56.1 \pm 0.3}{\sqrt{E}}\% & (\pi^+, \pi^- \quad \text{combined}) \\ \left(\frac{\sigma}{\mu}\right) &= (4.2 \pm 1.4) \oplus \frac{56.6 \pm 0.6}{\sqrt{E}}\% & (p) \end{aligned}$$

The fits to the pion data were performed over the entire momentum range from 400 MeV/c to 10 GeV/c, but for protons the fits were restricted to the region above 1.5 GeV. Below 1.5 GeV the proton energy resolution was better than $1/\sqrt{E}$ scaling would indicate.

364

The response curves were presented in terms of the MIP units defined by the cosmic ray calibration procedure of Ch. 5.3. Though useful, the MIP unit explicitly depended on the calibration methodology and also implicitly depended, through dE/dx, on the cosmic ray energy spectrum. Since the energy spectrum varies between the detector locations, results derived in terms of CalDet MIPs are not portable. Stopping muons were used to derive a new energy unit, the MEU, so as to wrap the results presented here in a more portable package. Two definitions for the MEU were examined, one of which was used to derive a conversion between MIPs and visible energy of $0.734\,\mathrm{MeV}\ \mathrm{cm}^2/\mathrm{g}$ MIP.

Chapter 10

Hadronic Response in Neutrino Events

In each CC event at the Near and Far detectors MINOS will attempt to measure the energy of the incoming neutrino by reconstructing the muon momentum (p_μ) and the energy transferred to the target nucleus ($\nu = yE_\nu$), here labeled E_{had}). The muon momentum will be derived from the muon's range or from the curvature of its trajectory in the detector's magnetic field. The energy transfered to the target nucleus will appear as a hadronic shower with a composition that is similar, but by no means identical, to the showers observed with the CalDet. The energy of these neutrino induced hadronic showers will, in general, be carried by multiple hadrons and, as such, the detector response will be a convolution of the single particle response measured at CalDet.

As an example, consider a neutrino induced hadronic shower with $3\,\mathrm{GeV}$ of available energy carried by a number of charged pions and protons. A first expectation is that the measured signal in this scenario will be approx-

imately equal to the mean signal measured in single $3\,\mathrm{GeV}$ pion (or proton) events. That is, the response to neutrino induced showers is presumed to follow the single particle response. Figure 10.1 graphically displays the veracity of this assumption. The figure was constructed by simulating 50000 ν_μ charged and neutral current events in the CalDet, with interaction vertices that were restricted to a circular region $3\,\mathrm{cm}$ in radius and centered on the detector axis in plane eight. The NEUGEN3 code was used to model the neutrino interactions [88], and the flux was distributed as $1/E_\nu$ between 0.5 and $10\,\mathrm{GeV}$[1]. All other aspects of the simulation (physics settings, light output, cable lengths, etc.) were identical to the single particle simulations discussed previously. Only neutral current events were used to construct Fig. 10.1. The mean calorimeter signal is shown on the ordinate and the abscissa corresponds to E_{had} in the case of neutrino induced events but the available energy in the case of single particle events.

Figure 10.1 makes it clear that the response to neutrino induced hadronic showers does not precisely follow the single particle response. Continuing the example, at $3\,\mathrm{GeV}$ the response to single π^+ simulated with GCALOR was $51\,\mathrm{MIP/GeV}$ (see Fig. 9.1) but the response to neutrino induced showers was $55.8\,\mathrm{MIP/GeV}$, a $\sim 9\%$ difference. Part of the disrepancy is due to the production of π^0 and protons at the vertex rather than just $\pi^\pm$. The MINOS calorimeter has a larger repsonse to electrons (and by analogy to neutral pions) than it does to charged pions, and therefore the presence of π^0s in the final state (of the neutrino interaction) should cause the average signal to increase.

Figure 10.2 shows, as a function of E_{had}, the average fraction of the

---

[1]A $1/E_\nu$ flux results in a nearly flat energy spectrum. Technical problems frustrated efforts to use a more realistic beam spectrum (like the ones in Fig. 2.3).
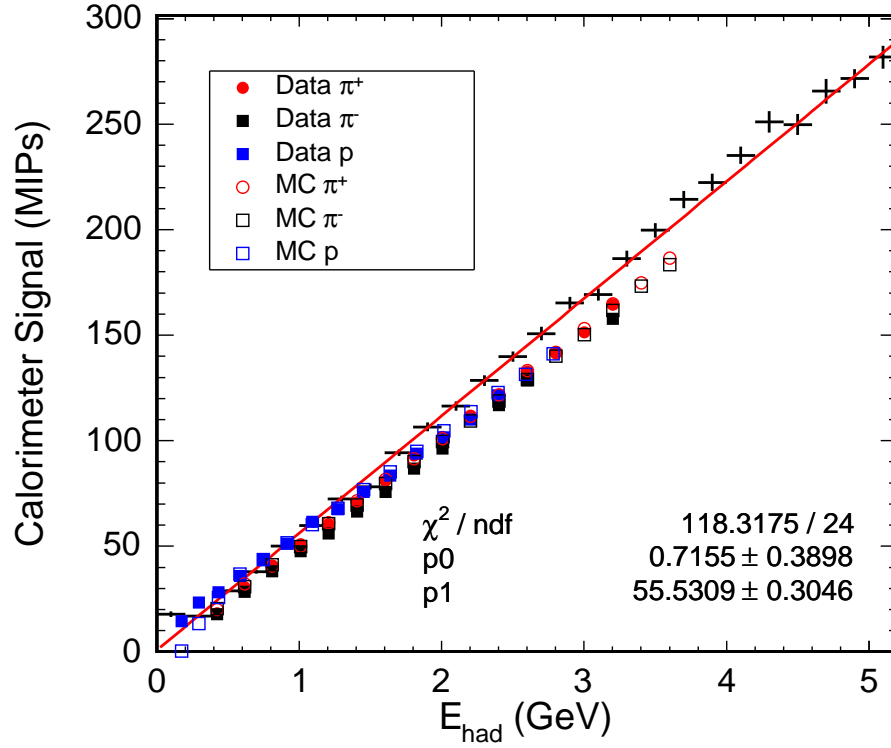
Figure 10.1: The calorimeter signal as a function of $E_{had} = yE_\nu$ for simulated NC events (crosses). GCALOR was used to model the hadronic interactions and the measured and simulated single particle response curves are shown overlaid. For the single particle data points the abscissa corresponds to the available energy.
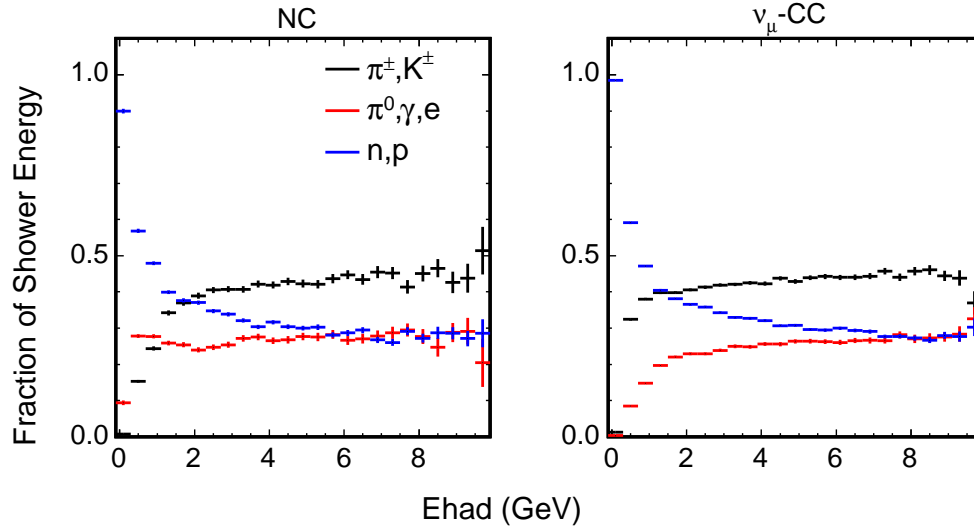
Figure 10.2: Fraction of shower energy carried from the vertex by nucleons, mesons and electromagnetic particles as a function of $E_{had} = yE_\nu$.

shower's available energy carried from the vertex by nucleons (n,p), charged mesons ($\pi^\pm, K^\pm$) and electromagnetic particles ($\pi^0, \gamma, e^\pm$). At 3 GeV approximately 41% of the shower energy is carried by charged pions, 32% by nucleons and 27% by electromagnetic particles, and, for the sake of argument, we will assume that the shower energy is carried by a single particle with 3 GeV available energy. In the simulation the e/π response ratio is approximately 1.27 and the p/π ratio (at 3 GeV) is approximately 1. Using this information, the respose to 3 GeV neutrino induced showers (R_ν) may be estimated in terms of the response to single pion events (R_π) as:

$$R_\nu = \left[\left(\frac{e}{\pi} \right) f_{em} + \left(\frac{N}{\pi} \right) f_p + f_\pi \right] \times R_\pi$$
$$= [1.27 \times 27\% + 32\% + 41\%] \times 51 \, \text{MIP/GeV}$$
$$= 54.7 \, \text{MIP/GeV}$$

369

The response calculated above is to be compared to 55.8 MIP/GeV, the number directly determined from Fig. 10.1.

The brief discussion above was presented to highlight one of the additional complexities that MINOS must confront when dealing with neutrino induced hadronic showers. The result was encouraging for such a simple calculation but must be considered as an approximation. For example, although the fraction of energy carried by nucleons includes both protons and neutrons, the calculation only recognized protons. As another example, the momentum spectra of various shower particles are presented in Figure 10.3, and Fig. 10.4 displays the average number of different shower particles and their average momentum as a function of E_{had}. The two figures make it clear that, even in multi-GeV neutrino induced showers, most of the shower energy is carried by a number of low energy shower particles, rather than single particles having an energy equal to the shower energy.

The computation discussed above may be repeated using Fig. 10.4 instead of Fig. 10.2. Showers at 3 GeV contain, on average, 1 nucleon, 2 charged pions and 1.2 π^0s. The average (available) energy carried by each particle was 1 GeV (nucleons) and 0.62 GeV (pions). At these energies, the mean signal expected for single charged pions was 31.6 MIP, for single protons 57.5 MIP, for neutrons 48.9 MIP, and for neutral pions 40.2 MIP. The expected signal is then

$$
\begin{aligned}
S_\nu &= n_p \times S_p + n_n \times S_n + n_\pi \times S_\pi + n_{em} \times S_{em} \\
&= 0.5 \times 56.0 + 0.5 \times 48.9 + 2 \times 31.6 + 1.2 \times 40.2 \quad \text{MIP} \\
&= 164.6 \, \text{MIP} \quad \text{or} \quad 54.9 \, \text{MIP/GeV}
\end{aligned}
$$

Here S_p, S_n, S_π, S_{em} and n_p, n_n, n_π, n_{em} denote the average signal and multi-
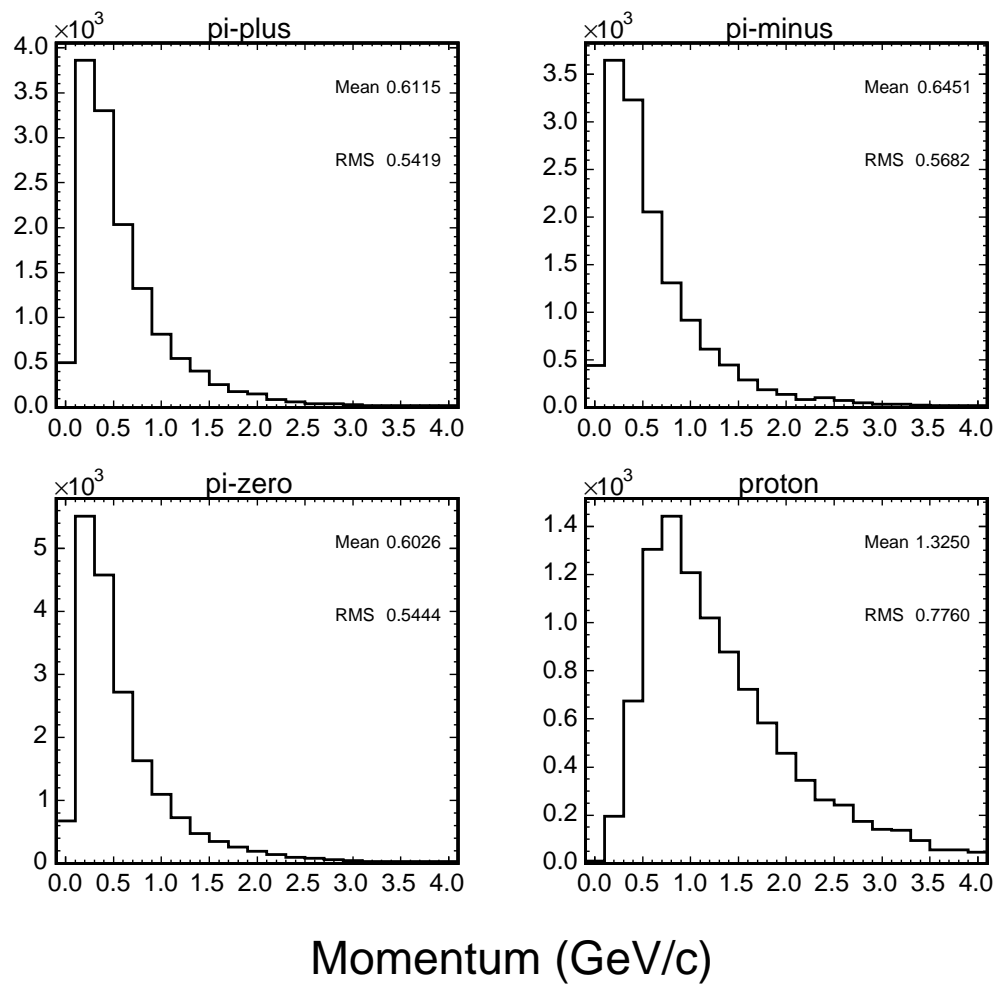
Figure 10.3: Momentum spectra for a few shower particles. The spectra were integrated over the entire 0.5 to 10 GeV neutrino energy range.
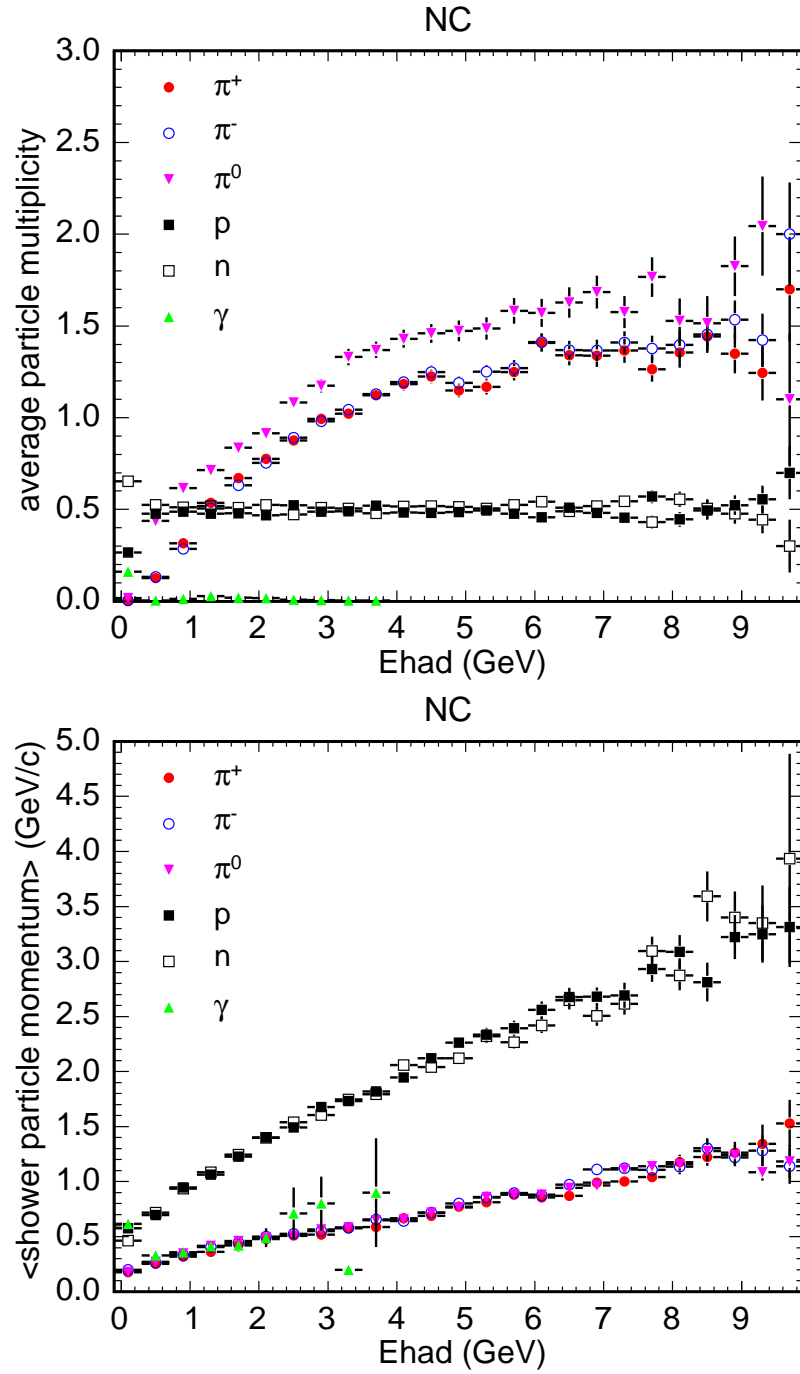
Figure 10.4: The average shower particle multiplicity (top) and momentum (bottom) as a function of $E_{had} = yE_\nu$.

plicity of protons, neutrons, pions and electromagnetic particles (mostly π^0). The actual detector response was $55.8\,\mathrm{MIP/GeV}$.

The calculations above were intended to demonstrate the way in which the detector response to neutrino induced hadronic showers is related to the response to single particle events. A number of factors, such as any dependence of the response on the angle of the shower particles, were ignored in the discussion. Because the comparison was made to simulated neutral current events, the numeric values used for the single particle response were taken from the Monte Carlo rather than the data. MINOS's task will be to construct a response curve, like the one shown in Fig. 10.1, using the predicted shower particle multiplicities, angular distributions and energies, along with the measured single particle curves presented in Ch. 9. The task is obviously non-trivial.

Finally, the discussion here dealt only with neutral current events so as to avoid complications regarding the muon signal, which must be subtracted out before the hadronic shower energy can be estimated. The topic of muon subtraction brings to the forefront a more general issue, which is that the signal attributed to hadronic showers, and hence the response, will depend on the reconstruction methods used. This seems a more particular issue for the Near detector, in which the relatively high rate will result, in some cases, in leakage between individual events. In addition, the hadronic energy in some event topologies may be best reconstructed by considering quantities other than, or in addition to, the signal. For example, as discussed in Ch. 9, some low energy protons range out in the detector and for those events it seems advisable to consider the proton range in addition to the signal when estimating the hadronic energy. Most events which contain a proton also contain a number

373

of charged and neutral pions in the hadronic shower, obscuring the proton track and any attempt to reconstruct its range. On the other hand, Fig. 10.5 shows two quasi-elastic events that contain clean proton tracks for which the range can be estimated. Events like these are probably the only ones in which MINOS will be able to completely reconstruct the final state.

In summary, the response to neutrino induced hadronic showers is not expected to follow the response for single particles. Instead, the signal measured from such showers must be considered a convolution of the signals from charged pions, nucleons and electromagnetic particles. The CalDet program was undertaken to measure the detector's response to single hadrons, muons and electrons, thereby providing (at least part of) the knowledge needed to reconstruct the energy of hadronic showers in the Near and Far detectors.
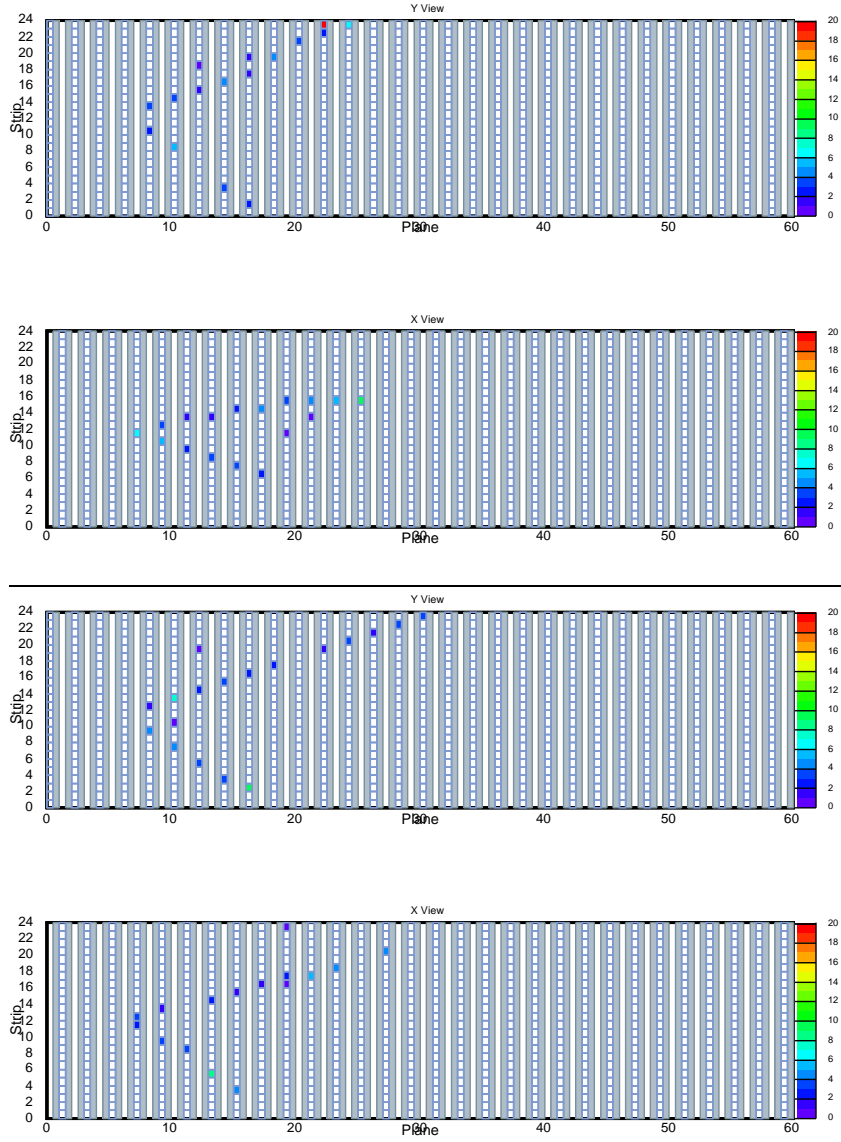
374

Figure 10.5: An example of two charged current quasi-elastic events in which the recoil proton can be rather easily reconstructed. The incoming neutrino in the upper figure had an energy of 4 GeV and created a 2.8 GeV/c proton (upper track in both views) and a 1.9 GeV/c muon. In the lower figure, the incoming neutrino had an energy of 2.9 GeV, and created a 2.1 GeV/c muon (upper track in both views) and a 1.4 GeV/c proton. Events like these are likely to be the only ones in which MINOS can reconstruct the exclusive final state.

Chapter 11

Conclusions

MINOS, the Main Injection Neutrino Oscillation Search, will use a neutrino beam produced by the Neutrinos at the Main Injector (NuMI) facility at Fermi National Accelerator Laboratory (Fermilab) to study neutrino flavor transformations over a long baseline. The composition of the beam will be measured with a Near detector located at Fermilab and a Far detector located in the Soudan Underground Laboratory in northern Minnesota. The Near and Far detectors are iron-scintillator tracking-sampling calorimeters and were constructed so as to respond in the same way. The two detectors feature relatively fine grained transverse and longitudinal segmentation and are magnetized so as to allow the momentum and charge sign of muons produced in charged current interactions to be determined.

MINOS will attempt to conclusively demonstrate the mechanism responsible for the ν_μ disappearance observed in atmospheric neutrino experiments and, in the case of oscillations, make a precision measurement of the parameters $(\sin^2 2\theta_{atm}, \Delta m_{23}^2)$. In addition, MINOS will search for the sub-dominant $\nu_\mu \to \nu_e$ mode and attempt to set a tighter constraint on

$\nu_\mu \to \nu_s$. The experimental goals of MINOS require that the detector response to hadrons, muons and electrons be known with an absolute precision of 5% so that the neutrino energy can be accurately reconstructed. Moreover, the experiment will classify events as muon neutrino charged current (ν_μ-CC), neutral current (NC) or electron neutrino charged current (ν_e-CC) based on the topological pattern of hits induced in the detector. The classification efficiencies will be determined, in large part, on the basis of Monte Carlo simulations of neutrino interactions in the MINOS detectors. The accuracy of the classification efficiencies then depends crucially on the ability of the Monte Carlo to correctly simulate muon tracks and electromagnetic and hadronic showers.

To determine the topological and signal response to hadron, muon and electron induced events, MINOS constructed the CalDet, a smaller version of the Near and Far Detectors. The CalDet was also used to verify MINOS's calibration procedures and compare the performance of the Near and Far detector readout schemes. In addition, the CalDet data were used to confront the Monte Carlo in the relatively simple case of single particles with a well known momentum and identity.

The CalDet was exposed to the T11 and T7 test-beams in the CERN PS East hall during the years 2001-2003. The beamlines provided a mixed sample of hadrons, electrons and muons with a tunable central momentum between 0.2-10 GeV/c. Time of flight and Čerenkov counters were used to identify the particle initiating each event. The TOF resolution and Čerenkov efficiencies were sufficient to define electron, proton and combined pion and muon, samples with negligible cross contaminations. The worst contaminations were a 2.3% leakage of electrons into the pion sample at 10 GeV/c and a 3.5% con-

tamination of the pion sample by kaons at 3.6 GeV/c in T11.

The CalDet was the first detector constructed by MINOS and, at the time of this writing, was the only detector to fully exercise the calibration chain. A blue LED based light injection system was used to measure the gain of each channel, track variations in those gains over time and establish the response of the phototubes and electronics over the range of light levels relevant to MINOS. The gain variations, which were largely caused by temperature fluctuations in the experimental hall, were tracked with a 0.5% accuracy. Cosmic rays were used to correct for differences in light output between strips, attenuation in the fiber optic readout cables, and variations in the quantum and light collection efficiency of the phototubes. After applying the cosmic ray calibration, beam muons were used to demonstrate that plane-to-plane variations in the response were approximately 2%.

The optics of the T11 and T7 beamlines were studied with the DECAY-TURTLE program. The modeling was undertaken to understand the behavior of the beam for different magnet and collimator settings and to predict the muon composition and momentum spectrum. A GEANT based simulation of the downstream portion of the beamline was developed, initially to predict the energy lost by beam particles in time of flight and Čerenkov counters and the air in the experimental hall. The beamline simulation was later extended to extract events from TURTLE prior to the most upstream Čerenkov counter and propagate them to the detector. In addition to predicting the energy loss, the GEANT simulation was used to improve knowledge of the muon content and estimate the trigger acceptance.

The FLUKA 2003 code was used to characterize the particles produced by a 24 GeV/c proton beam impacting the T11 and T7 targets. The yields at

378

the target were corrected for π and K decays and trigger acceptance to predict the beam composition at CalDet. The predicted compositions agreed with the data to within 10% at momentum settings below $6\,\text{GeV/c}$[1]. The target modeling was used to estimate that the kaon contamination of the pion and proton was less than 3% after accounting for the particle identification criteria.

The topology of pion and proton induced events was studied over a 0.4-$10\,\text{GeV/c}$ momentum range. Single particle events were simulated in the CalDet with the MINOS experiment's GEANT3 based detector Monte Carlo, GMINOS. GMINOS simulated particle interactions in the detector and recorded energy deposited in the scintillator strips. The composition and structure of the CalDet, which differed slightly from the Near and Far detectors, was carefully accounted for. Events were read in from the GEANT beamline simulation discussed above. The two hadronic shower codes most commonly used with GEANT3, GHEISHA and GFLUKA, were found to be in poor agreement with the data and are not recommended for use by MINOS in their current implementations. Instead, pion and proton events were generated at all momentum settings, both polarities and in both beamlines with the GCALOR shower code and at approximately half of the settings with the SLAC-GHEISHA code. Muon events were also generated at each setting and polarity.

Events output by GMINOS were read into the MINOS offline framework in which the DetSim and PhotonTransport packages were used to model the active detector response. All relevant effects, such as cable attenuations, phototube response and inter-pixel cross talk were simulated. The light output of the scintillator strips and the conversion from photoelectrons to MIPs was tuned to the data with $1\,\text{GeV/c}$ electrons.

---

[1]Here, 10% agreement is meant in the absolute sense, as in $60 \pm 10\%$

The pion sample contained a background of muons. A linear discrimination procedure was developed to separate pions and muons on the basis of topology. Pion events were characterized by energy depositions inconsistent with a minimum ionizing particle, isolated hits larger than a ~ 2 photoelectrons, large differences in activity between adjacent planes and between the horizontal and vertical views of the detector, and multiple strips per plane with a signal larger than a few photoelectrons. The discriminant procedure was tuned and its efficiency was estimated using events simulated with GCALOR. Above $1.0\,$GeV/c pions and muons were classified with larger than 90% efficiency but the ability to seperate pions and muons decreased with the beam momentum.

The MINOS detectors were not optimized to measure hadronic events in the $1\,$GeV/c range and below. Low energy pion events had few large hits and little information that distinguished them from muons. In addition, the muon momentum momentum spectrum had a long off-momentum tail which descended to the kinematic limit of 57% of the nominal beam setting. Events in that tail made the discrimination task significantly more difficult since a simple cut on the range could not be used. Pions which interacted but produced little visible shower energy were the most likely to be misidentified as muons. Muon tracks in which there was a large Landau fluctuation were often identified as pions. The MINOS Near and Far detectors will have to confront similar problems.

The discriminant procedure was used to count the number of muons. After correcting for the efficiency, the composition of muons was found to be much larger than the GEANT beamline simulation predicted. Pions and muons could identified with little ambiguity at high energies but, even there,

the muon content was about a factor of two higher than the predictions. At high energy, the muon content established with simple cuts was in good agreement with the content determined from the discriminant procedure. In addition, the muon content was found to vary significantly between runs repeated at the 9 and 10 GeV/c settings. Identical selection criteria were used for runs taken at the same momentum setting in the T11 and T7 beamlines; At 2 GeV/c (and positive polarity) the content disagreed by about a factor of two between T11 and T7. The simulation predicted that the beamlines would have identical muon content. The cause of these discrepancies is not understood but is hypothesized to be due to differing beam conditions. A better understanding of the muon content will require a detailed simulation, in GEANT or FLUKA, of the entire beamline so as to include interactions in collimators, magnet apertures and beam-pipe walls.

A variety of topological quantities were used to compare the data and Monte Carlo. The results of the comparison indicate that, while neither GCALOR nor SLAC-GHEISHA perfectly modeled the data, positive pions and protons at momentum settings below 6 GeV/c were best simulated with GCALOR; SLAC-GHEISHA generally predicted too little activity in the detector. Negative pions were observed to produce somewhat less activity in the detector than positives and in that case GCALOR cannot be so strongly preferred over SLAC-GHEISHA. For momentum settings above 6 GeV/c the GCALOR code began to gradually over-predict the detector response. The behavior may be due to the use of GFLUKA, which was called by GCALOR with a frequency proportional to the energy of the hadronic interaction. In the future it should be possible to replace the calls to GFLUKA with calls to GHEISHA.

Studies of the muon range found a discrepancy between the data and the simulation. Part of the difference was due to a deficiency in GEANT's treatment of the density effect which caused the muon dE/dx to be overestimated by about 2%. Even after the deficiency was corrected the range of on-momentum muons was 3–4% longer than the simulation predicted. The discrepancy could be consistent with a shift in the beam momentum or a mismodeling of the muon flux but additional studies are needed before any firm conclusions may be drawn.

The detector response to pions and protons was parameterized as

$$
\begin{aligned}
S(E) &= 0.10 + 50.52E + 0.172E^2 & (\pi^+) \\
S(E) &= 1.20 + 44.72E + 1.69E^2 - 0.100E^3 & (\pi^-) \\
S(E) &= 9.80 + 45.34E + 0.421E^2 & (p)
\end{aligned}
$$

where S is the signal in MIPs and E denotes the available energy in GeV. The response to positive and negative pions was found to differ by $\sim 7\%$ in the 1-3 GeV/c region, with positives having a higher response. The asymmetry, which was observed in both beamlines and with simple cuts on the event length, decreased with the beam momentum and disappeared above 6 GeV/c. A careful scrutiny of the data and beam conditions was conducted and other experiments may have observed a similar effect [83, 84]. One hypothesis is that the discrepancy is related to the proton/neutron imbalance in iron coupled to the $\pi^+ + n \to \pi^0 + p$, $\pi^- + p \to \pi^0 + n$ and similar charge exchange reactions.

Beam muons were used to derive a calibration constant which may be used to to relate measurements made in MIPs to energy deposited in the scintillator. The value of the constant is

$$
0.734 \, \frac{\text{MeV cm}^2}{\text{g MIP}}.
$$

This result should be considered as preliminary since muons were not tracked,

the signals in each plane were summed, and multiple scattering effects were ignored.

The pion and proton energy resolutions were described by

$$
\begin{aligned}
\left(\frac{\sigma}{\mu}\right) &= (4.2 \pm 1.5) \oplus \frac{55.7 \pm 0.5}{\sqrt{E}}\% \quad (\pi^+) \\
\left(\frac{\sigma}{\mu}\right) &= (0.0 \pm 3.3) \oplus \frac{56.2 \pm 0.3}{\sqrt{E}}\% \quad (\pi^-) \\
\left(\frac{\sigma}{\mu}\right) &= (2.1 \pm 1.5) \oplus \frac{56.1 \pm 0.3}{\sqrt{E}}\% \quad (\pi^+, \pi^- \quad \text{combined}) \\
\left(\frac{\sigma}{\mu}\right) &= (4.2 \pm 1.4) \oplus \frac{56.6 \pm 0.6}{\sqrt{E}}\% \quad (\text{p})
\end{aligned}
$$

where the $\oplus$ indicates the two terms should be added in quadrature. The expression applies to pions over the entire range but only above $1.5\,\text{GeV}$ for protons. Below $1.5\,\text{GeV}$ protons lost much of their energy via ionization and the resolution was better than the $1/\sqrt{E}$ scaling would imply.

The task ahead for MINOS is to utilize the measured pion and proton response curves to parameterize the detector response to neutrino induced hadronic showers. Since the shower energy will be carried by multiple particles there is no simple relationship between the single particle responses measured with CalDet and the shower response. Instead, signals observed by the Far and Near detectors will correspond to a convolution of signals from individual hadrons, including, in contrast to the CalDet, π^0s and other electromagnetic particles produced at the vertex. Construction of the shower response curve is likely to be a non-trivial task.

The CalDet program, a small experiment in its own right, was a major effort of the MINOS collaboration. As the first detector constructed by MINOS, CalDet was a crucible in which nearly seven years of research and development finally confronted reality. Many problems were initially encoun-

tered and solved at the CalDet, smoothing the way for the construction and operation of the Near and Far detectors. A veritable gold mine of data was collected during the three year operating period. All of it was surveyed but much remains unexcavated. The CalDet data have already demonstrated their worth and their value is only expected to grow with time. The author was pleased to have been a part of the effort.

Appendix A

Selected CalDet Events

A selected sample of CalDet events is shown on the next few pages. Except where noted, all events were accepted into the final analysis. Beam particles enter the detector from the left, within $\sim 10\,\mathrm{cm}$ of the detector center. The detector consists of sixty $1\,\mathrm{cm}$ thick scintillator planes backed by $2.50\,\mathrm{cm}$ iron absorber plates. Each scintillator plane contains twenty-four strips, visible in the figure as small cells. Successive scintillator planes are rotated by $\pm 90°$, permitting three dimensional track reconstruction. In each of the figures, both the horizontal (lower) and vertical views are shown. The aspect ratio is approximately correct. Cells are colored according to the observed signal in MIPs, shown on the color scales on the right. Unless noted, only hits with a signal larger than $1.5\,\mathrm{PEs}$ on one of the ends are shown. The cut removes approximately 85% of single-photoelectron cross talk hits and 7-12% of minimum ionizing hits.
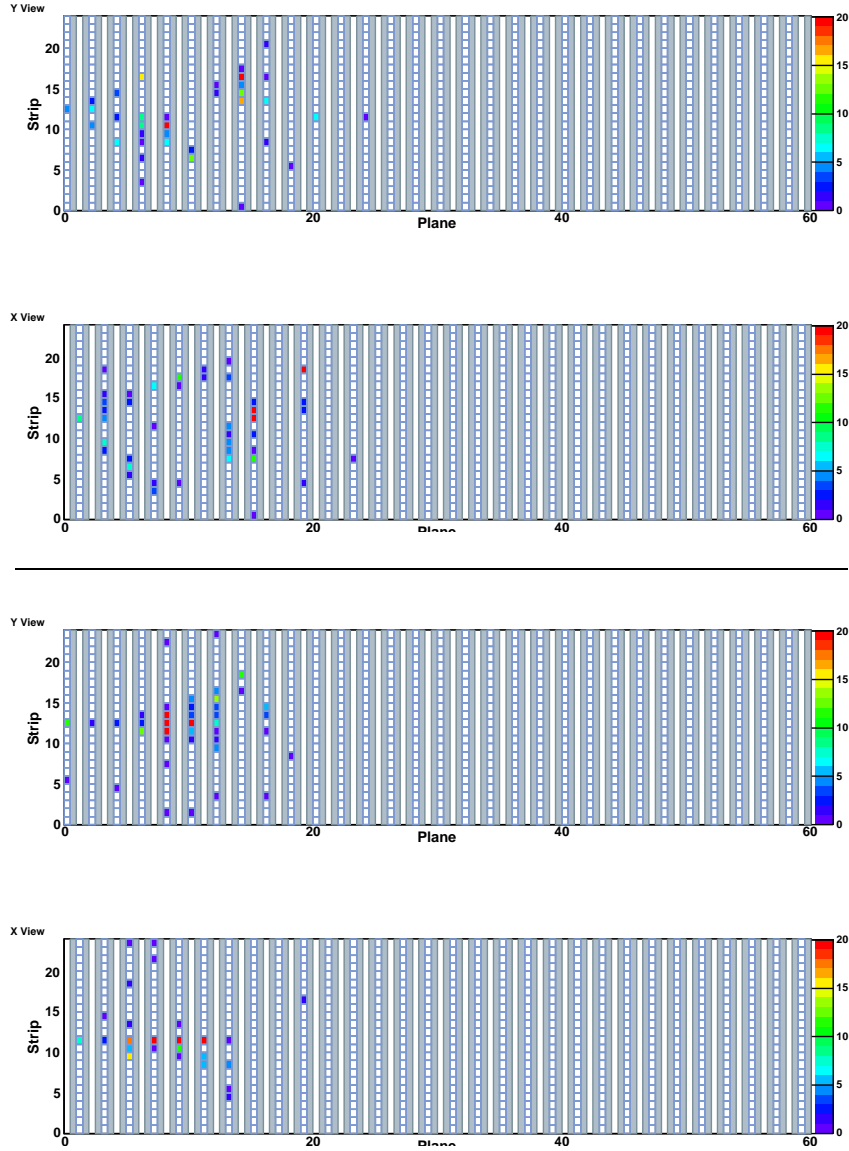
Figure A.1: Two 8.0 GeV/c pions.
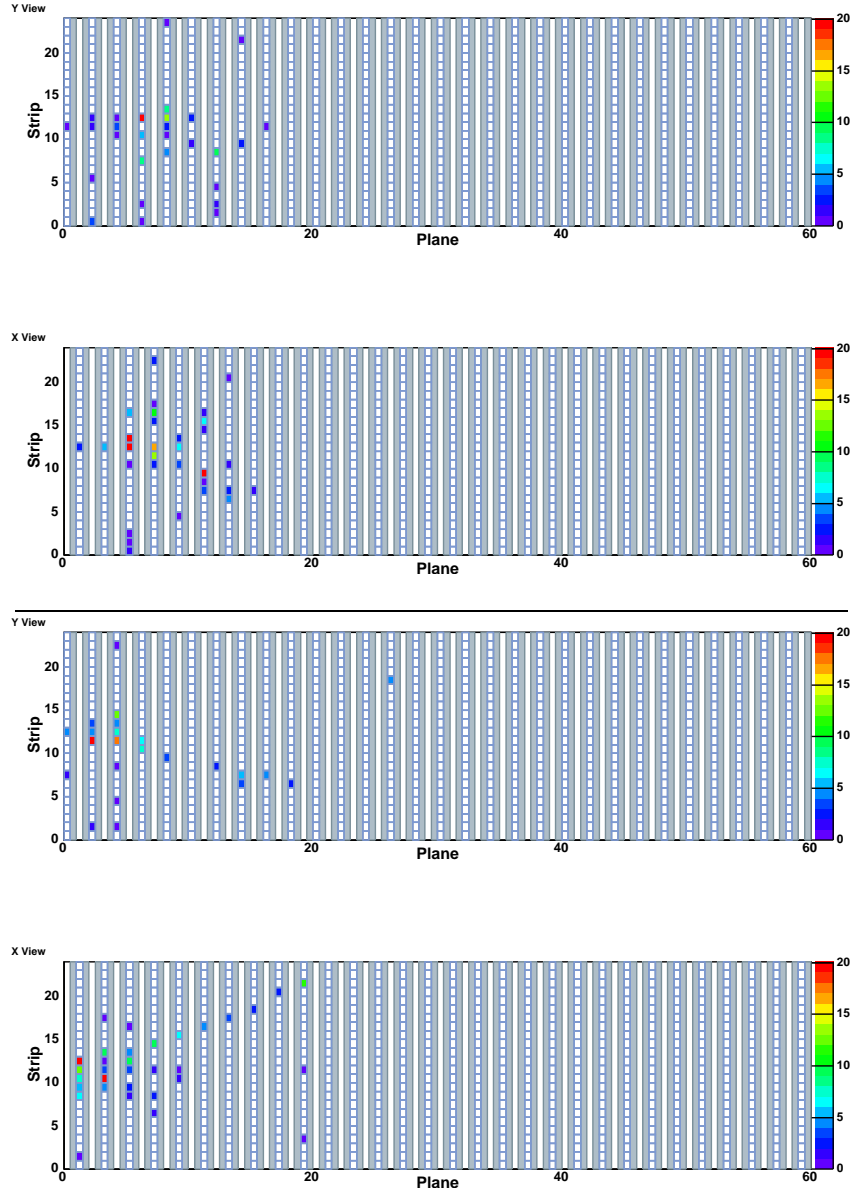
Figure A.2: Two 5.0 GeV/c pions.
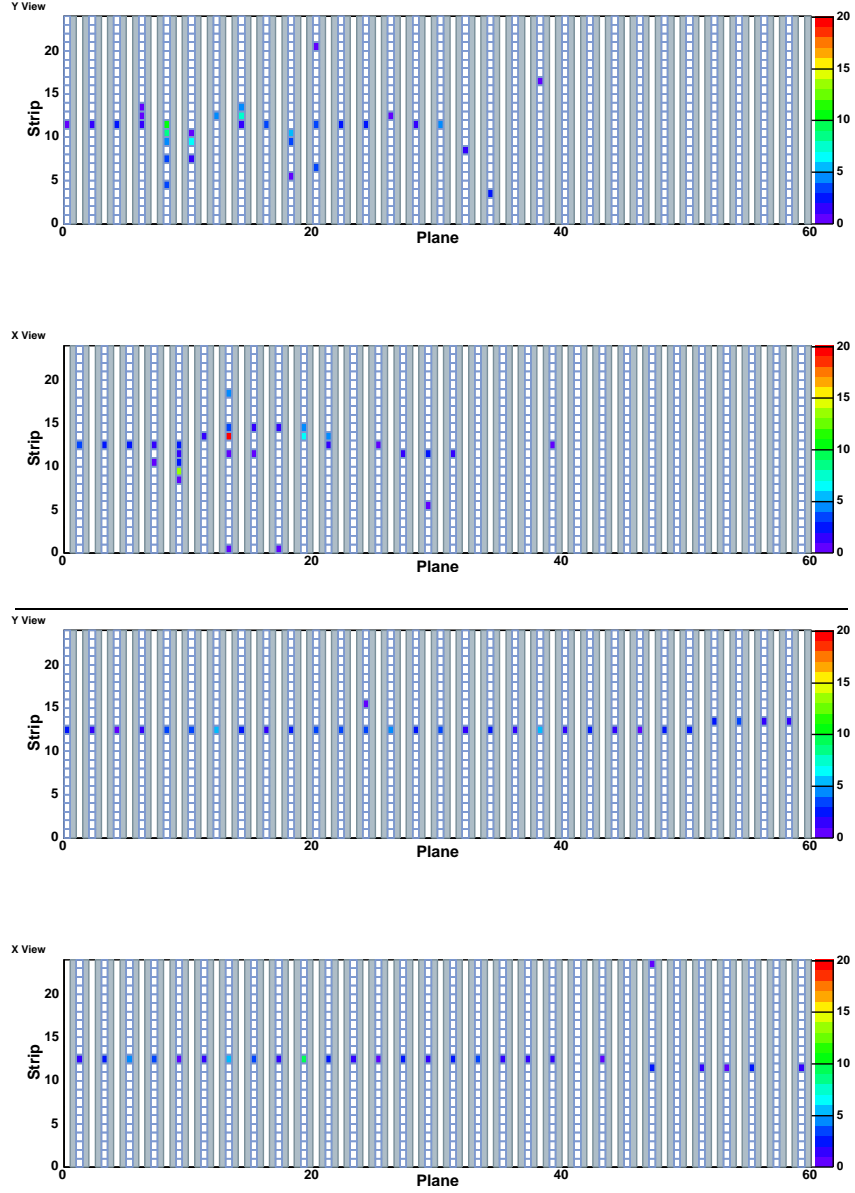
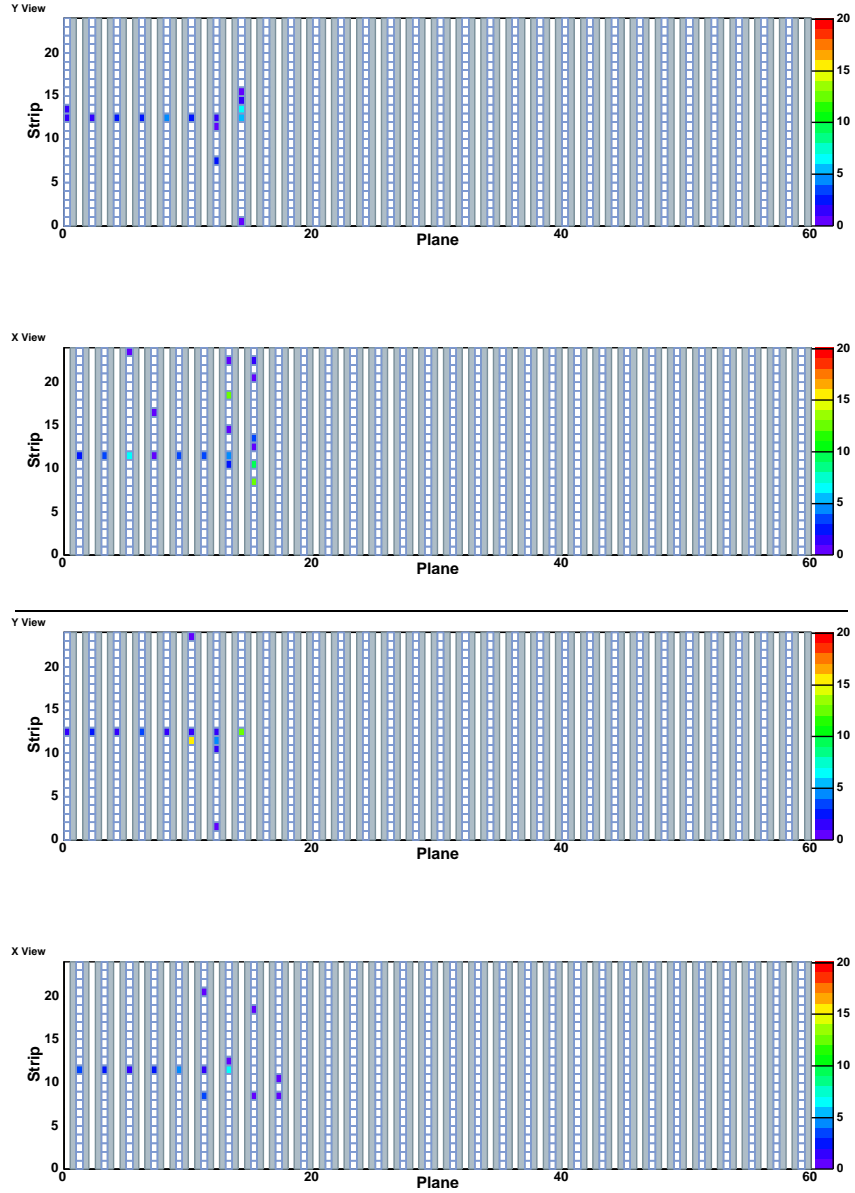Figure A.3: A 5.0 GeV/c pion (top) and a muon (bottom).
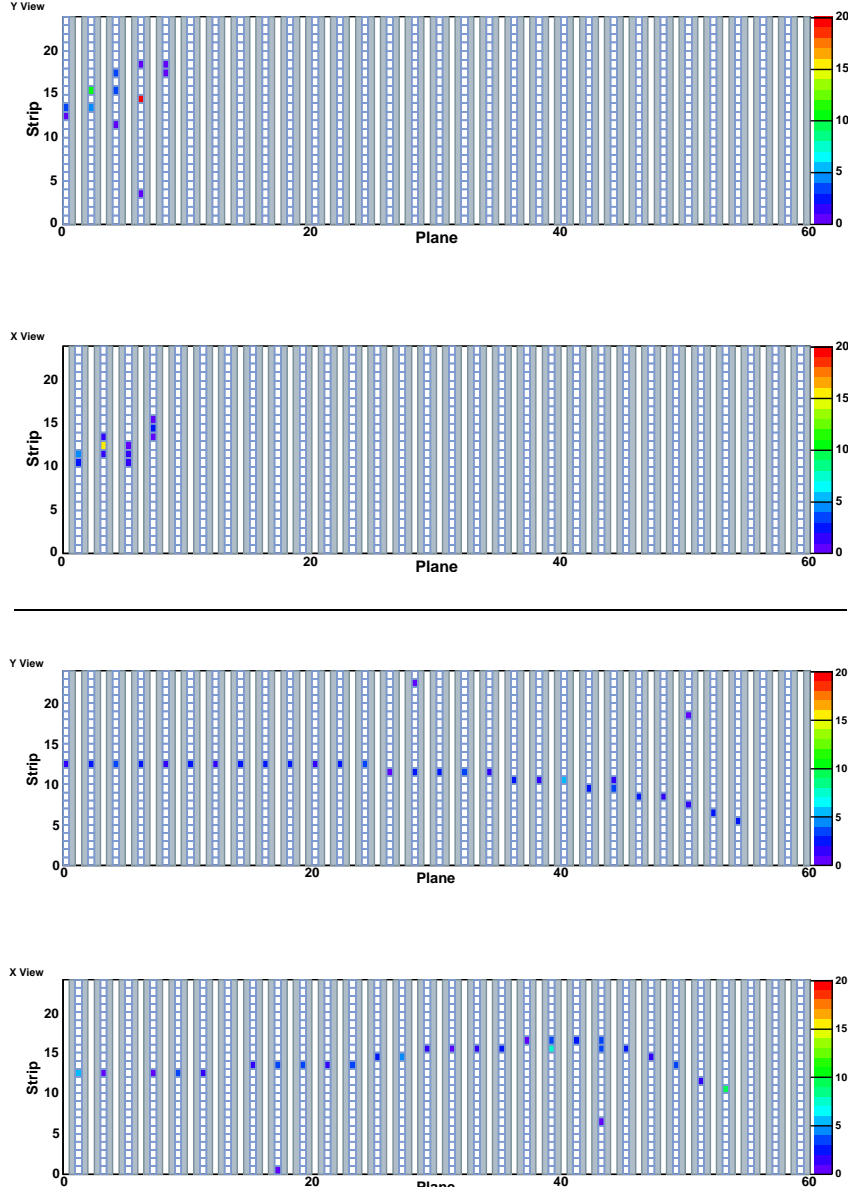
Figure A.4: Two 2.0 GeV/c pions.

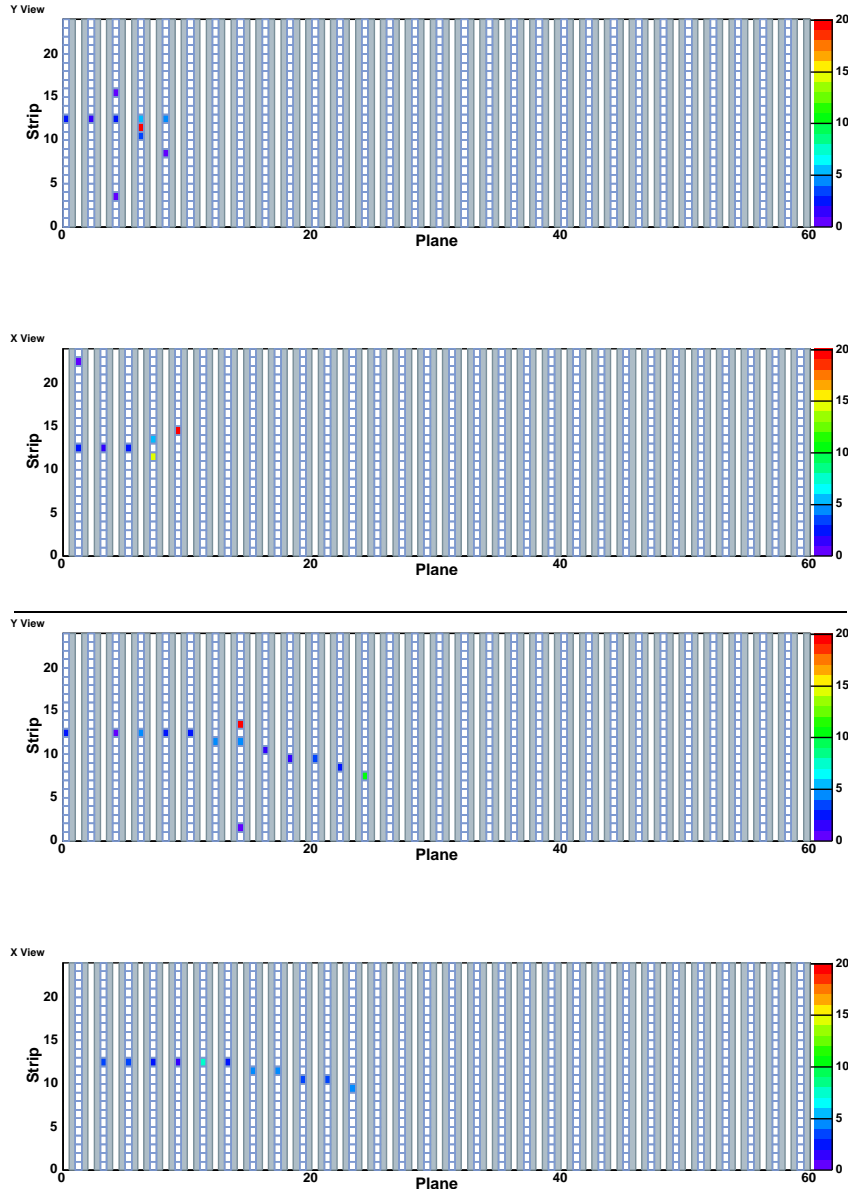Figure A.5: A 2.0 GeV/c pion (top) and muon (bottom). Judging by the range, the muon was nearly on-momentum.

Figure A.6: Two 2.0 GeV/c protons. The lower event is interesting, as a clear track is visible but there is a strip with 20 MIPs slightly off the track, making the track very inconsistent with a muon. The majority of events look more like the upper figure.

391
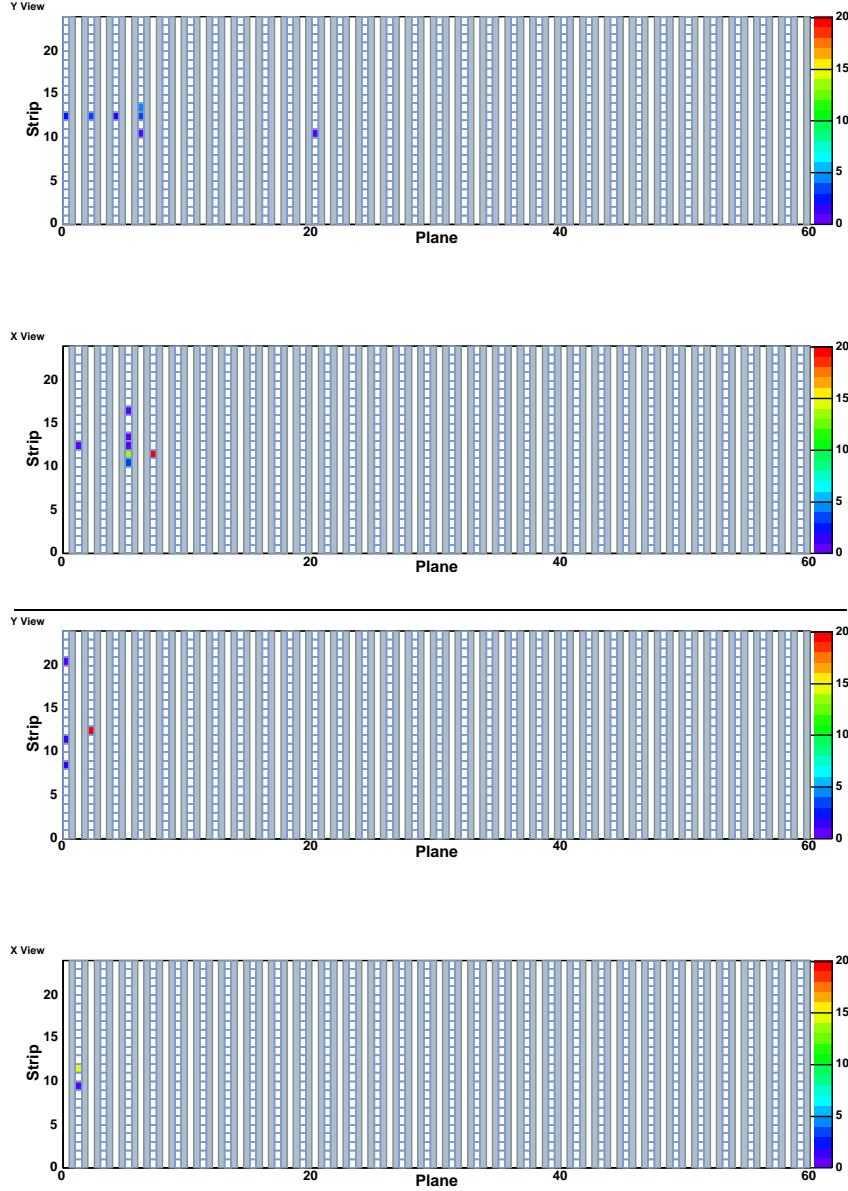
Figure A.7: Two $1.0\,\text{GeV}/c$ pions. Pion events at $1\,\text{GeV}$ are characterized by large fluctuations in the activity induced in the detector.
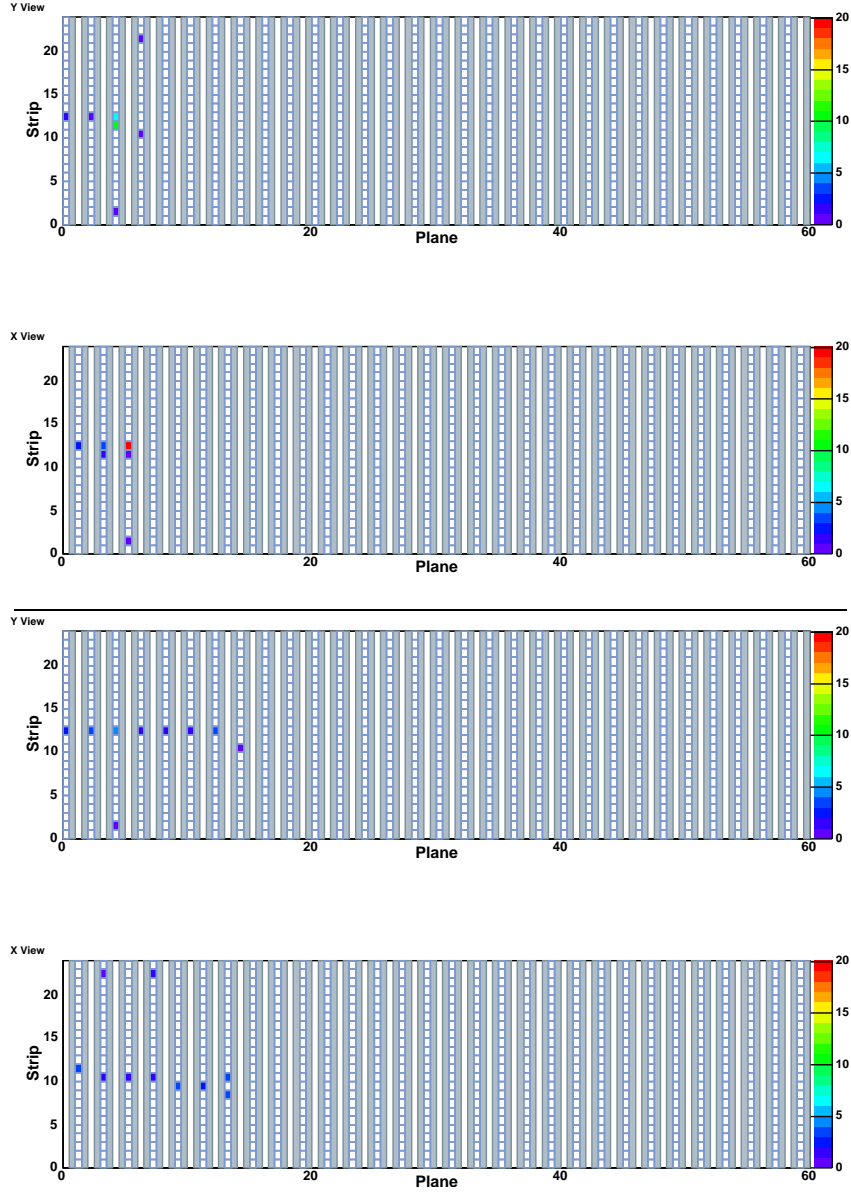
Figure A.8: A 1.0 GeV/c pion (top) and a muon (bottom). The identification of the lower event as a muon is not unambiguous: some Monte Carlo pions have a similar appearance. Judging by the range, the muon has a momentum of approximately 530 MeV/c. The additional hit at the end of the track in the x-view is most likely due to cross talk.
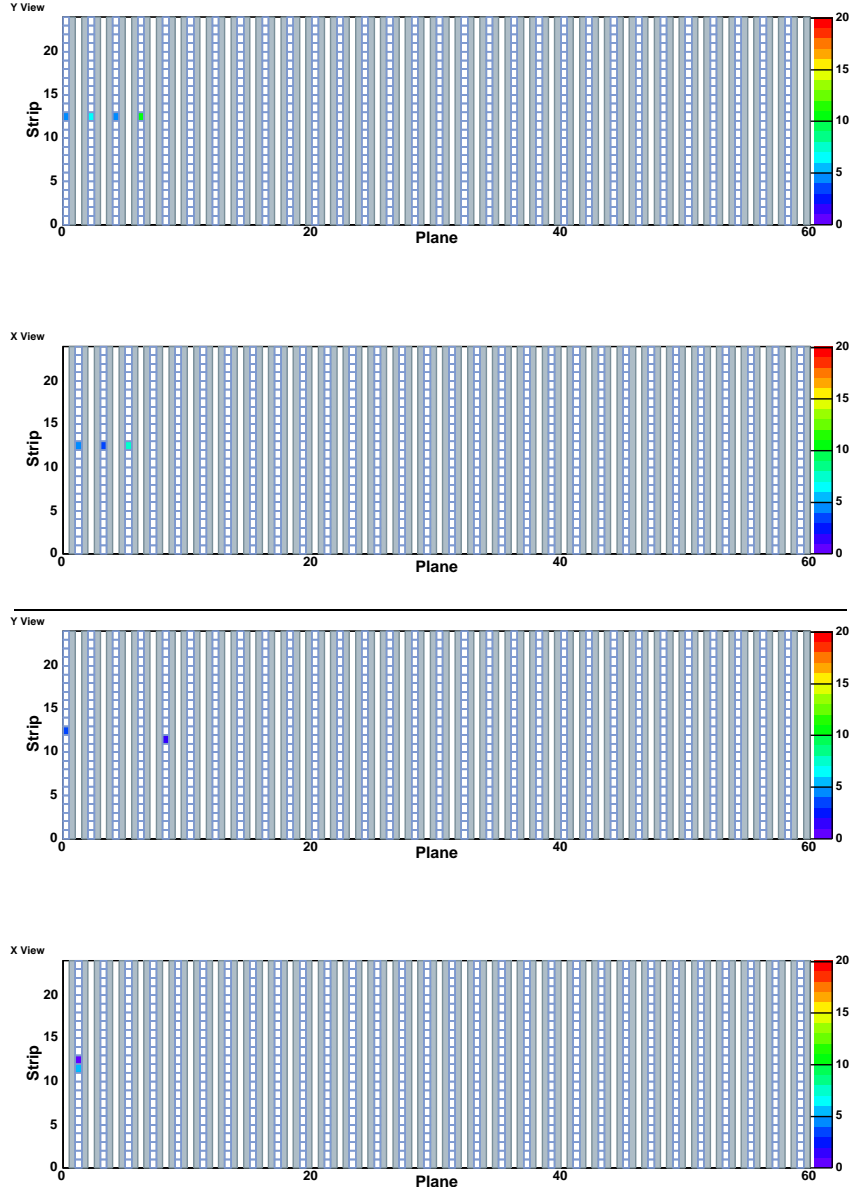
Figure A.9: Two 1.0 GeV/c protons. Many 1 GeV/c protons range out without interacting hadronically, leading to events like the one shown in the upper figure. MINOS should be able to identify such protons in quasi-elastic events. The lower figure shows an event in which MINOS has little hope of extracting any meaningful information.
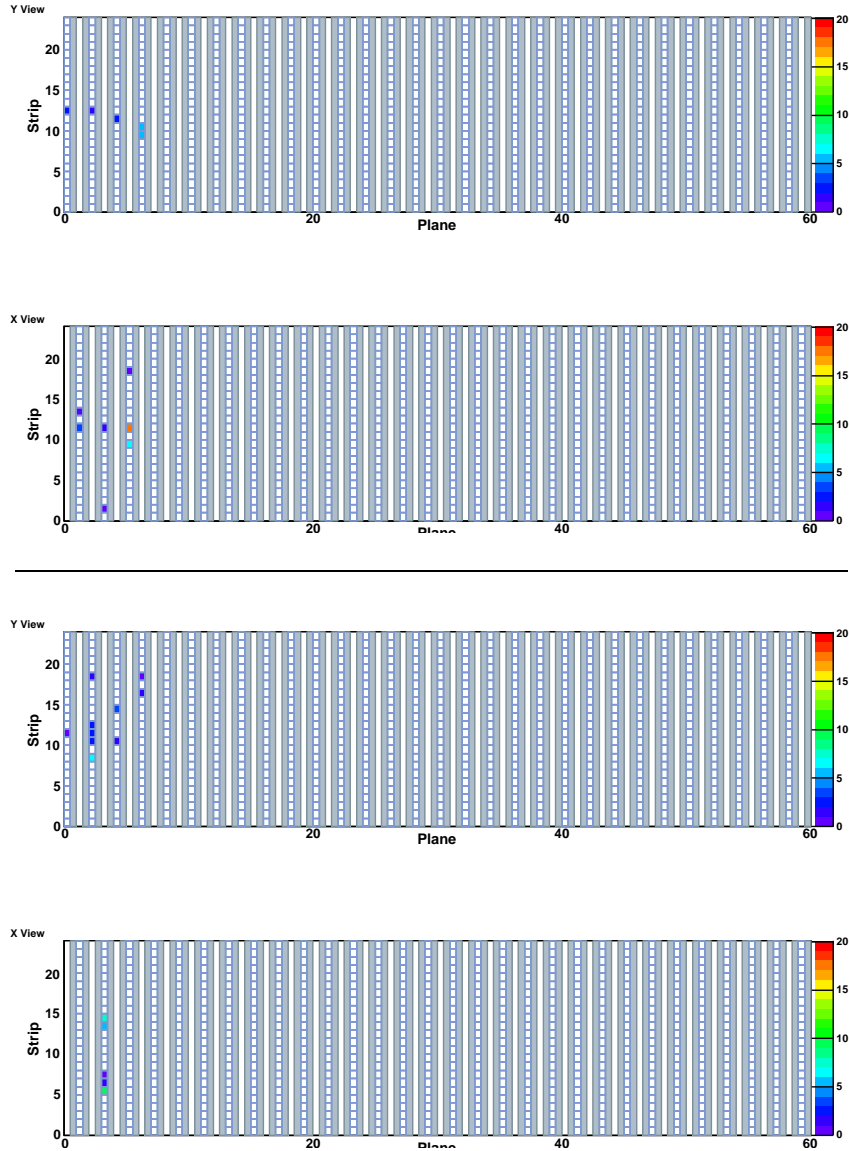
Figure A.10: Two 600 MeV/c pions. These events are unambiguously pions, but many events at 600 MeV/c are not so easily identified.
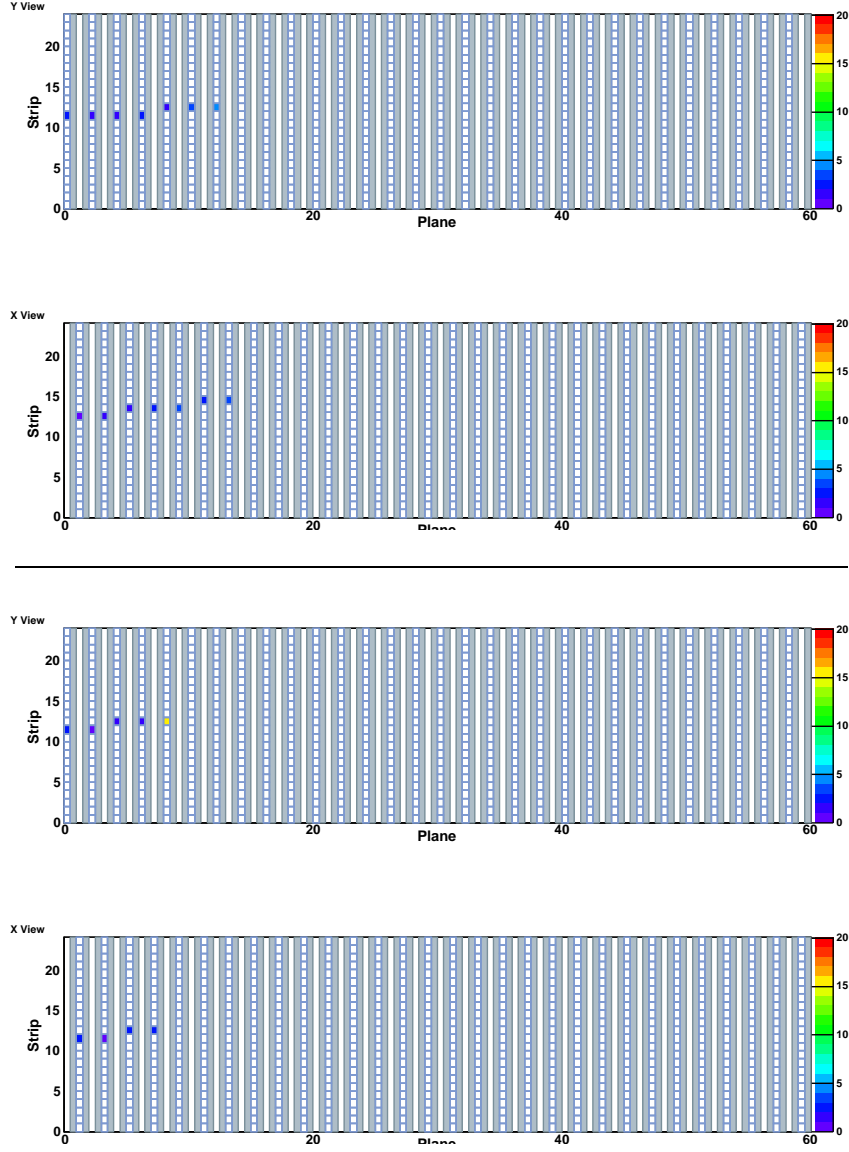
Figure A.11: A 600 MeV/c muon (top) and pion (bottom). The lower event was identified as a pion due to the 15 MIP signal at the end of the track. The identification is not without ambiguity.
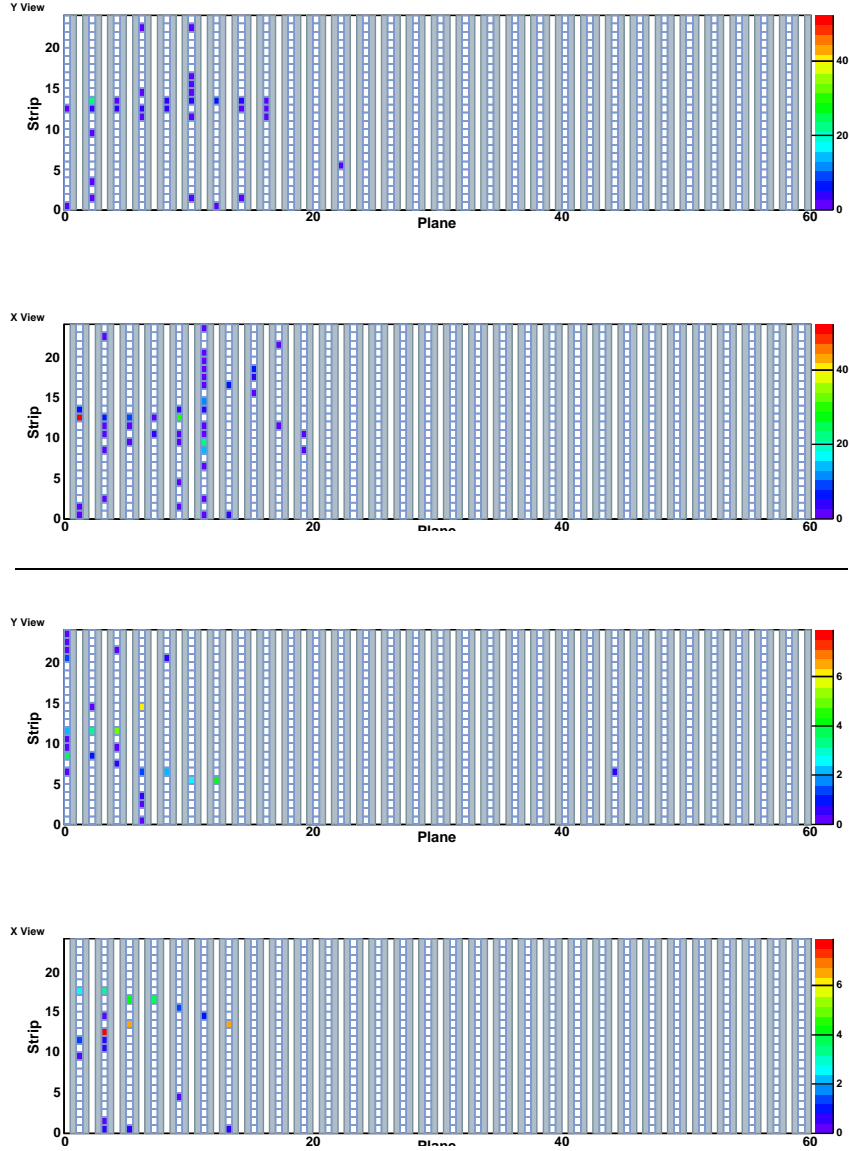
Figure A.12: Two events removed by the olchi2 cut. Both events are from a 2 GeV/c run. No 1.5 PE cut was applied on these events.
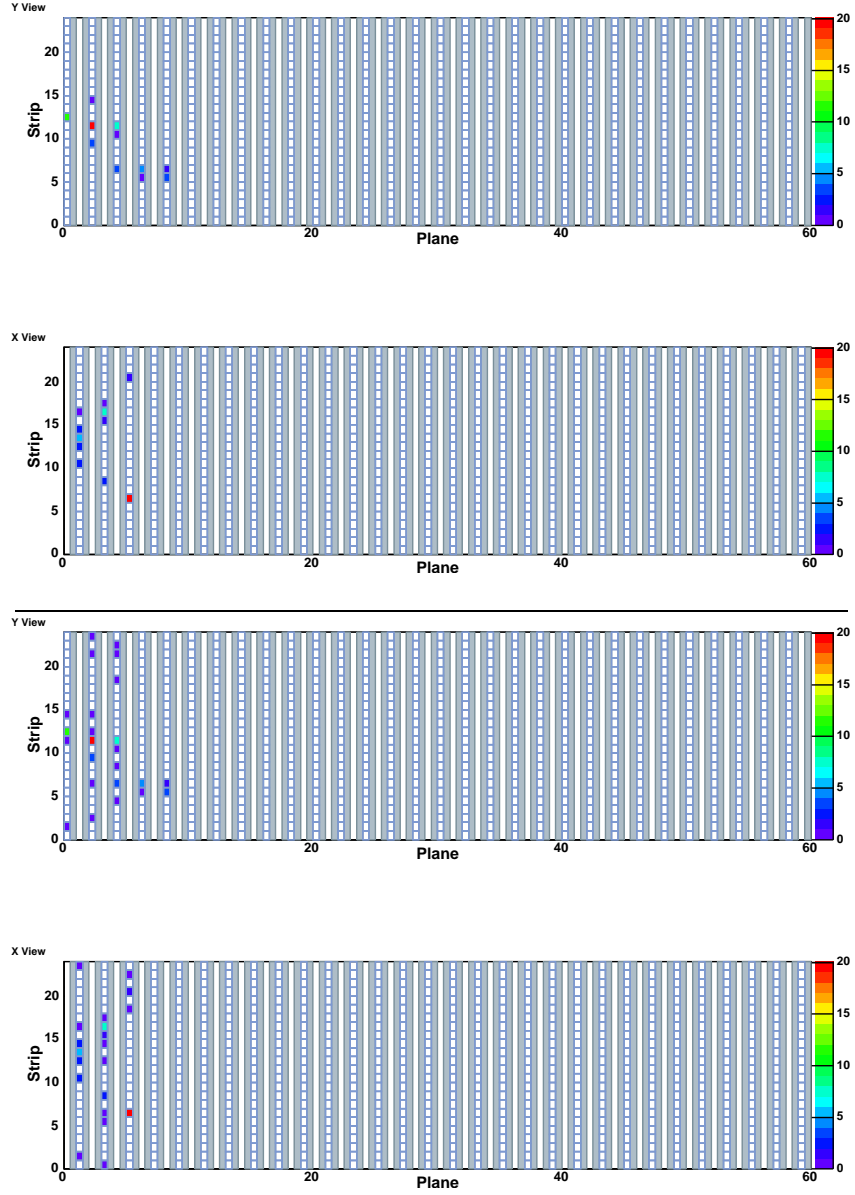
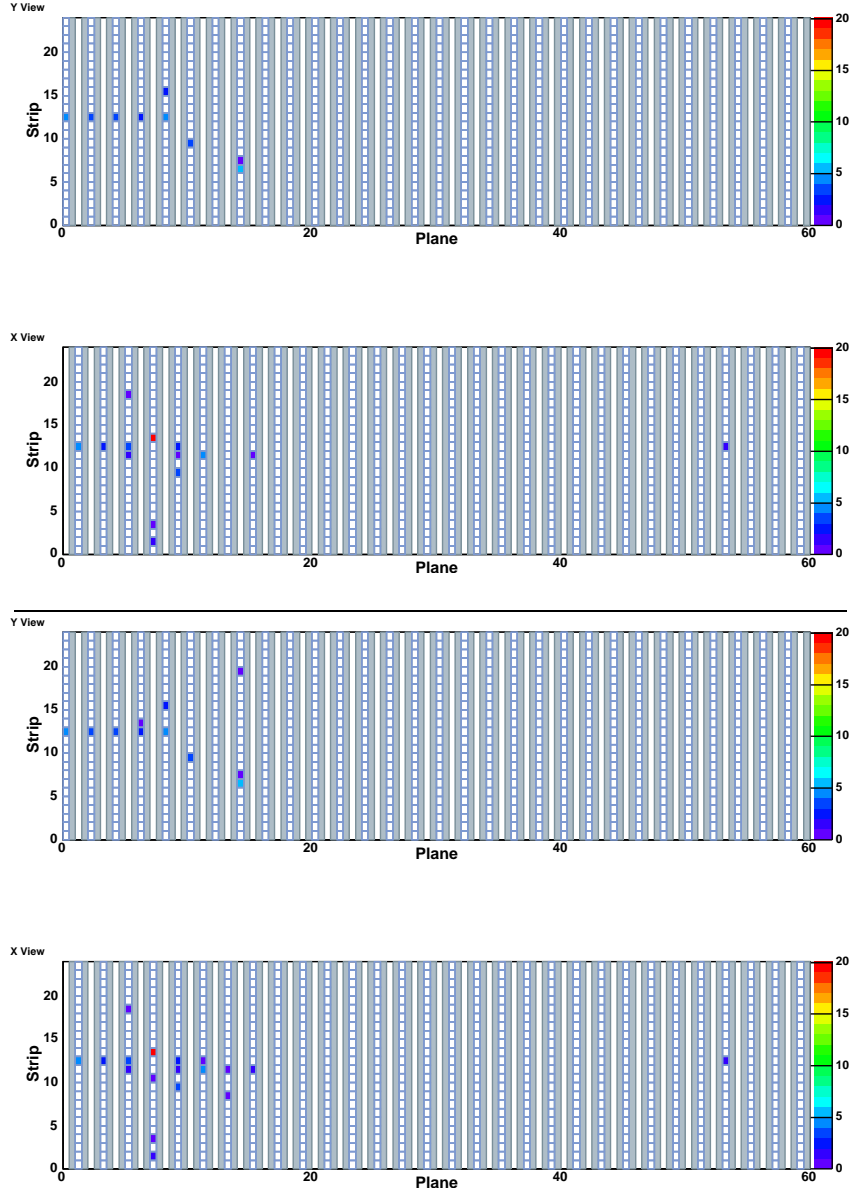Figure A.13: A 2 GeV/c pion event with a 1.5 PE cut (top) and without (bottom).

Figure A.14: A 2 GeV/c proton event with a 1.5 PE cut (top) and without (bottom).

Bibliography

[1] C. L. Cowan, F. Reines, F. B. Harrison, H. W. Kruse, A. D. McGuire, Detection of the free neutrino: A confirmation, Science 124 (1956) 103–104.

[2] K. Hagiwara, et al., Review of Particle Physics, Physical Review D 66 (2002) 010001+.
URL http://pdg.lbl.gov

[3] Y. Fukuda, et al., Evidence for oscillation of atmospheric neutrinos, Phys. Rev. Lett. 81 (1998) 1562–1567.

[4] Q. R. Ahmad, et al., Direct evidence for neutrino flavor transformation from neutral-current interactions in the sudbury neutrino observatory, Phys. Rev. Lett. 89 (2002) 011301.

[5] B. T. Cleveland, et al., Measurement of the solar electron neutrino flux with the homestake chlorine detector, Astrophys. J. 496 (1998) 505–526.

[6] Y. Fukuda, et al., Solar neutrino data covering solar cycle 22, Phys. Rev. Lett. 77 (1996) 1683–1686.

[7] B. Pontecorvo, Inverse beta processes and nonconservation of lepton charge, Sov. Phys. JETP 7 (1958) 172–173.

[8] H. Murayama, Theories of Neutrino Masses and Mixings, Lecture given at the XXVIII SLAC Summer Institute (August 2000).

[9] A. Y. Smirnov, Neutrino Physics and Astrophysics, Biedenharn Lectures at the University of Texas-Austin (April 2002).

[10] Y. Fukuda, et al., Study of the atmospheric neutrino flux in the multi-gev energy range, Phys. Lett. B436 (1998) 33–41.

[11] Y. Fukuda, et al., Measurement of a small atmospheric nu/mu / nu/e ratio, Phys. Lett. B433 (1998) 9–18.

[12] C. K. Jung, T. Kajita, T. Mann, C. McGrew, Oscillations of Atmospheric Neutrinos, Annual Review of Nuclear and Particle Science 51 (2001) 451–488.

[13] S. Fukuda, et al., Tau neutrinos favored over sterile neutrinos in atmospheric muon neutrino oscillations, Phys. Rev. Lett. 85 (2000) 3999–4003.

[14] M. B. Smy, Neutrino experiments with super-kamiokande, AIP Conf. Proc. 655 (2003) 20–41.

[15] L. Wolfenstein, Neutrino oscillations in matter, Phys. Rev. D17 (1978) 2369.

[16] V. D. Barger, et al., Neutrino decay and atmospheric neutrinos, Phys. Lett. B462 (1999) 109–114.

[17] E. Lisi, A. Marrone, D. Montanino, Probing possible decoherence effects in atmospheric neutrino oscillations, Phys. Rev. Lett. 85 (2000) 1166–1169.

[18] G. L. Fogli, et al., Solar neutrino oscillation parameters after first kamland results, Phys. Rev. D67 (2003) 073002.

[19] K. Eguchi, et al., First results from kamland: Evidence for reactor anti-neutrino disappearance, Phys. Rev. Lett. 90 (2003) 021802.

[20] C. Athanassopoulos, et al., Evidence for nu/mu −− > nu/e neutrino oscillations from lsnd, Phys. Rev. Lett. 81 (1998) 1774–1777.

[21] C. Athanassopoulos, et al., Evidence for anti-nu/mu −¿ anti-nu/e oscillation from the lsnd experiment at the los alamos meson physics facility, Phys. Rev. Lett. 77 (1996) 3082–3085.

[22] K. Anderson, et al., The NuMI Technical Design Report, (Fermi National Accelerator Laboratory) (December 2002).

[23] The MINOS Collaboration, Proposal for a Five Year Run Plan for MINOS, MINOS internal Note 930 (May 2003).

[24] M. Kostin, S. Kopp, M. Messier, D. Harris, J. Hylen, A. Para, Proposal for Continuously-Variable Beam Energy, MINOS internal note 783 (October 2001).

[25] D. Indurthy, et al., Ion chambers for monitoring the numi neutrino beam at fermilab .

[26] D. Petyt, an official MINOS figure (December 2000).

[27] M. Diwan, M. Messier, L. Wai, B. Viren, A Study of $\nu_\mu \to \nu_e$ Sensitivity in MINOS, MINOS internal note 714 (February 2001).

[28] S. Wojcicki, A Parametric Study of MINOS Sensitivity to $\nu_\mu \to \nu_e$ Oscillations, MINOS internal note 929 (May 2003).

[29] D. Petyt, $\nu_\mu \to \nu_s$ in MINOS, MINOS internal note 691 (November 2000).

[30] G. L. Fogli, E. Lisi, A. Marrone, Four-neutrino oscillation solutions of the atmospheric neutrino anomaly, Phys. Rev. D63 (2001) 053008.

[31] R. Hatcher, Active Detector (fls) simulation in GMINOS and RECOMINOS, MINOS internal note 479 (March 2001).

[32] The MINOS Collaboration, The MINOS Detectors Technical Design Report, (Fermi National Accelerator Laboratory) (October 1998).

[33] J. Alner, Private Correspondence (March 2004).

[34] J. Kilmer, Specification For Carbon Steel Plate For MINOS Detectors, MINOS internal note 330 (October 1998).

[35] J. Kilmer, J. Nelson, Private Correspondence (March 2004).

[36] A. Godley, et al., Air Fields Measured While Commissioning the SM1 Magnet at Soudan, MINOS internal note 859 (August 2002).

[37] A. Pla-Dalmau, Extruded plastic scintillator for the minos calorimeters To be published in the proceedings of 9th Conference on Calorimetry in High Energy Physics (CALOR 2000), Annecy, France, 9-14 Oct 2000.

[38] T. Chase, Private Correspondence (May 2001).

403

[39] Fermilab Visual Media Services, `http://www-visualmedia.fnal.gov`.

[40] K. Lang, et al., Results of Characterization of 1600 Sixteen-Anode PMTs for the MINOS Far Detector, Unpublished (June 2003).

[41] A. Cabrera, et al., Hamamatsu R5900-00-M64 PMT Characteristics Measured by the Oxford Test Stand, MINOS internal note 934 (April 2003).

[42] B. Rebel, S. Mufson, A Demultiplexing Algorithm for the MINOS Far Detector, MINOS internal note 725 (March 2001).

[43] The Far Detector Electronics Design Team, The Far Detector FEE User's Manual, MINOS internal note 901 (September 2001).

[44] S. Avvakumov, et al., Background dark rates in the MINOS detectors, In preparation (July 2004).

[45] G. Drake, J. Dawson, C. Nelson, Overview of the Front End Electronics for the MINOS Near Detector, MINOS internal note 628 (November 1999).

[46] D. Simon, et al., Secondary Beams for Tests in the PS East Experimental Area (1993).
URL `http://ps-div.web.cern.ch/ps-div/Reports/PA9321/Welcome.html`

[47] L. Durieu, private communication.

[48] O. Ferrando, East Hall Operations Manual, manual provided to testbeam users at the CERN PS East Hall.

[49] H. Grote, F. C. Iselin, E. Keil, J. Niederer, The MAD Program Presented at 1989 Particle Accelerator Conf., Chicago, IL, Mar 20-23, 1989.

[50] P. Vahle, Electromagnetic Interactions in the MINOS Calorimeter, Ph.D. thesis, University of Texas-Austin (2004).

[51] P. Adamson, et al., The MINOS Light Injection Calibration System, Nucl. Instrum. Meth. A492 (2002) 325–343.

[52] R. Nichol, Calibration of the MINOS Detectors, Ph.D. thesis, University College London (2002).

[53] R. Nichol, Light Injection Calibration at the Calibration Detector, MINOS internal note 974 (October 2003).

[54] P. Adamson, et al., On the linearity of the minos light-injection calibration system, Nucl. Instrum. Meth. A521 (2004) 361–366.

[55] C. Smith, Calibration of the MINOS Detectors and Extraction of Neutrino Oscillation Parameters, Ph.D. thesis, University College London (2002).

[56] C. Smith, R. Nichol, Strip-to-Strip Calibration at the Calibration Detector, MINOS internal note 972 (October 2003).

[57] P. Adamson, P. Vahle, The CalDet Trigger, MINOS internal note 978 (November 2003).

[58] U. Rohrer, PSI Graphic Turtle Framework by U. Rohrer based on a CERN-SLAC-FERMILAB version by K.L. Brown et al., Code was only released as binary and author was not communicative. (2003).
URL http://people.web.psi.ch/rohrer_u/turtle.htm

405

[59] D. C. Carey, K. L. Brown, F. C. Iselin, Decay TURTLE(Trace Unlimited Rays Through Lumped Elements): A Computer Program for Simulating Charged Particle Beam Transport Systems, Including Decay Calculations SLAC-0246.

[60] D. C. Carey, The Optics of Charged Particle Beams, 2nd Edition, Harwood Academic Press, 1992.

[61] A. Fasso', et al., The FLUKA Code: Present Applications and Future Developments, ECONF C0303241 (2003) MOMT004.

[62] R. Brun, et al., GEANT Detector Description and Simulation Tool, CERN Program Library Long Writeup W5013 (October 1994).

[63] R. Hatcher, A Comparison of the GMINOS Simulation to Prototype Module Data, MINOS internal note 478 (April 2001).

[64] R. Hatcher, Numbering Conventions and Coordinate Systems in GMINOS, MINOS internal note 243 (February 1997).

[65] N. Tagg, http://www-numi.fnal.gov/offline_software/srt_public_context/WebDocs/detsim/DetSim_Documentation.html (October 2003).

[66] D. Michael, Private Correspondence (March 2003).

[67] A. Fasso, A. Ferrari, J. Ranft, P. R. Sala, Fluka: Present status and future developments Given at 4th International Conference on Calorimetry in High-energy Physics, La Biodola, Italy, 19-25 Sep 1993.

[68] H. Fesefeldt, GHEISHA The Simulation of Hadronic Showers: Physics and Applications, As reproduced by CERN, 1985.

[69] G. Bower, R. Cassel, unpublished version of the GHEISHA code with bug fixes.

[70] C. Zeitnitz, T. A. Gabriel, The geant - calor interface and benchmark calculations of zeus test calorimeters, Nucl. Instrum. Meth. A349 (1994) 106–111.

[71] T. A. Gabriel, J. E. Brau, B. L. Bishop, The physics of compensating calorimetry and the new calor89 code system, IEEE Trans. Nucl. Sci. 36 (1989) 14–22.

[72] H. W. Bertini, A. H. Culkowski, O. W. Hermann, N. B. Gove, M. P. Guthrie, High-energy (e ¡= 1000-gev) intranuclear cascade model for nucleons and pions incident on nuclei and comparisons with experimental data, Phys. Rev. C17 (1978) 1382–1394.

[73] D. E. Groom, N. V. Mokhov, S. I. Striganov, Muon Stopping Power and Range Tables 10-MeV to 100-TeV, Atom. Data Nucl. Data Tabl. 78 (2001) 183–356.

[74] R. M. Sternheimer, General Expression for the Density Effect for the Ionization Loss of Charged Particles BNL-29872.

[75] R. M. Sternheimer, M. J. Berger, S. M. Seltzer, Density Effect for the Ionization Loss of Charged Particles in Various Substances, At. Data Nucl. Data Tabl. 30 (1984) 261.

[76] M. Kordosky, K. Lang, J. Liu, P. Vahle, M16 Cross Talk Measurements, MINOS internal note 1030 (August 2004).

[77] M. Kordosky, K. Lang, J. Liu, P. Vahle, M16 Response and Cross Talk Simulation, MINOS internal note 1044 (August 2004).

[78] G. Cowan, Statistical Data Analysis, Oxford Univ. Press, 1998, Ch. 7.

[79] R. Wigmans, Calorimetry : Energy Measurement in Particle Physics, Oxford Science Publications, 2000.

[80] M. Berger, J. Coursey, M. A. Zucker, Stopping-Power and Range Tables for Electrons, Protons, and Helium Ions, http://physics.nist.gov/PhysRefData/Star/Text/contents.html, program based on the methods in ICRU Reports 37 and 49.

[81] R. K. Bock, T. Hansl-Kozanecka, T. P. Shah, Parametrization of the longitudinal development of hadronic showers in sampling calorimeters, Nucl. Instr. Meth. 186 (1981) 533.

[82] E. Hughes, Study of Hadronic and Electromagnetic Shower Development Between 10-GeV and 140-GeV by an Iron Scintillator Calorimeter, SLAC-PUB-5404 (1990).

[83] J. Kruger, Response of the zeus uranium scintillator calorimeter to pions, protons and electrons for kinetic energies from 0.2- gev to 10-gev and study of the calorimeter uniformity, Nucl. Phys. Proc. Suppl. 16 (1990) 513–516.

[84] T. Akesson, et al., Properties of a Fine Sampling Uranium - Copper Scintillator Hadron Calorimeter, Nucl. Instr. Meth. A241 (1985) 17.

[85] D. Groom, Atomic and Nuclear Properties of Materials for 292 Substances, http://pdg.lbl.gov/AtomicNuclearProperties/.

[86] C. Schilling, J. Ritchie, private Communication (June 2004).

[87] R. Seitz, Describing Energy Deposit in CsI Crystals, BABAR Note # 294 (1996).

[88] H. Gallagher, The neugen neutrino event generator, Nucl. Phys. Proc. Suppl. 112 (2002) 188–194.

School he e███ d at St. John's Un██ rsity, a 13█ r old catholic university operated by the Benedictine order of St. John's Abbey, Minnesota. At St. John's he studied physics, mathematics and the history and philosophy of the Enlightenment period. He graduated magna cum laude with a Bachelor of Arts in physics and mathematics in the spring of 1998, and entered the physics department at the University of Texas that autumn. He began working on the MINOS experiment in the fall of 1999 and as part of his studies has lived in Austin, Texas and at CERN in Geneva, Switzerland. He currently resides in Austin.

This dissertation was typeset with ██████ 2_ε[1] by the author.

---

[1] LaTeX 2_ε is an extension of LaTeX. LaTeX is a collection of macros for TeX. TeX is a trademark of the American Mathematical Society. The macros used in formatting this dissertation were written by Dinesh Das, Department of Computer Sciences, The University of Texas at Austin, and extended by Bert Kay and James A. Bednar.